Studies of Molecular Precursors Used in FEBID Fabrication of Nanostructures

Maria Pintea

School of Physical Sciences

Canterbury

University of Kent

A thesis submitted for the degree of Doctor of Philosophy

November 2021

“The universe is not only queerer than we imagine, it's queerer than we can imagine.”

J. B. S. Haldane

DECLARATION

I hereby declare that the present work is my personal work entirely unless stated otherwise. This work has not been previously submitted, in whole or in part, for any other academic degree.

Maria Pintea

November 2021

ABSTRACT

The adoption of nanotechnology is increasingly important in many aspects of our daily life influencing the clothes we wear and most of the electronic devices we use while also underpinning the development of drugs and medical techniques that we will need at some point in our lives. The methods by which nanoscale devices are fabricated is changing from a 'top down' etching based procedure to a 'bottom up' molecule by molecule deposition and assembly. The focus of the present research is the development, design, and analysis of new precursors for focused electron beam induced deposition (FEBID) and extreme ultraviolet nanolithography (EUVL) through a large pool of experimental and computational resources. The research is divided into two areas: gas – phase analysis of precursors (largely used for fragment and radicals' analysis, and molecular design) and surface and deposition science (physical deposition of precursors, simulation analysis of surface – molecule interactions and characterization of deposition processes to obtain optimal process parameters for molecular structures). It is necessary to collect data such as cross sections of electron – molecule interactions e.g., dissociative ionization (DI) and dissociative electron attachment (DEA) to provide accurate simulations that can be used to improve the FEBID and EUVL while understanding surface processes such as molecular absorption and diffusion to determine the structure and purity of the nanostructures formed by these methods. The objective of this thesis is to provide a gas – phase and deposition analysis of potential and widely used precursors for FEBID and EUVL at the nanoscale. To achieve this the experimental technique of velocity sliced map imaging (VsMI) was used in conjunction with theoretical tools such as density functional theory (DFT) simulations using Gaussian 16 software and evaluation of cross-section data for molecular dissociation at low electron energies of 0 – 20 eV using Quantemol-N. Results of the gas – phase analysis of negative ionic fragments formed by DEA and DI with their appearance, dissociation and ionization energies, angular distributions and kinetic energies, cross-sections for DEA fragmentation at low energy and excited states calculations at values up to 10 eV are presented. These results are used as the inputs to the models of the FEBID processes. The electronic, structural, and kinetic properties of several FEBID precursors are explored, and FEBID method used to create nanostructures using a Zeiss MeRiT SEM with GEMINI column operated at 20 kV. Analysis of the deposits was performed using EDX and atomic force microscopy (AFM) analysis as well as electron stimulated desorption (ESD) and temperature programmed desorption (TPD). Complementary simulations of the dynamics of processes at the surface were studied using MBN Explorer and surface – molecule interactions with great results in simulating the deposition process of islands and structures (results presented in Chapter 8).

ACKNOWLEDGEMENTS

I want to take the chance of thanking to the people that have been beside me during the development of this research, and to the ones who had a profound influence on how the things would turn, with great results as well. I would start by thanking my professor, prof. Nigel Mason, and the teaching staff at University of Kent for making the research journey a greatly enjoyable experience. I decided to join the team at the University of Kent at professor Nigel Masons invitation mostly due to the great reputation in teaching the university had, receiving The Gold in Teaching Award and The Most European University of UK Award a year earlier in 2018, and partly due to the novelty of the place and good connections to London, the great oysters and the good seafood. Most of all to my father and mother, Mariana Pintea and Dumitru Pintea, both professors/teachers, for helping even with moral support, being the first influence and guidance towards appreciating the university work and the research community, especially, to my father who was beside me even the day he went to the hospital with COVID and through his last moments of life. What a dark day to finish my thesis the same day he died, but he's love for teaching being a professor at University of Bucharest and a pastor before all, always in search for good and right, looking for the right path, was an inspiration for me. And my mother, as well always keeping the calm and silent side of things, and guiding me to the love of books, but more than anything helping in controlling my emotional destructive nature, as we all humans are more prone to break things /relationships when upset than to make them work.

As well, I would like to thank prof. Michael Probst for accepting me into his group at the University of Innsbruck to finish my Density Functional Theory calculations and computational work, that indeed set up for me a different view to the field of molecular physics, to broadening my understanding of its evolution to AI and the implications this has on our lives, through the high simulation capabilities that rather sooner will gives us the cure for cancer or show us the evolution of the universe. I want to thank the technical team at the University of Kent for their support with the laboratory preparation and while moving the equipment from The Open University to where it is today, at the University of Kent, and making that possible in such a brief time. Other thanks to my sister Silvia-Laura Pintea whom I visited for conferences in Amsterdam and who herself has been a postgraduate student for taking the time to meet during my research trips, and to the rest of my family (siblings). Last, but not least, I would like to thank to the group of prof. Stefan Matejcik, and Peter Papp at Comenius University Bratislava, where I performed experimental work multiple times, and for the hearty welcome and support over the time I spent there.

TABLE OF CONTENTS

Table of Contents

TABLES OF FIGURES AND TABLES

TABLE OF FIGURES

TABLE OF TABLES

ACRONYMS

AES – Auger Electron Spectroscopy

AFM – Atomic Force Microscopy

AI – Artificial Intelligence

BSEs – Backscattered Electrons

BZW-EF – Bagayoko, Zhao and Williams enhanced by Ekuma and Franklin

CAS – Complete Active Space

CASSCF – Complete Active Space Self-Consistent Field

CVD – Chemical Vapour Deposition

DD – Direct Dissociation

DEA – Dissociative Electron Attachment

DFT – Density Functional Theory

DI – Dissociative Ionization

EBI-CVD - Electron Beam Induced Chemical Vapour Deposition (EBI-CVD)

EBID – Electron Beam Induced Deposition

EBIE – Electron Beam Induced Etching

EDS/EDX – Energy Dispersive X-Ray Spectroscopy

EELS – Electron Energy Loss Spectroscopy

EH – Electron Holography

ESD - Electron Stimulated Desorption

EUVL – Enhanced Ultraviolet Lithography

FEBID – Focused Electron Beam Induced Deposition

FEBIP – Focused Electron Beam Induced Processing

GGA – Generalized Gradient Approximation

MD – Molecular Dynamics

ML – Machine Learning

MTL - Mass Transport Limited Regime

PEs – Primary Electrons

RAIRS – Reflection Adsorption Infrared Spectroscopy

REELS – Reflection Electron Energy Loss Spectroscopy

RRL – Reaction Rate Limited Regime

SAED – Selected Area Electron Diffraction

SCF – Self-Consistent Field

SEM – Scanning Electron Microscope

SEs – Secondary Electrons

TDS – Thermal Diffuse Scattering

TEM – Transmission Electron Microscopy

TPD - Temperature Programmed Desorption

VMI – Velocity Map Imaging

XANES – X-ray Absorption Near Edge Structure

LPCVD – Low Pressure Chemical Vapor Deposition

TTIP – Titanium Tetra Isopropoxide

CHAPTER 1. INTRODUCTION

1.1 GENERAL INTRODUCTION

The research reported in this thesis was performed as part of a larger pan-European Initial Training Network (ITN) entitled "Low energy ELEctron driven chemistry for the advantage of emerging NAno – fabrication" under the acronym of ELENA, *www.elena.hi.is*, which was the result of an earlier COST action CELINA, where a group of researchers shared their interest in developments in induced chemistry for nanotechnology applications and nanolithography. The project was a network of 14 participants (universities, research centres and institutes: University of Iceland, ARCNL, Universität Bremen, The Open University, Technische Universität Wien, FAU Erlangen, University of Oslo, University of Bielefeld, TUDelft, Empa, IMEC Belgium, Tescan Ltd, Zeiss Ltd, University of Kent) and 8 partners including John Hopkins University, University of Florida, CEI - Europe (CEI), Minerva, University Paris - Sud, and Comenius University of Bratislava. The project received funding from European Union HORIZON 2020 Research and Innovation Program under the grant agreement ID 722149 and operated as a Marie Curie Initial Training Network (ITN). The ELENA project sought to bring together researchers from both industrial and academic institutions to share knowledge and expertise and to train 15 Early Career Researchers (ECRs) in the skills needed in the nanotechnology industry. The primary focus of the ELENA project was towards developing two nanofabrication methods, (i) Focused Electron Beam Induced Processing (FEBIP) and (ii) Extreme Ultraviolet Lithography (EUVL). Focused electron beam induced processing is presented in Chapter 1, while extreme ultraviolet lithography finds its place in Section 2 of Chapter 6.

Fig 1.1.1. ELENA $Si(OEt)_4$ deposits on Au(111) done with Clone 1 MeRiT column at Zeiss Gmbh, Rossdorf, Germany

The ELENA international training network performed research on both well-established precursor molecules and in-house designed molecular compounds used to fabricate the nanostructures. Sophisticated and specialized simulation software (Gaussian 16, CASINO 3.2, MBN Explorer/Studio,

Quantemol-N) was used to model the molecular compounds and processes involved in the chemical reactions at the nanoscale, whether on surface or gas-phase. My work described in this thesis covers aspects in all these areas.

The thesis is conveniently divided into two sections. The first section focuses on the study of electron interactions with FEBIP precursors in the gas phase. Experiments were performed using the Velocity Sliced Map Imaging instrument (VsMI) to study Dissociative Electron Attachment (DEA) at low electron energies. Experimental studies were complemented by density functional theory studies using Gaussian 16 software to compute structural parameters, excited states, PDOS/TDOS, as well as deriving computational based cross-sections using Quantemol-N software. During the course of the ELENA project (pre-pandemic) experimental research trips were made to the molecular research group at Comenius University, Bratislava led by Professor Stefan Matejcik and Dr. Peter Papp to acquire mass spectrometry data for $Fe(CO)_5$, $Si(OEt)_4$ and $Ti(OPr)_4$ precursors. The second section of the thesis focuses on surface science studies of $Si(OEt)_4$, $Me_2Au(acac)$ and $Fe(CO)_5$ precursors. The experiments include Temperature Programmed Desorption (TPD) and Electron Stimulated Desorption (ESD) of FEBID precursors on a Cu surface performed in Dr. Anne Lafosse's group at the Institute des Sciences Moléculaires d'Orsay (ISMO), Orsay - France, and deposition of precursors using electron beams with the aid of SEMs in collaboration with Zeiss Gmb in Rossdorf – Germany in Fig 1.2.1. These experiments were complemented by simulations of surface processes using molecular dynamics (MD) performed using MBN Explorer software developed by the MBN Research Centre in Frankfurt, Germany.

The present thesis report is structured in two sections and eleven chapters as below:

Chapter 1: Introduction – The ELENA project and its importance to nanotechnology developments is described. The Focused Electron Beam Induced Deposition (FEBID) process, its characteristics and the main process parameters are discussed.

Chapter 2: Tools in Experimental and Computational Molecular Physics for FEBID Investigations - The tools used to perform both experimental and computational investigations of FEBID are presented.

Chapter 3: Tools for Surface Science and Deposition Studies of FEBID Precursors –A detailed presentation of TPD, ESD, SEM – EDX, AFM is presented and MBN Explorer modelling capabilities of FEBID processes are presented.

Section 1: Gas-Phase Studies of FEBID Precursor.

Chapter 4: Studies of Ti and Si Based Compounds Used as Precursors in FEBID; Gas-Phase Studies – A mass spectrometric analysis of the $Ti(OPr)_4$ and $Si(OEt)_4$ in combination with infra-red spectroscopy with implications to FEBID deposition studies.

Chapter 5: Study of the Carbonyl Group Based Compounds in Gas-Phase – This chapter reports new data on the molecular structure and dynamics of electron induced dissociation of the FEBID precursors $Fe(CO)_5$ and $W(CO)_6$ studied in the gas – phase using velocity sliced map imaging. The results are compared to earlier data.

Section 2: Surface Science and Deposition Studies of FEBID Precursors

Chapter 6: Deposition Study of $Si(OEt)_4$ Precursor – A deposition study of the SiO_2 from $Si(OEt)_4$ using SEM, EDX and AFM analysis.

Chapter 7: A Study of Gold Based FEBID Compounds and Their Processes on Surfaces – A study of the $Me_2Au(acac)$ precursor deposited on Cu surface using TPD and ESD studies.

Chapter 8: A Computational Simulation of FEBID Production of Iron Nanostructures Using $Fe(CO)_5$ as the Gaseous Precursor – A simulation approach-based study of the $Fe(CO)_5$ using MBN Explorer and MD simulations on SiO_2 and Au(111) substrates.

Chapter 9: Conclusions and Future work.

ANNEX 1: $Fe(CO)_5$ Computational Parameters.

ANNEX 2: Acetylacetone from $Me_2Au(acac)$ – A gas – phase study of cross – section data obtained from Quantemol-N simulations representing DEA cross – sections, excitation cross – sections and total cross – sections.

ANNEX 3: Acetylacetone Radical from $Me_2Au(acac)$ – Where a study of the structure and morphology of acac radical is done using DFT simulations run with the Gaussian 16 software investigating bonding of the acac to the Co and Au atoms.

ANNEX 4: Pt Based Compounds - A thorough DFT analysis is run using Gaussian 16 calculations for excited states of $Pt(PF_3)_4$ and $Pt(acac)_2$, first for $Pt(PF_3)_4$ which may be compared with earlier work in the literature and then for $Pt(acac)_2$ and $Pt(NH_3)_4(NO_3)_2$.

ANNEX 5: Artificial Intelligence (AI) and machine learning (ML) in Molecular Physics - Future work and approaches using AI and ML for precursor analysis using neural networks as simulation tools.

ANNEX 6: A Study of Gold Based FEBID Compounds in gas-phase.

ANNEX 7: Tables and Supporting information on the deposition of $Si(OEt)_4$

1.2 The FEBID Process

From its first appearance in 1934 when Steward found contamination in his optical microscope in the form of small elemental growths, to determining its viability as a deposition method in 1960, Focused Electron Beam Induced Deposition has been studied and, today, it is recognised as part of the wider lithographic family of processes being developed into a viable manufacturing method for complex structures at the nanometre scale. As a lithographic technique, FEBIP deals with processes associated with electron beam induced etching (EBIE), electron beam induced deposition (EBID), electron beam induced resist and electron beam induced chemical vapour deposition (EBI-CVD). Based on the use of varying diameter electron beams and the use of a scanning electron microscope in high and ultrahigh vacuum chambers, the physics associated with the growth of the structure on the surface is governed by interactions of the electrons with both the gas-phase molecules and the substrate (reviewed in Surface Science Section 6.2 and 6.3 in Chapter 6, and the type of electrons (explained in detail in section 2.1 in Chapter 2) inducing the fragmentation processes. The two main FEBID processes, EBID and EBIE, are schematically presented in Fig 1.2.1. In the EBID/EBIE process, the electron beam energy is usually > 1 keV, representing the magnitude of the primary electrons (or so-called PE) energy result of the collision with the precursor. Such a high energy allows a well-focused electron beam to be created. However, it should be noted that, the primary fragmentation processes involved in FEBID, dissociative electron attachment (DEA), dissociative ionization (DI) and direct dissociation (DD) have their peak cross-section values around 100 eV [1] or lower than 100 eV.

Electron interaction processes in FEBIP. For an atom to be deposited on the substrate, the probability of this event is the cartesian product of the dissociation cross section, σ, with the density coverage, N, of the adsorbed molecules on the substrate. For this to occur, though not only the cross section is needed, but there are other factors such as the type of electrons (PEs, SEs, BSEs; see Fig 1.2.2) the compound used (kinetic energy, dissociation energy) and the type of substrate, as well as the deposition type (pillar, thin film, complex structure) and direction of deposition. The deposit growth is determined by both PEs and SEs. The PEs are mainly responsible for the height of the structure, while the SEs are responsible for the lateral growth of the structures with some influence to the height growth as well. When it comes to molecular simulations of the growth of the pillar, Monte Carlo calculations have been used in Ref. [2

- 3] to explore the effect of SEs. Liu et al. 2006 [4] studied FEBID deposited structures on a substrate and found that the process was dominated by forward scattered PEs and SEs and the penetration depth of the beam.

The processes at the surface are governed by three types of electrons: primary electrons (PEs; with energy higher than 1 keV), backscattered electrons (BSEs; with energies higher than 50 eV, but lower than PEs energy) and secondary electrons (SEs; with energies peaking at 50 eV). The electrons governing the DEA process are secondary electrons. The backscattered electrons are higher energy electrons able to deposit structures, create secondary electrons through collision and create elongated structures or additional structures around the main structures.

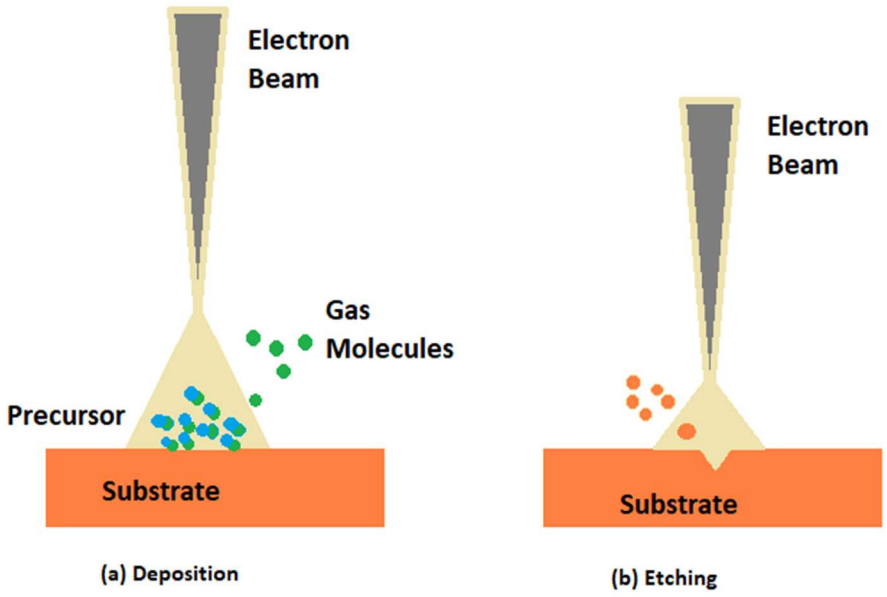

Fig 1.2.1. EBID and EBIE schematics

The modifications the SEs make to the substrate and deposits may be studied using the Koshikawa and Shimizu 1974 [5] model, a single scattering model, with electron energies with values up to 0.1 keV. The scattering energy distribution is modelled by the excitation function in Ref. [2] for classical binary collisions with atomic electrons of the solid:

$$S(E) = e^4 k^3_F / [3\pi E_p (E - E_F)] \text{ (Streitwolf excitations)} \quad (1.2.1)$$

where E_p is the energy of the PEs exciting the SEs, E_F is the Fermi energy, k_F is the wave factor at Fermi level.

Considering that the PEs, BSEs and SEs have different energy and spatial distributions, the role of the electrons in the deposition process is determined by the density of electrons, energy of the electrons and the location of the electrons to the target substrate. The SEs and BSEs widely modelled through Monte Carlo simulations, have an unchanged spectrum with the increase or decrease of PEs energy, changing only in the case when the PEs energy is close to the SEs energy in Ref. [1].

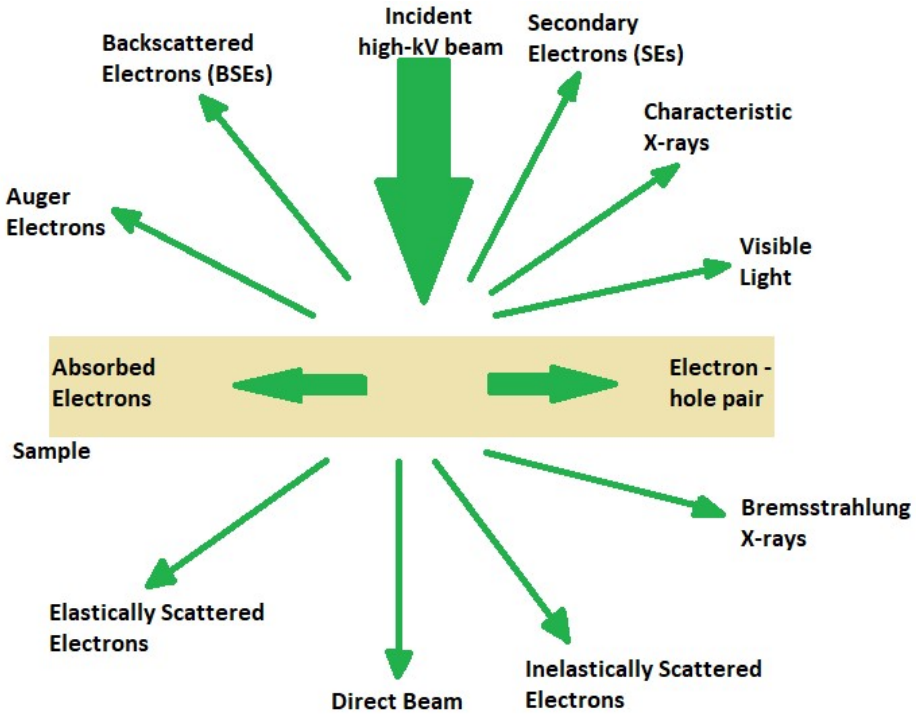

Fig 1.2.2 Types of electrons in FEBIP; reproduced from C. Colliex 2005 in Ref. [321]

The two models for electron scattering, Murata et al. 1981 [6] and Koshikawa and Shimizu 1974 [5], based on Monte Carlo simulations of the SEs trajectory, explain their effect on the deposition process. A more practical approach to the path of an electron between the source and its molecular target is the probability in Ref. [7] of an electron to scatter between x and x + dx:

$$p(x)dx = 1/\lambda\, e^{-x/\lambda}\, dx \qquad (1.2.2)$$

where λ is the mean free path between x and x + dx.

The model of Murata et al. 1981 [6] introduces a hybrid model for lithography applications based on the single scattering model, Monte Carlo routine and the fast secondary electron production. The hybrid model is based on the initial Bethe law for two calculations:

(a) Energy loss:

$$\left[\frac{dE}{dS}\right]_{\varepsilon_C} = \left[\frac{dE}{dS}\right]_{Bethe} - \left[\frac{dE}{dS}\right]_{single}$$

$$\left[\frac{dE}{dS}\right]_{single} = \sum n_i Z_i \int_{\epsilon_C}^{\frac{1}{2}} E\epsilon \left[\frac{d\sigma}{dE}\right] dE \quad (1.2.3)$$

where ε_C is the cut-off value of the energy transfer, E is the initial energy, Z_i is the atomic number, ε is the energy transfer normalized by E, σ cross-section value in $Å^2$.

(b) Scattering angle:

$$sin^2\Phi = \frac{2(1-\epsilon)}{2+\tau\epsilon} \quad (1.2.4)$$

where ε is the energy transfer normalized by E and τ is the time for an electron to travel the mean free path.

Monte Carlo simulations have also been used to describe the processes involved in the inelastic scattering in bulk materials (Si, Cu, Al) in Ref. [7] with charged projectiles (electrons) with energies of 1 keV. The model uses the Maxwell equations to describe the electrical field induced by the photon or electron on a trajectory described by the function $\varepsilon(q, \omega)$ to determine the stopping power and the distribution of energies per unit path length. The induced electric field is described by the relation (1.2.5):

$$E_{ind}(q,\omega) = -i4\pi\ (q/q^2)\ \rho(q,\omega)\ [1/\varepsilon(q,\omega) - 1] \quad (1.2.5)$$

and r the stopping power S,

$$S = -d\mathcal{E}/ds = v\ E_{ind}(r,t) \quad (1.2.6)$$

where $\mathcal{E}$ is the kinetic energy of the photons or electrons.

The energy losses per unit path length, $d\mu/d\omega$ are defined by the relation (1.2.7), representing the Monte Carlo approach for simulating REELS energy loss distribution in Ref. [8]:

$$d\mu/d\omega = 2(Z^2_0/\pi)\ (1/v^2)\int dq\ 1/q\ Im[-1/\varepsilon(q,\omega)] \quad (1.2.7)$$

Models of FEBID. Multiple models have been developed to describe the deposition process in Ref. [1-2]. The fragmentation and recombination of molecules is governed by the molecular density at the surface, the density of electrons and the number of molecules undergoing fragmentation and the molecules desorbing from the surface without undergoing the fragmentation processes.

$$dN / dt = gF(1 - N/N_0) - \sigma(E)NJ - N/\tau\ [1] \quad (1.2.8)$$

where g is the sticking coefficient, F is the gas flux on the substrate ($cm^{-2}s^{-1}$), N_0 is the site density of a monolayer (cm^{-2}), J is the current density ($e^{-}s^{-1}cm^{-2}$), N is the number of molecules on the substrate and τ(s) is the time molecules stick to the surface.

The growth rate of the nanostructures on the surface is defined according to Ref. [1, 9] as:

$$R = V_{molecule}\, N_0\, [(gF/N_0)\sigma J] / [(gF/N_0) + \sigma J + 1/\tau) \quad (1.2.9)$$

with two states:

$gF/N_0 >> \sigma J$, where growth is limited by current density

$gF/N_0 << \sigma J$, where growth is limited by the number of molecules

where $V_{molecule}$ is the volume of the molecules and τ(s) is the duration of the molecules sticking to the surface.

The effects of the PEs and SEs on the structures are more pronounced in the case of widened tips a deformation due to prolonged usage that would change the shape of the resulting structures, and change with the surface conditions, inhomogeneous surfaces having a higher probability of creating SEs and BSEs.

The final height and width of the deposit are dependent on the primary electron flux as a function of the growth rate R, the dwell time t_{dwell} and the area of the deposition as:

$$V_{deposit} = R\, t_{dwell}\, A_{deposit}\, [1] \quad (1.2.10)$$

where the value of the volume of the deposit is $V_{deposit}$, the lateral growth of the structure depends on I (the current) that further depends on d_{beam}, diameter of the beam, and $d_{deposit}$, diameter of the deposit.

The two growth regimes are denominated as reaction-rate limited (RRL) regime with longer dwell times, and, mass transport-limited regime (MTL regime, depending on the electron flux) with shorter dwell times, in Ref. [1, 8]. The RRL regime, where the regime is limited by the number of the molecules on the surface being dissociated, and, the MTL regime characterized by depletion of the adsorbed precursor on the surface, are described by the relation:

$$Y_i = \sigma_i / t_D \int 0 \rightarrow t_D\, n_i(t)dt\, [8] \quad (1.2.11)$$

where n is the adsorbed precursor density, and Y_i is the ratio of the dissociation rates for the primary electrons.

The metal content, the tips and the electrons create a magnetic environment in Ref. [9-11] characterized by an average magnetic inductance, B_x:

$$|B_x(x,y)| = [\hbar/(e\ t)]\ [\delta\rho_{MAG}(x,y) / \delta y] \quad (1.2.12)$$

where ħ is Planck constant, ρ_{MAG} is the magnetic component of the phase shift ρ(r), e is the electron charge, t is the variable thickness.

High metal content was observed in Co nanowires formed by deposition of $Co_2(CO)_8$, with values of 85 % and diameters higher than 120 nm in Ref. [11]. For lower diameters, 80 % Co metal content was observed for ~ 80 nm structures and 45 % Co metal content for 60nm structures, with improved Co metal content and elimination of oxygen, obtained in annealing process leading to a Co content of 90 % for diameters smaller than 100 nm. Typical nanowires present oxidized shells in the range of ~ 5 nm with the metal content decreasing as the wire diameter decreases. The same oxidation layer effect in Co deposits is reported by Sangiao et al 2017 [11] where an 110 nm structure was grown with a contamination layer of C and O of more than 7 nm. Variable range hopping conductivity and Mott formalism have been used in combination with Bethe-Born calculations for the characterization of doped sites in disordered Al/Ti/Mn-doped ZnO in Ref. [33] and in p-type $CuIn_3Te_5$ semiconductors results of electrically inactive ($In^{+2}_{Cu} + 2V^{-1}_{Cu}$) donor - acceptor defect pairs in Ref. [32] with the only acceptor state in the range of ~ 200 meV and available only at temperatures of 200 K. As a result, variable range hopping is present for specific doped materials and semiconductors at higher temperatures, between 45 K and 210 K. The occupation probability defined by the Fermi-Dirac distribution function in the variable range hopping conductivity mechanism is given by relation (1.2.13):

$$f_i = \{\exp [\ E_i - \mu_i] / k_B T] + 1\}^{-1} \quad (1.2.13)$$

and the transition rate probability of the variable range hopping is defined by relation (1.2.14):

$$w_{ij} = \Upsilon p_{ij} \quad (1.2.14)$$

where P_{ij} is the successful hopping between two states and ϒ is the number of attempts.

The common variable range hopping models and metal conduction models do not consider the tunnelling probability through the material. The tunnelling probability is defined by the distance R_{ij} between two states, i and j, and the localization parameter of these states, α, that depends on the gaps, defects, weak bonding, and degeneration. The tunnelling probability is described by the relation in Ref. [12] (1.2.15):

$$P_{tunnel\ i \rightarrow j} = \exp(-2\alpha|R_{ij}|) \quad (1.2.15)$$

1.3 FEBID PRECURSORS

Choosing the right precursor for deposition is one of the most important initial processes in creating a viable structure with a controllable level of impurities and low resistivity. To date most precursors used in FEBID were designed for thermal deposition and spontaneous ligand release, mostly for CVD where precursors are intended to have higher stability at temperatures < 200 °C and to decompose at higher temperatures through multiple chain reactions, the example of Pt and Pd precursors fragments at temperatures in the range of ~ 350 °C. The precursors used to date for FEBID are divided according to their bonding groups and rings see Ref. [13] and include: homoleptic carbonyl complexes ($Fe(CO)_5$, $W(CO)_6$, $Mo(CO)_6$, $Co_2(CO)_8$), homoleptic phosphine complexes ($Pt(PF_3)_4$), monodentate ligands ($Co(CO)_3NO$), chelating ligands ($Pt(hfac)_2$, $Pd(hfac)_2$, and $Cu(hfac)_2$), anionic polyhapto ligands ($MeCpPtMe_3$). By the type of metal they contain, the precursors are divided in Au-, Pt-, Cu-, Co-containing precursors, and heterobimetallic precursors as the newest ones developed for alloy deposition. The criteria used to select the right type of precursors are subject to a series of characteristics: vaporization, sublimation temperature, type of metal and/or organic ligands (C, O or Br, I, F), sensitivity to light, toxicity (highly toxic compounds are forbidden to be used).

Iron based precursors. Iron structures with sizes smaller than 20 nm have been obtained using SEM – EUVL (15 nm), TEM (<1 nm) and SEM/TEM with reactive gases in Ref. [14-15] using $Fe(CO)_5$, a highly volatile precursor. The Fe deposits derived from $Fe(CO)_5$ were low in C content, with structures obtained using an electron exposure of 185.9 $nA \cdot s \cdot \mu m^{-2}$ having a metal content of 95 % Fe at room temperature. The Fe deposits appear as dots, attributed to the scattering of the primary electrons from the already deposited structures, or due to a high tensile strength relative to the initially deposited layer that forces the formation of Fe clusters at the surface (Stranski – Krastanov growth mode). At lower temperatures, in the range of 200 K, the purity of the Fe deposits is lower, with a metal content of only 79 %. There is an increasing interest in creation of nanostructures composed of bimetallic complexes. (e.g., RuCo, FeCo, FeMn). Two of the most used bimetallic precursors are $HFeCo_3(CO)_{12}$ in Ref. [16] and $H_2FeRu_3(CO)_{13}$ in Ref. [16], producing metal content in the final deposits in the range of ~80wt% for $HFeCo_3(CO)_{12}$ and ≤30wt% for $H_2FeRu_3(CO)_{13}$, while their magnetic properties are defined by the size and shape of the alloys. In the dissociative ionization process, $HFeCo_3(CO)_{12}$ and $H_2FeRu_3(CO)_{13}$ decompose, $HFeCo_3(CO)_{12}$ forming a mixture of $HFeCo_3(CO)_2$, $HFeCo_3(CO)_3$, $HFeCo_3(CO)_4$ and $HFeCo_3(CO)_5$, with the highest number of $[HFeCo_3(CO)_3]^-$ fragments. The high fragmentation ratios on

removing H and CO ligands make $HFeCo_3(CO)_{12}$ and $H_2FeRu_3(CO)_{13}$ highly researched and used precursors in the FEBID deposition of semiconductor nanowires [14-16] .

Other bimetallic precursors, such as $Cp(CO)_2FeMn(CO)_5$ in the deposition stage are characterized by the reaction schematics in (1.3.1), a process that has two intermediary steps:

$$Cp(CO)_2FeMn(CO)_{5(ads)} + e^- \rightarrow CpFeMn(CO)_{2(ads)} + 5(CO)_{(g)}\uparrow$$

$$CO_{(ads)} + e^- \rightarrow ROS + C_{(ads)}$$

$$CpFeMn_{(ads)} + ROS \rightarrow Fe(Mn_xO_y)_{(ads)} + C_{(ads)} \quad (1.3.1)$$

Gold precursors. Au containing precursors are complexes with chelate rings or anionic polyhapto ligands containing Me and Cp groups or simpler bonding to P or CO groups. Trying to remove the presence of the C in the structure often comes with its replacement with either F, Br or I. Studies of Au with chelate rings in Ref. [14] reported low Au content in the deposits with values lower than ≤ 20 wt% for acac containing Au precursors, ≤ 40 wt% for tfac containing Au precursors and ≤ 3 wt% for hfac containing gold precursors. Two other Au-complexes containing CO and PF_3 groups, Cl – Au – CO and Cl – Au – PF_3, show higher Au content up to 95 wt% Au for Cl – Au - CO and pure metallic Au grains in the case of Cl – Au – PF_3, though their low thermal decomposition temperature, room temperature for CO and 40 – 45 °C for PF_3, and high sensitivity to air moisture and light make them not suitable for use in large scale manufacturing. However, based on these two compounds other similar compounds have been proposed to develop more stable structures following the mechanism presented in relation (1.3.2) in Ref. [14]:

$$X - Au - L_{(ads)} + e^- \rightarrow X - Au_{(ads)} + L_{(g)}\uparrow$$

$$X - Au_{(ads)} + e^- \rightarrow Au_{(ads)} + X^-_{(g)}\uparrow \quad (1.3.2)$$

where the Au – L ligand is the result of σ donor interaction and a smaller almost zero π-back bonding.

Other precursors intended for deposition such as Me – Au – PMe_3 present higher thermal stability during volatilization, but as is the case of Cl – Au – PMe_3 decompose before reaching the gas phase undergoing a recombination and clustering process. At clustering forming $[ClAuPMe_3]_n$, they are presenting longer Au – Au bond distances in the range of ~ 3.313 Å. Post-growth treatment of FEBID deposits may reduce carbon content as discussed in Ref. [17]. The $Cu(hfac)_2$ and $Me_2Au(acac)$, deposit Cu – C and Au – C structures with diameters of a few nm: ~35 nm for Cu and ~6 nm for Au. Subsequent annealing of the deposits at temperatures over 300 °C show the average agglomerates almost doubling to 70 ± 20 nm for

Cu and 18 ± 8 nm for Au. As hydrocarbons become volatile at temperatures higher than 300 °C, the sub-10nm dispersed grains with the annealing turn into Au structures with average size of 15.6 nm. The Co content of $Co_2(CO)_8$ in Ref. [17] improves from 67 wt% at 100 °C to form a compact metallic film at 300 °C with average Co content of 84 wt%.

Cobalt Precursors. Deposits of Co in Ref. [17] on natively oxidized silicon wafers have been analysed using EDX, showing a high Co content in the range of 80 wt%. The FEBID process of Co containing precursors is shown to remove through irradiation all the ligands leaving Co deposits with low contamination from commercially available precursors, $Co_2(CO)_8$ and $Co(CO)_3NO$, with purities higher than 95 wt%, following the reaction schematics presented in relation (1.3.3) in Ref. [14] for the fragmentation pathway:

$$Co(CO)_3NO_{(ads)} + e^- \rightarrow Co(CO)_xNO_{(ads)} + (3\text{-}x)CO_{(g)}\uparrow$$

$$Co(CO)_xNO_{(ads)} + e^- \rightarrow (CO)_xOCoN_{(ads)}$$

$$(CO)_xOCoN_{(ads)} + e^- \rightarrow (CoO_yN)C_{(ads)} \quad (1.3.3)$$

The Co deposits have been found to create a 4 – 5 nm thin halo film around the structures which may be reduced by irradiation at 60 mC^2/cm^2 in an initial step observing a diminishing of the halo, with full reduction at 85 mC^2/cm^2 in Ref. [17] raising questions related to the different domains (MTL or RRL) where the deposition is happening. FEBID has been applied to building other structures, for example domain wall conduits from Co, with the intent of trapping and manipulating magnetic nanoparticles or biological material on nanoparticles, Ref. [17]. EELS and EDS studies in Ref. [18] of Co from $Co_2(CO)_8$ deposition revealed the presence of CoO species at 531 eV in EELS spectrum and the presence of pure deposits from O K edge and $L_{2/3}$ edge. Deposits of SO_2 show a content of O/Co ratio of 0.04 wt% and at $L_{2/3}$ an oxygen ratio of 0.3 wt%. Similar studies employing EELS, EDS, and electron holography (EH) in Ref. [11] present higher Co contents of 80 at% in nanowire deposits from $Co_2(CO)_8$ depositions with diameters of up to 100 nm and 85 at% Co content in nanowires with diameters of ~ 120 nm. From EDS analysis, wires with 60 nm diameter and Co content of 45 at% and a value of the magnetization in the bulk of ¼ have been obtained.

Platinum Precursors. The $MeCpPtMe_3$ precursor was used for FEBID deposition of a thin layer of < 100 nm with a substrate temperature of 120 °C and a conductivity of ~70 ± 8 μΩ·cm, a value approximately six times higher than that obtained for bulk Pt (10.6 μΩ cm) in Ref. [20]. In the regular EBID process, a deposit purity of only ~ 15 % was achieved, while using EBID and post-annealing in O_2 at 300 – 550 °C a deposition Pt content of 70 % was achieved. The rate of net intensities obtained

from experimental data, C/Pt = 0.12 at a temperature of 200 °C, shows a low C content with the Pt content reaching values close to the bulk Pt value. For $Pt(PF_3)_4$ deposited on the substrate in Ref. [334], from room temperature (RT) to 350 K, the Pt/(Pt+P) ratio increased from 0.15 – 0.24 % at RT to 0.60 % at 350 K. Platinum precursors ($MeCpPtMe_3$) are some of the most widely used giving high purity metal content with values higher than 80 % in Ref. [20] reaching an average of ~82 at% on the 4th deposition layer. Studies of Pt precursors have been presented in more details in ANNEX 3.

Ruthenium Precursors. A Ru purity content of 83 % has been achieved by Kapusta et al 2019 [21] using $(\eta^3\text{-}C_3H_5)Ru(CO)_3X$ precursor, where X = Cl, Br. Compared to $(EtCp)_2Ru$ precursor that creates deposits with a higher C content, the removal of which requires the use of O_2 jets with the effect of increasing the oxidation level of the metal. The $(\eta^3\text{-}C_3H_5)Ru(CO)_3X$, X = Cl, Br precursor in Ref. [22] has smaller numbers of C ligands and as a result less C content in the final nanostructure, though the final nanostructure will be contaminated by other organic elements such as Cl, Br or F. The NH_3 ligands in $(\eta^3\text{-}C_3H_5)Ru(CO)_3Cl$ in the electron irradiation process dissociate from the parent and form HCl with the free/released Cl atoms, following the relation (1.3.4):

$$NH^+_3 + Cl^- \rightarrow HCl + NH_2 \qquad (1.3.4)$$

ESD and TDS measurements of the $(\eta^3\text{-}C_3H_5)Ru(CO)_3Cl$ on Ta deposited at 110 K show that it decomposes at 31 eV electron energy with the fragmentation peak at 220 K, while another similar Ru containing precursor, $(\eta^3\text{-}C_3H_5)Ru(CO)_3Br$, deposited on Au decomposes at very high energies close to 500 eV electron energy. The desorption of the organic part on Ta and Pt(111) takes place at temperatures between 300 K and 400 K on Ta, and 300 K and 350 K on Pt(111). Before ESD process three bands corresponding to CO are observed, 2122 cm^{-1} (0.263 eV), 2072 cm^{-1} (0.256 eV) and 2034 cm^{-1} (0.252 eV), but after the ESD and annealing only one band corresponding to CO is observed at 1990 cm^{-1} (0.246 eV). In the post-annealing process, the substrate and molecules are irradiated with an electron beam of 1.25 x 10^{17} e^-/cm^2 finding the HCl content at less than 1 % in Ref. [22].

Copper Precursors. Selected area electron diffraction (SAED) and EDX measurements have been performed in conjunction with RAIRS studies in Ref. [23] for $C_{16}H_{26}CuO_6$ with the purpose of finding the elemental content of the deposited structure. Six bands were observed at 150 cm^{-1} (0.018 eV), 220 cm^{-1} (0.027 eV) and 630 cm^{-1} (0.078 eV) corresponding to partially oxidized copper, and 1580 cm^{-1} (0.195 eV), 1300 cm^{-1} (0.161 eV) and 1500 cm^{-1} (0.185 eV) corresponding to highly amorphous carbon with pure Cu embedded in a carbonaceous matrix presenting a deposit content of 26 wt% Cu, 13 wt% O and 61 wt% C. An EDX comparative analysis of $Cu(hfac)_2$, (hfac)Cu(VTMS) and (hfac)Cu(DMB) has been reported in Ref. [23]. A lower thermal stability is observed for (hfac)Cu(VTMS) with a

disintegration temperature of 63 °C compared to $Cu(hfac)_2$ with a stabilization limit temperature of 250 °C, coming from the structure characteristic to amorphous or nanocomposite materials of the $Cu(hfac)_2$ and (hfac)Cu(VTMS). The (hfac)Cu(VTMS) higher grain size of up to ~150 nm is the result of the annealing process, and the lower $Cu(hfac)_2$ nanocrystal size in the range of 2 nm to 20 nm comes from its amorphous structure; no notable difference was observed when changing the thermal source, from conventional to laser induced heating. The resultant deposits are non-conductive pre-annealing and conductive upon heating forming lattices.

Silver Precursors. Other precursors with intended FEBID use are Ag precursors in Ref. [24 - 26]. The $Ag(PMe_3)_n$, n = 2, 3, 4 have been analysed to suitability as FEBID precursors using DFT calculations. Out of the three precursors, $Ag(PMe_3)_2$ and $Ag(PMe_3)_4$ have been found to have the highest suitability as deposition complexes. The Ag content from $AgO_2CC_2F_5$ deposition by EDX measurements has a value of 70 wt% and for dots deposition from the same precursor an Ag content of 54 % in Ref. [26] was achieved. The resistivity of the deposits has a value of $\rho = (3.68 \pm 0.05) \times 10^3$ μΩ·cm which is approximately 500 times better than for amorphous C and 1000 times higher than of pure Ag. The other two precursors investigated for decomposition pathways using DFT calculations, the $\{AgO_2CCH_2OMe\}_n$ and $\{AgO_2CCH_2OMe(PPh_3)\}_n$, in Ref. [27], in the initial state at low electron energy of 1.3 eV, are giving a high number of carbonyl groups, $\{AgO_2CCH_2OMe(PPh_3)\}_n$ forming the resultant ionic fragment $[AgCH_2OMePPh_3]^-$ through the bond cleavages induced in Ag-P and Ag-C bonds. The FEBID technique has been employed in the fabrication of Ag nanostructures from dissociation of $[AgO_2F_5Prop]$ and $[AgO_2Me_2Bu]$ in Ref. [30]. The $[AgO_2F_5Prop]$ precursor creates deposits with unexpectedly high Ag content of 74 wt% and 75 nm size, though the final content suffers from contamination of F as well as C. The $[AgO_2Me_2Bu]$ precursor provides a lower Ag content of the final deposits with an Ag content of 50 wt% in the nanopillar shapes compared to bulk deposition which shows an Ag content of 67 wt% and size of 105 nm. The three parameters influencing the growth of the nanopillars in Ref. [27] are the primary beam current, the beam current (comprises of primary and secondary electrons current) and the patterning velocity dividing the growth region into three regions: the cylindrical shaft with high parallelism, the topmost conical region, and the apex region. The growth rates for both precursors are influenced by the dwell time, a low deposition rate caused by desorption of the molecules is observed in the $[AgO_2Me_2Bu]$ precursor and a reduction in temperature to 10 - 15 K triggers the condensation improving the height of the final deposit. For the $[AgO_2F_5Prop]$ precursor, the height and volume are related entirely to deposition dwell times, with little influence from temperature.

Nickel Precursors. Nickel precursors have been widely used in FEBIP. A detailed study of Cordoba et al. 2016 [29] compares the use of the $(MeCp)_2Ni$ and $Ni(CO)_4$, with the formation of NiO under electron

beam irradiation with O_2 creating deposits with resistivity of 2000 Ωcm. The conductance mechanism in the resulting Ni deposits from the deposition of $(MeCp)_2Ni$ is governed by the variable range hopping in nano-granular systems, with the formation of a carbonaceous matrix with embedded Ni clusters of 1 – 2 nm in Ref. [28] and resistivity values of 40 Ωcm at 270 K and 0.113 Ωcm at room temperature with the metal content 1.7 times higher than the metal content obtained at 270 K. DFT calculations in Ref. [29] were carried out to determine the changes (catalyst size and geometry) in the structure morphology of the surface and the clusters lattice for H_2 and CH_4 on N_{13} icosahedral clusters and Ni(111) surface. Earlier studies of CH_4 and H_2 on Ni surfaces experimentally determined values of 9.7 kcal/mol to insert a Ni atom in the C - H bond from CH_4, while Liu et al 2009 [30] calculates the value to be 9.9 kcal/mol on Ni(111) and for a single Ni to be lower to 1.7 kcal/mol; H_2 has a value of 3.5 kcal/mol, determining that H atoms have a higher probability to bind on c_3 sites of Ni_{13}, while CH_3 would bind to t_1 and b_2 sits of Ni_{13}, and, H_2 and CH_4 would bind at t_1 sites on Ni_{13}. The values for the Ni(111) substrate in Ref. [30] are 0.6 kcal/mol for H_2 and 21.4 kcal/mol for CH_4. The binding energy for H at c_3 sites is 63.88 kcal/mol, 70.53 kcal/mol and 72.16 kcal/mol and for CH_3 at t_1 and b_2 are 59.59 kcal/mol, 59.33 kcal/mol and 58.04 kcal/mol.

1.4 Conclusions To Chapter 1

From the multitude of available compounds for the FEBID process several of them have been used to be analysed using either the surface science tools (TPD, ESD, deposition, MBN Explorer simulations) or gas-phase analysis tools such as Velocity Map Imaging in combination with DFT studies. The chemical complexes chosen for the analysis are $Fe(CO)_5$, $W(CO)_6$, $Si(OEt)_4$, $Ti(OPr)_4$, $Me_2Au(acac)$ and $Cl_2ImEtCF_3Au$, from which $Cl_2ImEtCF_3Au$ has been designed at the University of Oslo specifically designated for the nanolithography research carried at the University of Kent, School of Physical Sciences. The 5 precursors will be discussed in 9 chapters over 2 sections, while ANNEX 1 - 5 have conclusive information on Pt containing compounds used for deposition purposes, with the intent of separating surface science from the gas-phase science.

CHAPTER 2. EXPERIMENTAL TOOLS USED IN STUDIES OF FEBID PROCESSES

In this chapter the different methods and instrumentation used in FEBID processing and in the analysis if the final FEBID nanostructures will be described. These were used to perform the set of experiments detailed in Chapters 4, 5, 6, 7 and 8.

2.1 ELECTRON INDUCED DISSOCIATION OF FEBID PRECURSOR MOLECULES

2.1.1 DISSOCIATIVE ELECTRON ATTACHMENT (DEA), DISSOCIATIVE IONIZATION (DI) AND NEUTRAL DISSOCIATION (ND) PROCESSES

Of the three processes governing the FEBIP (ND, DI, DEA) the focus in this thesis is on the DEA process, a process taking place at low electron energy looking into the fragmentation of the precursors up to 20 eV with implications to the FEBID produced nanostructures and possible causes of noise in the final products (MEMS, electronics, sensors, devices) and contamination influencing the resistivity and conductivity of the final structure through composition.

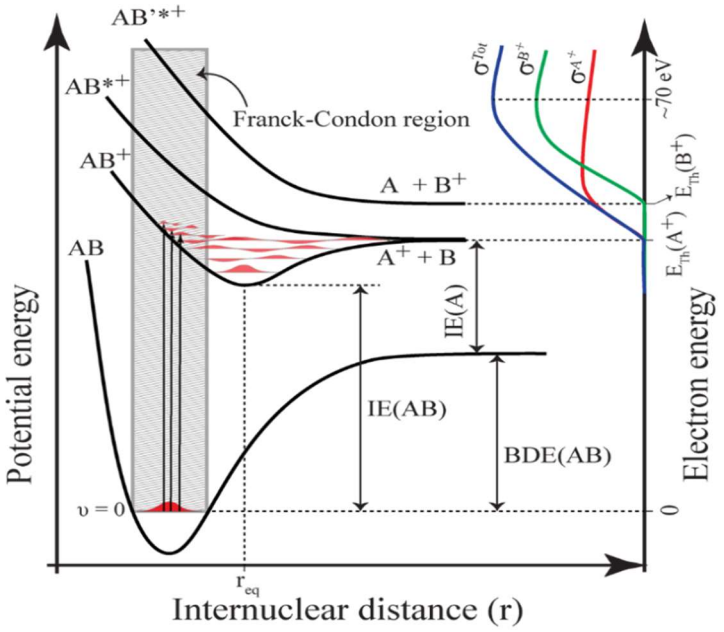

Fig 2.1.1.1 Dissociative ionization process of a molecule; courtesy of Thorman et al 2015 in Ref. [275]

DI is the process of dissociation of a molecule into one positively charged ion (cation) and a neutral ion. (See relation (2.1.1.1) and Fig 2.1.1.1).

The process is explained schematically by:

$$AB + e- \rightarrow AB^* \rightarrow A^+ + B \text{ or } A + B^+ \quad (2.1.1.1)$$

ND (see Fig 2.1.1.2) is the process of dissociation of a molecule into two neutral fragments where the fragments may be in the ground state or excited state e. The process is explained schematically by:

$$AB + e- \rightarrow AB^* \rightarrow A + B \text{ or } A^* + B \quad (2.1.1.2)$$

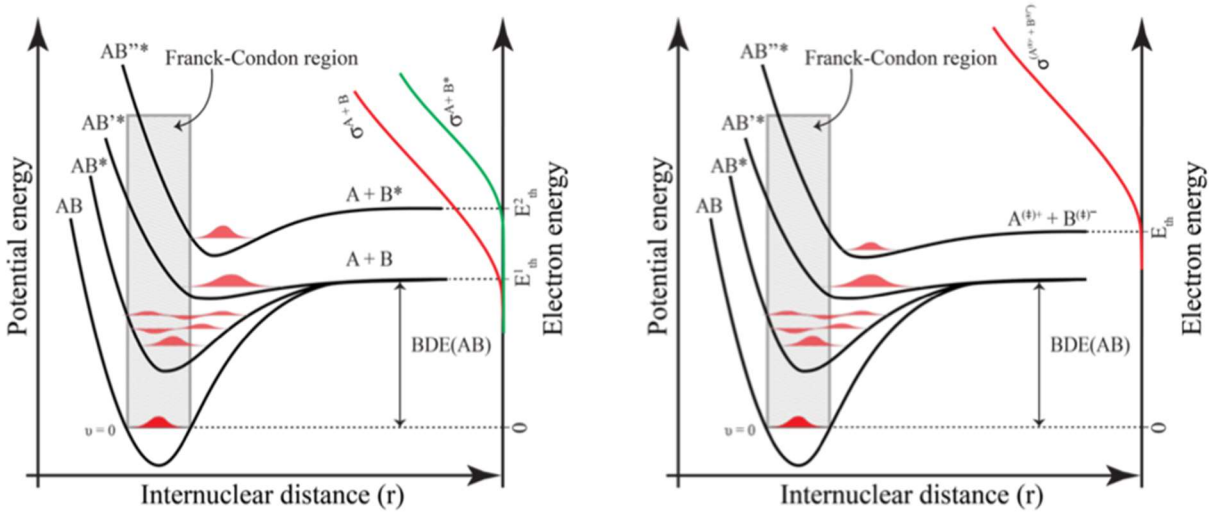

Fig 2.1.1.2 Neutral Dissociation and Dipolar Dissociation of a molecule; courtesy of Thorman et al 2015 in Ref. [275]

Ion – Pair Formation (see Fig 2.1.1.3 and Fig 2.1.1.2) also known as DD (Dipolar Dissociation) is the process of dissociation of the molecule into two charged fragments one cation and one anion.

The process is explained schematically by:

$$AB + e- \rightarrow A^- + B^+ \text{ or } A^+ + B^- \quad (2.1.1.3)$$

Dissociative Electron Attachment (DEA) (see Fig 2.1.1.4) is the process of molecular fragmentation of a compound in two or more stable fragments one of which is an anion.

The process is explained schematically by relation (2.1.1.4):

$$AB + e \longrightarrow AB^{-*} \rightarrow A^{-} + B \quad \text{or} \quad A + B^{-} \tag{2.1.1.4}$$

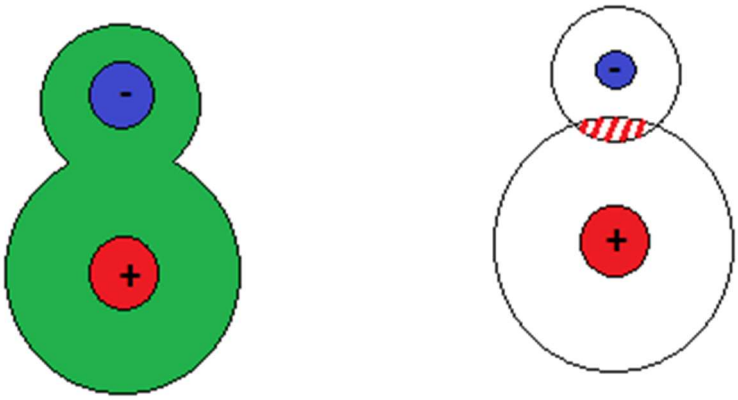

Fig 2.1.1.3 Ion-Pair formation of a molecule; courtesy of Krishnan et al 2009 in Ref. [319]

The Dissociative Electron Attachment (DEA) process is a process that takes place at relatively low energies, from 0 – 20 eV, Schulz 1973 [35] governed by the formation of a temporary negative ion (TNI) formed at specific incident electron energies and is often called an "electron scattering resonance".

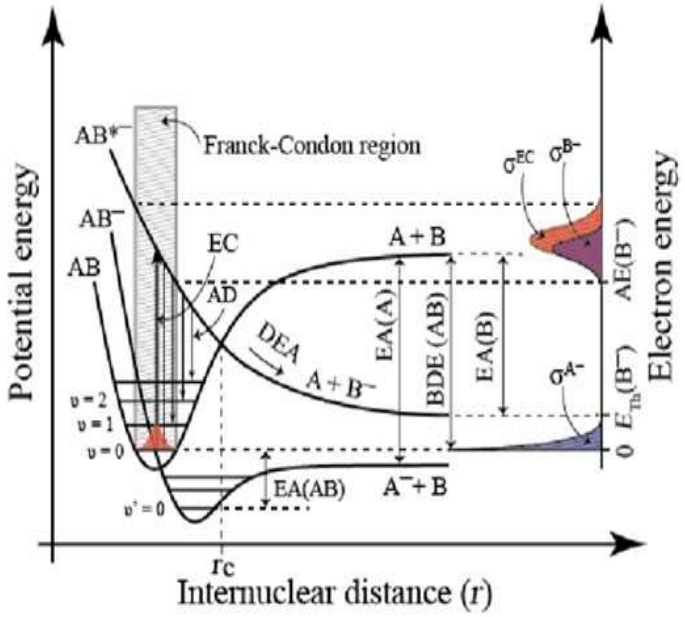

Fig 2.1.1.4. Dissociative Electron Attachment Process, courtesy of Thorman et al 2015 in Ref. [275]

The TNI may then undergo one of two decay process, auto-detachment (2.1.1.5) or dissociation (2.1.1.6):

$$e^{-} + AB \rightarrow AB^{-} \rightarrow AB + e^{-} \tag{2.1.1.5}$$

$$AB^- \rightarrow A + B^- \qquad (2.1.1.6)$$

The life of a temporary negative ion is in the order of 10^{-12} to 10^{-15} s, too short to measure. The appearance of the resonances and as such of the temporary negative ions is strongly correlated to the environment: temperature pressure and state (gas or solid).

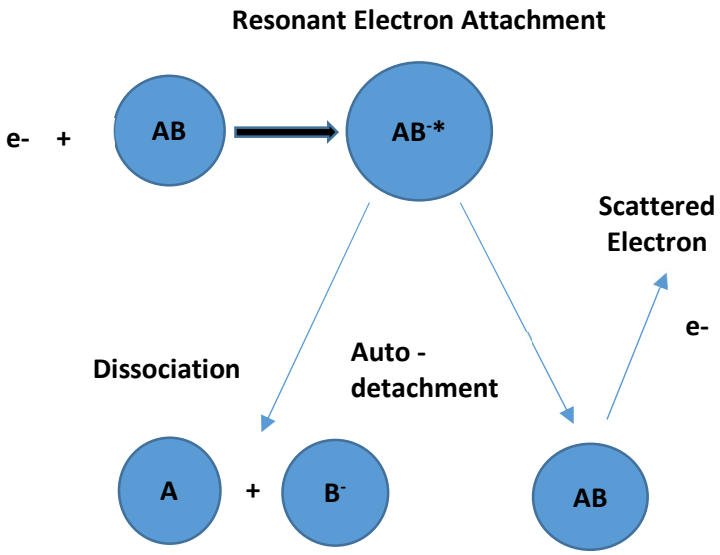

Fig 2.1.1.5. Resonant Electron Attachment Schematics

When the distance between the molecule and incident electron is larger than a few tens of Bohr radii to a few hundred Bohr radii, the resultant interaction is a long-range electron-molecule interaction capable of giving rise to a virtual anion state through attachment of an electron leading to what is called a vibrational Feshbach resonance. The resonances or the temporary negative ions are formed in two ways, as single particle excited resonances (1p) and as two particle – one-hole excited resonances (2p 1h). In the case of the electronically excited Feshbach resonances, a two particle – one-hole resonances, the energy of the excited anion is below the energy of the parent molecule. In a shape resonance where the anion energy is higher than the energy of the parent molecule single particle excited resonances are obtained. A schematic of the energy levels for the different type of resonances is presented in Fig 2.1.1.6.

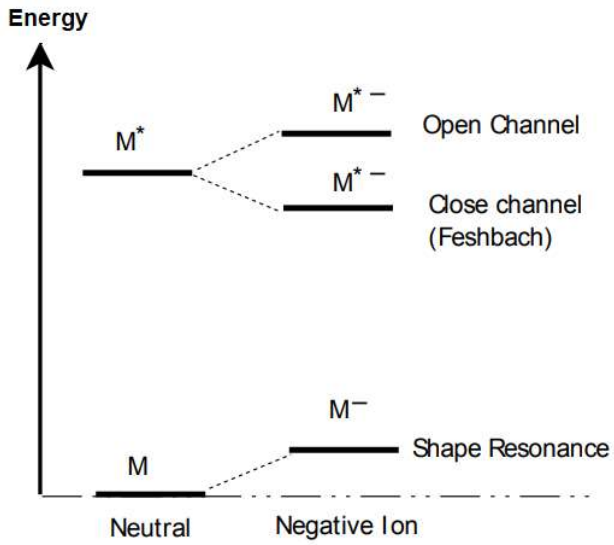

Fig 2.1.1.6. Types of resonances in electron induced chemistry; courtesy of Illenberger et al 1992 in Ref. [318]

The Heisenberg uncertainty (1927) helps in defining the lifetime of a temporary negative ion according to its energy width Γ in relation (2.1.1.7):

$$\Gamma \sim \frac{\hbar}{\tau} \qquad (2.1.1.7)$$

where $\hbar = \frac{h}{2\pi} = 6.6 \times 10^{-16}$ eV·s is the reduced Planck constant and τ is the temporary negative ion's state lifetime.

The resonances can be singular resonances or non-overlapping resonances and coupled resonances when in the vicinity of one resonant state lies another resonant state. The lifetime of the temporary negative ion can be increased through coupled resonances when the resonant state combines with a longer-lived resonant state.

2.1.2 Scattering Theory

When defining the scattering process, there are a few basic assumptions applied to the system, such as the same potential operates for the duration of the scattering event the target is subject to a single collisions and scattered electron undergoes no further collision post collision Taking all these into account for a beam of particles with the density n = dN/dV and a current density J_i, the total cross-section σ_{tot} can be explained as being the integral of all solid angles (see relation (2.1.2.1)):

From resolving the energy eigenvalue equation for the stationary scattering states:

$$(H-\varepsilon)|\psi\rangle = 0 \qquad (2.1.2.2)$$

and considering that the Hamiltonian is reduced to the kinetic energy $H \rightarrow H_0 = P^2/2m$, the equation is going to change to:

$$\langle (H_0 + V)\,|\varphi_\varepsilon\rangle = \varepsilon \mid \varphi_\varepsilon \qquad (2.1.2.3)$$

We obtain a relation between the scattering length and the cross-sections:

$$\frac{d\sigma(\theta,\Phi)}{d\Omega} = |f(\theta, \varphi)|^2 \qquad (2.1.2.4)$$

$$\sigma_{tot} = \int_{sphere} \frac{d\sigma(\theta,\Phi)}{d\Omega}\, d\Omega \qquad (2.1.2.1)$$

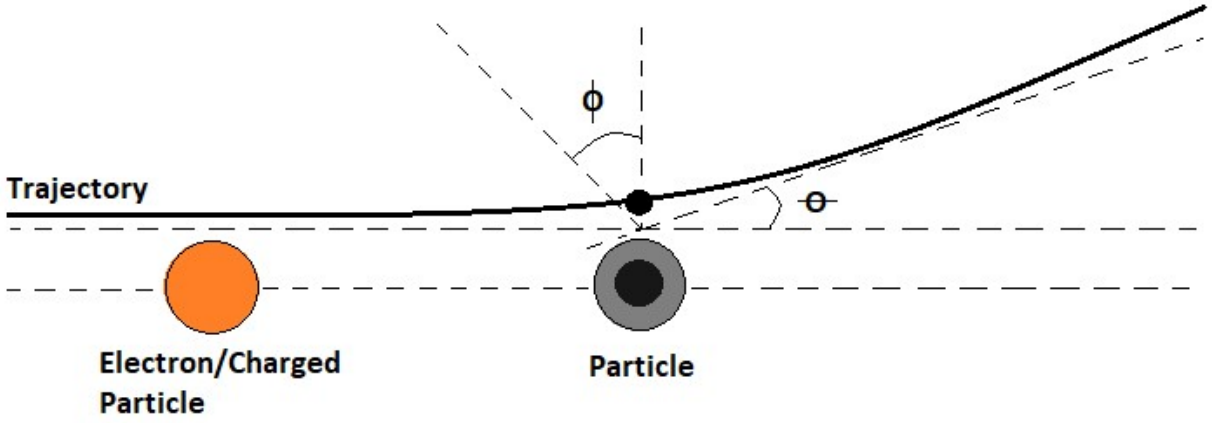

Fig 2.1.2.1. Area scattering (dσ) in solid angles (dΩ) of particles, courtesy of Griffiths D. J. 1994 in Ref. [36]

The Eigen function is defined by the relation (2.1.2.5), deduced from relation (2.1.2.4) by using the Green's function and Lipmann-Schwinger equation:

$$\boldsymbol{r} = \left(\underset{r}{\rightarrow'}\right)$$

$$f(\theta, \varphi) = -\frac{m}{2\pi\hbar^2} \int d^3 e^{-ik\hat{r}\cdot\boldsymbol{r}} r' V(\boldsymbol{r}) \Phi_\varepsilon(\boldsymbol{r}) \qquad (2.1.2.5)$$

For low energy scattering, the Eigen function with the Born approximation is reduced to:

$$f(\theta, \varphi) = -\frac{m}{2\pi\hbar^2} \int d^3 V(\boldsymbol{r}) \qquad (2.1.2.6)$$

2.1.3 Electron Collision Cross-Sections

Each electron scattering process may be quantified by its cross-section, defined as the "area around a particle in which the centre of another particle needs to be in order for the collision to occur" in Ref. [37 - 39]. Different types of cross-sections can be defined in Ref. [36] to describe different collision processes:

The **total cross section** is determined from electron beam attenuation using Beer-Lambert's law:

$$I = I_0 \exp(-\sigma N l) \tag{2.1.3.1}$$

where I is the scattered electron current, I_0 is the incident current , N is the target density, l is the gas cell in length.

The **momentum transfer cross sections** is obtained by integrating the differential cross-section and is defined as:

$$\sigma_{MT} = 2\pi \int_0^{\pi} \frac{d\sigma}{d\theta} sin\theta(1 - cos\theta)d\theta \tag{2.1.3.2}$$

The **total dissociative attachment cross-section** is defined as:

$$\sigma_T(E) = C \sum_i S_i \sigma_{ri}(E) \tag{2.1.3.3}$$

where E is the electron incident energy; C is a constant to adjust for the missing variables in the model.

$$\sigma_r(E) = \int_0^{\infty} \Psi^*(r)\sigma_{BW}(E,r)\,\Psi(r)dr \tag{2.1.3.4}$$

The **ionization cross section** is dependent on the ratio of the measured current I^+/I^- of ions and electrons

$$\sigma_I = \frac{I^+}{I^-} \tag{2.1.3.5}$$

2.2 Velocity Map Imaging

To study DEA to several FEBIB precursor molecules the Velocity Map Imaging (VMI) technique also called Velocity Map Imaging Mass Spectrometry (VMImMS) was used. Ref. [40]. This technique combines the use of a time-of-flight mass spectrometer (TOF) with the use of a fast pulsed high-resolution camera (CCD). The method itself does not consider how the ions were created in the

spectrometer, at what moment in time or their initial position, but focuses on the dynamics of the molecular fragmentation, the final products, and their characteristics. The dissociative electron attachment processes lead to fragmentation of the parent molecule. The result of the dissociation processes is an anion which is focused by a set of ion optics onto a position-sensitive detector. The position-sensitive detector has a chevron pair of microchannel plates coupled to a phosphor screen, where ions are transformed into pulses that appear as luminescence points on the phosphor screen and can be further imaged using a camera. The final products of a VMI from the image processing are velocity components of the ion and the scattering angle. Legacy VMI spectrometers used 2D projections for Abel transformations, while velocity sliced map imaging uses the three-dimensional momentum without the need for processing of the cylindrical symmetry in Ref. [41]. In velocity sliced map imaging, the middle slice of the 3D ion Newton sphere contains all the dynamical information needed. The VMI equipment used in this work has a 400 mm flight tube, 80 mm MCP stack, 10 kV repelling voltage for creation of ions at electrons energies up to 100 eV.

2.2.1 Kinetic Energies of the Anionic Products Measured Using VMI

The electrons from the electron gun are focussed into the gas chamber with an incident energy E_i in the range 0 to 20 eV and collide with the molecules in the ground state. The collision forms a temporary negative ion, AB^{-*}, with an energy higher than the parent molecule, which will further dissociate into fragments A + B^- with an electron affinity EA of neutral B ion. The molecule in its ground state is characterized by a bond dissociation energy BDE.

The kinetic energy of the fragment is the available energy E_e:

$$E_e = EA - BDE + E_i \quad (2.2.1.1)$$

The kinetic energy can be calculated by using the relation (2.2.1.2):

$$E_e = (1 - \frac{m}{M}) [E_i - (BDE - EA - E^*)] \quad (2.2.1.2)$$

where m and M are the masses of the two fragments.

The kinetic energy calculations give a maximum of kinetic energy, rather than a kinetic energy spectrum. When the velocity slice map imaging technique is applied, the kinetic energy is a curve with multiple points obtained by integrating over the area of the picture that contains the ions data points.

2.2.2 Angular Distribution of Anionic Products Measured Using VMI

The angular distribution of the anionic fragments is a macroscopic quantity that can be derived from velocity slice map imaging data. Considering that the molecule should not be in high level of rotational motion prior to dissociation, determining the angular distribution of a certain anionic fragment after the fragmentation process means that once the molecule goes from an initial state of symmetry to a final state of symmetry, for certain orientations of the internuclear axis to $\vec{k}$, the state transition probability will be non-zero, in other words, there will be an angular distribution. The initial conditions for this to happen is an incident electron beam defined by $e^{i\vec{k}\cdot\vec{r}}$ that is symmetric to rotations around $\vec{k}$ and reflections about $\vec{k}$, a particular symmetry of the molecule with respect to $\vec{k}$ and the internuclear axis of the molecule with a particular alignment with respect to $\vec{k}$.

The measured angular distribution is characterized by the relation (2.2.2.1):

$$\sigma_{DA}(\Omega, k) \propto \left| \sum_{l=\mu}^{\infty} i^l e^{i\delta_i} a(k)_{l\mu} Y_{l\mu}(\Omega) \right|^2 \qquad (2.2.2.1)$$

where k is the incident electron wave, Ω is the scattering direction of the anion, $a(k)_{l\mu}$ is the energy-dependent expansion coefficient, $Y_{l\mu}$ is a spherical parameter, δ_l is a phase shift, $\mu = |\Lambda_r - \Lambda_I|$, Λ_r and Λ_I are angular momentum resonances.

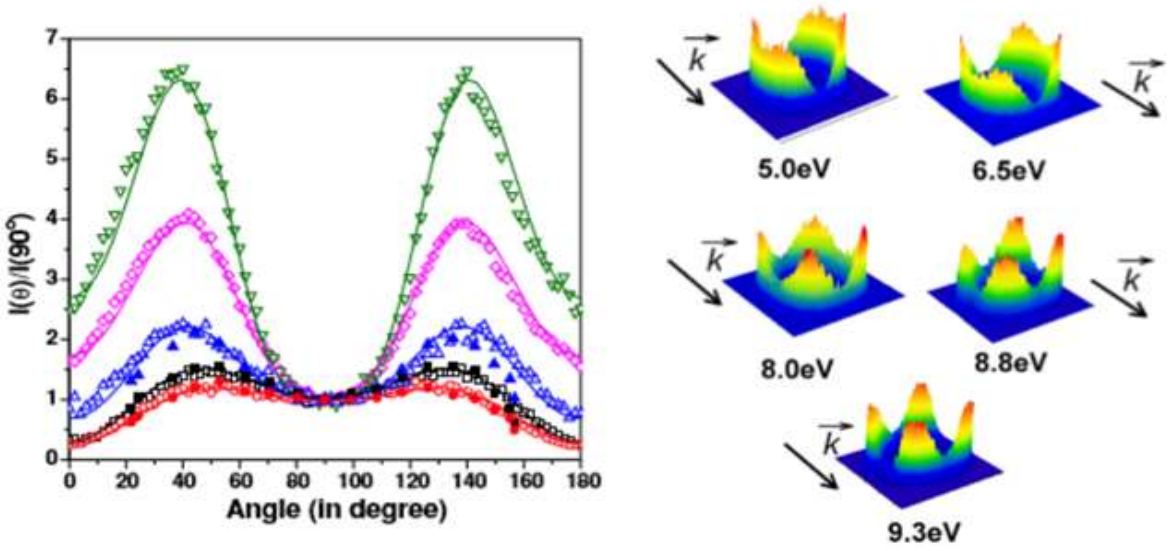

Fig 2.2.2.1. Angular distribution from O^-, courtesy of Prabhudesai et al 2006 in Ref. [320]

The theory predicting the angular distribution of ions by using the differential cross-section theory is defined in relation (2.2.2.2):

$$\frac{d\sigma(\Omega)}{d\Omega} = \frac{4\pi^3}{k_i^2} e^{-\rho_{Jr}} \cdot g \cdot \sum_{\Lambda_r} \left| \sum_{L=|\mu|}^{\infty} \langle \chi_{Jr} | V_{L,|\mu|} | \chi_v \rangle \, Y_{L,\mu}^*(\Omega) \right|^2 \quad (2.2.2.2)$$

where χ_{JR} and χ_v are vibrational wave functions of the molecule, $Y_{L,\mu}$ are spherical harmonics, k_i is the incident electron momentum.

We approximate in (2.2.2.3) $\langle \chi_{Jr} | V_{L,|\mu|} | \chi_v \rangle = i^l a_{l|\mu|}$, where $a_{l|\mu|}$ are real coefficients and we solve for:

$$I(k, \theta, \varphi) \sim \left| \sum_{L=|\mu|}^{\infty} a_{L,|\mu|}(k) Y_{L,\mu}(\theta, \varphi) \right| \quad (2.2.2.3)$$

Depending on the number of states describing the angular distribution, the equation (2.2.2.3) takes the form in relation (2.2.3.4):

$$I(\theta) \sim \sum_{|\mu|} \left| \sum_{L=|\mu|} a_L \, Y_{L,\mu}(\theta) e^{i\delta_L} \right|^2 \quad (2.2.2.4)$$

2.2.3 Velocity Map Imaging Experimental Apparatus

The experimental apparatus (Fig 2.2.3.1) consists of a high vacuum chamber, a set of pumps and measurement systems. The high vacuum chamber is evacuated by an oil free scroll vacuum pump, SCROLLVAC SC5D and a turbo pump which allows a base pressure of 10^{-9} mbar to be easily reached. Within the chamber an electron gun, a time-of-flight system and the anion detector are mounted.

The experimental chamber and vacuum system. The experimental chamber containing the VMI apparatus (Fig 2.2.3.1) is evacuated by an oil free scroll vacuum pump, SCROLLVAC SC5D and a turbo pump which allows a base pressure of 10^{-9} mbar to be easily reached. The molecular samples enter the chamber through a gas line evacuated by an Edwards oil pump RV3. In the case of liquid samples a freeze thaw cycle is followed to remove any dissolved gases prior to their entry into the chamber.

The electron gun. The negative ions (anions) are formed by electrons from an electron gun, the electrons being formed through thermionic emission from a metal filament, in our case made of 0.5 mm tungsten. The energy of the electrons is selected by a series of electron lenses which determine the collision energy of the electrons on the molecular target. A schematic diagram of a typical electron gun is presented in Fig 2.2.3.1.

Such electron guns (Fig 2.2.3.1) are used in commercial FEBID devices and operate at higher energies (e.g., 200 kV) allowing more focused electron beams ~10 nm with a relative brightness of ~1 x 10^9 A/cm^2·sr. The typical electron gun is characterized by variables such as inclination angle of emission electrode, applied voltage to electrode, the gap width between the emission electrode and diameter of

focusing electrode in Ref. [44]. To define these parameters and find information such as temperature, current density, maximum current, and emission current ORTEC software (Ortec Ltd.) was employed.

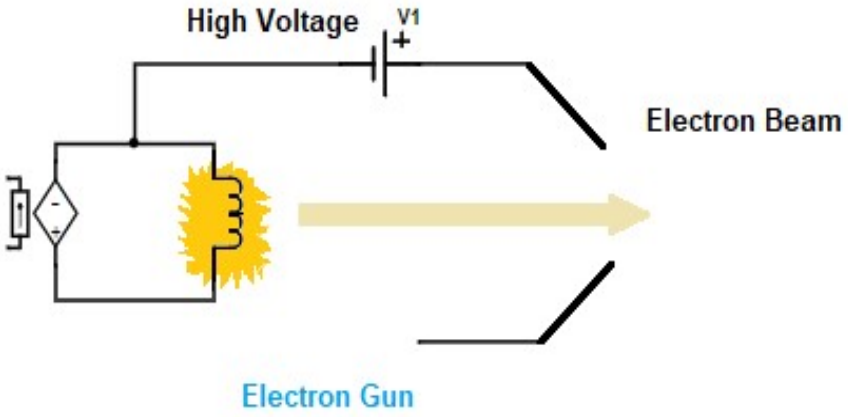

Fig 2.2.3.1 A schematic diagram of a typical electron Gun

From Ref. [44] we have characteristic equations for density of electrons of the emission current:

$$J = C\frac{V^{\frac{3}{2}}}{d^2}, \tag{2.2.3.3}$$

where C is the so-called Child constant and, V the potential between cathode and anode.

The thermionic current density emission is defined through the Richardson Dushman's law:

$$J_{eT} = AT^2\, e^{\frac{-e\phi}{KT}} \tag{2.2.3.4}$$

where A is Richardson's constant of 120 A/cm^{2}k, ϕ the cathode work function and T the temperature of the cathode.

The maximum total current from the electron gun is:

$$j_e = 2.33 \times 10^{-6}\,\frac{\pi}{2}V_0^{\frac{3}{2}} \tag{2.2.3.5}$$

where V_0 is the applied voltage in volts.

The temperature of the filament is given by:

$$T = \left(\frac{P}{e\sigma A}\right)^{\frac{1}{4}} \tag{2.2.3.6}$$

where P is the radiated power in Watts, e is the emissivity of the material, σ is the Stefan-Boltzmann constant, A is the surface area and T is the temperature of the filament.

The perveance of the electron gun is then given by the relation (2.2.3.7):

$$P = \frac{I}{V_0^{\frac{3}{2}}} \qquad (2.2.3.7)$$

where V_0 is gun anode voltage.

Fig 2.2.3.2. Velocity map imaging experimental setup

The Helmholtz Coils. As DEA is a low energy process it is necessary for the collision region to be 'field free' as even the Earth's magnetic field may deflect the electron beam and the product ions. To provide a field free region, the apparatus has a set of Helmholz coils such that a counteracting magnetic field is present in the interaction region to ensure collisions occur in a field free region. The magnetic field at the centre of the coil is dependent upon the coil current I, the number of wire windings N, the radius and distance of the coils R:

$$B \approx 7.48 \cdot 10^{-4} \frac{T}{A} \cdot I \qquad (2.2.3.8)$$

$$B = \mu_0 \cdot \frac{8 \cdot I \cdot N}{\sqrt{125}\, R} \qquad (2.2.3.9)$$

The magnetic field in the centre of the two coils is established to be equal and opposite to the Earth's field providing the field free region in which the electron scattering experiments occur.

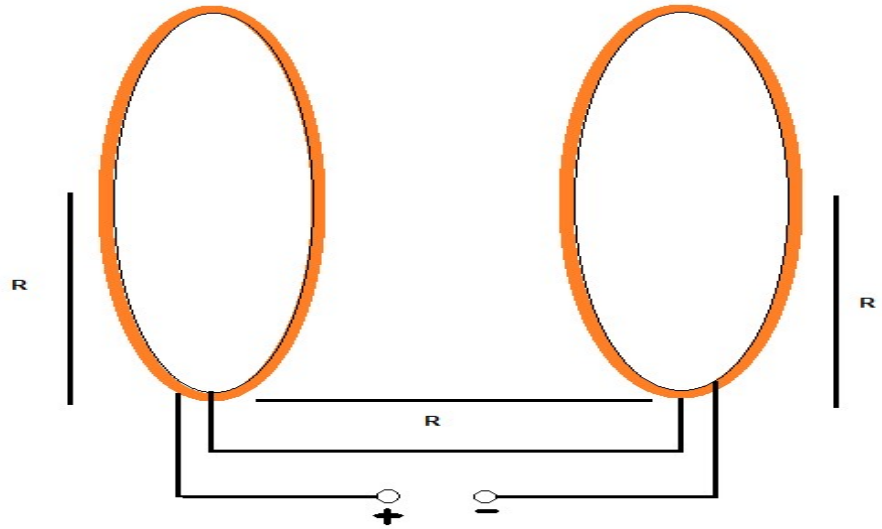

Fig 2.2.3.3. Helmholtz Coils

The anions produced in the scattering region are then repelled and deflected into a flight tube prior to striking the detector system. The detector is a three-channel plate Z-stack Chevron MCP detector. The ensemble of the MCP, Faraday cup for electron collection, extractor, puller and repeller is presented in Fig 2.2.3.4(). After extraction, the ions pass along the flight tube to reach the phosphor screen and they are captured by the CCD camera.

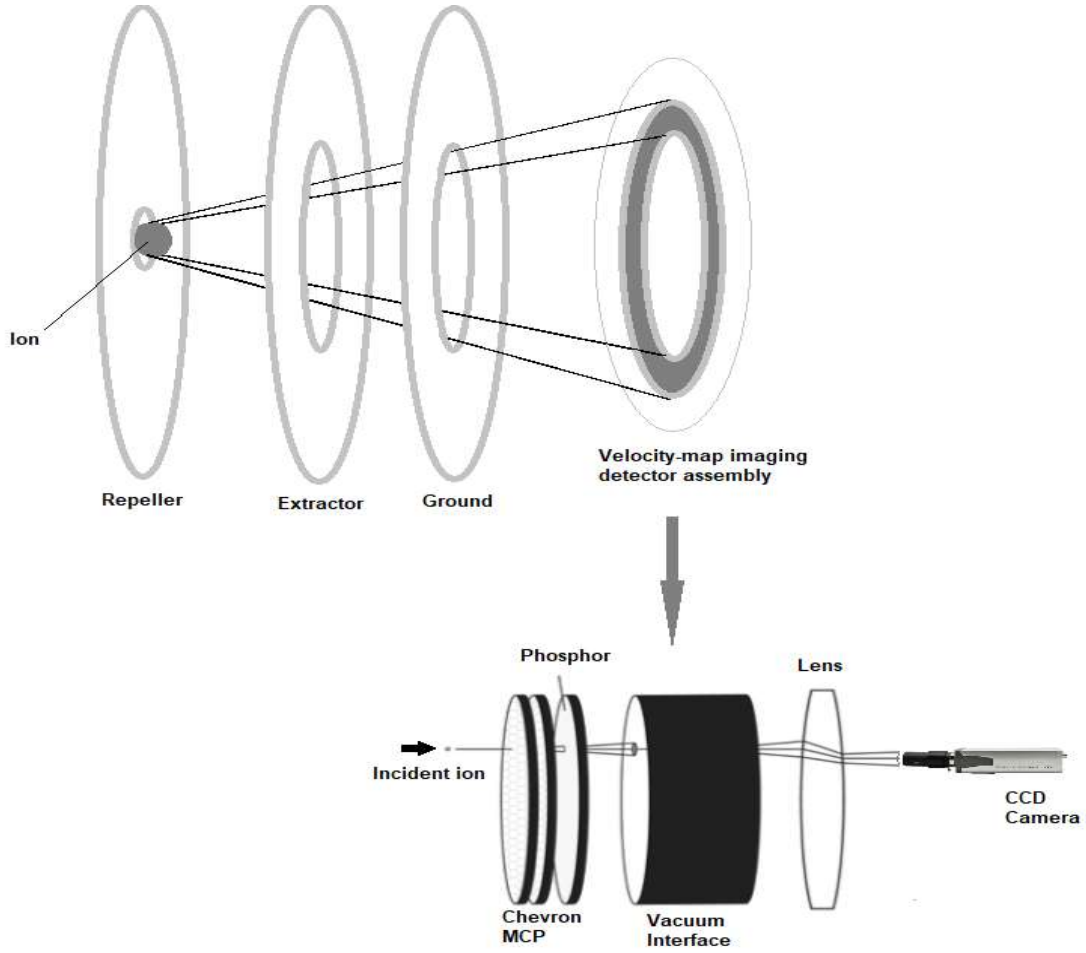

Fig 2.2.3.4. MCP assembly and detector schematics, Bull and Lee (2014) [47]

2.2.4 O^- FROM O_2

Calibration and testing of the VMI apparatus was performed by studying dissociative electron attachment to molecular oxygen. The oxygen used had a quoted 99.9 % purity and was introduced to the high vacuum chamber at a base pressure of 1.1 x 10^{-8} mBar rising to a pressure of 1.1 x 10^{-7} mBar with oxygen present. The oxygen gas was assumed to have a temperature of 297 K. Oxygen has been used in many nanofabrication processes and is one of the most commonly used compounds in the chemical vapour deposition processes as well as in plasma etching. In FEBID and EUVL, oxygen is used to enhance dissociation of precursors and improve purity of the deposits (see Section 2). DEA of O_2 to form O^- and neutral O is observed at an electron energy of 6.5 eV arising from a $\sigma \rightarrow \sigma^*$ transition and following the dissociation pathway presented in relation (2.2.4.1).

$$O_2 + e^- \rightarrow O_2^* \rightarrow O^- + O \qquad (2.2.4.1)$$

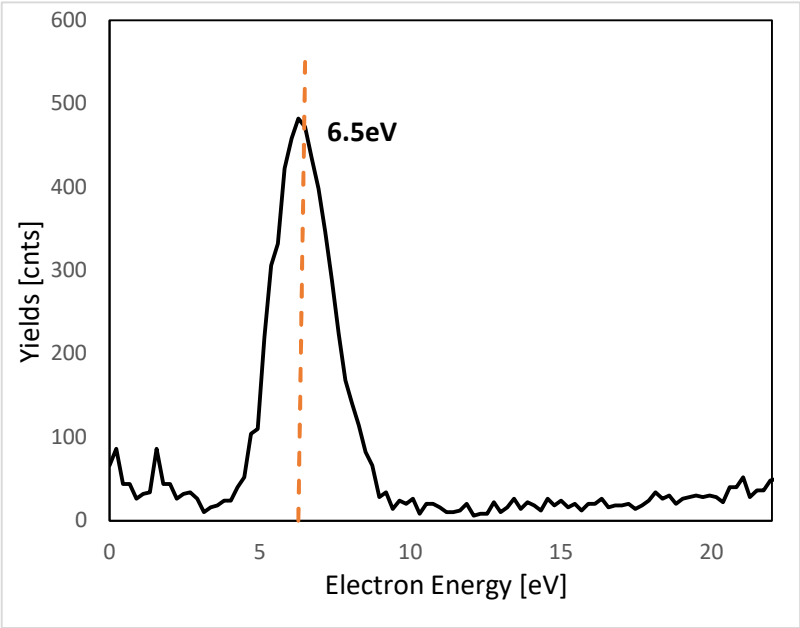

Fig 2.2.4.1. Oxygen anion yields to energy spectrum with resonance peak at 6.5 eV from TOF VMI

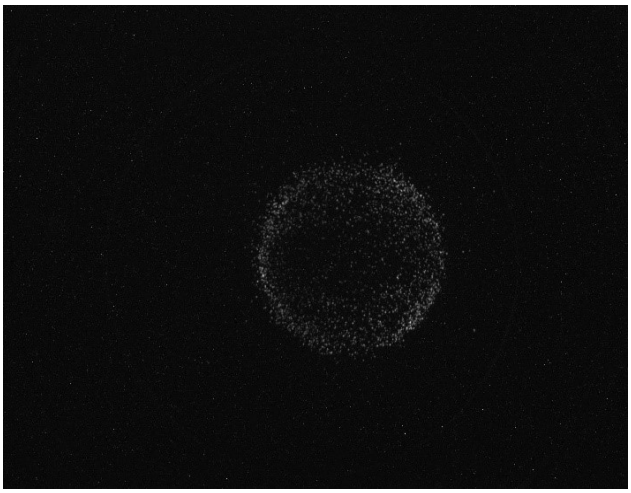

Fig 2.2.4.2. Raw oxygen anion velocity map image at 6.5 eV (10 V and 3725 ns gate delay)

The spectrum recorded from our time-of-flight velocity map imaging equipment is presented in Fig 2.2.4.1 and was recorded at room temperature (293 K). The peak of O^- anion yield was found at 6.5 eV, in good agreement with the study of Prabhudesai et al 2005 [51] corresponding to a $\Sigma_g \rightarrow \Sigma_g^*$ transition. The velocity map image of the ion was recorded with different voltages and gate delays for better accuracy, with the closest values to the centre of the Newton sphere and with the least amount of noise at 10 V and 3725 ns. The recorded anion image is presented in Fig 2.2.4.2. The VMI images of the O^- anion at 12 V / 3725 ns and 14 V / 3725 ns gate delay are presented in Fig 2.2.4.3. An image comparison can be made looking at the noise levels in all three images (Fig 2.2.4.2, 2.2.4.3 (a) and (b)), the centrality

of the O^- ring and the size of the ring, as well as the roundness of it (Abel inversion), all providing quality checks for the optimization of the VMI.

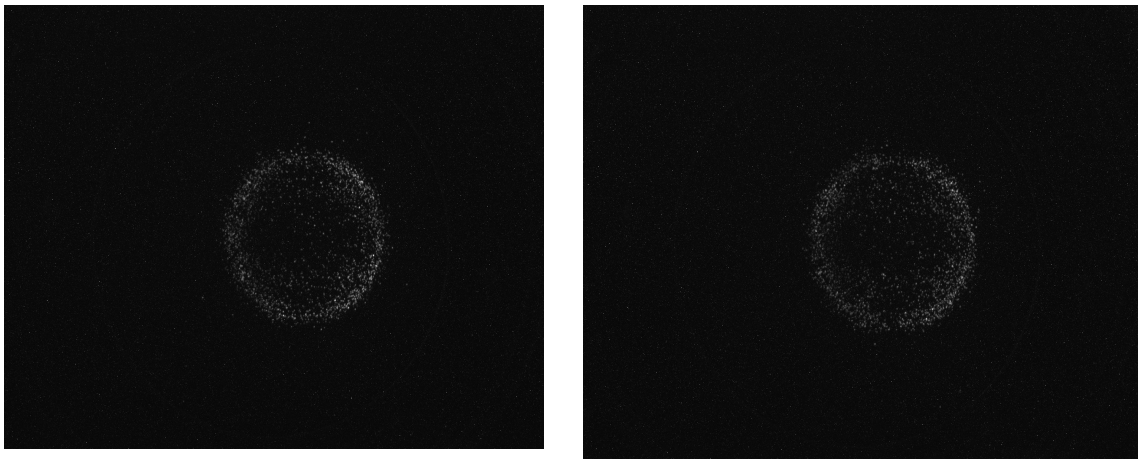

(a) (b)

Fig 2.2.4.3. Velocity sliced map imaging of O^-: (a) 12 V / 3725 ns; (b) 14 V / 3725 ns

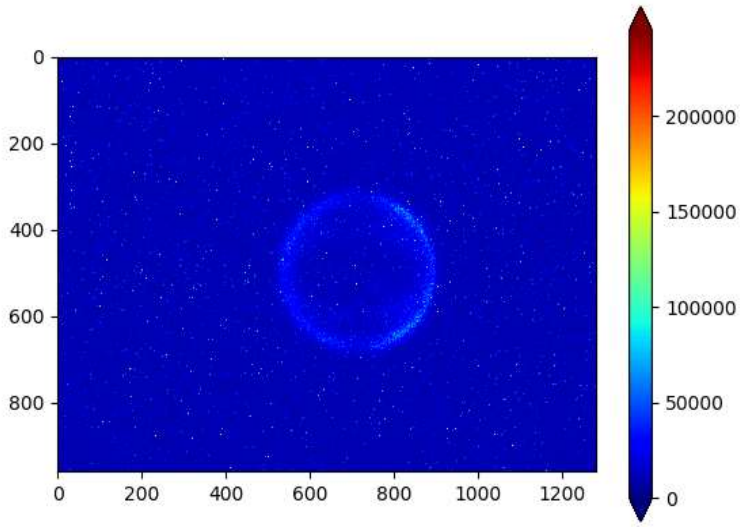

Fig 2.2.4.4. Velocity sliced map imaging of O^- at 6.5 eV

In Fig 2.2.4.2 the two images present O^- anions collected at two different extractor voltages. We can observe the elongation of the inner circular feature of Fig 2.2.4.3 (a) and (b), uncorrected this induces errors in the values of the angular distributions and kinetic energies. There was no evidence of the parent O_2^-, this can only be formed by reactions between the neutral O_2 and the negative O^- ion (relation (2.2.4.2)), suggesting that the pressure in the chamber is sufficiently low during experiment to avoid any three-body problem:

$$O_2 + O^- \rightarrow O_2^- + O \quad (2.2.4.2)$$

Kinetic energies of O^-. The kinetic energies of the O^- anions derived from the velocity sliced map imaging of O_2 are presented in Fig 2.2.5.5. The maximum of kinetic energy is obtained from electron affinity of the ion, the bond dissociation energy, and the incident electron energy:

$$Ee = EA - BDE + Ei \quad (2.2.4.3)$$

The maximum value of the kinetic energy obtained experimentally is 1.801 eV.

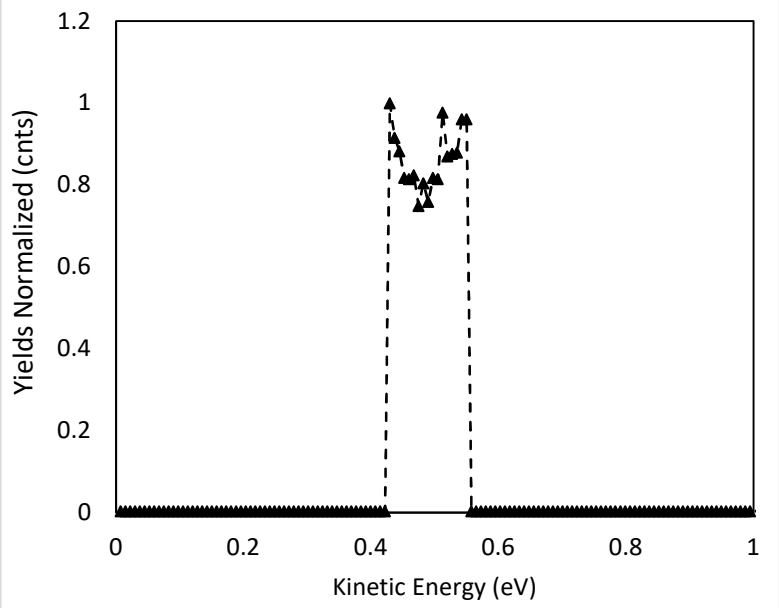

Fig 2.2.4.5. Kinetic energy of O^- from O_2 at 6.5 eV

The data recorded using the Behlke discriminator, MCP data acquisition module and the CCD camera was processed using Python v.3.8.1 adding a number of 11 pictures. Even though the number of recorded images of the negative ions arriving at the phosphor screen is still low, the data was processed with small errors that were reduced by fitting it to a 5^{th} order polynomial. Kinetic energy values were reported in Ref [48] at 204.8 nm, where the O^+ and O^- pair was found to have a corresponding kinetic energy peak at a value of 0.415 ± 0.016 eV characterised by a peak width of 0.080 ± 0.006 eV and a total energy of 0.83 ± 0.03 eV.

Angular distribution of O^-. The angular distribution of O^- is presented over a 0 deg to 360 deg scale, expecting symmetry around 90 deg, as the dissociation of O_2 is a process that divides the molecule into two similar mass atoms, one in neutral state and one anion. The C1 symmetry was used in the calculations for simplification, the O_2 molecule's symmetry point group being D_{2h}. The angular distribution is defined theoretically by the relation (2.2.4.4), presented by Nandi et al 2005 [51] and modelled earlier for the

scattering processes in dissociative electron attachment and electron-molecule collisions by O'Malley et al 1968 [53]:

$$I(k, \theta, \Phi) = \sum_{|\mu|} |\sum_{|\mu|}{}^{\alpha} a_{l\mu}(k)\, Y_{l\mu}(\theta, \Phi)|^2 \qquad (2.2.4.4)$$

where k is electron incident momentum, I is ion intensity at angular coordinates (θ, Φ), $a_{l\mu}(k)$ is energy dependent expansion coefficient, $Y_{l\mu}(\theta, \Phi)$ is spherical harmonics with $\mu = \Lambda_f - |\Lambda_i|$, $l >> |\mu|$.

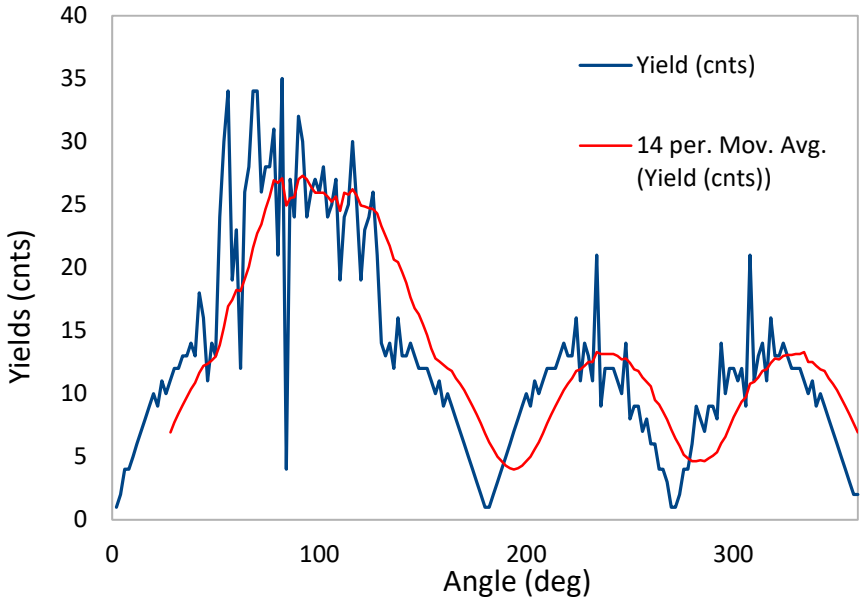

Fig 2.2.4.6. Angular distribution of O^- from O_2 at 6.5 eV with fitting, 0 – 360 deg

The resonant scattering processes in O_2, result of the interaction between electrons and O_2 molecules are characterized by an electronic ground state $^4\Sigma^-_u$ in Ref. [51] to excited state of the fragment anion $^3\Sigma^-_u$ with 90 deg symmetry. The resulting angular distribution plots were normalized at 90 deg. The distribution of O^- from O_2 has higher yields though other literature sources present a fully symmetric structure in Ref. [51, 52 - 54]; our structure is symmetric in shape to 90 deg with a reduction in amplitude from 90 – 180 deg, that can be observed from the velocity sliced map imaging picture as well, where, on the right side, 2 lobs with higher number of counts have been collected. A fully symmetric structure at the expected angle of 90 deg represents a perfect ring with homogeneous number of counts at each point on it. The induced symmetry through different number of counts has the result of creating two more angles where the shape could be symmetric, 42 deg and 135 deg. One of the potential causes of the reduced amplitude of the angular distribution angles after 90 deg could be from the reduced number of pictures collected and the low number of counts in each picture, though fitting of the graph to a 5th order polynomial comes with a fix to this problem.

2.3 TPD, ESD and Surface Irradiation

Temperature programed desorption, electron stimulated desorption and surface irradiation studies of the $Me_2Au(acac)$ precursor on Cu(110) have been conducted with the purpose of exploring the fragmentation of a set of FEBID precursor compounds on a surface by irradiation with electrons. These experiments were performed in the Laboratory of Surface Science and Interfaces at the Institute des Sciences Moléculaires d'Orsay at the University of Paris-Saclay, led by Professor Anne Lafosse, and sr. lecturer Dr. Amiaud Aionel.

2.3.1. Equipment Set-up at Institute des Sciences Molèculaires d'Orsay

Experiments were performed in an ultra-high vacuum chamber capable of producing pressures in the range of ~10^{-11} mbar using a pumping system that combines an SH-110 Dry Scroll Vacuum Pump from Agilent Technology and a turbo pump with an ion pump used to further reduce the pressure to 10^{-10} mbar.

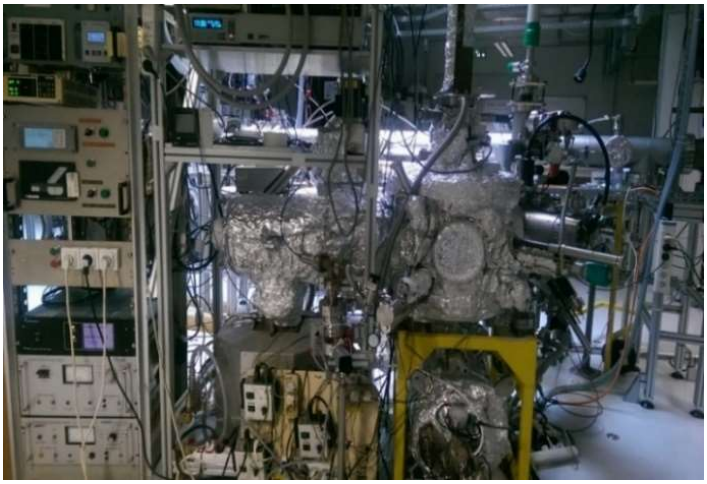

Fig 2.3.1.1. Left: inside of UHV chamber. Right: deposition and measurement mechanism

Electron Gun. To produce the necessary beam of electrons for irradiation of the $Me_2Au(acac)$ sample, a Kimball Physics ELG 2A electron gun (Fig 2.3.2.1) was used. An EGPS-1022 Power Supply aids the use of the electron gun and comprises of beam energy, X - Y deflection, floating source/ECC, grid, first

anode and focus supplies. The electron gun uses a Wehnelt electrode and an electrostatic lens system, beam-shaping anode lenses and electron beam deflection plates.

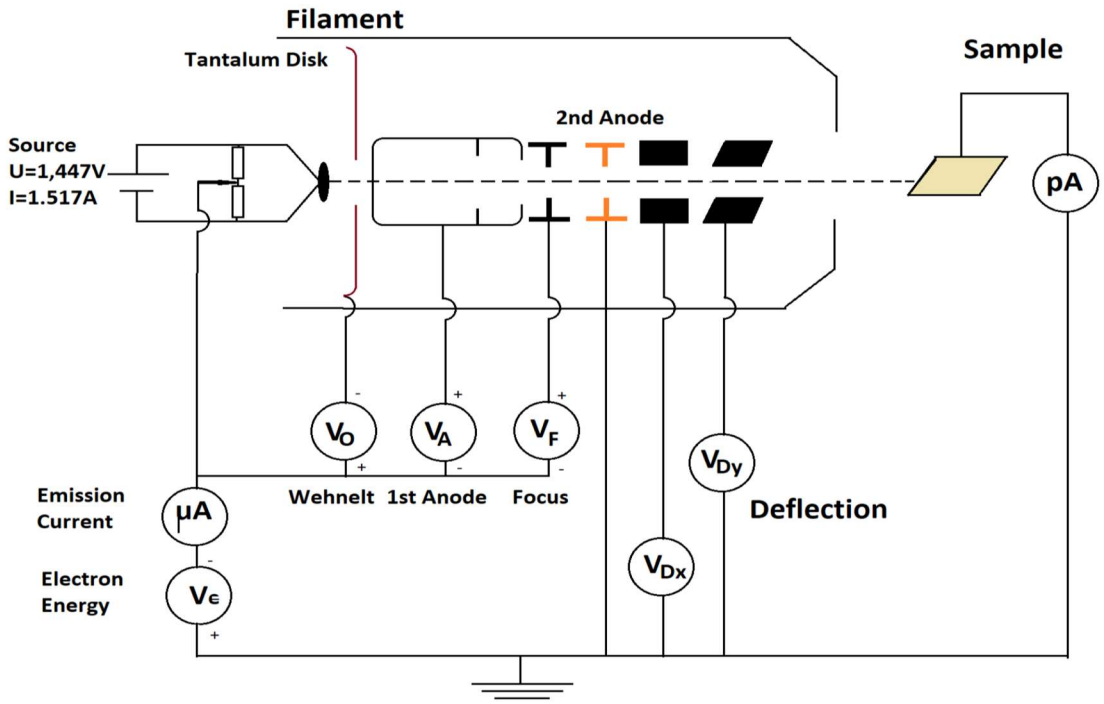

Fig 2.3.2.1. Electron gun schematics: *Leo Albert Sala, Low-Energy Electron Induced Chemistry in Supported Molecular Systems

The electron gun can not be run at pressure values higher than 10^{-5} torr and is suitable for baking only up to 350 °C without cables. It has a variable energy range between 1 eV to 2000 eV, delivering 1 μA into a 1 mm spot at 2 cm distance and 10 eV in Ref. [153]. The specifications of the electron gun when operated in these experiments were ~1 μA, 500 meV resolution, and a total dose of ~10^{15} electrons/cm^2. The control grid provides two options: fast capacitive beam pulsing, by using a pulse Junction Box, and fast beam pulsing to 20 ns with 20 % maximum duty cycle and dual grid pulsing.

2.3.3 Electron Stimulated Desorption (ESD) of Neutral Species from Condensed Films

In order to study Electron Stimulated Desorption (ESD) from condensed films on the substrate a quadrupole mass spectrometer (QMS) was used. The QMS used was a HIDEN Analytical Model HAL 301/3F, which consists of a HALO or single filter mass spectrometer for multipurpose HV/UHV applications and a 3F or a triple filter mass spectrometer for precise analytical capability, having a m/z

range option of 300 and 4 lens ion optics with integral ionizer (hot filament electron generator) highly similar to the one presented in Ref. [154-156].

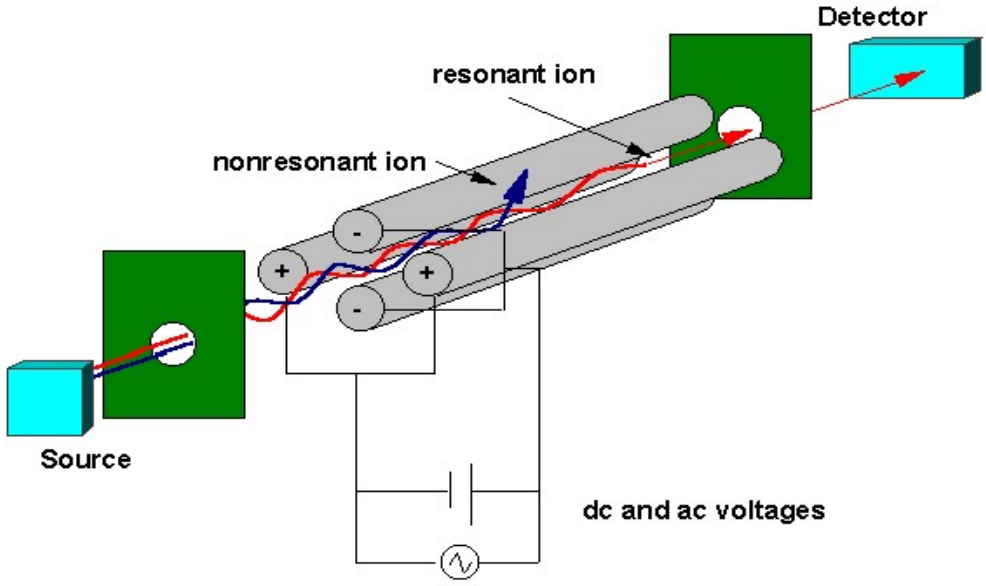

Fig 2.3.3.1. Quadrupole Mass Spectrometer; *Brian M. Tissue, https://www.tissuegroup.chem.vt.edu/chem-ed/ms/quadrupo.html

To be more precise, between the four plates we have a division of the masses of the ions being accelerated, the heavier ions and the smaller ions are attracted to the two negative electrodes, the X-direction being a high-pass mass filter and the Y-direction being a low-pass mass filter. The mass filter is tuned by changing the amplitude of the RF voltage in Ref. [154]. In order to find specific mass ions, a specific dc and ac voltage needs to be applied to the electrodes.

The QMS is characterized by Mathieu's equations in Ref. [154]:

$$\frac{d^2x}{dt^2} = -\left(\frac{e}{m}\right)\left(\frac{[U+Vcos(\omega t)]}{r0^2}\right)x \tag{2.3.3.1}$$

$$\frac{d^2y}{dt^2} = \left(\frac{e}{m}\right)\left(\frac{[U+Vcos(\omega t)]}{r0^2}\right)y \tag{2.3.3.2}$$

$$\frac{d^2z}{dt^2} = 0 \tag{2.3.3.3}$$

where m is the mass of the ion, q is the charge, $2r_0$ is the distance between the four electrodes, e is the magnitude of the electron charge.

The electron stimulated desorption process may be simulated by using models such as Menzel-Gomer Redhead model for desorption from covalent adsorbates, the Knotek-Feibelman model for desorption

from ionic substrates, DIET in multilayer films and Antoniewicz model. All these models have three steps in common as described in Ref. [153]: (i) fast initial electronic excitation (10^{-16} s), (ii) fast electronic rearrangement (10^{-15} s) to an electronic state of 10^{-14} s and (iii) changes in energy, charge state and trajectory of desorbing species.

2.4 SEM/EDX Equipment and Physics at Carl Zeiss Gmbh

SEM/EDX/AFM equipment was used at Carl Zeiss Gmbh to analyze the nanostructures deposited using the $Si(OEt)_4$ precursor determining their composition, height and morphology as a function of deposition characteristics e.g., electron beam diameter and energy, deposition time and substrate temperature.

2.4.1. SEM Physics

A scanning electron microscope is a microscope that creates an image using secondary electrons emissions. The principle of image formation is based on focusing primary electrons on the area of interest, called a specimen, where, by applying electrostatic or magnetic fields at right angles, the direction of travel is changed. The image resolution of a SEM is in the range of 1 nm to 10 nm. The electron field-emission source is a tungsten tip placed within an intense electric field.

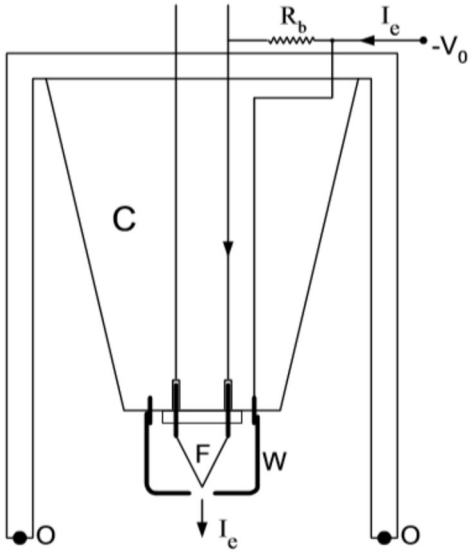

Fig 2.4.1.1. Electron gun used in a typical SEM comprising a tungsten filament F and Wehnelt electrode W, C is a ceramic high-voltage insulator, O is the O-ring seal, R_b is an autobias resistor in Ref. [156]

For the production of electrons, the SEM uses an electron gun with a tungsten filament, similar to the one used in the VMI equipment, though specific to the SEM. When the electron gun is on, a dc current is applied to the filament until the temperature value of 2700 K is reached and the filament emits the electrons by the process of thermionic emission (Fig 2.4.1.1).

The electron emission rate is characterized by Richardson's law:

$$J_e = AT^2 e^{-W/kT}, \quad (2.4.1.1)$$

where T is the absolute temperature, A is the Richardson constant ($\approx 10^6$ $Am^{-2}K^{-2}$), k is the Boltzmann constant (1.38×10^{-23} J/K) and W is the working function of the metal.

The brightness of the source is given by:

$$\beta = \frac{J_e}{\Omega} = constant, \quad (2.4.1.2)$$

where Ω is the solid angle over which electrons are emitted. The source brightness follows the principle of conservation; the brightness of the source should be the same in each plane.

From the cathode, after the emission of the electrons from the tungsten filament, the electrons undergo a process of acceleration to their final kinetic energy E_0, by using an electric field parallel to the optical axis. The kinetic energy E_0 is defined by the formula:

$$E_0 = (\Upsilon - 1)\, m_0 c^2 \quad (2.4.1.3)$$

Maxwell stated in 1958 that an image is perfect if for each point of the object there is a corresponding point in the image (or the ray path), the object and the image object are similar, and the perpendicularity and planarity are conserved in the image as in real life. When the electrons have electrostatic charges and are deflected by electric fields, we have electrostatic lenses, on the other hand, when we use the fact that the electrons in the beam are moving and they can be deflected by a magnetic field, we have magnetic lenses.

Electrostatic lenses - The electrostatic lenses used for imaging of electrons are made of a circular conducting electrode with a circular hole and a negative potential. The electrons passing along the optic axis suffer no deflection compared to electrons travelling off the axis that are deflected back towards the optical axis. In an Einzel lens, the electrons (electric fields) that give the focusing have axial symmetry, meaning that the electrons are taken at a radial distance from the optical axis, and it does not depend on the azimuthal direction.

Magnetic lenses – A magnetic lens is a lens made by using a magnetic field produced by a coil through which a direct current pass. The force acting on an electron in a magnetic field is defined by the relation:

$$F = -e\ (v \times B) \text{ or } F = evB\sin(\varepsilon), \tag{2.4.1.4}$$

where e^- is the charge of the electron, v is the velocity vector and B is the magnetic field. If the tangential, radial and axial components of the magnetic force on an electron are requested, the (2.4.1.5) relation can be used:

$$F_\Phi = -e\ (v_z B_r) + e\ (B_z v_r) \tag{2.4.1.5}$$

$$F_r = -e\ (v_\Phi B_z) \tag{2.4.1.6}$$

$$F_z = e\ (v_\Phi B_r) \tag{2.4.1.7}$$

A thin magnetic lens is characterized by a focusing power defined by:

$$\frac{1}{f} = \frac{e^2}{8mE_0} \oint B_z^2\, dz, \tag{2.4.1.8}$$

where E_0 is the kinetic energy of the particle, *e* and *m* are the charge and mass of the electron and B_z the z-component of the magnetic field.

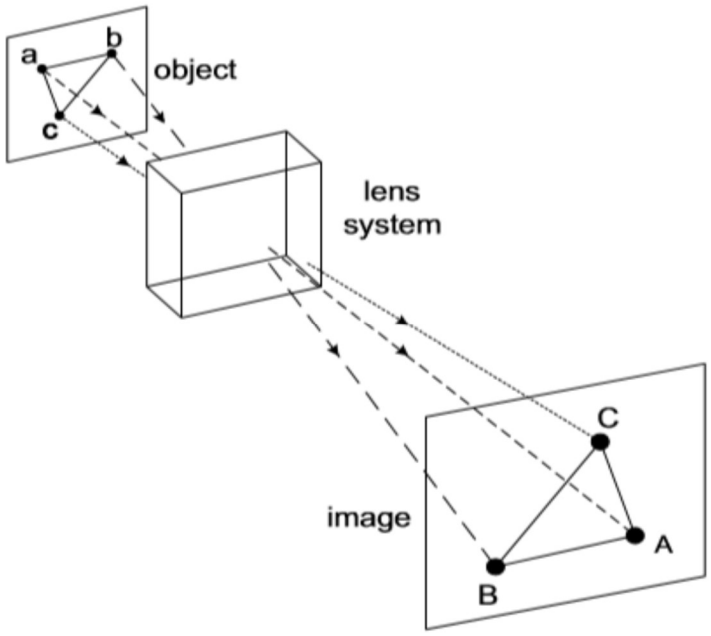

Fig 2.4.1.2. Object imaged with magnification and inversion, Ray F. Egerton 2005 in Ref. [322]

Defects of Electron Lenses

The most common type of defects in electron lenses are spherical aberration, chromatic aberration, axial astigmatism, and distortion and curvature of field-emission.

Spherical aberration – The electrons arriving at the lens are located at a shorter distance f_1 from the optical axis of the center of the lens. The aberration is characterized by:

$$\Delta f = f - f_1 \tag{2.4.1.9}$$

$$\Delta f = c_2 x^2 + c_4 x^4 + \textit{higher even powers of } x \tag{2.4.1.10}$$

$$r_s \approx [c_2 (f\alpha)^2]\alpha = C_s \alpha^3, \tag{2.4.1.11}$$

where c_2 and c_4 are replaced by a constant C_s.

Chromatic aberration – Chromatic aberration is caused by the spread in wavelengths in any beam direction. This spread is characterized by the spread in kinetic energy of the electrons and leads to different foci for electrons with different energies.

Defining:

$$\Delta f = A\ \Delta E_0 = \frac{f}{E_0}\ \Delta E_0 \tag{2.4.1.12}$$

we obtain:

$$r_c \approx \alpha\ C_c \frac{\Delta E_0}{E_0} \tag{2.4.1.13}$$

considering that we are approximating the lens with a thin lens and $C_c = f$.

Axial astigmatism –This is important for magnetic lenses because the pole piece material is not perfectly smooth such that the magnetic field varies giving rise to different focusing powers.

Distortion and curvature of field-emission – If every point on a picture is displaced outward, then the picture suffers what is called pincushion distortion. The distortion is described by the relation:

$$R = Mr + C_d r^3, \tag{2.4.1.14}$$

where r is the distance from the axis, and C_d is a constant.

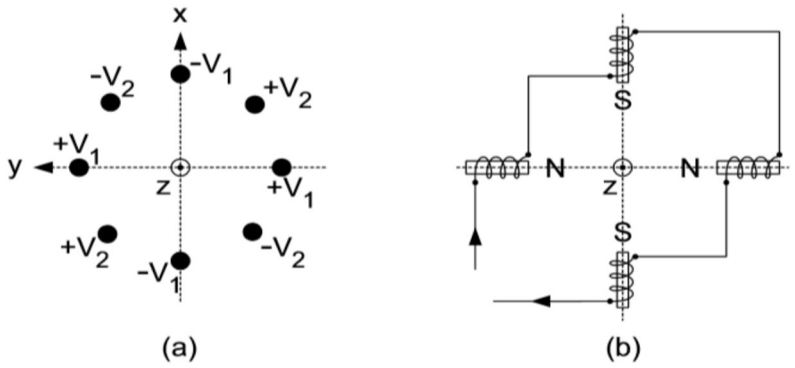

Fig 2.4.1.3. Axial stigmator (a) and the magnetic quadrupole for the axial stigmator (b) from Ref. [156]

2.4.2. Equipment Used at Carl Zeiss SMT GmbH

The condenser lenses control the size of the electron beam that controls the size of the nanostructures formed, while the objective lenses focus the beam onto the sample. Besides these two lenses extra equipment is used to enhance the equipment's capabilities, apertures that control the size of the beam, and scanning coils used to raster the beam onto the sample. The Gemini column used had a single condenser lens for controlling the electron beam, though the possibilities of combining the parts could provide higher focusing with multiple condenser lenses or nano-twin mirrors. The scanning electron microscope (Fig 2.4.2.1) used for deposition of the nanostructures was a microscope with a LEO 1500 series Gemini column producing a maximum field of view resolution of 1.0 nm at 20 kV, 2 mm down to 5.0 nm at 0.2 kV, in high vacuum, and 1.2 nm at 20 kV, 7.0 nm at 1 kV in variable pressure mode, with an acceleration voltage in the range 0.1 kV to 30 kV. The column, in our case, of Gemini type and denomination, is formed by the electron source (electron gun) and a set of lenses (condenser lenses for condensing the electrons, objective lenses for focusing of the electrons), placed in the vacuum under normal functioning conditions.

The SEM equipment with the Gemini column, as per product developer's specification is presented in Fig 2.4.2.1. The electron source is a Shottky field emitter, characterized by high beam brightness and low beam energy spread. The infrared CCD camera has a focusing distance of 1 mm to 50 mm with eight poles electromagnetic stigmator. The stage is a 5 axis eccentric stage with motorized movements on x, y in the range of 75 mm and z in the range of 55 mm.

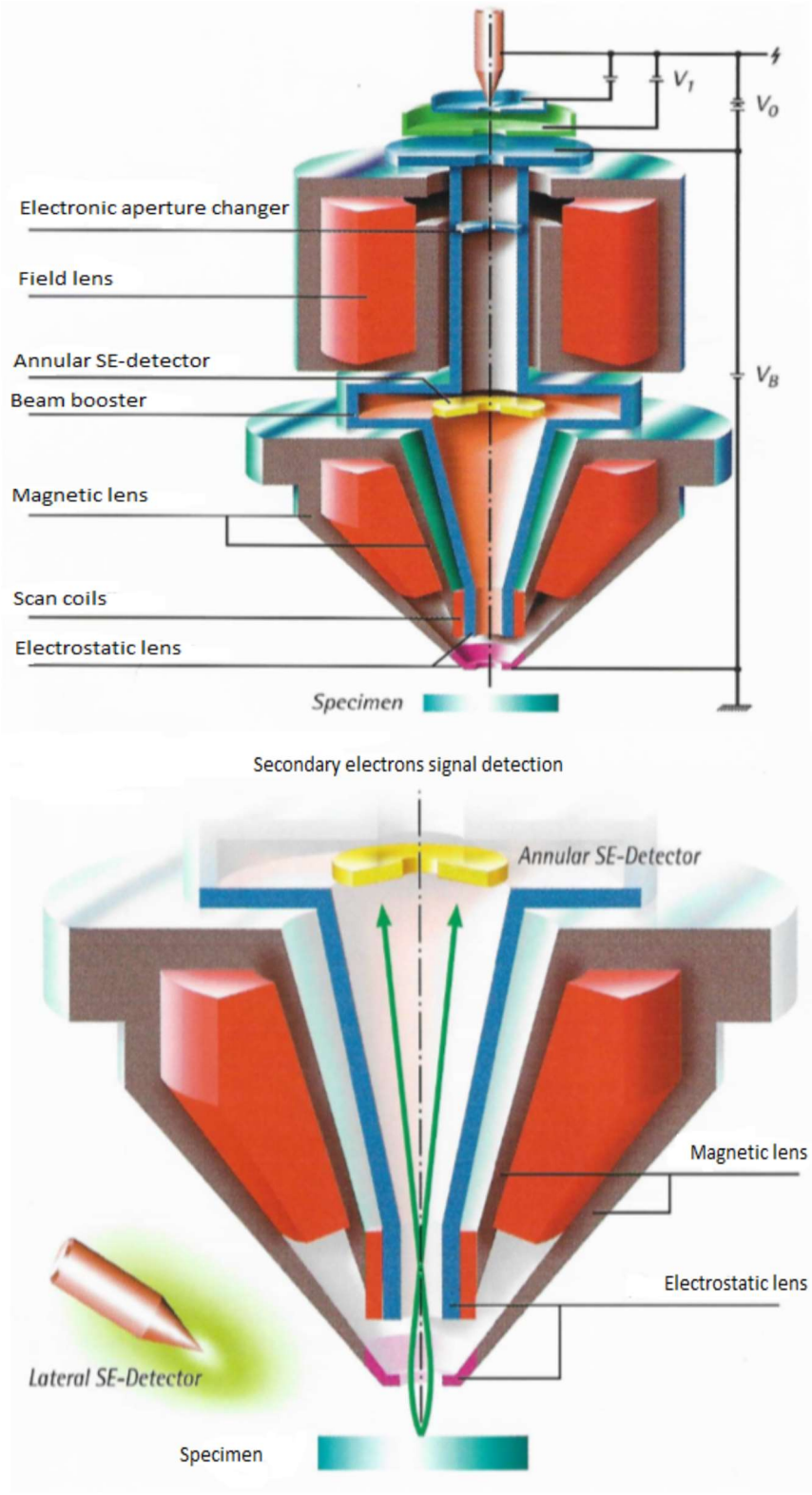

Fig 2.4.2.1. Operating principle of LEO 1500 series with GEMINI column (first upper); Secondary electron signal detection (second upper)

2.4.3. SEM - EDX

The Scanning Electron Microscopy with Energy – Dispersive X-ray Spectroscopy (EDS, EDX) is an imaging scanning technique that allows morphological analysis, as well as the elemental composition of the desired structure by focusing an electron beam onto a surface. Electrons in the target are excited in their inner shell and ejected leaving an electron hole in the electronic structure of the element. In principle, the area of analysis is isolated and scanned using the SEM that will provide an image, and by additional EDX measurement an elemental spectrum of that particular area is made.

Si	O	C
1.739	0.525	0.277

Table 2.4.3.1. Characteristic X-rays values for EDX voltage

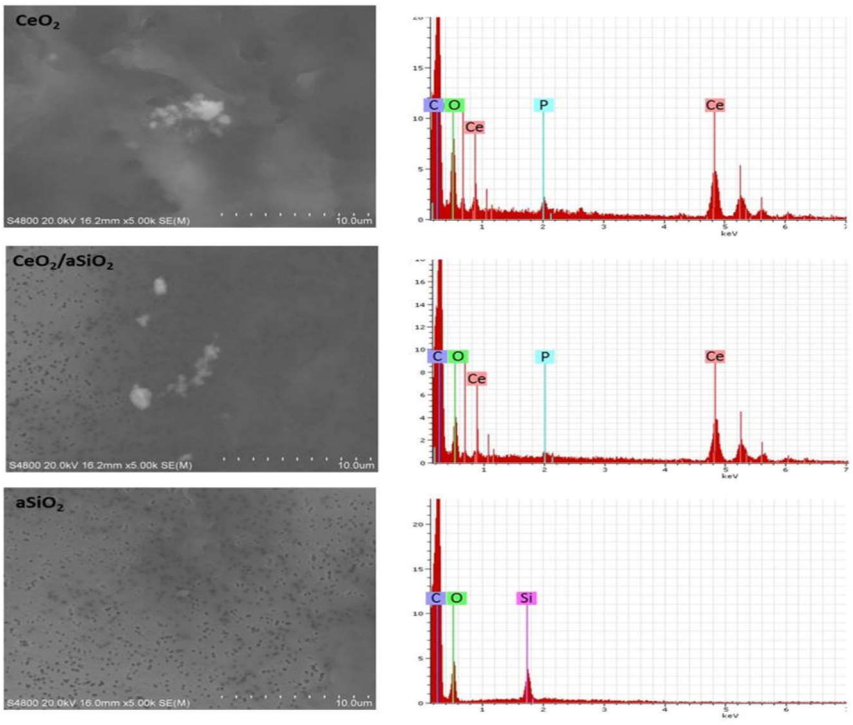

Fig 2.4.3.1. SEM with EDX image of amorphous silica coating on cerium oxide nanoparticles in Ref. [159]: Ma et al., Toxicol Appl. Pharmacol., 2015, 288(1):63-73

The EDX measurements beam settings used in these studies were a beam voltage of 5 keV and have been calculated according to relation (2.4.3.1) for the $Si(OEt)_4$ precursor. According to the EDX physics when an electron strikes a molecule or an atom, a hole is created in the inner shell and an electron from the outer shell will take its place emitting a set of characteristic X-rays specific to each element from the periodic table and with a characteristic acceleration voltage:

$$z_m = 0.033\ (E_0^{1.7} - E_c^{1.7})\ A/\rho Z \qquad (2.4.3.1)$$

For the elements in our compounds, we have the values of Kα (characteristic X-ray) presented in Table 2.4.3.1 with a resulting minimum accelerating voltage of 5 kV.

2.4.4 AFM – Atomic Force Microscopy

The atomic force microscopy (AFM) is used to measure the height and width of the nanostructures using the proprieties of repulsion and attraction between the AFM tip and the surface. The AFM tip is mounted on a very flexible joint that gives freedom of movement on all directions of the tip. There are five types of forces influencing the functioning of the AFM: van der Waals forces, electrostatic force, capillary forces, adhesive forces and double layer forces. Multiple imaging modes are available: contact DC mode, tapping and non-contact AC modes, tapping in air, tapping under liquid and true non-contact AC mode. The characteristic of the system considering both attractive and repulsive forces is presented in equation (2.4.4.1):

$$E^{pair}(r) = 4\varepsilon\left[\left(\frac{\sigma}{r}\right)^{12} - \left(\frac{\sigma}{r}\right)^{6}\right] \qquad (2.4.4.1)$$

where r is the separation between the tip and the surface, ε and σ are constants; σ is equal to the diameter of the atoms involved and is called the "hard sphere diameter".

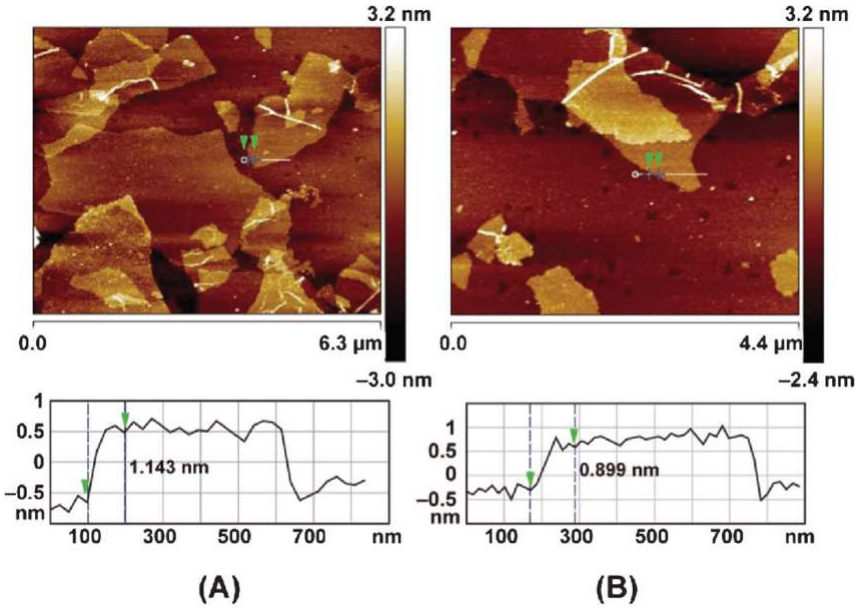

Fig 2.4.4.1 AFM images in Ref. [159] of graphene oxide (GO; (A)) and reduced graphene oxide (rGO; (B)) on mica substrate

2.5 Conclusions To Chapter 2

In this Chapter the experimental apparatus used in this thesis are described together with a brief guide to their operational principles. The method of Velocity Mapping Imaging (VMI) used to explore electron impact induced Dissociative Electron Attachment (DEA) is described and the VMI apparatus used as the University of Kent to measured DEA to selected FEBID precursors is presented. Calibration and text data for VMI or DEA to molecular oxygen is presented. The apparatus used to study electron induced desorption and DEA from absorbed films of a new FEBID precursor $Me_2Au(acac)$ is also described. Finally apparatus used in Carl Zeiss to produced FEBID structures and the SEM and AFM used to analyze the product nanostructures and their metal purity is presented. Gas-phase experimental studies of several FEBID precursors were undertaken using multiple tools at different laboratories, with greatest importance given to the VMI and LS/MS measurements. From the VMI analysis we could obtain molecular dynamics (MD) data from the DEA process, such as kinetic energy of the anions and the system, velocities of the anions, position and orientation (structural distribution of the molecule with implications to the symmetry associated with the excited state of the anion) and angular distributions, all as a function of electron energy and time representing continuous models of the resonances (fragmentation energies and spectrum), symmetry point groups and angles (ligands, orientation of the molecule, bond lengths and excited state), and kinetic energies and appearance energies for each particular ion (from the number of anion counts and their position on the detector). The mass spectrum (LS/MS), on the other hand, would present more limited data on MD, but high content information on the mass spectrum and resonances, and contribution of each anion in the fragmentation process; with higher resolution the research was carried forward to presenting clustering data of anions up to 40 eV. The surface science tools offer information on already deposited material and look into the parameters needed to obtain good deposition of the structures. AFM and EDX are two of the most common tools used in the deposition looking at the composition percentage of each elements in the deposited nanostructure, while the EDX offers valuable information on the height and width of the as deposited nanostructures. Different beam characteristics have been used with the SEM to obtain a complete analysis of the behaviour of the molecule with the change in the parameters. The neutral dissociation of the molecule on the surface was exemplified with the use of the quadrupole mass spectrometer in a high vacuum chamber at low temperatures using a cooling unit of the deposition Cu rod. The measurements were run with temperatures between 160 K and 298 K, and 0 eV to 25 eV. TPD and ESD spectrums were recorded for a Au compound, looking into the fragmentation patterns and experimental cross-sections. The results of experimental studies using this apparatus are presented in Chapter 4, 5 and 6 (VMI), Chapter 7 for surface studies and Chapter 8 for FEBID processing.

CHAPTER 3. COMPUTATIONAL TOOLS

The aim of this chapter is to introduce the computational codes and theories used to determine the characteristics of the precursor molecules in both the gas phase and interacting with a substrate. The first part of the chapter introduces the Quantemol-N and UKRmol codes and how they are used to calculate molecular cross-sections. This is followed by a summary of the DFT theory its limitations leading into higher level quantum mechanical simulations to determine molecular structures, vibrotational modes, excitation energies, etc. The final part of the chapter presents molecular dynamics simulations to extend the gas phase models to surface adsorption using the MBN software.

3.1 QUANTEMOL-N AND UKRMOL CODE

3.1.1 UKRMOL CODE

The UKRmol code has been developed to run scattering electron theory calculations for compounds up to 17 atoms by its integration into the Quantemol-N code. The Quantemol-N software compared to the rest of the Quantemol software family focuses on low electron energy calculations for a wide range of process in astrophysics, plasma fusion, ignition, and engines. A wide range of cross-sections can be run using the R-matrix calculations, from simple total cross-sections to rotational and vibrational cross-sections.

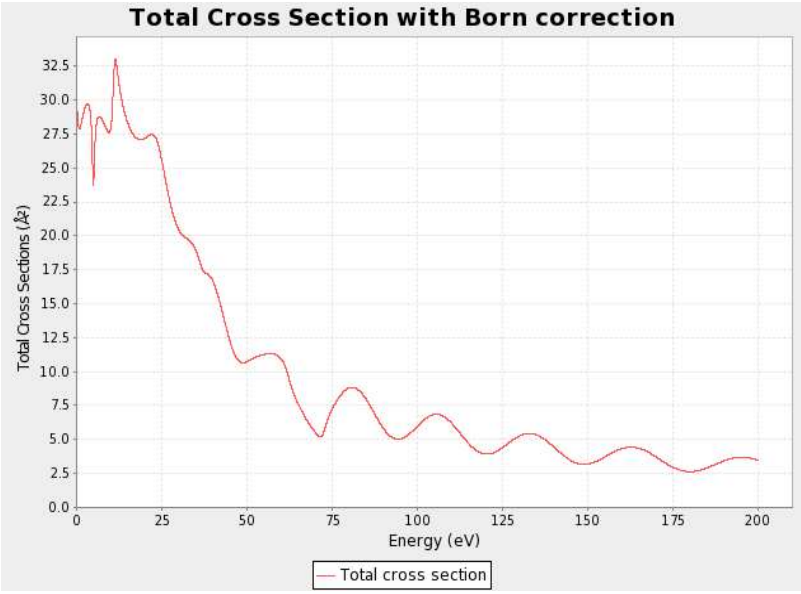

Fig 3.1.1.1. Total cross sections for SF_6 from Quantemol-N

The UKRmol code consists of two parts: UKRmol-in and UKRmol-out, as the R-matrix is divided into the inner region and outer region of the molecule, for which the radius is optimised for each individual structure. The program makes use of a number of routines, for example, the SWMOL3 that calculates the integrals between the GTO basis functions, SWORD that calculates the integrals, SWEDMOS used for orthogonalization of the orbitals, SWTRMO that transforms the integrals and CONGEN used for the configuration state functions for CI. The CONGEN and SWTRMO outputs are used for the Hamiltonian transformations in Ref. [55]. The schematics of the R-matrix process is presented in Fig 3.1.1.2 comprising of the processes related to the R-matrix simulations and refinement of the results

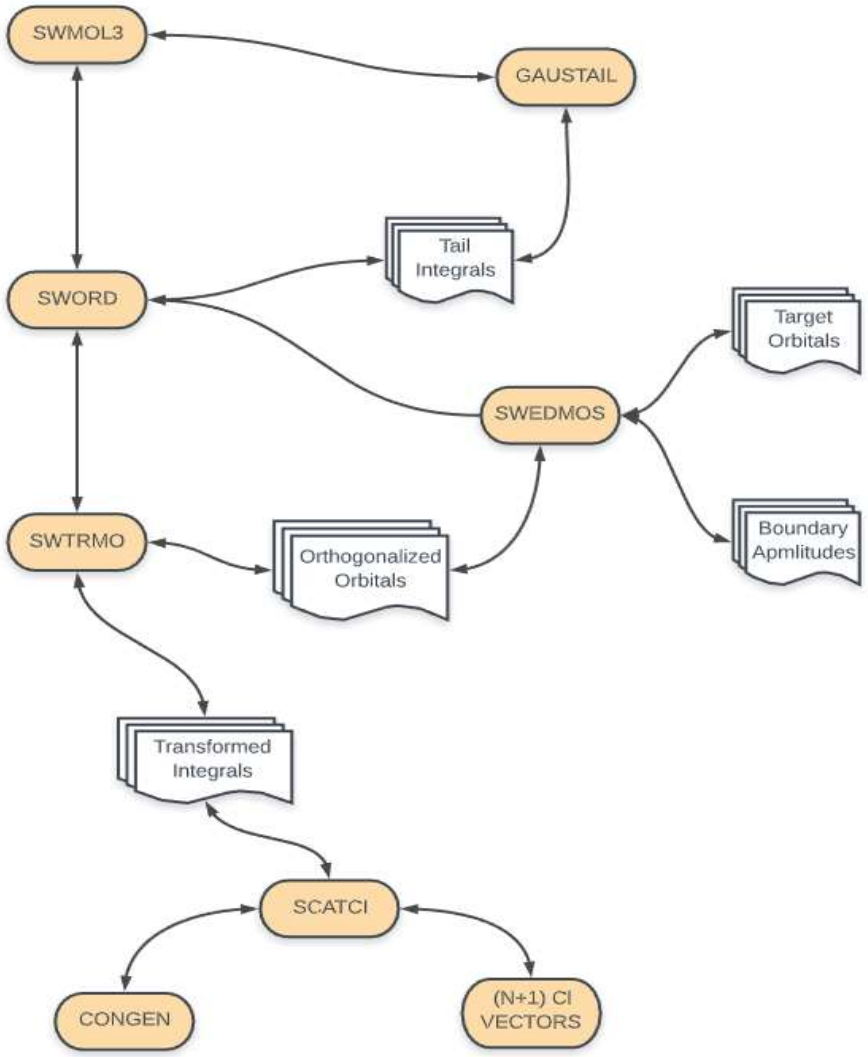

Fig 3.1.1.2. Carr et al 2012 [56] Quantemol-N algorithmic structure for cross-section determination

3.1.1.2 R-Matrix Calculations and Theory

The R-matrix calculations have been used integrated in different simulation software for cross-section determinations such as DUO [57], Quantemol-N [56], Quantemol-QEC [58] making use of additional GUI interfaces with software such as the MOLPRO quantum chemistry package. The R-matrix method divides the space into two regions: the inner region and the outer region with the conditions at the boundary.

The inner region Ref. [59] is characterized by the wave function and the integrals solving the target orbitals:

$$u_l^{int}(r) = \frac{\hbar^2}{2\mu a R_l(E,B)} u_l^{ext}(a) \sum_{j=1}^{N} \phi_j(r) \sum_{i=1}^{N} (C^{-1})_{ij} \phi_i(a) \quad (3.1.3.1)$$

determined from the radial Schrödinger equation and solving for the Hamiltonian H_l:

$$(H_l - E)u_l = 0 \quad (3.1.3.2)$$

$$H_l = T_l + V(r) \quad (3.1.3.3)$$

The outer region uses the boundary calculations for r, the radius of the inner region, equal to a constant "a". To solve the outer region function, the boundary properties need to be solved, knowing that these properties are the excited states energies.

$$V_{ij}(r) = \sum_{\lambda} \frac{\alpha_{ij}^{\lambda}}{r^{\lambda+1}} \quad (3.1.3.4)$$

$$\alpha_{ij}^{\lambda} = \left(\frac{2l_i+1}{2l_j+1}\right)^{\frac{1}{2}} C(l_i \lambda l_j;\ m_i m_\lambda m_j)\, C(l_i \lambda l_j; 000) Q_{ij}^{\lambda} \quad (3.1.3.5)$$

To optimize for the boundary conditions C(E, B)c = 0 needs to be solved and further to determine the cross-sections there is a need to determine the resonances.

$$B = L_l \quad (3.1.3.6)$$

The resonance energy Ref. [59] has the form:

$$E_R = E_{nl} - \Upsilon_{nl}^2 S_l(E_R) \quad (3.1.3.7)$$

with the width:

$$\Gamma(E) = 2\Upsilon_{nl}^2 P_l(E) \quad (3.1.3.8)$$

and the internal wave function close to the resonance:

$$u_l^{int}(r) = e^{i\left(\delta_l - \pi\frac{1}{2}\right)} C_l \left[\frac{\hbar v \Gamma}{(E_R - E)^2 + \left(\frac{\Gamma}{2}\right)^2}\right]^{\frac{1}{2}} \phi_{nl}(r) \qquad (3.1.3.9)$$

3.1.3 DEA Cross Sections of O_2

As a test of the Quantemol-N software ability to calculate DEA cross-sections, cross-section data for the molecular oxygen was run with the aid of the simulation software Quantemol-N and compared with the available literature. The parameters set for the simulation are the specificity value of 1556 cm^{-1} (0.192 eV) and the electron affinity of 0.451 eV, using a C1 molecular symmetry and a cartesian coordinates structure presented in Table 3.1.3.1.

Atom	X(Å)	Y(Å)	Z(Å)
O1	0	0	0
O2	0	0	1.21

Table 3.1.3.1. Cartesian structure of O_2 in XYZ coordinates

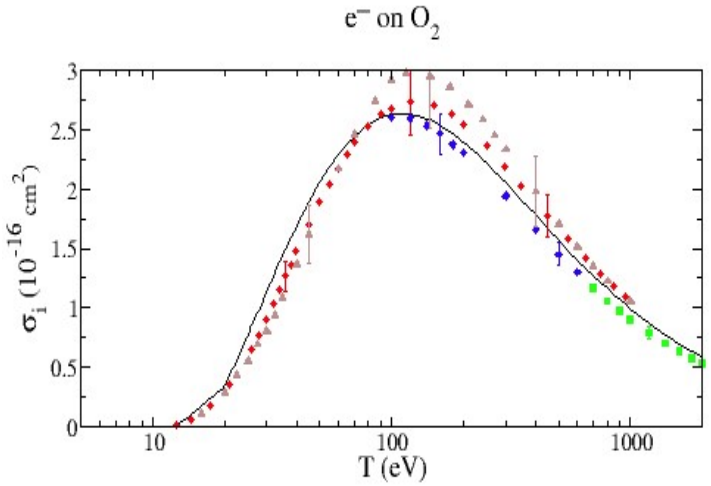

Fig 3.1.3.1 Total Ionization Cross Sections of O_2 from NIST Database: black continuous line (W. Hwang, Y.-K. Kim and M.E. Rudd, J. Chem. Phys. 104, 2956 (1996)), red diamond (D. Rapp and P. Englander-Golden, J. Chem. Phys. 43, 1464 (1965)), green square (B. L. Schram, F. J. de Heer, M. J. van der Wiel and J. Kistenmaker, Physica 31, 94 (1965)), blue diamond (B. L. Schram, H. R. Moustafa, J. Schutten and F. J. de Heer, Physica 32, 734 (1966)), brown triangle (E. Krishnakumar and S. K. Srivastava, Int. J. Mass. Spectrom. Ion Processes 113, 1 (1992))

The ground state of O_2 from Quantemol-N is $^1A_g^2$, $^2A_g^2$, $^3A_g^2$, $^1B_u^2$, $^4A_g^2$, $^2B_u^2$, $^1A_u^2$, $^2A_u^2$. The ground state symmetry applied is C_{2h} and a higher basis set was used, aug-cc-PVTZ, for the computation of DEA cross-sections. The total cross-section of O_2 is presented in Fig 3.1.3.2. The value of the cross-section in $Å^2$ close to zero is 92 $Å^2$. The total cross-section reveals multiple resonances between 0 and 12 eV corresponding to the excited states ^1A_g 0.0 eV, ^3B_g 2.76 eV, ^3A_g 4.17 eV, ^1B_g 4.34 eV, ^3B_g 4.48 eV, ^3A_g 5.04 eV, ^1A_g 6.15 eV, ^1B_g 6.33 eV, ^3B_g 8.06 eV, ^3B_g 8.66 eV, ^1A_g 9.05 eV, ^3A_g 9.13 eV, ^3B_g 9.50 eV, ^1B_g 9.64 eV, ^1A_g 10.37 eV, ^1A_g 10.60 eV and ^1B_g 10.90 eV.

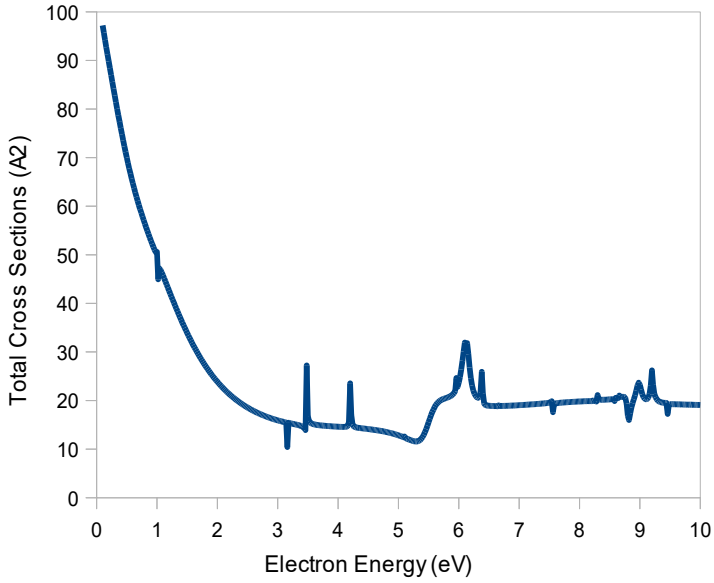

Fig 3.1.3.2. Total Cross Sections of O_2 from Quantemol-N

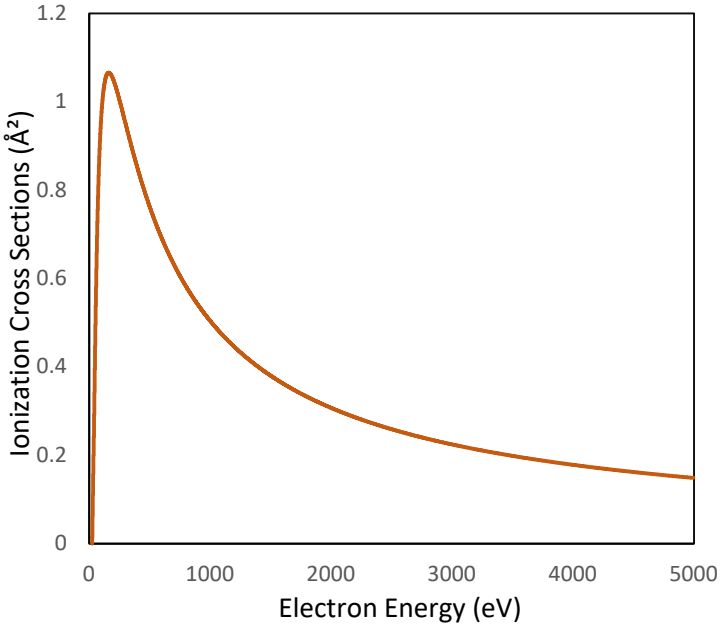

Fig 3.1.3.3. BEB ionization cross-sections from Quantemol-N

Quantemol-N software also allows total ionization cross-sections to be evaluated using the well-known BEB method (see Fig 3.1.3.3). The BEB cross-section data compared to the values from the literature and *NIST database* is presented in Fig 3.1.3.4, and the BEB cross-sections result of our simulation are presented in Fig 3.1.3.3 with lower maximum at 1.05 $Å^2$ and 1800 eV closer in values to the ones reported by Schram et al 1965 *NIST database*.

Joshipura and Mason 2019 [61] characterize the total cross-sections as well as the differential elastic cross-sections by CSP-ic, a method that uses the values (Q_{ion}/Q_{inel}) at three different energies for the Q_{ion}/Q_{inel} determined initially for the water molecule, the ionization threshold and the peak position of Q_{inel}. The reported cross-sections values from our Quantemol-N calculations fall closer to the values of Thompson 1995 [62], than to the values calculate by the CSP-ic method or data from Deutsch et al 2001 [61]. The comparison of all the cross-sections from Joshipura and Mason 2019 [61] and other sources with the one from Quantemol-N calculations is presented in Fig 3.1.3.4.

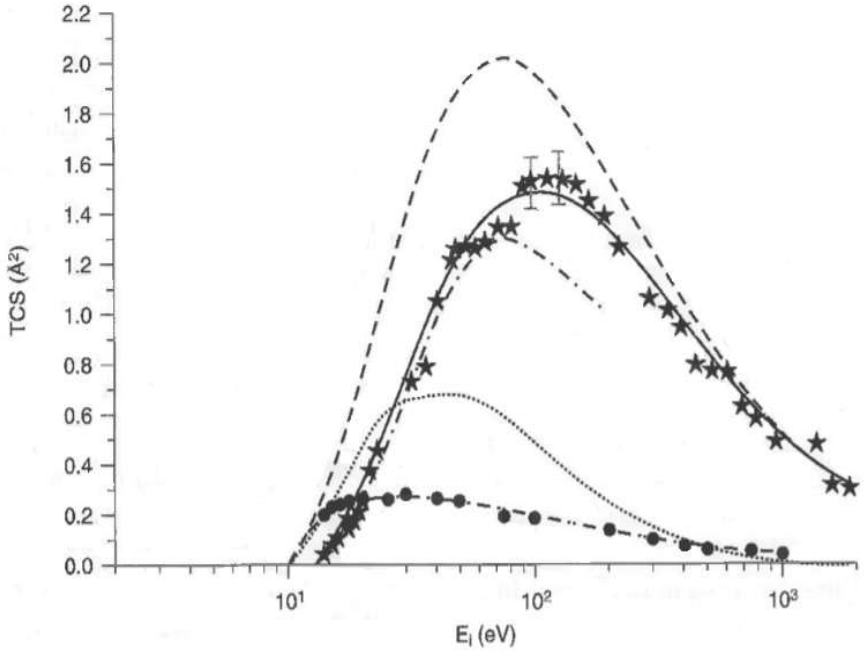

Fig 3.1.3.4. Cross-sections from Mason & Joshipura 2009 [61] for oxygen collision with electrons: dashed CSP-ic Mason & Joshipura 2009 [61], continuous Thompson et al 1995, star Deutsch et al 2001, dot dashed, and double dot dashed calculated by Mason & Joshipura 2009 and dot Johnson et al

The DEA cross-sections have a visible resonance close to the 6.5 eV, dissociation energy used experimentally by Nandi et al 2005 [51] and the present work, at a value of 6.1 eV and a shoulder around 6.8 – 7 eV, with further two peaks at 7.8 eV and 9 eV, all corresponding to the dissociation of the

molecular oxygen in the negative ion O^- and the neutral O. For an electron affinity of 0.451 eV, the maximum value of the cross-section is 0.48 $Å^2$.

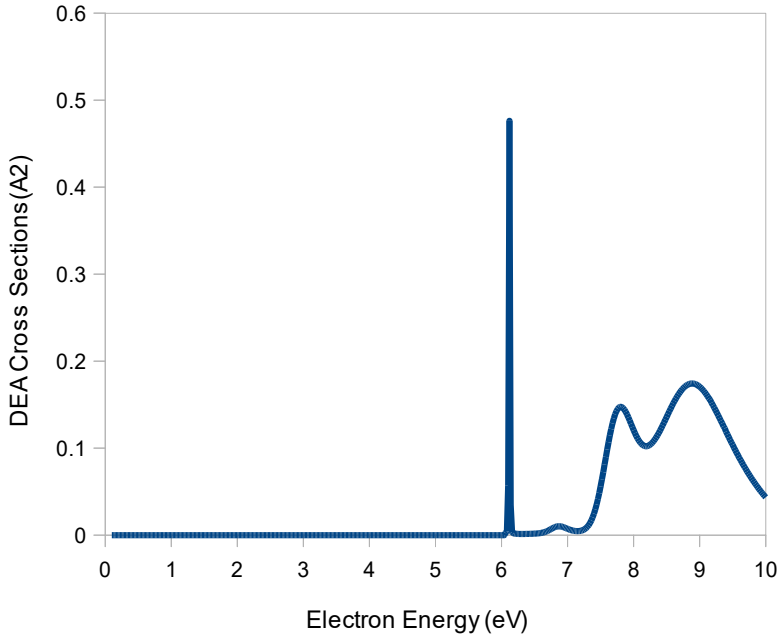

Fig 3.1.3.5. DEA cross-sections of O_2 from Quantemol-N

3.1.4 CH_4, SF_6 AND CF_4 CALIBRATION CROSS-SECTIONS

CH_4 is a common compound studied for its importance to astrophysics, stars formation and plasmas, on the other hand the SF_6 is used in generators, transformers, circuit breakers and is known to be a strong 'electron scavenger'. Similar to SF_6, CF_4 is used in plasma industry, both being well-known greenhouse gases used for refrigeration. As being relatively simple compounds, CF_4, SF_6 and CH_4 are used for the calibration of cross-sections values to unknown compounds, for which the cross-sections data is not available. The CH_4 cross-sections measured in Ref. [61] are total ionization cross-sections graphically presented in comparison with works from Gluch et al (2003), Vallence et al (1997), Tian and Vidal (1998), Adamczyk et al (1966), Chatham et al (1984), Djuric et al (1991), are smooth and have similar maximum values ranging from 3.4 – 4 $Å^2$. For CF_4 cross-section data, a total ionization cross-section from *NIST database* is compared to the cross-section data simulated with Quantemol-N. The same smooth features of the graph are observed with maximum values around 5 $Å^2$. The *NIST database* presents a collection of cross-sections from Nishimura (1999), Poll (1992), Bruce (1993), Rao (1997), Christophorou (1996). The values from the Quantemol-N simulation are similar to the ones of Rapp (1965), following the same smooth slope.

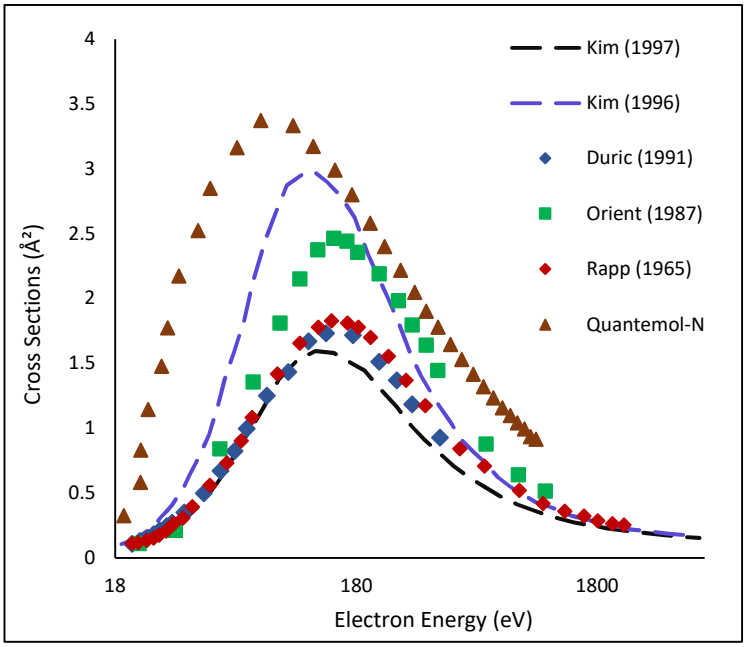

Fig 3.1.4.1. CH_4 total ionization cross sections, 0 to 5000 eV from NIST Database: black dashed Kim (1997), blue dashed Kim (1996), red diamond Rapp (1965), green square Orient (1987), blue diamond Duric (1991), brown triangle Quantemol-N

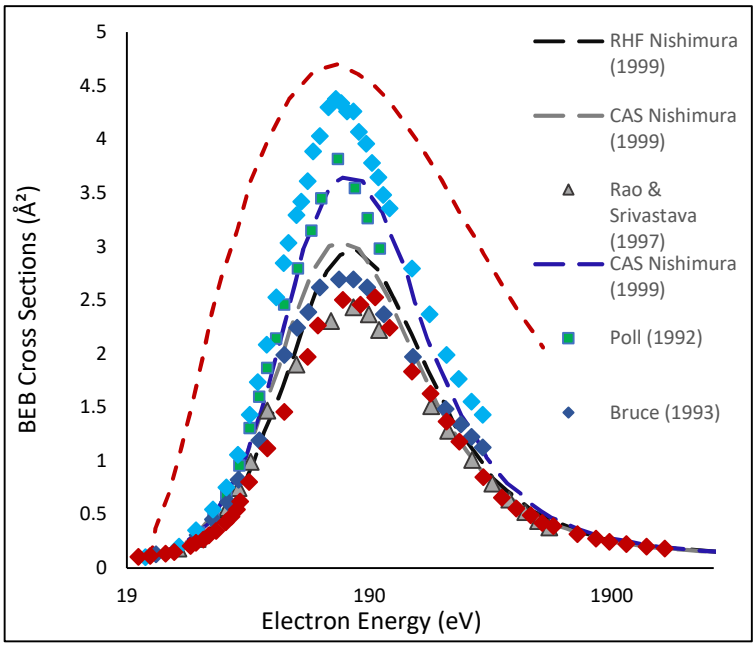

Fig 3.1.4.2. CF_4 total ionization cross-sections 10 to 5000 eV range, NIST Database: black dashed RHF wavefunction Nishimura (1999), blue dashed CAS wavefunction Nishimura (1999), grey dashed CAS wavefunction Nishimura (1999), red diamond Nishimura (1999), green square Poll (1992), blue diamond Bruce

(1993), grey triangle Rao & Srivastava (1997), light blue diamond Christophorou (1996), red dashed Quantemol-N

The SF_6 cross-sections from Quantemol-N were compared to the SF_6 cross-sections from NIST database, where multiple cross-sections have been presented from Ali (2000), Margreiter (1990), Rapp (1965), Margreiter (1992). The cross-sections have similar amplitudes in the range of 7.5 Å², with smooth curves falling under 50 %, close to 1000 eV.

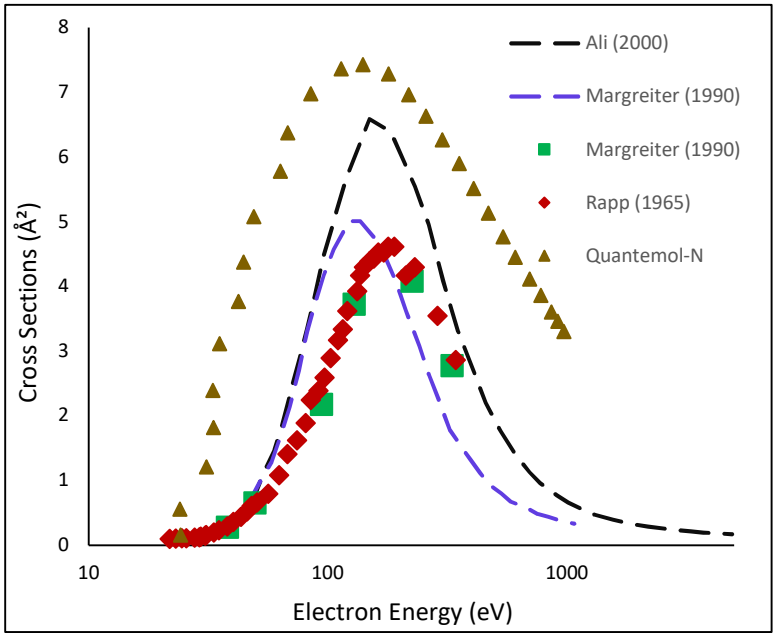

Fig 3.1.4.3. SF_6 total ionization cross-sections: 5 to 5000 eV range, NIST database 2019: black dashed Ali (2000), dashed blue Margreiter (1990), red diamond Rapp (1965), green square Margreiter (1990), brown triangle Quantemol-N

3.2 Density Functional Theory Calculations

3.2.1 Density Functional Theory Overview of Theoretical Background

The energy as a solution of the Schrödinger equations based on Born-Oppenheimer approximation is given by the relation (3.2.1.1):

$$\hat{H}\,\Psi(r_1, r_2, \dots, r_N) = E\,\Psi(r_1, r_2, \dots, r_N) \qquad (3.2.1.1)$$

where $\hat{H}$ is the Hamiltonian operator equal to the sum of the kinetic energy, interaction with the external potential V_{ext} and electron-electron interaction V_{ee}.

In the Hartree-Fock theory, Ψ is the product of the electron functions Φ_i each depending on a single electron, and replaced in the initial Schrödinger equation we obtain the Self-consistent Field (SCF) equations where the classical Coulomb energy is written based on orbitals (ϕ) and exchange energy:

$$[-1/2\nabla^2 + V_{ext(}r) + \int\rho(r')/|r-r'|\ dr'] \Phi_i + \int V_x(r, r')\ \Phi_i(r')dr' = \varepsilon_i\ \Phi_i\ (r) \quad (3.2.1.2)$$

As result the exchange energy in the Hartree-Fock energy is exact, but it is lacking correlation energy.

The Hamiltonian operator, based on the Hohenburg-Kohn theorem, can be resolved only by the electron density, where the second part of the theorem is defined by:

$$\int\rho t(r)\ dr = N \quad (3.2.1.3)$$

and is a restriction to the ground states that according to this are expressed only by the exact ground state density leading to the development of the density functional theory (DFT).

Density functional theory (DFT) is a method developed in 1965 having its roots in Fermi-Dirac rationalism and was put into practice by the inclusion of the Kohn-Sham formalism (KS-DFT). Other developments on this framework have been included over the years; the example of Bagayoko, Zhao and Williams 1999 [62] and Amsterdam density functional code in Ref. [63] being only a few of the many adaptations to it.

The fundamental statement of the density functional theory is presented in relation (3.2.1.4):

$$\rho\ |E(\rho) - \mu\ (\int\rho(r)dr - N)\ | = 0 \quad (3.2.1.4)$$

where ρ represents the density of electrons/states.

Exclusive to DFT is the exchange correlation function expressed by relation (3.2.1.5):

$$E_{xc}(\rho) = (T(\rho) - T_s(\rho)) + (V_{ee}(\rho) - V_H(\rho)) \quad (3.2.1.5)$$

is based on the energy being defined by the three terms, kinetic energy, interaction with the external potential and electron - electron interactions as:

$$E(\rho) = T(\rho) + V_{ext}(\rho) + V_{ee}(\rho) \quad (3.2.1.6)$$

The local density approximation, LDA, refers to the $E_{xc}(\rho)$ that is explained by the Hartree potential and the density of electrons as:

$$E_{xc}(\rho) \approx \int\rho(r)\ \varepsilon_{xc}\ (\rho(r))\ dr \quad (3.2.1.7)$$

The GGA approximations, $\nabla\rho$, and hybrid GGAs (relation (3.2.1.9)), and for better adaptation meta-GGAs, $\nabla^2\rho$, are introduced and account for the exchange hole as being always negative, and applied to relation (3.2.1.7) we obtain the local density approximation $E_{xc}(\rho)$:

$$E_{xc}(\rho) \approx \int \rho(r)\, \varepsilon_{xc}\, (\rho(r), \nabla\rho)\, dr \qquad (3.2.1.8)$$

$$E_{xc}(\rho) \approx a\, E_{Fock} + b E_{xc}^{GGA} \qquad (3.2.1.9)$$

The novelty of BZW and BZW-EF methods over classical DFT come with the criteria used for adding the reference orbitals in Ref. [64 - 65] and obtaining the absolute minima of the occupied energies by using the Rayleigh theorem where the classical theory was not able to give accurate values. For BZW, depending on the added orbitals (s, p, d, f) the dimension of the Hamiltonian increases with 2, 6, 10 and 14, where enhanced BZW-EF defines the criteria of first polarization, as p, d, f orbitals would go first in comparison to s orbitals. On the other hand, Jarlborg et al 2011 [67] comes with an adaptation of the local density approximation to local spin density approximation and the characterization of the muffin tin orbitals (LMTO), where they calculate the total energy for systems with N-1, N and N+1 electrons. They applied it to $Nd_{2-x}Ce_xCuO_4$, where he used DFT for the relaxation energies of the electrons from an occupied excited state to a hole and for f-bands electrons where these electrons appear far from the Fermi level energy (E_F). The Amsterdam density functional code with Becke - Perdew functional and TZP basis set in Ref. [63] have been used to calculate structural and vibrational data for predictions of photo detachment. Other advances in the Schrödinger equations are employing the use of the variational quantum Monte Carlo approach in Ref. [57 - 58]. To simplify and to reduce the number of steps, it is sought to avoid the solutions of the Schrödinger equations and introduce the density functional theory matrix that uses only the density probability of only two particles (the r_1 and r_2 from relation (3.2.1.2)) for the computation of 3N-dimensions wavefunctions.

3.2.2 GAUSSIAN 16 SOFTWARE

For the purpose of the DFT calculations reported in this thesis, Gaussian 16 software was used. Gaussian 16 offers a wide range of molecular computations of molecular structures, vibrational frequencies, chemical reactivity, prediction of transition structures, potential energy surfaces and stationary points, reaction energies and barriers as well as excited states using molecular mechanics methods, semi-empirical methods, the Hartree-Fock method, the DFT method, the CASSCF method, Møller-Plesset perturbation theory, coupled cluster theory, Brueckner doubles, outer valence Green's function, high accuracy energy models and excited states methods. Two types of calculations can be run: open shell

and closed shell. Open shell systems are usually unrestricted systems using different orbitals for the spin-up and spin-down electron pair, denominated by U, while closed shell systems are restricted systems forcing each electron pair into one single spatial orbital, denominated by R. The approximation methods used in the Gaussian 16 software are: Hartree - Fock Self-Consistent Field (HF), Becke - style 3-Parameter Density Functional Theory (B3LYP), 2nd Order Møller - Plesset Perturbation Theory (MP2), 4th Order Møller - Plesset Perturbation Theory (MP4), Quadratic CI (QCISD(T)). Single point energy calculations are used to check the molecular structure of a molecule to be further used for geometry optimization and to obtain accurate values of the energy or when other type of simulation is rendered impossible. Multiple options on advancing single point energy calculations are available: lower and higher five orbitals, or full field of orbitals, tight SCF computing the energy using strict convergence criteria, or predicting NMR properties.

The optimization of the molecular system is based on finding the energy minima of the potential surface by using the convergence criteria. For the system to be optimized, from the initial input geometry, the potential surface is calculated and the point of lowest energy, where all forces convergence to zero, is called the global stationary point characterized by zero gradient, and the state of the system denominated converged state or convergence. The convergence criteria are setting the maximum component of the forces cut-off to 0, root-mean-square of the forces to 0, the calculated displacement to be smaller than 0.0018 and the root-mean-square of the displacement to be smaller than the cut-off value of 0.0012. Another option in the optimization of the system is locating the transition states of the structures, essentially providing an intermediate geometry between the reactants and products of the optimization of the reactants. Frequency calculations is one of other options when using DFT to determine properties of molecular systems, with the purpose of predicting infra - red (IR) and Raman spectra of molecules, compute force constants for geometry optimization, identify stationary points on the potential energy surface and to compute zero-point vibration and thermal energy corrections. The error obtained in the raw frequency generation from computations at Hartree - Fock level are in the range of ~10 – 12 %. In this study a scaling factor of 0.8929 has been applied. Thermochemistry information at certain temperatures and pressures such as thermal energy corrections, heat capacity and entropy are obtained running frequency-optimization jobs, as well as polarizability and hyperpolarizability tensors. The thermal energy corrections used are zero-point thermal corrections (for vibrations at energies close to 0K) and thermal energy corrections to account for the effects of molecular translation, rotation and vibration at the specified temperature and pressure. Different model chemistries are defined for selected basis sets, based on the Hartree-Fock functionals and Schrödinger equations, presented schematically in Table 3.2.2.1. The types of basis sets used depends on the size of the molecule or molecular system to

be analysed, divided by their size in minimal basis sets (containing the minimum number of basis functions for each atom), split valence basis sets (uses two sizes of functions to define each orbital), polarized basis sets (basis sets that allow orbitals to change size, but not to change shape), diffuse functions (occupy a larger region of the space), high angular momentum basis sets (add multiple polarized functions to the triple ζ basis set), post-third-row atoms basis sets (for large atoms, beyond the third line in the periodic table).

	Electron correlation →						
	HF	MP2	MP3	MP4	QCISD(T)	….	Full CI
Minimal STO-3G							
Split Valence 3-21G							
Polarized 6-31G(d)							
6-311G(d,p)							
Diffuse 6-3111+G(d,p)							
…							
∞	HF Limit					….	Schrödinger Equation

Table 3.2.2.1. Basis set schematics from the smallest to the largest, taken from Ref. [67]

The functions used for model chemistries and basis sets are Gaussian - type atomic basic functions with the general form given in relation (3.2.2.1):

$$g(\alpha, \check{r}) = c\, x^n y^m z^l e^{-\alpha r^2} \quad (3.2.2.1)$$

where the exponent α defines the size of the function.

The linear combination of many Gaussian - type atomic basic functions from the basis functions used in the basis sets for structure calculations is characterized by:

$$\chi_\mu = \sum_p d_{\mu p}\, g_p \quad (3.2.2.2)$$

where $d_{\mu p}$ are fixed coefficients in the basis set.

All calculations run at a lower-level (see Table 3.2.2.1 for reference) HF, MP2, MP3, MP4 and the more advanced versions of MP4, MP4(DQ) and MP4(SDQ), included in the MP4(SDTQ) calculations.

The open shell molecular complexes are used for calculating unpaired electrons, with the output in two α and β sets of Hartree-Fock matrices:

$$\Phi_i^\alpha = \sum_\mu c_{\mu i}^\alpha\, \chi_\mu \quad (3.2.2.3)$$

$$\Phi_i^{\beta} = \sum_{\mu} c_{\mu i}^{\beta} \chi_{\mu} \quad (3.2.2.4)$$

There are multiple theoretical methods that can simplify, adapt and correct the calculations by using different methods: semi-empirical methods (simplify the approximation to the Schrödinger equation; best known methods are AM1, PM3, MNDO), electron correlation and post - SCF methods (add correlation corrections to the basic Hartree - Fock model – the energy contributions from the electrons interacting between each other; Møller – Plesset perturbation theory [MP2, MP3, MP4, MP5], quadratic CI energies [QCISD, QCISD(T), QCISD(TQ)], coupled cluster methods [CCD, CCSD, CCSD(T)], Brueckner doubles energies [BD, BD(T), BD(TQ)]), the MPn methods, coupled cluster and quadratic configuration interaction methods, density functional theory (partition the electronic energy into components – kinetic energy, electron - nuclear interaction, the Coulomb repulsion, exchange – correlation accounting for electron – electron interactions; based on functionals – local, gradient - corrected). Important for the excited state calculations are conical intersections. The calculations are made for non-adiabatic effects and non-crossing rule, where more than two electronic states can be degenerate. By definition, the conical intersection (Fig 3.2.2.1) is the intersection between two electronic states that have different symmetries, accidentally allowed symmetry. The conical intersection between two electronic states is represented through the Hamiltonian matrix:

$$\begin{pmatrix} H_{11}(\vec{R}) & H_{12}(\vec{R}) \\ H_{12}(\vec{R}) & H_{22}(\vec{R}) \end{pmatrix} \quad (3.2.2.5)$$

Where only two states are calculated by Hamiltonian matrix in a real spatial wavefunction configuration, the number of degrees of freedom reduces to two and two conditions need to be fulfilled: $H_{11}(R) = H_{22}(R)$ and $H_{12}(R) = 0$ in Ref. [68], and the resulting conical intersection is a single R_x point. The components of R are varied, and the two components define a two-dimensional subspace called a branching space in Ref. [69]. The branching space is defined by two vectors, the gradient difference (x_1) and interstate coupling vectors (x_2):

$$x_1 = \delta(E_2 - E_1) / \delta\xi \quad (3.2.2.6)$$

$$x_2 = < C^i_2 \mid \delta\hat{H}_e / \delta\xi \mid C_1> \quad (3.2.2.7)$$

where ξ is the vector of displacements of the nuclei, $\hat{H}_e$ is the Hamiltonian operator, C_i are the configuration interaction eigenvectors.

The existence of conical intersections in polyatomic molecules was first presented by Neumann and Wigner 1929 [71], and similar to Renner-Teller effect (Fig 3.2.2.1) using the potential energy surface topology similar in orbital degenerate molecules, the Jahn-Teller conical interactions describe the

photochemical processes and spectroscopy of molecules using the quadratic expansion in curvilinear coordinates (second order degeneracy), where the decay from the minimum energy point of crossing is the dominant process. Neumann and Wigner theorem states that two points are independently varied to obtain a degeneracy eigenvalue. Further Jahn-Teller (1937) defines the existence of non-totally symmetric vibrations that lift the degeneracy and lower the symmetry. According to that, a molecule for which the electronic state is degenerate, would be on a conical intersection between the potential energy surfaces of the degenerate electronic state (example, intersection between A_1 and B_2 in C_{2v} symmetry).

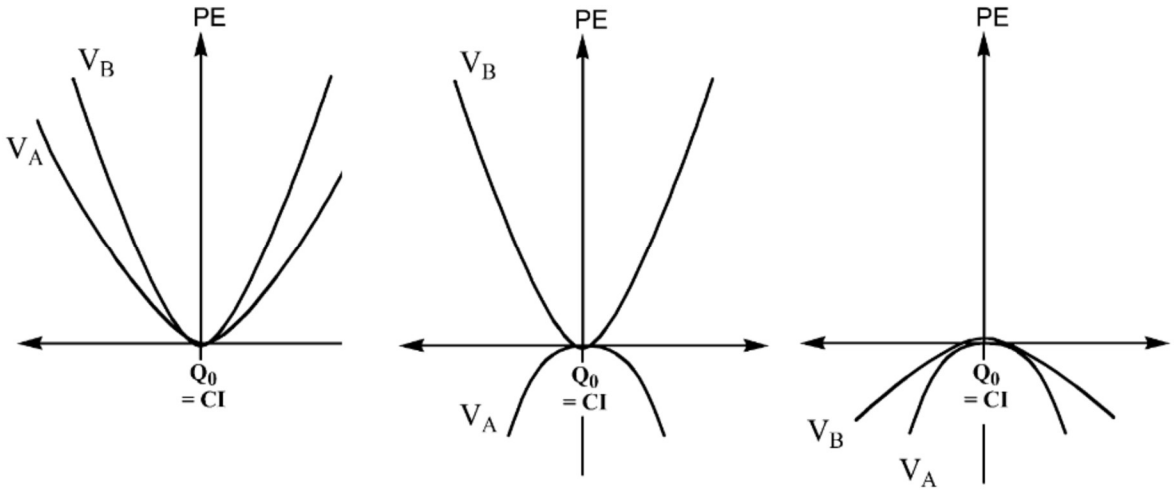

Fig 3.2.2.1. Renner-Teller effect, from left to right, type I to III, from Ref. [72]

The CASSCF model for calculations was developed on the definition of an active space comprising the active orbitals and free electrons involved in the excitation process. Methods of Newton-Raphson and Hartree-Fock matrices simplifying calculations at the Hessian level are used for determining the active space and modelling of the excited states, ground state geometry and chemical reactions in Ref. [71]. For our calculations and modelling of $Pt(PF_3)_4$, basis sets as B3LYP, LANL2DZ and methods as MP2, HF, MP4 were used. A first CI calculation and an initial CASSCF were run for determining the active space.

3.3 MBN Explorer (Molecular Dynamics at Surface Simulation Package) at MBN Research Center GmbH

"MBN" from the acronym "MBN Explorer" stands for Meso-Bio-Nano systems and is the software program used to run a range of molecular dynamic simulations of our FEBID precursors. IDMD that stands for Irradiation Driven Molecular Dynamics is one of the newest features integrated into the MBN

Explorer package and is particularly useful in the simulation of FEBID and helps us compare our experimental results with the results obtained from simulations. The MBN Explorer package makes use of tools such as many-body theory, DFT, TDDFT, collision theory to simulate processes based on Born - Oppenheimer theory in Ref. [160] in femto-seconds time steps. The software supports classical molecular dynamics, Monte-Carlo simulations with applications to large molecular biological and nano-systems, nanostructured materials, hybrid materials, gases, liquids, solids, atomic clusters, fullerenes, nanotubes, polypeptides, proteins, composite systems and nanofractals [160-161].

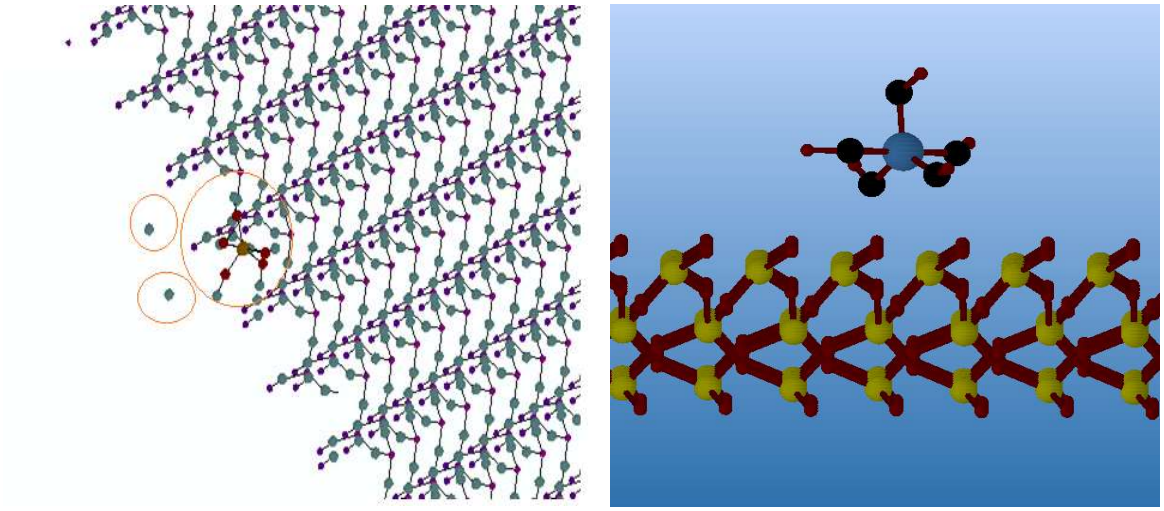

Fig 3.3.1. $Fe(CO)_5$ on SiO_2 substrate, MBN diffusion simulation

The effects of induced chemistry on the systems are the appearance of secondary electrons, ions, radicals or reactive species and excited or ionized molecules that can further react. The probability of the dissociation process in the molecules is governed by the cross-section values with the probability of attachment characterized by the irradiation parameters: time, incident energy and angle in Ref. [161]. As presented in Chapter 2 the cross-sections are elastic scattering, inelastic scattering, vibrational and rovibrational excitation or dissociative electron attachment cross-sections. The molecular systems under irradiation are characterized by molecular bond breakage, redistribution of electrons through dissociative electron attachment and electron capture, reorganization of free radicals resulting new compounds, structural and morphological transformations in vicinity of the substrate with the formation of chains, clusters and organized structures in Ref. [161]. For FEBID simulations, the theory of classical molecular dynamics cannot be applied as the systems and processes are characterized by induced chemical reactions. Classical molecular dynamics is mostly used for simulations with packages such as CHARMM, AMBER, GROMACS and NAMD; the MBN Explorer implemented the use of these packages with its functions but uses extra functions for creating the environment of the induced chemical

transformation on the structure, bonds, system's energy and resultant reactants. In Chapters 9 we report results of MBN Explorer FEBID simulations of $Fe(CO)_5$ precursor deposited on Au(111) and SiO_2.

3.3 Conclusions To Chapter 3

All the gas-phase analysis tools presented in Chapter 2 are combined to offer a complex view of the processes that take place at molecular and atomic level as result of a collision between an electron and a molecule in neutral state. Combined studies of VMI are run with Quantemol-N cross-sections simulations, while density functional theory studies are complemented with the use of VMI, LS/MS, mass spectrometry and cluster analysis (Chapter 3).

The DFT and ab-initio studies (Hartree – Fock level of theory) are used in conjunction with the VMI to determine point bond dissociation energies, fragmentation energies (using reaction products and resultants or complexation energies), for structure determination and optimization of the charged ions (anions) or the parent compounds, potential energy surfaces (PES), determination of electron occupation of the orbitals involved in the transitions and fragmentation (density of states (DOS) and partial density of states (PDOS)), calculation of excited states of the molecules using time - dependent density functional theory and CIS, excited states that are involved in the process of fragmentation, exciting the molecule from ground states to higher excited states in DEA, DI and DD, as well as electron affinities of the anions and vertical electron attachment/detachment energies and vertical electron affinities of parent molecules and anions. The Quantemol-N code was used specifically for cross-section determination at DEA, for particular molecules to complement the VMI and LS/MS studies of the fragmentation of the precursors, obtaining a set of cross-sections, DEA cross-sections, total cross-sections, excitation cross-sections and ionization cross-sections. Another set of tools related to surface and deposition studies is presented, that provides an insight into the processes that take place on the substrate and at the surface. The wide range of tools used for FEBID precursor deposition and deposition analysis have been described in this chapter, from SEM MeRiT tools to EDX and AFM, and surface science tools such as quadrupole mass spectrometers (QMS) running temperature programmed desorption (TPD) and electron stimulated desorption (ESD) studies of the neutral species from the surface. These experimental tools are complemented by simulation tools such as MBN Explorer and DFT/ab-initio calculations of binding energies to substrate molecules offering a broader view to what happens at the surface on the substrates when precursors are deposited on them, and Monte Carlo electron trajectories simulations using the CASINO code.

SECTION 1. GAS-PHASE STUDIES OF FEBID PRECURSORS

CHAPTER 4. STUDIES OF TI AND SI BASED COMPOUNDS USED AS PRECURSORS IN FEBID; GAS-PHASE STUDIES

Tetraethyl orthosilicate ($Si(OEt)_4$ (TEOS); with characteristic linear formula $Si(OC_2H_5)_4$) and Titanium(IV) isopropoxide ($Ti(OPr)_4$ (TTIP); with characteristic linear formula $Ti(OCH(CH_3)_2)_4$), are two compounds that have been extensively used as precursors for deposition in mask repair and for substrates deposition by the focused electron beam induced process (FEBID) of the TEOS/TTIP to form SiO_2 and TiO_2 on the surface. $Ti(OPr)_4$, mixed in different ratios with acetylacetone or other stabilizers, is used for the deposition of TiO_2 thin films and substrates. There has been an increased interest in the creation of TiO_2 thin films because of its use in the construction industry for coating the skyscraper windows with a film that reacts to a band of light equal to the band gap of the TiO_2 of ~ 3.2 eV, and for the tunnel lamps that coated with $Ti(OPr)_4$ emit light at 3 $mWcm^{-2}$, a value sufficient for maintaining the cleanliness of the lamp surfaces from car debris in Ref. [117]. In the context of this research, $Ti(OPr)_4$ and $Si(OEt)_4$ have been used as FEBID precursors to fabricate nanostructures with Ti and Si content between 13 – 22 %.

Earlier uses of $Si(OEt)_4$ and $Ti(OPr)_4$ were in sol-gel processes [117, 244-245] where hydrolysis of $Si(OEt)_4$ and $Ti(OPr)_4$ in combination with acids and acetones led to the formation of dry sol-gels, powder sol-gels and fluid sol-gels. Widely used for titanium coatings [246], $Ti(OPr)_4$ is obtained through the deposition of nanostructures by low pressure chemical vapor deposition (LPCVD) with good results. Thermal treatments of $Ti(OPr)_4$ [247] are used to obtain TiO_2 with temperatures in the range of 800 °C – 900 °C. Newer applications of $Ti(OPr)_4$ come in the field of dye-sensitized nanocrystalline TiO_2 with electrolyte interfaces [248]; where the electrolyte is in liquid state with the linear formula CH_3CN, while the sensitized dye used are $Ru(dye)N_3$. Graphene based nanocomposites [252] using hybrid nanostructures based on TiO_2 photocatalysis processes are one of the newest applications of the use of titanium oxides. Experimental work on graphene based nanocomposites has been carried at BESSY synchrotron SoLiAS beam light to determine the binding energies of the adsorption of CH_3CN to TiO_2. Nanocomposites have been obtained in the study of Petrella et al [248] in 2005 using hydrolysis [249] of created rodlike and thin films of colloidal TiO_2 nanocrystals by MEH-PPV of the $Ti(OPr)_4$ precursor. Later studies by Yokoi et al [250] from 2011 have analysed the silica nanospheres obtained from $Si(OEt)_4$ through hydrolysis of the precursor and sublimation with acidic compounds in the regrowth process of the particles and homogenization of the particles' size.

Other applications of the TiO_2 and SiO_2 - nanoparticles focus on the drug delivery [252] at the nanoscale and cancer treatment [253]. The SiO_2 – nanoparticles can be administered through the blood stream carrying drugs to the affected zones, considered safe through the degradation of the SiO_2 in silicilic acid by its solubility in H_2O contributing to good functioning of the bone processes. In 2012, the work of Rosenholm et al [254] states that preclinical trials have begun on the application of SiO_2 in cancer therapy, while newer sources [255] look into a wide range of benefits coming from injecting SiO_2 to affected places in irradiation cancer therapy. The DEA mass spectrum of $Si(OEt)_4$ and $Ti(OPr)_4$ were recorded at Comenius University, Bratislava, and further analysis was performed using velocity sliced map imaging apparatus at the University of Kent collecting anions angular and kinetic data. SEM deposition of these materials in surfaces was studied using Clone 1 apparatus at Zeiss Gmbh, Roβdorf, Germany, as one of the main precursors for their mask repair processes; these results are discussed further in Chapter 7. The aim of this chapter is to investigate DEA of $Ti(OPr)_4$ and $Si(OEt)_4$ by using velocity map imaging and mass spectroscopy tools (quadrupole mass spectroscopy). Experiments revealing electron scattering resonances in the formation process of negative ions at low electron energies are revealed with implications to the FEBID process.

4.1. Ti(OPr)$_4$

4.1.1 Introduction of Titanium (IV) Isopropoxide

.

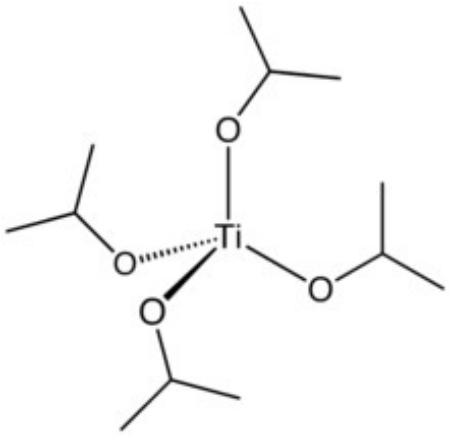

Fig 4.1.1.1. $Ti(OPr)_4$ molecular bar structure

IR study of Titanium (IV) isopropoxide. The structure of $Ti(OPr)_4$ (Fig 4.1.1.1) has been determined in gas-phase using infrared spectroscopy. The IR spectrum of the $Ti(OPr)_4$ recorded at the University of Kent is presented in Fig 4.1.1.2. ν(Ti – O(Pr)) vibrational bands were observed between 507 cm^{-1} (0.06 eV) and 614 cm^{-1} (0.08 eV), with higher values than the vibrational bands for ν(Ti – O) bonds in TiO_2

obtained from $Ti(OPr)_4$ deposition and sol-gel formation at 394 cm^{-1} (0.05 eV). The same ν(Ti – O) band from the TiO_2 sub microspheres formed through $Ti(OPr)_4$ decomposition reaction and calcination at 400 °C was found at 568 cm^{-1} (0.07 eV) in Ref. [117]. The ν(C – O) vibrational band has signature values of 1114.86 cm^{-1} (0.138 eV) and 1116.15 cm^{-1} (0.138 eV), compared to the values declared by Hwang et al 2004 [118] of 1131.9 cm^{-1} (0.14 eV) from Ti – OPr monodentate. The ν(Ti – OPr) monodentate would suffer a symmetry change to keep its stability. Our spectrum presents two other peaks at 848.68 cm^{-1} (0.105 eV) and 852.53 cm^{-1} (0.1057 eV) corresponding to the ν(C – O) stretches of $Ti(OPr)_4$. The peaks between 1330 cm^{-1} (0.165 eV) and 1463 cm^{-1} (0.181 eV) are assigned to ν(C – C) stretches of the bidentate acetyl groups with vibrational frequencies at 1361.74 cm^{-1} (0.168 eV) and 1462.04 cm^{-1} (0.181 eV), other sources assigning the ν(C – C) to 1014.9 cm^{-1} (0.125 eV) in Ref. [120]. In Ref. [117], Hazifah and Sopyan 2009 identify the ν(C – H) aliphatic peak at 2942 cm^{-1} (0.365 eV) and the ν(C – H) alkane peak at 987 cm^{-1} (0.122 eV). From our IR spectrum we identify the ν(C – H) methyl group peaks at 2966.52 cm^{-1} (0.367 eV), 2926.01 cm^{-1} (0.363 eV) and 2864.29 cm^{-1} (0.355 eV), and the ethyl group peaks at 985.62 cm^{-1} (0.122 eV) and 941.26 cm^{-1} (0.117 eV).

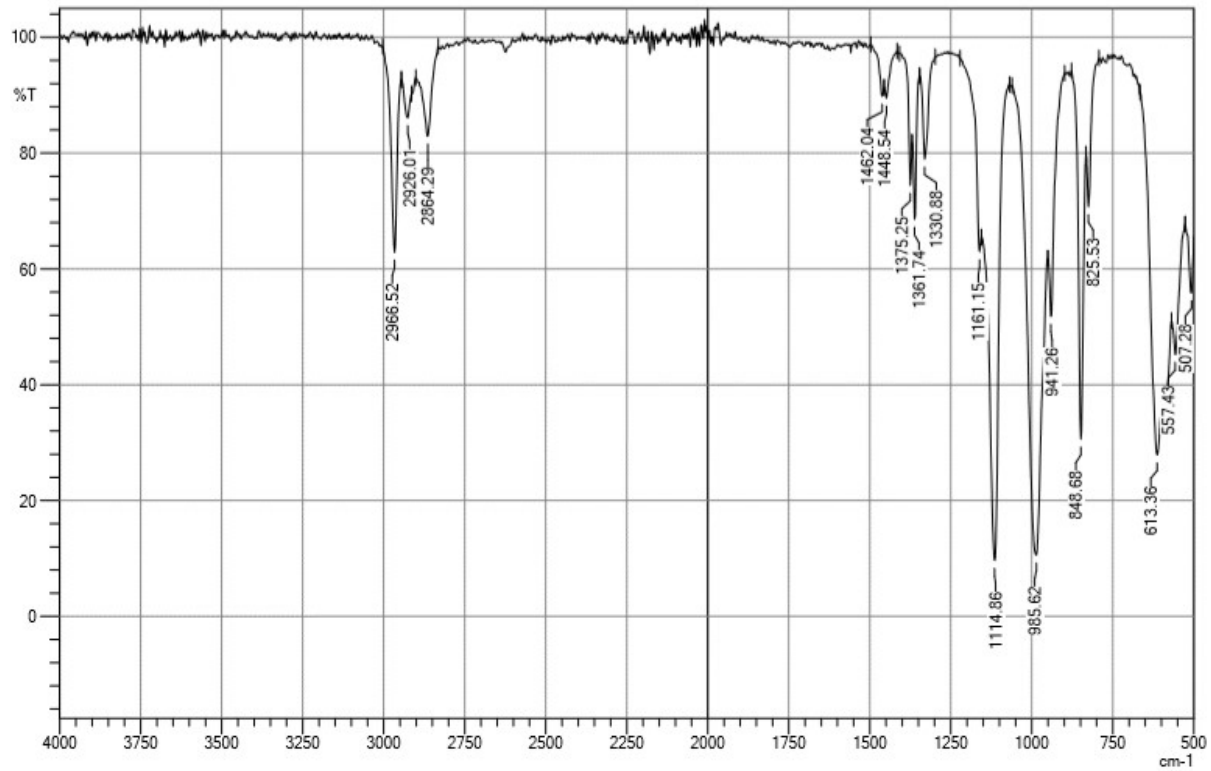

Fig 4.1.1.2. IR spectrum of titanium isopropoxide, $Ti(OPr)_4$

4.1.2 Previous Work

Ershov et al 2018 [123] studied the dissociation pathways of the $Ti(OPr)_4$ at different energies and for different bonds, though they do not specifically declare the presence of anions or cations, but the presence

of excited fragments. A number of 10 charged fragments have been analysed with bond dissociation energies between 48.9 kcal/mol in the formation of $Ti(OPr)_3H\cdot$ and 164.3 kcal/mol for the formation of $(OPr)_2Ti\text{-}OH\cdot$. The calculations of Ershov et al 2018 [123] were performed at M06-2X/6-311++G(2df,p) level of theory and at a temperature of 0 K. In their simulation work at photodissociation they declare the presence of Ti^+ and TiO^+ cations, as the only positively charged fragments identified. The study focuses on a range of bond dissociation energies obtained from calculations for the TTIP compound (titanium isopropoxide) with focus on the obtained Ti^+ and TiO^+ and the reaction photon energy.

Reference	DEA fragments spectra	Electron Energy (eV)
Ref. [123]		*dissociation energy (kcal/mol)
Ershov et al 2018	$Ti(OPr)_3OH\cdot$	57
	$Ti(OPr)_3\cdot$	85
From photodissociation	$TiO(OPr)_3\cdot$	85
M06-2X/6-311++G(2df,p)	$Ti(OPr)_3H\cdot$	48.9
level of theory	$Ti(OPr)_2H_2\cdot$	104.1
	$Ti(OPr)_3\cdot$	97.7
	$Ti(OPr)_2\cdot$	99.7
	$Ti(OPr)_2H\cdot$	153
	$(OPr)_2Ti{=}O\cdot$	159
	$(OPr)_2Ti\text{-}OH\cdot$	164.3
Present work (QMS)	H^-	n/a
	$Ti(OPr)_4^-$	5.9
	$TiO_4C_{10}H_{10}^-$	8.7
	$TiO_3C6H_{15}^-$	9.6
	$COOCH^-$	5.5 / 7.3
	$CH_3 - (CH_2)_2^-$	5.7 / 8.6

Table 4.1.2.1. DEA anion spectrum data from different sources and comparison with current work

In this work DEA anion fragments have been studied and compared with the work of Ershov et al 2018 [123] looking at the possibility of the existence of other charged fragments (anions). Bond dissociation energies of 85 kcal/mol have been calculated in the dissociation of TTIP in $Ti(OPr)_3\cdot$ and OPr, 57 kcal/mol in the dissociation of the TTIP with the resulting fragment $Ti(OPr)_3OH\cdot$ and 48.9 kcal/mol in the dissociation of TTIP with the resulting fragment $Ti(OPr)_3H\cdot$. A higher bond dissociation energy is

obtained for the charged fragment $Ti(OPr)_2H\cdot$ by breaking one Ti – OPr monodentate bond and a O – C bond at a dissociation energy of 153 kcal/mol. The highest bond dissociation energy [123] is obtained for the two bonds dissociation of Ti – OPr and O – C from the OPr monodentate bond. The two bonds exhibit a dissociation energy of 164.3 kcal/mol at the formation of $(OPr)_2Ti$ - $OH\cdot$.

Reference	DFT electronic states [1]*, [2]*
Present work DFT calculations from Gaussian 16 in neutral state at B3LYP/cc-pVTZ	1A 4.9448 eV 1A 5.2652 eV 1A 5.3319 eV 1A 5.3321 eV 1A 5.6627 eV 1A 5.7191 eV 1A 5.7195 eV 1A 5.7416 eV
Present work DFT calculations from Gaussian 16 in charged state at B3LYP/cc-pVTZ	2A 0.7335 eV 2A 1.3227 eV 2A 1.3537 eV 2A 1.6138 eV 2A 2.1193 eV 2A 2.5787 eV 2A 2.6297 eV 2A 2.6801 eV 2A 3.5929 eV 2A 3.6083 eV

Table 4.1.2.2. DFT electronic states, cross-sections from different sources and comparison with current work

4.1.3 Experimental Set-up

The experimental work has been run using a quadrupole mass spectrometer presented in details in Chapter 2. The computations of the excited states and the calculations of EA and BDE were run using Gaussian 16 software, while the TDOS was done using Multiwfn software (Chapter 3).

[1] Data not available from literature sources on excited states

[2] Excitation cross-section data was not determined as the Ti atom is not implemented in the Quantemol-N software

4.1.4 Results and Discussions

The anion data determined experimentally was carried using a quadrupole mass spectrometer (see Section 1 Chapter 2) at Comenius University, Bratislava in the group of Dr. Lect. Peter Papp. Five negative ions were found, produced by DEA of $Ti(OPr)_4$ (Fig 4.1.4.1) at m/z from 1 to 284: 1, 57, 178, 199 and 242 (Fig 4.2.4.1). At m/z 1, H^- is expected, and compared to $Si(OEt)_4$, where we barely see any H^- ions, H^- yields from $Ti(OPr)_4$ are abundant. However, it should be noted that the detection efficiency of the quadrupole under m/z 10 is subject to systematic effects depending on the kinetic energy of the anion.

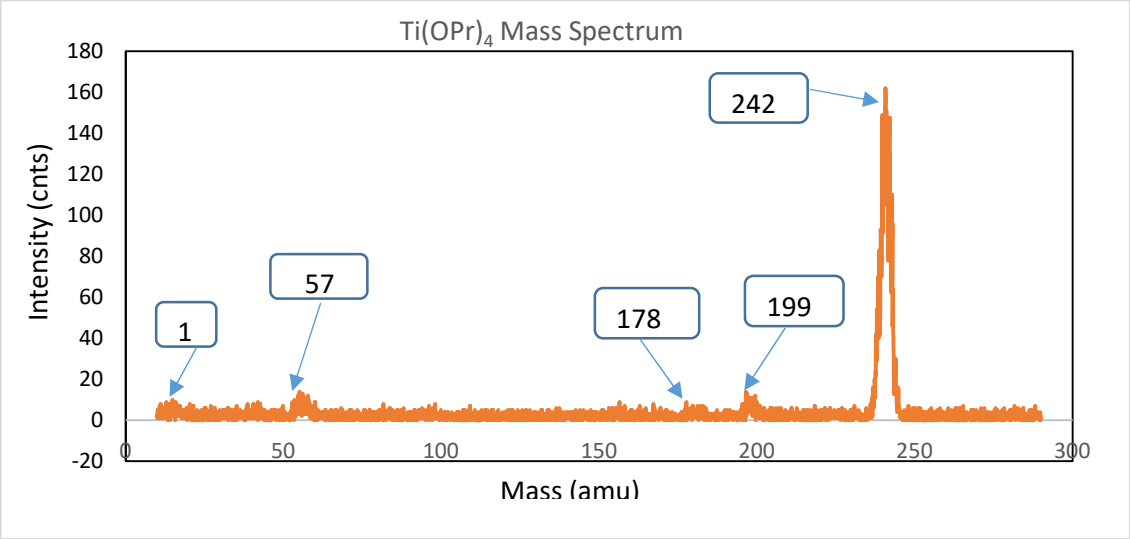

Fig 4.1.4.1. Mass spectrum of $Ti(OPr)_4$

The peak at m/z 57 is the third highest yield in the mass spectrum, and there are two possible fragments depending on the ligand breakage energy, either C-$COOH^-$ or C_2H_4-CO^- (Fig 4.1.4.6). The peak observed at m/z 178, can be assigned to $TiO_3H_9C_6^-$ or $TiO_3H_{10}C_6^-$ with dissociation energy values close to each other; but a lower BDE value is assigned to the $TiO_3H_{10}C_6^-$ anion. The peak at m/z 199 can be assigned to one of several possibilities according to the lowest ligand breakage: $TiO_4H_{15}C_6^-$, $TiO_2H_{11}C_9^-$, $TiO_4H_3C_7^-$, $TiH_7C_{12}^-$, $TiOH_3C_{11}^-$ and $TiO_3H_7C_8^-$. The highest anionic yield was found at m/z 242 with multiple possible fragmentation paths $TiO_4H_{10}C_{10}^-$, $TiO_4H_9C_{10}^-$, $TiO_4H_8C_{10}^-$ and $TiO_3H_{12}C_{11}^-$. The dissociation paths and resonances will be further discussed. The negatively charged parent ion was also observed at the expected m/z 284.146.

The total anion yield was measured over the electron energy range 0 to 15 eV and suggests the presence of three resonances, at 0.1 eV, 0.9 eV and 8.9 eV, though it could be argued that the first two resonances represent only one peak with a shoulder, as the interpeak minimum is higher than the median height of both resonances. The anionic yield of the parent m/z 284.14 is shown in Figure 4.1.4.3 together with the

corresponding mass spectrum. A higher lying resonance (or overlapping set of resonances) is observed around 5.9 eV. The FWHM width of the parent ion resonance peak is ~ 2 eV. The dissociation and excitation path of the anion parent is presented in relation (4.1.4.1).

$$Ti[OCH(CH_3)_2]_4 + e^- \rightarrow Ti(OPr)_4^* \rightarrow Ti(OPr)_4^- \quad (4.1.4.1)$$

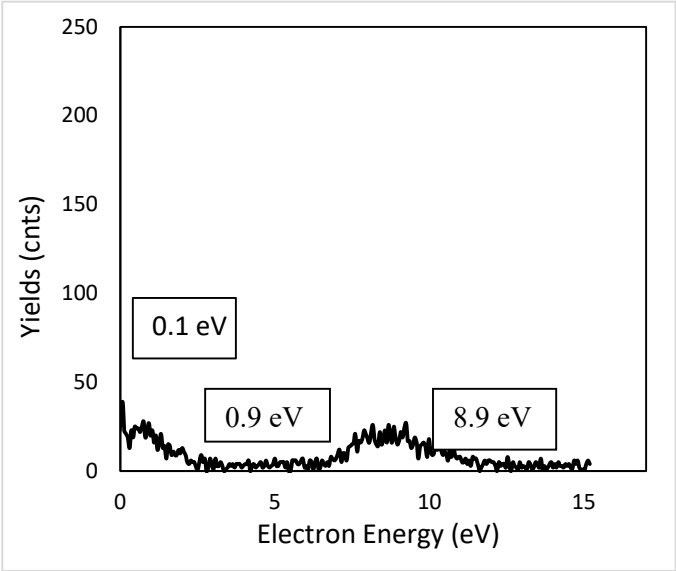

Fig 4.1.4.2. Measured yield of all anions produced by DEA of $Ti(OPr)_4$ as a function of electron energy with two resonances, one low lying around 0.9 eV and a higher resonance around 8.9 eV

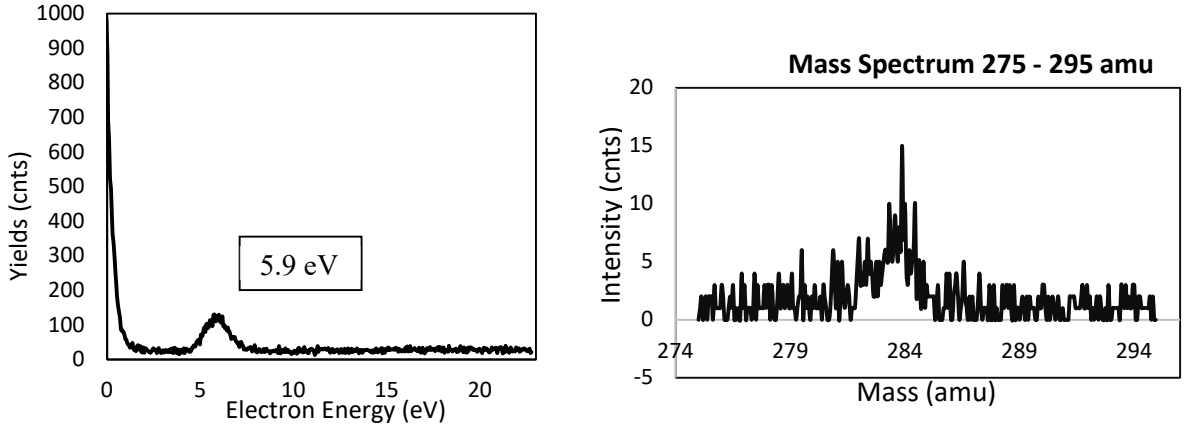

(a) (b)

Fig 4.1.4.3. (a) Anion yields of m/z 284 peak created by DEA of $Ti(OPr)_4$ as a function of electron energy and (b) mass spectrum of m/z 275 to m/z 295

The mass spectrum of the negative ions of $Ti(OPr)_4$ between m/z 230 to m/z 250, with the presence of the m/z 242 is shown in Fig 4.1.4.5 (a). In this region there are three possible product anions with m/z very close in value: 240 ($TiO_4C_{10}H_8^-$, $TiO_3C_{11}H_{12}^-$), 241 ($TiO_4C_{10}H_9^-$) and 242 ($TiO_4C_{10}H_{10}^-$). The quadrupole resolution is insufficient to separate these, but from the mass spectrum, the highest amplitude peak falls at m/z 242. Additionally, Ti has several isotopes (Table 4.1.4.1) which may lead to multiple m/z although ^{48}Ti is the dominant (74 %) one in nature. The anion yield for this m/z range is shown in Fig 4.1.4.4 (b) and shows a single resonance at 8.7 eV.

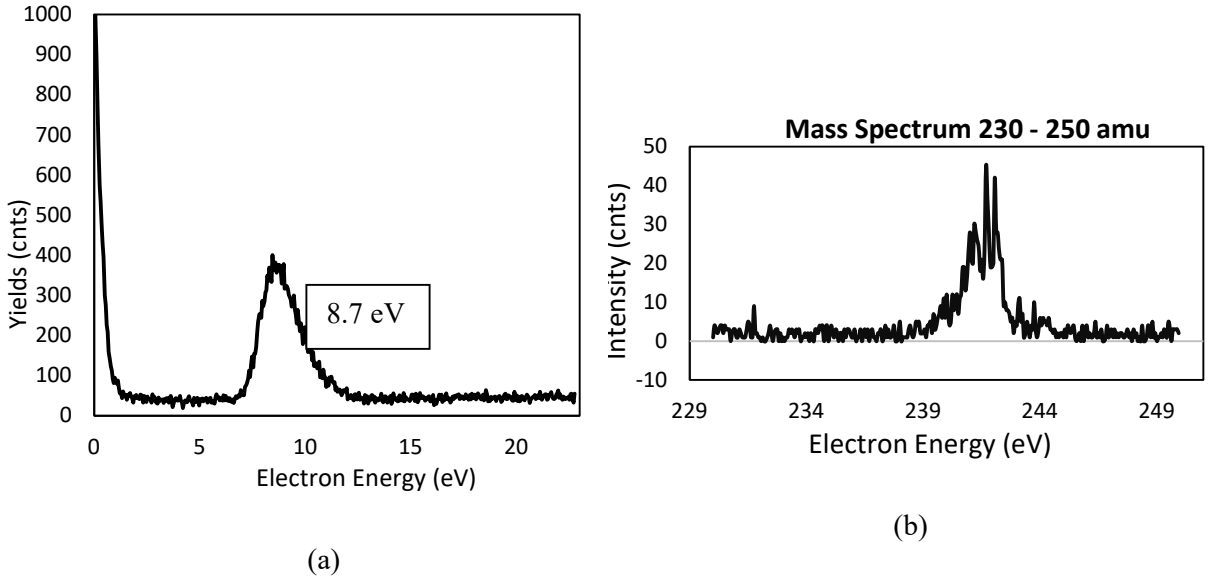

Fig 4.1.4.4. (a) Anion yield of m/z 242 produced by DEA of $Ti(OPr)_4$ (b) mass spectrum of m/z 230 to m/z 250

In an earlier FEBID study on the deposition of the titanium isopropoxide [119], two negative ions in the energy range 0 to 10 eV were observed, results of the DEA fragmentation, with formulae $TiO_4(C_3H_7)_3^-$ and $TiO_4(C_3H_7)_2H^-$. The anion mass at m/z 241 has the peak yield at 0.2 eV. In [119], the authors also showed an anion at m/z 199 with a peak yielding at 9.4 eV, in good agreement with our observed higher resonance at 9.6 eV (Fig 4.1.4.5). The corresponding anion to mass m/z 199 is $TiO_3C_8H_9^-$. The $TiO_3C_8H_9^-$ anion presents one resonance at 9.6 eV, with a FWHM width of 7 eV and the maximum peak yields with a value of 118 counts. The dissociation path of the TTIP in $TiO_3C_8H_9^-$ anion and OC_4H_{19} is a fast process and characterized by high stability observed from the width of the resonance peak. In the gas-phase analysis it is expected to find TiO^-, $TiCH^-$ or $TiCH_3^-$, but the closest peak we find is at m/z 57 assigned to $COOCH^-$, corresponding only to organic elements. The anionic yield as a function of incident electron energy for m/z 57 shows a resonance at near zero energy and two higher lying ones at 5.7 eV and 8.6 eV (Fig 4.1.4.6).

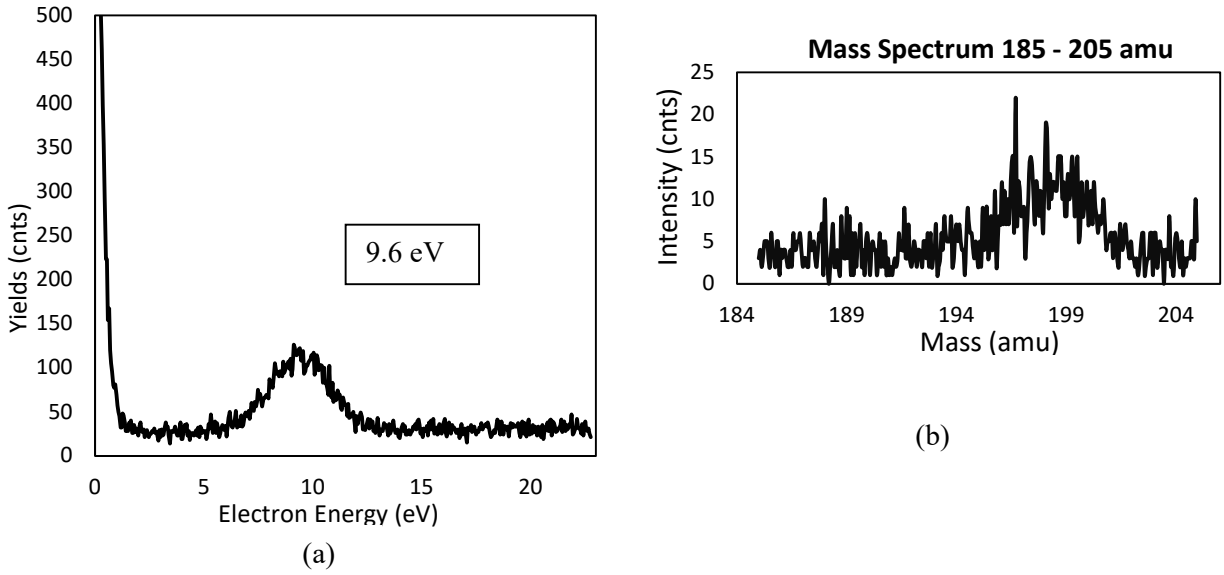

Fig 4.1.4.5. (a) Anion yields m/z 199 from $Ti(OPr)_4$; (b) mass spectrum from m/z 185 to m/z 205

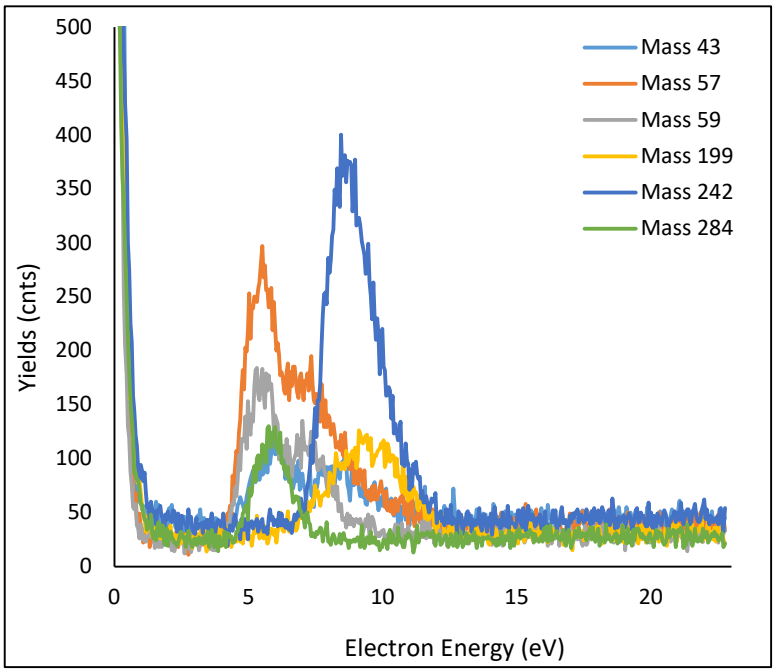

Fig 4.1.4.6. Anion yields of negative ions produced by DEA of $Ti(OPr)_4$

Two separate ions were identified at m/z 59 and m/z 43 and are evidence of the decay of heavier fragments into organic radicals, with the metal atom part of the neutral anion. From the anion yield at m/z 43, we observe two resonances at 5.7 eV and 6.5eV with a FWHM width of the resonance of 3.4 eV (presented in Fig 4.1.4.7). The resonance at m/z 43 presents two peaks interlinked with the maximum of the peaks with a value of 119 counts at 5.7 eV and 107 counts at 6.5 eV. The interlink value of the

resonance is decreasing to 53 counts, proving the existence of two peaks of the same resonance. A high FWHM width of the two resonances of 2.8 eV each is observed in the electron energy to yields spectrum.

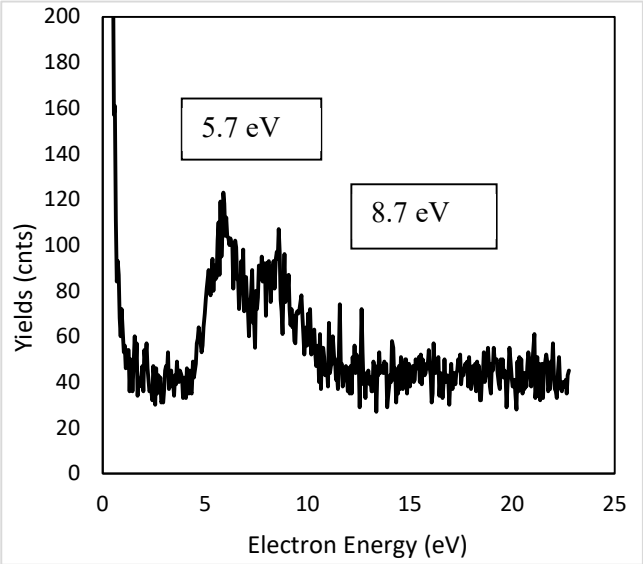

Fig 4.1.4.7 Anions yields of m/z 43 anions produced by DEA of $Ti(OPr)_4$

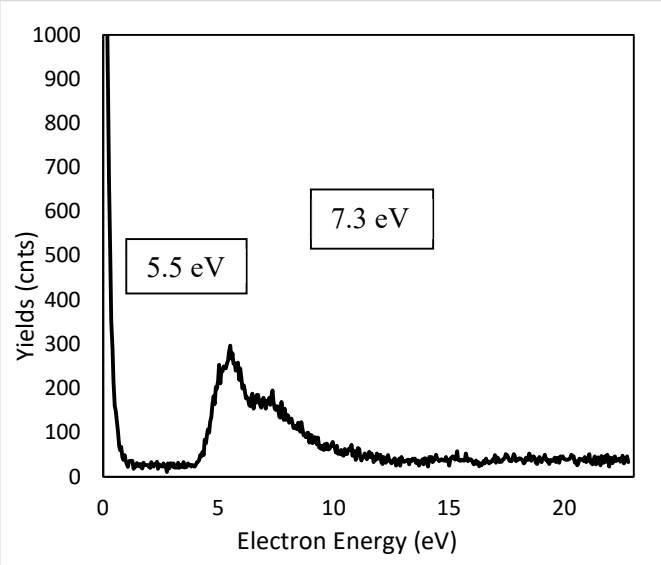

Fig 4.1.4.8 Anion yield of m/z 57 produced by DEA of $Ti(OPr)_4$

The anion yield of the mass m/z 57 (Fig 4.1.4.8) which corresponds to $COOCH^-$ anion shows a maximum peak of the resonance at 5.5 eV with a shoulder at 7.3 eV, further resonances higher than 15 eV might be present, but their low amplitude makes them indistinguishable from the high noise. The value of the shoulder yields is 200 counts, while the maximum value of the resonance peak at 5.5 eV is 297 counts.

The largest FWHM resonance width is obtained for m/z 57 anion ($COOCH^-$), with a value of 8.8 eV taking into calculation the length of the shoulder.

Ion	m/z	Resonance (eV)	Width of the peak (eV)
$Ti(OPr)_4^-$	284	5.9	2.9
$TiO_4C_{10}H_{10}^-$	242	8.7	4.7
$TiO_4C_6H_{15}^-$	199	9.6	4.8
$CH_2(CH_3)_3^-$	59	5.5; 7.3	2.7; 3.1
$COOCH^-$	57	5.7; 8.6	2.5; 3.5
$CH(CH_3)_2^-$	43	5.7; 6.5	2.3; 5.3

Table 4.1.4.2 Resonances of $Ti(OPr)_4$ anions

EAs and BDEs. The electron affinities and bond dissociation energies have been calculated using DFT calculations at B3LYP/Def2TZVPP level of theory. The two anions we ran calculations on to determine the maximum kinetic energy, the m/z 43 $CH_3(CH_2)_2^-$ and m/z 199 $TiO_4C_6H_{15}^-$, have electron affinities lower than 0.2 eV, 0.145 eV for the lightest anion and 0.07 eV in the case of the Ti - containing anion $TiO_4C_6H_{15}^-$. The electron affinities have been calculated using the relation $EA = (E_{el\ neutral} + ZPE_{\ neutral}) - (E_{el\ anion} + ZPE_{anion})$. The bond dissociation energy (BDE) in the case of the lightest anion ($CH_3(CH_2)_2^-$) is close to 0.60 eV corresponding to the rupture of a C – O bond to the higher containing Ti neutral fragment. The $TiO_4C_6H_{15}^-$ anion has a value of the BDE of 3.25 eV, in the interaction with an electron the molecule is breaking a C – C bond. In the calculation of the excess energy the value of the second peak of the resonance was used, found at an incident electron energy - Ei of 9.6 eV. A resulting excess energy – Ee and maximum kinetic energy of 6.42 eV is obtained using the relation Ee = EA – BDE + Ei (eV).

Ion	Ei (eV)	EA (eV)	BDE (eV)	Ee (eV)
$CH_3 – (CH_2)_2^-$	5.7	0.145	0.60	5.245
$TiO_4C_6H_{15}^-$	9.6	0.07	3.25	6.42

Table 4.1.4.3 Excess energy of $Ti(OPr)_4$ anions at DFT B3LYP/cc-pVTZ level of theory

PDOS/TDOS and TD-DFT. The TDOS/PDOS as total density of states and partial density of states are obtained from time-dependent density functional theory calculated at B3LYP/cc-pVTZ level of theory (Fig 4.1.4.9). The excited states computed are 11 states $^2A_1$ to $^2A_1$' at 0.73 eV, 1.32 eV, 1.35 eV, 1.61 eV, 2.12 eV, 2.58 eV, 2.63 eV, 2.68 eV, 3.54 eV, 3.59 eV and 3.61 eV. The fragments used for the PDOS evaluation are the anion $TiO_4C_{10}H_{10}^-$ and C_2H_{18} neutral fragment. The HOMO position is at 0.02 a. u. on

the energy scale. Higher values of density of states between -0.20 a. u. and -0.40 a. u. shows the leverage for additional transitions from lower energy orbitals to higher excited states, while at -0.80 a.u. no transitions are possible. Higher occupation is observed in the -0.40 a. u. to 0.00 a. u. region than for the orbitals between -0.70 a. u. and -0.40 a. u and 0.05 a. u. to 0.20 a. u.

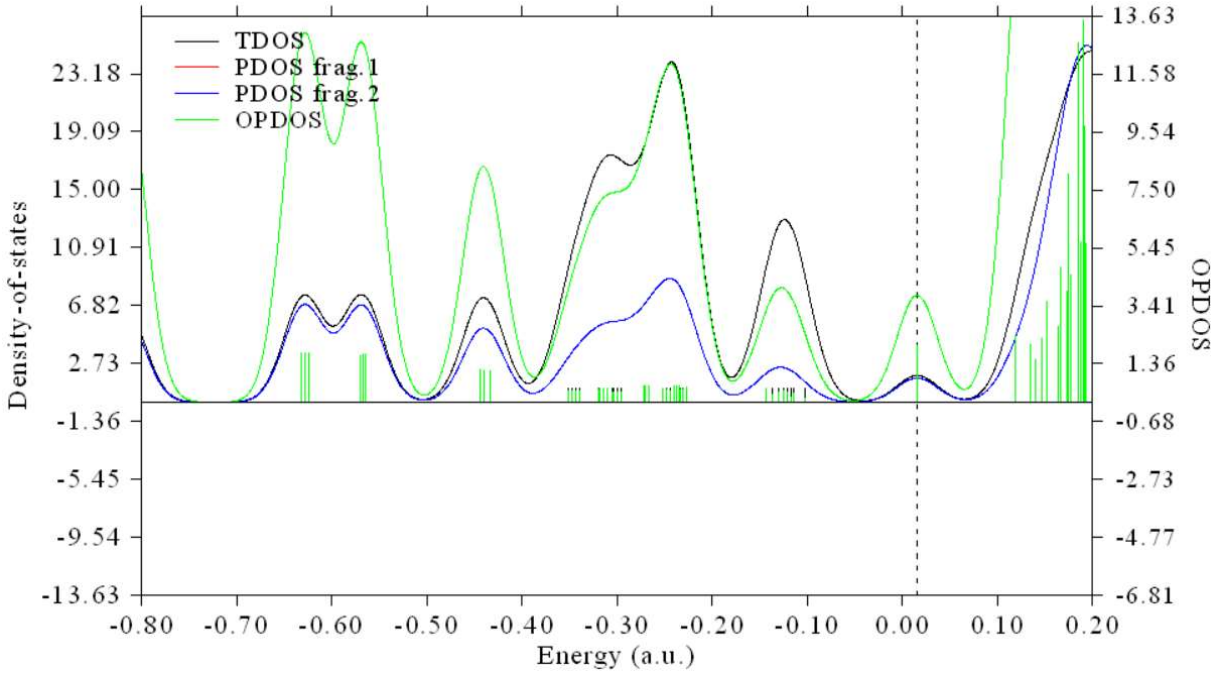

Fig 4.1.4.9 TDOS of $Ti(OPr)_4$ in charged state with PDOS anion $TiO_4C_{10}H_{10}^-$ (fragment 1) and C_2H_{18} (fragment 2)

4.1.5 Summary and Conclusions

DEA to the $Ti(OPr)_4$ precursor, mainly used in the FEBID for the production of Ti – nanoparticles and substrate repair (TiO_2), is shown to be dominated by three resonances one at threshold of 0.1 eV, one at 0.9 eV and one at 8.9 eV. Six product anions are formed; three higher mass anions, the $TiO_4C_6H_{15}^-$ (m/z 199), $TiO_4C_{10}H_{10}^-$ (m/z 242) and the parent anion $Ti(OPr)_4^-$ (m/z 284), and three lower mass fragments which are tentatively assigned as $COOCH^-$ (m/z 57), $HCO(CH_3)_2$ (m/z 59) and $CH_3 – (CH_2)_2^-$ (m/z 43). From the six compounds researched in this study, $Ti(OPr)_4$ is the only one to present a parent anion. The parent anion $Ti(OPr)_4^-$ presents one resonances at 5.9 eV. The resonances of the masses m/z 242 and m/z 199 anions, both showing only one peak at 8.7 eV ($TiO_4C_{10}H_{10}^-$) and 9.6 eV ($TiO_4C_6H_{15}^-$), respectively, have lower FWHM width 5.4 eV ($TiO_4C_{10}H_{10}^-$) and 6.4 eV ($TiO_4C_6H_{15}^-$). The lightest anions have wider resonance peaks with 1 - 2 peaks between 7.6 eV FWHM width ($CH_3 – (CH_2)_2^-$) and 8.7 eV FWHM

width ($COOCH^-$). The BDEs have been calculated for the highest counts anions $CH_3 – (CH_2)_2^-$ and $TiO_4C_6H_{15}^-$ with electron affinities between 0.07 eV and 0.145 eV. The BDEs of the two anions range between 0.60 eV for $CH_3 – (CH_2)_2^-$ to 3.25 eV for the higher mass anion. The maximum of the kinetic energy has been calculated with values of 5.245 eV ($CH_3 – (CH_2)_2^-$) and 6.42 eV ($TiO_4C_6H_{15}^-$), though the kinetic energy distribution could not be determined. The low number of counts and vaporization pressure are difficult conditions, and the substrate compounds can hardly be imaged using VMI.

4.2 Si(OEt)$_4$

4.2.1 Introduction To structure and spectroscopy Si(OEt)$_4$

Tetraethyl orthosilicate, formally named tetraethoxysilane (TEOS), is the organic chemical compound with the formula $Si(OC_2H_5)_4$ abbreviated as $Si(OEt)_4$ (Fig 4.2.1.1) and has been widely used in the fiber optics industry [257, 258], wafer industry [172] and as a chemical complex for the production of SiO_2 nanoparticles [257]. With the use of FEBID [1, 9] the applications of the $Si(OEt)_4$ have widened to its use in mask repair (substrates) [259], chip-based substrates [260] and isolators [261] between other metals deposited in complex 3D shapes. However, $Si(OEt)_4$ contains multiple C and H atoms, known to create impurities in FEBID deposits similar to (acac)-metal and halides-metal compounds. Compounds containing only H, the silanes (SiH_2, SiH, SiH3), deposit only Si through the easy release of the H.

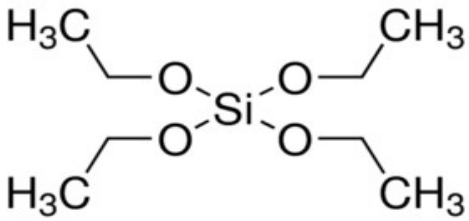

Fig 4.2.1.1. $Si(OEt)_4$

IR Study of Tetraethyl Orthosilicate. The IR spectrum of $Si(OEt)_4$ recorded at the University of Kent is presented in Fig 4.2.1.2. The IR spectrum presents features in the area 3050 – 2810 cm^{-1} (0.38 eV – 0.35 eV) corresponding to ν(C – H) stretching and 1520 – 1280 cm^{-1} (0.19 eV – 0.16 eV) of the CH deformation. The values are lower for the ν(Si – O – Si) mode stretching at 1090 cm^{-1} (0.14 eV), 450 cm^{-1} (0.06 eV) and 820 cm^{-1} (0.10 eV) and the ν(Si – O – C) band at 1090 cm^{-1} (0.14 eV). The ν(Si - OH) absorption bands appear at 960 cm^{-1} (0.12 eV), 3650 cm^{-1} (0.45 eV) and the bonded OH at 3400 cm^{-1} (0.42 eV). The Si - H bond is present at 2200 cm^{-1} (0.27 eV), 2135 cm^{-1} (0.26 eV) as seen in HMDSN (hexamethyldisilazane) amorphous films and the C = O at 1720 cm^{-1} (0.21 eV). In the HMDSO

(hexamethyldisiloxane), the IR spectrum bands appear at 2150 cm^{-1} (0.27 eV), 2300 cm^{-1} (0.29 eV) for the Si - H bond. The $Si(OEt)_4$ precursor dissociates to form SiO_2 on a backbone chain like structure with component atoms Si, O, H and C. In Ref. [121], the deposition of the TEOS on SiO_2 is a mixture of $(SiO)_2$ - $Si(OC_2H_5)_2$ and SiO - $Si(OC_2H_5)_3$ adsorbed at the surface of the SiO_2 with similar values to what we expect from the deposition studies of the precursor deposited without the aid of O_2 jets (surface science section Chapter 8).

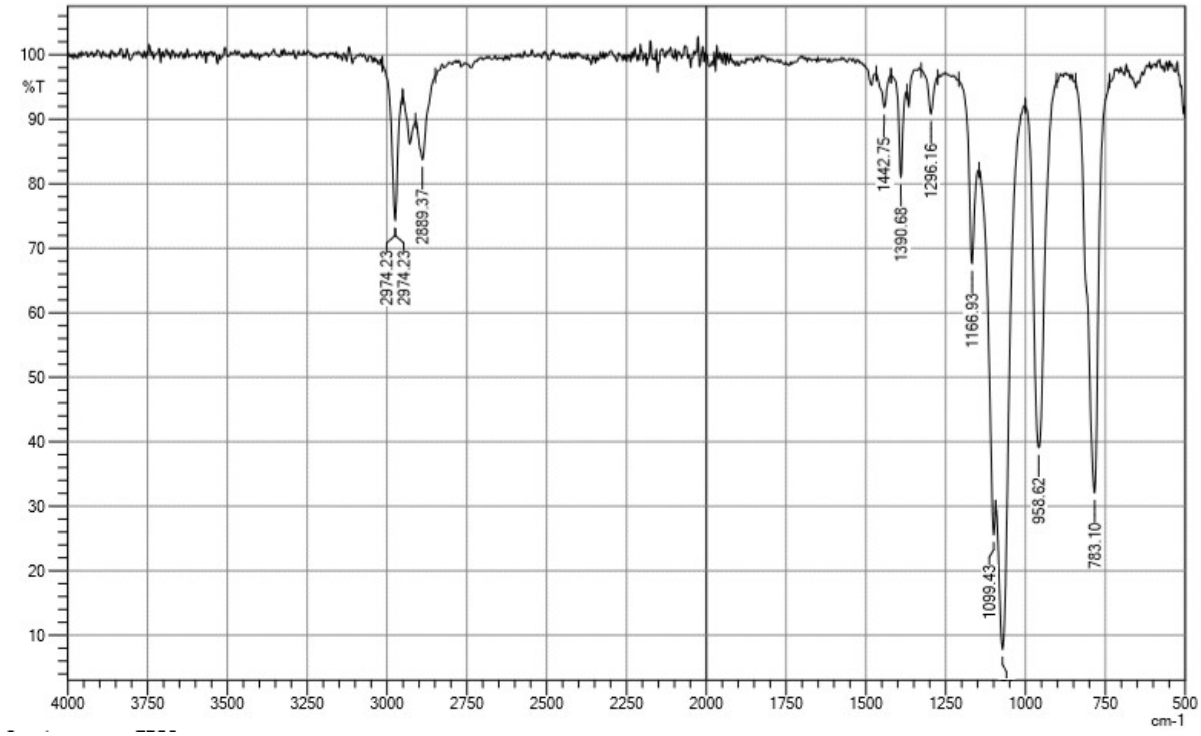

Fig 4.2.1.2. IR spectrum of tetraethyl orthosilicate, $Si(OEt)_4$ (TEOS)

UV – Vis Of TEOS. For the UV – Vis measurement, the $Si(OEt)_4$ was mixed with ethanol 2/5, as the compound is not soluble in water. The compound was transferred to the vial in a glove box to keep the vapors contamination by air intake lower.

For liquid phase, the UV-Vis spectrum (Fig 4.2.1.3, Table 4.2.1.1) presents peaks at:

Peak 1	Peak 2	Peak 3
204 nm	221 nm	280 nm
6.09 eV	5.61 eV	4.43 eV
1.47 x 10^{15} Hz	1.36 x 10^{15} Hz	1.07 x 10^{15} Hz

Table 4.2.1.1. $Si(OEt)_4$ liquid phase from UV-Vis measurement

For gas phase, the UV-Vis spectrum (Fig 4.2.1.4, Table 4.2.1.2) peaks are at:

Peak 1	Peak 2	Peak 3
206 nm	222 nm	277 nm
6.02 eV	5.58 eV	4.48 eV
1.46 x 10^{15} Hz	1.35 x 10^{15} Hz	1.08 x 10^{15} Hz

Table 4.2.1.2. $Si(OEt)_4$ gas phase (vapor) from UV-Vis measurement

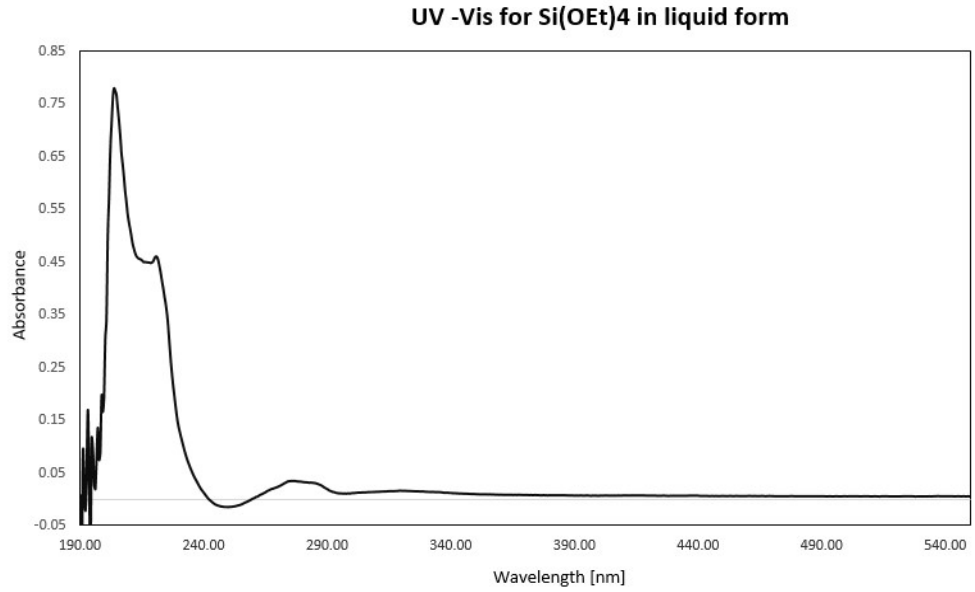

Fig 4.2.1.3. UV-Vis spectrum of $Si(OEt)_4$ liquid form

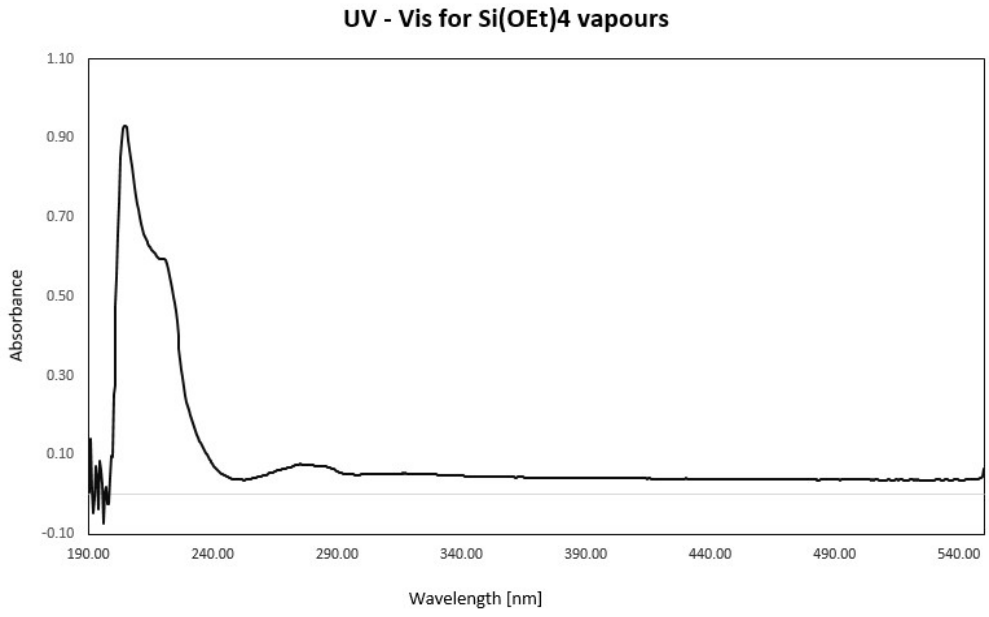

Fig 4.2.1.4. UV-Vis spectrum of $Si(OEt)_4$ in gas-phase (vapor)

Comparing to the liquid and gaseous SiO_2 UV-Vis spectra very small differences are observed between the peaks for the dried sample at 110 °C and calcinated sample at 300 °C, Table 4.2.1.2.

4.2.2 Previous Work

Da Silva et al [124] present a number of ten fragments resulting from the photodissociation of the $Si(OEt)_4$ precursor that are not specified as cations or anions as their evaluation is done by DFT and ab-initio calculations, but the importance in having their bond breaking energy and the possibility of being present in experimental conditions as cations or anions make the work of particular importance to a further DEA experimental study. To date there is no previous DEA study of TEOS.

Reference	DEA anion spectra	Electron Energy (eV)
Ref. [124]		*dissociation energy (kcal/mol)
Da Silva et al 1997	$(EtO)_3SiOCH_2\cdot$	108
From photodissociation	$(EtO)_2(MeO)SiOCHMe\cdot$	116
	$[(EtO)_2Si(OMe)(OCH{=}CH_2)]H\cdot$	101
	$(HO)(EtO)_2Si\text{-}O{=}CHMe\cdot$	94
	$[(HO)(EtO)_2Si(OC_2H_3)]H\cdot$	108.5
	$(EtO)_2Si\text{-}H\cdot$	86
	$(EtO)_2Si\text{-}O{=}C(H)Me\cdot$	91
	$(EtO)_2(MeO)Si\cdot$	36.2
	$H(EtO)(MeO)SiOCHMe\cdot$	32.9
	$H(EtO)_2SiOCH_2\cdot$	25.3
Present work (VMI)	CH_3^-	8.7
	$CH-(CH_3)_2^-$	1.4 / 6.6
	$SiO_2C_4H_{12}^-$	0.3 / 2.6 / 9.1
	$SiO_3C_7H_{17}^-$	2.7 / 8.9
	$SiO_4C_6H_{16}^-$	2.5 / 8.8

Table 4.2.2.1. DEA anion spectrum data from different sources and comparison with current work

The highest dissociation energy is obtained for the charged fragment $(EtO)_2(MeO)SiOCHMe\cdot$ of 116 kcal/mol, by the fragmentation of the $Si(OEt)_4$ in a charged fragment and one H. The $Si(OEt)_4$ is stable

and no spontaneous dissociation is possible at low temperatures (higher than RT), but in air it decomposes forming SiO_xC_x. By the loss of one CH_2 radical the charged fragment $(EtO)_3SiOCH_2\cdot$ is formed through the dissociation of a C – C bond and a value of the dissociation energy of 108 kcal/mol. Quite opposite than expected, the breaking of one Si – OEt bond is very low and results in the loss of a high number of atoms. The obtained value of the resultant dissociation energy is of 25.3 kcal/mol with the resulting charged fragment $H(EtO)_2SiOCH_2\cdot$. A higher dissociation energy is reported for the charged fragment $(EtO)_2(MeO)Si\cdot$ through the breaking of one Si – O bond and one C – C bond with the loss of an OEt and CH radical with a dissociation energy of 36.2 kcal/mol. The bond dissociation in the formation of $(EtO)_2(MeO)Si\cdot$ charged fragment is higher than for the dissociation of a Si – OEt bond with a C – CH_3 resulting in the loss of two hydrogens to a CH_3 and reorganization through the formation of a O – H bond and Si – H bond. The formation of the second ion is less probable than a straight dissociation as in the case of the ion $(EtO)_2(MeO)Si\cdot$.

Reference	DFT electronic states [3]*, [4]*
Present work DFT calculations from Gaussian 16 in neutral state at B3LYP/LANL2DZ	1A 7.4895 eV 1A 7.9396 eV 1A 8.3821 eV 1A 8.3845 eV 1A 8.8054 eV 1A 8.9495 eV 1A 9.2162 eV 1A 9.2793 eV 1A 9.2835 eV 1A 9.3233 eV 1A 9.3257 eV 1A 9.5780 eV
Present work DFT calculations from Gaussian 16 in charged state at B3LYP/LANL2DZ	2A 4.2736 eV 2A 4.2845 eV 2A 4.4461 eV 2A 4.7912 eV 2A 4.9356 eV

[3] No literature data is available on $Si(OEt)_4$ excited states

[4] Excitation cross-section data was not determined as the Si atom is not implemented in the Quantemol-N software

	2A 5.1348 eV 2A 5.3481 eV 2A 5.4085 eV 2A 5.5311 eV 2A 5.5962 eV 2A 5.6159 eV 2A 5.7083 eV 2A 5.7979 eV 2A 5.9468 eV 2A 5.9671 eV 2A 5.9846 eV 2A 6.1187 eV

Table 4.2.2.2. DFT electronic states, cross-sections and resonances from different sources and comparison with current work

4.2.3 Equipment Set-up

The experimental setup for the acquisition of the anions was a quadrupole mass spectrometer. The computational data and the EA and BDE calculations were run using Gaussian 16, while the TDOS and TD-DFT calculations were done using Multiwfn.

4.2.4 Results and Discussions

The DEA experiments of TEOS were done using a quadrupole mass spectrometer (see Section 1 Chapter 2) in collaboration with dr Lect. Peter Papp, Comenius University, Bratislava. The mass spectrum of anionic fragments produced by DEA from $Si(OEt)_4$ is presented in Fig 4.2.4.1. Four definite peaks with m/z values of 177, 181, 120, 41, 43 and 15 were observed. The lowest mass peak corresponding to m/z 15 is indicative of the fragmentation of $Si(OEt)_4$ into a neutral fragment and the negative ion CH_3^-.

The highest mass fragment containing Si is at m/z 180 and is assigned to $SiO_4C_6H_{16}^-$ following the dissociation pathway $Si(OC_2H_5)_4 \rightarrow SiO_4C_6H_{16}^- + O_2C_4H_{12}$. A further discussion is supported by Fig 4.2.4.1, Fig 4.2.4.6, and Fig 4.2.4.7.

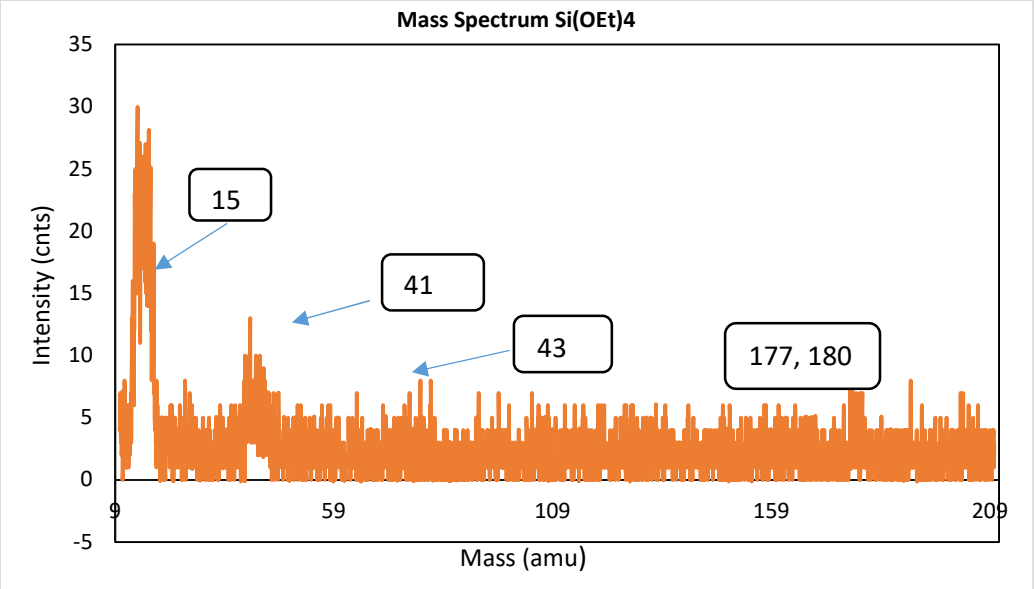

Fig 4.2.4.1. Mass spectrum $Si(OEt)_4$

The peak at m/z 43 is assigned to $CH(CH_3)_2^-$. The mass spectrum of the $Si(OEt)_4$ is presented in Fig 4.2.4.1 with the three visible peaks at m/z 15, m/z 41 and m/z 177. The anion corresponding to mass m/z 15 is CH_3^- (Fig 4.2.4.8 (a)), with an intensity of counts of 747 at the maximum peak energy of 8.4 eV. The anion with a higher mass, but similar resonance, falling at an electron energy of 6.8 eV at the peak maximum yields a value of ~ 60 counts and was assigned to $CH(CH_2)_2^-$ (Fig 4.2.4.8 (b)) corresponding to m/z 41.

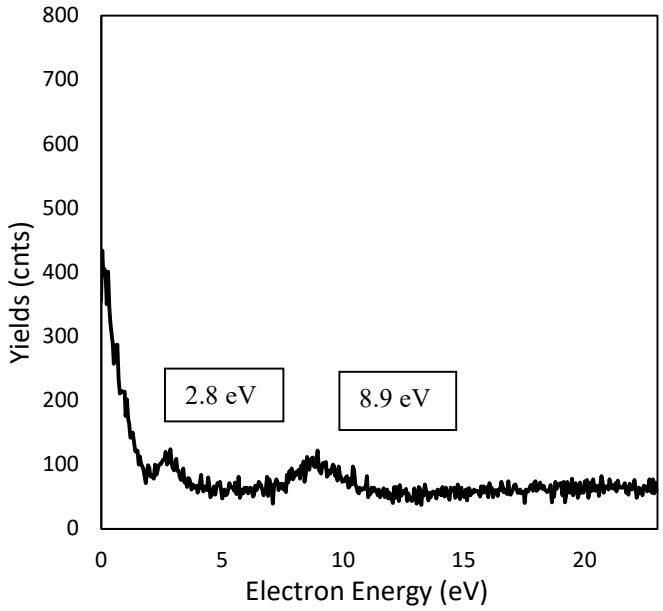

Fig 4.2.4.2. Spectrum of all ions yields produced by DEA of $Si(OEt)_4$

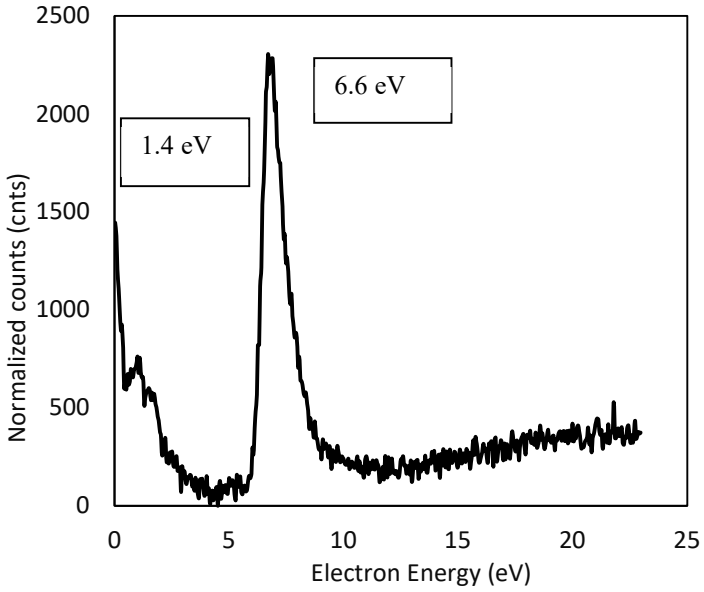

Fig 4.2.4.3. Anion yield for m/z 43 produced by DEA of $Si(OEt)_4$

The fragment with m/z 43 is ascribed to $CH(CH_3)_2^-$. The m/z 43 anion yield as a function of incident electron energy is shown in Fig 4.2.4.3. Two distinct resonances are observed, one at 1.4 eV energy and the other with a higher cross section at 6.6 eV. A shoulder is observed at 1.7 eV, but the drop in counts is too low to be considered a second resonance of the same anion. The fragment with m/z 120 is ascribed to $SiO_2C_4H_{12}^-$ (Fig 4.2.4.4). A low energy resonance (close to zero) is observed with a larger magnitude peak at 0.29 eV characterized by the presence of a shoulder at 2.6 eV and a higher lying resonance at 9.1 eV.

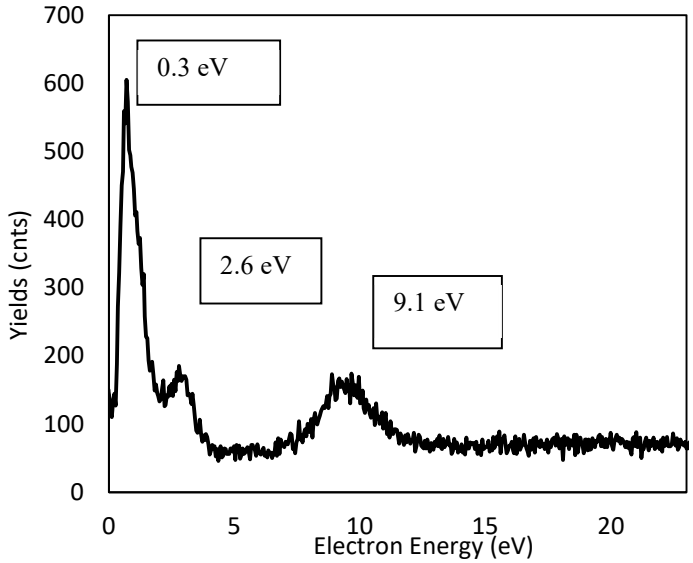

Fig 4.2.4.4. Anion yield of m/z 120 produced by DEA of $Si(OEt)_4$

Anion yields of the m/z 177 corresponding to the negative ion $SiO_3C_7H_{17}^-$ and m/z 180 assigned to $SiO_4C_6H_{16}^-$ are presented in Fig 4.2.4.5 and Fig 4.2.4.6 respectively. Both figures show a similar series of resonances, one at 2.7 (m/z 177) / 2.5 eV (m/z 180) and a second resonance at higher energy 8.9 (m/z 177) / 8.8 eV (m/z 180) (see Table 4.2.4.2). There is no evidence for a lower (zero energy) peak for m/z 180 as there is for m/z 177. Both anions contain similar resonances at similar electron energies, but with very high difference in amplitude. On the mass spectrum, the anion $SiO_3C_7H_{17}^-$ at m/z 177 is covered by the high intensity peaks of the $SiO_4C_6H_{16}^-$ at m/z 180.

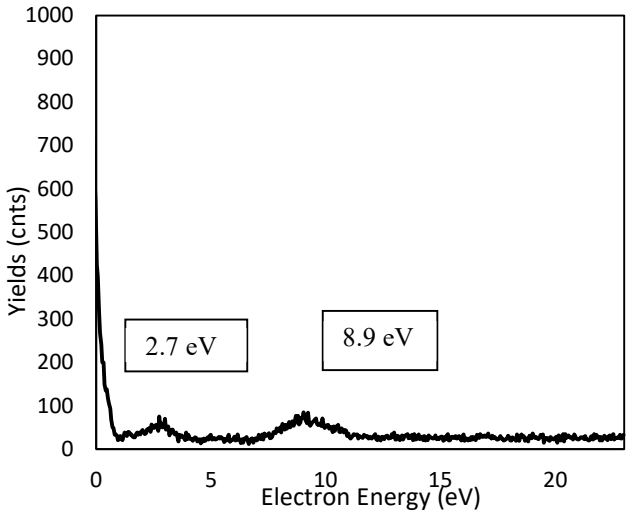

Fig 4.2.4.5. Anion yield of m/z 177 produced by DEA of $Si(OEt)_4$

.

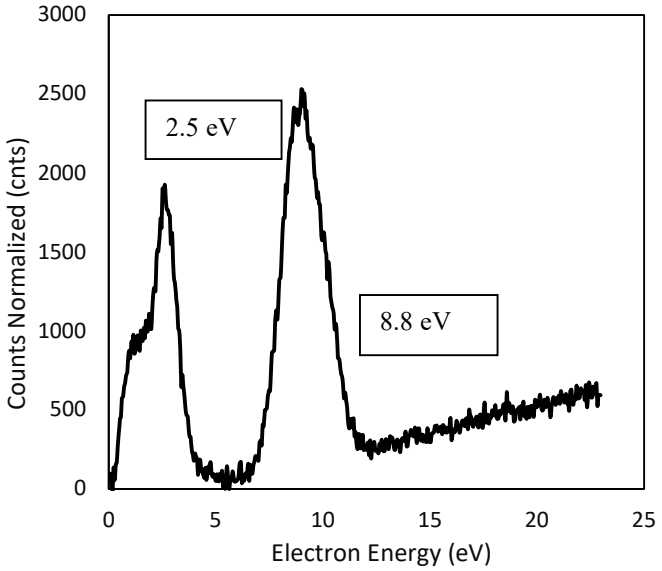

Fig 4.2.4.6. Anion yields of m/z 180 produced by DEA of f $Si(OEt)_4$

The spectra in Fig 4.2.4.7 presents the anion yield curves for each of the anionic fragments. The mass spectrum at m/z 177 corresponds to the negative ion $SiO_3C_7H_{17}^-$. With the addition of one O at m/z 180 $SiO_4C_6H_{16}^-$ was formed. Fig 4.2.4.7 presents masses m/z 15 and 43, corresponding to fragments containing only organic elements, their formation is assigned to the O – C bond rupture and dissociation; similar behavior is observed for the anions at m/z 41 ($CH(CH_2)_2^-$) and m/z 57 ($CH(CH_2)(CH_3)_2^-$). The anions with masses from m/z 120 to m/z 180 are all containing Si and have resonances peaking at very low energies close to 0 eV and very high over 8 eV, assigned to both C – H bonds and Si – O bonds strength. Compared to the rest of the masses, mass m/z 57 corresponding to $CH(CH_2)(CH_3)_2^-$ anion presents one resonance at 6.4 eV with rather low yields and a primary resonance with two peaks at 1.5 eV and 2.6 eV, and FWHM widths of 1.2 eV (res 1.5 eV), 1.8 eV (res 2.6 eV) and 3 eV (res 6.4 eV).

Ion	m/z	Resonance (eV)	Width of the resonance (eV)
CH_3^-	15	8.4	4.1
$CH(CH_2)_2^-$	41	6.8	3.5
$CH(CH_3)_2^-$	43	1.4; 6.6	1.5; 3.2
$CH(CH_2)(CH_3)_2^-$	57	1.5; 2.6; 6.4	1.2; 1.8; 3
$SiO_2C_4H_{12}^-$	120	0.29 shoulder 2.6; 9.1	4; 5.3
$SiO_3C_7H_{17}^-$	177	2.7; 8.9	2.6; 3.4
$SiO_4C_6H_{16}^-$	180	2.5; 8.8	4; 5.1

Table 4.2.4.2 $Si(OEt)_4$ resonances and negative ions

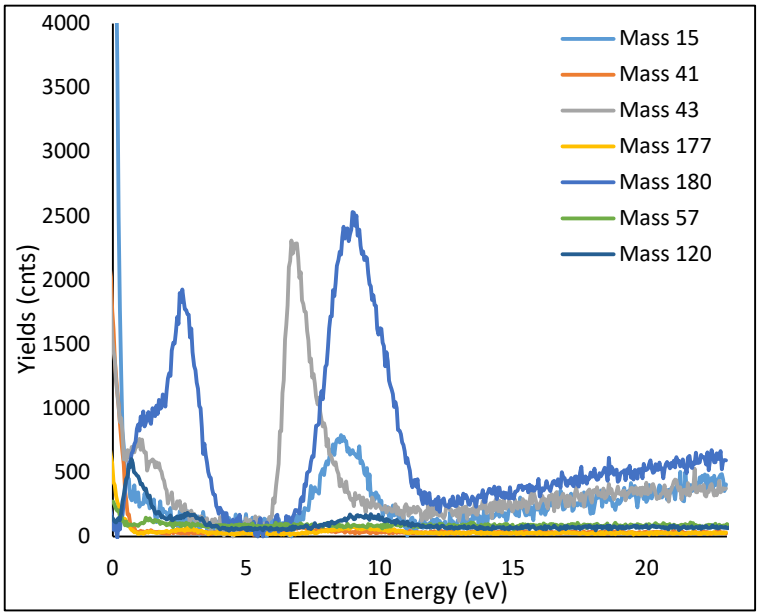

Fig 4.2.4.7. Yields to electron energy spectrum of negative ions of $Si(OEt)_4$

The lower mass anions as presented in Fig 4.2.4.7 are $CH(CH_2)_2^-$ (m/z 41), $CH(CH_2)(CH_3)_2^-$ (m/z 57), $SiO_2C_4H_{12}^-$ (m/z 120) and $SiO_3C_7H_{17}^-$ (m/z 177). The other three masses have very high counts compared to the four masses presented before. At m/z 41 we observe an anion (see in Fig 4.2.4.8 (b)) that we identified as $CH(CH_2)_2^-$ as the most probable anion in the dissociation of the excited $Si(OEt)_4$ into a neutral fragment $SiO_4C_5H_{13}$ and the negatively charged $CH(CH_2)_2^- + O_2$, the yield shows a single resonance at 6.84 eV.

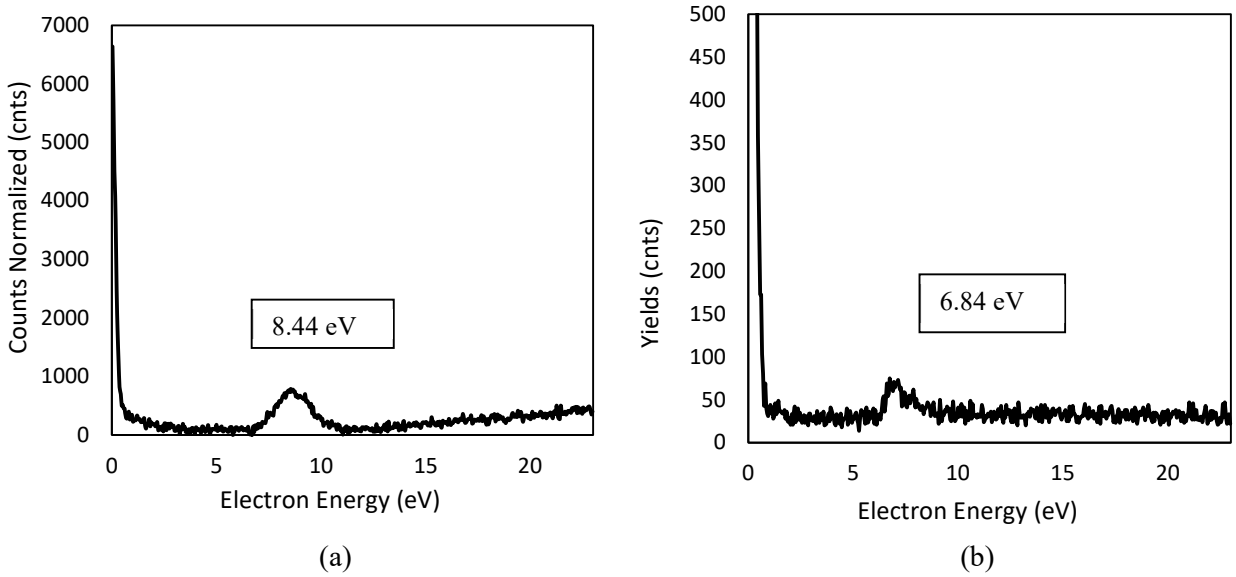

Fig 4.2.4.8. Anion yield m/z 15 (a) and m/z 41 (b) produced by DEA of $Si(OEt)_4$

EAs and BDEs of anions. The EAs and BDEs of the highest counts anions have been calculated, offering insight into the maximum kinetic energies of the particular fragments, the fragmentation channels and resonances. We used the experimental incident electron energies to determine the bond dissociation energies in our DFT calculations at B3LYP/LANL2DZ level of theory. The electron affinities have been computed using the same DFT calculations by the relation EA = [E_{el} (optimized neutral) + ZPE (optimized neutral)] – [E_{el} (anion) + ZPE (anion)]. The value of the excess energy (see Table 4.2.4.3) representing the maximum of the kinetic energy for the m/z 43 CH - $(CH_3)_2^-$ anion is 6.23 eV, while higher mass anions have an excess energy of 4.14 eV ($SiO_2C_4H_{12}^-$; m/z 120), 8.55 eV ($SiO_3C_7H_{17}^-$; m/z 177) and 5.5 eV ($SiO_4C_6H_{16}^-$; m/z 180). For the maximum of the resonance of $SiO_2C_4H_{12}^-$ anion found at an electron energy of 9.1 eV, the bond dissociation energy of removing two Si – O ligands has a value of 5.23 eV. The bond dissociation energies are in the range of 0 – 1.4 eV, with a value of dissociation of one Si – O bond of 0.44 eV and an excess energy (Ee) of 8.55 eV for an electron incident energy (Ei) of 8.9 eV. A very small electron affinity of the $SiO_3C_7H_{17}$ anion is observed compared to the rest of the anions in neutral state.

Ion	Ei (eV)	EA (eV)	BDE (eV)	Ee (eV)
CH - $(CH_3)_2^-$	6.6	0.96	1.33	6.23
$SiO_2C_4H_{12}^-$	9.1	0.27	5.23	4.14
$SiO_3C_7H_{17}^-$	8.9	0.09	0.44	8.55
$SiO_4C_6H_{16}^-$	8.8	3.69	0.39	5.5

Table 4.2.4.3 Excess energy of anions calculated at DFT B3LYP/LANL2DZ level of theory

TDOS and TD-DFT. The TDOS/PDOS has been run using the optimized structure and TD-DFT calculations at B3LYP/LANL2DZ level of theory for a number of 17 excited states representing allowed transitions from $^2A_1$ to $^2A_1$' at 4.27 eV, 4.28 eV, 4.45 eV, 4.79 eV, 4.94 eV, 5.13 eV, 5.35 eV, 5.41 eV, 5.53 eV, 5.60 eV, 5.62 eV, 5.71 eV, 5.80 eV, 5.95 eV, 5.97 eV, 5.98 eV and 6.12 eV. The HOMO orbital (dashed line) falls at 0.015 a. u.

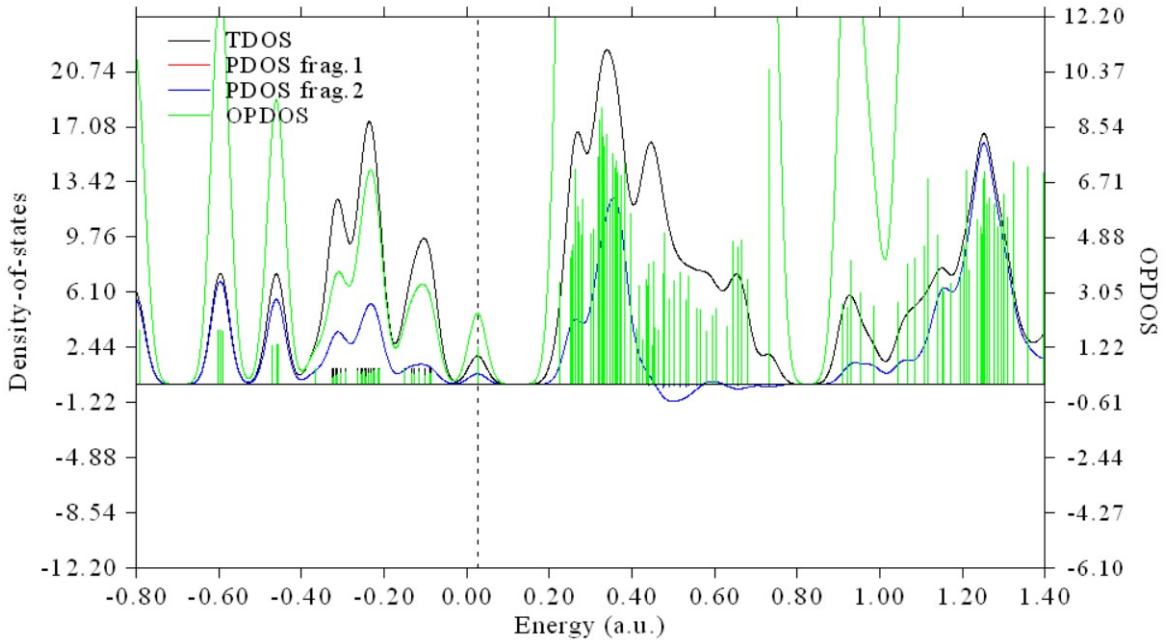

Fig 4.2.4.11 TDOS/PDOS of $Si(OEt)_4$ in charged state with fragments $SiO_4C_6H_{16}^-$ (fragment 1) and C_2H_4 (fragment 2)

Higher occupation of orbitals is seen between -0.45 a. u. and 0.05 a. u., while lower occupation characterizes the rest of the TDOS/PDOS spectrum. Discrepancies in the fragments appear over HOMO line, between 0.20 a. u. and 0.75 a. u. representing changes in the hydrogenation level of the fragment compared to the parent. The HOMO of the fragment 2 $(CH_2)_2$ falls right through the middle of the resonance peak showing a high occupancy and no fragmentation coming from the C – $(CH_2)_2$ bond in

the transition from HOMO to LUMO and dissociation of the compound, while the OPDOS shows the level of overlap occupation coming from the fragmentation of the PDOS with the level of allowed transition from occupied states to unoccupied states. The fragmentation channel used to simulate the TDOS/PDOS of the compound is likely not to be one of the channels with the highest probability of apparition in the dissociation of the $Si(OEt)_4$ complex.

4.2.5 Summary and Conclusions

With increased used of the $Si(OEt)_4$ precursor in the Si – nanoparticles production, fiber optics applications and as a substrate repair material for SiO_2 in mask repair industry, the compound has received high interest from the research community. Despite the wide applications of the compound, the $Si(OEt)_4$ has not been enough studied to DEA and FEBID in the process of induced chemistry reactions to form anions; the limitations came with the experimental equipment used and its dissociation to form SiO_2 with the exposure to air is inducing high level of contamination in UHV chambers. In this work we have studied DEA to $Si(OEt)_4$ revealing the formation of seven anions. The lower mass anions do not contain Si atoms. At mass m/z 15, the CH_3^- anion presents a resonance at 8.4 eV with a FWHM width of 4.5 eV. Lower mass anions m/z 41 ($CH(CH_2)(CH_3)_2^-$), m/z 43 ($CH – (CH_3)_2^-$) and m/z 57 ($CH(CH_2)(CH_3)_2^-$) present one peak of the resonance at 6.8 eV ($CH(CH_3)_2^-$), 0.78 eV ($CH(CH_2)(CH_3)_2^-$), while $CH – (CH_3)_2^-$ (m/z 43) presents two resonances at 1.4 eV and 6.6 eV. The higher mass anions each containing one Si atom have 2 – 3 resonances at m/z 120 ($SiO_2C_4H_{12}^-$) 0.3 eV, 2.6 eV and 9.1 eV, m/z 177 at 2.7 eV and 8.9 eV ($SiO_3C_7H_{17}^-$) and the highest mass anion m/z 180 ($SiO_4C_6H_{16}^-$) at 2.5 eV and 8.8 eV. The bond dissociation energies and electron affinities have been calculated at B3LYP/LANL2DZ level of theory with values of EA ranging from 0.09 eV ($SiO_3C_7H_{17}^-$) to 3.69 eV ($SiO_4C_6H_{16}^-$) and BDE from 0.39 eV ($SiO_4C_6H_{16}^-$) to 5.23 eV ($SiO_2C_4H_{12}^-$). Excess energies of the anions have been calculated and tabulated in Table 4.2.4.3 with values between 4.14 eV ($SiO_2C_4H_{12}^-$) to 8.55 eV ($SiO_3C_7H_{17}^-$).

4.3 Conclusions To Chapter 4

The formation of nanostructures specific to FEBIP using $Si(OEt)_4$ and $Ti(OEt)_4$ as starting materials have major implications in the deposition of SiO_2 and TiO_2 substrates in a range of applications e.g. construction industries (civil applications) and hardware industry (nanoscale circuits on microchip

boards and devices, and supermaterials/superconductors). Despite its high importance in the fiber optics and lately in the development of batteries, the literature data is scarce in studies of the DEA and FEBID of $Si(OEt)_4$ and $Ti(OPr)_4$. Electron impact dissociation of these two compounds has been studied successfully obtaining a number of negative ions as a result of DEA induced fragmentation. Anionic kinetic energies and the reaction pathways for the ions formation have been determined. The $Ti(OPr)_4$ fragments in six anions with the presence of the parent anion. The anions with their resonance energies are $TiO_4C_6H_{15}^-$ (m/z 199), $TiO_4C_{10}H_{10}^-$ (m/z 242) and the parent anion $Ti(OPr)_4^-$ (m/z 284), while the lower mass fragments are $COOCH^-$ (m/z 57), $CH(CH_2)(CH_3)_2^-$ (m/z 59) and $CH_3 – (CH_2)_2^-$ (m/z 43). The parent anion $Ti(OPr)_4^-$ presents one resonances at 5.9 eV, while the resonances of the lower masses m/z 242 and m/z 199 anions both show only one peak at 8.7 eV ($TiO_4C_{10}H_{10}^-$) and 9.6 eV ($TiO_4C_6H_{15}^-$). The anions $CH_3 – (CH_2)_2^-$ and $COOCH^-$ present resonances at 7.6 eV and at 8.7 eV. A number of 11 excited states have been calculated at TDDFT B3LYP/Def2TZVPP level of theory with values of 0.73 eV, 1.32 eV, 1.35 eV, 1.61 eV, 2.12 eV, 2.58 eV, 2.63 eV, 2.68 eV, 3.54 eV, 3.59 eV and 3.61 eV with a $^2A_1$ symmetry allowed transitions from $^2A_1$' ground state.

The $Si(OEt)_4$ precursor at DEA does not exhibit a parent anion compared to $Ti(OPr)_4$, but slightly increases the fragmentation ratio with a number of seven obtained anions. The $Si(OEt)_4$ has five higher mass anions m/z 120 ($SiO_2C_4H_{12}^-$) 0.3 eV, 2.6 eV and 9.1 eV, m/z 177 at 2.7 eV and 8.9 eV ($SiO_3C_7H_{17}^-$) and the highest mass anion m/z 180 ($SiO_4C_6H_{16}^-$) at 2.5 eV and 8.8 eV, while the organic anions are m/z 41 ($CH(CH_2)(CH_3)_2^-$), m/z 43 ($CH – (CH_3)_2^-$) and m/z 57 ($CH(CH_2)(CH_3)_2^-$) presenting only one resonance peak at 6.8 eV ($CH(CH_3)_2^-$), 0.78 eV ($CH(CH_2)(CH_3)_2^-$). The $CH – (CH_3)_2^-$ (m/z 43) has two resonance peaks at 1.4 eV and 6.6 eV. A number of 17 excited states have been calculated at TDDFT B3LYP/LANL2DZ level of theory with energies ranging from 4.27 eV, 4.28 eV, 4.45 eV, 4.79 eV, 4.94 eV, 5.13 eV, 5.35 eV, 5.41 eV, 5.53 eV, 5.60 eV, 5.62 eV, 5.71 eV, 5.80 eV, 5.95 eV, 5.97 eV, 5.98 eV to 6.12 eV with a $^2A_1$' symmetry representing allowed transitions from ground state $^2A_1$. Particular states have been run for $Si(OEt)_4$ using CIS orbitals at 1A' 9.5780 eV, 7.4895 eV, 7.9396 eV, 8.3821 eV, 8.3845 eV, 8.8054 eV, 8.9495 eV, 9.2162 eV, 9.2793 eV, 9.2835 eV, 9.3233 eV and 9.3257 eV from 1A ground state, and for $Ti(OPr)_4$ CIS orbitals at 1A' 4.9448 eV, 5.2652 eV, 5.3319 eV, 5.3321 eV, 5.6627 eV, 5.7191 eV, 5.7195 eV and 5.7416 eV from 1A ground state. The EAs and BDEs have been calculated for both compounds, with values ranging from 0.09 eV ($SiO_3C_7H_{17}^-$) to 3.69 eV ($SiO_4C_6H_{16}^-$) EAs and 0.39 eV ($SiO_4C_6H_{16}^-$) to 5.23 eV ($SiO_2C_4H_{12}^-$) BDEs for $Si(OEt)_4$, and between 0.07 eV ($CH_3 – (CH_2)_2^-$) and 0.145 eV ($TiO_4C_6H_{15}^-$) EAs and between 0.60 eV ($CH_3 – (CH_2)_2^-$) to 3.25 eV ($TiO_4C_6H_{15}^-$) BDEs of $Ti(OPr)_4$. For both compounds a set of PDOS/TDOS data has been run using Multiwfn software and calculated structures at TDDFT B3LYP/LANL2DZ and Def2TZVPP level of theory.

CHAPTER 5. STUDY OF THE CARBONYL GROUP BASED COMPOUNDS IN GAS-PHASE

The aim of this chapter is to analyse the processes involved in the DEA of carbonyls and explore its potential implications to the FEBID deposition of the compound. Carbonyl group-based compounds are amongst the most common precursors used in the FEBID process; with a number of (CO) groups (carbonyls) under electron irradiation dissociating from the metal or bimetallic radical as $M_nZ_m(CO)_x + e^- \rightarrow M_nZ_m + (CO)_x$ to produce a metallic nanostructure. There has been considerable research into the study of carbonyl precursors in Ref. [218, 220, 222 - 224]. The CO radical is known to be highly volatile and through rupture of the metal – CO ligand, CO is liberated leaving a metallic deposit on the surface. The research literature in the field of carbonyls focuses on precursors as $Fe(CO)_5$, $W(CO)_6$, $Co(CO)_3NO$, $Co(CO)_6$, $Ni(CO)_4$, and therefore they are the subject of the most extensive electron collision studies, in particular focusing on DEA and DI, dissociation processes that are most relevant to FEBID.

In contrast, heteronuclear and bimetallic carbonyl precursors have received interest with the intent of perfecting the process of combining carbonyl radicals and two metals in one compound to obtain bimetallic FEBID structures. The $HFeCo_3(CO)_{12}$ in Ref. [220], $HFeCo_3(CO)_{12}$ and $H_2FeRu_3(CO)_{13}$ in Ref. [2212] have been shown to exhibit high metal purities in the deposited nanostructures. The Ru/Fe rate obtained in the deposition of $H_2FeRu_3(CO)_{13}$ in Ref. [213] is of 1 : 0.35 representing 26 at% metal purity with a lower deposition purity than $HFeCo_3(CO)_{12}$ characterized by a metal purity in the deposited nanostructures of 80at%. Other carbonyl precursors Ref. [220] present higher metal content at room temperature with purities in the range of ~40 at% compared to 26 at% in Ref. [2212] for $Mn_2(CO)_{10}$. Comparatively, the bimetallic precursor $SiH_3Mn(CO)_5$ in Ref. [221] containing Mn element and silicon has lower metal content than typical carbonyl precursors with values of ~34 at% Mn and 17 at% Si. Used extensively in the EUVL and mask repair industry, the $Ru(CO)_4I_2$ and $Ru(CO)_4Br_2$ in Ref. [224], at DEA, fragment in $RuI_2 + (CO)_4$ and $RuBr_2 + (CO)_4$, containing Ru – CO bonds, a typical behaviour is observed where the CO groups are removed in the interaction with the electrons, and Ru is deposited on the surface with atoms of I_2 or Br_2. The wide applications of $Fe(CO)_5$ in nanotechnology through its decomposition in pure Fe and volatile (CO) fragments is a sought characteristic in the development of silicon carbide fibres (SiC) in Ref. [224] with a content of 3.6 wt% Fe increasing the value of the tensile strength up to 2.37 GPa. Earlier studies present the fragmentation of the $Fe(CO)_5$ on Ag(111) surfaces in Ref. [227] with cross-sections values of ~1 - 14 x 10^{-16} cm^2. The bombardment of the $Fe(CO)_5$ precursor with Ar^+ ions in Ref. [225] has the result of full fragmentation of the compound on the surface and a desorption

of the volatile fragments of 80% with implications to the carbon nanotube industry. Applications in the development of carbon nanotubes by the use of uniform nanoparticles with the addition of $W(CO)_6$ in the reduction of metal salts have been reported in Ref. [229], and by the epoxidation of alkenes with the addition of H_2O_2, $W(CO)_6$ and 1,2-diaminobenzene have been reported in Ref. [230], and, with the increase in the tensile strength has known to improve the manufacturing process in the carbon nanotubes production. In this chapter new results on using the VMI method to dissociative electron attachment of $Fe(CO)_5$ and $W(CO)_6$ will be presented. The results on earlier CF_3, SF_6 and CH_3 are compared with earlier work to calibrate and test the cross-sections obtained from Quantemol-N methodology and apply it to $Fe(CO)_5$. The VMI allowed angular distributions and kinetic energies of the ions have been measured and calculated for the two carbonyls. Experimental results may also be compared with theoretical calculations to test the reliability of the Quantemol-N code to derive cross sections for higher electron density compounds. In contrast there are fewer studies of $W(CO)_6$ despite its increasing importance in the FEBID field.

5.1 $Fe(CO)_5$

5.1.1 Introduction of $Fe(CO)_5$

Iron pentacarbonyl (Fig 6.1.1.1) is widely used to create nanowires, alloys of different strengths, magnetic nanostructures as magnetic dots and tips for information storage, nano-Hall sensors for bead detection, many of which are produced by using the FEBID process. $Fe(CO)_5$ is therefore, one of the most commonly used FEBID precursors particularly because the resulting nanostructures demonstrate unique magnetic properties.

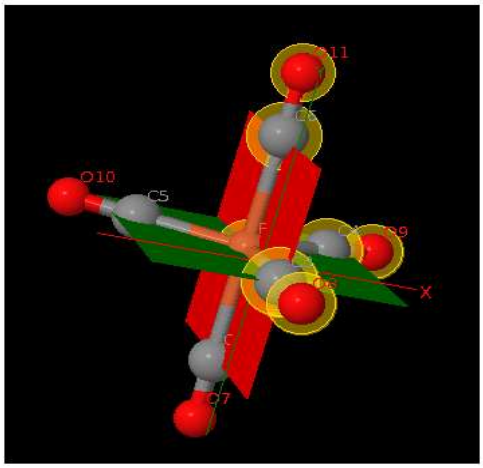

Fig 5.1.1.1. $Fe(CO)_5$ molecular structure from Quantemol-N (Fe – orange, C – grey, O – red)

Measurements of the resistivity of Fe nanostructures in Ref. [74] indicate a value of the residual resistivity ρ_{300K}/ρ_{2K} of 70% Fe containing deposits close to 1Ω, while the ferromagnetic induction in Fe nanorods is between 0.61 T and 0.45 T.

5.1.2. Previous Studies of DEA to $Fe(CO)_5$

The $Fe(CO)_5$ precursor has been shown to fully fragment using dissociative electron attachment (DEA) stripping off all five of the (CO) carbonyl groups leaving a single Fe atom to deposit on the surface at electron energies as low as 0 – 10 eV. All FEBID precursors containing carbonyl groups have been shown to produce high purity deposition structures (over ~ 90 at%) Ref. [74] by the lose of the carbonyl (CO) groups in the process of DEA fragmentation. A comprehensive list of previous experiments on DEA and DI using mass spectroscopy is presented in Table 6.1.2.1. The ions recorded in the DEA process of $Fe(CO)_5$ are anions with a number of $(CO)_x$ (x = 1 - 4) groups with dissociation energies between 2 – 20 eV. The highest anion (m/z 168) has a resonance peaking close to 0 eV, with high cross-section and a shoulder at 0.6 eV. Ref. [75], Ref. [79] present two high peaks of the highest anion acquired with two different apparatus, a quadrupole mass spectrometer with lower mass resolution and a CLUSTER apparatus with higher mass resolution. Small differences were observed in the $Fe(CO)_3^-$ anion spectra with resonance peaks at 1.2 eV in Ref. [79] and 1.4 eV in Ref. [75], and similar discrepancies for $Fe(CO)_2^-$ resonance peaks observed at 4.3 eV in Ref. [75] and 4.2 eV in Ref. [79]. The $FeCO^-$ shows even higher differences in the value of the resonance peaks at 4.9 eV and 7.9 eV comparing the values in Ref. [75] with the values in Ref. [79]. The smaller differences in the peak values in the anion data may be due to the resolution of the equipment used and the calibration.

*DEA anions from Ref. [75] and [79] are taken from graph data

Reference	**DEA anion spectra**	
	Anion	Electron Energy (eV) of the Resonance Peaks
Ref. [75] Lacko et al 2018 Quadrupole mass spectrometer	$Fe(CO)_4^-$ $Fe(CO)_3^-$ $Fe(CO)_2^-$ $FeCO^-$ Fe^-	0.26/ 0.98 1.4/ 3.8 4.3/ 8.9 5.9/8.5 8.9
Ref. [208]	$Fe(CO)_4^-$	0.6

Lengyel et al 2016 CLUSTER apparatus	$Fe(CO)_3^-$ $Fe(CO)_2^-$ $FeCO^-$ Fe^-	1.2/ 3.6 4.2/ 8.9 5.9/ 8.5 n/a
Present work (VMI)	$Fe(CO)_4^-$ $Fe(CO)_3^-$ $Fe(CO)_2^-$ $FeCO^-$ Fe^-	0.2 /0.6 / 1.2 1.3 / 3.4 4.2/8.9 4.9/ 7.9 7.9

Table 5.1.2.1. DEA anion spectrum data from different sources and comparison with current work

In the stretching modes vibrational analysis, the dissociation of $Fe(CO)_5$ is characterized by the loss of between one to five ligands to carbonyls. From the 33 basis vectors (3 x 11 atoms) we can reduce the basis set to only the five C = O bonds by using a C_{2v} symmetry and a user predefined basis set that combines LANL2DZ, 6-31G* and 31-STO. The stretching modes for carbonyl ligands fall in the range of 1700 – 2100 cm^{-1} (0.21 eV – 0.26 eV) in Ref. [77-778] with five vibrational excitations at 2093.4 cm^{-1} E' (0.259 eV), 2118.85 cm^{-1} A_1' (0.262 eV), 2120.24 cm^{-1} A_2" (0.263 eV) and 2192.65 cm^{-1} A_1' (0.27 eV) from JSmol (Table 5.1.2.2).

Reference	Excited Electronic States
Ref. [77-778] Korobtsov et al 2007 [778] Pauling et al 1948 [789]	$^1A_1$' to E' (0.26 eV) $^1A_1$' to A_1' (0.26 eV) $^1A_1$' to A_2" (0.26 eV) $^1A_1$' to A_1' (0.27 eV)
Ref. [76] from photofragmentation Lacko et al 2018	$^1A_1$' to E', E", A"$_2$ (4.4 eV) $^1A_1$' to E', E", A"$_2$ (5.15 eV) $^1A_1$' to E', A"$_2$ (6.2 eV)
Ref. [856] Rubner et al 1999	$^1A_1$' to ^{1,3}E' (3.97 eV) $^1A_1$' to ^{1,3}E" (4.41 eV) $^1A_1$' to b^{1}E' (4.83 eV)
Present work (Gaussian 16) DFT of $Fe(CO)_5$ in neutral state; B3LYP/6-31G*	$^1B_1$ (3.19 eV) $^1B_2$ (3.87 eV) ^1E (3.87 eV)

	^1E (4.17 eV) ^1E (4.35 eV) $^1A_1$ (4.36 eV) ^1E (4.7 eV) $^1B_2$ (4.9 eV) ^1E (4.95 eV) $^1A_2$ (4.97 eV) ^1E (5.06 eV) ^1E (5.2 eV) ^1E (5.24 eV) ^1E (5.27 eV)
Present work (Gaussian 16) DFT of $Fe(CO)_5$ in charged state; B3LYP/6-31G*	$^3A_1$ (3.1 eV) $^3A_1$ (3.14 eV)
Present work (Quantemol-N)	$^3A_2$ (2.58 eV) $^1A_2$ (2.77 eV) $^3B_2$ (3.13 eV) $^3B_1$ (3.27 eV) $^1B_2$ (3.4 eV) $^1B_1$ (3.67 eV) $^3B_1$ (4.35 eV), $^1B_1$ (4.51 eV)

Table 5.1.2.2. Excited electronic states, cross-sections, and resonances from different sources and comparison with current work

A number of excited states have been calculated and determined experimentally by Lacko et al 2017 [75] in the photofragmentation process resulting in cations if high enough, and excited states in DEA processes obtained by Rubner et al 1996 [86], Korobtsov et al 2007 [77] and Pauling et al 1948 [78] for low electron energies (Table 5.1.2.2). For comparison, a set of excited states from TDA at TD-DFT level using the $Fe(CO)_5$ molecule in neutral and charged state has been done using Gaussian 16 software at the B3LYP/6-31G* level of theory (Chapter 3 in 3.2.2. Gaussian 16 Software). Between 0.26 eV and 6.2 eV a number of 7 excited states have been obtained with the predominant symmetry states $^1A_1$' to E', A_1', A_2" (0.26 eV), A_1' (0.27 eV) [78, 79] and E', E", A"$_2$ (4.4 eV), E', E", A"$_2$ (5.15 eV), E', A"$_2$ (6.2 eV) [75]. In the charged state, the calculations of the excited states limit to two obtained symmetries and

allowed transitions $^3A_1$ close to the electron energy of ~3.1 eV. Smaller energy values in the excitation cross-sections have been reported in Ref. [78, 79] around 0.2 eV as different compared to the ones reported in Ref. [86] and Ref. [75] with values between 3eV and 5.5 eV, corresponding to the presence of $Fe(CO)_4^-$ anion only.

5.1.3 SUMMARY OF EXPERIMENTAL SET-UP

The VMI apparatus used in these experiments has been presented in Chapter 2 including details on the method of calibration of the equipment. SIMION v2020 (https://simion.com/) was used to confirm the focussing elements. The resolution of the VMI equipment was 0.1 eV. The set of 3D plots (Fig 6.1.3.1) of the anions produced by DEA was obtained from the VMI images processed with Phyton v3.10.

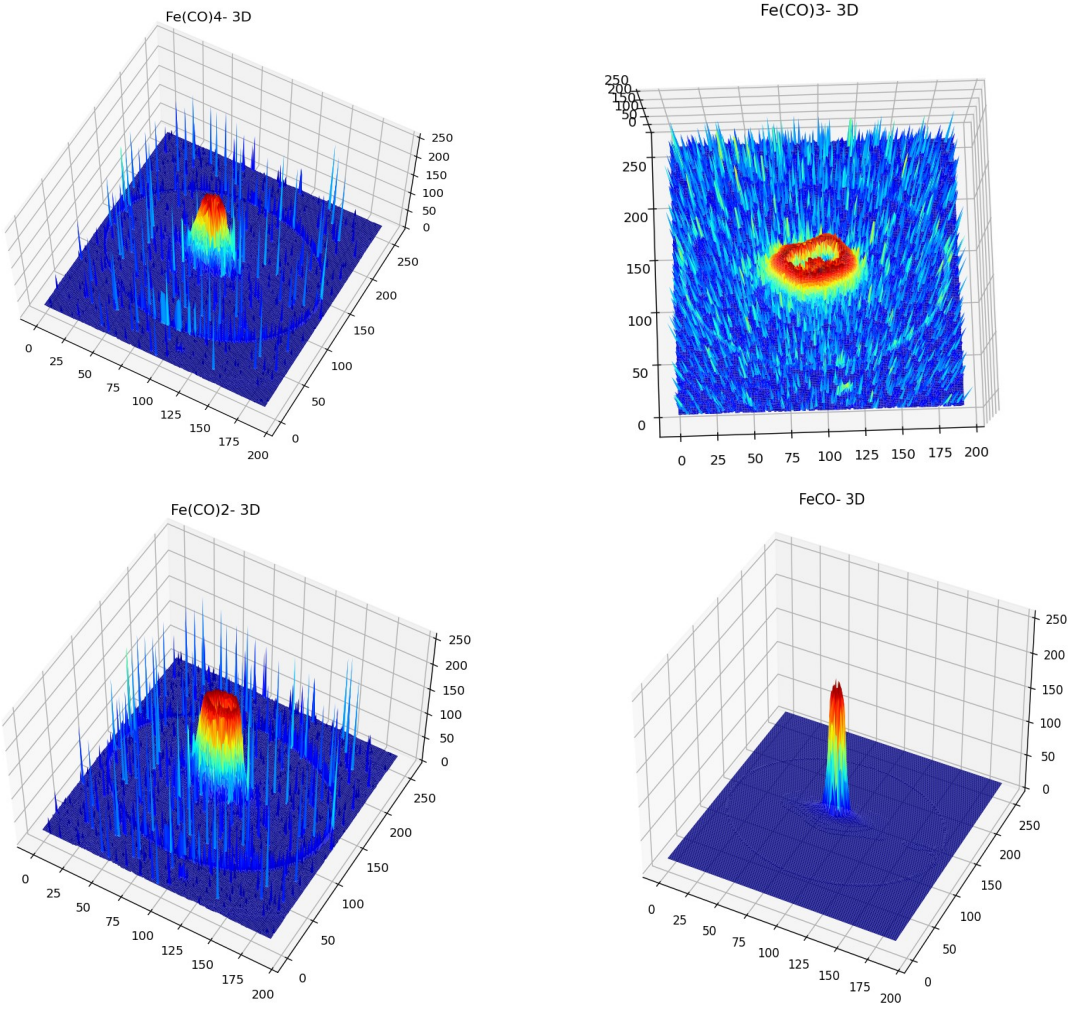

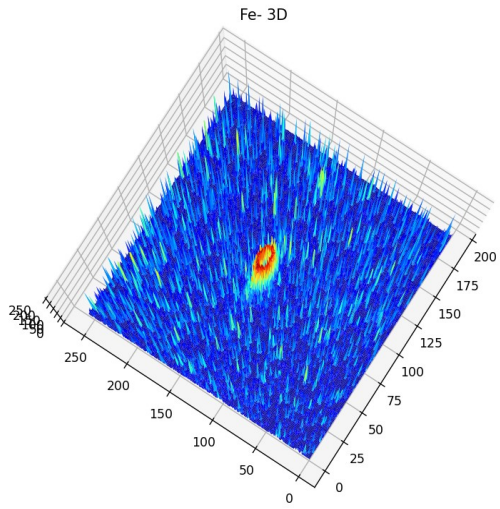

Fig 5.1.3.1. 3D velocity sliced map images of the anions of $Fe(CO)_5$ at different incident electron energies

5.1.4 Results and Discussions

DEA induced anion fragments. The $Fe(CO)_5$ dissociation process is characterized by high collision cross-sections at energies as low as 0.2 eV.

$$Fe(CO)_5 \rightarrow Fe(CO)_4^- + CO \rightarrow Fe(CO)_3^- + 2(CO) \rightarrow Fe(CO)_2^- + 3(CO) \rightarrow Fe(CO)^- + 4(CO)$$

$$\rightarrow Fe^- + 5(CO) \qquad (5.1.4.1)$$

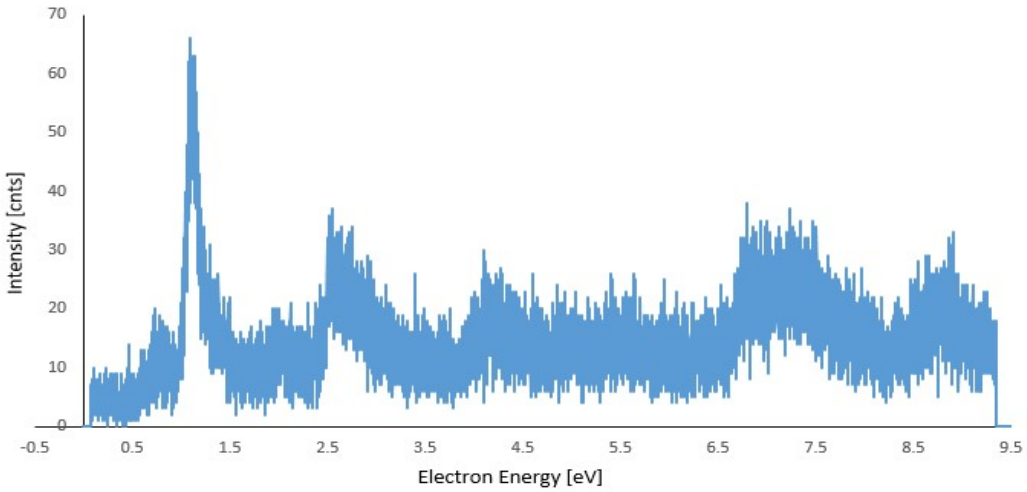

Fig 5.1.4.1. $Fe(CO)_5$ A spectrum of total anion yield produced by DEA to $Fe(CO)_5$

Using the VMI apparatus described in Chapter 2 and the quadrupole mass spectrometer instrument in Comenius University, Department for Molecular Physics, the mass spectrum of anionic fragments from the VMI of $Fe(CO)_5$ was acquired and is presented in Fig 5.1.4.1. Higher intensity (number of counts) is observed for the higher mass fragments compared to the lighter anions containing one to two CO groups. From the velocity map imaging spectrum, we observe multiple peaks and higher energy bands corresponding to fragmentation channels of the compound, in close agreement to the data of Lacko et al 2018 [75]. Even though the spectrum of the $Fe(CO)_5$ negative ions is very noisy, one can clearly distinguish between the five negative ions and their peak structures, anionic fragments resulting from the striping-off of the five ligands. Cross-sections (anion yields as a function of incident energy) were calculated for each fragment. In the present work, the resonance has a maximum peak at 0.6 eV with a smaller amplitude peak at 0.2 eV in agreement with the data presented in Lacko et al 2018 [75] at 0.26 eV (Fig 5.1.4.2; Fig 5.1.4.3). The high-count rates for the dissociation resonances peaking around 0 eV shows that the dominant process at these energies is intramolecular vibration causing the breakage of the ligand and a high rise in the dissociation cross-section. The loss of one ligand in the DEA process at energies close to 0 eV is considered a transition process of the $Fe(CO)_5$ from the neutral ground state σ to π* excited state ($Fe(CO)_5$*), losing one of the axial CO bonds to metal forming $Fe(CO)_4^-$.

Negative Ion	Incident Electron Energy [eV]	Maximum Kinetic Energy [eV]
$Fe(CO)_4^-$	0.2 / 0.6 / 1.2	0.79
$Fe(CO)_3^-$	1.3	1.375
$Fe(CO)_2^-$	4.2	3.87
$FeCO^-$	8.5	8.197
Fe^-	9	8.998

Table 5.1.4.1. Excess energy calculations for $Fe(CO)_5$ negative ions obtained in the dissociation process

The electron affinity of the ions formed in the photo-dissociation process is presented by Engelking et al 1989 [84]. He experimentally determined the values by using an electrical discharge ion source and a Wien filter with an Ar ion laser. The values are comparable with the work of Shuman et al 2013 [52]. The Fe atom's electron affinity experimentally determined is higher in the range of ~0.164 ± 0.02 eV compared to the work of Chen et al 2016 [85] exhibiting a value of 0.153 eV determined by the slow electron velocity map imaging (SEVI) method. The thermochemistry data from Shuman et al 2013 [52] falls back to the measurements of Engelking et al 1969 [84] with changes to the uncertainty corrections. They employed variable electron and neutral density attachment spectroscopy (VENDAMS) technique and flowing afterglow Langmuir probe mass spectrometer (FALP), for the determination of accurate

values on electron affinity and bond dissociation energies for the negative ions formed in the DEA of $Fe(CO)_5$.

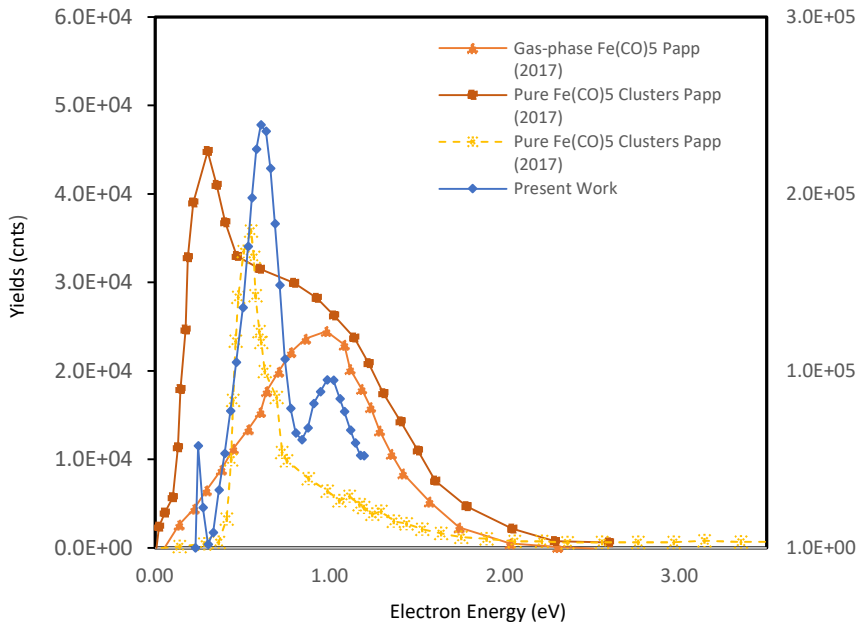

(a)

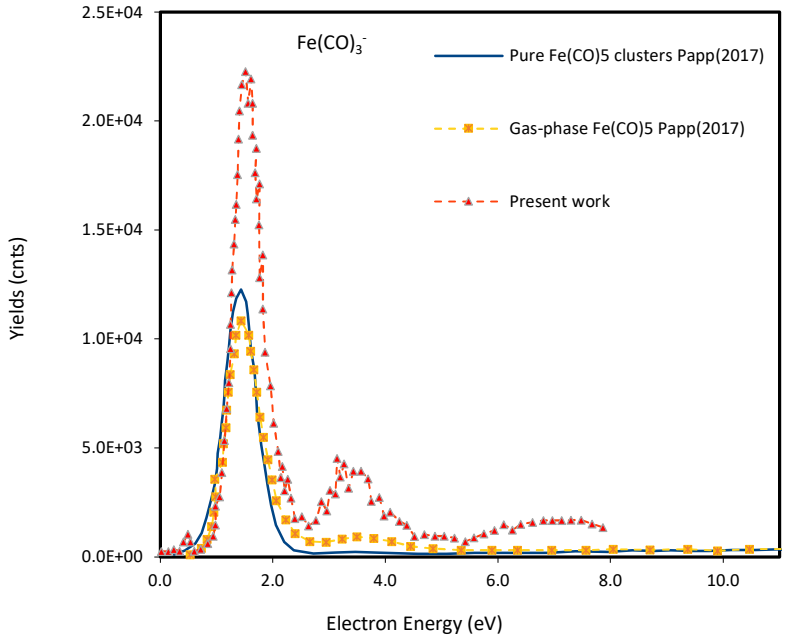

(b)

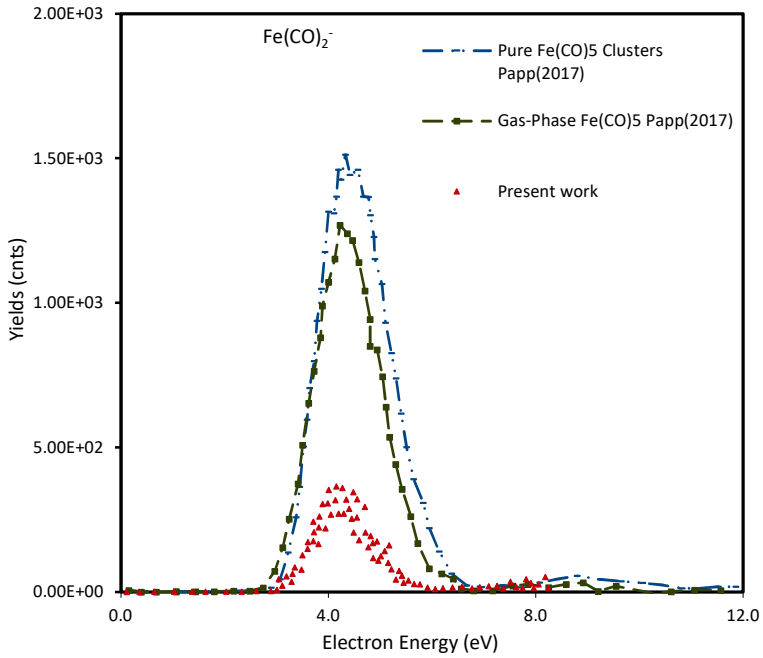

(c)

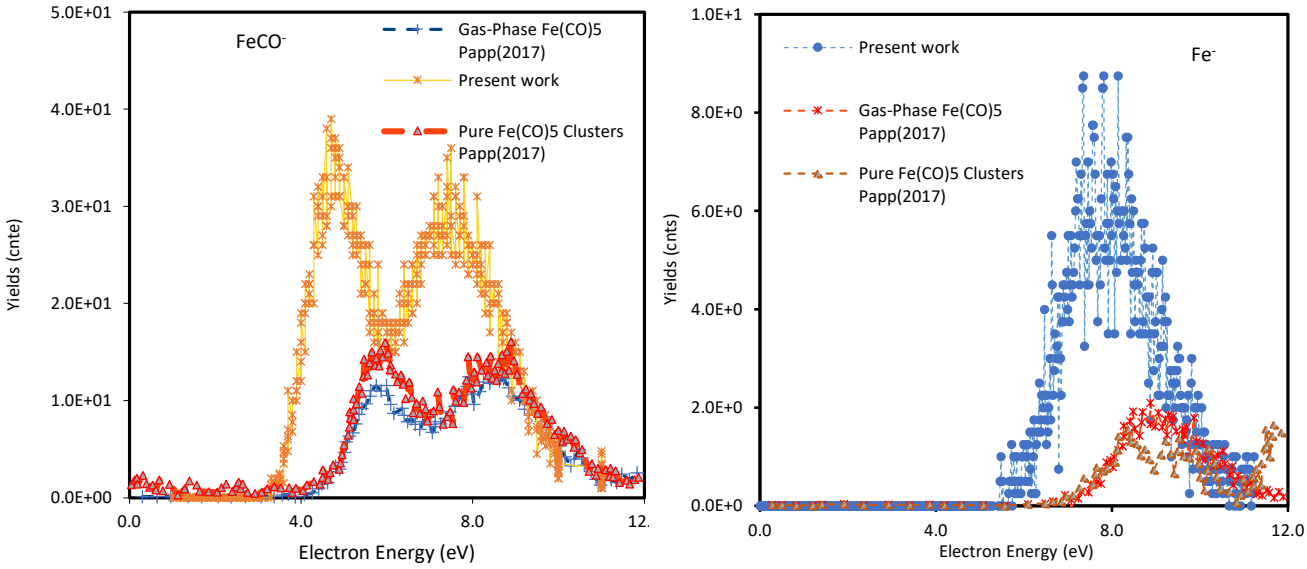

(d) (e)

Fig 5.1.4.2. $Fe(CO)_5$ negative ion spectrum reproduced from Lengyel et al 2017 [82]: (a) $Fe(CO)_4^-$, (b) $Fe(CO)_3^-$, (c) $Fe(CO)_2^-$, (d) $FeCO^-$ and (e) Fe^-

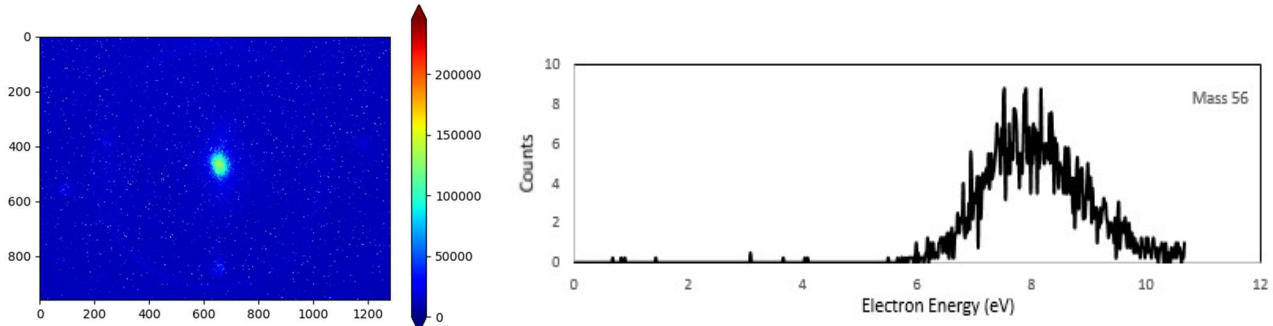
Mass 56
Counts
Electron Energy (eV)

(a)

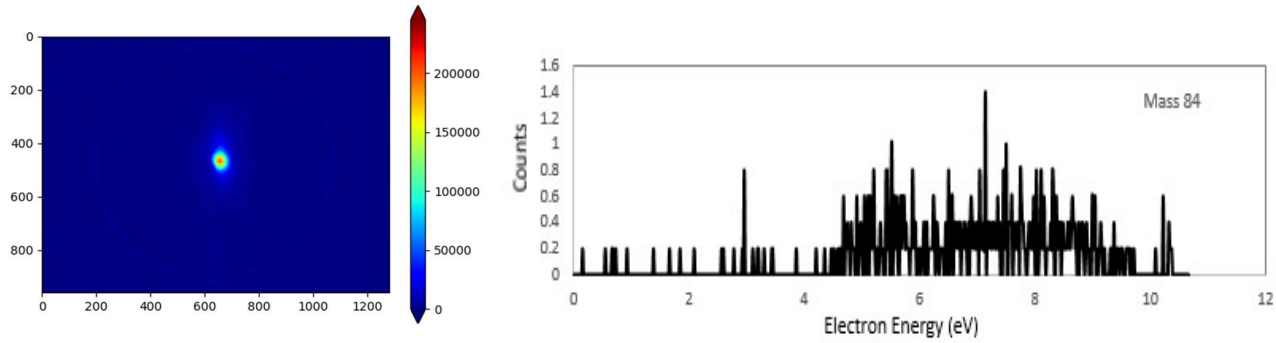
Mass 84
Counts
Electron Energy (eV)

(b)

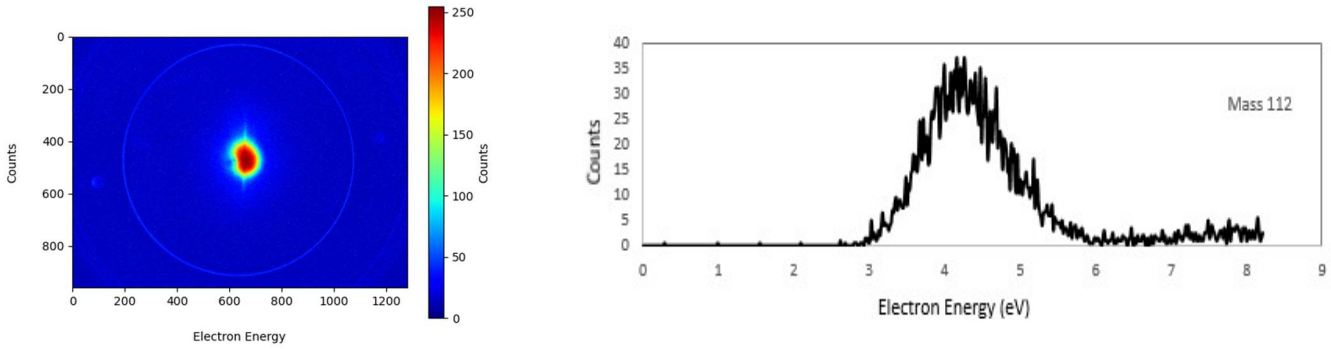
Mass 112
Counts
Electron Energy (eV)
Counts
Electron Energy

(c)

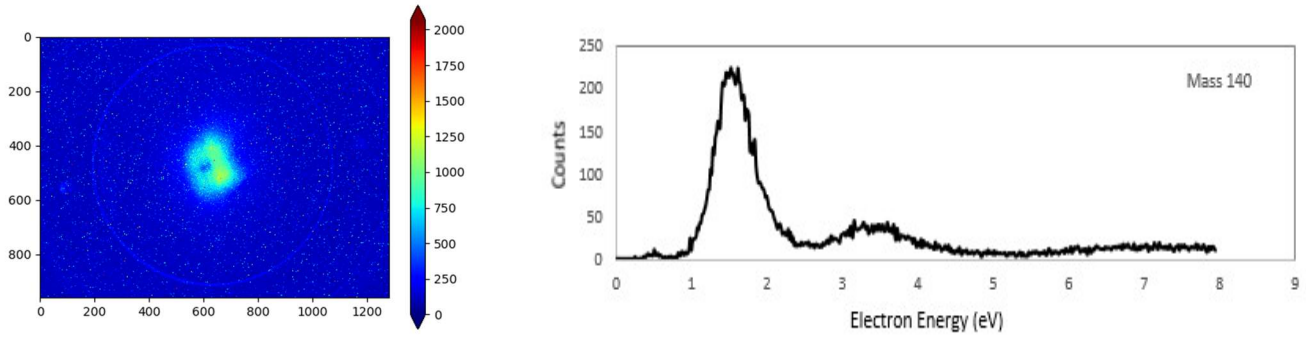

(d)

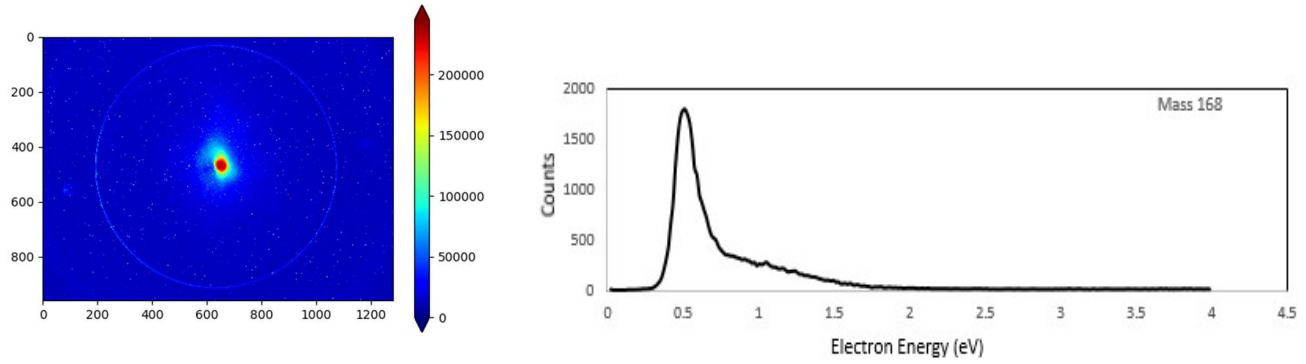

(e)

Fig 5.1.4.3. Anions of $Fe(CO)_5$: (a) Fe^- (m/z 56) (b) $FeCO^-$ (m/z 84) (c) $Fe(CO)_2^-$ (m/z 112) (d) $Fe(CO)_3^-$ (m/z 140) (e) $Fe(CO)_4^-$ (m/z 168)

Kinetic energy of the fragments. The kinetic energy of each of the fragments are presented in Fig 5.1.4.4. The maximum values of the kinetic energies for each of the negative ions formed in the velocity sliced map imaging chamber in the dissociation process are presented in the Table 5.1.4.1. Lacko et al 2018 [75] defines the kinetic energy of the $Fe(CO)_4^-$ negative ion as being only 14 % of the excess energy or of the maximum kinetic energy with a value of 0.15 ± 0.04 eV. From our experimental data, 14 % of our maximum kinetic energy or excess energy is 0.11 eV, 0.04 eV lower than the cited value.

The symmetry of the negative fragment $Fe(CO)_4^-$ is a result of the dissociation induced by the interaction of the charged electron with the neutral molecule of $Fe(CO)_5$ in ground state, with a conserved D_{3h} symmetry, the loss of one axial ligand is not affecting the system's final state of symmetry. The maximum of the kinetic energy for the $Fe(CO)_4^-$ fragment is determined using the electron affinity of the fragment, for the present measurement the value of Schuman et al 2013 [52] of 2.4 ± 0.3 eV was used, the bond dissociation energy of 1.81 eV and the electron incident energy of 0.2 eV, with a resultant value of 0.61 eV. Changes at the electronic level in the case of the second fragment of $Fe(CO)_5$, the $Fe(CO)_3^-$ that as a result of the fragmentation looses its symmetry undergoing a transition to C_{2v} are the result of a $\sigma \rightarrow \sigma^*$ transition and an electron incident energy of the maximum peak of the resonance at 4.2 eV.

Ions	Shuman et al 2013 [52] EA	Shuman et al 2013 [52] BDE	Engelking et al 1979 [84] EA	Engelking et al 1979 [84] BDE_{Fe-C}	Chen et al 2016 [85] EA
$Fe(CO)_4^-$	2.4 +/- 0.3	1.81	1.26 +/- 0.02	1.0 +/- 0.3	n/a
$Fe(CO)_3^-$	1.915 +/- 0.085	1.84	1.22 +/- 0.02	1.0 +/- 0.3	n/a
$Fe(CO)_2^-$	1.22 +/- 0.02	1.55	1.8 +/- 0.2	1.4 +/- 0.3	n/a
$Fe(CO)^-$	1.157 +/- 0.005	1.46	2.4 +/- 0.3	0.2 +/- 0.4	n/a
Fe^-	0.151 +/- 0.003	n/a	n/a	n/a	0.153

Table 5.1.4.2. $Fe(CO)_5$ electron affinity (EA) and bond dissociation energy (BDE)

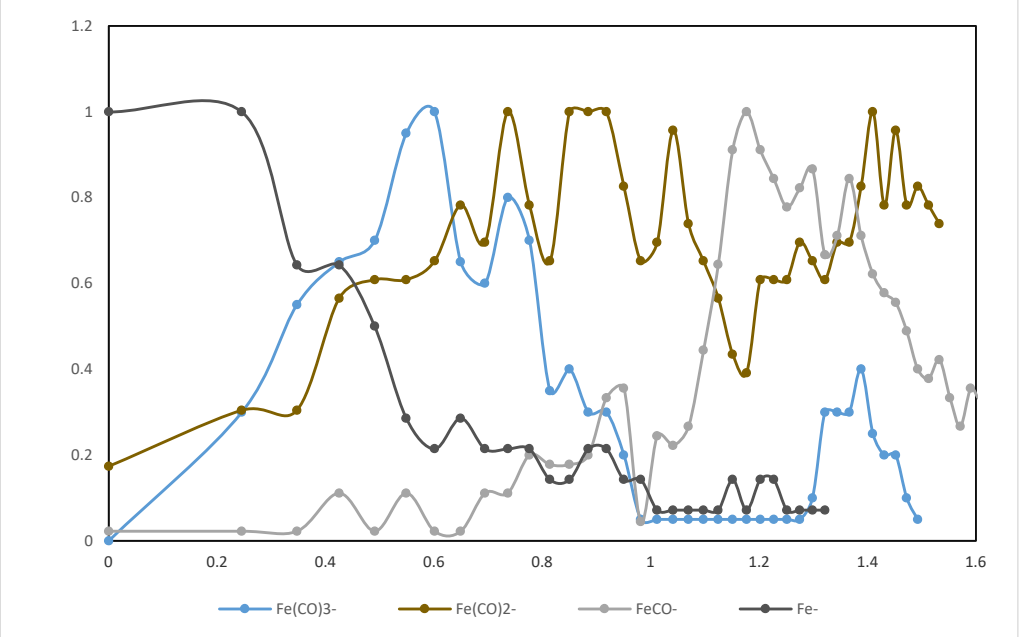

(a)

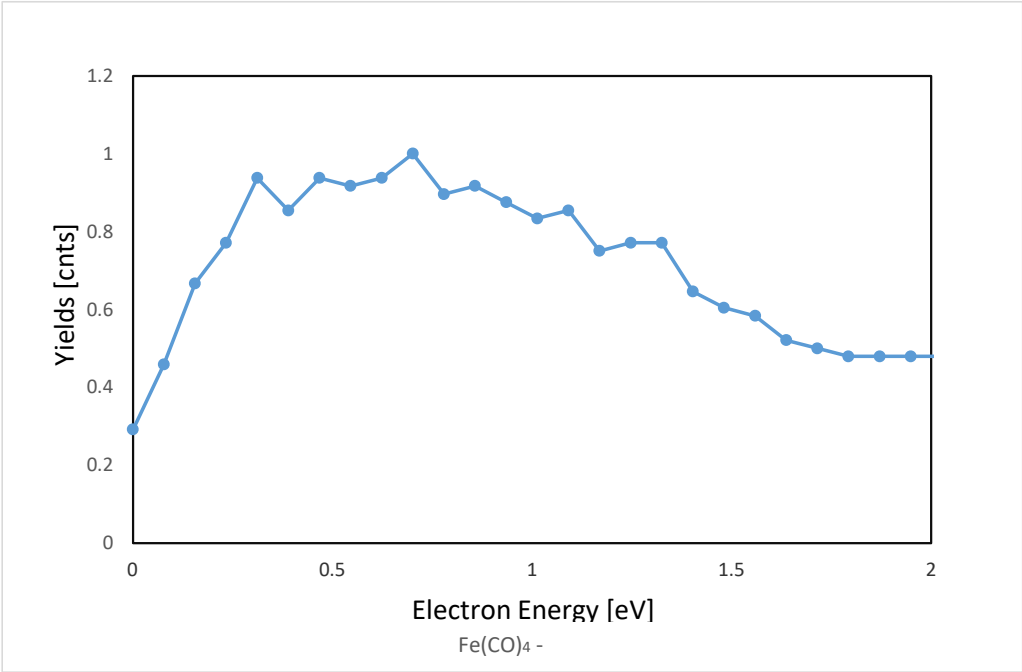

(b)

Fig 5.1.4.4. Kinetic energies of $Fe(CO)_5$ anions: (a) $FeCO^-$; Fe^-; $Fe(CO)_2^-$; $Fe(CO)_3^-$ (b) $Fe(CO)_4^-$

The kinetic energy measurement from the velocity slice map imaging recorded data, shows a high-rise slope between 0.2 eV and 1 eV (Fig 5.1.4.4 (b)), with the two maximum points with similar amplitude at 0.2 eV and 0.6 eV. An increase in the electron affinity is observed in the transition from Fe to FeCO, assigned to the bond strength within the Fe - CO, though the work of Engelking et al 1979 [84] explains this by a stabilization of d orbitals of π symmetry in the interaction with the CO π* orbitals and a destabilization of d orbitals with σ symmetry by the σ orbitals of CO. Vibrational features showing up at 1815 cm^{-1} (0.225 eV), 1735 cm^{-1} (0.215 eV), 1695 cm^{-1} (0.21 eV) are attributed to the neutral state of FeCO fragment and a smaller peak at 780 cm^{-1} (0.097 eV) to the Fe-C bond. The vibrational frequencies of the $FeCO^-$ ion appear at 1980 cm^{-1} (0.245 eV), assigned to the C - O stretch. The negative ion fragments are presented in Fig 5.1.4.3.

Angular distribution of $Fe(CO)_5$ anions. The angular distribution of the anions of $Fe(CO)_5$ is presented in Table 5.1.4.3. The angular distribution data from our VMI measurements processed using Python 3.8 is presented in Fig 5.1.4.5 using the "best feature" algorithm and OpenCV package for picture analysis (see ANNEX 5). The real-time counts were recorded as distributions of ions in the pictures. The symmetry for all the ions can be observed as being between 92 deg – 100 deg.

Anion	Symmetry angle	Symmetry
$Fe(CO)_4^-$	50°, 120°	C_{2v}
$Fe(CO)_3^-$	48°, 140°	C_{2v}
$Fe(CO)_2^-$	48°, 140°	C_{2v}
$FeCO^-$	30°, 148°	C_{3v}
Fe^-	48°, 140°	C_{3v}

Table 5.1.4.3. Angular distribution and symmetry of $Fe(CO)_5$ from Ref. [82]

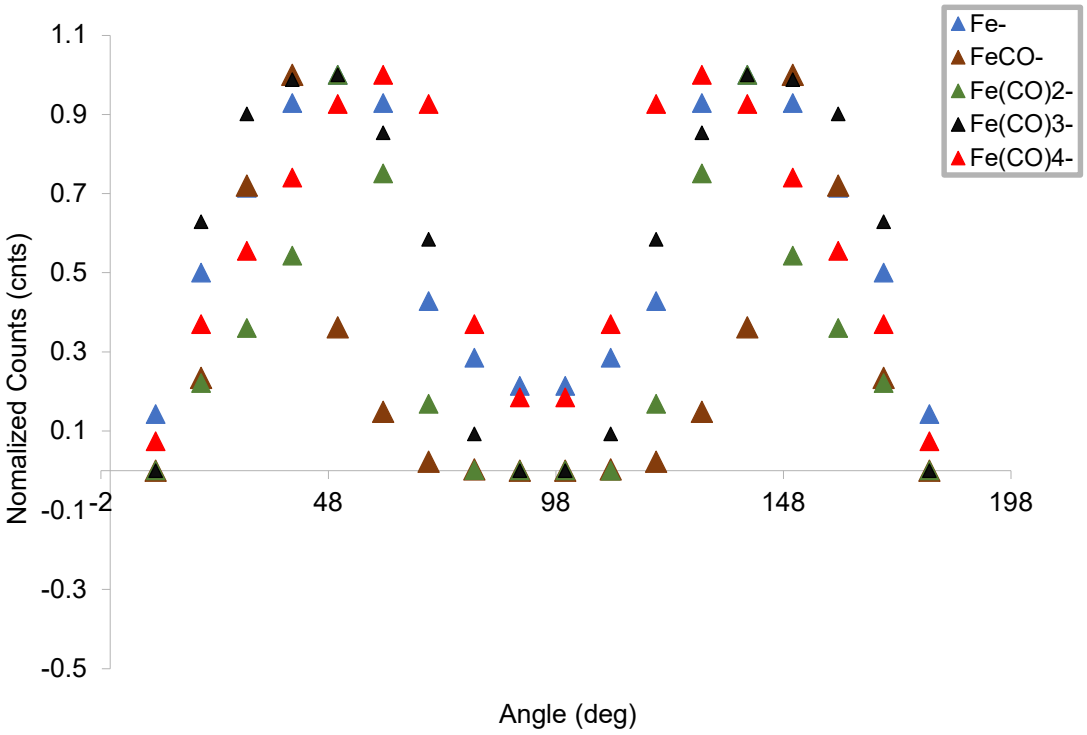

Fig 5.1.4.5. $Fe(CO)_5$ anions angular distributions

The angular distribution of the anions is at 50 deg and 120 deg corresponding to a C_{2v} symmetry state $Fe(CO)_4^-$, while $Fe(CO)_3^-$ and $Fe(CO)_2^-$, are found in C_{2v} symmetry state, but with lower symmetry amplitudes found at 148 deg and 140 deg. For the two lighter anion fragments, $FeCO^-$ and Fe^-, the first symmetry peak changes to lower values bellow 50 deg, at 30 deg and 48 deg, while the higher symmetry peak shifts to higher values at 148 deg and 140 deg, and as well their symmetry changes from C_{2v} to C_{3v}. No angular distribution data of the $Fe(CO)_5$ anions has been found reported in the cited literature to this date.

Calculated $Fe(CO)_5$ Electron Scattering Cross Sections Data. Using Quantemol-N software (described in Chapter 3 Subsection 3.1) cross-sections of several electron scattering processes were evaluated: elastic cross-sections, inelastic cross-sections, excitation cross-sections and dissociative electron attachment cross-sections.

The ground state structure for $Fe(CO)_5$ is D_{3h} with vibrational frequency bands for $^1A_1'$ at 2034 cm^{-1} (0.252 eV) for A_2'', 2121 cm^{-1} (0.263 eV), 2042 cm^{-1} (0.253 eV) for A_1' and 2013 cm^{-1} (0.249 eV) for E'. The bond distance is between Fe - C of 1.8240 Å and 1.1450 Å between C - O *NIST database*. The bond distances in Ref. [83] for $Fe(CO)_5$ are: 1.807 Å metal – CO and 1.152 Å C-O bond. The X, Y, Z atomic coordinates used in the Quantemol-N calculations are presented in Table A1 (ANNEX 1). These parameters have been adapted from the configuration on the *NIST database* to obtain D_{3h} symmetry for the Quantemol-N simulations. For simplification of the simulations and reduction of the number of electrons and orbitals, a C_{2v} symmetry work point group has been used.

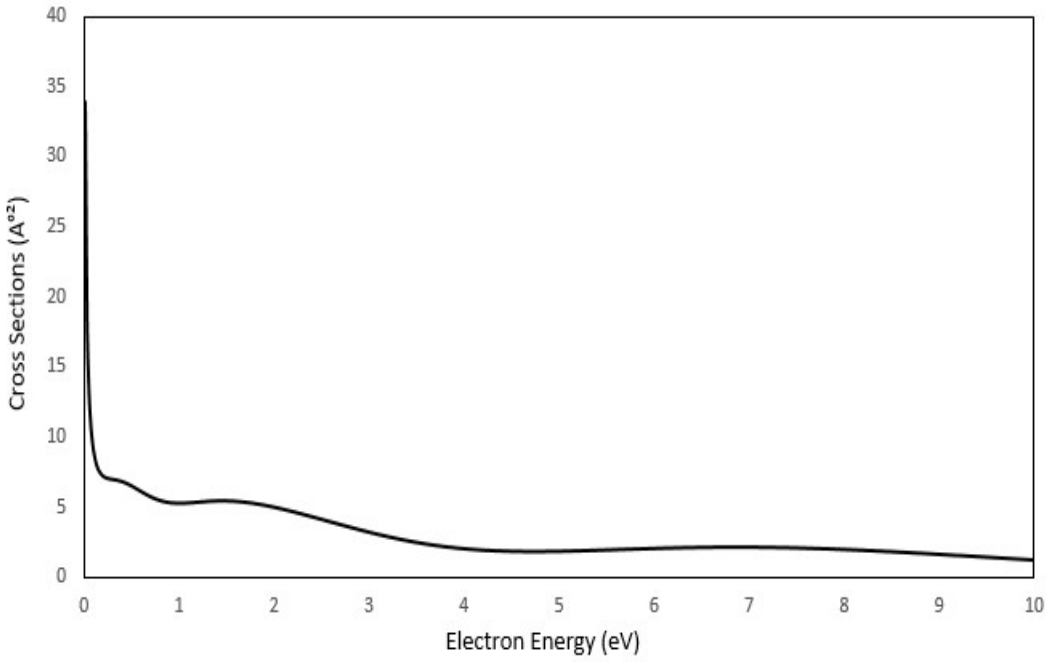

Fig 5.1.4.6. Dissociative electron attachment cross-sections of $Fe(CO)_5$ (from Quantemol-N with 1800cm^{-1} specificity, 0.2 eV fragmentation energy and 1.8 eV bond dissociation energy)

As the configuration orbitals needed for the evaluation of dissociative attachment cross-sections require larger computational resources, a larger data set in SUPERMOLECULE format defined by the user has been used. The R-matrix radius has a value of 13 Å with a 10 eV cut-off. The basis set (see ANNEX 1 for details) is a user defined basis set. The metal – to – CO transition bond mechanism is a σ to π* transition, from a lower energy level to a higher excited state, the donation of metal – to – CO back

bonding π* in agreement to Ref. [83]. This transition process is a typical process for the carbonyls. The bond dissociation energy and electron affinity for the $Fe(CO)_5$ negative ions are presented in Table 5.1.4.2. The fragmentation energy of the $Fe(CO)_4^-$ anion was taken from the VMI experimental data. High cross-section values are observed for low energies, close to zero, where we have a dissociation process caused mostly by the increase in the vibration of the molecule leading to bond breakage. The highest cross-section value (Fig 5.1.4.6.) is observed in the formation of the $Fe(CO)_4^-$ anion with values in the range of 5.7E+02 $Å^2$. The highest cross-section value is 1.63E+03 $Å^2$ close to 0 eV, reaching 4.69E+01 $Å^2$ at an incident electron energy of 10 eV. The cross-section values correspond to the fragmentation energies of the anions with peaks visible close to the bond dissociation energy of the anions, and the highest cross-section value close to 0, corresponding to the $Fe(CO)_4^-$ anion. The DEA cross-section curve is in good agreement to the experimental data from VMI and to the experimental data of Lacko et al 2018 [745] with the presence of all the anions and peaks of the resonance. Multiple BDEs and specificities (cm^{-1}) have been used in Fig 5.1.4.8 to calculate and compare different DEA cross-section curves.

Data presenting different bond values, electron affinities, and specificities (vibrational frequency corresponding to excited state) [52, 84-85] are presented in Table 5.1.4.2. The values presented by Shuman et al 2013 [52] decrease with the lowering of the mass of the charged fragment, while Engelking et al 1979 [84] present values that increase with the stripping-off of the CO radicals. The electronic state excitation cross-sections with the respective channels are presented in Fig 5.1.4.7. The electronic configuration used for the doubly occupied orbitals run in Configuration Interaction (HF Orbitals) mode is 22(a1)2, 10(b1)2, 11(b2)2 and 5(a2)2. We observe that at 0.6 eV, the first excitation resonance appears corresponding to $^3B_2$ with the highest peak amplitude at 1.6 eV and a value of 1.29E+00 $Å^2$. The specific channels in the excitation cross-sections graph correspond to vibrations at different incident electron energies. If further compared with the excitation energies related to the DEA cross-sections, each resonance channel corresponds to excitation energies higher than 3 eV. The DEA fragmentation channels are presented in Table 5.1.4.4 and are inputs to the simulation software for cross-sections determination. The excited states for the C_{2v} geometry used in our simulations are the result of a transition from the ground state $^1A_1$ to eight electronically excited states with excitation energies between 2.5 eV and 5 eV. The excited states are $^3A_2$ (2.58 eV), $^1A_2$ (2.77 eV), $^3B_2$ (3.13 eV), $^3B_1$ (3.27 eV), $^1B_2$ (3.4 eV), $^1B_1$ (3.67 eV), $^3B_1$ (4.35 eV) and $^1B_1$ (4.51 eV) and were obtained results of the Quantemol-N simulation in the Configuration Interaction Orbital mode. Three allowed transitions $^1A_1$' → ^{1,3}E', $^1A_1$' → ^{1,3}E" and $^1A_1$' → b^{1}E' presented by Rubner et al 1999 [86] may be linked to the three higher mass fragments $Fe(CO)_4^-$, $Fe(CO)_3^-$ and $Fe(CO)_2^-$ (the two higher mass fragments $Fe(CO)_4^-$ and $Fe(CO)_3^-$ correspond to ^{1,3}E'

transition; all three of them have a corresponding transition to b^1E') and similar in corresponding energy value to our experimental work. The resonances for each cross-section corresponding to the excited states can easily be identified in Fig 5.1.4.7 with their corresponding energy.

DEA fragmentation channel	Energy range (eV) *taken from experimental work	Vibrational frequency (cm^{-1})
$Fe(CO)_5 + e^- \rightarrow Fe(CO)_4^- + CO$	0 - 1	2093.4 (E')
$Fe(CO)_5 + e^- \rightarrow Fe(CO)_3^- + 2(CO)$	1 - 2.5	2118.85 (A1')
$Fe(CO)_5 + e^- \rightarrow Fe(CO)_2^- + 3(CO)$	2.5 - 6	2093.4 (E')
$Fe(CO)_5 + e^- \rightarrow Fe(CO)^- + 4(CO)$	4 - 10	2120.24 (A2")
$Fe(CO)_5 + e^- \rightarrow Fe^- + 5(CO)$	6 - 10	2192.65 (A1')

Table 5.1.4.4. DEA fragmentation channels and resonances used for cross-sections simulations; work done in collaboration with M. Tudorovskaya (Quantemol-N)

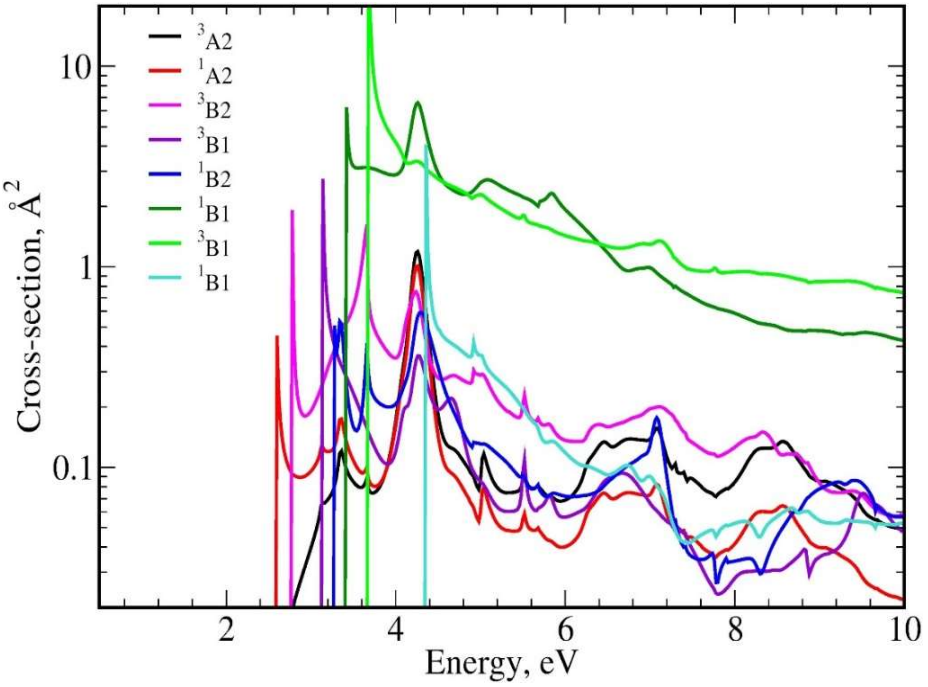

Fig 5.1.4.7 Excitation cross-sections of $Fe(CO)_5$; work done in collaboration with M. Tudorovskya (Quantemol-N)

The analysis of the cross-section values may be performed using different values of the electron affinity of the molecule and specificity. The difference in the resulting resonances can clearly be seen for the two

red curves (Fig 5.1.4.8) where the same electron affinity value is used (EA = 2.4 eV), the same bond dissociation energy value (BDE = 1.8 eV), but different specificities (red dashed 1000 cm^{-1} and red continuous 2093 cm^{-1}). A higher peak value and as well higher cross-sections values are observed for the continuous red curve with a higher specificity value, but the curve follows the same changes presenting the same shoulder at higher incident electron energy and with lower amplitude. The same behaviour is observed for the green and blue curves and further for the two black curves (dashed and continuous) corresponding to lower values of EA of 1.9 eV.

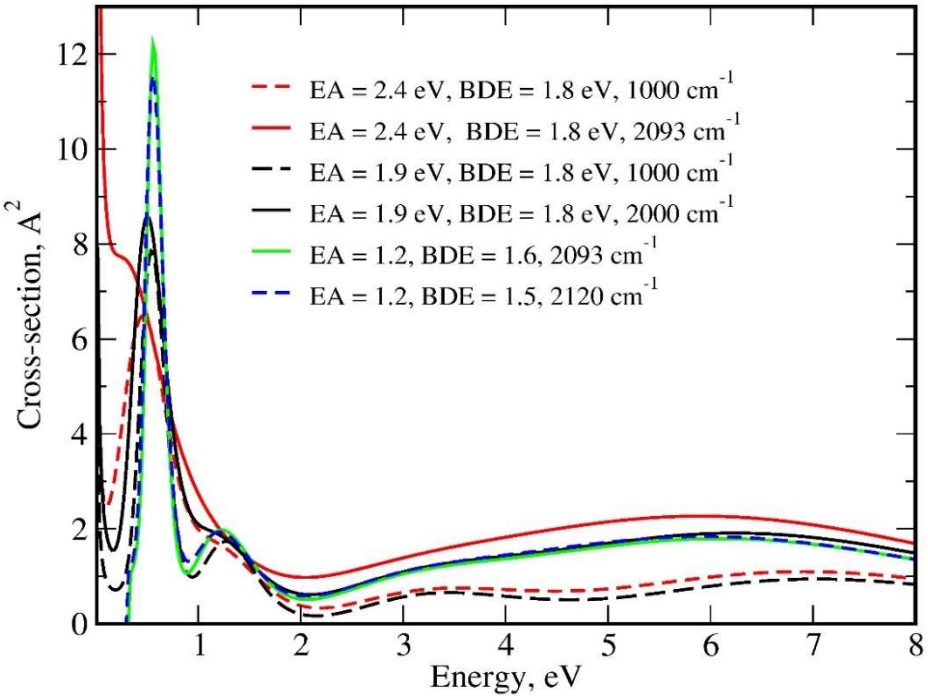

Fig 5.1.4.8 DEA cross-sections of $Fe(CO)_5$ obtained from Quantemol-N using different electron affinity; work done in collaboration with M. Tudorovskya (Quantemol-N)

5.1.5 Summary and Conclusions

In the DEA study of the $Fe(CO)_5$ molecule, characterized by one metal core and five CO bonded to the metal core with BDEs between 1 eV to 2 eV, the VMI technique was used to identify all the product anions and determine their kinetic energy data and angular distribution data. The present data is in good agreement with earlier work reported in Ref. [52] and Ref. [84]. Lacko et al 2017 [82] present their BDE estimation energies in good agreement with the work of Shuman et al 2013 [52] and Engelking et al 1984 [84] of 1 eV for 3 – 5 CO radicals in the formation of $Fe(CO)_{3\text{-}5}^-$ and 2 eV for the molecule containing 1 - 2 CO radicals in the formation of $Fe(CO)_{1\text{-}2}^-$. Values of ~1 eV of the bond dissociation energies have been used in the determination of cross-sections and maximum kinetic energies. The kinetic energies

determined from the sliced Newton sphere using a Python developed code have values between 0 – 1.2 eV with 0.7 eV (for $Fe(CO)_4^-$), 0.6 eV (for $Fe(CO)_3^-$), 0.8 eV (for $Fe(CO)_2^-$), 1.17 eV (for $FeCO^-$) and 0.24 eV (for Fe^-). The angular distribution of the fragments ranges in symmetry from C_{4v} (D_{3h}) to C_{2v} and C_{3v} for the excited anionic fragments. The higher excited fragments ($Fe(CO)_4^-$ and $Fe(CO)_3^-$) present symmetry at 40 deg and 140 deg, while the smaller excited fragments present symmetries between 20 – 60 deg and 115 – 140 deg. Quantemol-N software has been used to evaluate total DEA cross-sections with a maximum value of 1.63E+03 $Å^2$ between 0 eV and 1 eV, reaching values of 4.69E+01 $Å^2$ at higher energies of 7 eV.

5.2 $W(CO)_6$

5.2.1 Introduction of $W(CO)_6$

$W(CO)_6$ has been widely used as a precursor gas for nano- and micro-scale prototyping in Ref. [99] delivering structures with good electrical conductivity, isolation, and ferro-magnetic behaviours. In FEBID, $W(CO)_6$ has delivered magnetic nanostructures with a resistance of 50 kΩ and resistivity of 0.01 Ωcm in Ref. [99] and purity of the nanostructures of up to 56 %.

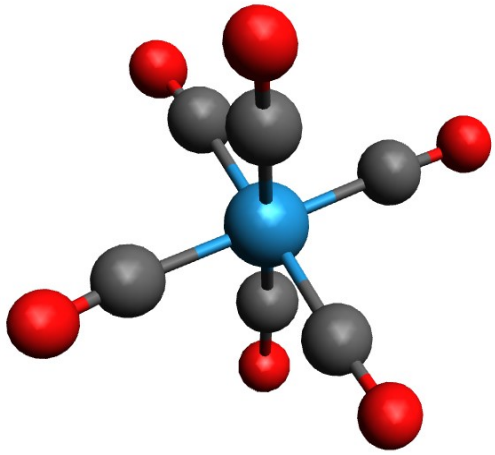

Fig 5.2.1.1 View of $W(CO)_6$ (W - blue, C – grey, O – red)

Its use in the manufacturing of carbon nanotubes in Ref. [229] has increased the importance of having electronic data available (anions and fragmentation pathways, electronic excited states, cross-sections

data) on the molecule and its behaviour in different conditions, gas-phase, surface deposition, beam assisted deposition.

Similar to other carbonyl compounds, $W(CO)_6$ strips off from one to multiple metal – CO ligands, the difference comes in its partial dissociation at low energies forming the lightest anion WCO^- leaving on the substrate structures with C and O in their content. UHV studies of the deposition of the $W(CO)_6$ in Ref. [14] at 500 eV show the decomposition of the precursor after a short irradiation cycle into $W(CO)_3$ and $W(CO)_2$, loosing in the C(1s) and O(1s) Xray photoelectron spectroscopy regions from one to two (CO) radicals, characteristic to its high volatility and low fragmentation energy; though its powder form makes it harder to use, creating high levels of contamination in the chamber upon usage. Higher chamber pressures (vaporization) suit better this compound due to its commercialization in solid/powder state up to one level compared to the $Fe(CO)_5$ produced in liquid state.

5.2.2 Previous Work

Earlier work has identified five anions formed by DEA to $W(CO)_6$, with no observation of W^- ion electron induced dissociation or as a result of the photofragmentation in cation form, and as a result in the FEBID process a higher number of C and O will deposit in the nanostructures at low energies. The anions in Ref. [88] and Ref. [97] disagree in the incident electron energy with more than 0.4 eV. The higher mass anion fragment $W(CO)_5^-$ is found at energies of 1.5 eV in Ref. [88] and 1.8 eV in Ref. [97], and at 0.2 eV in our own experimental measurements from VMI. Similar discrepancies are found in the other four anions.

Reference	DEA anion spectra	Electron Energy (eV) of Resonance Peaks
Ref. [97]	$W(CO)_5^-$	1.8
Seebauer et al 1995	$W(CO)_4^-$	2.6
	$W(CO)_3^-$	3.6
	$W(CO)_2^-$	7.5
	WCO^-	10.8
Ref. [88]	$W(CO)_5^-$	1.5
Wnorowski et al 2012	$W(CO)_4^-$	1.8/ 3.3/ 7.6
	$W(CO)_3^-$	3.9/ 4.7/ 7.5
	$W(CO)_2^-$	8.8
	WCO^-	n/a

Present work (VMI)	$W(CO)_5^-$	0.2
	$W(CO)_4^-$	3.3
	$W(CO)_3^-$	4.7
	$W(CO)_2^-$	8.8
	WCO^-	17

Table 5.2.2.1. DEA anion spectrum data from different sources and comparison with current work

The anions with higher masses have values of the incident electron energies as high as 1.8/ 3.3/ 7.6 eV (Ref. [88]) and 2.6 eV (Ref. [97]) for $W(CO)_4^-$, 3.9/ 4.7/ 7.5 eV (Ref. [89]) and 3.6 eV (Ref. [97]) for $W(CO)_3^-$, 8.8 eV (Ref. [88]) and 7.5 eV (Ref. [95]) for $W(CO)_2^-$ and 10.8 eV (Ref. [97]) the lightest WCO^-. Wnorowski et al 2012 [87] present their anion data in comparison to the data of Winters and Kiser [89], though Winters and Kiser [89] present only one peak of the resonances at 1.8 eV ($W(CO)_5^-$) , 2.6 eV ($W(CO)_4^-$), 3.6 eV ($W(CO)_3^-$), 7.5 eV ($W(CO)_2^-$) and 10.8 eV (WCO^-). Wnorowski et al 2012 [88] found the $W(CO)_2^-$ at 8.8 eV, 1.3 eV higher, and no data is present for the lightest anion WCO^-. In comparison, Seebauer et al 1995 [97] present only one peak of the $W(CO)_4^-$ resonance at 2.6 eV, 0.7 eV lower than the work of Wnorowski et al 2012 [87] and Winters and Kiser [89]. The electron affinities in Ref. [87] calculated for each ion based on the appearance energy of the anion follow the relation EA = AE – (6 – x) BDE, where x is the number of CO radicals, with values between 1.5 eV and 3.1 eV ($W(CO)_5 \leq 2$ eV, $W(CO)_4$, $W(CO)_3 \leq 3.1$ eV, $W(CO)_2 \leq 1.5$), higher than the values presented by Stano et al 2012 [90] for the higher mass anions $W(CO)_5$ (0 eV), $W(CO)_4$ (0.9 ± 0.01 eV) and $W(CO)_3$ (2.9 ± 0.01 eV) and smaller for $W(CO)_2$ (6.5 ± 0.01 eV) for a BDE value of 2.15 ± 0.01 eV. Based on the values of their calculated electron affinities and BDE and using a time dependent data acquisition system, Wnorowski et al 2012 [87] declared the process as a step process due to the time it takes to break the ligands, and according to their values of EA and BDE they declare three peaks of the $W(CO)_4^-$ and $W(CO)_3^-$ resonances.

Reference	DFT electronic states
Ref. [87] Wnorowski et al 2012	3^3E_u (8.146 eV) 3^3T_{2u} (8.264 eV) 3^3T_{1u} (8.329 eV) $^1A_{1g}$ (8.25 eV and 8.34 eV)
Ref. [232] Mendes et al 2017	$^{1\text{-}3}T_{1u}$ (<4 eV) $^{4,6}T_{1u}$ (4.32 eV)

$^{1}A_{1g}$ ground state	$^{9}T_{1u}$ (5.59 eV) $^{10}T_{1u}$ (7.63 eV) $^{11\text{-}14}T_{1u}$ (8.35 eV) $^{21\text{-}37}T_{1u}$ (10.38 eV)
Present work (Quantemol-N)	*Excitation cross-section data was not determined as the W atom is not implemented in the Quantemol-N software
Present work Gaussian 16; neutral state	$^{1}A_{1}$ (3.4 eV) $^{1}A_{1}$ (3.49 eV) $^{1}A_{1}$ (3.55 eV) $^{1}A_{1}$ (3.89 eV) $^{1}A_{1}$ (4.07 eV) $^{1}A_{1}$ (4.11 eV) $^{1}A_{1}$ (4.22 eV) $^{1}A_{1}$ (5.17 eV) $^{1}A_{1}$ (5.22 eV)
Present work Gaussian 16; charged state	2A (0.25 eV) 2A (0.97 eV) 2A (1.03 eV) 2A (1.61 eV) 2A (1.87 eV; 1.89 eV) 2A (2.88 eV) 2A (3.13 eV) 2A (3.14 eV) 2A (3.16 eV) 3A (3.27 eV) 3A (3.35 eV)

Table 5.2.2.2. DFT electronic states, cross-sections, and resonances from different sources and comparison with current work

A number of sources report excited states over 4 eV electron energy in Ref. [87], Ref. [232], while one of the sources, in Ref. [232] and our DFT calculations in charged and neutral states of the $W(CO)_6$ molecule report excitation states at electron energies lower than 4 eV. In Ref. [87] excited states with energies over 8 eV are presented at $3^{3}E_{u}$ (8.146 eV), $3^{3}T_{2u}$ (8.264 eV), $3^{3}T_{1u}$ (8.329 eV) and $^{1}A_{1g}$ (8.25

eV, 8.34 eV). Similar excitation energies and state configurations are presented in Ref. [232] transitions from the $^{1}A_{1g}$ ground state to $^{4,6}T_{1u}$ (4.32 eV), $^{9}T_{1u}$ (5.59 eV), $^{10}T_{1u}$ (7.63 eV), $^{11\text{-}14}T_{1u}$ (8.35 eV) and $^{21\text{-}37}T_{1u}$ (10.38 eV).

The density of electrons for the two alpha orbitals, the electron occupied 49 orbital and the electron unoccupied 50 orbital, representing the HOMO and LUMO involved in the fragmentation of the compound and in the transition from a lower excited state (HOMO) to a higher excited state (LUMO) are presented in Fig 5.2.2.1. The HOMO is characterized by an orbital energy of E = - 0.2714 (Hartree) ~ -7.385 eV, while LUMO has an orbital energy of E = - 0.1030 (Hartree) ~ -2.803 eV. The transition $\pi \rightarrow \pi^*$ in the formation of the temporary negative ion (TNI) has a value of 4.582 eV, sources reporting the DEA fragmentation process (Lacko et al 2018 [75]; Wnorowski et al 2012 [95]) as a multiple step process, but we declare it as being one step process and the electron – molecule collision taking place between one electron and one molecule.

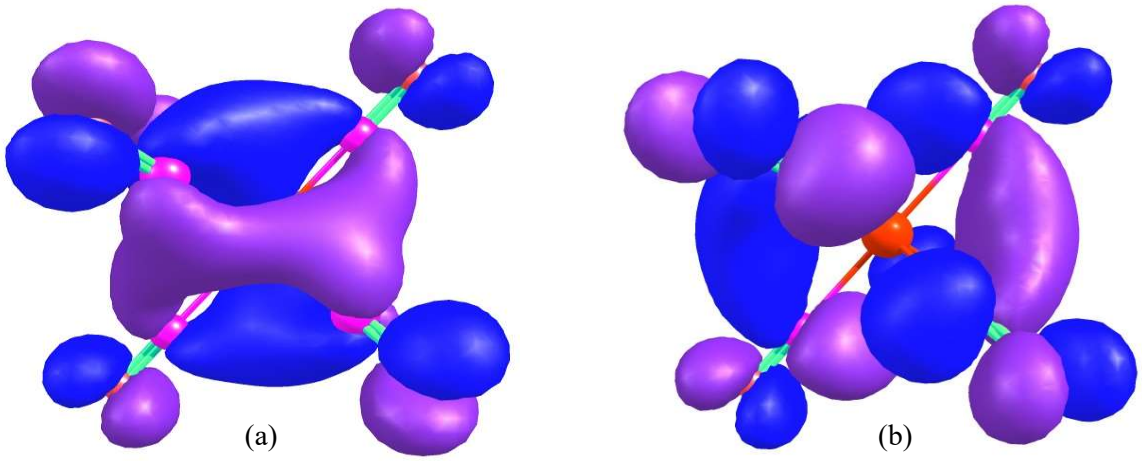

Fig 5.2.2.1. Density of electrons of the occupied orbitals HOMO (a) and unoccupied LUMO (b) from DFT calculations of $W(CO)_6$ optimized in neutral state at B3LYP/SDD level of theory

5.2.3 Summary of Experimental Set-up

The experimental set-up used for the acquisition of the $W(CO)_6$ anions is the one presented in Chapter 2 of Section 1, and follows the guide lines presented in Subsection 3.1.3 of Chapter 3. As the resulting 3D Newton sphere of anions is sliced at central plane by using a 100 ns Behlke slicer with negative polarity, the inner circle is accumulated through the collection of a large number of images (every 5s) and processed with the use of Python programming language with Scikit, Pandas, OpenCv and Matplotlib

libraries. Processing and fitting of data was necessary, but due to the equipment set-up no Abel inversion of the anion data was needed in the processing step. Experimental set-ups as the one at Tata Institute, India in Ref. [51] similar to the one available at University of Kent make use of Matlab scripts to process the anion counts and images acquired. A set of 3D pictures of the anions is presented in Fig 5.2.3.1 with the anion flux coming from 90 deg (inward to the paper) to the plane of relaxation (dark blue) and with good data quality (very low levels of noise are characteristic to the $W(CO)_6$ anions measurements).

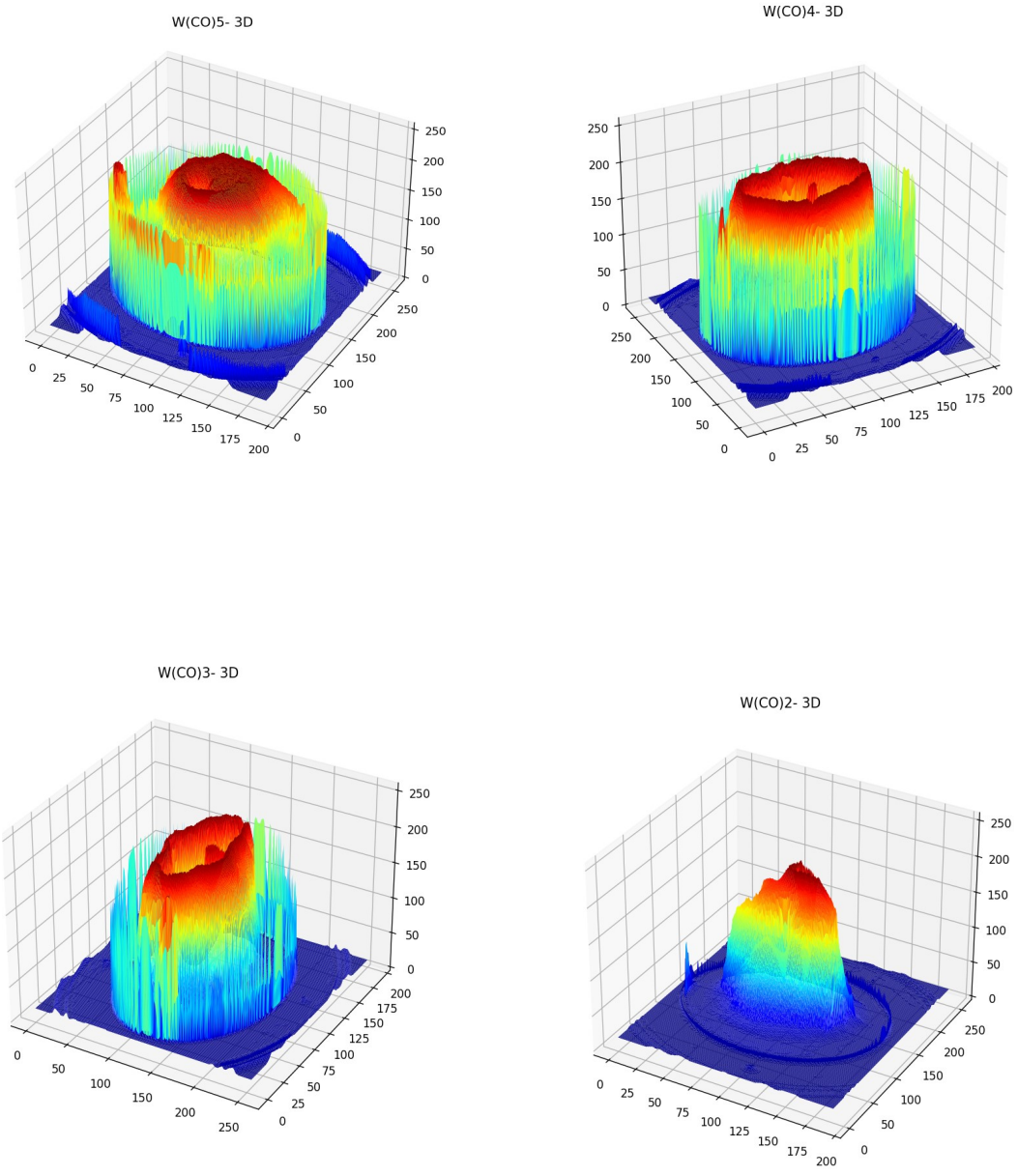

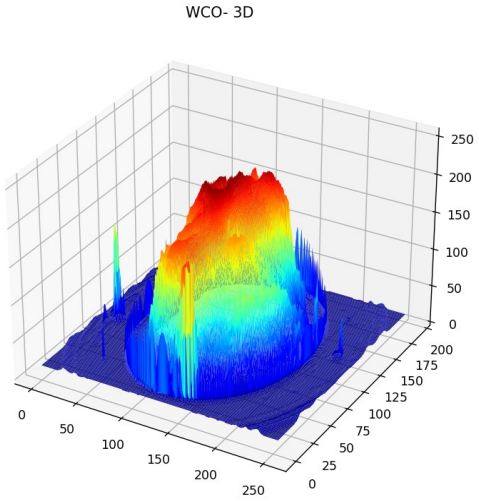

Fig 5.2.3.1. 3D velocity sliced map images of anions at different electron energies

5.2.4 Results and Discussions

DEA induced anion fragments from $W(CO)_6$. The fragment types produced by DEA of $W(CO)_6$ are very similar to $Fe(CO)_5$ when it comes to the dissociation, the $W(CO)_6$ undergoes the same process steps as for $Fe(CO)_5$ resembling some similitude in the step fragmentation process (relation (5.2.4.1)):

$$W(CO)_6 + e^- \rightarrow W(CO)_6^* \rightarrow W(CO)_5^- + CO \rightarrow W(CO)_4^- + 2(CO) \rightarrow W(CO)_3^- + 3(CO) \rightarrow$$

$$W(CO)_2^- + 4(CO) \rightarrow WCO^- + 5(CO) \rightarrow W^- + 6(CO) \qquad (5.2.4.1)$$

Winters and Kiser 1966 [89] showed the dissociation of the $W(CO)_6$ into $W(CO)_5^-$, $W(CO)_4^-$, $W(CO)_3^-$, $W(CO)_2^-$ and WCO^- with peaks yields at 1.8 eV, 2.6 eV, 3.6 eV, 7.5 eV and 10.8 eV. The values for the incident electron energies for the different $W(CO)_6$ anions from our experimental data and different sources are presented in Table 5.2.4.1. The $W(CO)_6$ is rather a difficult dissociation process due to the short-lived life of the $W(CO)_6^*$. Stano et al 2012 [90] presents the short life of the $W(CO)_6^*$ as the effect of the extra electrons that need to occupy the anti-bonding e_g orbital. The same source presents as the most abundant species, results of the dissociation, three fragments: $W(CO)_5^-$, $W(CO)_4^-$ and $W(CO)_3^-$. Considering the morphology of the molecule, the $W(CO)_6$ belongs to the O_h group with its orbital configuration in the ground state as $(7e_g)^4(3t_{2g})^6(1t_{1g})^6(11t_{1u})^6(4t_{2g})^6$ and $^1A_{1g} - {}^1T_{1u}$ allowed transitions. Under the 4 eV the only possible transitions are $^1A_{1g}$ to $^1T_{1u}$, $^2T_{1u}$ and $^3T_{1u}$ for 0.2 eV and 3.3 eV, metal-

to-ligand charge transfer. Over this energy range, there are multiple bands associated with the specific energies. For the case of $W(CO)_3^-$, a $^1T_{1g}$ - $^1A_{1g}$ and $^1T_{2g}$ - $^1A_{1g}$ are the most probable transitions at an incident electron energy of 4.7 eV, close to the 4.609 eV presented in Ref. [87].

Anions of $W(CO)_6$	Incident Electron Energy [eV]	Stano et al 2012 [88], Incident Electron Energy [eV]	Winters and Kiser 1966 [89], Incident Electron Energy [eV]	Stano et al 2012 [88] EA	Li et al 1994 [93] BDE	Wnorowski et al 2012 [90] BDE cations
$W(CO)_5^-$	0.2	0; 1.5	1.8	0	2.1	1.84 ± 0.12
$W(CO)_4^-$	3.3	1.8; 3.3	2.6	0.9 ± 0.1	-	1.70 ± 0.12
$W(CO)_3^-$	4.7	4.7; 7.5	3.6	2.9 ± 0.1	-	1.90 ± 0.12
$W(CO)_2^-$	8.8	8.8	7.5	6.5 ± 0.1	-	2.52 ± 0.12
$W(CO)^-$	17	10.8	10.8	-	-	1.92 ± 0.12

Table 5.2.4.1. The electron affinity (EA) and bond dissociation energy (BDE) for $W(CO)_6$

At energies of >8 eV, with the closest to our 8.8 eV value, the three transitions allowed are 3^3E_u, 3^3T_{2u} and 3^3T_{1u} at 8.146 eV, 8.264 eV and 8.329 eV, respectively. At lower values of 8.25 eV and 8.34 eV, only spin-forbidden transitions are present $^1A_{1g}$ - $^1A_{1g}$. For values over 9 eV, the highest transition is in the $^1T_{1u}$ state, with low contributions from $^3T_{1u}$ and ^3E_u. From the six – CO vibrational structures we get three vibrational stretching modes: a doubly degenerate forbidden E_g, a totally symmetric one A_{1g}, and the T_{1u} mode, the active vibrational CO mode in Ref. [90]. This vibrational stretching modes change with the state of the compound (vapor, powder, or crystal) and with its deposition on the surface, by shifting to the left. The $W(CO)_6$ bond distances are metal – to - CO with a length of 2.058 Å and C-O with a length of 1.148 Å from experimental data in Ref. [92].

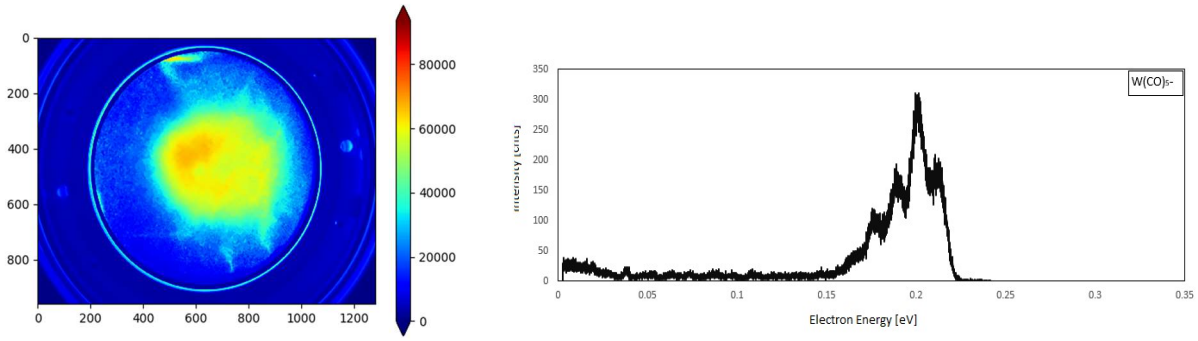

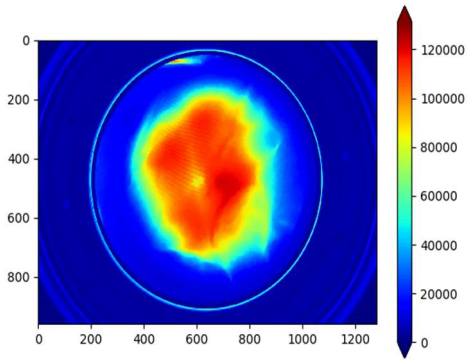
0
200
400
600
800
0 200 400 600 800 1000 1200
120000
100000
80000
60000
40000
20000
0

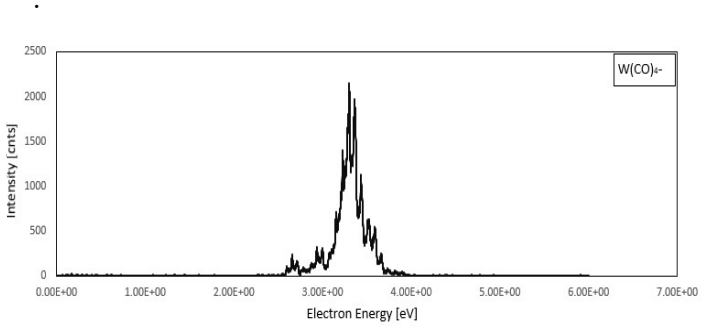
W(CO)4-
Intensity [cnts]
2500
2000
1500
1000
500
0
0.00E+00 1.00E+00 2.00E+00 3.00E+00 4.00E+00 5.00E+00 6.00E+00 7.00E+00
Electron Energy [eV]

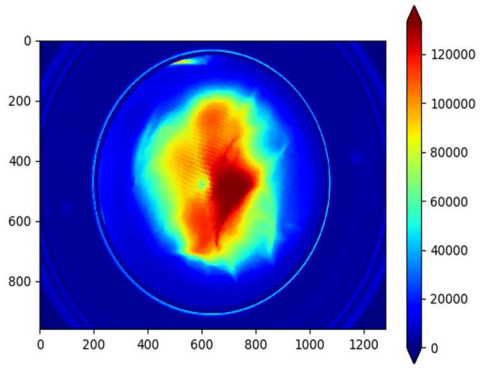
0
200
400
600
800
0 200 400 600 800 1000 1200
120000
100000
80000
60000
40000
20000
0

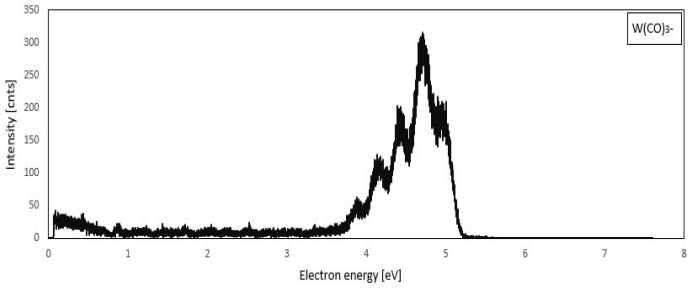
W(CO)3-
Intensity [cnts]
350
300
250
200
150
100
50
0
0 1 2 3 4 5 6 7 8
Electron energy [eV]

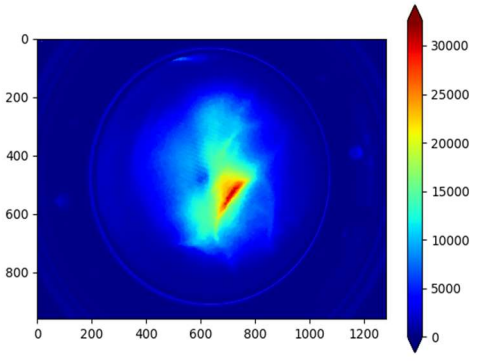
0
200
400
600
800
0 200 400 600 800 1000 1200
30000
25000
20000
15000
10000
5000
0

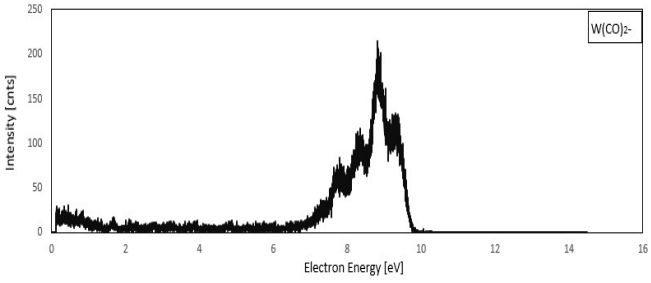
W(CO)2-
Intensity [cnts]
250
200
150
100
50
0
0 2 4 6 8 10 12 14 16
Electron Energy [eV]

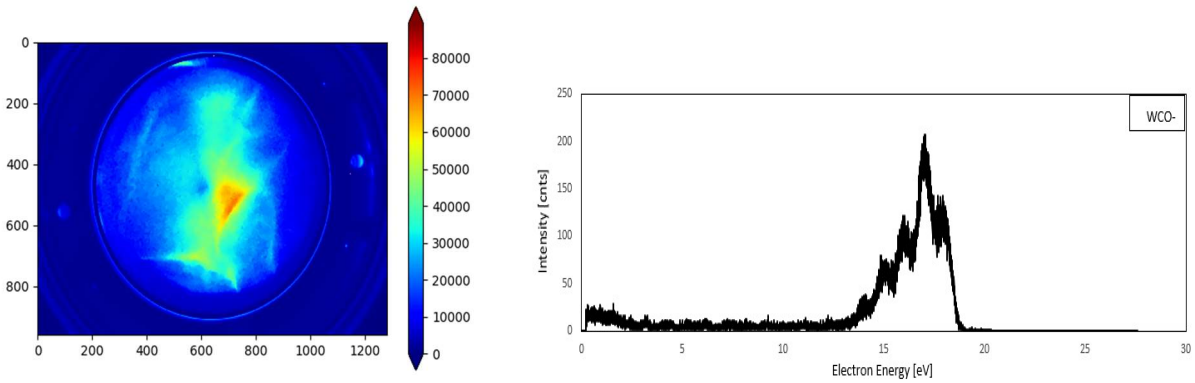

Fig 5.2.4.1 Negative ions of $W(CO)_6$ using velocity map imaging: (a) $W(CO)_5^-$ (b) $W(CO)_4^-$ (c) $W(CO)_3^-$ (d) $W(CO)_2^-$ (e) WCO^-

The CO active vibrational stretching mode changes with the state of the compound: in gas phase, the band is found at 1998 cm^{-1} (0.246 eV), in condensed phase the band is found at 1980 cm^{-1} (0.245 eV) and in crystal form it is found at 1956.5 cm^{-1} (0.243 eV). At 1950 cm^{-1} (0.242 eV), the CO stretching band is assigned to the ^{13}C isotope species in Ref. [90], forming $W(^{13}CO)(^{12}CO)_5$ with natural abundance of 1.1 %. Dissociative ionization process resulting in the full dissociation of the $W(CO)_6$ and formation of W^+ and W^{2+}, similar to the negative ion formation, was demonstrated by Ershov et al 2019 [94]; the absorption spectrum presents high values of cross-sections of 1.4 x 10^{-17} cm^2 peaking at 4.317 eV. The TDDFT calculations in Ref [95] assigned this band to a metal – to – ligand charge transfer and intra-ligand excitation.

Kinetic Energies of Negative Ions. The kinetic energies of each of the negative ions of the $W(CO)_6$ are presented in Fig 5.2.4.2. The present kinetic spectra are in better agreement with Stano et al [88] than with the work of Winters and Kiser [89] with three of the resonances presenting the same dissociation electron energies.

$W(CO)_5^-$. The kinetic energy of the negative ions of $W(CO)_6$ is in the range of 0.7 – 3.8 eV. The $W(CO)_5^-$ anion is formed through the dissociation of $W(CO)_6$, by the interaction with an electron, in $W(CO)_5^-$ and CO, as a $^1A_1 \rightarrow {}^1T_{1u}$ transition from the ground level $^1A_1$ to the higher excited state $^1T_{1u}$ (essentially a $\sigma \rightarrow \pi^*$ transition). The maximum of kinetic energy of the $W(CO)_5^-$ ion is 0.78 eV from the experimental data and 0.36 eV from the calculation using relation (eq. 5.2.4.2) with the ~10 % of the maximum value at 0.04 eV, in close agreement with the graph data (see Fig 5.2.4.2). The $W(CO)_5^-$ ion from the experimental data has multiple peaks that could be fitted to one wider peak with the maximum value of

1.15 eV. The reaction channel that involves the dissociation of the $W(CO)_6$ in $W(CO)_5^-$ and the CO neutral fragment, has a threshold close to ~0 eV in Ref. [95], lower than the VMI experimental value of 0.2 eV.

$W(CO)_4^-$. The experimental data for the $W(CO)_4^-$ ion shows a peak at 3.3 eV, compared to the data of Wnorowski et al 2012 [90] that presents three peaks of the resonance at 1.8 eV, 3.3 eV and 7.6 eV. The calculated kinetic energy maximum is 4.63 eV, with its ~10 % value at 0.46 eV. The dissociation energy of $W(CO)_4^-$ is < 5 eV, and it is linked to a $^1T_{1u}$, $^1T_{2u}$, transition from the $^1A_1$ ground state. Wnorowski et al 2012 [90] presents the $W(CO)_4^-$ fragment with a DEA dissociation threshold of 0.9eV lower in value, compared to our experimental value of 3.3 eV. A fit of the experimental graph values of kinetic energies would bring the peak value in the range of ~1.5 – 2 eV.

$W(CO)_3^-$. The $W(CO)_3^-$ ion results from the dissociation of $W(CO)_6^* \rightarrow W(CO)_3^- + 3(CO)$. At the dissociation energy value of 4.7 eV, the maximum value of the kinetic energy from the graph is 4.2 eV. The calculated maximum of the kinetic energy is 5.99 eV. The dissociation process is either a straightforward process where the ionized $W(CO)_6^*$ parent dissociates in the two fragments or a step process where the intermediary fragment dissociates forming the $W(CO)_3^-$ ion. The absorption spectrum in Ref. [103] presents a peak at 4.317 eV with a cross-section value of 1.4 x $10^{-17}cm^2$, as a metal – to - ligand charge transfer and intra-ligand excitation occurs close to the dissociation energy of the parent into the $W(CO)_3^-$ and the neutral fragment. The $W(CO)_3^-$ kinetic energy distribution is very noisy with multiple peaks; a graphical fit brings the value of the maximum kinetic energy in the range of ~ 4.2 eV.

Ion	m/z	AE in Ref. [89]	Resonances (eV) in Ref. [89]					Ref [95]	VMI
$W(CO)_5^-$	324	0	0	1.5	-	-	-	1.8	0.2
$W(CO)_4^-$	296	0.9	-	1.8	-	3.3	7.6	2.6	3.3
$W(CO)_3^-$	268	2.9	-	-	3.9	4.7	7.5	3.6	4.7
$W(CO)_2^-$	240	6.5	-	-	-	-	8.8	7.5	8.8
WCO^-	212	-	-	-	-	-	10.8	10.8	17

Table 5.2.4.2. $W(CO)_6$ negative ion appearance energy (AE) and resonances (eV)

The appearance energies of the negative ions of the $W(CO)_6$ are calculated based on the bond dissociation energies (BDEs) in the range of ~2 eV and the electron affinity of each fragment.

$$AE\ (W(CO)^-_x) = EA(W(CO)^-_x) - BDE(W(CO)_x - CO)\ [89] \quad (5.2.4.2)$$

Ions	EA (eV)	BDE (eV)	AE (eV) in Ref. [89]	BDE(eV) in Ref. [89]	BDE(eV)* in Ref. [97]	Ei (eV)
$W(CO)^-_5$	2	1.84	0	~2eV	2.15 (0)	0.2
$W(CO)^-_4$	3.1	1.77	0.9 ± 0.1		2.18 (2.2)	3.3
$W(CO)^-_3$	3.1	1.81	2.9 ± 0.1		1.98 (3.8)	4.7
$W(CO)^-_2$	1.5	1.99	6.5 ± 0.1		2.16 (6.5)	8.8
WCO^-	1.2	1.98	-		-	17

Table 5.2.4.3. The electron affinities (EA), bond dissociation energies (BDE) and incident electron energies (Ei) of W(CO)6 ions. *with the AE(eV) values in brackets

$W(CO)_2^-$. The experimental data presents a value of 2.4 eV for the kinetic energy maximum. The calculated value of excess energy is 8.31 eV. With a computed fit of the graph (Fig 5.2.4.2), the value of the peak kinetic energy is shifted to ~3 eV. The threshold value in Ref. [94] of the dissociation energy is ~6.5 eV. Our experimental dissociation electron energy (Table 5.2.4.2) value is 8.8 eV, higher than the presented experimental value in [96] of 7.5 eV.

WCO^-. In Ref. [96] the dissociation of the W - CO ligand has a value of 1.8 eV. The spectrum of the WCO^- is wider and attenuated compared to the spectrum of the other fragments, as a result, the dissociation energy is higher than 15 eV, with a value of 17 eV. The kinetic energy from the experimental data has a value of 1.1 eV for this fragment, with a calculated kinetic energy maximum or excess energy of 16.22 eV. The value is smaller than the 17 eV dissociation threshold, the process happening as an interaction with a single charged particle. The data from Wnorowski et al [90] is in agreement with our results, no W^- was found result of the induced chemical dissociation of the molecule by the electron beam.

The values of the BDE and EA from our calculations are in good agreement with slight differences of only 0.17 eV to 0.31 eV compared to the values obtained by Nakashima et al [97], though the authors do not report any BDE for the lightest anion WCO^-. All five ions have bond dissociation energies of over 1.5 eV with values between 1.84 eV for the highest mass anion $W(CO)_5^-$ to 1.98 eV for the lightest mass anion WCO^-. The appearance energies corresponding to the anions found experimentally by Wnorowski et al [90] are between 0.4 eV and 1.3 eV higher than the values reported in Ref. [97] based on an electron

energy of 1.5 eV to 10.8 eV, though our lightest anion is found at an electron energy of 0.2 eV compared to the value of 1.5 eV reported in [90], while the higher mass anion is found at 17 eV with an appearance energy of 9 eV.

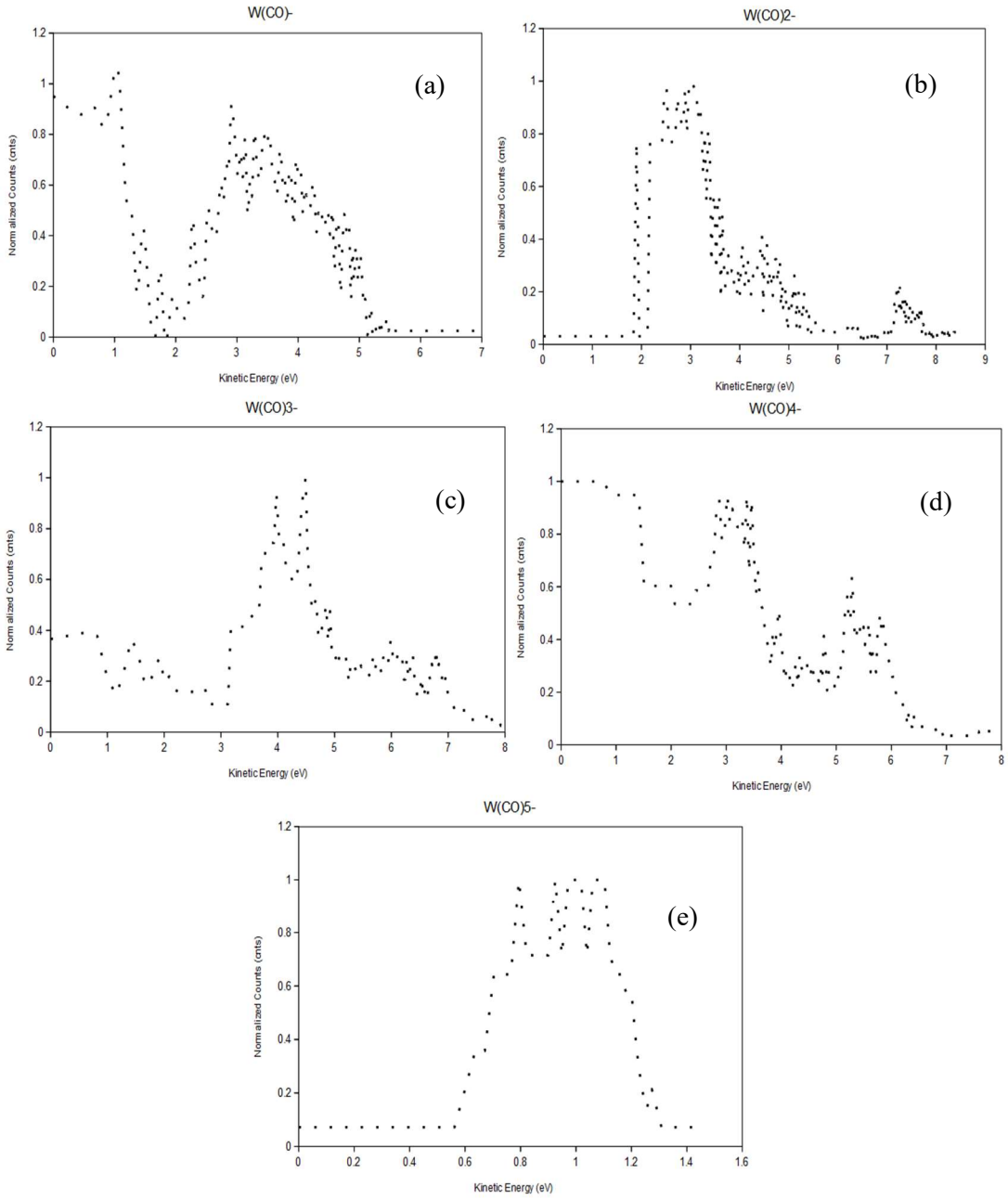

Fig 5.2.4.2. Kinetic energies of negative ions of $W(CO)_6$ using velocity map imaging: (a) $W(CO)_5^-$ (b) $W(CO)_4^-$ (c) $W(CO)_3^-$ (d) $W(CO)_2^-$ (e) WCO^-

Angular distribution of negative ions. The angular distribution was determined using Python 3.8 for image processing and real-time counts (see ANNEX 5). We analysed the images in a comparable manner

to $Fe(CO)_5$ data processing using the best fit algorithm and OpenCV. In cleaning the data, the symmetry of the initial features was kept. The angular distribution of the negative ions is visibly symmetric about 85 deg, although the peaks are noisy due to the irregular shape of the acquired ions. The data is in good agreement with Ref. [90] and the VMI ions are similar in amplitude and shape. The $W(CO)_5^-$ (blue) and $W(CO)_4^-$ (red) ions are symmetric to 90 deg in the case of $W(CO)_5^-$ and to 85 deg in the case of $W(CO)_4^-$. Similar, but with higher values for the angular distribution, the symmetry points of the $W(CO)_3^-$ (yellow) ion appears at 100 deg. The other two smaller negative ions, $W(CO)_2^-$ (green) and WCO^- (violet), have their symmetry points at 87 deg and 75 deg, respectively.

Anion	Symmetry angle in Ref.	Symmetry angle (Present	Symmetry in Ref. [90]
$W(CO)_5^-$	144°	35°, 150°	C_{2v}
$W(CO)_4^-$	144°	55°, 130°	C_{2v}
$W(CO)_3^-$	120°	52°, 130°	C_{2v}
$W(CO)_2^-$	120°	48°, 130°	C_{2v}
WCO^-	144°	48°, 138°	C_{2v}

Table 5.2.4.4. $W(CO)_6$ anions symmetry

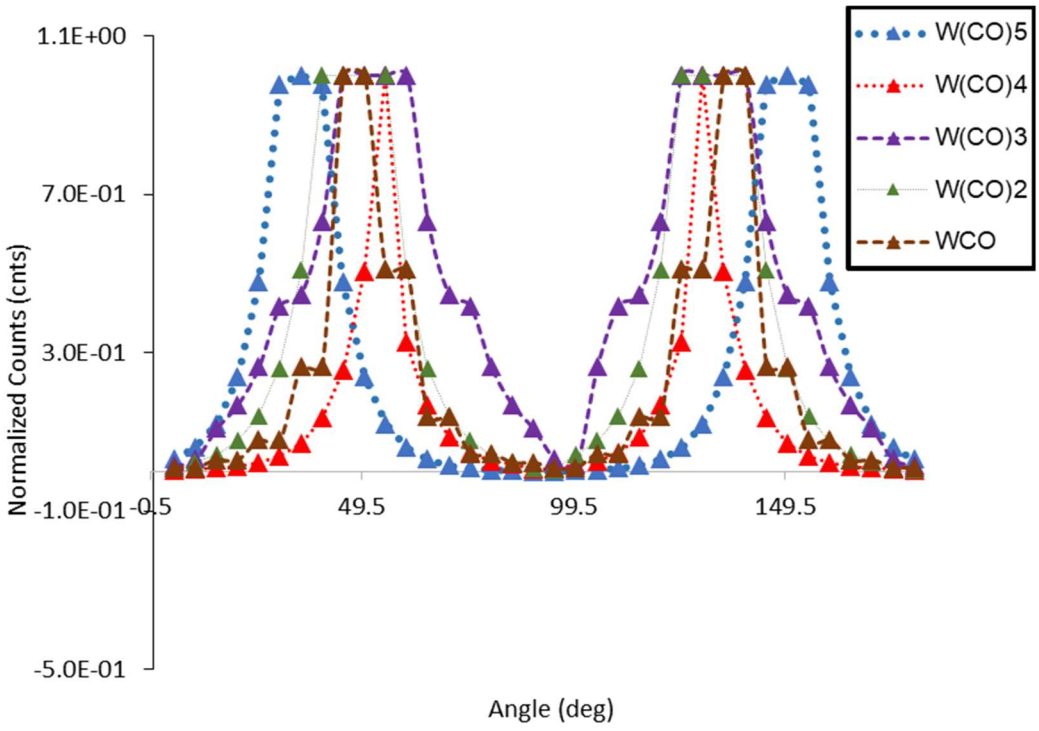

Fig 5.2.4.5. $W(CO)_6$ anions angular distribution

The symmetry of the anions is reduced from the parent neutral found in C_{4v} to C_{2v} and C_{3v} for the anions $W(CO)_3^-$ to WCO^-, respectively, and is preserved for the higher mass anions $W(CO)_4^-$ and $W(CO)_5^-$. The DEA process is usually a two step process, formation of a temporary negative parent anion and

fragmentation of this negative parent into a lower mass anion and a neutral fragment (in this case a CO radical), but for this compound no parent anion was observed as a result of the DEA fragmentation. This is likely to be assigned to the very short-lived life of the temporary negative parent ion, where an obvious reduction in the symmetry would take place from C_{4v} of the parent anion to the C_{2v} symmetry state of the individual anions.

Calculated $W(CO)_6$ Cross Sections Data. The cross-section data using Quantemol-N could not be obtained as the W element (group 5, 6 and 7 elements) is not implemented in the routine; to be implemented in the future versions of Quantemol-QEC.

5.2.5 Summary and Conclusions

The $W(CO)_6$ precursor fragments into five anions with resonances up to 18 eV from our experimental measurements and to 11 eV in the experiments presented in Ref. [90]. The five ions are formed by stripping off 1 - 4 CO radicals. The formed anions are still containing CO that at low energies deposit structures with C and O content; the lightest anion is WCO^- falling at an energy over 15 eV. The bond dissociation energies and electron affinities have been calculated using experimental data and DFT calculations with values between 1.77 eV and 1.99 eV in close agreement with the values reported in Ref. [90] and Ref. [97]. In Ref. [90] multiple resonances have been assigned to the formation of the anions being one of the few sources reporting this, though we declare the presence of only one peak of the resonance. Excited states have been calculated using DFT simulations at B3LYP/SDD level of theory with values between 3 eV and 6 eV. From the images acquired using VMI, the kinetic energies with values between 0.1 eV and 4.2 eV and angular distributions showing mainly C_{2v} symmetry of the anions with angles between 35 deg and 150 deg have been collected. Unfortunately, due to the current lack of the implementation of W atom in Quantemol-N, we were unable to calculate cross-sections using the code.

5.3 Conclusions To Chapter 5

For the first time VMI was used to experimentally determine kinetic energies and angular distributions of all the anionic fragments of $Fe(CO)_5$ and $W(CO)_6$ at DEA, earlier studies focusing on imaging the W^+ and Fe^+ in cationic states at higher electron energies (over 15 eV). Complementary studies of $Fe(CO)_5$

using Quantemol-N for inelastic collisions with molecules up to 17 atoms were run obtaining a full set of DEA cross-sections, excitation cross-sections, ionization cross-sections and total cross-sections. Unfortunately, for the study of the $W(CO)_6$ molecule Quantemol-N software could not be used due to the lack of implementation of group 5, 6 and 7 elements in the routine.

The decomposition and fragmentation of the $Fe(CO)_5$ and $W(CO)_6$ takes place with the loss of a 1 - 5 (for the iron compound) or 1 - 6 (for the tungsten compound) number of CO ligands to the metal atom, a characteristic behaviour of carbonyl – metal compounds. Their fragmentation starts at ~0 eV with the loss of the highest energy CO ligand and ends at energies over 5 eV, but lower than 12 eV (the threshold limit for the Fe-carbonyl bonds at low electron energies) and 17 eV (the threshold limit for the W-carbonyl bonds at low electron energies). Relatively less complex than the acac-metal compounds or fluorines - and broms - metal compounds their cross-sections feature very high peaks close to 0eV. Angular distributions with symmetries between 25 – 55 deg ($W(CO)_6$, $Fe(CO)_5$) and kinetic energies between 0 – 2 eV ($Fe(CO)_5$) and 0 – 5.5 eV ($W(CO)_6$) have been recorded, and all the anions results of the fragmentation in FEBID process have been imaged.

The removal of all metal – CO ligands has been observed in the case of $Fe(CO)_5$, while only 1-5 metal – CO ligands have been removed for $W(CO)_6$ with lightest anion WCO^- around 17 eV. Values of bond dissociation energies (BDE) have been reported for both $Fe(CO)_5$ and $W(CO)_6$ in close agreement with the literature data in Ref. [75] and Ref. [90] with values of ~2 eV. The calculated values of the BDEs of $W(CO)_6$ anions are in the range of 1.7 eV and 1.99 eV. Values of $Fe(CO)_5$ BDE have been reported in Ref. [52] between 1.46 eV and 1.84 eV, while in [84] authors report values between 0.2 ± 0.4 eV and 1.4 ± 0.3 eV. In the dissociation of $Fe(CO)_5$ electron affinities of 0.151 ± 0.003 eV to 2.4 ± 0.3 eV have been reported in Ref. [52], 1.22 ± 0.02 eV to 2.4 ± 0.3 eV in Ref. [84] while [85] report a single value of 0.153 eV of the lightest anion Fe^-. The excited states for the two compounds obtained from DFT calculations, $Fe(CO)_5$ and $W(CO)_6$, have symmetries in $^1A_1$ state with energies between 3.4 eV to 5.22 eV for the neutral molecule, 2A with energies between 0.25 eV and 3.35 eV in charged state, optimized at B3LYP/SDD ($W(CO)_6$), and a set of excited states of $Fe(CO)_5$ with different symmetries $^1B_1$ (3.19 eV), $^1B_2$ (3.87 eV), ^1E (~4 eV), $^1A_1$ (4.36 eV), ^1E (4.7 eV), $^1B_2$ (4.9 eV), $^1A_2$ (4.97 eV), ^1E (5eV to 5.27 eV) in neutral state, $^3A_1$ (3.1 eV), $^3A_1$ (3.14 eV) in charged state at B3LYP/6-31G*, while the excited states obtained from interactions at low electron energy with the precursor molecules through Configuration Interaction Orbitals mode in Quantemol-N are $^3A_2$ (2.58 eV), $^1A_2$ (2.77 eV), $^3B_2$ (3.13 eV), $^3B_1$ (3.27 eV), $^1B_2$ (3.4 eV), $^1B_1$ (3.67 eV), $^3B_1$ (4.35 eV), $^1B_1$ (4.51 eV). The kinetic energies obtained from the processing of the data of $Fe(CO)_5$ are calculated for each ion separately from the VMI images exhibiting values of 0.79 eV $Fe(CO)_4^-$, 1.38 eV $Fe(CO)_3^-$, 3.87 eV $Fe(CO)_2^-$, 8.2 eV $FeCO^-$ and 9 eV Fe^-

, while for the $W(CO)_6$ anions values between 0.78 eV and 4.4 eV are obtained with 0.78eV $W(CO)_5^-$, 1.5 – 2 eV $W(CO)_4^-$, 4.4 eV $W(CO)_3^-$, 2.4 eV $W(CO)_2^-$ and 1.1 eV WCO^-.

The extent of details of the calculations, experimental data and through the multiple software used (Chemcraft, Gaussian 16, Quantemol-N, Python, Avogadro) makes the study of these two carbonyl precursors rather comprehensive and complex. Further development work in reducing the time of the calculations and the extra experimental work needed could focus on the use of AI and ML for molecular physics, we intended a first step by implementing the use of Python with ML and Image Processing for data manipulation of the experimental work.

SECTION 2. SURFACE SCIENCE AND DEPOSITION STUDIES OF FEBID PRECURSORS

CHAPTER 6. STUDY OF GOLD BASED FEBID COMPOUNDS AND THEIR PROCESSES ON SURFACES

$Me_2Au(acac)$ (Fig 6.1.1.1) is an acetylacetonate metal-based compound commonly used as a precursor in FEBID deposition. Since 1977 in Ref. [162] acetylacetonate metal-based compounds have been used in chemical vapor deposition (CVD), but lately with the increase of importance of FEBID process they have successfully been used as precursors for FEBID nanostructures. The applications of $Me_2Au(acac)$ to FEBIP are: plasmonic gold nanostructures, soldering of the carbon nanotubes, gold electrodes and field emitter tips in Ref. [163]. However, the high carbon content of the precursor through the high number of carbon atoms, even after ligand breakage, might not make it the most suitable precursor for FEBIP and there is the need for an in-depth analysis of its fragmentation, an urgency increased with the need to design, create and use precursors that give high purity in the focused electron beam induced nanolithography. Gold metal precursors have been used for CVD as early as 1985 by Baum and Jones 1985 in [292], where they studied the deposition of $Me_2Au(acac)$ on native oxide layers thermally grown with 3000 – 4000 Å. The Au structures of 3.7 μm height and 60 μm width were deposited at 4.01 x 105 W/cm^2 10 – 20 time higher than with a deposition rate of 2.9 x 105 W/cm^2 using an argon ion laser. The deposition temperature used was 180 °C, with line resistivities of 10 μΩcm, four times higher than the bulk Au resistivity. A later study of Baum and Jones 1987 [293] presented a density of atoms for 60 μm width lines of 8.45 x 10^{17} atoms/cm^2 with the structures purity of 98 % Au, 1.9 % O and no C. The structures have been reported as having been treated in a post-annealing process at 300 – 350 °C for 30 min exhibiting resistivities only 2 – 3 times higher than bulk Au.

Pratti and Villa 2012 [294] in their study report the deposition of $Me_2Au(acac)$ with the addition of H_2O with resultant Au_2O_3 deposited on surface. Resistivities of two times higher than then bulk Au have been obtained [294] with values in the range of ~4.6 μΩcm of Au/O_2/Ar for an average film thickness between 600 – 1000 Å. The deposits formed have the composition of Au_2O_3 with a Au content of 98 % and a density of 11.1 g/cm^3 exhibiting very good adhesion to the substrate. Other studies report in the CVD of $Me_2Au(Acac)$ a composition of the structures of 95 % Au and 5 % C [299] at a deposition temperature of 200 – 300 °C. Recent studies of Winkler et al 2017 [300] report the 3D synthesis of nanostructures with compositions of 95 at% C impurities at electron energy beams of 30 keV, current in the range of ~21 pA. With the aid of the post annealing process at 10 Pa and H_2O and EELS studies, the C content of the $Me_2Au(acac)$ deposits its reduced to under 10 at%. The deposited structures are disks with diameter ranging from 250 nm to 400 nm and 60 nm thick deposited on Si_3N_4 membranes. Parkhomenko et al

2015 [301] report vacuum ultraviolet (VUV) studies of $Me_2Au(acac)$ with thin film purities of more than 99 % with the addition of H_2 into the deposition process, with the increase in the H_2 content an increase in the Au film purities is observed. De Los Santos et al 2009 [304] studied the crystallization and annealing of Au on SiO_2 substrates at temperatures of 350 – 400 °C. The obtained crystallites diameters are in the range of 90 nm, characterized by a free activation energy of the grain boundary shifts of 0.2 eV for a temperature of 360 °C. The Au crystallizes over the SiO_2 surfaces creating an intermediary layer of Au_xSi_y in a thermal reaction with the substrate over which pure Au nano islands appear. The processes in which the Au nano islands are created are flame annealing and furnace annealing with resulting nanostructures in the range of 90 nm, furnace annealing is a slower process taking longer to create pure nanostructures. A temperature of ~ 80 °C is needed to create Au structures and SiAu alloys on the Si(100) substrate. Design of alternative Au precursors have been developed and carried successfully by McElwee-White et al 2017 [232] and Tilset et al 2021 [317] correlating Br, I, Cl ligands and CNMe, PMe_3, $P(NMe_2)_3$ with the Au – Au distances. In the Surfaces and Interfaces group of Prof. Dr. Anne Lafosse at the Institute des Sciences Moléculaires d'Orsay, University of Paris – Saclay, under the supervision of sr. lecturer Dr Lionel Amiaud, the evolution and fragmentation of $Me_2Au(acac)$ using low energy electrons (0 – 20 eV) has been studied using three experimental methods: ESD, TPD and HREELS.

6.1 Previous Work

XPS and RAIRS studies [163] have been performed for the $Me_2Au(acac)$ precursor with a specific electron energy of 520 eV. The $Me_2Au(acac)$ precursor was deposited on two types of substrates, a : C (amorphous carbon) and Ag. The deposits of the $Me_2Au(acac)$ precursor were measured as ~ 1ML corresponding to a thin layer of ~ 15 nm thickness. The power density of the electron beam was 2×10^{-4} $\mu W/\mu m^2$ at low temperature and 2×10^2 $\mu W/\mu m^2$ at room temperature. The Au(4f) peak from RAIRS / XPS measurements was found at an electron energy 86.2 ± 0.3 eV representing the binding energy of the Au atoms to the O(s) atoms. $Me_2Au(acac)$ fragmentation [163] was studied by electron impact using a QMS (6.1.1):

$$Me_2Au(acac) + e^- \rightarrow Au^{III}C_7O_2 + e^- + \text{neutral fragments} \rightarrow Au^0C_6O_{0.8} + H_2(g) + CH_4(g) + C_2H_6(g) + CO(g) \quad (6.1.1)$$

Reported cross-sections of 3.6 x 10^{-16} cm^2 at an electron energy of 175 eV have been compared to the values of the cross sections for a : C substrate with a value of 3.4 ± 0.1 x 10^{-16} cm^2 and for Ag substrate with a value of 3.9 ± 0.4 x 10^{-16} cm^2, both with the maximum of the cross section peak between 150 eV and 200 eV.

Reference	Fragments	Substrate	Energy (eV)	Temperature (K)
Ref. [163] Wnuk et al 2010 $Me_2Au(acac)$ precursor	$AuC_6O_{0.8}$ CH_4 H_2 C_2H_6 CO	Ag a : C	520 eV	RT
Ref. [302] Mäkelä et al 2017 $Me_2Au(S_2CNEt_2)$ precursor	Au_2O_3 Au_2O	SiO_2	500 eV	170 °C
Ref. [296] Guzman et al 2003 $Me_2Au(acac)$ precursor	$Au(OH)_3$ $Au(CH_3)_2$ acac	$\gamma - Al_2O_3$	500 eV	RT
Ref. [305] Bessonov et al 2007 $Me_2Au(OAc)_2$ and $Me_2Au(piv)_2$ precursor	$COCH_2$ C_2H_6 CO CO_2 H_2O	Si - substrate	Thermal decomposition	120 °C

Table 6.1.1 Previous work on $Me_2Au(acac)$, $Me_2Au(S_2CNEt_2)$, $Me_2Au(OAc)_2$ and $Me_2Au(piv)_2$

Studies of EXAFS and XANES [296] report the presence of $Au(CH_3)_2$ species on the substrate, resulting from the decomposition of $Me_2Au(acac)$ on $\gamma - Al_2O_3$. Acac unevaporated groups have been reported that with annealing at 473 K, fragment and convert into acetate groups. The presence of another fragment at the surface, $Au(OH)_3$, with the increase in the calcination temperature is probed by XANES.

6.2. Experimental Section

6.2.1. Substrate Preparation

The substrate used for deposition was a plain copper bar. Experiments were performed in a vacuum chamber (Chapter 2 Section 2.3) that was pumped down and baked at 80 °C such that a base pressure of

~10^{-11} mbar was reached. Degassing of the filament was performed before and after baking the chamber, followed by a flash heating TPD to remove any possible traces of gas coming from the use of previous compounds.

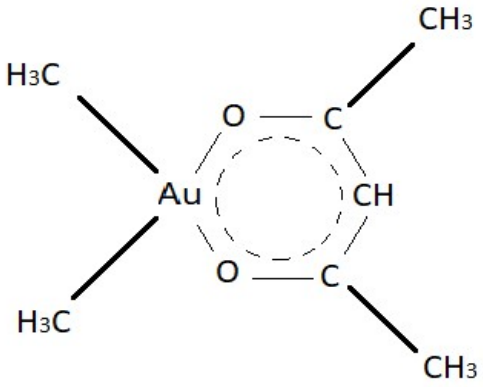

Fig 6.2.1.1. Molecular structure of $Me_2Au(acac)$

The $Me_2Au(acac)$ compound was purchased from Strem Chemicals Inc. with a purity of 98 % and Au purity of 99.9 %. It was placed in a glass vial attached to the gas line with a regulatory valve. To deposit a $Me_2Au(acac)$ sample on the copper plate or introduce it to the chamber in gaseous phase, the valve is opened enough to achieve a chamber pressure of 10^{-9} mbar. Background (residual gas) spectra were recorded after baking the chamber and before the introduction of the compound. To measure the thickness of the thin film layer deposited on the copper bar, several methods can be employed: (i) the use of a quartz crystal (this is a measurement of mass charge per crystal area made by measuring changes in frequency), (ii) by deposition rate, where the thickness of deposited film is determined by the deposition time., or (iii) a newly employed technique called modulation-based structured illumination microscopy (MSIM) in Ref. [165], where a pico-amperemeter measures the current transmitted through the sample. In this case the integral over the transmitted current and charge density gives the layer thickness. At a background pressure of 2 x 10^{-9} mbar for 8 minutes the resulting thickness is 3.4 Langmuir (L) = 0.002 x 10^{-6} x 1.698, where 1L ~ 1 x 10^{-6} mbar for 1 s.

6.3 Results and Discussion

6.3.1 ESD from Thin Films of $Me_2Au(acac)$

To measure the direct electron impact dissociation of $Me_2Au(acac)$, the compound is introduced in the chamber to a pressure of 10^{-9} mbar (compared to a base pressure of 7 x 10^{-11} mbar). The QMS was used

to measure the mass spectrum of the compound and to look for any contamination compared with a gas spectrum recorded without any precursor present. The decomposition of $Me_2Au(acac)$ takes place in the head space of the QMS by electron impact at 70 eV. Electron impact of $Me_2Au(acac)$, has been shown to form low mass fragments of methane, ethane, carbon monoxide and hydrogen. Fragments with higher masses are presented in Fig 6.3.1.1 and in Fig 6.3.1.2.

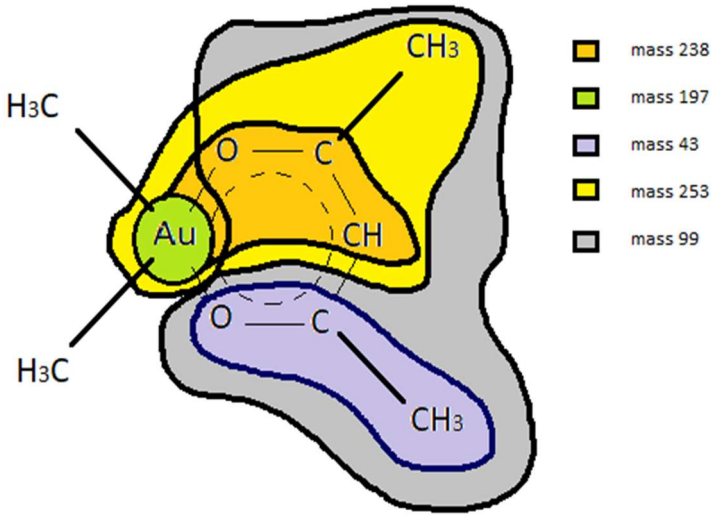

Fig 6.3.1.1. $Me_2Au(acac)$ precursor

The next step of the experiment was to explore the products of electron stimulated desorption (ESD) from thin films of $Me_2Au(acac)$ and compare these with a spectrum of the irradiated surface with no thin films deposited on it. In both cases, the copper block was cooled to its lowest temperature at 20 K. These spectra are shown in the Fig 6.3.1.3. By collecting a spectrum with the gun on and striking a bare surface, all possible sources of contaminants may be realized (e.g., desorption from the electron gun, the filament, background gases in the UHV chamber). Subtraction of this spectrum from that recorded exposed only to the empty chamber environment provides reliable calibration and proves the cleanliness of the chamber at the beginning of the experiment. Several new mass peaks were found in the ESD spectrum at m/z 14 and can be ascribed to CH_2, m/z 15 which can be assigned to CH_3, a peak at m/z 16 that could be either O or CH_4, the peak at m/z 18 most likely H_2O and the peak at m/z 28 ascribed to CO. Masses are observed at m/z 41 – 43, matching the production of CH_3CO (m/z 43) and CHCO (m/z 41) similar to the dissociative fragments of $Me_2Au(acac)$ in the gas phase. The mass at m/z 99 is basically the ring structure with gold and both methyl groups (CH_3) removed. The present ESD results are similar to the data presented by Wnuk et al 2010 [163] who reported peaks of CH_4 (m/z 16) and CO (m/z 28) from the $Au_2Me(acac)$ mass spectrum. The first gold containing fragment is observed at m/z 238.6 (m/z 239) which may be ascribed to the fragment AuC_3H_6. There are two heavier fragments, the peak at m/z 253.6

(m/z 254) corresponding to the AuC_3H_5O fragment and the peak at m/z 294 corresponding to $AuO_2C_5H_7$, both characterized by the removal of two CH_3 ligands. A schematic representation of these fragmentation patterns is shown in Figure 6.3.1.4.

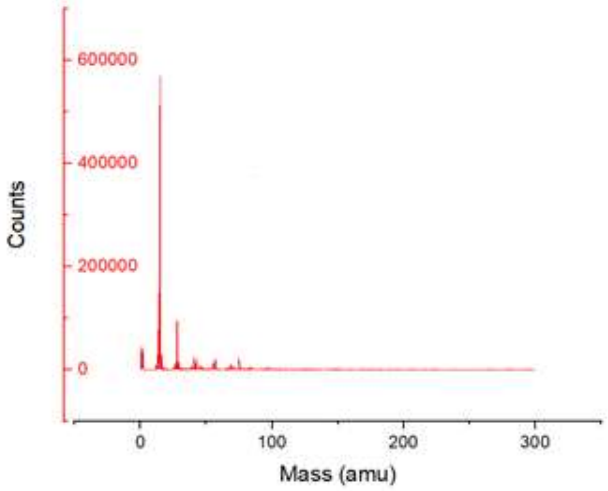

Fig 6.3.1.2. Mass spectrum of ESD Cycle 1 electron gun off subtracted from cycle 2 electron gun on without any $Me_2Au(acac)$ in the chamber

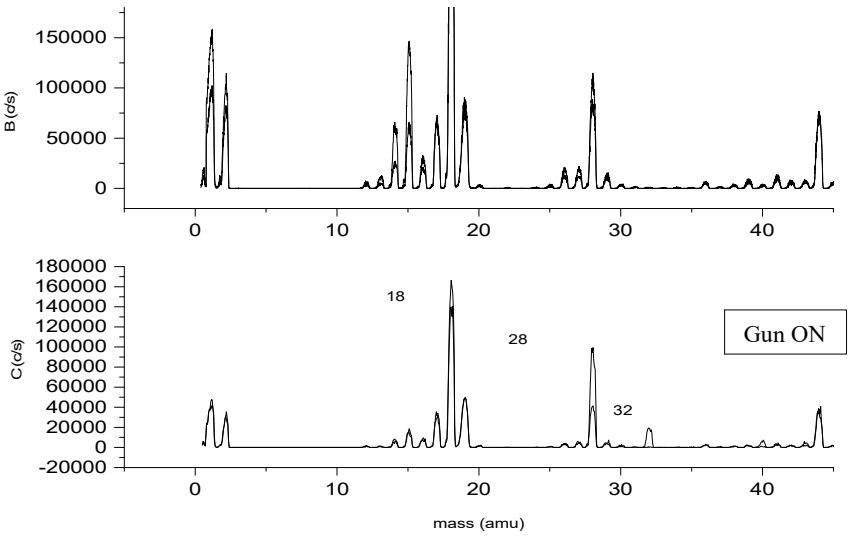

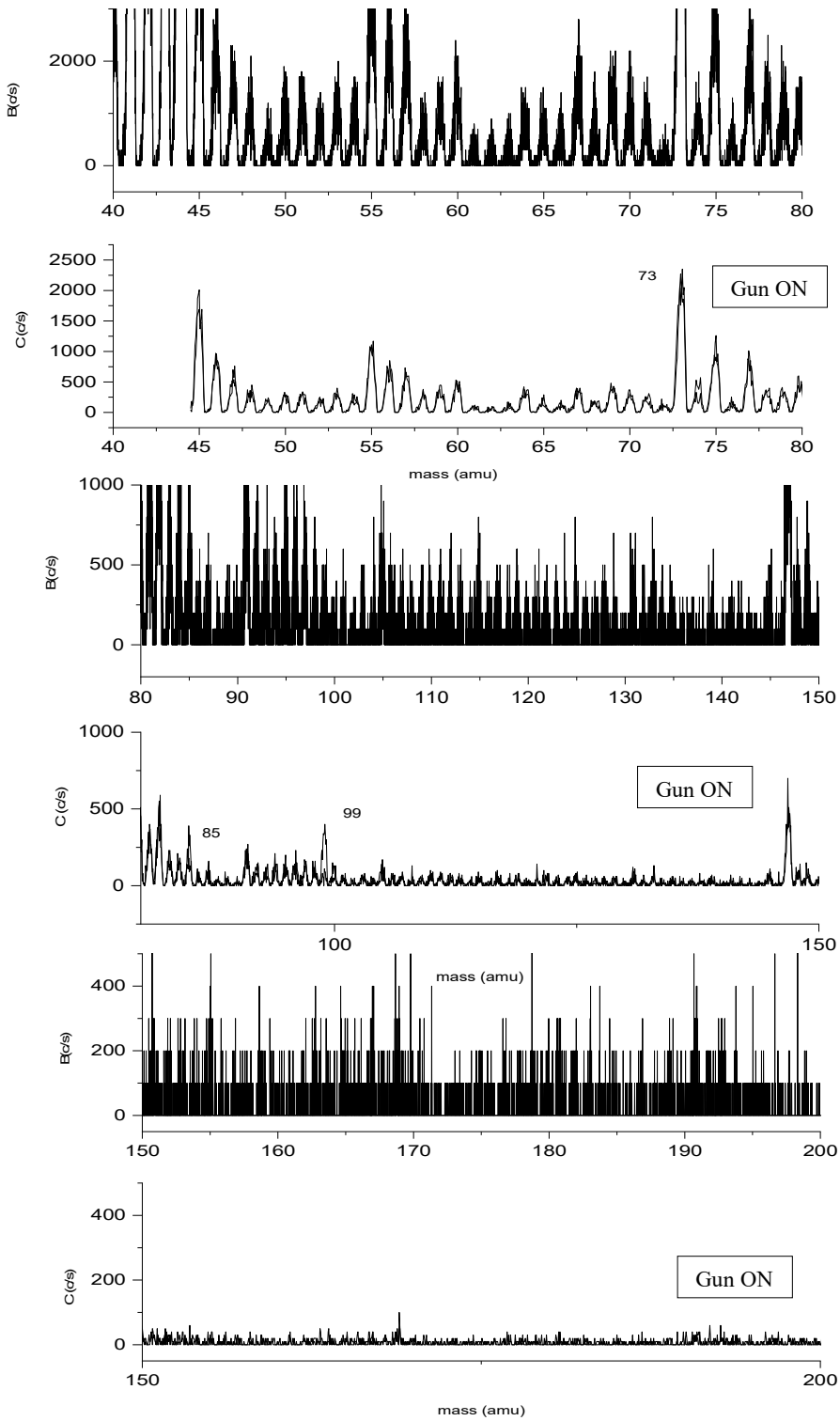
B(cts)
C(cts)
mass (amu)
73
Gun ON
85
99
Gun ON
mass (amu)
Gun ON
mass (amu)

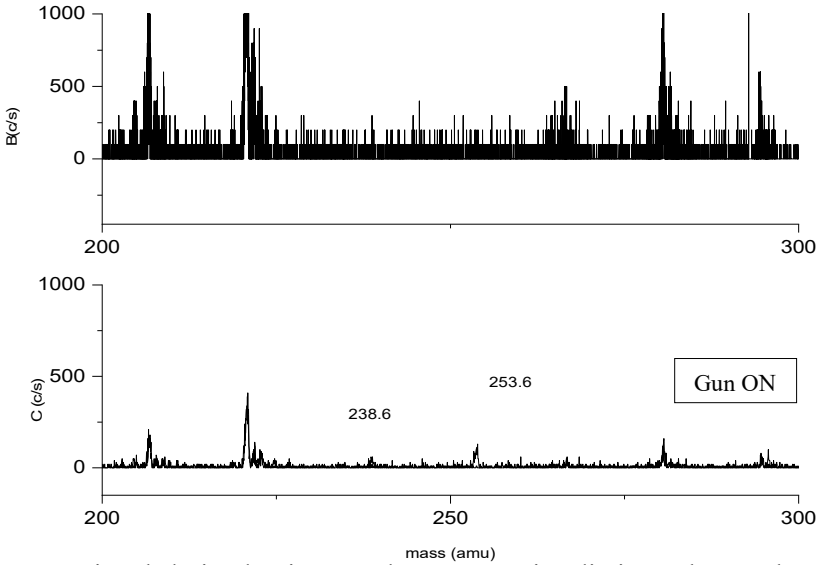

Fig 6.3.1.3 ESD QMS signal derived using an electron gun irradiating a bare substrate surface (top) compared to electron gun irradiating a thin film of $Me_2Au(acac)$ (bottom over range) to m/z 300. The new peaks observed in ESD of thin films are marked

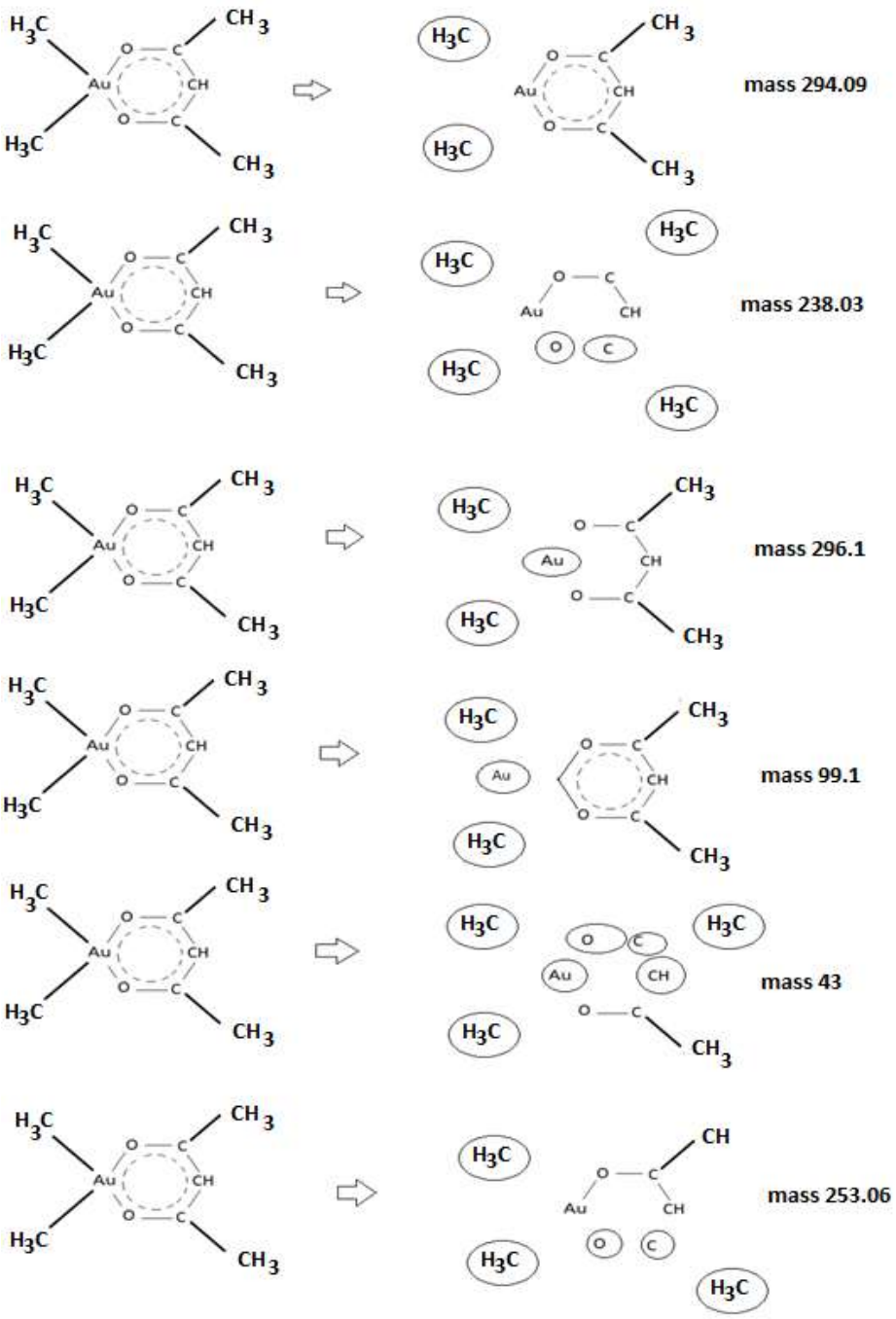

Fig 6.3.1.4 $Me_2Au(acac)$ fragments from background deposition

6.3.2 Temperature Programed Desorption of $Me_2Au(acac)$

The method of Temperature Programed Desorption (TPD) as described in Ref. [166] is one commonly used method in surface science to study the bonding between an adsorbate and the surface on which they

are absorbed. A mass spectrum of the desorbing species is recorded as a function of the temperature of the surface. The temperature at which molecules desorb is characteristic of the molecule-surface bonding. In the set of experiments performed at University of Paris-Sud two methods were used to desorb $Me_2Au(acac)$ from the copper substrate. The first was flash heating used for sample cleaning, the second was a slower TPD study used for compound analysis.

For the TPD measurements, the chamber environment is characterized by the gas density N, given by the relation:

$$VdN/dt = F_F - NS_F + F_A - NS_E, \quad (6.3.2.1)$$

where V is the volume of the chamber, N is the instant gas density, F_A is the supply rate from cell walls or gas source, F_F is the rate of supply of gas from the filament, S_E is the pumping out speed of the system. If the pumping out speed is much smaller than the heating rate, described by the relation $1 >> S_E t/V$, we simplify the (6.3.2.1) equation to: $\Delta N = \int_0^t (F_F/V)dt$. Further, using the Arrhenius equation, the rate of desorption for a surface of area A is characterized by the relation (6.3.2.2):

$$F_F/A = -dn/dt = n^x v_x \exp(-E_d/RT), \quad (6.3.2.2)$$

where n is the surface concentration, v_x is the frequency factor, x should be in the order of 1 or 2. The order depends on the type of molecules on the surface, as it is the case of CO or O_2. As the system is in continuous transformation and state change, the relation needs to be corrected for any loss of the gas in the system or any gain from the walls or filament, by integrating the $\int_0^t (F_A - NS_E)$.

6.3.2.1 TPD Spectrum of $Me_2Au(acac)$ from 160 K to 300 K

In these TPD experiments a multilayer thin film of $Me_2Au(acac)$ with thickness between 6 – 10 ML was deposited on the cooper bar substrate. The dosing valve was opened for 35 s resulting a deposition thickness of 6 ML, determined by integrating the area of the curves for selected masses at the peak width and taking into account the cryostat heating rate. During deposition, the QMS and sample were positioned at x = 14.3 mm, y = 19 mm, z = 12.9 mm for the sample and d_{QMS} = 40 mm from the sample. During TPD, the sample was positioned at x = 20.6 mm, y = 19 mm, z = 2.6 mm and the QMS remained at 40 mm. TPD curves were then recorded for different mass peaks in the QMS (Fig 6.3.2.1.2) using heating rates of 30 K/min, 20 K/min and 10 K/min. The TPD curves were found to be strongly dependent of heating rate and a stronger signal was observed at higher rates and a smaller shift in the TPD peak temperature.

TPD curves of m/z at 28, 236.5, 253.6, 99, 43, have a visible desorption peak compared to m/z 32, 40, 294.5, 85, where the desorption is less evident, the peak being hidden in the noise. TPD for all major m/z was observed between 200 K and 240 K with an increase at 210 K suggesting the $Me_2Au(acac)$ is desorbing intact and then being dissociated into fragments once in the gas phase (as observed in direct dissociation of the molecules). Some m/z TPD curves as in the case of m/z 85 show desorption over the whole temperature range, a characteristic of highly vaporizing compounds and radicals in large quantities, or low vaporization, and low sensitivity to temperature over the specified range, a dry-out of the compound, a process that is more likely if the number of counts is low, similar to our case for the $Au_2Me(acac)$ compound.

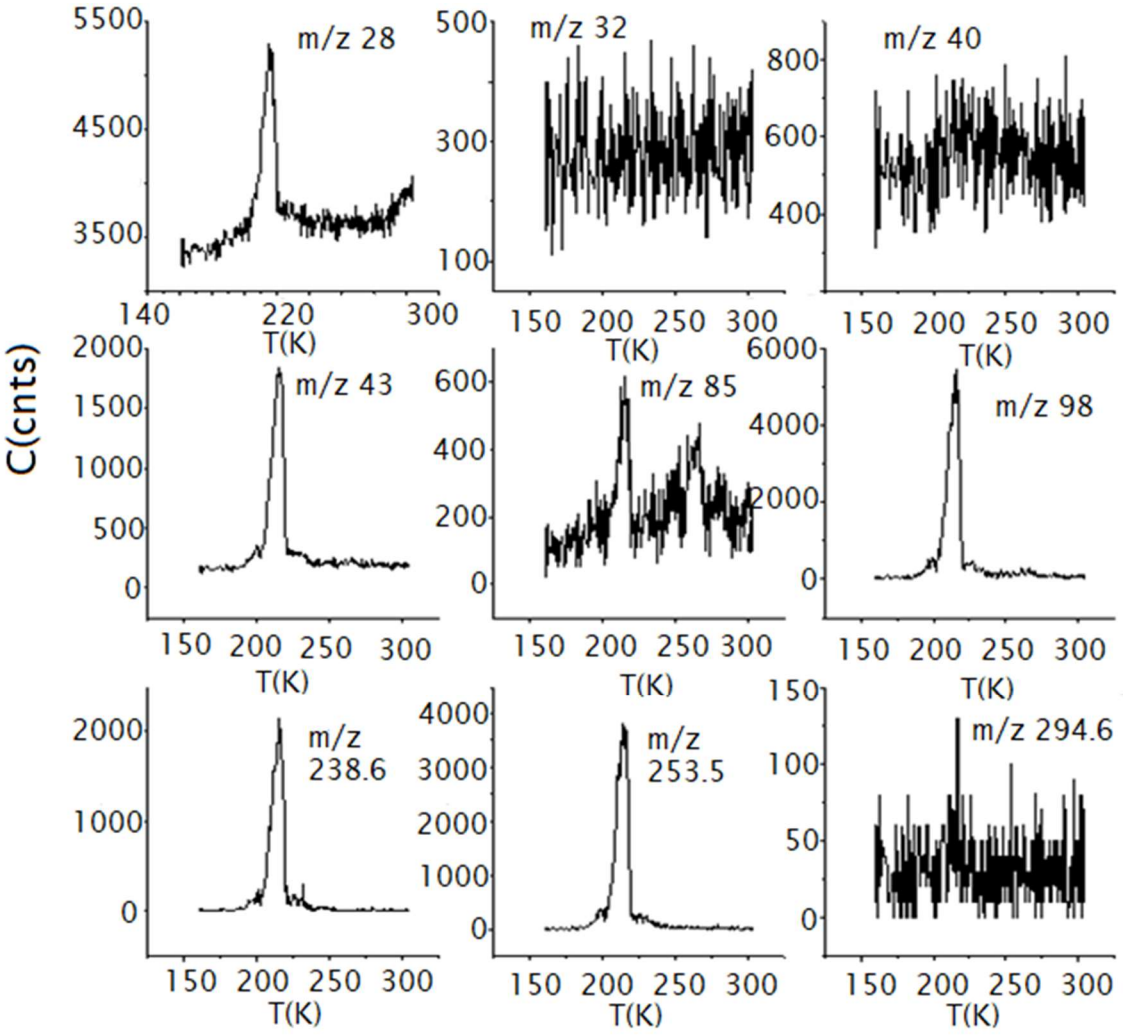

Fig 6.3.2.1.1 TPD of $Me_2Au(acac)$ from 160 K to 300 K at 20 K/min

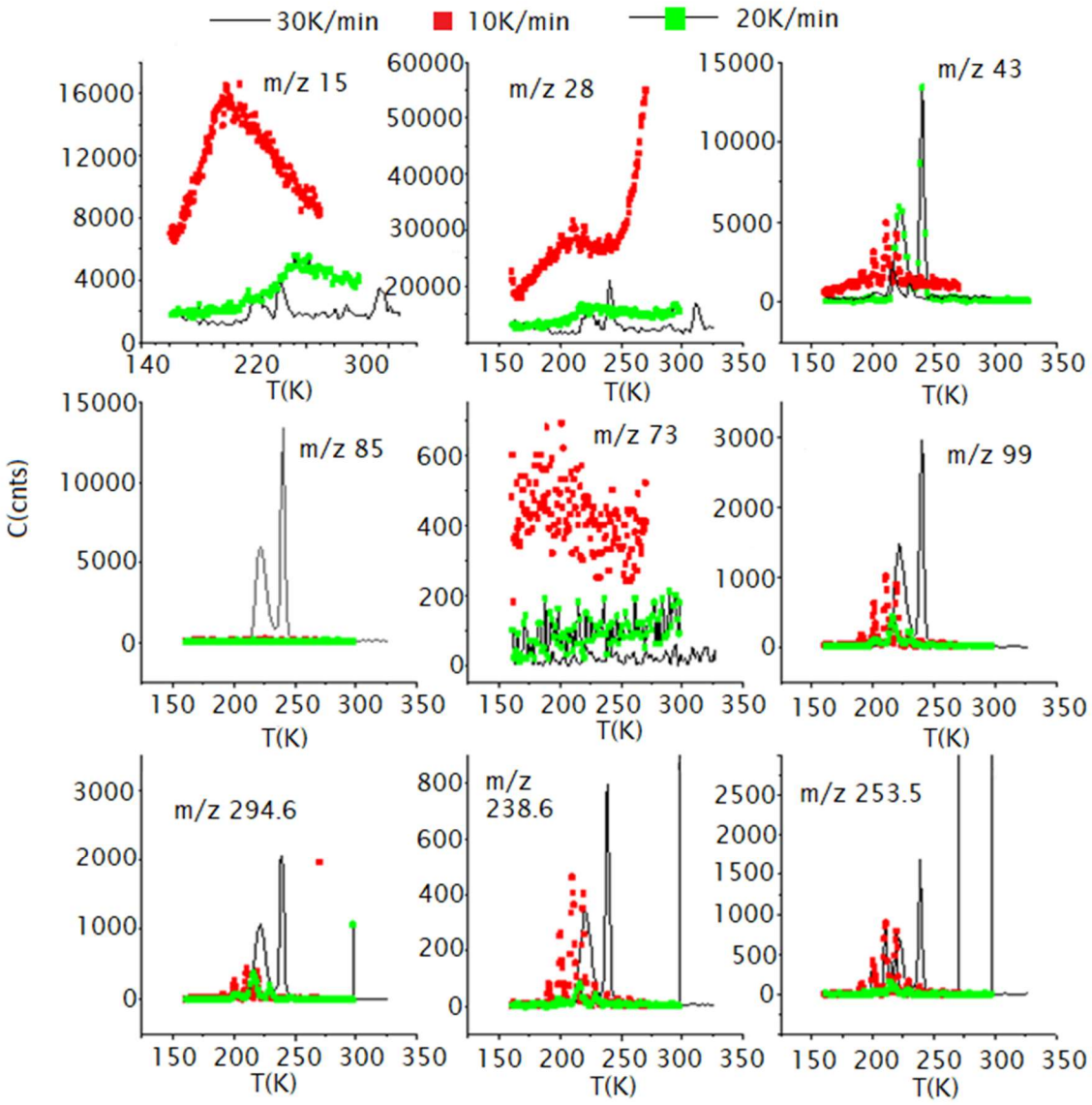

Fig 6.3.2.1.2 TPD with different temperature desorption rate: 10 K/min, 20 K/min, 30 K/min

6.3.3 ESD Spectrum of $Me_2Au(acac)$ Recorded as a Function of Incident Electron Energy

An ESD spectrum was recorded for a thin film of $Me_2Au(acac)$ on the copper substrate cooled first to 20 K and then heated to a temperature of 160 K. The m/z of interest was set in the QMS software, and the signal recorded as a function of the electron energy from 1 to 29 eV. Electron gun parameters were set to grid voltage 30 V / 1 V for OFF/ON, 20 μA range, for a duration of 5 min / 5 min.

Ion yields as a function of electron energy for m/z of 26 and 43, corresponding to $(CH)_2$ and CH_3CO respectively, are shown in Figure 6.3.3.1 to 6.3.3.2. The two selected masses show yield variations at 6, 10, 12 and 16 eV.

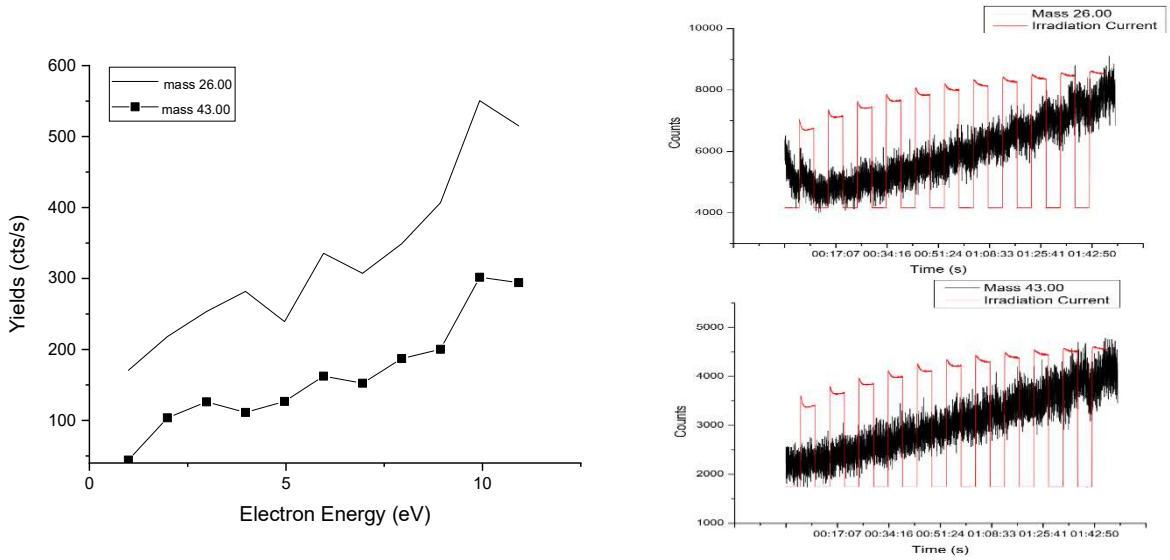

Fig 6.3.3.1 Yields of m/z 26 and m/z 43 from 1 eV to 11 eV

From a series of spectra there is evidence of peaks around 3 eV and 6 eV and a double peak at 9 eV and 11 eV. These are typical energies for an electron induced resonance. Above 20 eV there is a steep rise in yield which may coincide with electron induced dissociative ionization. The peak of both m/z 26 and 43 appears to be between 20 eV and 25 eV.

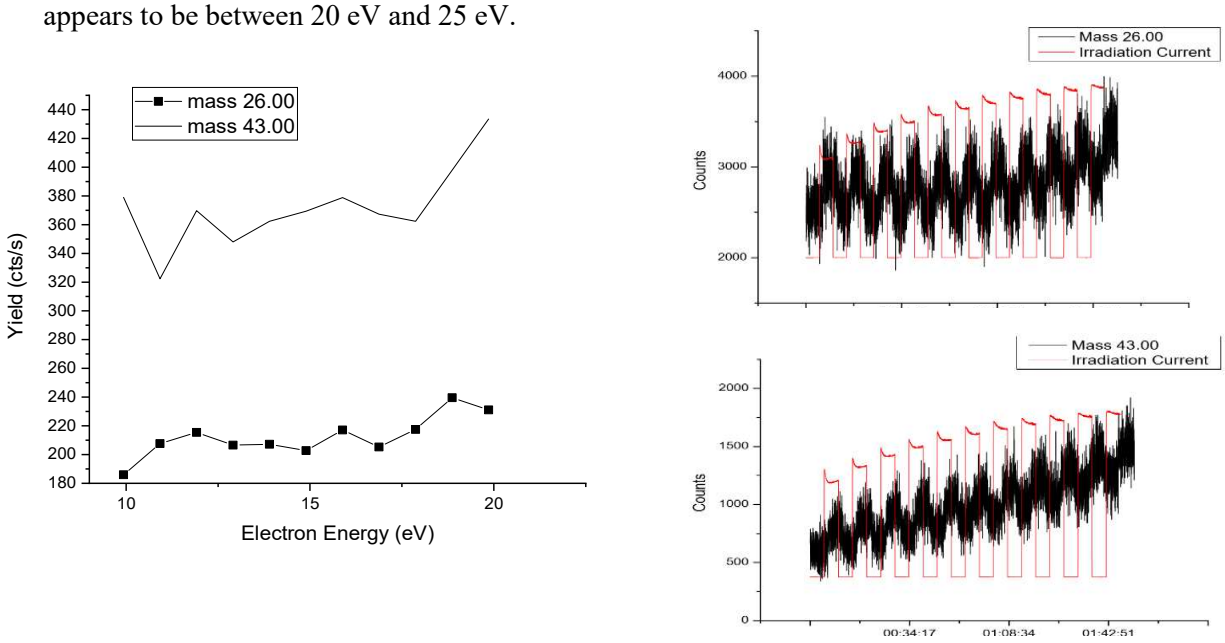

Fig 6.3.3.2 Yields of masses m/z 26 and m/z 43 from 10 eV to 20 eV

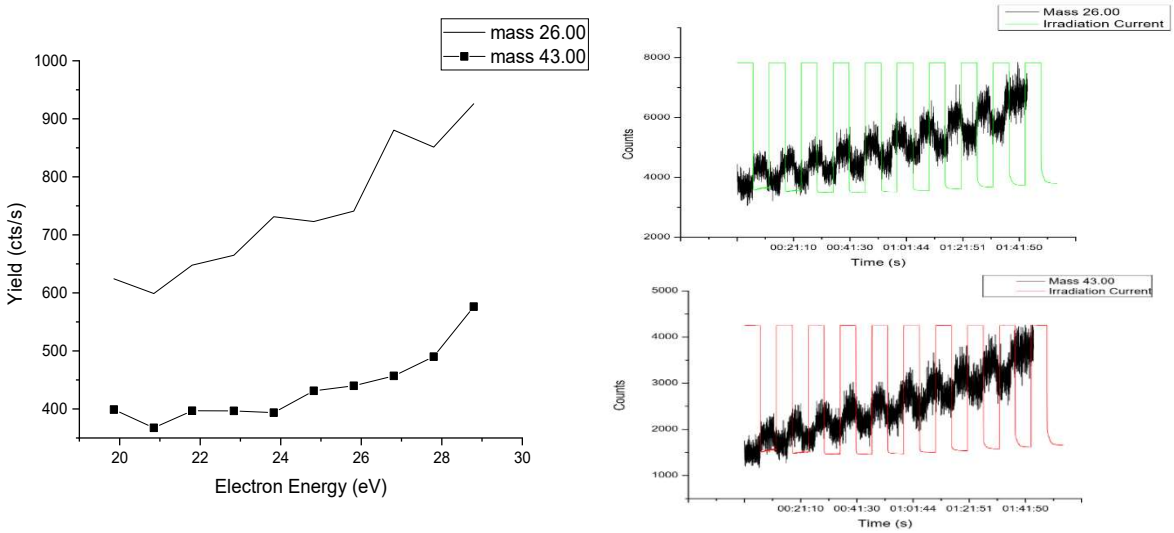

Fig 6.3.3.3 Yields of masses m/z 26 and m/z 43 from 20 eV to 29 eV

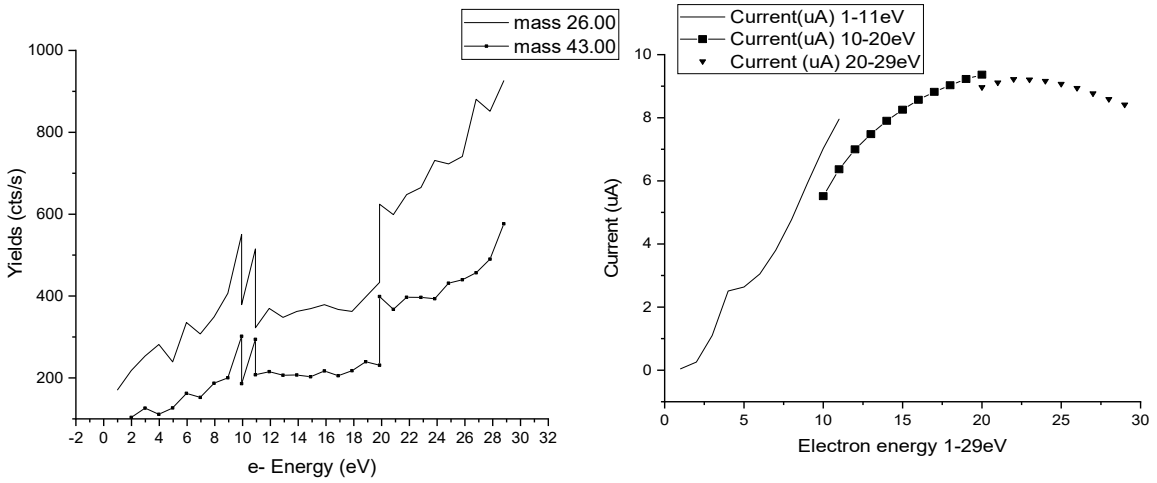

Fig 6.3.3.4 Left: Yields of masses 26 and 43 from 1 eV to 29 eV; Right: Irradiation current I(μA) to electron energy (eV)

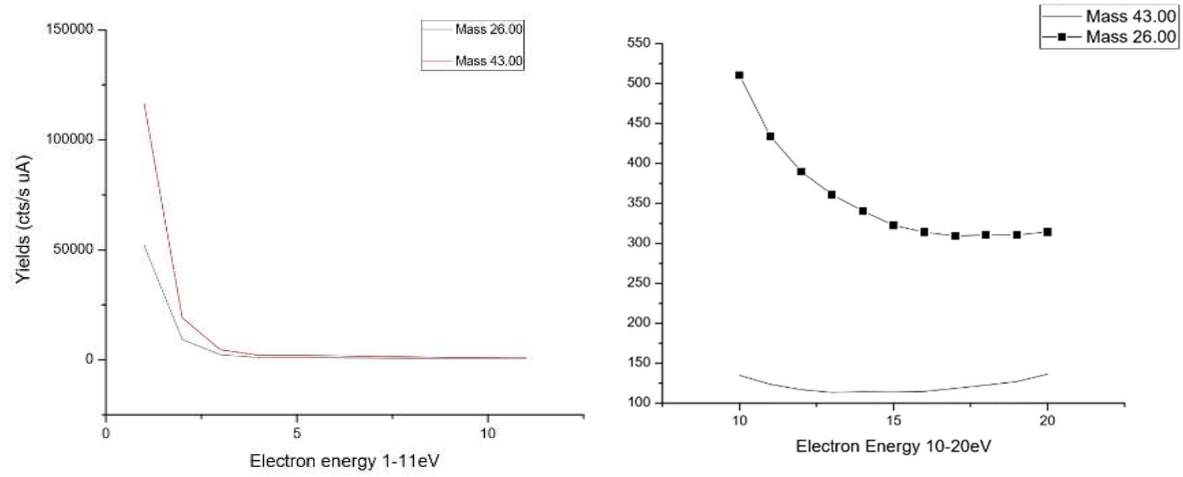

Fig 6.3.3.5 Yields for selected masses from 1 eV to 20 eV with current dependence (fragmentation rate): 1 – 11 eV (left) 10 – 25 eV (right)

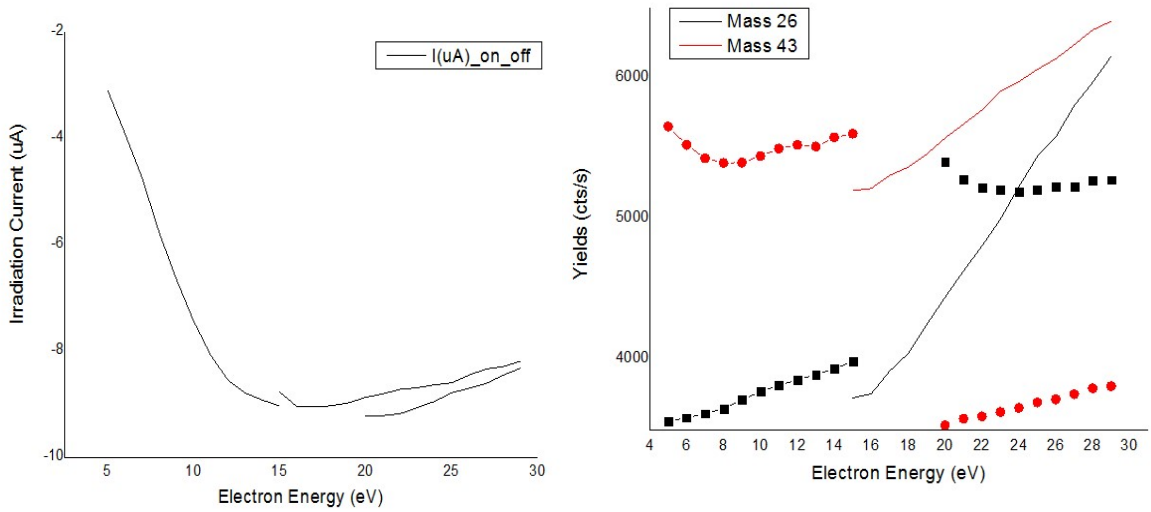

Fig 6.3.3.6 Current (μA) and yields (cts/s) for masses 43 and 26 from 5 – 29 eV

6.3.4 TPD AFTER ESD 7MIN (A) AND 15MIN (B) IRRADIATION

In the next set of experiments thin films were irradiated. A TPD curve was then recorded for each of the fragments observed and may be compared with those recorded without any irradiation. If the electron irradiation had caused any chemical changes in the films, different TPD curves and different products should be observed. The TPD curves after these two irradiation times are shown in Fig 7.3.4.1.

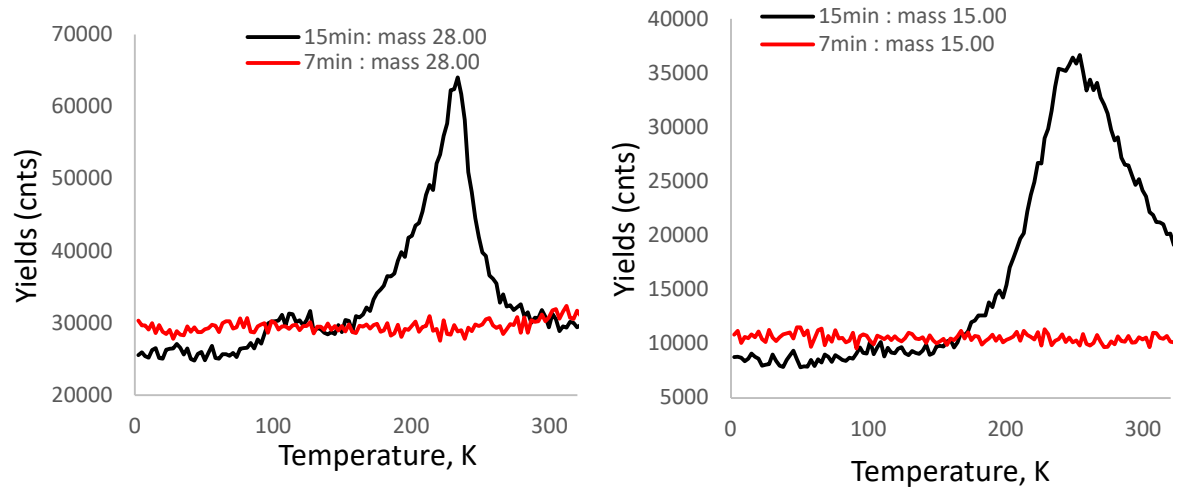

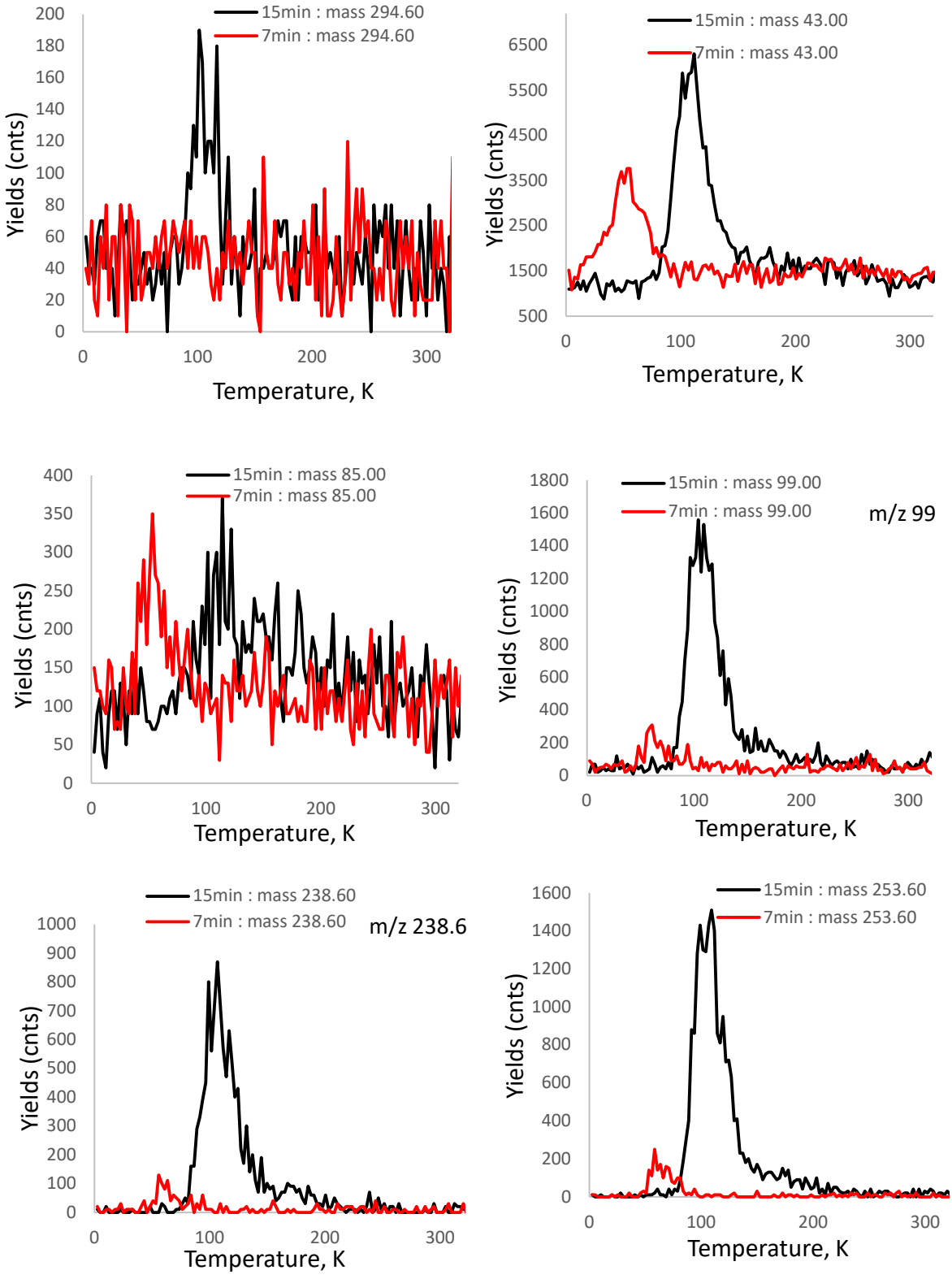

Fig 6.3.4.1 TPD after irradiation 7 min compared to 15 min at 25 eV electron energy irradiation

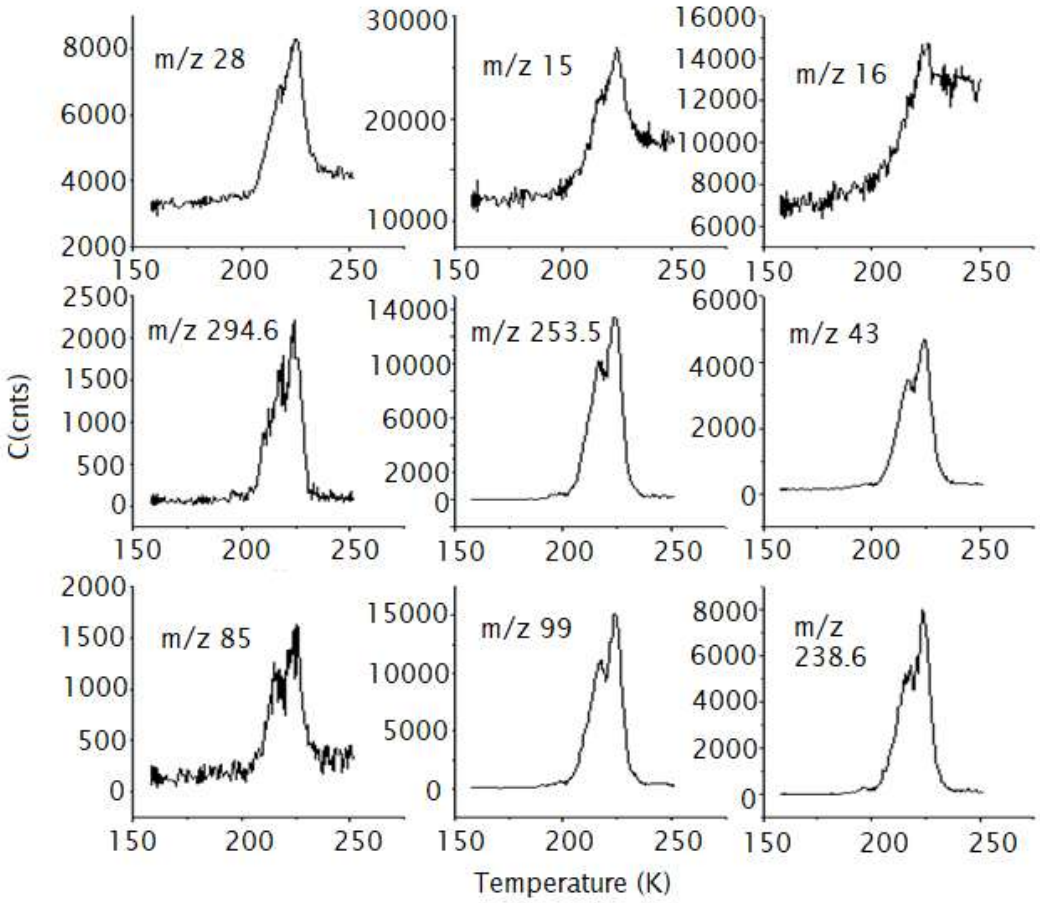

Fig

6.3.4.2. TPD after ESD of $Me_2Au(acac)$ from 160 K to 300 K

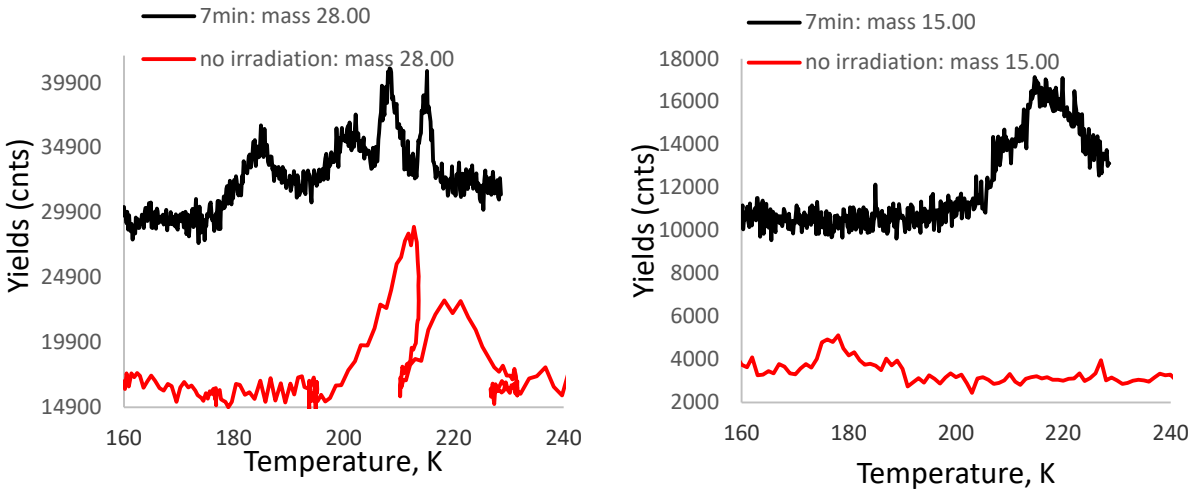

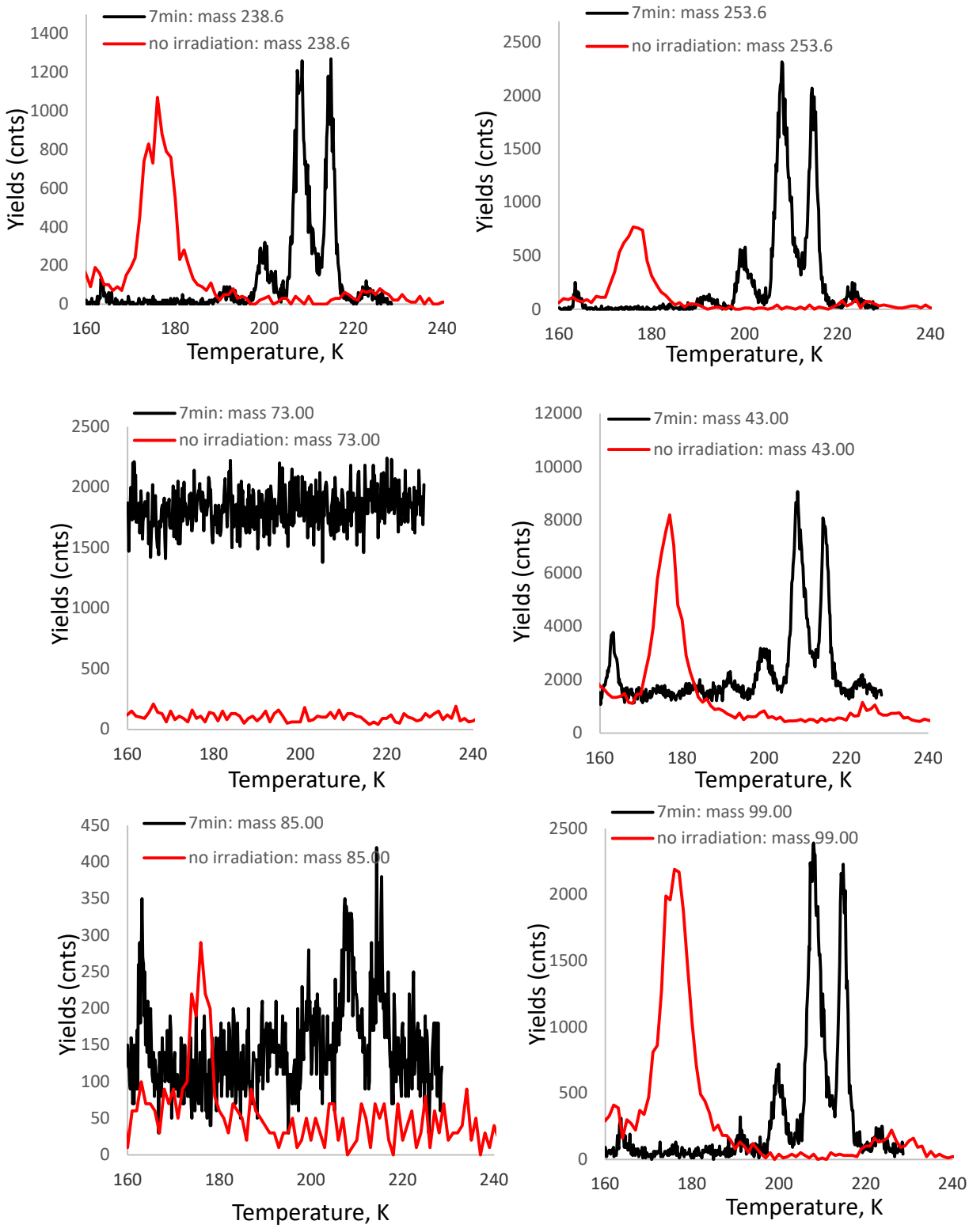

Fig 6.3.4.3 TPD after ESD of $Me_2Au(acac)$ from 160 K to 300 K with 7 min irradiation (a) TPD without ESD of $Me_2Au(acac)$ from 160 K to 300 K (b)

A separate comparison was done for TPD after ESD and irradiation at 7 min and 20 K/min rate and TPD without irradiation at 20 K/min rate. A lower desorption rate is observed in the case of the TPD with 7 min ESD, while the regular TPD at 20 K/min without irradiation has a higher desorption rate characterized by broader peaks with lower amplitude.

6.3.5 ESD Spectrum of $Me_2Au(acac)$

Irradiation was performed at 21 eV with ON/OFF grid values of 1 V / 30 V and duration of 10 min / 5 min. The thin film was deposited on the Cu plate for 35 s with the position set at x = 14.3 mm, y = 19 mm, z = 12.9 mm. The total electron dose is given by the relation (6.3.5.1), and it defines the number of electrons on cm^2:

$$N_e = \int I_t/e \, dt, \qquad (6.3.5.1)$$

Where $e \approx 1.6 \times 10^{-19}$ C.

For: $1\mu A = 1 \times 10^{-6} Cs^{-1} = 1 \times 10^{-6}/1.6 \times 10^{-19} e^{-}s^{-1}cm^{-2} = 6.25 \times 10^{12} e^{-}s^{-1}cm^{-2}$

The highest electron dose in the case of mass 26 is 1.8E16 electrons/cm^2, with a similar dose value for the degradation through irradiation of the thin films of $Me_2Au(acac)$ for an m/z of 43, but with a reduced number of counts from 2450 cnts for m/z 26 to 900 cnts for m/z 43, describing the number of specific fragments obtained at a certain electron dose and for a particular mass.

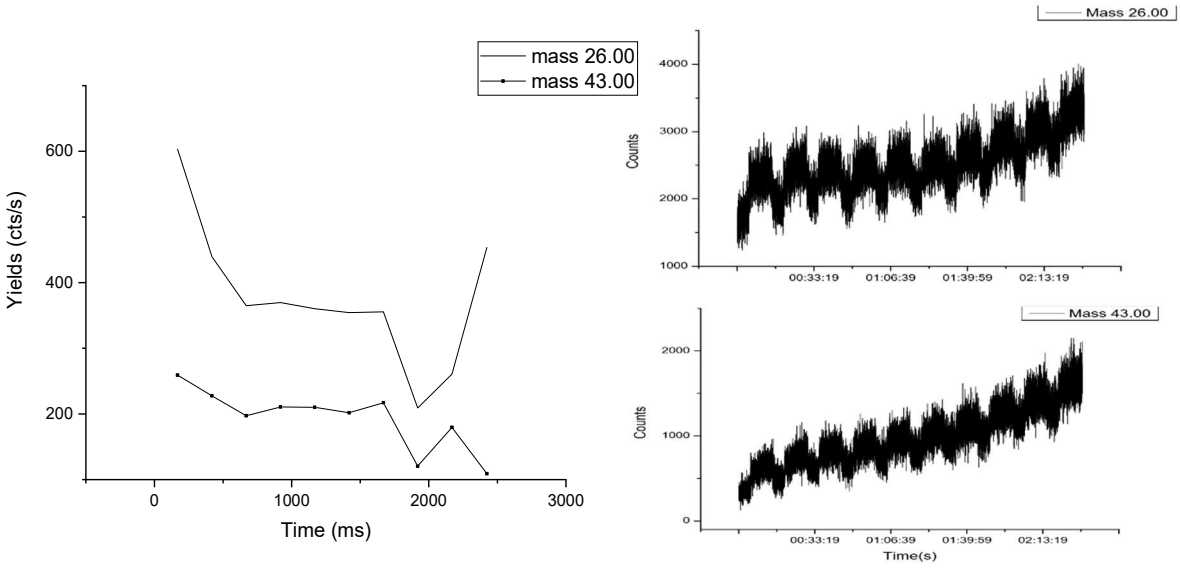

Fig 6.3.5.1 Irradiation spectrum at 21 eV electron energy with 1 V / 30 V ON/OFF grid voltage for electron gun

The electron dose according to the masses irradiated at 21 eV is presented in Fig 6.3.5.2 for mass 26 and mass 43.

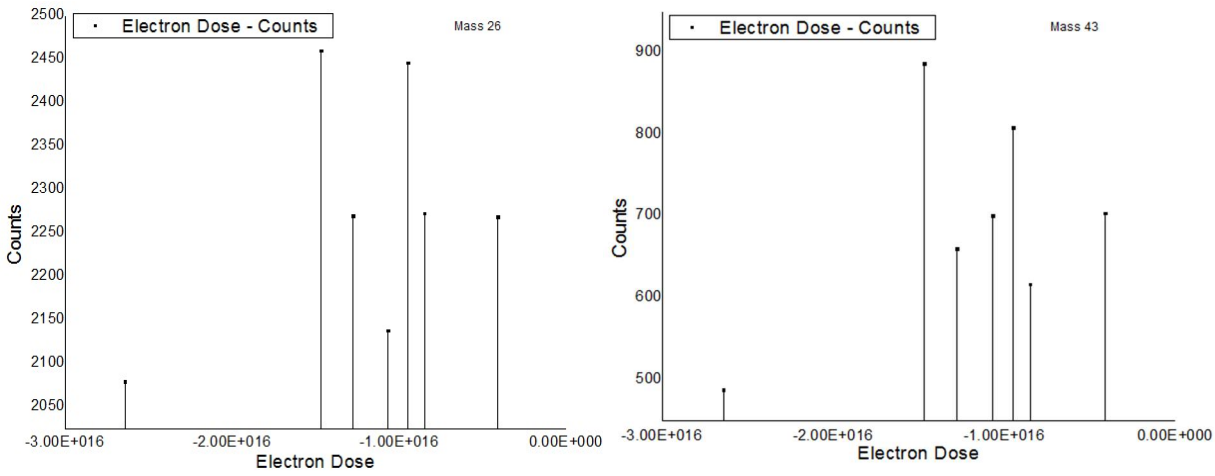

Fig 6.3.5.2 Counts to electron dose for m/z 26 and m/z 43, at 21 eV electron energy, with 1 V / 30 V ON/OFF grid voltage and 10 min / 5 min exposure

6.4 Conclusions To Chapter 6

In this chapter we report results of a detailed study of $Me_2Au(acac)$ irradiation (0 – 20 eV) upon deposition on a Cu(110) bar using a QMS spectrometer. Three types of measurements were performed on the sample: direct electron impact dissociation, electron stimulated desorption and temperature programmed desorption. The $Me_2Au(Acac)$ sample was deposited in thin films of 6 ML thickness on the copper surface. We obtained a detailed overview of the fragmentation pathways of the $Me_2Au(acac)$ precursor at low temperatures (160 K and 298 K), and, in order to determine whether there had been major chemical changes in the $Me_2Au(acac)$ thin films, the process of electron beam induced irradiation of the sample at 25 eV for 15 min and 7 min irradiation and 21 eV irradiation for 5 min and 10 min periods of time. The results show that fragmentation on the surface is similar to that in the gas phase. By studying fragment yields as a function of incident electron energy there is evidence of electron induced resonances on the surface adsorbate. Temperature programed desorption (TPD) studies focus on three rates 30 K/min, 20 K/min and 10 K/min, between 160 K and 298 K. In this step, the desorption of the compound from the surface was observed between 200 K and 250 K with the maximum of the yields at a temperature of 210 K.

The graphical data in the desorption process at TPD studies was obtained for a rate of 30 K/min, though the high rate for fragments with masses 238.6, 253.5 and 294.6 induces spikes in the yields to temperature spectrum coming from the very fast heating of the thermostat. A second step in the surface desorption studies is the electron stimulated desorption (ESD); a first check of the behavior of the $Me_2Au(acac)$ precursor was performed by doing a step irradiation between 1 eV and 29 eV looking into the resonances of the fragments with mass 26 and 43 with a voltage of 30 V ON / 1 V OFF, a current of 20 µA and a duration of 5 min ON / 5 min OFF. Resultant resonances at low electron energies, between 0 eV and 20 eV, with neutral fragmentation on the surface, for fragments with mass 26 (CH_2 fragment) and 43 (CH_3CO fragment), were present at 3 eV, 6 eV, 9 eV and 11 eV. Above 20 eV, a steep increase in the yields to electron spectrum is observed, a sign of induced dissociative ionization. The current from the irradiation step was recorded as a current to electron spectrum presenting the maximum value at 20 eV in the range of ~ 9 µA.

A third irradiation step was done for fixed electron energy of 25 eV for a duration of 7 min and 15 min recording all fragments. As a result of the irradiation of the $Me_2Au(acac)$ thin film at 25 eV we observed a shift in the peak to a lower temperature, while at 7 min irradiation lower amplitude of the resonances was recorded and fragments with mass 15, 294.6 and 28 were missing signaling that no desorption or fragmentation was achieved yielding at those masses. A second TPD was done after the irradiation step at 25 eV analyzing the behavior of the irradiated $Me_2Au(acac)$ thin films and presence of all fragments upon ramping the temperature from 160 K to 298 K. All fragments were found desorbing between 200 K and 250 K. In the comparison of the obtained graph from 7 min irradiation at 25 eV and the thin films without any irradiation step (recorded at 70 eV QMS) a rather constant behavior is observed without major changes, the only difference being in the shift of the spectrum amplitude and the shift of the spectrum with the desorption temperature. The electron dose was recorded in an additional step of irradiation at 21 eV, with 30 V ON / 1 V OFF, 5 min ON / 10 min OFF for a maximum counts in the yields to electron dose spectrum of 2470 cnts (mass 26). The electron dose recorded for fragments with mass 26 and 43 was of 1.8E+16 electrons/cm^2. At the same electron dose the maximum of the mass 43 was found with 890 cnts.

CHAPTER 7. DEPOSITION STUDY OF THE $Si(OEt)_4$ PRECURSOR

The present chapter discusses the experimental work performed on the formation of silica nanostructures by FEBID using $Si(OEt)_4$ as the precursor gas. The experiments were conducted at Zeiss Gmbh, Rossdorf in the research group of Dr. Felix Hermanns. Although $Si(OEt)_4$ has been widely used in the nanotechnology industry there are relatively few articles on its deposition while its use was mostly limited to being a substrate material. This chapter will relate entirely to FEBID deposition studies of this precursor as the fragmentation channels leading to the formation of negative ions of $Si(OEt)_4$ have been discussed in Chapter 3. For the analysis of the deposited nanostructures both AFM and EDX methods were used in conjunction with simulation tools such as CASINO software to determine structural morphology and composition of the created nanostructures.

7.1 PREVIOUS WORK

A study of three precursors, TEOS ($Si(OEt)_4$), TMOS ($Si(OCH_3)_4$) and TMS ($Si(CH_3)_4$), published in 2007 [285] presents a comparison of the composition of elements in the FEBID deposited nanostructures with the addition of O_2 and without. The chemical composition of the TEOS deposited nanostructures of $SiO_{1.8}C_{3.8}$ on the substrate was obtained following the dissociation pathway $Si(OCH_2CH_3)_4 + 12\ O_2 + e^- \rightarrow 10\ H_2O + 8\ CO_2 + SiO_2$ [285] for primary electron beam energies in the range of 1 keV to 30 keV. A threshold of the Si ratio from the assisted deposition with O_2 flux of $Si(OEt)_4$ of 1.75 is obtained, a level representing the lower limit of Si over which C is not detectable in the nanostructures. Perentes and Hoffman 2007 in [285] report the Si threshold ratios in the range of 0.15 for O_2 + TMOS precursor and 0.05 for O_2 + TMS precursor, more than 1.5 lower than the $Si(OEt)_4$ ratio. The deposition Si purity obtained for the $Si(OEt)_4$ in [285] is increasing from 15 at% to 33 at% with the O_2 / TEOS ratio increasing from 0 to 2 : 1, while at higher than 2 O_2 / TEOS ratios, the Si composition in the nanostructures remains constant with O_2 flux and precursor flux. Etching rates of the Si deposits at 150 nm min^{-1} from 0 to 3 :1 ratios have been reached. The same behavior of maintaining a constant Si composition with the dwell time and O_2 / TEOS ratio was reported by Perentes and Hoffman 2007 in [286], the study was focused on the O_2 assisted processes of the $Si(OEt)_4$ precursor and the growth dynamics with the dwell time. Very low dwell times were used to deposit the precursor in the range of ~ 15 µs, with constant growth rates of the SiO_2 constant at currents of 50, 125 and 250 nA. The elemental composition investigation revealed that the C concentration in the final structure increases with the increase in the replenishment time and decreasing dwell time.

Reference	Deposition process	Si Composition (at%)
[285]	FEBID	15 – 33 at%
[274] $Si(CH_3)_4$ precursor	FEBID	3.8 – 35.6 at%
[290] Si_5H_{12} precursor	FEBID	28 - 47 at%
[291]	FEBID	26.9 – 28.6 at%

Table 7.1.1 Composition purity of deposited $Si(OEt)_4$

In the study of the development of the field effect transmitters (FETs), SiO_2 plays a major role. Created in the FEBID process of the $Si(OEt)_4$ precursor at electron beam energies between 5 keV and 30 keV with the addition of H_2O, nanostructures with Si content [291] between 26.9 at% (30 keV) and 28.6 at% (5 keV) have been obtained. In the same paper the authors report earlier development of SiO_2 insulators with low C content in the range of ~ 3 at% that for the $Si(OEt)_4$ precursor is independent of the beam energy, while for their H_2O hydrated structures they observe similar behavior of the precursor with different H_2O / TEOS ratios. Chapman et al 2022 in [291] report values of the effective resistance of the hydrated deposited nanostructures of ~ 20 GΩ. A comparison of the breakdown voltage of dielectric strength with the values of the Si thin films depositions of ~ 0.5 Vnm^{-1} to 1 Vnm^{-1} shows values higher over 40 time in the range of ~ 40 ± 20 Vnm^{-1} of the deposited SiO_xC_y nanostructures. Efforts have been focused towards the development of binary nanostructures of Pt precursors with Si from $Si(OEt)_4$. The resulting structures are Si – stabilized Pt heteroatomic clusters [287] on graphene surfaces. The structures have been created in the FEBID process of the $MeCpPtMe_3$ and Si precursors, after prior development of sputter sites on the graphene using FEBID. An obtained Pt – Si triple vacancy at -3.9 eV was observed with defect as high as 1 Pt atom and 6 Si surrounding atoms. Other Si and metal containing precursors for the development of binary structures and alloys have been investigated in [274], [289], [290]. In the use of $MeCpPtMe_3$ and $Si(SiH_3)_4$ precursors in the FEBID deposition [274], ratios of Si / Pt of 3 : 2 have been obtained, with an increase in the resistivity observed with the aging and exposure to air of the binary amorphous phase Pt – Si nanostructures. Similar purities to $Si(OEt)_4$ precursor deposited FEBID structures have been obtained with Si contents between 3.8 at% to 35.6 at%, and a C and Pt content between 47.2 at% and 12.7 at% corresponding to a decrease with the increase in the $Si(SiH_3)_4$ precursor ratio. Other applications use the Au precursor $Au(III)Me_2(acac)$ [289], where Au nanostructures have been deposited on Si nanorods with Au purities of 10 at% and the growing direction and height independent of the Si nanowires diameter and electron beam with heights in the range of ~ 80 nm. In the deposition of the Co - Si binary alloys, precursors as $Co_2(CO)_8$ and Si_5H_{12} have been tried with behavior similar to TEOS obtaining tunneling effects of the resultant CoSi and $CoSi_2$ [290], at Si content purities between 28 at% and 47 at%, and Co content of ~ 24 at%. Resistivities of 7 x 10^3 μΩcm (Si / Co ratio of

1.5) and 2.8 x 10^4 μΩcm (Si / Co ratio of 2.2) have been obtained from the electrical transport properties studies of the nanowires.

7.2. Sample Preparation and Substrate Characterization

The experimental set-up used in this work has been presented in Chapter 2 Section 2.4 SEM/EDX Equipment at Carl Zeiss Gmbh. Here some details on sample preparation and substrate characterization will be given. In these experiments a gold coated silicon substrate was used (Fig 8.1.2.1). The dimensions of the substrate were 6 mm x 12 mm. The substrate was cleaned in a sonic bath, using isopropanol, for ten minutes to remove any traces of dirt, grease or dust. After cleaning, the substrate was dried with compressed air until all traces of liquid have been removed. In the last step, the substrate was placed in a mask holder and screwed tightly in place.

Fig 7.2.1. Silicon / Au substrate

TEOS, due to its low toxicity level, and being biodegradable and easily assimilated, is used for the fabrication of silica nanoparticles in biomedical applications extensively presented in Ref. [167]. It has also been used extensively in the semiconductor industry as a semiconductor silicon source for the thin film deposition of doped and undoped silicon dioxide films. It is also used as a silane and pyrophoric source, and precursor for the sol-gel synthesis of oxides in Ref. [168]. $Si(OEt)_4$ has been shown not to diffuse into the substrate but forms thin films on the surface as presented in Ref. [169]. FT-IR spectroscopy investigations have revealed the polymerization of TEOS on a surface in Ref. [170]. The formation of the Si – O - Si network is the result of Si - OH condensation on the surface. If the thin film is heated above 368.15 K then $Si(OEt)_4$ dissociates. It has been observed that the C - H bonds break with the increase in temperature, as well as the Si – C and C = C bonds Ref. [172]. Forming either Si - OH

from $Si(OEt)_4$ detected at 1200 cm^{-1} (0.15 eV), 1147 cm^{-1} (0.14 eV), or Si – O – Si from multiple $Si(OEt)_4$ molecules. The C - H bond is easier to break than a Si - O bond, though the O would form new bonds to silica while C bonds to organic radicals will not restructure over time forming new bonds and will be pumped away. The contributions of O and C have been analyzed for the particular TEOS deposition where a high content of organic material has been found in the deposits.

7.3 Results and Discussion

7.3.1 Modelling Electron Interaction Processes Using Monte Carlo Routine

The intention of the simulation was to gain information on the experimental process through the study of a sample (substrate + structure) that is irradiated with 1 keV, 2 keV and 5 keV. The simulation is designed to provide data on the behavior of different types of electrons (backscattered, secondary) and their effect on the formation of the nanostructures. The electron – gas - substrate interactions can be modelled using CASINO software (version 3.3.0.4) that uses a Monte Carlo algorithm for electron trajectory simulation using as inputs the parameters of the electron microscope from the experiments. The number of electrons used in a typical simulation are presented in Table 8.3.1.1 with the electron beam characteristics of the microscope.

Number of electrons [cnts]	Beam radius [nm]	Beam spacing [nm]	Beam energy [keV]
1000000	3	1	5
500000	2.5	1	2
100000	2.5	1	1

Table 7.3.1.1. Electron beam characteristics used for simulations

In this simulation, a 3D shape was created from one box of 100 nm x 100 nm x 20 nm and a pyramid set to intercept the box with 50 nm x 50 nm x 50 nm at angles (70, 90, 70, 90) (Fig 7.3.1.1). The simulation focuses on the electron transport characteristics and quantities for the 3D structure simulated by the shape. The models used for our electron trajectory simulation use data from Mott (Browning 1994) for the total cross-section and partial cross-sections, and Joy and Luo (1989) for the ionization potential. The structure is defined by splitting it into multiple triangles using the model developed by Akenine – Möller (1997) and the electron energy and current region are redefined every time the triangular regions are in collision with an electron and further recorded as a vector product. An improvement to the triangle method was made by Mark de Berg (2008) by adding the triangles in a 3D partition tree. Experiments

on Si samples have been conducted by Demers et al 2012 [215] and Joy 1995 [174] at an electron energies of 1 and 5 keV with exploration of the contamination and oxidation of the sample surface. Our 5 keV simulations were run with a beam radius of 3 nm and 1000000 electrons. Two points on the surface of the sample have been taken and the trajectory of the electrons simulated; the distribution of the energy of the backscattered electrons, the distribution of the surface radius of backscattered electrons, the distribution of the backscattered angle and the distribution of the maximum depth of electrons were determined using a cylindrical distribution with Z in the range of 1000 nm and 50 divisions set relative to the scan point (1, 1, 1). A set of electron energy parameters has been set as the input to the simulation; the minimum secondary electron energy we use for our simulations is 1 eV, the minimum incident electron energy is 0.05 eV and the minimum generated electron energy of 1 eV, with an energy residual loss of 0.1 eV.

7.3.1.1 SIMULATIONS AT 5 KEV

The backscattering coefficient determined in the simulation of 5 keV (Fig 7.3.1.1.1) primary electrons has a value of 0.008139 and the secondary electron yield has a value of 0.047829. The graphical data for the surface radius of BE at 5 keV and backscattered angle at 5 keV are presented in Fig 7.3.1.1.2 and Fig 7.3.1.1.3.

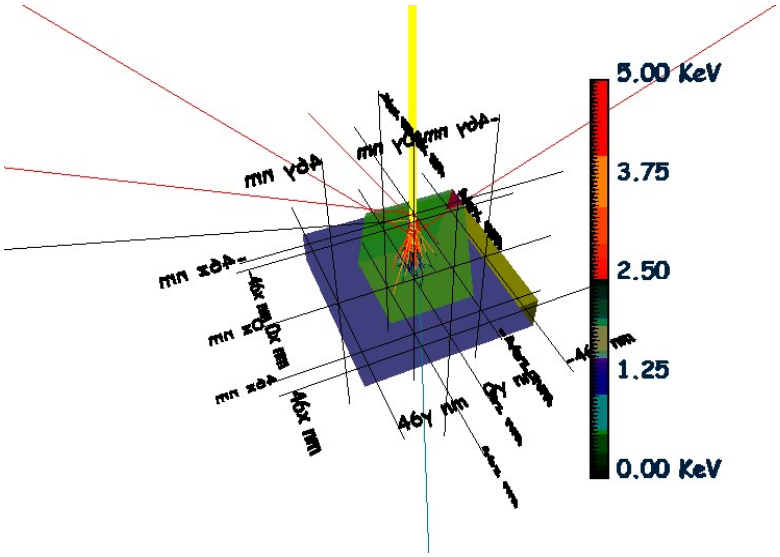

Fig 7.3.1.1.1. CASINO simulation of a 3D sample with 1 eV minimum secondary electrons energy and a 5 keV beam with 3 nm radius

The maximum backscattered radius is in the range of ~26 nm with a maximum of 0.03617 hits/nm^2 (Fig 7.3.1.1.3) and the maximum of the electron energy of the backscattered radius at 0.134 keV/nm^2 is less

than 2 nm from the point of measurement. The backscattered angle has a distribution with the highest peak value between 40 deg and 90 deg and maximum at 0.02 hits/nm^2 with the BSE density between 50 % and 100 % at this angle values, and 10% at 1deg.

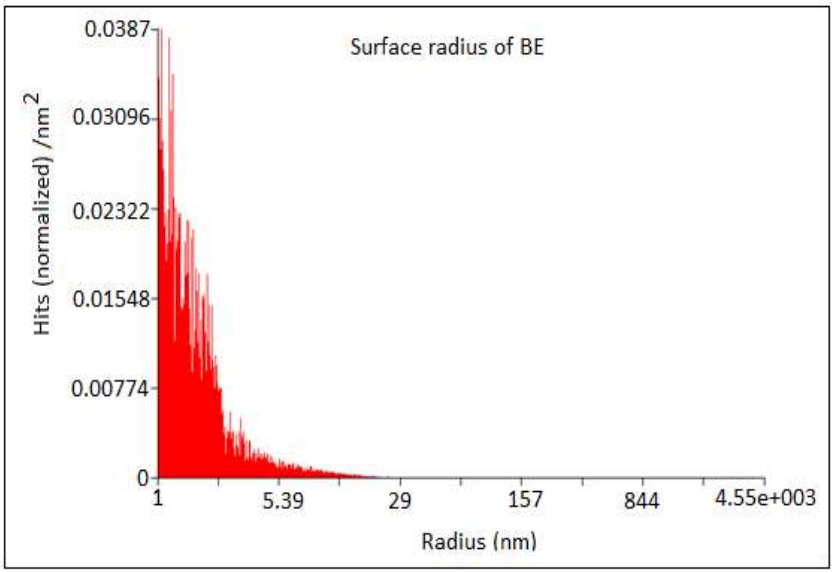

Fig 7.3.1.1.2. Surface radius of BE at 5 keV

From this simulation, the backscattered electrons are the second highest in importance when it comes to the simulation of the electron effects in the FEBID induced nanostructures, secondary electrons that have energies in the range of 1 – 40 eV are responsible for the structure elongation on both the lateral and creation of thin halo depositing extra intermediary fragmented material, while the backscattered electrons have energies over 40 eV and follow gradually the PE electron beam in a radial distribution.

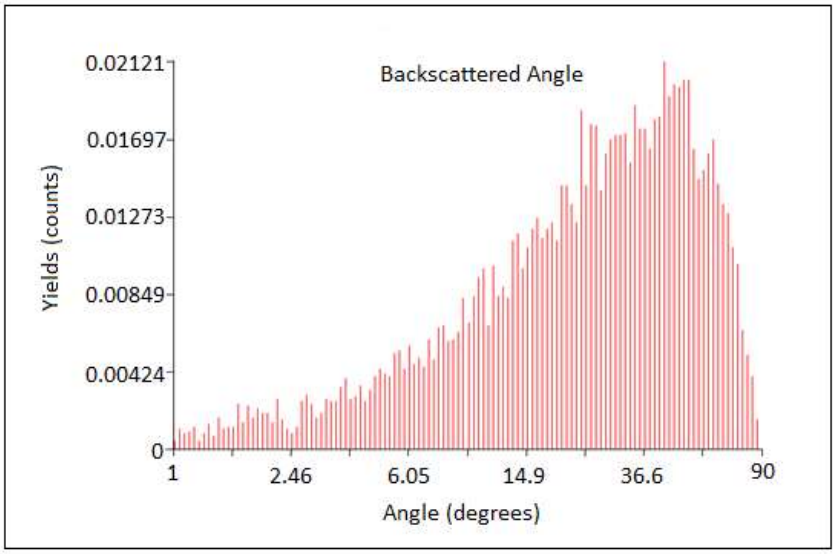

Fig 7.3.1.1.3. Backscattered angle at 5 keV electron beam energy

7.3.1.2 SIMULATIONS AT 2 KEV

The same points are used for the 2 keV distribution of the backscattered electrons and the secondary electrons. The simulation is presented in Fig 7.3.1.2.1. The backscattering angle distribution for a 2 keV primary electron beam follows the same pattern as for the 5 keV simulation, but with higher maximum value in the range of ~0.02482 hits, and the maximum peak falling between the same values of 40 deg and 90 deg. The same 10 % of all backscattered electrons falls between 0 – 2 deg and 50 – 100 % falls between 40 – 90 deg. The backscattered electron angle spectrum is presented in Fig 7.3.1.2.2. The backscattering coefficient for the 2 keV electron beam has a value of 0.009848 and the secondary electron yield has a value of 9.2 x 10^{-5}. The surface radius BSE distribution has a maximum surface radius of 12.2 nm from the defined point and a maximum value of 0.05316 hits/nm^2.

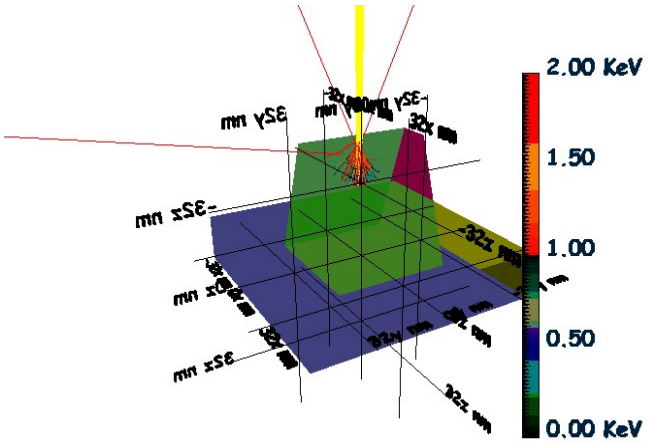

Fig 7.3.1.2.1. CASINO simulation of a 3D sample with 1 eV minimum secondary electrons energy and a 2 keV beam with 2.5 nm radius

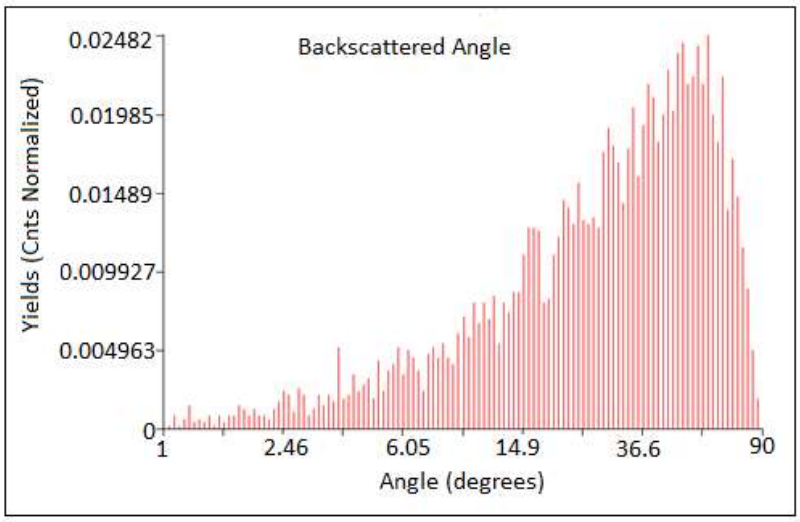

Fig 7.3.1.2.2. Backscattered angle at 2 keV electron beam energy

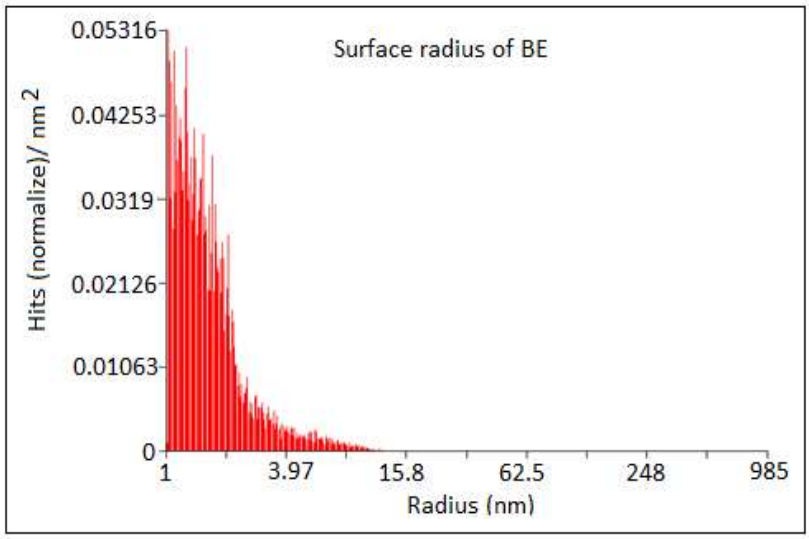

Fig 7.3.1.2.3. Surface radius of BE at 2 keV electron beam energy

7.3.1.3 Simulations at 1keV

Another set of simulations were run for an electron beam of 2.5 nm radius, 1 keV electron beam energy and a number of 100000 electrons (Fig 7.3.1.3.1). The sample used is the same sample as in the case of an electron beam of 2 keV and 5 keV. The models used for the distributions are the same as in the case of 5 keV electron beam: Mott (Browning, 1994) for total cross-sections and partial cross-sections, and Joy and Luo (1989) for the ionization potential. The minimum secondary and generated electron energy used was 1 eV and the residual energy loss of 0.1.

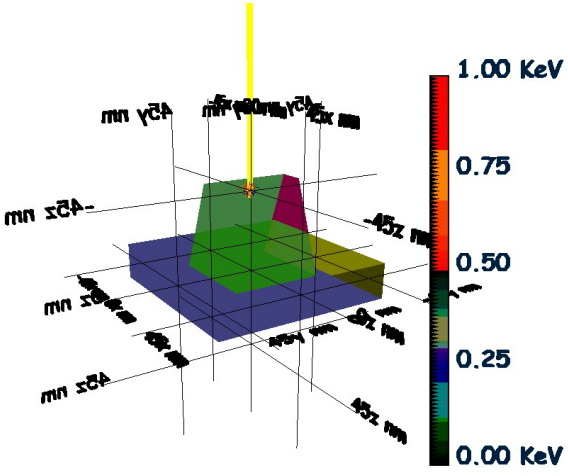

Fig 7.3.1.3.1. CASINO simulation of a 3D sample with 1 eV minimum secondary electrons energy and a 1 keV beam with 2.5 nm radius

The radius of dispersion of electrons inside the sample and atop the sample is visibly reduced compared to that generated with a 2 keV or 5 keV electron beam, though the maximum energy of the surface radius increases to 0.151 hits/nm^2, close to the main target of the beam meaning that the higher the energy the lower the scattering as the majority of electrons are primary electrons.

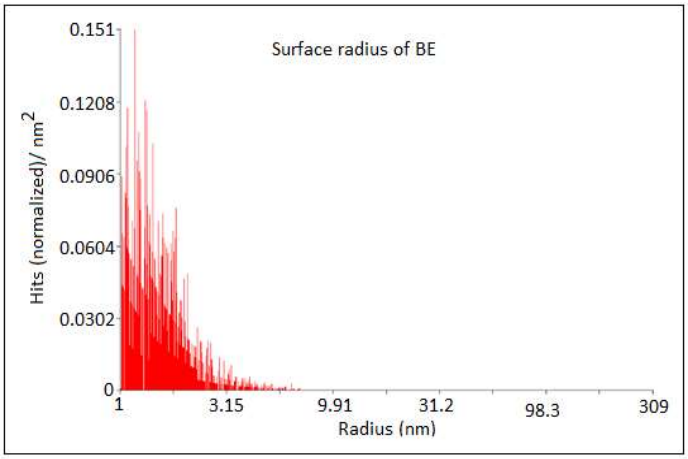

Fig 7.3.1.3.2. Surface radius of BE at 1 keV electron beam energy

The backscattering radius lowers to a value of 7 nm, and the maximum value of the backscattering radius on the surface is close to 1.2 nm. The obtained backscatter coefficient is 0.01219 and the secondary electron yield has a value of 0.08492. The energy of the surface radius of BSE has a maximum value of 0.121 keV/nm^2 at the maximum surface radius. The sample used is the same sample as in the case of an electron beam of 2 keV and 5 keV. The models used for the distributions are the same as in the case of 5 keV electron beam: Mott (Browning, 1994) for total cross-sections and partial cross-sections, and Joy and Luo (1989) for the ionization potential. The minimum secondary and generated electron energy used was 1 eV and the residual energy loss of 0.1.

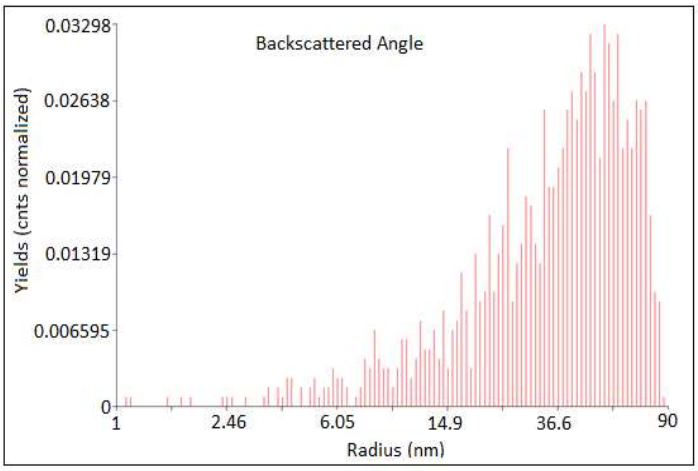

Fig 7.3.1.3.3. Backscattered angle at 1 keV electron beam energy

The electron beam radius of the backscattered electrons coming from a 1 keV electron beam is almost at half value to the one from the 2 keV BSE distribution and 3x lower than for the 5 keV. The distribution reported values though are not consistent with a linear increase, but rather polynomial. The simulation schematics, surface radius and backscattered angle are presented in Fig 7.3.1.3.2 and Fig 7.3.1.3.3 and Table 7.3.1.3.1.

Beam Voltage (keV)	Maximum energy of surface radius (hits/nm$^{2)}$	Backscattered Radius (nm)	Energy of surface radius of BSE keV/nm^2
1	0.151	1.2	0.121
2	0.05316	12.2	0.08172
5	0.03617	26	0.134

Table 7.3.1.3.1 Results of electron trajectory simulations using CASINO software for 1 keV, 2 keV and 5 keV

7.3.2 FEBID Studies Using Si(OEt)$_4$ (TEOS) Deposition

Si(OEt)$_4$ (TEOS) was used in a SEM environment to develop FEBID nanostructures on a 100 nm gold substrate layered on a silica support. The aim of these experiments was both to determine the behavior of Si(OEt)$_4$ as a precursor and to determine the level of oxidation of the structures with time and exposure to air. Two types of nanostructures were deposited, first deposits are 'line' like/rectangular structures, the second type of deposits are 'dots' or small silica pillars. The SEM apparatus used has already been described in Chapter 2, Section 2.4. The beam characteristics are detailed in Table A7.1 in ANNEX 7 for each of the deposits. A loop is defined as a one-time exposure of all exposure points used to create a particular structure. An acceleration voltage of 1000 eV is used for all deposits presented in this research. These deposits were analyzed eight months after deposition.

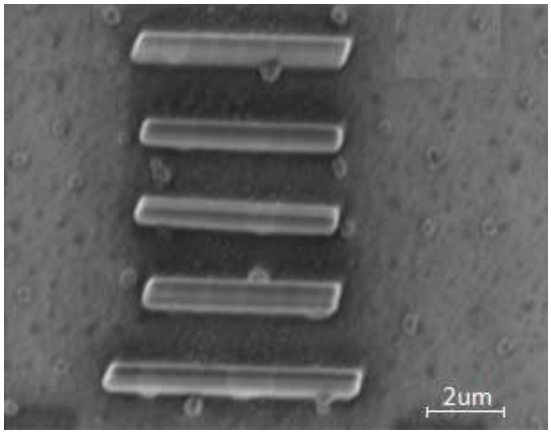

Fig 7.3.2.1. Si(OEt)$_4$ FEBID deposition on Au(111) substrate; line deposition at 750ns dwell time

A second set of experiments was performed using a Gemini column Zeiss SEM with a 1 keV electron beam; this instrument having a higher resolution than that used for the first set of data and the deposition of the shapes was performed to create structures of varied sizes using different dwell times. The second set of deposits were kept no longer than 12 hours in air. In this experiment only 4 deposits were made, with dwell times and beam characteristics presented in ANNEX 7 Table A7.2.

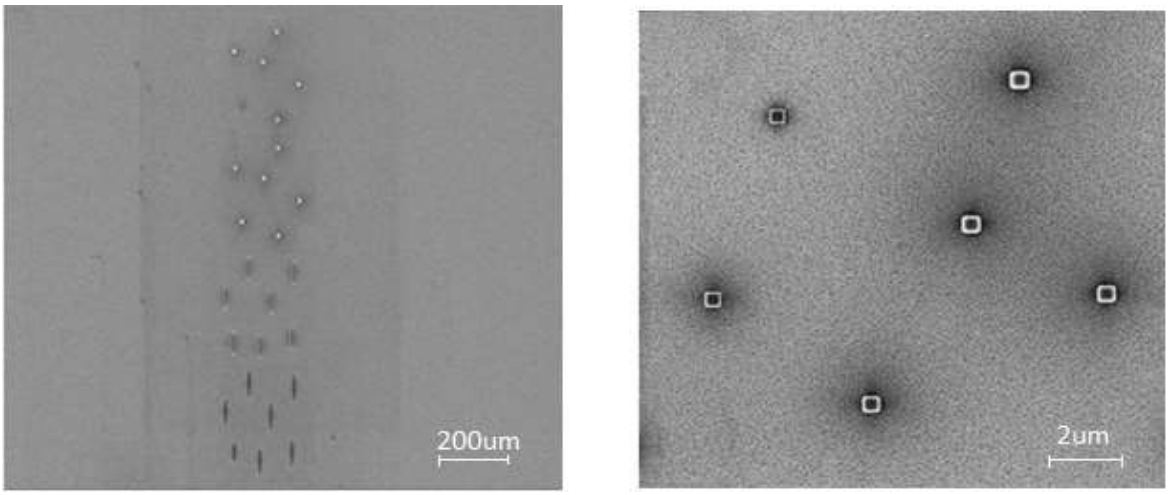

Fig 7.3.2.2. One day old deposits of $Si(OEt)_4$ on Au(111)/silica, 6 points

7.3.3. $Si(OEt)_4$ FEBID Deposition Analysis Using EDX and AFM Measurements

7.3.3.1 $Si(OEt)_4$ FEBID Deposition Analysis Using EDX and AFM Measurements of 8 Months Old Deposits

The deposits were measured using AFM and EDX analysis no later than 12 hours after fabrication to determine both their spatial and chemical composition characteristics. One set was then kept at room temperature for over 8 months and then analyzed again for structural integrity and chemical composition. For commercial purposes it is essential to understand any 'ageing' processes of the surface and deposition. The oxidation state values, and elemental composition of the structures is influenced by the substrate smoothness and homogeneity. The aged substrate presented a higher number of defects. The inhomogeneity of the surface, the holes in the Au(111) layer and kinks affect the deposits height and width, as well as their shape. Higher Si signal might be observed for the old substrate due to the higher number of surface defects (Table A7.7).

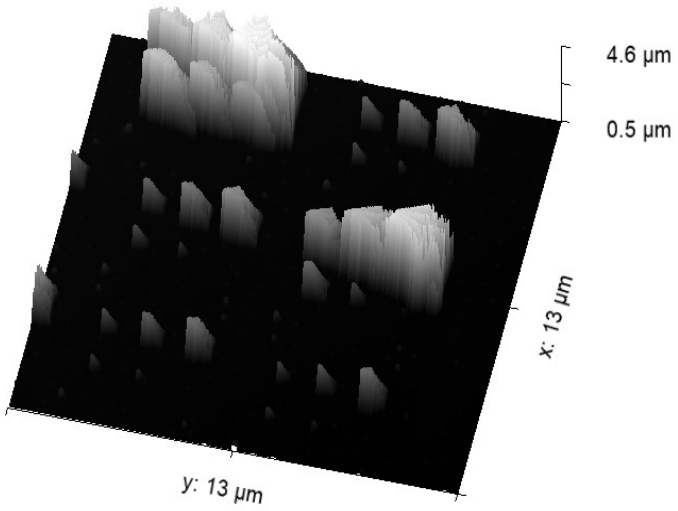

Fig 7.3.3.1.2. $Si(OEt)_4$ FEBID pillar depositions 3D view of Fig 7.3.3.1.1

After eight months line deposits look smooth, without visible damage, tilting or oxidation over time. However, a few of the point deposition structures have merged as a result of tilting (Fig 7.3.3.1.2), their initial size (> 500 nm) being larger than the rest of the deposited structures. The height and width of the structures is presented in Table 7.3.3.1.2. The 8 months old profiles correspond to a number of line profiles (Fig 7.3.3.1.1) and dot profiles (pillar structures; Fig A7.6), presented in Table 7.3.3.1.1 and Table 7.3.3.1.2.

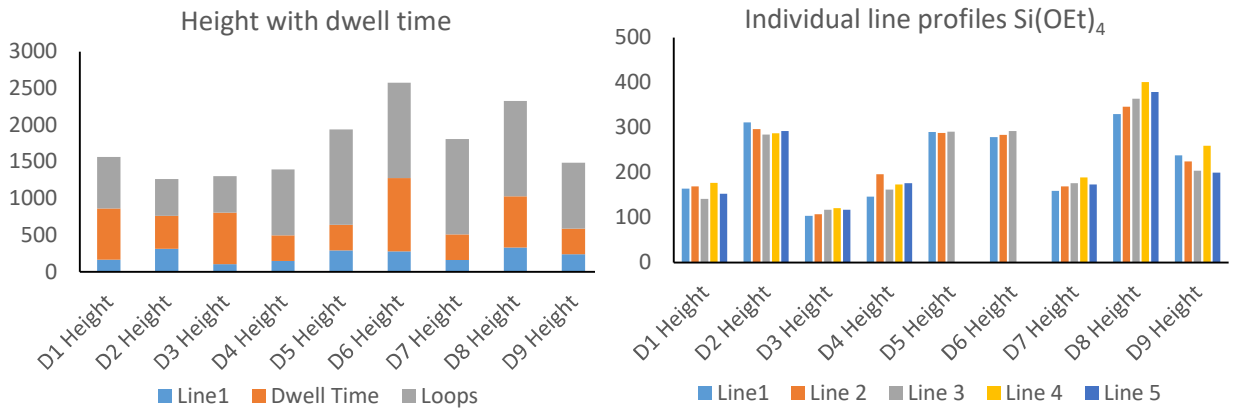

Fig 7.3.3.1.3. Height vs dwell time (a) data of individual line profiles of 8 months old structures (b)

The 9 line profiles have each a group of 5 lines created with different dwell times and number of loops creating deposits with different heights; the height difference is in the range of tens (10x) of nm. The data analysis of the width and height of the structures was performed using Gwyddion 2.65 software and shows the merging of the two biggest peaks in the structures with the smaller peaks/dot profiles on the

lateral of the structure obtained at lower dwell times, these small structures disappear completely. The tilting of the structures could have led to the collapse of the pillars over the 8 months merging the two rows of pillars. A 3D view of the pillars can be seen in Fig 7.3.3.1.2 where the merged structures can be observed. From the analysis of the height profiles with dwell time and number of loops, an increase in the height with the increase in the dwell time and the number of loops is seen. This is expected up to the precursor limited growth regime, but the best growth ratio (dwell time to height and width) can be seen for a set of parameters of 500 µs loops and 450 µs dwell time. From Table 7.3.3.1.2, the structure D2 has a height similar to structure D8 where the number of loops doubled, characterized by 1300 loops (D8 structure) compared to 500 loops for the D2 structure, and a dwell time of 250 µs higher than the 450 µs dwell time used for D2. The heights and widths of the merged structures and the well-preserved structures are presented in Fig 7.3.3.1.3 (a) and (b). The chemical composition of the structures may be derived from the EDX spectra presented in Fig 7.3.3.1.4 showing for D2 Line 5 structure a higher signal coming from Au. The C and O content is similar in value for all the profiles analyzed. However, in all structures there is evidence of the presence of nitrogen contamination most probably from the air, this can be seen from the compositional analysis graph (Fig 7.3.3.1.4). The Si content is fairly constant over all the deposits; the presence of Au is assigned to kinks or Au asperities (growths) on the Au(111) surface present there at the time of the FEBID deposition.

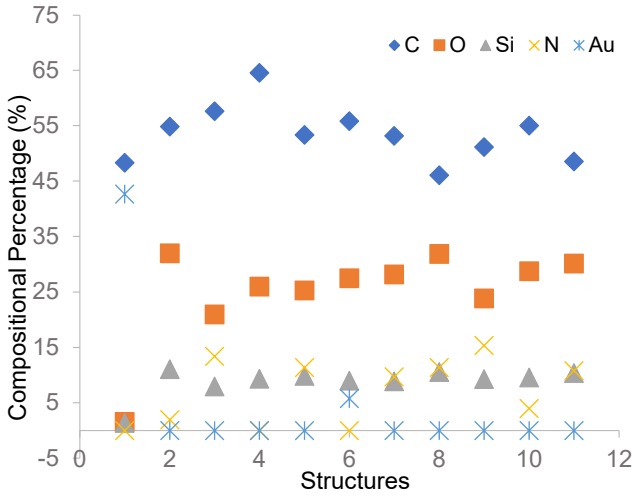

Fig 7.3.3.1.4. Compositional content of individual line profiles of 8 months old structures

The dot deposits for the 8 months in-air stored samples unfortunately could not be analyzed for elemental compositional percentage due to the low resolution of the EDX equipment used. Only a morphological analysis and height/width analysis has been obtained, knowing that oxidation would change the height and width of the structures with the addition of oxygen from the air.

7.3.3.2 Si(OEt)$_4$ FEBID Deposition Analysis Using EDX and AFM Measurements of 12 Hours Old Deposits

With the aid of the Gemini column SEM from Zeiss Gmbh 1 keV beam individual line depositions with 7 lines each and 2 dot deposits with 6 and 7 points have been performed. The height and width characteristics for each of these profiles are presented in ANNEX 7 Table A7.3 as well as the dwell time and number of loops. All deposits have been done with a 1 keV electron beam and a current of 28 pA.

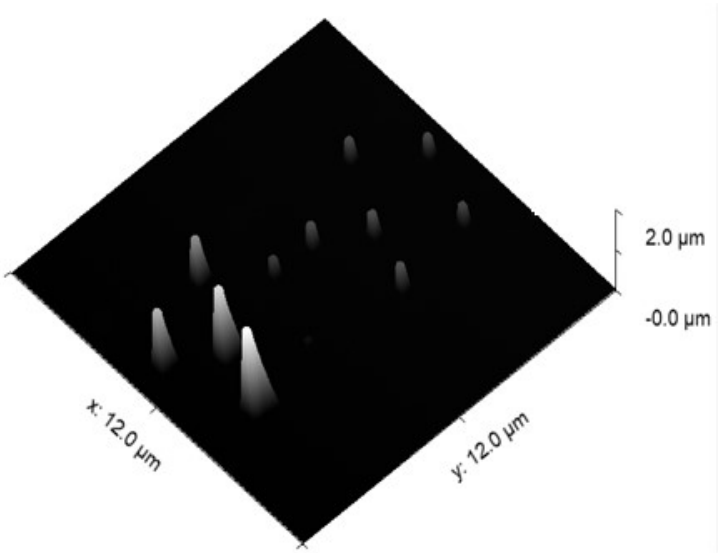

Fig 7.3.3.2.1. Dot profiles of 12 hours old Si(OEt)$_4$ deposits

In the 12 hours old pillar-shaped deposits no merging between structures is observed, the structures show a clear height profile, going from a higher base to a thinner top for deposited pillars at high deposition rates. When using a low dwell time and a high number of loops similar to the dwell time, the pillars do not have a constant width from bottom to top and the pillar growth is increased. The 3D profile of the 12 hours old dot deposits is presented in Fig 7.3.3.2.2. In the case of the deposition 2 (12 hours old) the individual line profiles, the dwell time and height are showing a growth regime affected by the electron beam (electron limited regime). A smaller dwell time and smaller number of loops used have the effect of higher structure growth. From analysis of the profile of the FEBID grown dots, we see that higher loops and higher dwell time results in smaller structures, while constant loops of 1000 and varying dwell time has better results in the height of the structures (ratio of dwell time to height, taking into account that higher dwell time means longer precursor flow); a value of 503.0 µs dwell time appears to give the best results and the highest structures. These can be seen from Fig 7.3.3.2.4 (a) as well, where Point 6

has the biggest height and width value. The lateral growth of the structure is more of a concern though as the intent is to grow thin controlled width and height structures.

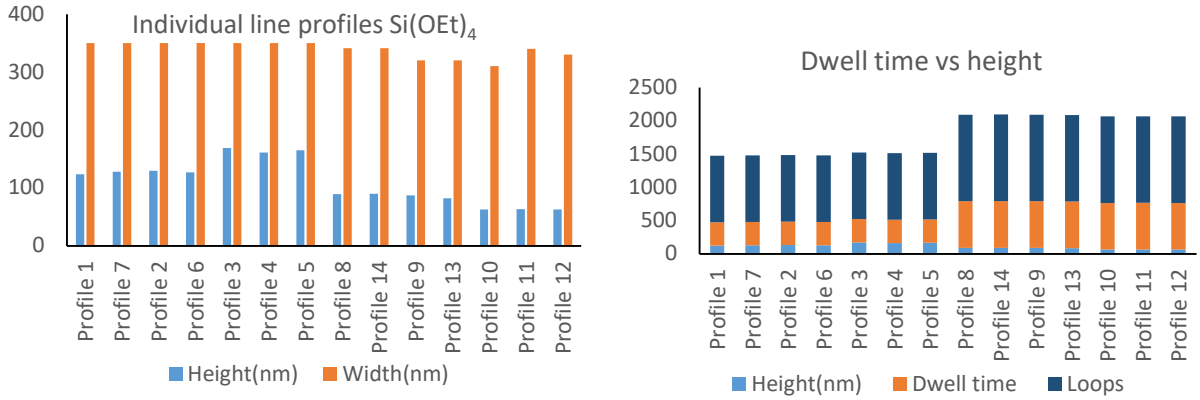

(a) (b)

Fig 7.3.3.2.3. Height and width of the individual line profiles (a) and height versus dwell time (b) of 12 hours old structures

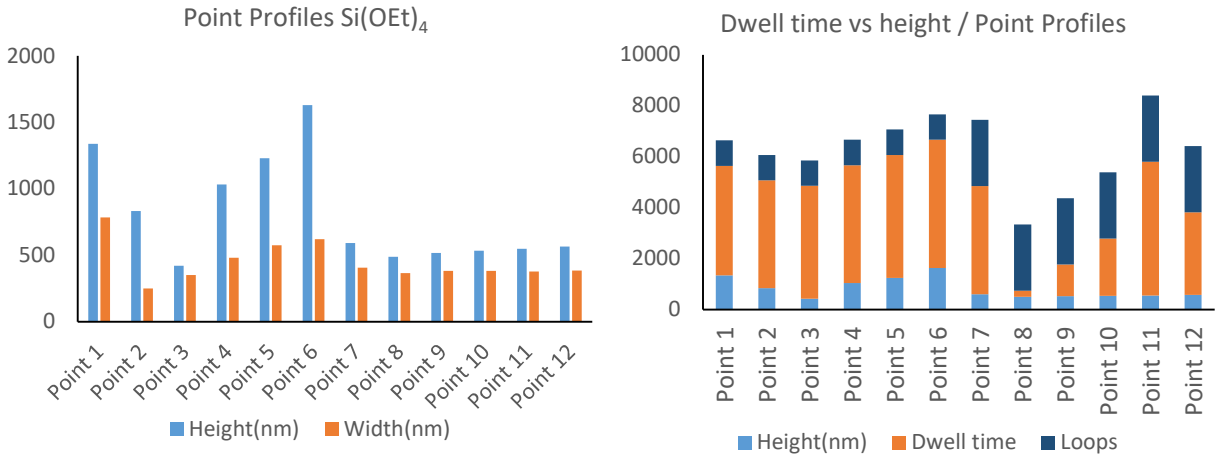

(a) (b)

Fig 7.3.3.2.4. Height and width of the point profiles (a) and height versus dwell time (b) of 12 hours old structures

Knowing it is possible to deposit as small as ~1 nm height, the challenge comes in controlling the parameters for the optimized shape and width of the structure, and composition. The lateral growth of the structure with the height is an undesired effect. In the line profiles and point profiles, in contrast to the first set of experiments, we see no evidence of nitrogen contamination, but we do see the presence of gold. We attribute this to the deposits being too thin, EDX having > 100 nm penetration depth, we see

the underlying gold. Higher dwell times, for Profile 9 and Profile 10, give higher C, O and Si content. See Fig 7.3.3.2.9 and Fig 7.3.3.2.6.

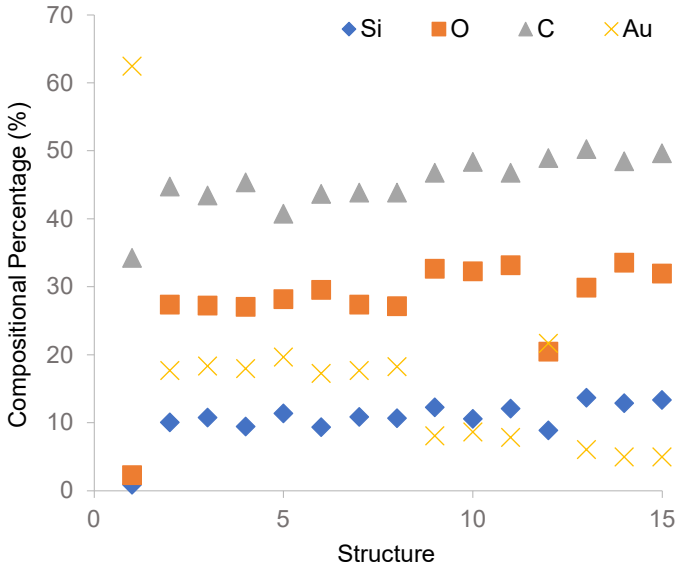

Fig 7.3.3.2.5. Point profiles of 12 hours old $Si(OEt)_4$ FEBID deposition structures

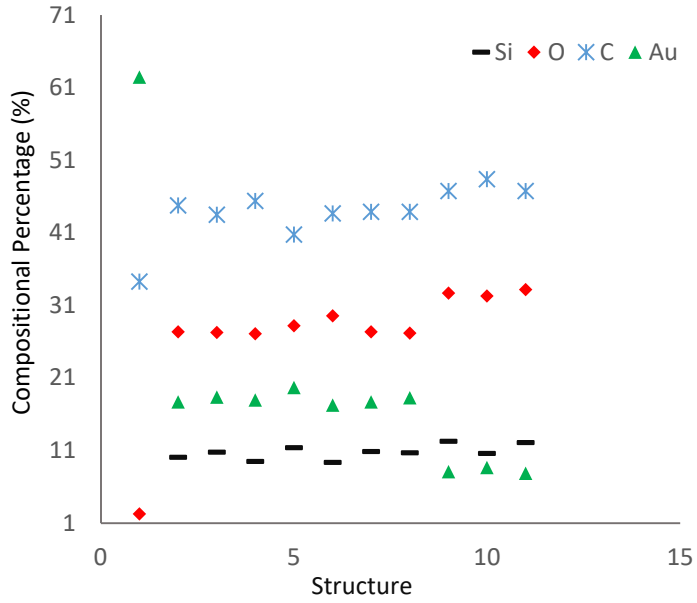

7.3.3.2.6. Individual line profiles of 12 hours old $Si(OEt)_4$ FEBID deposition structures

7.3.4 $Si(OEt)_4$ FEBID Deposition Analysis Using EDX and AFM Measurements

Comparison of Measurements

In Table A7.5 we present the concentrations of compositional elements for each measured structure, and we can see that for dwell times of 700 ns and 1300 loops the elements Si, C and O have higher percentage, and we can determine that the height and width of the structure increases. The nitrogen content in this case is limited to 0.8 % and present only in Profile 12. Further comparison is done between the 8 months old deposits and the 12 hours deposits considering only the compositional change in the deposits. In Fig 7.3.4.2, the profiles of the two structures 12 hours (N) and 8 months (N') are presented, with the nitrogen having high values for the 8 months old deposits, up to ~15.4 % for Profile 10. The oxygen content does not appear to change significantly over all the deposited structures for the 8 months old deposits compared to the 12 hours old deposits. Significant changes are observed only for profiles 1 and 10.

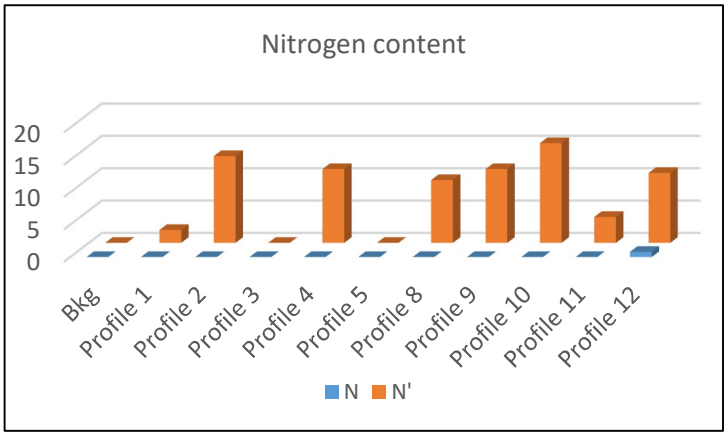

Fig 7.3.4.1. Comparison of the nitrogen in the structures composition: 12 hours (N); 8 months (N')

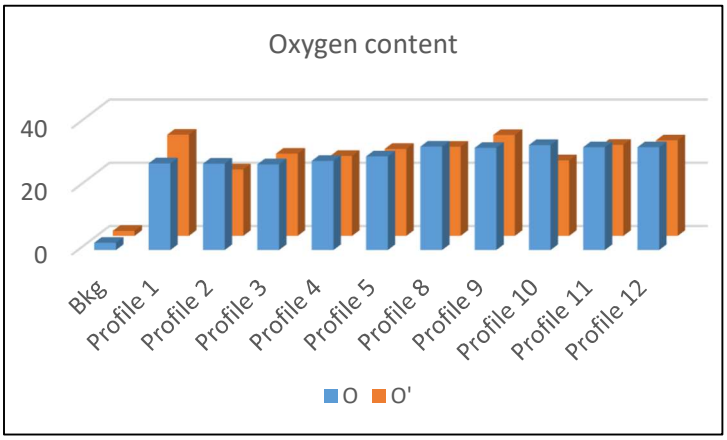

Fig 7.3.4.2. Comparison of the oxygen in the structures composition: 12 hours (O); 8 months (O')

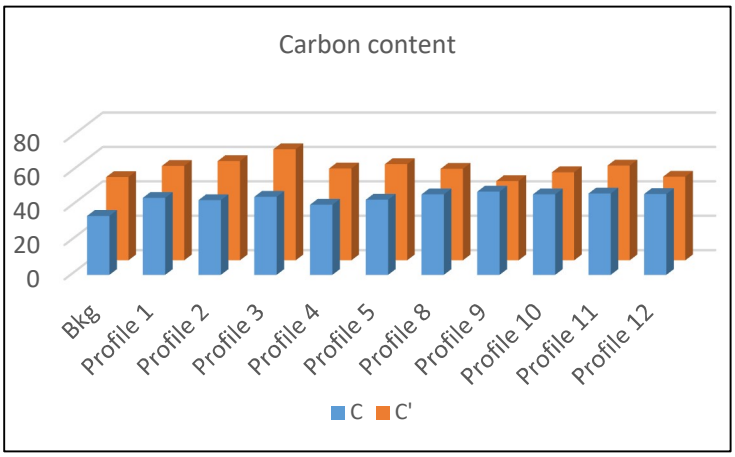

Fig 7.3.4.3. Comparison of the carbon in the structures composition: 12 hours (C); 8 months (C')

For the 8 months old deposits, the carbon content increases compared to the carbon content of 12 hours old deposits. Profile 3 shows the highest carbon content compared to Profile 2, Profile 1 and Profile 11.

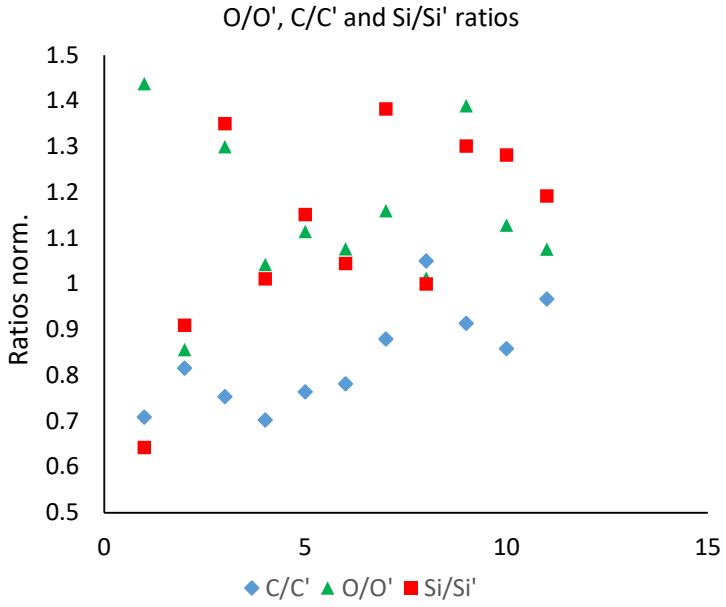

Fig 7.3.4.4. O, C and Si content with time ratios 12 hours () and 8 months (')

From these results we can conclude that the carbon content increases with time. The intake of carbon in the structures after the deposition would come only once the structures react with H_2O from air (moisture degrading the structures). The same process would be happening with the nitrogen, increasing its quantity and its concentration in the structures. The ratios of the three elements present in the deposits Si, C and O, are presented in Fig 7.3.4.5, Fig 7.3.4.6 and Fig 7.3.4.4. The ratios of O/O' and Si/Si' have values

higher than 1 (Fig 7.3.4.4). The ratio of C/C' is lower than 1, showing that the carbon content increased when keeping the structures in air, while the O and Si content decreased, suggesting that some kind of reaction formed in air with the release of oxygen and small amounts of Si.

7.4 Conclusions To Chapter 7

Monte Carlo simulations of the electron trajectories and BSEs / SEs have been performed using Casino simulations at 1 keV, 3 keV and 5 keV electron beam energy. The sample was declared as a 3D dihedral structure made of $Si(OEt)_4$ material, while the substrate is a flat polygon made of Au. For the 5 keV and 3 nm wide electron beam on the $Si(OEt)_4$ surface, the backscattered electron yields are of 0.008139 while the SEs yields have a value of 0.047829. A maximum of 26 nm of BSEs radius is obtained for the 5 keV beam, with a BSEs scattered angle with the maximum density of BSEs of 50 – 100 % between 40 deg and 90 deg. The electron energy of the BSEs / SEs has a value of 0.134 keV/nm^2 measured at less than 2 nm from the center of the beam. The value of the electron energy of the BSEs is lower for the 2 keV beam with a value of 0.08172 keV/nm^2. The BSEs yields are in the range of 0.009848, and the SEs reach values of 9.2 x 10-5, with an angle of ejection from the primary beam between 40 deg and 90 deg and a electron population density of 50 – 100 %. For 1 keV, the radius of backscattered electrons lowers to values of 1.2 nm, though the BSEs electron energy exhibits high values in the range of 0.121 keV/nm2. The BSEs yields and SEs yields are computed with values of 0.01219 (BSEs) and 0.08492 (SEs). The direction of projection of the BSEs/SEs follow the primary electrons direction with very low shifts.

Two types of nanostructures have been created as a result of FEBID deposition, a line like structure and a 'dot' or pillar with heights from 9 nm to 1.2 µm and widths from 30 nm to 700 nm. The FEBID deposits were created at different dwell times with different shapes with the intention of obtaining a wide range of structures. The structures were deposited using a Zeiss SEM with Gemini column. A full set of nanostructure measurements were performed using EDX and AFM analysis. Two sets of measurements were taken, one of 12 hours old nanostructures and the other one 8 months old nanostructures, deposited with the same beam characteristics and dwell times, and similar conditions of the precursor (temperature, pressure). Older structures (8 months old) were found to have undergone merging arising from the tilting and collapse of taller structures for the point profiles deposited with dwell times between 350 µs and 1000 µs, and loops between 300 and 1300. For a variable dwell time and similar number of loops different nanostructures height was observed, while for similar dwell time and higher number of loops an increase in the height of the pillar structures was observed from 163.8 nm to 445 nm. A first attempt to determine the elemental composition of the profiles was made hoping to find higher O content that

could be an indication of water, but the hypothesis was not viable. The second approach to find the cause of the collapse was looking into the height over the bottom width ratio; structures with higher width to height ratios, close to 0.5 (1/2 width/height) seem to behave properly after being left in air for a long time, while structures with lower width to height ratios suffered from collapse. The 12 hours old nanostructures present similar behavior to the 8 months old structures, but no collapse of the pillars is observed. A smaller height is achieved for higher dwell times and loops (Fig 7.3.3.2.3) indicating an electron beam limited regime. Point 6 from the point profiles (Fig 7.3.3.2.4) is the highest width/height structure with dwell time and number of loops. Constant dwell time and variable number of loops results in different heights of the nanostructures, while variable dwell time and constant loops creates similar height structures (point profiles 8 – 12).

When looking at the elemental composition of the structures, a decrease in the Si content and an increase in the C and O content was observed for the older structures, while for the newer structures smaller amounts of carbon were observed using EDX analysis. The presence of elements like N_2 is assigned to contamination from the air to the sample. The 8 months old line profiles (Fig 7.3.3.1.4) show a 48.5 at% - 64.6 % C, 1.4 % - 32 % O, 1 – 11.1 % Si and 0 % - 15.4 % Au elemental content. The 12 hours old dot profiles (Fig 7.3.3.2.5) present an elemental content of 34.3 at% - 50.3 at% C, 0.9 % - 13.7 % Si, 2.3 % - 33.2 % O and 5 % - 62.5 % Au (the starting values representing the background values). The 12 hours old line profiles (Fig 7.3.3.2.6) compared to the 8 months old profiles exhibit 34.3 % - 48.4 % C, 2.3 % - 33.2 % O, 9.4 % - 12.3 % Si and 7.9 % - 62.5 % Au. Nonetheless small nanostructures as low as 9nm with high Si composition content such as 50.3 % were fabricated. For the deposition of SiO_2, the deposition ratio is 1 : 2 (one Si atom to two O atoms), a content of Si close to 33 % is expected for a perfect deposition ratio. In the present deposition analysis, composition purity of 11.2 % in the FEBID line deposits for 8 months old structures and 12.3 % in the FEBID line deposits for 12 hours old structures have been obtained without any addition of H_2 or H_2O. The ratios of the atomic elements in the deposits for the 12 hours old structures to the 8 months old structures have values under 1 for C and between 0.6 – 1.4 for O and Si. A higher O ratio is expected to be from exposure to air, while the Si higher ratio we assign it to the degradation of the 100 nm Au layer on the substrate and upward moving of ‘stray’ Si atoms increasing the Si content of the structures.

CHAPTER 8. A COMPUTATIONAL APPROACH OF FEBID PRODUCTION OF IRON NANOSTRUCTURES USING $Fe(CO)_5$ AS THE GASEOUS PRECURSOR

$Fe(CO)_5$ has been widely used as a FEBID precursor to create iron nanostructures with the promise of producing novel magnetic arrays. The FEBID method using $Fe(CO)_5$ has been used to build deposits on different surfaces, SiO_2, Au(111) [225], Au(100), Al_2O_3, β - Si(111) doped substrate [310], Si(111), Pt(111), TiO_2 [247 - 248]. At electron beam irradiation of $Fe(CO)_5$ thin films [225] a desorption of 50 % of the CO ligands and partial loss of ligands to C atoms are obtained, while for Ar^+ bombardment 80 % desorption of CO radicals takes place. A purity of the Fe metal content of 85 at% is obtained from Auger electron spectroscopy measurements. Further XPS studies of the precursor deposited on Au substrates under UHV conditions have been done revealing almost no changes in the thin films, but probing the presence of the graphitic C, and partially decarbonylated species and oxides by inoculation in the Au surface, a process typical for the Au(111) surfaces and hcp/bcc structures of Au (further details on Au surface reconstruction are presented in section 8.3.2.4). The XPS study probes the presence and changes in the graphitic C and CO species on the surface with the result of an increase to 0.2 of the C/C0 graphitic species and decrease to 0.2 of the C/C0 ratio from CO species at 500 eV XPS irradiation. Other sources [15], [190] report Fe purities of 85 at% with an Fe / O ratio of 11.8 : 1 [190] and > 95 at% Fe purity [15].

Hydrated species of $Fe(CO)_5$ with cluster formation have been analysed in the work of Lengyel et al 2021 in Ref. [187] with resulting products containing OH^- and $(H_2O)_n$ at electron irradiation with electron energies between 0 eV and 20 eV (DEA studies). The highest cross-section anion found, formed through the hydrated $Fe(CO)_5$ clusters irradiation, was $Fe(CO)_4^- \cdot (H_2O)_n$, and with smaller contributions the presence of $Fe_2(CO)_9^- \cdot (H_2O)_n$ and $Fe_2(CO)_y \cdot (H_2O)_n$, n = 7, 6, 5 could be probed. Other fragments results of the dissociation at low electron energies, containing OH^- and $OH^- \cdot (H_2O)_n$ radicals with n = 1 - 2, are $Fe_x(CO)_y \cdot OH^-$ and $Fe_x(CO)_yOH^- \cdot (H_2O)_n$, x = 1 – 2, y = 5 – 9, where the $(H_2O)_n$ fragments are found to come from pure $(H_2O)_n$ pure clusters. Three resonances of the anions have been recorded, at 3 eV $Fe(CO)_4^- \cdot (H_2O)_n$ n = 4, 3, 2 was found, at 5.5 eV the presence of $Fe_x(CO)_y^- \cdot (H_2O)_n$ x = 2 - 3, y = 7 – 8, n = 1 - 4 is seen, while at 7.5 eV the anion population is mostly made of dimer and singlets species of $Fe_2(CO)_y \cdot OH^-$ y = 7 - 9 and $Fe(CO)_y \cdot OH^-$ y = 2 - 5 and their formation mostly characterized by a self-scavenging process [187]. Physical and chemical transformation of the iron pentacarbonyl ($Fe(CO)_5$) under pressure up to 20 GPa has been studied in the work of Young and Choong 2014 in Ref. [107]

isolating three solid polymorph and polymeric phases at 0.3 GPa, 1.5 GPa and 4.9 GPa, observing over 15.2 GPa a polymerization of the precursor. The $Fe(CO)_5$ precursor deposited in external heated diamond cells was studied at room temperature by in-situ micro-Raman spectroscopy. In phase I (0.3 GPa) a shift in the Raman curves is seen at 1990 cm^{-1} (0.247 eV) representing a change in the molecular symmetry of the molecule, while in phases II (1.5 GPa) and III (4.9 GPa) at 200 cm^{-1} (0.025 eV) a shortening of the bond lengths is observed. Another shift of the Raman curve is observed in phase III (4.9 GPa) at 2044 cm^{-1} (0.253 eV) resulting in a change in the polarizability of the $Fe(CO)_5$ molecule.

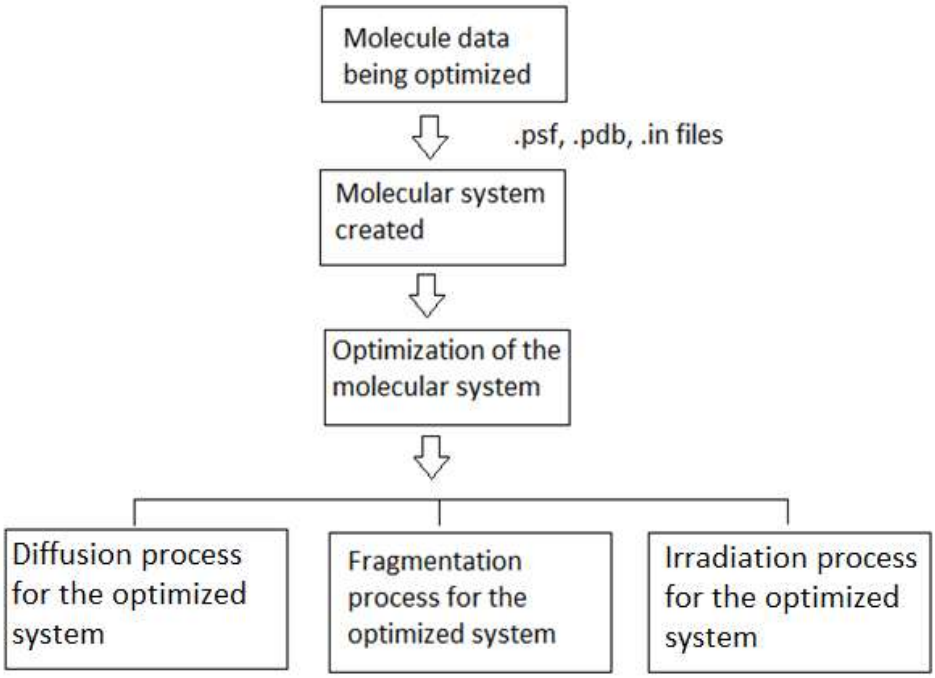

Fig 8.1. FEBID project steps for $Fe(CO)_5$ MBN Explorer irradiation task

The magnetic properties of the $Fe(CO)_5$ compound have been studied in [288], [308] and of $Fe_2(CO)_9$ precursor derived from clustering of $Fe(CO)_5$ in [312]. Poratti et al [288] in his 2011 study measures the anomalous Hall resistivity and longitudinal resistivity in deposited Fe magnetic nanowires at 400 pA and 15 keV obtaining a longitudinal resistivity of the nanostructures of 88 μΩcm at relatively low temperatures ranging from 4.2 K and 260 K. The Hall resistivity of the nanowires can be determined on the relation $\rho_{AN} = \rho_{xx}^{\ 2}$, where ρ_{xx} is the longitudinal resistivity in the nanowire. Fe vertical magnetic nanotips [308] have been obtained at deposition characteristics of the electron beam of 1.97 nA, 10 keV, and 0.5 mbar $Fe(CO)_5$ precursor pressure with growth rates of 48 nm/s and 84 at% Fe purity in the deposits, ranging from 48 at% at 0.97 nA current to 84 at% at 1.95 nA current. An Fe purity of the structures between 50 at% and 80 at% [189] was obtained with the variation of the electron beam energy

from 2 keV to 30 keV with the addition of H_2O to the irradiation step in the FEBID process. The presence of Fe_2O_3 and Fe_3O_4 iron oxides was proved and the saturation magnetization of the deposited nanowires was experimentally determined with values between 1129 ± 19 kAm^{-1} and 1371 ± 16 kAm^{-1} compared to the pure Fe bulk saturation magnetization value of 1700 kAm^{-1} and Fe oxide values between 300 kAm^{-1} and 600 kAm^{-1}. As seen from [288], [308], [312] and [189], the magnetic properties of the Fe nanostructures are highly sought in the nano – deposition industry relating entirely to their applicability to sensors, spectroscopy equipment, microchips and medical devices. The $Fe_2(CO)_9$ [312] widely used for magnetic applications in the field of magnetic nanowire modulation presents purities of the deposited Fe structures of 75 – 80 at% Fe. Deposited on β – Si dopped substrates [310] at 1 nA and 3 keV electron beam energy, the $Fe_2(CO)_9$ exhibits purities between 80 at% and 85 at% and high ferromagnetic signals. A comparison between the square deposited nanowires and bell-shaped deposited nanowires was done taking into account the value of the magnetization field H_c. The maximum value of the magnetization field was obtained for bell-shaped nanostructures and thicknesses in the range of ~15 nm. The existence of a 5 nm Fe – oxide layer with a Fe composition of 49.4 ± 2 at% and O composition of 50.6 ± 2 at% at the top of the nanostructures through its low magnetic behavior changes the magnetic behavior of the nanowire, especially in the areas where the nanowire is very thin creating an inhomogeneous magnetic field around the structure. The magnetization field has a high dependence on the nanostructure thickness over a critical t_c value, in the case of the study of Cordoba et al 2011 [189] this critical value is of 15 nm.

Other precursors used in FEBID, depositing bimetallic structures with high Fe content, (η^5 – Cp)$Fe(CO)_2Re(CO)_5$ on Au substrate [309] and $HFeCo_3(CO)_{12}$ on Au electrodes and Si wafer [311] show high C reduction in the electron irradiation process. The (η^5 – Cp)$Fe(CO)_2Re(CO)_5$ precursor [309] exhibits a desorption of all CO ligands at Ar^+ bombardment and 50 % desorption of CO ligands at e-irradiation for a 1 – 2 ML deposition layer of the precursor. At EDX, AFM, HRTEM and SAED (selected area electron diffraction) for an electron energy of 500 eV and Ar^+ of 860 eV, corresponding to e^- exposure of 6 mC/cm^2 and Ar^+ exposure of 0.048 mC/cm^2 the Fe yields fall in the range of ~ 708 eV and the Re yields fall in the range of 42.2 eV. The two reaction pathways result in a number of CO loss for e^- $CpFe(CO)_2Re(CO)_5 + e^- \rightarrow C_5FeRe(CO)_7 + (n\text{-}7)\ CO + 5/2\ H_2$, and for Ar^+ the dissociation process follows the path $CpFe(CO)_2Re(CO)_5 + Ar^+ \rightarrow C_5FeRe + 7\ CO + 5/2\ H_2$, in the last case the process being characterized by a dehydrogenation of the phenyl ring and sputtering of the atoms deposited on the surface. BDEs of the Cp – Fe 4 eV and 2.2 eV, C – C and C – H 5 eV have been obtained. Compared to (η^5 – Cp)$Fe(CO)_2Re(CO)_5$, the $HFeCo_3(CO)_{12}$ [311] is deposited on 100 nm thick Au electrodes and 200 nm thick Si wafer at 15 keV, 1.5 nA and a precursor flux of 2.6 x 1018 $s^{-1}cm^2$ and 65 °C, with an extra step of annealing at 100 °C, 200 °C and 300 °C. A Co to Fe ratio of 3 : 1 is obtained and no presence of

graphitic C in the annealing step, a decomposition of CoO into fcc Co at 300 °C taking place. The composition changes from Co : Fe : C : O 41 : 13 : 26 : 20 at% to Co : Fe : C : O 52 : 17 : 22 : 9 at% upon annealing, with resistivities of the obtained nanostructures in the range of 4200 μΩcm to 65 μΩcm upon annealing.

In this chapter a simulation of the FEBID of $Fe(CO)_5$ for magnetic nanostructures is discussed. This work was performed without the comparative experimental work due to closures and travel restrictions arising from the COVID-19 pandemic. However, simulation results were compared with earlier experimental data by Allan et al 2018 [75] and Gavagnin et al 2014 [186]. The simulations of Fe structures formed by FEBID on the SiO_2 / Au(ccp) substrate are presented as the focus of Chapter 8. The optimization and fragmentation process in the $Fe(CO)_5$ precursor using MBN Explorer software follows the steps shown in Fig 8.3.1.4.1. The simulations were run using the MBN Studio and MBN Explorer version 3 (discussed in detail in Chapter 5). A six step process is involved in the computation of the $Fe(CO)_5$ dynamics of the system on the Au(111) and Si(100) surfaces, involving the deposition of the precursor on the substrate, accommodation of the molecules on the substrate and irradiation of the molecules using the DEA and total cross-section values of the precursor. The single molecule structure is imported from DFT optimization calculations, based on pre-existent literature data and ***NIST Database***.

8.1 Computational Details

In the computation of the FEBID process we used MBN Studio and MBN Explorer provided under license by the MBN Research Center Gmbh, Germany.

8.2 Previous Work

The FEBID studies using MBN Explorer focus mostly on a small number of precursors, $W(CO)_6$, $Pt(PF_3)_4$ and Na nanoparticles deposited on MgO substrate, in part due to its novelty and to the extent of the complexity of the dynamical calculations at the surface that still require high computational power and up to a few hundred hours CPU time. Other codes based on Monte Carlo simulations are mostly in-house built and focus only on particular problems ignoring the FEBID process as a whole from the precursor to the electron beam characteristics and surface properties. Sushko et al [87] present the

simulation of the FEBID process of the $W(CO)_6$ computed with a precursor gas pressure of 0.33 Pa, a molecular flux of 2.7 x 10^3 l/nm^{2}s, 5 nm beam radius, 30 keV beam electron energy, 79 pA current, and a dwell time of 10 ms. The SiO_2 surface is modeled as a 3D square polygon with certain dimension and a specific density of the atoms representing the surface. Each of the Si atoms is bonded to two O forming a lattice modelled through Lennard – Jones potential and characterized by an interaction energy of 0.8 eV. A H layer is deposited at the surface of the SiO_2 and accustomed there by thermalization forming an hydrogenated layer atop the SiO_2 surface. The simulations of the $W(CO)_6$ precursor on SiO_2 surface [87] are run at room temperature. A diffusion coefficient of the $W(CO)_6$ atoms accustomed to the SiO_2 surface of 6.77 μm^2/s was obtained in the diffusion with the substrate step of the simulation. After 7 irradiation runs a number of 600 W atoms, 600 CO radicals and more than 200 free C (data collected in Table 8.2.1) are recorded as results of the fragmentation at 30 keV beam electron energy. The maximal island size containing most of the atoms, W, C and O is of 2000 atoms. Two models have been intended, in the first model the searching algorithm is between atoms beyond the molecular structure, while the second model searches over all the valence atoms. For the first model a maximal island size of 10500 atoms was obtained after 20 irradiation cycles, and a W purity of 25 at%, while in the second model the maximal island size recorded was of 2800 atoms after 20 irradiation cycles and W purity of 68 at%.

Based on the same principle, the simulations follow similar steps [87], [161], [315] in modelling the FEBID process (see Fig 8.3.1.4.1). At first an optimization of a single molecule obtained from literature, databases and DFT calculation is done on the chosen substrate, followed by and accommodation and thermalization of the molecule on the substrate. Using the results of the first step, a second optimization is done for an extended number of molecules created using the single molecule optimization. Lennard – Jones potentials and Coulomb interaction forces are used to define the physics between the molecules, atoms, and, molecules and atoms and the substrate. The thermalization and accommodation of the system is a third step of the simulation process with extensive CPU time used and high memory demands. Once accommodated on the substrate, the molecules are irradiated to the specified parameters obtained experimentally or intended to be experimental; the last two steps of the simulation comprising the accommodation and thermalization and irradiation with deposition of a new molecular layer are repeated a number of times, called irradiation cycles. A later article investigates the fragmentation of the $W(CO)_6$ precursor at different electron beam energies [161] looking into the ratios of dissociation between 0.5 – 30 keV of a deposited 1 – 2 ML of $W(CO)_6$ precursor on SiO_2 substrate. The obtained diffusion coefficient is in the range of 7.71 μm^2/s. The electron trajectories have been simulated using Monte Carlo simulations implemented in the SEED code [87]. The maximal island size obtained was of 4 x 10^4 atoms with 3 x 10^3 CO radicals and a W purity of 34 at% and 6 cycles of irradiation for an electron beam energy

of 30 keV indicating the highest fragmentation ratio from the 0.5 – 30 keV range. Comparatively the $Pt(PF_3)_4$ precursor [315] has lower vaporization pressure and lower fragmentation ratios with the maximal island size of 2500 atoms after 5 – 6 cycles. The $Pt(PF_3)_4$ precursor was deposited on SiO_2 substrate and irradiated with a beam of 2.8 nA and 1 – 2 keV. The electron beam energy is defined by declaring the bond breaking energy necessary to fragment a Pt – PF_3 bond to have a value of 300 kcal/mol.

Source	Precursor	Substrate	Island Size	Metal content (at%)	C Content (atoms no)	Cycles
Ref. [87]	$W(CO)_6$	SiO_2	2000	68 / 25	600	7
Ref. [161]	$W(CO)_6$	SiO_2	40000	34	75 from CO	6
Ref. [313]	Na nanoparticles	MgO	1067	1067 atoms	N/A	6
Ref. [315]	$Pt(PF_3)_4$	SiO_2	2500	361 atoms	N/A	5 - 6
Ref. [314]	$Fe(CO)_5$ thin films	SiO_2	1 – 2ML	90 - 93	1 – 6 %	Ab-initio

Table 8.2.1 Dynamic simulations of different precursors using MBNExplorer

MBN Explorer simulation package has been used to simulate nanoparticles behavior to aid in the nanoparticle design for medical applications. The study of Fortouna et al [313] investigates nanoparticles in the range of 4 nm with a number of 1067 atoms using Leapfrog algorithm to model and optimize the system deposited on MgO substrates for a deposition energy of 0.0068 eV/atom. A initial step of MgO substrate optimization using velocity quenching algorithm was carried with a time step of 0.1 fs. The resulting nanoparticle was found to undergo multiple phase transitions from liquid droplet, 2.5 ps to 40 ps and maximum temperature, and to recrystallize by reaching a temperature of 400 ps. Different simulations investigate the behavior of $Fe(CO)_5$ at CVD [314], at a temperature range between 130 °C and 250 °C, and a deposition pressure between 10 – 40 Torr. The main phenomena characterizing the events at the surface of the SiO_2 are the desorption of the radicals with 4.8 x 10^7 events, migration with 0.14 x 10^7 events and desorption with 0.14 x 10^7 events at a temperature of 250 °C. A decrease in the deposition rate with the increase in the temperature is observed between 160 °C with a Fe purity of 90 %, O 4 % and C 6 %, 200 °C Fe purity of 93 %, O 5.5 % and C 1.5 %, and 240 °C Fe 90 – 91 %, O 9 %, C 1 – 2 %. A deposition rate of 60 nm/min at 200 °C is obtained and a surface roughness between 0.67 μm at 150 °C decreasing to 0.48 μm at 200 °C and down to 0.16 μm between 230 – 250 °C. The multiscale model is in very good agreement with the experimental values [314], exhibiting a roughness value of 0.76 μm at 170 °C, 0.67 μm at 180 °C, 0.38 μm at 210 °C, and 0.16 μm at 250 °C.

8.3 Results and Discussion

8.3.1 Structure Optimization, Deposition, Irradiation and Fragmentation of $Fe(CO)_5$ on SiO_2

8.3.1.1 Optimization of the $Fe(CO)_5$ Molecular System

The optimization of the molecular system of $Fe(CO)_5$ molecule was made using the MBN step of structural optimization, and accommodation of the molecule on the substrate using specific characteristics: bond lengths, charges, atomic masses, and further, films and layers of molecular material with defined thicknesses. The SiO_2 substrate was modelled with a 5 nm thickness and one layer atom distribution with bonds at 94° angles, by defining a containing structure as a predefined box characterized by reflective boundary conditions with 200 x 200 x 480 (Å) dimensions. The substrate dimensions contained in the structure are 200 x 200 x 5 (Å) (x, y, z data). The rules governing the molecule-molecule interactions on the substrate and the $Fe(CO)_5$ molecular system are defined by the molecular forces acting on the substrate and the type of interaction potential these induce in the system: van der Waals interactions for molecule – substrate interactions, and a Sutton-Chen potential for the Fe – Fe interactions. The optimization process proceeds through multiple steps with different parameters: optimization of one molecule system, optimization of the many molecules system, optimization of the system after deposition, optimization with diffusion on the substrate of either the deposited layer or pre-deposited layer. In our simulations, the optimization method used is velocity quenching based on velocity Verlet algorithm for rigid body interactions approximations conjugated with linked cell interaction mode of 20000 / 0.1 fs steps spanned over 100 log steps simulation. The Verlet integrator (Verlet, 1967) preserves the physical properties of the system, such as phase-space and time-reversibility, and its novelty lies in the use of a Taylor expansion of the position of two coordinates in two different directions of time [175]:

$$x(t + \Delta t) = x(t) + v(t)\Delta t + f(t)/2m\ \Delta t^2 + \delta^3 x/3!\delta t^3\ \Delta t^3 + O(\Delta t^4) \quad (8.3.1.1.1)$$

$$x(t - \Delta t) = x(t) - v(t)\Delta t + f(t)/2m\ \Delta t^2 - \delta^3 x/3!\delta t^3\ \Delta t^3 + O(\Delta t^4) \quad (8.3.1.1.2)$$

The velocity Verlet algorithm developed after the Verlet integrator in 1982 in Ref. [175], uses the same approach for the molecular system, but incorporates the velocity in solving the system (relations (8.3.1.1.3) and (8.3.1.1.4)):

$$x(t + \Delta t) = x(t) + v(t)\Delta t + 1/2a(t)\ \Delta t^2 \quad (8.3.1.1.3)$$

$$v(t + \Delta t) = x(t) + [a(t) + a(t + \Delta t)]/2\ \Delta t \quad (8.3.1.1.4)$$

The output of the optimization of the $Fe(CO)_5$ molecule + SiO_2 surface compared to the output of the optimization of the $Fe(CO)_5$ molecules + SiO_2 surface comes in the high difference in the released energy of the system found almost four orders of magnitudes higher for a transition from one molecule to 812 molecules (8932 atoms). The kinetic energy ($\sum E_k$), total energy ($\sum E$) and potential energy ($\sum E_p$) of the system are presented in Table 8.3.1.1.1.

	Single molecule	Multiple molecules
$\sum E_k$	2.1292967E-08	7.6009748E-02
$\sum E_p$	-5.3209590E+01	1.1881794E+05
$\sum E$	-5.3209590E+01	1.1881838E+05

Table 8.3.1.1.1. Energy output (Hartree) of (a) $Fe(CO)_5$ molecule on SiO_2 and (b) multiple $Fe(CO)_5$ molecules on SiO_2

The SiO_2 substrate was declared frozen (fixed atoms), with only van der Waals interactions taking place, where no spontaneous reaction between the Fe and Si with the formation of FeSi or recombination with the substrate in the presence of increasing temperature (300 K with 1 K step) is possible.

8.3.1.2 Diffusion of $Fe(CO)_5$ on the SiO_2 Substrate

The diffusion mechanisms on a substrate are governed by multiple processes: standard site – to - site hopping, isotropic/anisotropic diffusion, migration through an exchange mechanism, migration of atomic clusters to diffusion with long hop lengths, characterized by different diffusion models, based on variation of temperature, time and energy of the system (through variation in the structure). The Wolf and Villain 1990 [179] model of diffusion is similar to the model of Edwards-Wilkinson. The model is based upon defining a quadratic lattice of height h, where sites of $h \leq 0$ are occupied, are part of the substrate, and the initiated growth is in a strip of infinite length and finite width ($1 \leq x \leq L$). In the Edwards - Wilkinson model the particle tends to settle at the lowest surface site from that particular surface area, while in the Wolf-Villain model the particles move to the lowest unoccupied site. For surface growth when defining only the diffusion coefficients and concept, the Kardar – Parisi – Zhang (KPZ) kinetic roughening equations [185] are used, and the gravitational forces neglected in the deposition of the thin films:

$$\delta h/\delta t = \lambda_0 + \lambda_1 (\nabla h)^2 + \nu^2 \nabla + \eta \qquad (8.3.1.2.1)$$

where h(x, t) is the height of the surface at time t above the substrate, ν roughness, λ is the average growth velocity and η is the white noise due to fluctuations in growth rate.

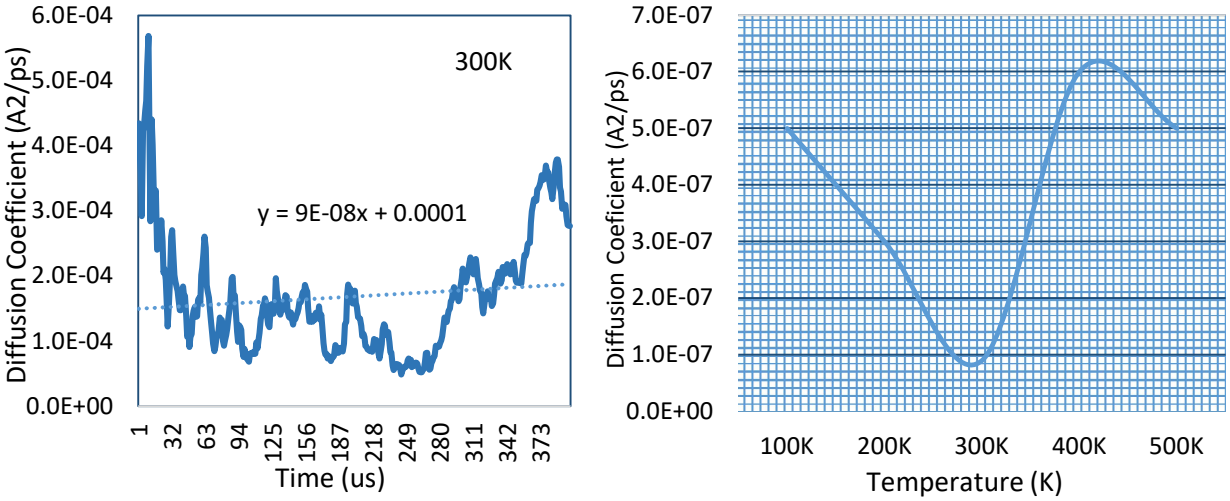

Fig 8.3.1.2.2. Diffusion coefficient for one $Fe(CO)_5$ on SiO_2: (left) 300 K (right) diffusion coefficient with temperature range 100 K – 500 K

The diffusivity obeys Arrhenius law and through the physics governing it, can be divided in intrinsic diffusion and mass transfer self diffusion, where the tunnelling effects are negligible, and the characteristic process depends on the temperature [180]:

$$D = D_0 \, e^{-E_{diff} / kt} \tag{8.3.1.2.2}$$

where D_0 is the pre-exponential factor, E_{diff} is the activation energy, k is the Boltzmann's constant, and the mass transfer relates to the intrinsic diffusivity by:

$$D_M = (N/N_s) \, D_I \tag{8.3.1.2.3}$$

The corrugation ratio is defined by:

$$\Omega = E_{diff} / E_{des} \tag{8.3.1.2.4}$$

Comparing the SiO_2 substrate with the MgO substrate, Si(100) and Au(110), a value of 550 kcal/mol is needed for creating a vacancy (lack of one or multiple Au atoms), while the diffusion energy for Au(110) is 17 kcal/mol (activation energy for $E_{diff,I}$ of 10 kcal/mol and activation energy for high-temperature mass transfer diffusion of 40 kcal/mol), and the diffusion energy for Si(100) of 30 kcal/mol (with an activation energy of 20 kcal/mol, and experimental activation energy of 53 kcal/mol). The dependence of the diffusion coefficient of $Fe(CO)_5$ molecules on the coverage as a function of time are presented in

Fig 8.3.1.2.2 and Fig 8.3.1.2.3. Low recombination and fragmentation of less than 1 % is observed in the diffusion and accommodation process of the molecules on the SiO_2 substrate, limited to the escape of a small number of O ions from the $Fe(CO)_5$.

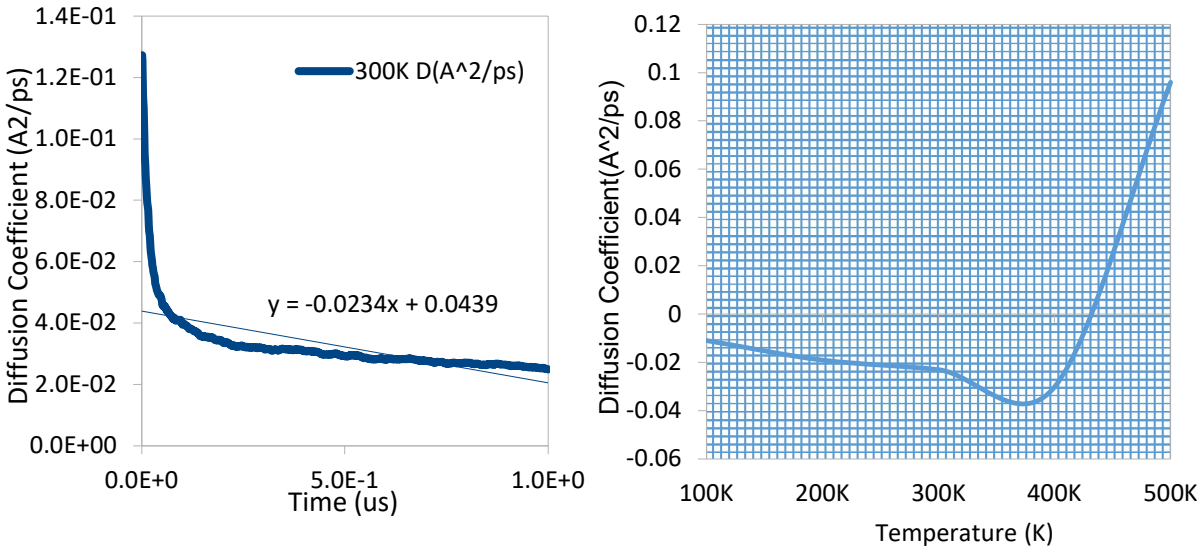

Fig 8.3.1.2.3. Diffusion coefficient for multiple $Fe(CO)_5$ molecules on SiO_2: (left) 300 K (right) temperature range 100 K – 500 K

	Single molecule	Molecular system of multiple molecules
$\sum E_k$	4.4594144E-01	3.4811920E+02
$\sum E_p$	1.1881794E+05	-4.0196340E+04
$\sum E$	1.1881838E+05	-3.9848221E+04

Table 8.3.1.2.1. Energy output (Hartree) of (a) $Fe(CO)_5$ molecule on SiO_2 and (b) multiple $Fe(CO)_5$ molecules on SiO_2

	Unhydrogenated Substrate	Hydrogenated Substrate
$\sum E_k$	3.4811920E+02	3.46453428E+02
$\sum E_p$	-4.0196340E+04	-4.03667071E+04
$\sum E$	-3.9848221E+04	-4.00202537E+04

Table 8.3.1.2.2. Energy output (Hartree) of (a) $Fe(CO)_5$ molecules on SiO_2 and (b) $Fe(CO)_5$ molecules on hydrogenated SiO_2

When the SiO_2 substrate has a layer of H atoms on top of the oxide layer, a higher conglomeration of molecules is observed with the formation of $Fe(CO)_5$ clusters without reorganization through

fragmentation and a lower kinetic energy of the system, though the whole final value of energy in the system does not decrease more than 0.54 eV. A comparison of the diffusion coefficient for the two processes shows a change in the system with hydrogenated substrate of 0.02 $Å^2$/ps. The hydrogenation of the silica substrate has the effect of creating a top layer of H on the last layer of SiO_2 that does not diffuse with the substrate but slows down the oxidation process of the substrate. The oxidation process of the substrate is the integration of multiple O ions in the structure, creating multiple "voids" in Ref. [181] and Si sites for oxidation. The oxidation process of the SiO_2 substrate may be defined by the equations (8.3.1.2.5) and (8.3.1.2.6):

$$A = A_0 + e^{-\Delta E/kt} \tag{8.3.1.2.5}$$

where ΔE is the activation energy, A_0 is the temperature constant.

$$T_{Ox} = At + L_0 \tag{8.3.1.2.6}$$

where T_{Ox} is the oxidation thickness, L_0 is the initial oxidation thickness.

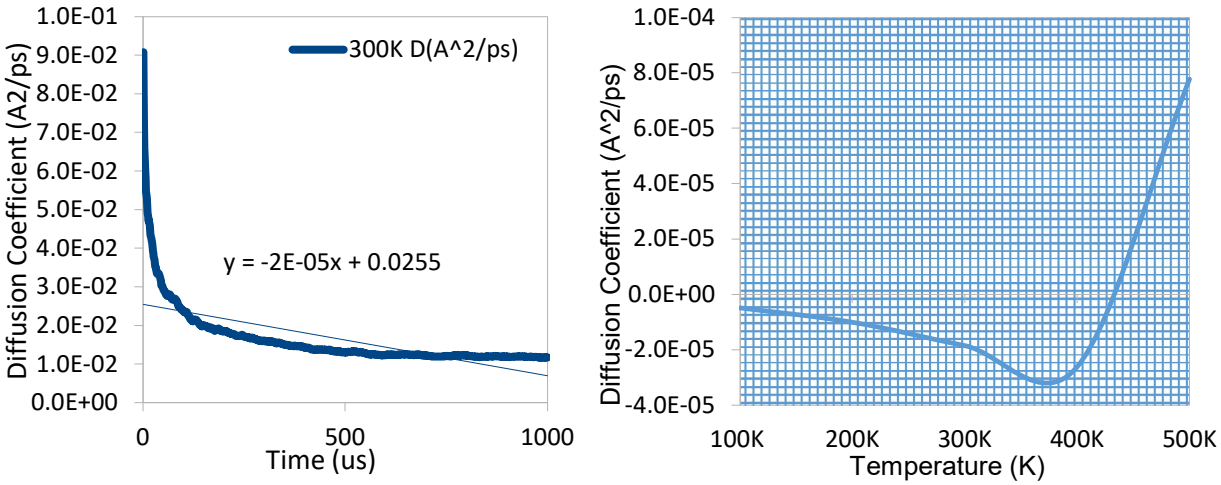

Fig 8.3.1.2.4. Diffusion coefficient for multiple $Fe(CO)_5$ molecules on hydrogenated SiO_2: (left) 300 K (right) temperature range 100 K – 500 K

Further analysis of the $Fe(CO)_5$ shows that in the event of void creation the oxidation process will be increased by the presence of Fe that recombines forming Fe_2O_3. For the purpose of our simulations, the substrate is considered frozen such that no recombination reaction occurs between the substrate and the molecular system. The forces acting on the substrate are the gravitational field forces and the van der Waals forces. The only recombination that takes place in the system is the recombination of $Fe(CO)_5$ molecules with neighboring $Fe(CO)_5$ molecules. In the diffusion process of multiple $Fe(CO)_5$ molecules

on the SiO_2 substrate, a reorganization of the molecules is observed with the formation of small clusters, but without structure modification or fragmentation, all bonds remaining intact.

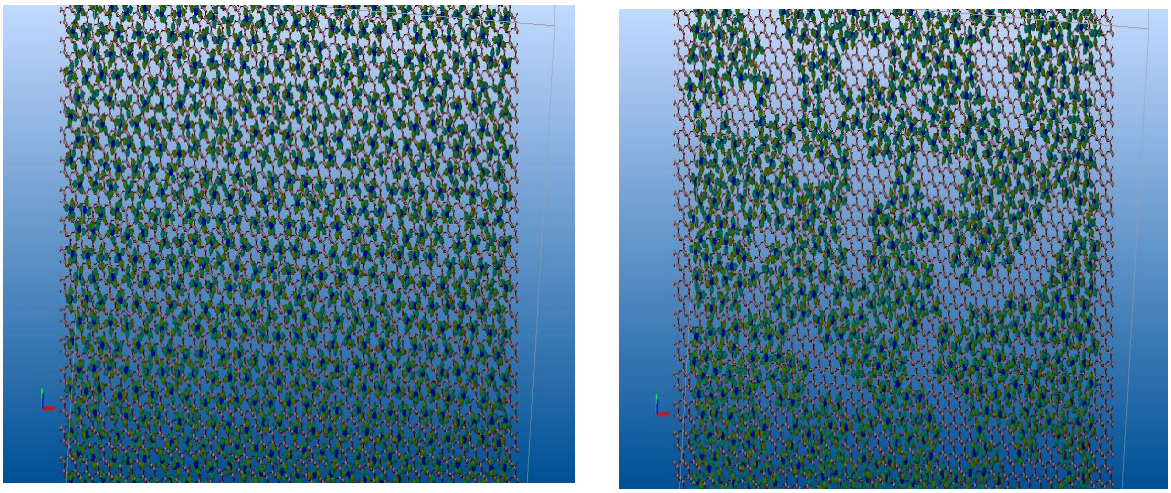

Fig 8.3.1.2.5. Schematics organization during diffusion of $Fe(CO)_5$ molecules on hydrogenated SiO_2 substrate: (left) initial organization of monolayer on SiO_2 (right) final organization of the monolayer on SiO_2

8.3.1.3 Relaxation Analysis with Time and Temperature

The relaxation process of a thin molecular film of $Fe(CO)_5$ is defined as a diffusion process followed by a desorption process, or the reverse in temperature of a diffusion process. In order to simulate this, the first diffusion task performed was diffusion of $Fe(CO)_5$ molecular system up to a temperature of 300 K using a Verlet integrator, linked cell method and pair nonperiodic interactions at 100 steps with 0.001-time step. The molecular dynamics task of relaxation uses an anti rotator to run the temperature from 300 K to 0 K in 1 K steps, and updates the molecular structure according to the reorganization of the molecular system on the substrate. During the relaxation process, the mass conservation equation is:

$$j = -\nu \nabla h \qquad (8.3.1.3.1)$$

where the current at the surface is induced by a chemical potential, the mass conservation equation takes the form:

$$j = k\, \nabla(\nabla^2 h) \qquad (8.3.1.3.2)$$

and may be represented by different chemical relation, dependent on Boltzmann's constant and temperature in Ref. [180]:

$$j = -D_c\, C/kT\, \nabla\mu \qquad (8.3.1.3.3)$$

where D_c is diffusivity, and if no particle interactions occur the relation (8.3.1.3.4) takes place:

$$\mu = \mu_0 + kTlnC \qquad (8.3.1.3.4)$$

For semiconductors, the corrugation factor is $\Omega = 0.6/M$, and $E_{diff,\,I} < E_{diff,\,M}$, while in the case of self diffusion, the desorption activation energy E_{des} is obtained equal to the heat of sublimation. The kinetic energy of the relaxed system is presented in Table 8.3.1.3.1.

	Relaxation of $Fe(CO)_5$ molecules	Diffused system from initial task
$\sum E_k$	3.44778701E+02	3.46453428E+02
$\sum E_p$	-3.74626407E+04	-4.03667071E+04
$\sum E$	-3.71178620E+04	-4.00202537E+04

Table 8.3.1.3.1. Kinetic energy (Hartree) of the $Fe(CO)_5$ molecular system on SiO_2

On the unhydrogenated SiO_2 substrate we observe a higher disorganization of the $Fe(CO)_5$ molecular layer and a reorganization with the change in temperature, from 300 K to 100 K, as well as the increase of atoms in particular areas of the substrate forming multiple layer islands conglomerating on the substrate. Fragments of CO are moving towards different islands before they are pumped away, though the extent of the phenomenon is very low with an occurrence of 0.0004 %, probability of occurrence obtained from the resulting fragments in the diffusion step.

8.3.1.4 IDMD Calculations in FEBID Studies of $Fe(CO)_5$ on SiO_2

The irradiation driven molecular dynamics (IDMD) approach is based on a number of steps defined by molecular dynamics rules (potentials, interaction forces, algorithms) to which a set of irradiation parameters is applied. A schematic of the process is presented in Fig 8.3.1.4.1. The irradiation driven molecular dynamics task and simulation makes use of cross-sections data, molecular dynamics using the MBN Explorer simulation environment, a combination of molecular structure files to an optimized number of atoms on a predefined optimized substrate, in our case SiO_2 and Au(111), and a set of interaction potentials and bonding/nonbonding characteristics of the $Fe(CO)_5$ molecule. The electron scattering and dissociation cross-sections data used was simulated using Quantemol-N software, combining the DEA cross-sections up to 10 eV with the dissociative ionization cross-sections between 10 eV and 1000 eV.

The Sutton Chen parameters used from Ref. [183] for the interaction potential in the simulations are presented in Table 8.3.1.4.1:

Parameters	ε(eV)	c	a(Å)	m	n
Sutton - Chen	0.0220225	28.8474	3.48501	8.14475	8.7932

Table 8.3.1.4.1 Sutton – Chen parameters used in the calculation

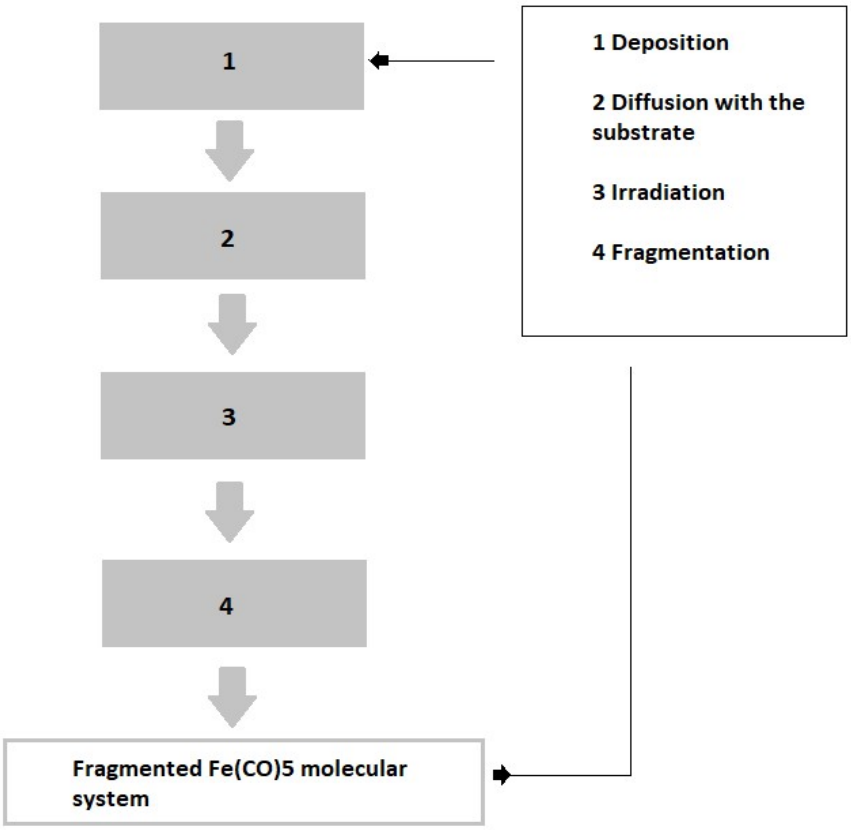

Fig 8.3.1.4.1. Deposition/irradiation steps of multiple $Fe(CO)_5$ molecular system

The islands (their characteristics are important to the growth of the deposits) are defined by the diffusion coefficient of the substrate, the duration of the diffusion on the substrate and the temperature. For the diffusion to take place three conditions need to be met: during the diffusion process the molecules need to diffuse with the substrate by attaching or either forming dimers, to detach, and to edge diffuse the weakly bonded molecules with the substrate (relation (8.3.1.4.1)).

$$\ell_2 \sim (D_s / F)^{ic/2(ic+4)} \qquad (8.3.1.4.1)$$

where i_c is the critical nucleation, F is the deposition flux, D_s is surface diffusion constant, and D_e is the detachment rate. The deposited molecules diffuse on a linear trajectory ℓ_2 during a period of time τ_2 [184]:

$$\tau_2 = \ell_2^2 / D_s \qquad (8.3.1.4.2)$$

and are characterized by a deposition density defined by the relation (8.3.1.4.3):

$$n_1 = F\ \tau_2 \tag{8.3.1.4.3}$$

where the molecules have a probability of encounter of: $n_1 \ell_2^2$.

If the SiO_2 layer has defects, as in a real-life process, the deposited Fe interacts with the Si substrate and forms silicide. Deformation and defect creation in the substrate are the effects of the annealing process, while in the deposition process, between 20 °C and 650 °C, the substrate does not deform in Ref. [75]. For the particular case of the iron (in solution), the diffusion coefficient is defined by relation (8.3.1.4.4):

$$D = 2.2 \times 10^{-2}\ e^{-3.05/kT} \tag{8.3.1.4.4}$$

with a value of $\lambda \sim 8.3 \times 10^{-19}$ nm for 10 min deposition at room temperature and $\lambda \sim 3.5 \times 10^{-3}$ nm for annealing at 470 °C over 30 min time range, and deposition at 470°C with a characteristic $\lambda \sim 2.0 \times 10^{-3}$ nm. The activation energy for the diffusion of the substrate has a value reported in Ref. [75] of 0.80 eV at 470 °C and 0.28 eV at 650 °C. Lengyel et al 2017 [82] presents a set of measurements on different mass spectrometers with cluster detection analysis confirming the presence of recombination of the $Fe(CO)_5$ and $Fe(CO)_4^-$ anions to form higher mass molecules. The yields for the different clusters and their electron energy of formation are presented in Fig 8.3.1.4.2. The clustering of $Fe(CO)_5$ on the surface, and its dissociation due to DEA and thermal electron-electron attachment measured in Ref. [186] through afterglow technique with a value of $8 \times 10^{-8}\ cm^3 s^{-1}$, has three causes: caging due to environment, long-range interactions and the formation of a polarized anion. The clusters investigated in Ref. [186] (Fig 8.3.1.4.2) are small pure $Fe(CO)_5$ clusters. The intensity or yield is the number of Fe atoms in the anion, with values of 12.6 % for two Fe atoms, 18.9 % for three Fe atoms, and the maximum contribution characterized coming from $Fe_2(CO)_9^-$ and $Fe_3(CO)_{14}^-$ at low energies, and $Fe_3(CO)_7^-$ and $Fe_4(CO)_{12}^-$ at high energies. In the range of 5 – 20 eV, the dissociation of metal – ligand – organic species are produced by a self-scavenging mechanism (the electron excites the molecule that releases one electron, that further causes DEA in another molecule) [75, 82, 228]. The $Fe(CO)_5$ clusters at low energies of 0.65 eV are forming $[Fe(CO)_5]_m Fe(CO)_4^-$, where m = 1÷4. Clustering and formation of islands of $Fe(CO)_5$ molecules is characterized by a reaction of the form presented in relation (8.3.1.4.5):

$$Fe(CO)^-_n + e^- + Fe_x(CO)_y \rightarrow Fe_z(CO)_{(n+y-m)} + mCO^* \tag{8.3.1.4.5}$$

where n = 0 ÷ 4, m < n+y, z = x+1, with high content of $Fe(CO)_5$ agglomeration in the form of $Fe_2(CO)_9$.

The further fragmentation of $Fe_2(CO)_9$, as a second process in the deposition of Fe on SiO_2 from $Fe(CO)_5$, has the result of higher Fe purity deposits reaching values close to 80 %, but still containing high amounts of O and C. These simulated results may be compared with previous experiments. FEBID deposits analyzed by Porrati et al 2016 [2166] (Table 8.3.1.4.1) have been produced on a Si substrate coated with a 100 nm layer of SiO_2 at a pressure of 2 x 10^{-6} mbar with a temperature of 27 °C, a beam energy 2 – 30 keV, and a beam current of 0.7 – 22 nA at a dwell time of 1 µs. The characterized structures have the dimensions of (width x height x length) 500 nm x 200 nm x 12 µm, with the beam current density defined in Table 8.3.1.4.2.

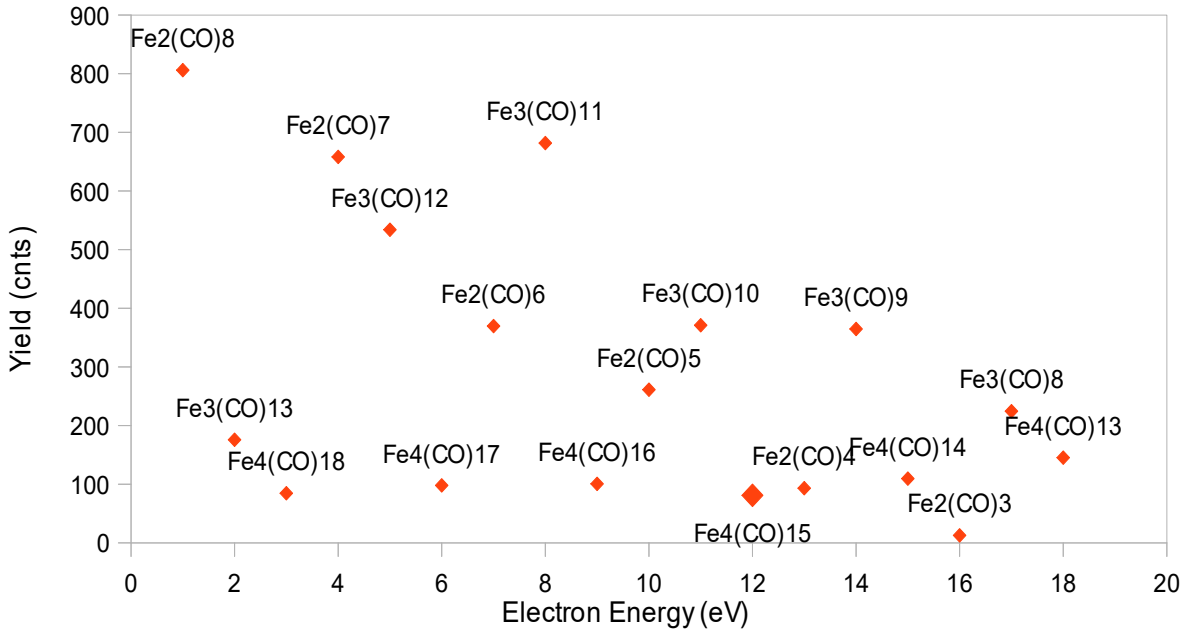

Fig 8.3.1.4.2. Cluster data for $Fe(CO)_5$ taken from Ref. [186]

Beam Energy (keV)	Beam current (nA)	Fe (at. %)	C (at. %)	O (at. %)
2	6.7	72.1	15.8	12.1
2	21.6	78.4	13.4	8.2
5	9.9	73.6	13.7	8.3
5	15.5	75.2	16.5	7.8
5	22.1	76.3	15.9	17.9
15	17.6	74.5	13.1	12.4
15	22.3	76.2	12.3	11.5
30	17	70.1	16.5	13.4
30	22	71.5	15.7	12.8

Table 8.3.1.4.1. Beam characteristics for $Fe(CO)_5$ irradiation on SiO_2 for deposits with Fe content higher than 70 at % from Ref. [188]

Current density (pA nm^{-2})	Voltage (kV)
0.49	2
1.29	5
3.91	15
7.95	30

Table 8.3.1.4.2. Current density for $Fe(CO)_5$ deposition on SiO_2 from Ref. [188]

The deposition rate is similar to other common precursors (carbonyls, acetylacetonates) with a constant yield of 3.2 x 10^{-4} $\mu m^3 nC^{-1}$. The use of H_2O is intended to increase the FeO content to the detriment of C content in the deposited structures obtaining an Fe content between 50 at. % and 80 at. %. If the Fe/O ratio (while keeping the C content to a constant value of ~16 ± 3 at. %,) is lower than 50 at. %, homogenous structures are formed containing both Fe_2O_3 and Fe_3O_4 (Fig 8.3.1.4.3 and Fig 8.3.1.4.4). For the analyzed structures in Ref. [188], a resistivity of 1000 μΩcm is measured (<55 at. % Fe content) and 100 μΩcm (>70 at.% Fe content). The results may be compared to other metal containing precursors, for example Co deposits, where the Co content varies with the C content, while the O ratio is kept constant. The resulting density and islands size from MBN simulations are presented in Table 8.3.1.4.3.

Density on Au	0.0017	0.0022
$Fe(CO)_5$ island size	17	34
Number of atoms in the island / cycle	17	34

Table 8.3.1.4.3. Density of $Fe(CO)_5$ molecules (%) and $Fe(CO)_5$ islands size on Au (number of atoms)

Characteristic varied	AV [kV]	BC [nA]	PoP [nm]	DT [μs]	Total Dose [nC]	Exposure Time [ms]
AV	1 - 20	0.86 - 2.28	1.1	204.8	0.80 – 2.12	931
BC	3	0.05 – 4.36	1.1	204.8	0.05 – 4.06	931
PoP	3	1.01	1.1 – 11.4	204.8	0.94 – 0.09	931 - 90
DT	3	1.01	1.1	12.8 – 1638.4	0.06 – 7.52	59 - 7522
WP	3	1.01	0.9	1638.4	5.52	5461

Topographical and chemical investigations of best characteristics in Ref. [189]						
	Fastest Deposition Rate		Highest Purity Fe/O		Highest Height FWHM	
AV	1 kV	$4.6 \cdot 10^6$ nm^3/s	1-5 kV	9	7 kV	0.35
BC	4.4 nA	$7.4 \cdot 10^6$ nm^3/s	1.0 nA	9.2	1.0 nA	0.25

PoP	11.4 nm	$2.1 \cdot 10^7$ nm^{3}s^{-1}	>1.6 nm	11.8	0.9 nm	0.32
DT	12.8 µs	$3.7 \cdot 10^7$ nm^{3}s^{-1}	<204.8 µs	9.7	1638 µs	0.73

Table 8.3.1.4.4. AC, DT, PoP and BC dependency of structures and content from Ref. [189]

The most important parameters of FEBID, the acceleration voltage (AC), beam current (BC), point pitch (PoP) and dwell time (DT), correlate with structural characteristics (width, length, height) and morphological characteristics (composition, purity, deposition rate, homogeneity). AC and BC account for the energy and number of electrons impinging on a substrate, and PoP and DT, account for the distance between neighbouring FEBID impinging points and to the exposure time per each point. See Table 8.3.1.4.4 for details.

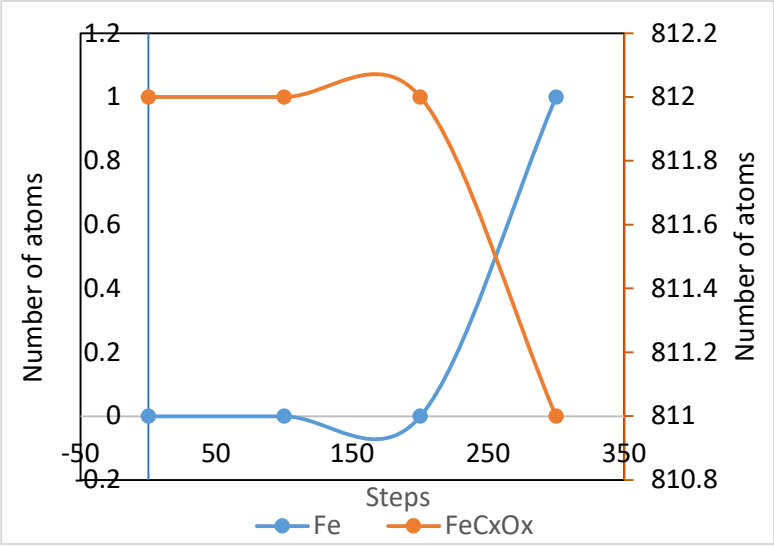

Fig 8.3.1.4.3. Fe island size and FeC_xO_x island size with 0.0022 $Fe(CO)_5$ layer density

The deposition dose is defined by the relation (8.3.1.4.6) considering AC, DT, PoP, and BC characteristics:

$$D = (BC \cdot DT / PoP)\, L \qquad (8.3.1.4.6)$$

where L is the nanowire length.

AFM investigations in Ref. [189] of four 1 µm long nanowires produced by FEBID (15 nm high, 60 nm wide, halo surrounding the structure of 3 nm thickness and 240 nm wide) show a Fe core structure covered by a 3 – 4 nm thin layer of oxide with FeO_x composition that would increase with the decrease in the size of the structure. An increase in the acceleration voltage would mean an increase in the electron energy, and an increase in the number of BSEs with further increase in the halo layers.

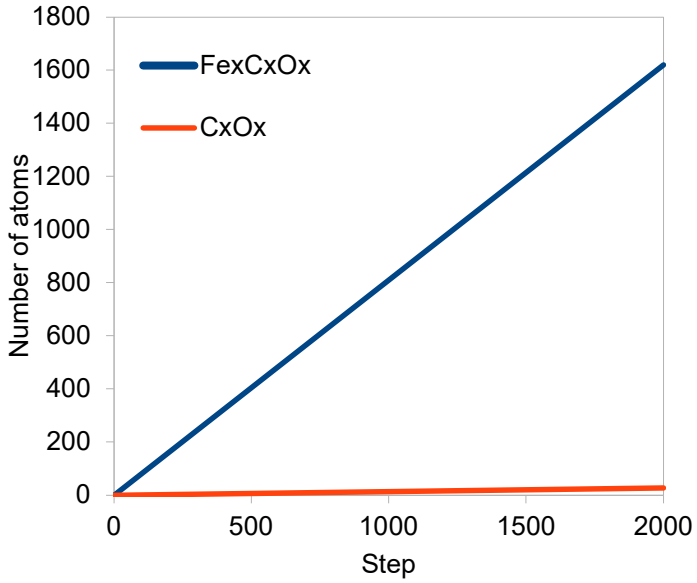

Fig 8.3.1.4.4. FeC_xO_x and C_xO_x island size with 0.0017 $Fe(CO)_5$ layer density

When analyzing the structures by their PoP time, a low PoP value for the same deposit size would mean a higher total electron dose for the structure, noting that at irradiation times higher than 409.6 µs the precursor molecules get depleted from the substrate. A good growth PoP rate would fall in values higher than 1.6 nm and DT values lower than 409.6 µs, resulting in higher surface roughness, metal islands layers with voids and gaps between metal deposits.

8.3.2 FEBID OF $Fe(CO)_5$ ON Au(ccp) SUBSTRATE

8.3.2.1 OPTIMIZATION OF THE MULTIPLE MOLECULE $Fe(CO)_5$ MOLECULAR SYSTEM ON Au(ccp)

The optimization of the multiple $Fe(CO)_5$ molecules and one single $Fe(CO)_5$ molecule on Au(ccp) substrate has been done using 20000 steps with 1000 trajectory steps, containing 100 chemical steps, characterized by velocity quenching optimization method. The interaction potential of the molecules with the substrate and each separate molecule with the Au(ccp) substrate is done by defining a pair of non periodic long range Coulomb potentials with a cut-off of 10 V and linked cell interaction mode. A velocity quenching time step of 1ms was used. The output of the structure optimization in the vicinity of the substrate has a factor of 10x difference between a single molecule and a multiple molecule system. The total energy of the final system for a molecular density of $Fe(CO)_5$ of 0.0017 corresponds to a number of 20047 atoms that need to be accommodated on the Au substrate and optimized according to the interaction potentials between the molecule and the level of van den Waals interaction forces with

the substrate. A density of molecules of 0.0022 Å was used for building the multiple $Fe(CO)_5$ molecular system, containing 29848 atoms on an Au(ccp) substrate of 200 nm x 200 nm x 5 nm (width x length x height). A similar step process is followed for the design, implementation, optimization and fragmentation of the multiple molecules system of $Fe(CO)_5$ on Au(ccp) with a reduced density at 0.0017 from the value of 0.0022 used in the first set of simulations.

	Single molecule	Multiple molecules
$\sum E_k$	1.7891404E-05	6.7233281E-02
$\sum E_p$	1.6245616E+05	4.8130700E+06
$\sum E$	1.6245616E+05	4.8130700E+06

Table 8.3.2.1.1. Energy output (Hartree) of (a) $Fe(CO)_5$ molecule on Au(ccp) and (b) multiple $Fe(CO)_5$ molecules on Au(ccp)

The $Fe(CO)_5$ molecular system was designed and built on Au(111) that has a ccp surface structure with orientation of the lines at 120° and a Chevron structural pattern of the substrate. The molecules would have to follow the orientation of the surface in the growth of films and deposits. A thorough analysis of the possible orientation of the molecular films of Fe $(CO)_5$ on Au(ccp) is done in the "IDMD calculations in FEBID studies of $Fe(CO)_5$ on Au(ccp)" section of the study, looking into different types of Au substrates, different molecular orientations with the hcp and bcc structures and the agglomeration of the molecular materials at kinks, holes and with the surface angle, as well as the threshold limits for surface hopping and hole accommodation. The deposition rates are further studied in comparison with the literature values of the system behavior when deposited on Au(ccp). The system optimization is the first step in the deposition and fragmentation of the $Fe(CO)_5$ on Au(ccp).

8.3.2.2 Diffusion of $Fe(CO)_5$ on the Au(ccp) Substrate

The literature lacks experimental data on diffusion of a single Au atom on Au(111) making it difficult to compare simulation data with experimental data, but certain behaviors of the molecules on the substrate can be predicted with good accuracy and high certainty using calculations. When choosing the substrate parameters such as temperature, diffusivity, film adhesion, morphology and composition (see Fig 8.3.2.2.1) need to be taken into account. With particular types of diffusion of the substrate molecules (step hopping, self-scavenging and inclusion) or $Fe(CO)_5$ molecules on the substrate (accommodation

and island formation), the values of the diffusion coefficients for different Au substrates are presented in Table 8.3.2.2.1.

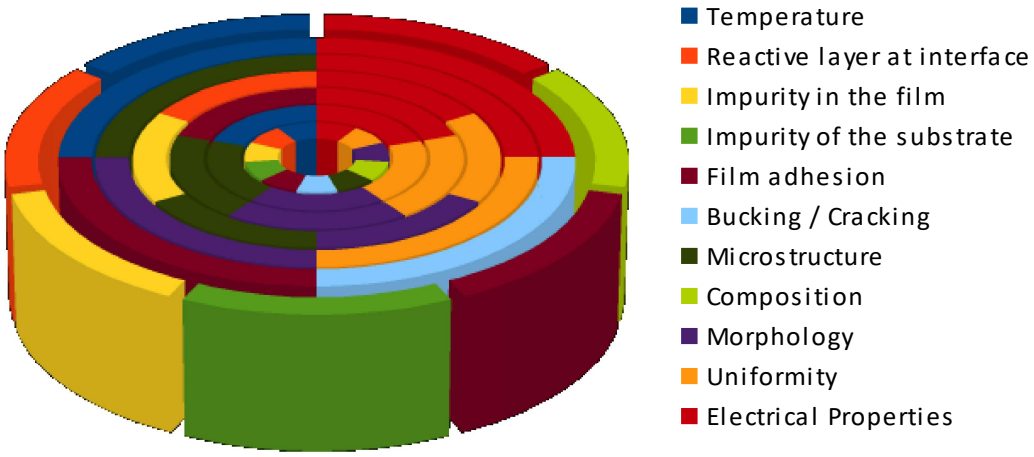

Fig 8.3.2.2.1. Characteristics in choosing the proper substrate from Ref. [190]

Substrate	In-channel (eV)	Cross-channel (eV)	Jumps (eV)	VC potential (eV)	Self-diffusion
Au(110)	0.14 (Ni); 0.27; 0.25 [191-192]	0.305 (Ni); 0.35; 0.40	-	0.34 [191]; 0.42	0.40; 0.38
Au(111)	0.1 [193]	-	0.013 [194]	0.04	0.22
Au(331)	0.35	-	-	0.42	-
Au(311)	0.35; 0.26	-	-	0.42; 0.34	-

Table 8.3.2.2.1. Activation energy for gold substrates in Ref. [195]

Diffusion of a $Fe(CO)_5$ single molecular system was simulated using MBN Explorer on a 5 nm thick Au(ccp) substrate. The comparison of system kinetic energy and the increase in the potential energy of the system at the transition from one molecule to multiple molecules is presented in Table 8.3.2.2.2. The simulation is run using 1000000 steps molecular dynamics (MD) simulation, with a Verlet integration algorithm and applying between the molecules and the substrate, and the molecule and the substrate van der Waals interactions. A Coulomb potential with a value of 1 is used for this particular case. Since the substrate is defined as being frozen, its structure and morphology will not change in time due to the molecule – substrate interaction. The type of the substrate chosen is an important part of the FEBID as the value of the overall kinetic energy and the total energy of the system changes. It is experimentally

proven that the $Fe(CO)_5$ is a very corrosive complex with high fragmentation and recombination when exposed to air and O_2 forming oxides and/or green rust. A particular study on the electrochemical deposition of green rust (pyroaurite group) on gold in Ref. [196] presents a detailed analysis of the size and morphology of the resulting structures of corrosion. The EDX, XPS, SEM and FTIR analysis shows the successful deposition of the rust on the Au and the bonding of the O with Fe^{3+} [196-196] from the $Fe(OH)_6$, as well as large resultant grains of ~0.7 μm (CO_3^{2-}) and a very porous environment in the case of chlorides. FTIR studies showed that the symmetry (T_d) reduces with the non-symmetric interactions between $Fe(OH)_6$ molecules that are intercalated in the octahedral H_2O molecules as a characteristic of corrosion presence. A similar mechanism we expect in the $Fe(CO)_5$ FEBID decomposition at exposure to air and humidity from environment.

	Single molecule	Multiple molecules
$\sum E_k$	1.7891404E-05	2.0611087E+02
$\sum E_p$	1.6245616E+05	4.6275167E+06
$\sum E$	1.6245616E+05	4.6277228E+06

Table 8.3.2.2.2. Energy output (Hartree) of (a) $Fe(CO)_5$ molecule on Au(ccp) and (b) multiple $Fe(CO)_5$ molecules on Au(ccp)

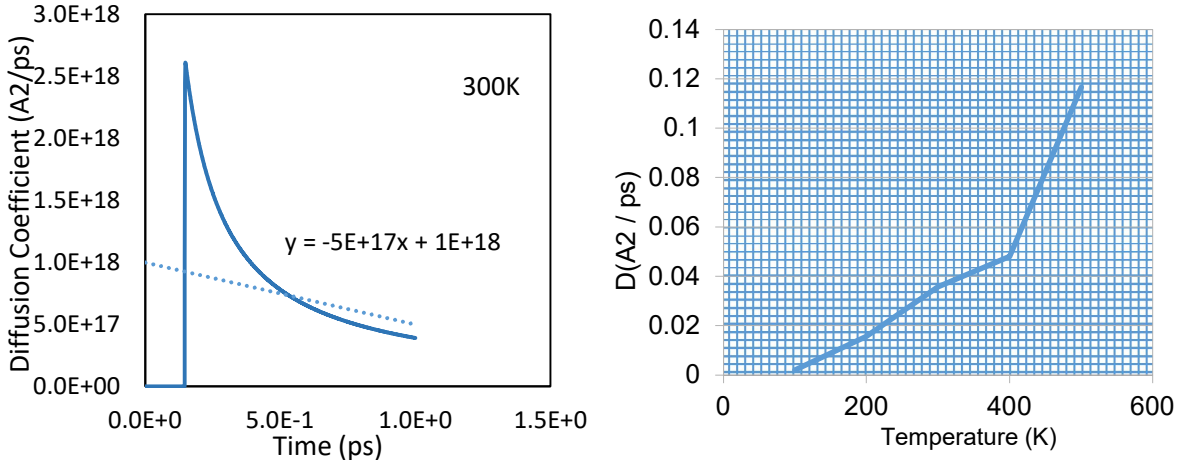

Fig 8.3.2.2.2. Diffusion coefficient for one $Fe(CO)_5$ on Au(ccp): (left) 300 K (right) temperature range 100 K – 500 K

In the case of one single molecule deposited on an inactive, non-reactive Au(ccp) substrate, the diffusion coefficient is in the range of ~-4E-05 A^2/ps. The full-length values for the simulation can be seen in Fig 8.3.2.2.4.

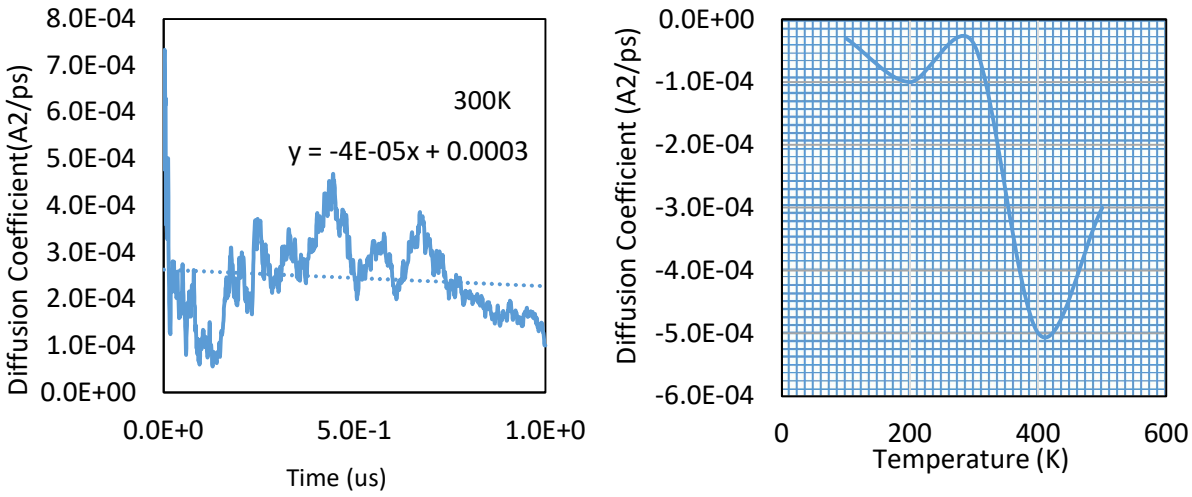

Fig 8.3.2.2.3. Diffusion coefficient for multiple $Fe(CO)_5$ molecules system on Au(ccp): (left) 300K (right) temperature range 100 K – 500 K

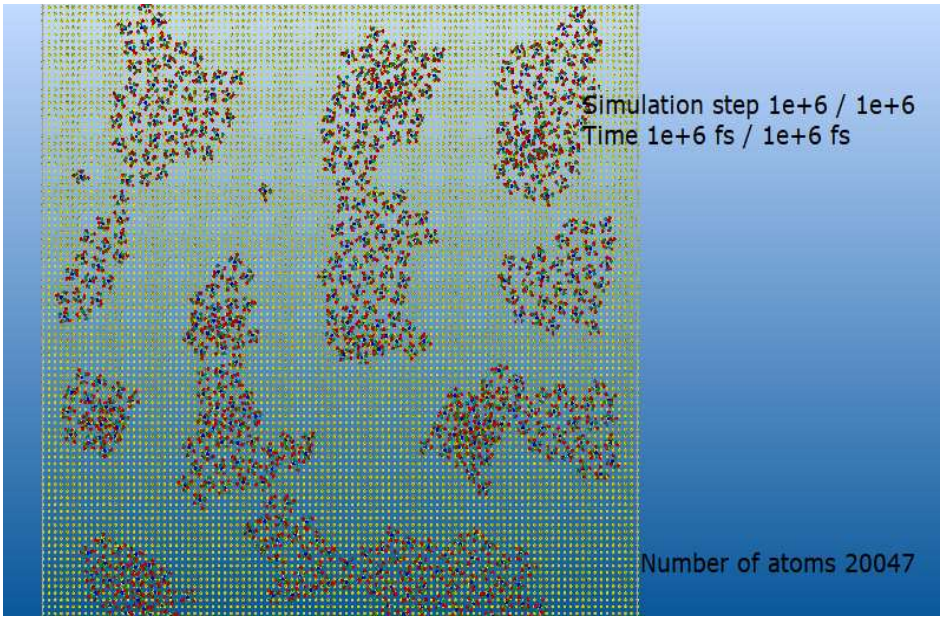

Fig 8.3.2.2.4. Diffusion of multiple $Fe(CO)_5$ molecules system on Au(ccp), clustering of molecules without recombination

The evolution of $Fe(CO)_5$ on Au(111) from a thin homogenous film of $Fe(CO)_5$ to resulting higher number of atoms islands was observed on the substrate (Fig 8.3.2.2.4). For higher thicknesses, lower levels of oxygen are observed, as well as the formation of oxygen islands at temperatures lower than 500 K. Characteristic of the surface deposition analysis, the two HREELs spectrum features at 380 cm^{-1} (0.047 eV) and 580 cm^{-1} (0.072 eV) are solely dependent on the layer thickness, where at lower coverages than 0.55 ML the features at 580 cm^{-1} (0.072 eV) disappear.

8.3.2.3 Relaxation Analysis with Time and Temperature

As reported in [198-202] morphological modifications of $Fe(CO)_5$ show similar results at IRRAS analysis (infrared reflection–absorption spectroscopy), with vibrational coupling dominating the features observed in the spectrum, as well as the process of Berry pseudo-rotation at energies higher than the barrier activation energy Ea = 2.5 ± 0.4 kcal mol^{-1}, and a broad range of temperatures. At lower temperatures, the values reported are not accurate enough. Different values of Berry pseudo-rotation energy in Ref. [201] were reported in other sources with values ranging between 2.0 - 2.3 kcal mol^{-1} in Ref. [198] and 1.6 ± 0.3 kcal mol^{-1} in Ref. [200]. In Ref. [198], the ν_{CO} vibrational resonances causing the change in the symmetry are characteristic to a_2" and e' excited states for D_{3h} symmetry, increasing its energy to a higher vibrational state a' and a change to C_{2v} symmetry; in Ref. [199] the C_{2v} symmetry state is characterized by the presence of e' final state from a a' ground state.

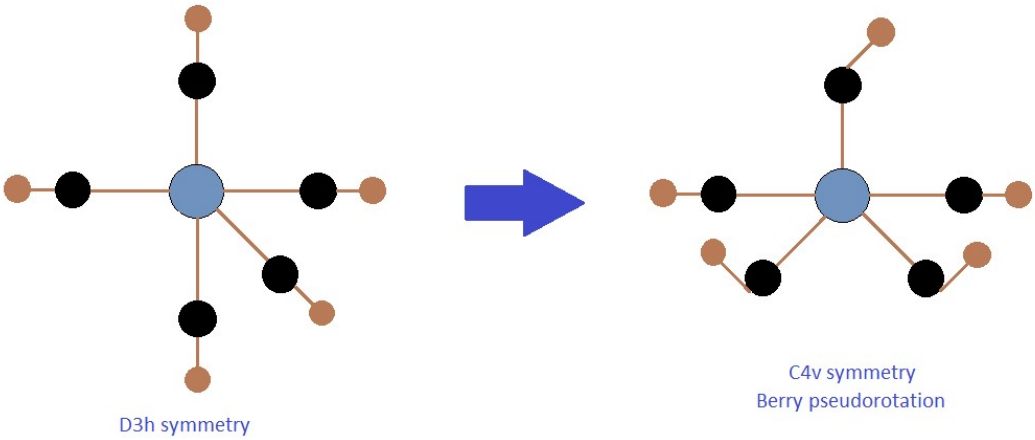

Fig 8.3.2.3.1. Schematics of CO ligand scrambling in Berry pseudo-rotation

The Berry pseudo-rotation is a process where the two axial Fe – CO bonds interchange with the equatorial ones, undergoing a bending of the Fe - CO ligands in the vibrational process. The process takes place at fast rates (1.1 x 10^{10} s^{-1}), and the CO scrambling for the molecule has an activation energy of 1.13 kcal mol^{-1}. The transition from the D_{3h} symmetry to C_{4v} symmetry in Ref. [198, 202] (top activation barrier in the Berry pseudo-rotation) in the ionization process obtained from DFT calculations has values of 2.25 kcal mol^{-1} DZ B3LYP, 2.28 kcal mol^{-1} DZP BP86 and 2.33 kcal mol^{-1} DZP B3LYP representing the energy difference between the two symmetry states. The isomers and IRRAS analysis in Ref. [199] were performed on two types of substrates, Au(111)/mica and C_4, C_8, C_{12}, C_{16} self-assembled monolayers (SAMs) / Au(111) / mica, where the number of C represent the number of C in the graphene ring. When $Fe(CO)_5$ thin films are on the surface, the spectra presents two frequencies, at 2012 cm^{-1} (0.249 eV) and 2050 cm^{-1} (0.254 eV). The lower deposition thickness or the low coverage regime is <5 ML on Au(111), <4 ML on C_4, C_8, and <2 ML on C_{12}, C_{16}.

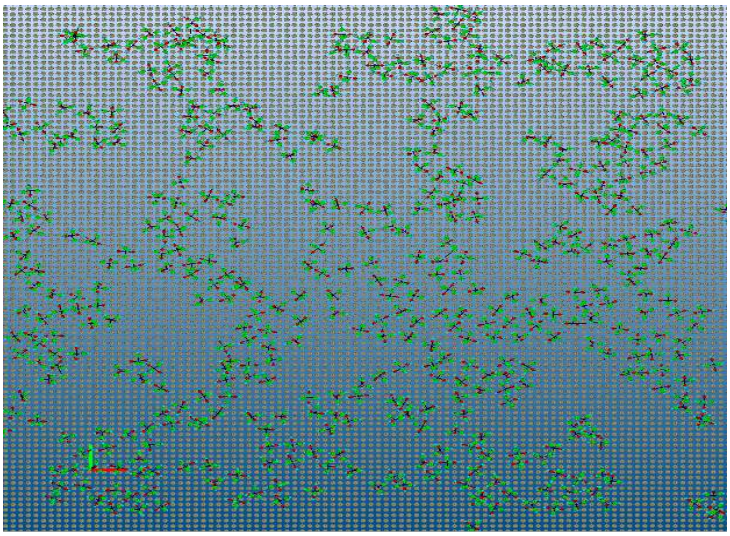

Fig 8.3.2.3.2. Relaxation process of the $Fe(CO)_5$ thin films deposited on Au(111)

The values of the frequency bands shift to higher values with the increase in the film thickness for the axial CO groups. An increase in the C – O stretching from 2050 cm^{-1} (0.254 eV) to 2063 (0.255 eV) – 2075 cm^{-1} (0.257 eV) is observed, with small contributions from the equatorial bands at 2014 cm^{-1} (0.249 eV), determined for a coverage between 10 ML and 40 ML. The defined bands in Ref. [199] compared to the data in Ref. [198] have higher values for the two declared transition states a_2" → a' and e' → a'.

Isomer	Bands	Symmetry	Stretching [cm^{-1}]	Stretching [eV]
$Fe(^{12}CO)_5$	1 2	A_2" E'	2023.9 cm^{-1} 1999. 6cm^{-1}	0.25 0.247
ax – $Fe(^{13}CO)(^{12}CO)_4$	3 6	A_1'	1988.5 cm^{-1} 2106.1 cm^{-1}	0.246 0.261
eq – $Fe(^{13}CO)(^{12}CO)_4$	4 5	A_1'	1963.2 cm^{-1} 2109.4 cm^{-1}	0.243 0.261

Table 8.3.2.3.1. Isomers of $Fe(CO)_5$ and bands in the Berry transition in Ref. [200]

In the molecular dynamics diffusion task, a step of 1 K from 200 K to 300 K was used, with a Verlet integrator over a time range of 1000000μs, characterized only by van der Waals interactions between the substrate and the $Fe(CO)_5$ molecular layer. Although the Au(111) in conjunction with Fe deposits is characterized by a higher reactivity, the substrate was defined as frozen. As the initial step to the relaxation process, the diffusion results for a layer of 0.0022 density and 300 K were used. The deposits of $Fe(CO)_5$ on Au(111) are brought up to a temperature of 300 K and then cooled down to 200 K using an anti rotator and a temperature step of 1 K (Fig 8.3.2.3.2). A decrease in the energy of the final system of two orders of magnitude compared to the initial system was observed, coming either from the

desorption on the substrate and bond reorganization, or simply reorganization of the $Fe(CO)_5$ molecular layer on the substrate.

	Relaxation of $Fe(CO)_5$ molecules	Diffused system from initial task
$\sum E_k$	2.05963931E+02	2.06110872E+02
$\sum E_p$	-2.30148219E+04	4.62751666E+06
$\sum E$	-2.28088580E+04	4.62772277E+06

Table 8.3.2.3.2. Kinetic energies (Hartree) of the $Fe(CO)_5$ relaxation process at a 0.0022 density of the deposits

From the relaxation task a reorganization of the $Fe(CO)_5$ molecules on Au(111) substrate occurs forming islands, but with little bond recombination, showing no sign of precursor degradation from 300 K to 0 K in the absence of irradiation. The same bending of the intermolecular bonds C – O and Fe – CO are observed in the interaction with the substrate assigned to the reactivity of the substrate and the Berry pseudo-rotation effect. A two order of magnitude lower overall kinetic and total energy of the system is observed compared to the initial system that underwent only diffusion with the substrate.

8.3.2.4 IDMD Calculations in FEBID Studies of $Fe(CO)_5$ Deposition on Au(ccp)

A number of deposition and irradiation cycles were performed for the Au(ccp) substrate, with two density levels, at 0.0022 and 0.0017. The purpose of these two multiple cycles simulations was to give a thorough insight into the kinetics of irradiation and fragmentation at the surface in the FEBID process of $Fe(CO)_5$. The steps of the deposition, accommodation and irradiation of $Fe(CO)_5$ precursor molecules on Au(ccp) substrate are presented in Fig 8.3.2.4.1. The kinetics of the system at deposition is defined by the values of the total energy and potential energy presented in Table 8.3.2.4.1. The FEBID principle states that the molecules are introduced to the gas line and vacuum chamber to be deposited on the substrate with a temperature lower than the transition temperature of the system, and at a pressure lower than the transition pressure, where a transition state is a state characterized by temperature, pressure, morphological and structural changes of the molecule undergoing fragmentation, oxidation, higher energy state transition, ionization, or undergoing chemical reactions within the environment, in essence any change that would take the system out of its stable state. Once accommodated on the surface, through the optimization and diffusion steps, the molecular layer of $Fe(CO)_5$ deposited on the substrate undergoes irradiation taking into account a set of FEBID processes using parameters that are illustrative of those used in experiment: beam characteristics (width, voltage, current), $Fe(CO)_5$ bonding data (cross-sections,

bond dissociation energies), a set of irradiation cycles being run in order to reach a certain height in the final deposits in coordination with beam parameters.

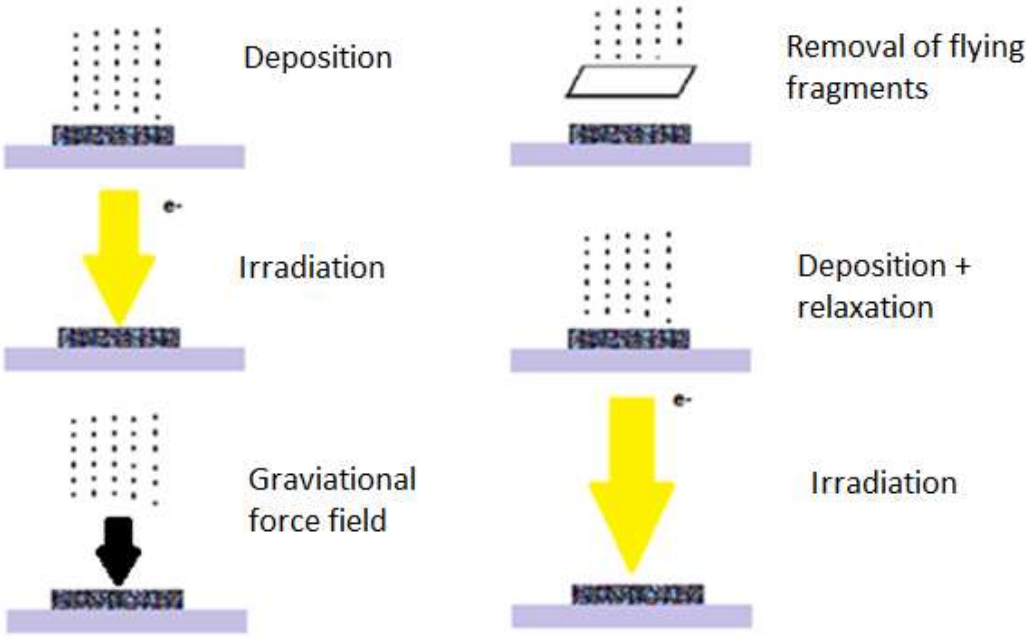

Fig 8.3.2.4.1. Deposition/irradiation steps of multiple $Fe(CO)_5$ molecular system on Au(ccp)

	Multiple $Fe(CO)_5$ molecules
$\sum E_k$	2.0696566E+02
$\sum E_p$	8.9611112E+06
$\sum E$	8.9613182E+06

Table 8.3.2.4.1. Deposition system characteristics for multiple $Fe(CO)_5$ molecules (Hartree) deposited on Au(ccp)

Analysis of the orientation of the Fe thin films and crystallites on Au(111) and vicinal Au(111) in Ref. [203] provides information on the structural and morphological modifications of the Fe structures, their orientation of the surface and the degree of orientation along certain directions. The Au(111) surfaces have a 22 x √3 reconstruction as a result of the non-uniform compression along [110] direction. The Au(111) surfaces are characterized by pattern lines separating the fcc regions from fault-stacked hcp regions, the lines being organized in a Chevron pattern across the surface with a corrugation of 0.2 Å and repetition rate of 20 nm. The crystal is trimmed along the [211] direction forming [111]-microfacets and terraces. The two metals have different structures at room temperature: while the Fe is a bcc structure

at room temperature, the Au has a fcc (ccp) structure at room temperature. The two characteristics for the metals govern the thickness of the layer at which the crystallites are formed and are incorporated in the deposits according to a critical thickness point. The critical thickness with a value of 1.7 ML for Fe / Au(111) and 1 ML for Fe / Au[23 25 25] is the limit for crystallite formation on the substrates, and with the increase in the thickness of the Fe layer to ~3 ML and 5 ML in Ref. [203], the crystallites disappear being incorporated in homogenous deposits. In Fig 8.3.2.4.2, two possible orientation models of the grains are presented, first the Nishiyama – Wassermann (NW), and the second one, a Kurdjimov – Sachs (KS) model of grain orientation set at a deviation of 5.25 °. The three types of Au substrates, usually have a combination of both the models with a variation of the orientation angle according to the $[211]_{fcc}$, $[011]_{fcc}$, $[110]_{bcc}$, $[001]_{bcc}$ and $[111]_{bcc}$ lines.

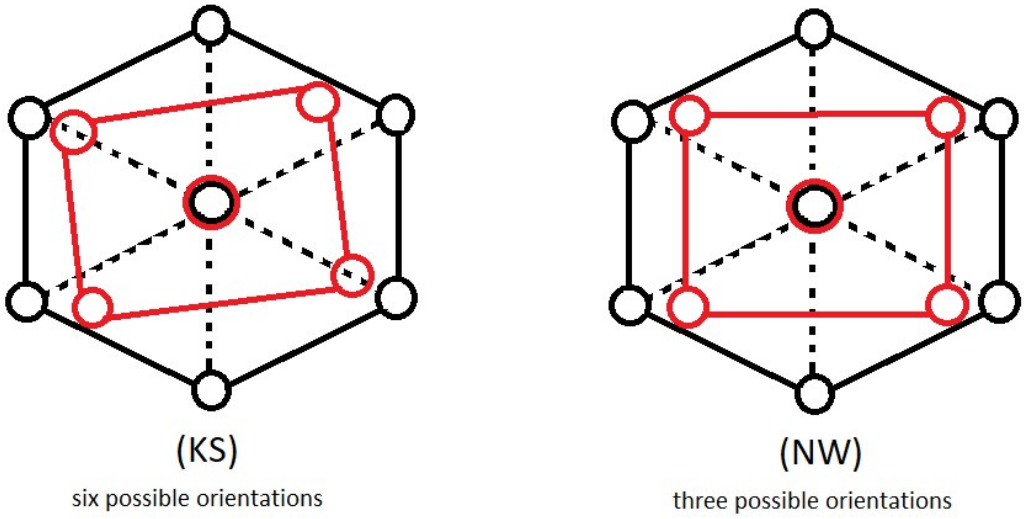

Fig 8.3.2.4.2. Fe orientation on Au(111), Au(788) and Au[23 25 25] in Ref. [203]

The scarcity of data on Fe deposition on Au substrates makes it difficult to predict the deposition rates and island sizes. Further analysis of another Fe containing compound reveals a different behavior with the interaction with the Au substrate. A higher reactivity is observed for the Au(111) substrate with Fe deposits from $Fe(dpm)_3$, with the linear formula $FeO_6C_{33}H_{60}$. The high content of C, O and H predicts a final composition on the substrate with higher doses of C and O. The study of Cimatti et al 2014 [204] tries to reveal through LEED and STM measurements of thin films deposited on the Au substrate. The presence of the $Fe(dpm)_2$ and $FeOH(dpm)_2$ was proven in Ref. [204], but no total fragmentation was found and the presence of intact $Fe(dpm)_3$ molecules on the substrate could not be determined. $Fe(dpm)_3$ has been denominated “an old workhorse for new applications” in Ref. [205], and has been widely used for low-temperature PECVD of nanomaterials. It has been proven to work at temperatures as low as 100

°C on a wide range of substrates obtaining pure Fe_2O_3 deposits. In the adsorption process on the Au(111) substrate, the $Fe(dpm)_3$ was found to nucleate only on the kinks of the herringbone reconstruction and terrace steps, known as reactive sites, where the deposits formed were patches of compound with regular shape (structural and morphological homogeneity) and different sizes. On the other hand, another PECVD study, but of the $Fe(CO)_5$ precursor, shows predilect presence of CO fragments with short lived ions, fragmentation of $Fe(CO)_n^-$ and Fe at DEA, and $FeC(CO)_n^+$ fragments at DI. A recombination with the formation of dimers and trimers, $Fe_2(CO)_m$ and $Fe_3(CO)_{m+5}$, involving a self-scavenging mechanism, a two-entered resonant process, where first a neutral dissociation occurs followed by a DEA process in Ref. [206] occurs. The resulting dimers and trimers have similar spectrum, with values of resonances ~5 eV higher than the monomer resonances, proving that the trimer is the result of a dimer and an intact $Fe(CO)_5$ monomer bonded to it.

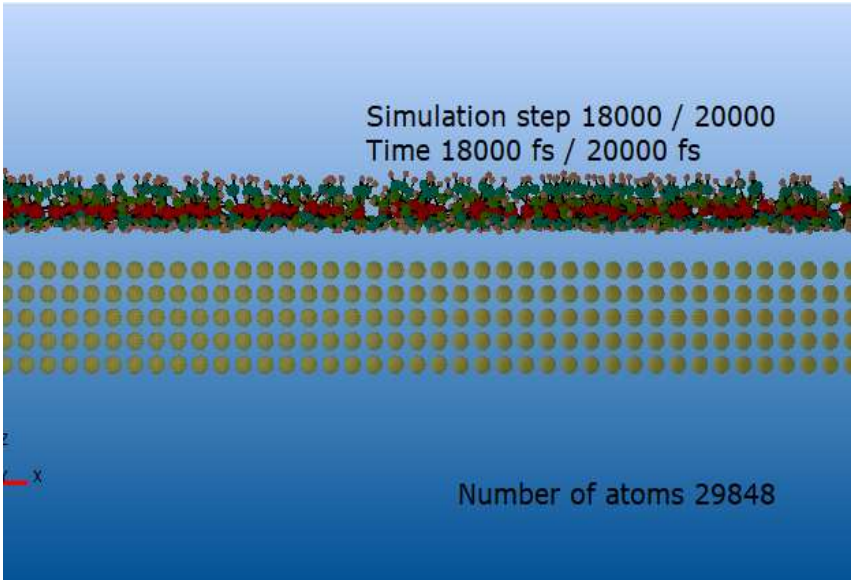

Fig 8.3.2.4.3. MBN Studio/MBN Explorer simulation of deposition process of multiple $Fe(CO)_5$ molecules on Au(ccp) substrate

Without the addition of another compound and catalyst, up to a constant temperature of 300 °C [207], the growth rate would decrease monotonically with the increase in the temperature and time, having an effect of surface poisoning atop the $Fe(CO)_5$ ions and molecules deposited on the substrate. XPS and SEM measurements in Ref. [207] show a change in the deposit size with the temperature without the addition of other gases or catalysts. Deposits of 50 nm were produced at temperatures of 200°C up to 300 °C for 10 min and a precursor pressure of 0.10 mTorr showed a decrease in the deposition rate from 120 nm/min to 5 nm/min. Further measurements, 50 nm thick @ 300 °C deposited for 10 min, 50 nm thick @300 °C deposited for 30 min, 50 nm thick @300 °C deposited for 10min and 200 °C deposited for another 10 min on top of the first one under combined flux of CO and $Fe(CO)_5$ with 3 mTorr of CO,

showed a similar behavior to $Fe(CO)_5$ films grown at 300 °C without flow of CO. A similar conclusion as in the first set of measurements could be drawn, the cause of the surface poisoning is the change in the surface, with one possible explanation being the reduction in the active surface sites. A reduction in the active surface sites would first mean a decomposition of the $Fe(CO)_5$, chemical reaction presented in relation (8.3.2.4.1):

$$Fe(CO)_{5\ (ads)} \rightarrow Fe + 5(CO)_{ads} \quad (8.3.2.4.1)$$

creating layers of Fe with adsorbed CO on it. The CO can undergo two chemical processes, in relation (8.3.2.4.2), following the Fischer-Tropsch process applied in the synthesis of hydrocarbons:

$$CO_{(g)} \rightarrow CO_{(ads)} \rightarrow C_{(ads)} + O_{(ads)} \quad (8.3.2.4.2)$$

These two processes produce structures of iron oxide and carbides (1), $CO_{2(g)}$ (2), and graphitic carbon (3). The cause of the surface poisoning coming from the deposition of graphitic carbon on top of the Fe structures, either blocking the active surface sites or covering them, is a process taking place at temperatures of 228 °C to 338 °C. Addition of olefin, H_2 and NH_3 to $Fe(CO)_5$ deposition was analyzed with good results in the case of olefin, and total elimination of surface poisoning at pressures of ~0.5 mTorr was obtained in the case of NH_3. The deposited structures of $Fe(CO)_5$ on Au(111) in Ref. [199] are characterized by an orientation to the substrate of the molecule depending on the monolayer, the first monolayer has one axial and two equatorial carbonyl groups towards the substrate and the second and subsequent monolayers with the C_3 molecular axis at an angle of 90 deg to the substrate. Similar orientation of a single molecule and multiple molecules have been obtained through MBN simulations.

Once deposited in thin layers and structures (created by depositing for longer periods of time higher number of layers), the $Fe(CO)_5$ molecules undergo irradiation, that would fragment them on the substrate to produce structures with the desired shape, width and height, depending on the irradiation characteristics: beam current, beam voltage, chamber pressure, deposition pressure (precursor pressure on the line), beam width (or radius) and the duration of time the irradiation takes place. For a 10 keV 2 μm diameter beam the effect of primary electrons injected to a depth of 1.3 μm has been calculated and compared to experimental data in Ref. [183]. A set of depositions of nanopillars grown with a vertical growth rate of 48 nm/s and 15 nm/s were done with the beam characteristics presented in the Table 8.3.2.4.2, presenting a Fe content of 48 % for the vertical growth regime, with 28 % O and 24 % C contamination, and a Fe content of 84 % in the self-sustained radial growth regime, with 10 % O and 6 % C contamination. Dendritic structures were found as a result of the electron beam (1.97 nA, 10 keV) at a precursor pressure of 0.5 mbar.

Growth regime	Beam (keV)	Pressure (mbar)	Current (nA)	Height (μm)	Aperture (μm)
Radial	10	0.5	1.97	2.5	60
Vertical	10	0.5	0.97	4.76	60

Table 8.3.2.4.2. Characteristics of growth regimes in Ref. [208]

The cross section data used in the simulations is presented in Chapter 5, Section 5.3. The most important cross-sections values are the values of DEA cross-sections up to 20 eV, DD cross-sections from 20 eV to 40 eV and DI cross-sections from 40 eV to 1000 eV. The cross-sections data was obtained running Quantemol-N simulations for the $Fe(CO)_5$ molecule. The same Sutton-Chen parameters in Ref. [183] used for $Fe(CO)_5$ on SiO_2 substrate simulation work have been used for Au(ccp) substrate, describing the interaction potential. The parameters are presented in Table 8.3.2.4.3.

Parameters	ε(eV)	c	a(Å)	m	n
Sutton - Chen	0.0220225	28.8474	3.48501	8.14475	8.7932

Table 8.3.2.4.3 Sutton-Chen parameters for Au(ccp) – Fe substrate interactions

The density and islands size from MBN simulations is presented in Table 8.3.2.4.4.

Density on Au(111)	0.0017	0.0022
$Fe(CO)_5$ island size	54	35
Number of atoms in the island / cycle	54	35

Table 8.3.2.4.4. Density of $Fe(CO)_5$ molecules and $Fe(CO)_5$ islands size on Au(111)

Island growth on the Au(111) in Ref. [210-213] is mostly determined by the surface reconstruction and terrace orientation, where oxides are used as isolation elements between the deposits and the surface. The Au(111) surface reconstruction is the 22 x √3 herringbone pattern (23 gold atoms packed on 22 bulk lattice sites along the [110] direction and two different 120° bends), and a complex pattern of corrugation lines on [112] direction repeating every 6.3 nm, and terraces with growth orientation and charge distribution on the surface to [100] and [111] and height of 2.35 Å. In Ref. [210] a lattice constant of 2.88 Å is obtained through the STM analysis of transition metals deposited on Au(111) with fcc regions (2.2 nm) combined with hcp regions (4.4 nm) and in between bridge separation regions. Chevron patterns on the parallel lines influenced by the temperature distribution and deposition conditions are characteristics of the repeating pattern of fcc-hollow-sites, bridge-site higher ridge, hcp-hollow-site, bridge-site higher ridge and fcc-hollow-sites in Ref. [212].

For isotropic substrates, the islands density saturation is defined by:

$$n_x = \eta\,(D/F)^{-1/3} \quad (8.3.2.4.4)$$

where D is the diffusion constant, F is the deposition flux, for a critical cluster size of i = 1 and $\eta = 0.25$. The surfaces are chosen to be governed only by van der Waals interaction forces between the molecules and the substrate, vdWDF/PBE calculations in Ref. [213] of the interactions and reactivity levels at the surface are run for Au 5d projected density of states (PDOS) and a 42 meV/surface atom:

$$\Delta E_{Au(111)} = E_{22x\sqrt{3}} - 44E_{1x1,ideal} - 2E_{Au,bulk} \quad (8.3.2.4.5)$$

where $E_{1x1,ideal}$ is the total energy of an ideal 1x1 six-layer surface cell, $E_{Au,bulk}$ is the total energy of an Au atom in the bulk.

The change of the structure across the entire unit cell depends on the position and different atomic layers:

$$\langle E_d \rangle = \int dE\, Eg_{PDOS,\,5d} / \int dE g_{PDOS,\,5d} \quad (8.3.2.4.6)$$

The Au model is a d-band model in Ref. [213]. Changes in the d states take place in the second layer of the atomic structure of the Au(111) surface, the first layer being frozen and immobilized on the substrate, similar to the bottom most layer. Multiple molecules have been analyzed at deposition rates particularly on the Au(111) substrate, due to the changes in reactivity with the molecular environment. NaCl on Au(111) has a (100) orientation following the Au corrugation lines reconstruction and characterized by a wetting energy of $\Upsilon_{Au(111)} = 1.28\ Jm^{-2}$ in Ref. [209]:

$$\Upsilon_{Au} > \Upsilon_{monolayer} + \Upsilon_i \quad (8.3.2.4.7)$$

where $\Upsilon_{monolayer}$ is the monolayer surface energy, Υ_i is the interface energy between the monolayer and the substrate.

Another common precursor for the Au(111) substrate is the iron carbide in Ref. [214], ε'-$Fe_{2.2}C$, ε-Fe_3C, θ-Fe_3C and χ-Fe_5C_2, forming an iron monolayer on top of the Au substrate in a pseudomorph fcc Fe(111) islands parallel with Au(111). With addition of ethylene, a moiré pattern at 3.3 ± 0.2 nm in a heteroepitaxial thin film growth is observed. Comparatively, the $MoSe_2$ in Ref. [211] deposited on Au(111) presents a moiré structure at 3.29Å ± 0.05 Å.

The Fig 8.3.2.4.4 presents the changes in the molecular fragmentation at parameters evaluated from Table 8.3.2.4.2 with resulting elemental changes in the system and maximal molecule size of 35 atoms containing Fe, and a number of $Fe_xC_xO_x$ fragments of 60 from the total initial deposited density of 0.0022. There was no presence of CO and C atoms in the fragmentation process, most of the CO radicals being released and removed, not accommodating on the substrate or integrating to the structure. This proves the lack of graphitic carbon on the surface and the low affinity of the surface at low temperatures to C.

Values of deposition rates with different island sizes from literature were gathered and presented in Table 8.3.2.4.5 for comparison with the MBN simulation data.

Type of islands	Monolayers	Temperature	Deposition rate	Nearest neighbor
Cr	0.07 / 0.25 ML	room temperature	0.25ML/min	7.2 nm
Fe(111)	0.2 ML	523K – 773K	0.2 ML/min	0.288 nm
Isotropic substrate	0.10 ML – 0.15 ML	0-500K	0.10 ML/min	0.285 ± 0.003 nm
NaCl	0.9Å - 1.1 Å 1.53Å – 0.7 Å	room temperature	~1 ML/min	4.0 ± 0.1 nm
C_2H_4 + Fe(111)	0.15 ± 0.02 nm	room temperature	0.25 ML/min	0.315 ± 0.2 nm

Table 8.3.2.4.5. Deposition rates for different molecules on the Au(111) substrate in Ref. [209]

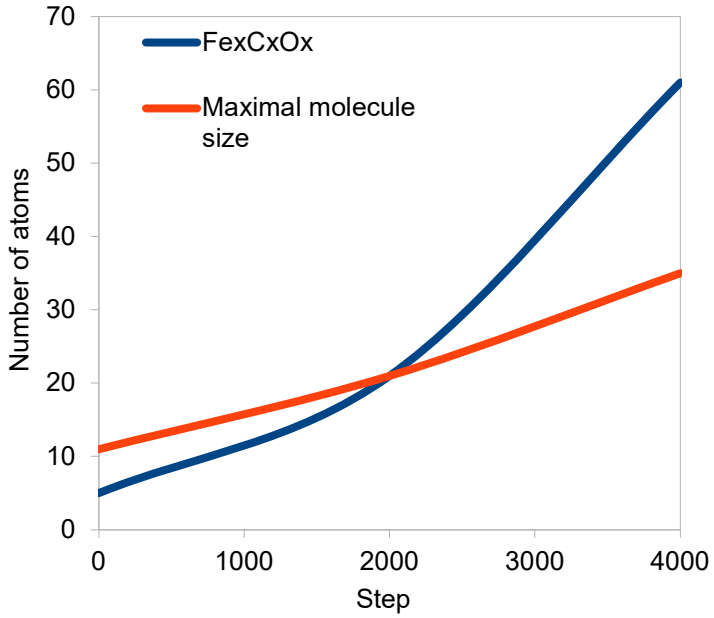

Fig 8.3.2.4.4. FeC_xO_x island size at 0.0022 $Fe(CO)_5$ density

8.4 Conclusions To Chapter 8

In this chapter simulations of the FEBID process using MBNExplorer are presented that focuses on three steps: diffusion, relaxation and irradiation of $Fe(CO)_5$ on a choice of two substrates, SiO_2 and Au(111). MBN Explorer is the software developed at MBN Research Center, Frankfurt, Germany to study the dynamics of the molecular reaction on the nano and micro scales making use of the classical chemistry

quantum approach and dynamics through the implementation of packages such as CHARMM, AMBER, GROMACS and NAMD, but with the addition of newer approaches to the field of induced chemical reactions, where a high number of parameters need to be implemented and used with the basic chemical approach, bond lengths, electron energies, bond dissociation, ion energies, bond breaking strengths, beam characteristics (current, voltage, dwell times). The software gives the user the opportunity to choose and create from a wide range of substrates, crystals, nanoparticles, and offer the means to create and optimize them from scratch. Ab-initio and dynamical simulations can be combined to create complex molecular systems with high number of atoms and dimensions in the range of μm. The MBNExplorer software is complemented by the availability of MBN Studio visualization and coding software that give the opportunity to make changes in real-time to the simulation programs and visualize the evolution step-by-step. The choice of the substrate comes with research and literature evaluation for higher or lower reactive substrates according to the users needs. Molecules and substrate can be imported from DFT, or other simulation software by the easy use of the available .pdb format.

The present study and simulation of the FEBID process of $Fe(CO)_5$ makes use of the available features, with the purpose of creating a complete evaluation of the possible complex relations between multiple environmental factors that can influence the deposition quality and the structural modifications on the substrate. Mostly three products of reaction are present with the result of fragmentation of the precursor molecules FeC_xO_x, Fe and C_xO_x. The lack of Fe_xO_x in the final nanostructures is a sign of the lack of oxidation of the iron. The fragmentation of the $Fe(CO)_5$ on SiO_2 deposited with a density of 0.0022 has a maximal molecule size of 34 with an average number of atoms corresponding to the $Fe_xC_xO_x$ products of reaction of 812, while for a density of 0.0017 a number of 1620 atoms corresponding to $Fe_xC_xO_x$ products of reaction are present. The SiO_2 substrate was modelled as a 5 nm thick monolayer with the bond angles of the Si – O bonds at 94 deg and the working space defined as 3D square polygon shape (box) of 200 x 200 x 480 Å. The interaction between the molecule and the substrate were defined by van der Waals interaction forces and the Sutton – Chen potential was used in the definition of the Fe – Fe interactions. In the optimization and thermalization (diffusion step) the substrate was declared as a perfect infinite substrate where no Fe – Si interaction can take place, the only forces acting on the molecules and the substrate in the vicinity of the substrate being the van der Waals forces. The optimization of the molecules with the substrate is based on the velocity quenching algorithm and 1982 Verlet algorithm for rigid bodies. In the diffusion and accommodation step a low recombination of the $Fe(CO)_5$ molecules with the SiO_2 substrate is observed limited to a small number of O atoms escaping the $Fe(CO)_5$ bonds and SiO_2 bonds with a value under 1 % from the total number of atoms. In the case of the hydrogenated SiO_2 substrate, where a monolayer of H is placed atop the SiO_2 a higher

agglomeration and conglomeration at particular sites of the $Fe(CO)_5$ molecules is observed, with an increase in the energy of the system with approximately 0.2 eV. The unhydrogenated SiO_2 substrate shows a lower migration and conglomeration of the $Fe(CO)_5$ molecules organizing to a less extent, but in wider island, with less free substrate places, and agglomerating the CO bonds to neighboring atoms are phenomena with an occurrence of 0.0004 % (an initial indication of a beginning of clustering process). At deposition and irradiation times over 409.6 μs the precursor is found as depleting from the surface, phenomenon influenced by the PoP rate at values higher than nm (> μs), resulting higher surface roughness, metal islands with voids and gaps between the metal deposits.

For the Au(111) substrate, a density of 0.0022 is deposited resulting in structures containing 61 atoms corresponding to $Fe_xC_xO_x$ products of reaction. In the case of Au(111) no pure Fe, and Fe without any $(CO)_x$ radical attached, are observed compared to the SiO_2 where for a density of 0.0022 only Fe deposits have been found. A wide description of all Au substrates and Au √23 reconstruction is presented with multiple precursors deposited on them to sample the behavior of the Au substrate at different parameters and environmental conditions. In the optimization process 2000 steps, 1000 trajectory steps, 100 chemical steps (0.1 fs) have been used with the velocity quenching method and Verlet algorithm. The interaction of the molecules with the substrate was modelled by a pair of non-periodic long range Coulomb potentials with a 10 V cut-off in linked cell interaction mode and a time step of 1 μs. The value of the systems energy in the optimization step compared to the value of a single optimized molecule on the substrate is ~ 10 times higher. The one single molecule diffusion coefficient is in the range of ~ -4E-05 Å/ps, and a predominant process of Berry pseudo-rotation with the substrate of the $Fe(CO)_5$ molecule is observed characterized by an activation energy of the molecule with the substrate of 2.5 ± 0.4 kcal mol^{-1}, and an activation energy of the CO scrambling of 1.13 kcal mol^{-1}. In the thermalization step, a low number of migration events forming islands and recombination of the CO to form $Fe_x(CO)_y$ clusters, x = 1 – 5, y = 1 – 20 is observed, while the energy of the whole system decreases with 2 orders of magnitude upon accommodation of the molecules on the substrate and increase in temperature.

CHAPTER 9. CONCLUSIONS AND FUTURE WORK

9.1 CONCLUSIONS

The research presented in this thesis has focused on four groups of compounds used as precursors for manufacturing of nanostructures using the FEBID process: two carbonyls ($Fe(CO)_5$, $W(CO)_6$), two gold precursors ($Me_2Au(acac)$, $C_8H_{10}Cl_2N_2AuF_3$), two substrate precursors ($Si(OEt)_4$, $Ti(OPr)_4$) and a set of Pt precursors ($Pt(acac)_2$, $Pt(PF_3)_4$, $Pt(NH_3)_4(NO_3)_2$). All have been studied in the gas-phase and three of the compounds ($Fe(CO)_5$, $AuMe_2(acac)$, $Si(OEt)_4$) were studied during deposition and irradiation on SiO_2, Au(111) and Cu(110). The studies are summarised in Table 9.1.1.

Gas - phase Studies	Surface Science and Deposition Studies
$Fe(CO)_5$	$AuMe_2(acac)$ / Cu(110)
$W(CO)_6$	$C_5O_2H_8$ / Cu(110) and SiO_2
$C_8H_{10}Cl_2N_2AuF_3$	$Si(OEt)_4$ / Au(111)
$C_5O_2H_8$	$Fe(CO)_5$ / SiO_2 and Au(111)
$Ti(OPr)_4$	
$Si(OEt)_4$	

Table 9.1.1. Compounds used for analysis

The focus of these studies has been on the fragmentation process of the molecules and the influence of such fragmentation on the height, width, morphology, composition, and shape of the final nanostructures. The fragmentation of the molecules at low electron energies has been studied in the range of 0-20eV and simulations of the secondary and backscattered electrons have been employed to analyse the deposition regime and the scattering extent of the electrons from the substrate and structures. In the dissociative electron attachment process the molecule undergoes fragmentation when irradiated with low energy electrons and was studied using the velocity sliced map imaging technique, to determine the resonance values, as well as cross-sections data through the processing of the ion Newton sphere and the angular distribution of velocities and kinetic energies.

$Fe(CO)_5$ and $W(CO)_6$

DEA of $Fe(CO)_5$ was shown to produce five negative ions each with highest yields at different incident energies: $Fe(CO)^-_4$ (0.2 eV), $Fe(CO)^-_3$ (1.3 eV), $Fe(CO)^-_2$ (4.2 eV), $FeCO^-$ (8.5 eV) and Fe^-(9 eV) with the maximum kinetic energies of 0.25 eV, 0.6 eV, 0.8 eV, 1.2 eV and 0.2 eV. DEA of $W(CO)_6$ was shown to produce the following anions (with maximum yields at different energies) $W(CO)^-_5$ (0.2 eV),

$W(CO)^-_4$ (3.3 eV), $W(CO)^-_3$ (4.7 eV), $W(CO)^-_2$ (8.8 eV) and WCO^- (17 eV) with the maximum kinetic energies associated with each resonance 0.8 eV, 0.15 eV, 4.3 eV, 2.4 eV and 1.2 eV. Compared to $Fe(CO)_5$ the DEA of $W(CO)_6$ has been found not to strip off all ligands in gas-phase or to present a negative ionized parent in the transition from $\pi \rightarrow \pi^*$ state. The angular distribution for the ions of $W(CO)_6$ precursors presents symmetry at (35, 150) deg ($W(CO)^-_5$), (55, 130) deg ($W(CO)^-_4$), (52, 130) deg ($W(CO)^-_3$), (48, 130) deg ($W(CO)^-_2$) and (48, 138) deg (WCO^-). All ions have been reported to have C_{2v} structure symmetry and the comparison to literature data of the angular symmetry is presented in Table 5.2.2.3 Chapter 5. The Fe(CO)5 anions present symmetry at (80, 120) deg ($Fe(CO)^-_4$), (48, 140) deg ($Fe(CO)^-_3$), (48, 140) deg ($Fe(CO)^-_2$), (30, 148) deg ($FeCO^-$) and (48, 140) deg (Fe^-) with C_{2v} symmetry for $Fe(CO)^-_{4-2}$ and C_{3v} symmetry for $FeCO^-$ and Fe^-. A set of cross-sections has been run for $Fe(CO)_5$ using Quantemol-N with the focus on the dissociative electron attachment cross-sections with a maximum value of 34 x $10^{-16}cm^{-1}$. The novelty in the analysis of the carbonyl group compounds comes in the use of velocity sliced map imaging for the first time in the determination of the DEA cross-sections for organo-metallic compounds using the experimental data as input to the calculation. The cross-sections data on organo-metallic compounds is scarce, both experimentally and theoretically.

A simulated FEBID study of $Fe(CO)_5$ deposited on two substrates, SiO_2 and Au(111), is presented in Chapter 8. Four simulations have been done for the diffusion of the $Fe(CO)_5$ on the SiO_2 and Au(111) substrates for both the densities, 0.0017 molecules·μm^{-1} and 0.0022 molecules·μm^{-1}, with values of the total energy of -3.9848221E+04 eV and a kinetic energy of the system of -3.4811920E+02 eV for the SiO_2, while for the Au(111) a diffusion total energy of the system of 4.6277228E+06 eV and a total kinetic energy of the system of 2.0611087E+02 eV was obtained from the simulations. The deposition of the $Fe(CO)_5$ on Au(111) was done with a total energy of the system of 8.9613182E+06 eV, 2x higher than the diffusion process. A separate simulation run with a hydrogenated SiO_2 substrate was run with values of the total energy of the system of -4.00202537E+04 eV and total kinetic energy of the system of 3.46453428E+02 eV, 20x lower than the unhydrogenated substrate. A diffusion coefficient was obtained for the SiO_2 substrate of -0.03 A^2/ps, while for the Au(111) a value of 0.048008851 A^2/ps was obtained. Comparing the SiO_2 hydrogenated substrate with the unhydrogenated substrate, a value of the diffusion coefficient of -2.61E-05 A^2/ps was obtained for the hydrogenated one, 1000 times lower than the unhydrogenated one. The irradiation process of the $Fe(CO)_5$ monolayers using MBN Explorer characterized by an electron beam of 130 eV and 30 eV binding energy with molecular dynamics routine has as a result a number of 812 fragmentation channels for the resultant FeC_xO_x and 8 full fragments for the resultant Fe_x. The numbers correspond to 8192 atoms deposited on the substrate with 0.0022 molecules·μm^{-1} density. For a smaller density of the $Fe(CO)_5$ on the SiO_2 a higher decomposition rate is

observed, where 1620 $Fe_xC_xO_x$ are obtained, but no Fe_x fragments are found. On the Au(111) for a density of 0.0022 molecules·μm^{-1} a number of 61 $Fe_xC_xO_x$ are obtained at a rate 10x to 50x smaller than for the SiO_2 with a maximal molecule island size of 35 atoms.

Au precursors

The $Me_2Au(acac)$ precursor has been deposited on Cu(110) at a pressure of 2.2 x 10^{-9} mbar (an initial pressure of 2.7 x 10^{-11} mbar) to create 6ML thin films. A temperature programmed desorption study and electron stimulated desorption study of the molecule was performed. Values of current density of 8.5 µA at 21 eV irradiation, and the fragments, results of desorption with m/z 15, 43, 28, 99, 73, 85, 294.6, 238.6 and 253.6 have been obtained. At 21 eV irradiation for 10 min /5 min with 1 V/ 30 V ON/ OFF grid voltage of the monolayers, the fragments at the masses m/z 26 and m/z 43 were characterized by a calculated electron dose on the substrate and thin films of 1.8E+16 electrons/cm^2.

Further studies of acetylacetone focus on the deposition of the acetylacetone on Cu(110) followed by temperature programmed desorption (as part of $Me_2Au(acac)$ precursor) using Gaussian 16, Multiwfn, Avogadro, ChemCraft and NewtonX in comparison with its deposition and binding to SiO_2 (Chapter 7). With a binding energy of one C = O bond of acetylacetone to SiO_2 we obtained a binding energy of the molecule to the substrate of -568.8721245 (*Hartree*), while binding of an O of acetylacetone to SiO_2 would have a binding energy of 1711.5528817 (*Hartree*), an O and H of acetylacetone bound to SiO_2 has a value of 1937.4145492 (*Hartree*). Comparing the value to the binding of the molecule on Cu with the formation of a Cu – O bond at a value of -8203.1672390 (*Hartree*), we obtain a binding energy of acetylacetone on the Cu(110) of 0.0098523 (*Hartree*). See ANNEX 4 for these results. A desorption/adsorption study of the molecule on the Cu(110) was run at separate temperatures with a rate of 30 K from 160 K to 310 K. A slight difference in the adsorption band at 160 K is observed compared with the rest of the adsorption curves at 190 K – 310 K.

Ti and Si precursors

We analyzed two compounds, $Ti(OPr)_4$ and $Si(OEt)_4$, two of the most used in the deposition of SiO_2 and TiO_2 for mask repair in FEBID processes. The DEA gas-phase analysis of the $Si(OEt)_4$ compound reveals a number of negative fragments. The anion yield from the quadrupole mass spectrometer presents contributions at 2-3 eV and 6-9 eV from the ions CH^-_3 (m/z 15), $SiO_3C_9H_6^-$ (m/z 180), $SiO_3C_9H_5^-$ (m/z 177), $CH(CH_3)_2^-$ (m/z 43), $SiOC_6H_4^-$ (m/z 120). DEA fragmentation of $Si(OEt)_4$ is mainly through electron scattering resonances at incident electron energies of 6.6 eV (m/z 43, $CH(CH_3)_2^-$), 2.4 eV and 8.8 eV (m/z 120, $SiOC_6H_4^-$), 2.9 eV and 9.2 eV (m/z 177, $SiO_3C_5H_5^-$) and 2.4 eV and 8.9 eV (m/z 180,

$SiO_3C_5H_6^-$). $Ti(OPr)_4$ is a compound with a lower vapor pressure than $Si(OEt)_4$ and a smaller number of negative ions are formed in the DEA process. The ions $TiCH_3^-$ (m/z 57), $TiOH_7C_9^-$ (m/z 179), $TiO_4C_6H_{15}^-$ (m/z 199), $TiOH_7C_9^-$ (m/z 179), $TiO_4H_{10}C_{10}^-$ (m/z 242) and the parent anion (m/z 284, $Ti(OPr)_4^-$) were found. Several resonances are observed, the lowest values have been found at 1eV, while a nested series of resonances have been observed between 8.3eV and 9.5 eV.

The FEBID deposition of $Si(OEt)_4$ (Chapter 7) was studied both experimentally and using the Monte Carlo routine integrated in the CASINO software version 3 for the three electron beam characteristics at 1 keV, 2 keV and 5 keV. Two sets of measurements were done: in the first set, the nanostructures were synthesized and then stored in air for 8 months and a second set deposited and kept in air for 12 hours before analysis. From the CASINO simulations we obtained the best beam characteristic as being the 1keV since both the 2 keV and 5 keV have higher secondary and backscattered electron density and wider radius with values of 12.2 nm (2 keV) and 2 nm (5 keV). The backscattered coefficient for a 2 keV beam as determined from simulations is 0.009848 with secondary electron yield of 9.2×10^{-5} and with a 50% of electrons falling 40 – 90 deg from the sample, while for a beam of 5 keV we obtained a value of the backscattered coefficient of 0.008139 with a secondary electron yield of 0.047829 and with 50 % of the backscattered electrons falling 40 – 90 deg to the sample. The simulations were done on a trapezoidal sample of $Si(OEt)_4$ deposited on Au(111). The parameters used for experimental studies where an electron beam of 1 keV was chosen, resulting a simulated radius of 1.2nm, secondary electron yield 0.08492, a backscattered coefficient of 0.01219, and 28 pA for the second set of depositions (12 h) and 24 pA for the first set of depositions (8 months), have been determined based on the CASINO simulations results in the intent of reducing the effects of the secondary electrons on the structures. A number of dots and line profiles were deposited on Au(111) at a deposition temperature of -25 °C, see Table 6.2.1.1 for 8 months old deposits and Table 6.2.1.2 for 12 - hour old deposits. The height/width and compositional content of the structure has been evaluated using an AFM and a STM. Over time, as observed experimentally (see Fig 6.2.1.4 Chapter 6) the deposits increase their C composition due to their reaction with the air, and we also observed a reduction in height in 10 % of the structures and fall in the O and Si content, the oxygen through reaction with the C and evaporation, while the Si through settlement and integration in the kinks and patterns of the substrate.

9.2 Future Work

Artificial intelligence has increasingly been applied to industrial focused fields, in the last few years it has changed the way that molecular physics evolves and how the simulations and calculations are done reducing the amount of time it takes to obtain the results, leaving room for increasing the complexity of the calculations and reducing the number of resources used for running the calculations. A large number of databases has been developed containing an increasing number of molecules that can be used in the simulations. The algorithms for running them are simplified by using the neural networks and decision trees, as well as the methods of reinforcement learning, direct learning, and deep learning. Running calculations based on AI would bring better and more accurate results, larger sets of data, surfaces and increased numbers of molecules are easier to simulate close to their real-life values reducing the total computing time and number of cores, making many of the simulations that were not possible before possible. A further step would be applying the AI to FEBID simulations of the fragmentation patterns on the surface and in the gas-phase. Software such as VASP with their AI interfaces available from the University of Colorado, Newton-X and Fleur, are tools that are planned to be used to carry the research needed, and further the development of in-house built decision trees and neural networks are guaranteed to offer novel results. Due to the COVID pandemics experimental results of the velocity map imaging could not be obtained on $Si(OEt)_4$ (done at J. Heyrovský Institute of Physical Chemistry of the Czech Academy of Sciences, but only with poor results due to the slicing type (>100 ns); images of the ions, kinetic energies and angular distributions could not be determined), $Ti(OPr)_4$, $Pt(NH_3)_4(NO_3)_2$ and $Cl_2ImEtCF_3Au$. The results were meant to be used in further publications supporting this thesis and being part of the ELENA project research and further Velocity Map Imaging measurements were supposed to be carried at the University of Kent, VMI and Fluorescence Laboratory during the year 2020. The work intended to be done at the time makes the topic of future work section. As well, my presence in Prague during the experimental work was limited by the COVID travel restrictions and lockdown. However, the lack of this work does not impediment the work done in this thesis. A trip to the SOLEIL synchrotron for FEBID research was intended for chemical complexes such as $Pt(acac)_2$, $Pt(NH_3)_4(NO_3)_2$ and $W(CO)_6$, but as well limited by the COVID as all applications were stalled for half a year during 2020 pushing the lack of availability of the equipment close to the final deadline of the project. At the Zeiss Gmbh research facility in Germany two more experiments were intended for the deposition of $Pt(acac)_2$ and $W(CO)_6$ but were stopped during 2020 due to COVID limiting the installation and delivery standby time for the experimental work. Work was done at their facilities on only the planned $Si(OEt)_4$ as that compound was more easily available and in-stock at the facility. As well, there was a draft plan for the development of GIS deposition equipment for highly complex FEBID structures in 3D, that could not be initiated as the COVID pandemics started and its construction was left as a draft, the work and its design making the topic of a future work section.

REFERENCE

1.Van Dorp W.F., Hagen C.W., A critical literature review of focused electron beam induced deposition, J. Appl. Phys. 104, 2018, 081301

2. Koshikawa T., Shimizu R., A Monte Carlo calculation of low-energy secondary electron emission from metals, J. Phys. D: Appl. Phys. 7, 1974, 1303

3.Kotera M., Kishida T., A Monte Carlo Simulation of Secondary Electron Trajectories in a Specimen, Jpn. J. Appl. Phys. 28, 1989, 148

4.Liu Z.-Q., Mitsuishi K., Furuya K., A dynamic Monte Carlo study of the in-situ growth of a substance deposited using electron-beam-induced deposition, Nanotechnology 17, 2006, 3832–3837

5.Koshikawa T., Shimizu R., A Monte Carlo calculation of low-energy secondary electron emission from metals, J. Phys. D: Appl. Phys. 7, 1974, 1303

6.Murata K., Kyser D.F., Ting C.H., Monte Carlo simulation of fast secondary electron production in electron beam resists, Journal of Applied Physics 52, 1981, 4396

7.Mitsuishi K., Monte Carlo Method in FEBID Process Simulations, Utke I., Moshkalev S., Russell P., Nanofabrication Using Focused Ion and Electron Beams: Principles and Applications, Oxford University Press, Chapter 8, 2012, Technology & Engineering

8.Salvat-Pujol F., Valentí R., Werner W.S., Surface excitations in the modelling of electron transport for electron-beam-induced deposition experiments, Beilstein J. Nanotechnol. 2015, 6, 1260–1267

9.Huth M., Porrati F., Schwalb C., Winhold M., Sachser R., Dukic M., Adams J., Fantner G., Focused electron beam induced deposition: A perspective, Beilstein J. Nanotechnol. 2012, 3, 597–619

10.De Teresa J.M., Fernández-Pacheco A., Present and future applications of magnetic nanostructures grown by FEBID, Appl. Phys. A, 2014, 117:1645–1658

11.Sangiao S., Magén C., Mofakhami D., de Loubenss G., De Teresa J.M., Magnetic properties of optimized cobalt nanospheres grown by focused electron beam induced deposition (FEBID) on cantilever tips, Beilstein J. Nanotechnol. 2017, 8, 2106–2115

12.Navarro J.P., Hernández D.S., Magén C., Pacheco A.F., de Teresa J.M., Tuning shape, composition and magnetization of 3D cobalt nanowires grown by focused electron beam induced deposition (FEBID), J. Phys. D: Appl. Phys. 50, 2017

13.van Hapert J.J., Chapter 4 – Variable range hopping, 2002

14.Carden W. G., Lu H., Spencer J. A., Fairbrother D. H., McElwee-White L., Mechanism-based design of precursors for focused electron beam-induced deposition, MRS Communications 2018, 8, 343–357

15.Lukasczyk T., Schirmer M., Steinrück H. -P., Marbach H., Electron-Beam-Induced Deposition in Ultrahigh Vacuum: Lithographic Fabrication of Clean Iron Nanostructures, Small 2008, 4, No. 6, 841–846

16.Kumar R. T. P., Unlu I., Barth S., Ingolfsson O., Fairbrother D. H., Electron Induced Surface Reactions of $HFeCo_3(CO)_{12}$, a Bimetallic Precursor for Focused Electron Beam Induced Deposition (FEBID), J. Phys. Chem. C 2018, 122, 2648−2660

17.Puydinger dos Santos M. V., Szkudlarek A., Rydosz A., Guerra-Nuñez C., Béron F., Pirota K. R., Moshkalev S., Diniz J. A., Utke I., Comparative study of post-growth annealing of $Cu(hfac)_2$, $Co_2(CO)_8$ and $Me_2Au(acac)$ metal precursors deposited by FEBID, Beilstein J. Nanotechnol. 2018, 9, 91–101

18.Idigoras O., Nikulina E., Porro J. M., Vavassori P., Chuvilin A., Berger A., FEBID fabrication and magnetic characterization of individual nanoscale and micro-scale Co structures, Nanofabrication 2014, Volume 1: 23–34

19.Córdoba R., Fernández-Pacheco R., Fernández-Pacheco A., Gloter A., Magén C., Stéphan O., Ibarra M. R., De Teresa J. M., Nanoscale chemical and structural study of Co-based FEBID structures by STEM-EELS and HRTEM, Nanoscale Research Letters 2011, 6:592

20.Mehendale S., Mulders J. J. L., Trompenaars P. H. F., A new sequential EBID process for the creation of pure Pt structures from $MeCpPtMe_3$, Nanotechnology 24, 2013, 145303

21.Jurczyk J., Brewer C. R., Hawkins O. M., Polyakov M. N., Kapusta C., McElwee-White L., Utke I., Focused Electron Beam-Induced Deposition and Post-Growth Purification Using the Heteroleptic Ru Complex $(\eta^3\text{-}C_3H_5)Ru(CO)_3Br$, ACS Appl. Mater. Interfaces 2019, 11, 31, 28164–28171

22.Rohdenburg M., Boeckers H., Brewer C. R., McElwee - White L., Swiderek P., Efficient NH_3 - based process to remove chlorine from electron beam deposited ruthenium produced from $(\eta 3\text{ - }C_3H_5)Ru(CO)_3Cl$, Sci Rep 10, 2020, 10901

23.Haverkamp C., Sarau G., Polyakov M. N., Utke I., Puydinger dos Santos M. V., Christiansen S., Höflich K., A novel copper precursor for electron beam induced deposition, Beilstein J. Nanotechnol. 2018, 9, 1220–1227

24.Szkudlarek A., Rodrigues Vaz A., Zhang Y., Rudkowski A., Kapusta C., Erni R., Moshkalev S., Utke I., Formation of pure Cu nanocrystals upon post-growth annealing of Cu–C material

obtained from focused electron beam induced deposition: comparison of different methods, Beilstein J. Nanotechnol. 2015, 6, 1508–1517

25.Tamuliene J., Ab initio studies of silver precursors for FEBID: $Ag(PMe_3)_n$ n=2, 3, 4, Materials Physics and Mechanics 39, 2018, 21-26

26.Berger L., Madajska K., Szymanska I. B., Höflich K., Polyakov M. N., Jurczyk J., Guerra-Nuñez C., Utke I., Gas-assisted silver deposition with a focused electron beam, Beilstein J. Nanotechnol. 2018, 9, 224–232

27.Tamuliene J., Noll J., Frenzel P., Rüffer T., Jakob A., Walfort B., Lang H., Synthesis of [{$AgO_2CCH_2OMe(PPh_3)$}n] and theoretical study of its use in focused electron beam induced deposition, Beilstein J. Nanotechnol. 2017, 8, 2615–2624

28.Plank H., Winkler R., Schwalb C. H., Hütner J., Fowlkes JJ. D., Rack P. D., Utke I., Huth M., Focused Electron Beam-Based 3D Nanoprinting for Scanning Probe Microscopy: A Review, Micromachines 2020, 11(1), 48

29.Córdoba R., Barcones B., Roelfsema E., Verheijen M. A., Mulders J.J.L., Trompenaars P.H.F., Koopmans B., Functional nickel-based deposits synthesized by focused beam induced processing, Nanotechnol. Vol. 27, 2016, No. 6

30.Liu B., Lusk M. T., Ely J.F., Influence of Nickel Catalyst Geometry on the Dissociation Barriers of H_2 and CH_4: Ni_{13} versus Ni(111), J. Phys. Chem. C 2009, 113, 31, 13715–13722

31.Höflich K., Jurczyk J. M., Madajska K., Götz M., Berger L., Guerra-Nuñez C., Haverkamp C., Szymanska I., Utke I., Towards the third dimension in direct electron beam writing of silver, Beilstein J. Nanotechnol. 2018, 9, 842–849

32.Essaleh L., Wasim S.M., Marín G., Rincón C., Amhil S., Galibert J., Mott type variable range hopping conduction and magnetoresistance in p-type $CuIn_3Te_5$ semiconductor compound, Journal of Applied Physics 122, 2017, 015702

33.Plugaru R., Sandu T., Plugaru N., First principles study and variable range hopping conductivity in disordered Al/Ti/Mn-doped ZnO, Physics, Volume 2, 2012, Pages 190-197

34.Schirmer M., Walz M.-M., Vollnhals F. Lukasczyk T. Sandmann A., Chen C., Steinrück H. -P., Marbach H., Electron-beam-induced deposition and post-treatment processes to locally generate clean titanium oxide nanostructures on Si(100), Nanotechnol., 2011, Vol. 22, No. 8

35.Schulz G. J., Resonances in Electron Impact on Diatomic Molecules, Rev. Mod. Phys. 45, 1973, 423

36.Griffiths D. J., Introduction to Quantum Mechanics, Prentice Hall, 1994

37. Laporta V., Celiberto R., Wadehra J. M., Theoretical vibrational-excitation cross sections and rate coefficients for electron-impact resonant collision involving rovibrationally excited N_2 and NO molecules, Plasma Source Sci. Technol. 21, 2012, 055018

38.Munro J., Harrison S., Fujimoto M., Tennyson J., A dissociative electron attachment cross-section estimator, J Phys : Conf Ser 388, 2012, 012013

39.Machado L. E., Brescansin L. M., Lee M. T., Elastic and Rotational Excitation Cross Sections for Electron Scattering by Polyatomic Molecules, Branzilian Journal Physics, vol. 32, 2002, no. 3

40.Bull J. N., Lee J. W. L., Gardiner S. H., Vallance C., Account: An Introduction to Velocity-Map Imaging Mass Spectrometry (VMImMS), European Journal of Mass Spectrometry, 20(2), 2014, 117-129

41.Kling N. G., Paul D., Gura A., Laurent G., De S., Li H., Wang Z., Ahn B., Kim C. H., Kim T. K., Litvinyuk I.V., Cocke C.L., Ben-Itzhak I., Kim D., King M. F., Thick-lens velocity-map imaging spectrometer with high resolution for high-energy charged particles, JINST (Journal of Instrumentaiton), 9, 2014, P05005

42.Arnot F. L., Milligan J. C., A New Process of Negative Ion Formation, Proceedings of the Royal Society A, Volume 156, Issue 889, 1 September 1936

43.Loeb L. B., Formation of Negative Ions, 1956

44.Borisov A. G., Esaulov V. A., Negative ion formation in the scattering of atoms and ions from dielectric surfaces, J. Phys.: Condens. Matter 12 (2000) R177-R206

45.Hoseinzade M., Sadighzadeh A., Design and numerical simulations of thermionic electron gun, Chinese Physics C, September 2015

46.Fabrikant Ilya I., Eden Samuel, Mason Nigel J., Fedor Juraj, Recent Progress in Dissociative Electron Attachment: From Diatomics to Biomolecules. In: Ennio Arimondo, Chun C. Lin and Susanne F. Yelin, editors, Advances in Atomic, Molecular, and Optical Physics, Vol. 66, Burlington: Academic Press, 2017, pp. 545-657

47.Bull J. N., Lee J. W. L., Gardiner S. H., Vallance C., Account: An Introduction to Velocity-Map Imaging Mass Spectrometry (VMImMS), European Journal of Mass Spectrometry, 20(2), 2014, 117–129

48.Zhou Y., Meng Q., Mo Y., Neutral dissociation dynamics of O_2 in the photon range 14.26-15.20eV studied by XUV laser pump and UV laser probe method, Journal of Physics: Conference Series 488, 2014, 022034

49.Baklanov A. V., Janssen L. M. C., Parker D. H., Poisson L., Soep B., Mestdagh J. M., Gobert O., Direct mapping of recoil in the ion-pair dissociation of molecular oxygen by a femtosecond depletion method, J. Chem. Phys. 129, 2008, 214306

50.Dhouiba A., Guesmi H., DFT study of the M segregation on MAu alloys (M = Ni, Pd, Pt) in presence of adsorbed oxygen O and O_2, Chem. Phys. Lett., Vol. 521, 2012, pg. 98-103

51.Nandi D., Prabhudesai V. S., Krishnakumar E., Chatterjee A., Velocity Sliced Map Imaging for dissociative electron attachment, Review of Scientific Instruments 76, 2005, 053107

52.Shuman N., Miller T. M., Friedman J. F., Viggiano A. A., Electron Attachment to $Fe(CO)_n$ (n=0-5), J. Phys. Chem. A., 2013, 117, 6, 1102-1109

53.O'Malley T. F., Taylor H. S., Angular Dependence of Scattering Products in Electron-Molecule, Phys. Rev. 176, 1968, 207

54.Fehsenfeld F. C., Albritton D. L., Associative-detachment reactions of 0^- and 0_2^- by $O_2(^1\Delta_g)$, Canadian Journal of Chemistry, 1969, Vol. 47

55.Midey A., Dotan I., Viggiano A. A., Temperature Dependences for the Reactions of O^- and O_2^- with $O_2(a^1\Delta_g)$ from 200 to 700 K, J. Phys. Chem. A 2008, 112, 3040-3045

56.Carr J. M., Galiatsatos P. G., Gorfinkiel J. D., Harvey A. G., Lysaght M. A., Madden D., Mašín Z., Plummer M., Tennyson J., Varambhia H. N., UKRmol: a low-energy electron- and positron-molecule scattering suite, Eur. Phys. J. D, 2012, 66: 58

57.Tennyson J., A new algorithm for Hamiltonian matrix construction in electron–molecule collision calculations, J. Phys. B: At. Mol. Opt. Phys. 29 (1996) 1817–1828

58.Tennyson J., McKemmish L. K., Rivlin T., Low-temperature chemistry using the R-matrix method, Faraday Discuss., 2016, 195, 31

59.Cooper B., Tudorovskaya M., Mohr S., O'Hare A., Hanicinec M., Dzarasova A., Gorkfield J. D., Benda J., Mašin Z., Al-Refaie A. F., Knowles P. J., Tennyson J., Quantemol Electron Collisions (QEC): an enhanced expert system for performing electron molecule collision calculations using the R-matrix method, 2019, Atoms, Vol. 7, Pages 97

60.Descouvemont P., Baye D., The R-matrix Theory, Rep. Prog. Phys., 2010

61.Joshipura K. N., Mason N., Atomic-Molecular Ionization by Electron Scattering. Theory and Applications, 2019, Cambridge University Press, Edition 1

62.Song M.–Y., Yoon J.-S., Cho H., Karwasz G. P., Kokoouline V., Nakamura Y., Tennyson J., Cross Sections for Electron Collisions with Methane, J. Phys. Chem. Ref. Data, Vol. 44, No. 2, 2015

63.Zhao G.L., Bagayoko D., Predictive ab-initio computations of properties of ferroelectric materials, International Journal of Modern Physics B, 1999

64.Visser B.R., Addicoat M.A., Gascooke J.R., Lawrance W.D., Metha G.F., First spectroscopic observation of gold(I) butadiynylide: Photodetachment velocity map imaging of the AuC_4H anion, The Journal of Chemical Physics 145, 2016, 044320

65.Bagayoko D., Understanding density functional theory (DFT) and completing it in practice, AIP Advances 4, 2014, 127104

66.Franklin L., Ekuma C.E., Zhao G.L., Bagayoko D., Density functional theory description of electronic properties of wurtzite zinc oxide, Journal of Physics and Chemistry of Solids 74, 2013, 729–736730

67.Jarlborg T., Barbiellini B., Lin H., Markiewicz R.S., Bansil A., Renormalization of f-levels away from the Fermi energy in electron excitation spectroscopies: Density functional results of $Nd_{2-x}Ce_xCuO_4$, Phys. Rev. B 84, 2011, 045109

68.Foresman J. B., Frisch Æ., Exploring Chemistry with Electronic Structure Methods, Second Edition, 1993, Gaussian Inc.

69.Malhado J.P., Bearpark M.J., Hynes J.T., Non-adiabatic dynamics close to conical intersections and the surface hopping perspective, Front. Chem. Vol. 2, 2014, 97

70.Atchity G. J., Xantheas S. S., Ruedenberg K., Potential energy surfaces near intersections, J. Chem. Phys. 95, 1991, 1862–1876

71.von Neumann J., Wigner E., Uber merkwürdige diskrete Eigenwerte, Z. Phys., 1929, 30, 467

72.Olsen J., The CASSCF Method: A Perspective and Commentary, International Journal of Quantum Chemistry, 2011, Vol 111, 3267–3272

73.Paterson M.J., Bearpark M.J., Robb M.A., Blancafort L., Worth G.A., Conical intersections: A perspective on the computation of spectroscopic Jahn–Teller parameters and the degenerate 'intersection space', Phys. Chem. Chem. Phys., 2005, 7, 2100-211

74.De Teresa J.M., Fernández-Pacheco A., Córdoba R., Serrano-Ramón L., Sangiano S., Ibarra M.R., Review of magnetic nanostructures grown by focused electron beam induced deposition (FEBID), J. Phys. D.: Appl. Phys. 49, 2016, 243003

75.Allan M., Lacko M., Papp P., Matejcik S., Zlatar M., Fabrikant I.I., Kocisek J., Fedor J., Dissociative Electron Attachment and Electronic Excitation in $Fe(CO)_5$, Phys. Chem. Chem. Phys., 2018, 20, 11692

76.Read S. T., Metastable Induced Electron Spectroscopy of Iron Pentacarbonyl on Gold, University of Guelph, PhD Thesis, Ontario, 2014, Canada

77.Korobtsov V. V., Balashev V. V., Pisarenko T.A., Chusovitin E. A., Markidonov E. V., Fe interaction with native SiO_2 on Si(001) studied by RHEED, e-J. Surf. Sci. Nanotech. Vol. 5, 2007, 45-50

78.Pauling L., Soldate A. M., The Nature of the Bonds in the Iron Silicide FeSi and Related Crystals, Acta Cryst., 1948, 1, 212

79.Saito Y., Kawasaki R., Two-Dimensional Island Shape Determined by Detachment, J. Phys. Soc. Jpn., 2007, 76(7)

80.Fowkes F. M., Contact Angle, Wettability, and Adhesion, Chap. 6, Advances in Chemistry Series, Vol. 43, 1964, American Chemical Societies

81.Mohimi E., Zhang Z., Liu S., Mallek J. L. M., Girolami G. S., Abelson J. R., Area selective CVD of metallic films from molybdenum, iron, and ruthenium carbonyl precursors: Use of ammonia to inhibit nucleation on oxide surfaces, Journal of Vacuum Science & Technology A 36, 2018, 041507

82.Lengyel J., Papp P., Matejcik S., Kocisek J., Farnik M., Fedor J., Suppression of low-energy dissociative electron attachment in $Fe(CO)_5$ upon clustering, Beilstein J. Nanotechnol., 2017, 8, 2200-2207

83.Kotzian M., Rösch N., Schröder H., Zerner M.C., Optical Spectra of Transition-Metal Carbonyls: $Cr(CO)_6$, $Fe(CO)_5$ and $Ni(CO)_4$, J. Am. Chem. Soc., Vol. 111, No. 20, 1989

84.Engelking P.C., Lineberger W.C., Laser Photoelectron Spectrometry of the Negative Ions of Iron and Iron Carbonyls. Electron Affinity Determination for the Series Fe(CO)n, n=0,1,2,3,4, Journal of the American Chemical Society, 1979, 101:19

85.Chen X., Luo Z., Li J., Ning C., Accurate Electron Affinity of Iron and Fine Structures of Negative Iron ions, Scientific Reports, 2016, 6:24996

86.Rubner O., Engel V., Hachey M.R., Daniel C., A CASSCF/MR-CCI study of the excited states of $Fe(CO)_5$, Chemical Physics Letters 302, 1999, 489-494

87.Sushko G.B., Solov'yov I.A., Solov'yov A.V., Molecular dynamics for irradiation driven chemistry: application to the FEBID process, Eur. Phys. J. D, 2016, 70:21

88.Wnorowski K., Stano M., Barszczewska W., Jówko A., Matejčik Š., Electron ionization of $W(CO)_6$: Appearance energies, International Journal of Mass Spectrometry 314, 2012, 42-48

89.Winters R.E., Kiser R.W., Unimolecular decomposition of negative ions formed from the transition-metal carbonyls of Ni, Fe, Cr, Mo and W, J. Chem. Phys., 1966, 44, 1964

90.Wnorowski K., Stano M., Matias C., Denifl S., Barszczewska W., Matejčik Š., Low-energy electron interactions with tungsten hexacarbonyl – $W(CO)_6$, Rapid Commun. Mass Spectrom., 2012, 26, 2093-2098

91.Broquier M., Crépin C., Dubost H., Galaup J.-P., IR spectra and vibrational dephasing of the CO stretching mode in $W(CO)_6$ doped cryogenic matrices, Chemical Physics 341, 2007, 207-217

92.Thon R., Chin W., Chamma D., Gutiérrez-Quintanilla A., Chevalier M., Galaup J.-P., Crépin C., $W(CO)_6$ in cryogenic solids: A comparative study of vibrational properties, Journal of Luminescence 191, 2017, 78-86

93.Li J., Schreckenbach G., Ziegler T., First Bond Dissociation Energy of $M(CO)_6$ (M = Cr, Mo, W) Revisited: The Performance of Density Functional Theory and Influence of Relativistic Effects, J. Phys. Chem., 1994, 98, 4838-4841

94.Ershov K.S., Kochubei S.A., Baklanov A.V., Tungsten Isotope-Specific UV-Photodecomposition of $W(CO)_6$ at 266nm, J. Phys. Chem. A 2019, 123, 7751-7757

95.Wnorowski K., Stano M., Matias C., Denifl S., Matejčík Š., Low-energy electron interactions with tungsten hexacarbonyl – $W(CO)_6$, Rapid Communications in Mass Spectrometry, 2012, Volume 26, Issue 17

96.Winters R.E., Kiser R. W., Unimolecular decomposition of negative ions formed from the transition-metal carbonyls of Ni, Fe, Cr, Mo, and W, J. Chem. Phys., 1966, 44, 1964

97.Seebauer E.G., Allen C.E., Estimating surface diffusion coefficients, Progress in Surface Science, Vol. 49, No. 3, 1995, pp. 265-330

98.Tanaka H., Nakashima N., Yatsuhashi T., Anisotropic Coulomb Explosion of CO Ligands in Group 6 Metal Hexacarbonyls: $Cr(CO)_6$, $Mo(CO)_6$, $W(CO)_6$, J. Phys. Chem. A 2016, 120, 6917-6928

99.Mulders J.J.L., Nanofabrication, 2014, Vol 1, 74-7

100.Arai F., Liu P., Dong L., Nakajima M., Fukuda T., Electron beam induced deposition of conductive nanostructures with carbon nanotube emitters, 2003 Third IEEE Conference on Nanotechnology, 2003, Vol 2, 811-814

101.Shawrav M. M., Taus P., Wanzenboeck H. D., Schinnerl M., Stöger-Pollach M., Schwarz S., Steiger-Thirsfeld A., Bertagnolli E., Highly conductive and pure gold nanostructures grown by electron beam induced deposition, Scientific Reports 6, 2016, 34003

102.Marashdeh A., Tiesma T., van Velzen N. J. C., Harder S., Havenith R. W. A., De Hosson J. T. M., van Dorp W. F., The rational design of an Au(I) precursor for focused electron beam induced deposition, Beilstein J. Nanotechnol., 8, 2017, 2753-2765

103.Moulders J.J.L., Veerhoek J.M., Bosch E.G.T., Trompenaars P.H.F., Fabrication of pure gold nanostructures be electron beam induced deposition with ClAuCO

precursor: deposition characteristics and primary beam scattering effects, J. Phys. D Appl. Phys. 45, 2012, 475301

104. Galassi R., Oumarou C.S., Burini A., Dolmella A., Micozzi D., Vincenzettic S., Pucciarellic S., A study on the inhibition of dihydrofolate reductase (DHFR) from Escherichia coli by gold(I) phosphane compounds. X-ray crystal structures of (4,5 – dichloro – 1H – imidazolate – 1 – yl) triphenylphosphane - gold(I) and (4,5 – dicyano – 1Himidazolate – 1 – yl) – triphenylphosphane - gold(I), Dalton Trans., 2015, 44, 3043-3056
105. Gil-Rubio J., Vicente J., Gold trifluoromethyl complexes, Dalton Trans., 2015, 44, 19432-19442
106. Chang S.-Y., Uehara A., Booth S.G., Ignatyev K., Frederick J., Mosselmans W., Dryfe R.A.W., Schroeder S.L.M., Structure and bonding in Au(I) chloride species: a critical examination of X-ray absorption spectroscopy (XAS) data, RSC Adv. 2015, 5, 6912-6918
107. Ryu Y. J., Yoo C. S., Physical and chemical transformations of iron pentacarbonyl under pressure, Journal of Physics: Conference Series 500, 2014, 022011
108. Squibb R.J., Sapunar M., Ponzi A., Richter R., Kivimäki A., Plekan O., Finetti P., Sisourat N., Zhaunerchyk V., Marchenko T., Journel L., Guillemin R., Cucini R., Coreno M., Grazioli C., Di Fraia M., Callegari C., Prince K.C., Decleva., Simon M., Eland J.H.D., Došlić N., Feifel R., Piancastelli M.N., Acetylacetone photodynamics at a seeded free-electron laser, Nature Communications, 2018, 9:63
109. Steinbach J.F., Freiser H., Acetylacetone. In the Dual Role of Solvent and Reagent in Extraction of Metal Chelates, Analytical Chemistry, Volume 25, 1953, No. 6
110. Spiridonova J., Katerski A., Danilson M., Krichevskaya M., Krunks M., Acik I. O., Effect of the Titanium Isopropoxide: Acetylacetone Molar Ratio on the Photocatalytic Activity of TiO_2 Thin Films, Molecules 2019, 24, 4326
111. Lowrey A.H., George C., D'Antonio P., Karle J., Structure of Acetylacetone by Electron Diffraction, Journal of the American Chemical Society, 1971, 93:24
112. Caminati W., Grabow J.-U., The C_{2v} Structure of Enolic Acetylacetone, J. Am. Chem. Soc. 9 Vol. 128, 2006, No. 3, 857
113. Tayyari S.F., Milani-nejad F., Vibrational assignment of acetylacetone, Spectrochimica Acta Part A56, 2000, 2679–2691
114. Ogoshi H., Nakamoto K., Normal-Coordinate Analyses of Hydrogen-Bonded Compounds. V. The Enol Forms of Acetylacetone and Hexafluoroacetylacetone, J. Chem. Phys. 45, 1966, 3113

115.Chiavassa T., Verlaque P., Pizalla L., Roubin P., Vibrational studies of methyl derivatives of malonaldehyde: Determination of a reliable force field for β-dicarbonyl compounds, Spectrochim. Acta 50A, 1993, 343

116.Bjarnason E. H., Ómarsson B., Engmann S., Ómarsson F. H., Ingólfsson O., Dissociative electron attachment to titatinum tetrachloride and titanium tetraisopropoxide, Eur. Phys. J. D, 2014, 68, DOI:10.1140/epjd/e2014-50091-9

117.Hafizah N., Sopyan I., Nanosized TiO_2 Photocatalyst Powder via Sol-Gel Method: Effect of Hydrolysis Degree on Powder Properties, International Journal of Photoenergy, Vol. 2009, 962783, 8 pages

118.Wang H., Li B., Yan Z., Lu Z., Cheng R., Qian D., Fast synthesis of monodisperse TiO_2 submicrospheres via a modified sol-gel approach, Rare Metals, 2008, vol. 27, no. 1, pp. 1– 4

119.Koo K.-K., Park H.-S., Hwang U.-Y., Behaviour of Barium Acetate and Titanium Isopropoxide during the Formation of Crystalline Barium Titanate, Ind. Eng. Chem. Res. 2004, 43, 3, 728–734

120.Kim M.T., Deposition kinetics of silicon dioxide from tetraethylorthosilicateby PECVD, Thin Solid Films 360 (2000) 60-68

121.Sanogo O., Zachariah M.R., Kinetic Studies of the Reaction of Tetraethoxysilane with Oxygen Atoms, J. Electrochem. Soc., 144, 1997, 2919

122.Toth M., Lobo C., Friedli V., Szkudlarek A., Utke I., Continuum models of focused electron beam induced processing, Beilstein J. Nanotechnol. 2015, 6, 1518–1540

123.Ershov K.S., Kochubei S.A., Kiselev V.G., Baklanov A.V., Decomposition Pathways of Titanium Isopropoxide $Ti(OPr)_4$: New Insights from UV - Photodissociation Experiments and Quantum Chemical Calculations, J. Phys. Chem. A2018, 122, 1064 – 1070

124.Da Silva M.L.P., Riveros J.M., A comparative study of gas-phase ion/molecule reactions in $Si(OCH_3)_4$ and $Si(OC_2H_5)_4$, International Journal of Mass Spectrometry and Ion Processes 165/166 (1997) 83-95

125.Campostrini R., Carturan G., Soraro G., Traldi P., HYDROLYSIS AND POLYCONDENSATION OF $Si(OEt)_4$ II. Identification of chemical species in condensed phase by mass spectrometry with fast atom bombardment, Journal of Non-Crystalline Solids 108 (1989) 315-322

126.Nandanwar R., Singh P., Haque F.Z., Synthesis and characterization of SiO_2 nanoparticles by sol-gel process and its degradation of methylene blue, American Chemical Science Journal, 5(1): 1-10, 2015, Article no.ACSj.2015.001

127. Rohdenburg M., Martinović P., Ahlenhoff K., Koch S., Emmrich D., Gölzhäuser A., Swiderek P., Cisplatin as a Potential Platinum Focused Electron Beam Induced Deposition Precursor: NH_3 Ligands Enhance the Electron-Induced Removal of Chlorine, J. Phys. Chem. C 2019, 123, 35, 21774–21787
128. O'Regan C., Lee A., Holmes J.D., Petkova N., Trompenaars P., Mulders H., Electrical properties of platinum interconnects deposited by electron beam induced deposition of the carbon-free precursor, $Pt(PF_3)_4$, J. Vac. Sci. Technol. B, Vol. 31, No. 2, Mar/Apr 2013
129. Dias R.J., O'Regan C., Thrompenaars P., Romano-Rodriguez A., Holmes J.D., Mulder (Hans) J.J.L., Petkov N., Low resistivity Pt interconnects developed by electron beam assisted deposition using novel gas injector system, Journal of Physics: Conference Series 371, 2012, 012038
130. Ritz C.L., Bartell L.S., Molecular structure of $Pt(PF_3)_4$ by gas-phase electron diffraction, Journal of Molecular Structure, 31, 1976, 73-76
131. Zlatar M., Allan M., Fedor J., Excited States of $Pt(PF_3)_4$ and Their Role in Focused Electron Beam Nanofabrication, J. Phys. Chem. C 2016, 120, 19, 10667–10674
132. May O., Kubala D., Allan M., Dissociative electron attachment to $Pt(PF_3)_4$—a precursor for Focused Electron Beam Induced Processing (FEBIP), Physical Chemistry Chemical Physics, No. 9, 2012, 2979-2982
133. Rezaei S. D., Ho J., Hong NG R. J., Ramakrishna S., Yang J. K. W., On the correlation of absorption cross-section with plasmonic color generation, Optics Express 27652, Vol. 25, No. 22, 2017
134. Allan M., Electron scattering in $Pt(PF_3)_4$: Elastic scattering, vibrational and electronic excitation, Journal of Physics: Conference Series 388, 2012, 05206
135. Błachucki W., Szlachetko J., Hoszowska J., Dousse J.-Cl., Kayser Y., Nachtegaal M., Sá J., High Energy Resolution Off-Resonant Spectroscopy for X-Ray Absorption Spectra Free of Self-Absorption Effects, PRL 112, 2014, 173003
136. Hämäläinen J., Munnik F., Ritala M., Leskelä M., Atomic Layer Deposition of Platinum Oxide and Metallic Platinum Thin Films from $Pt(acac)_2$ and Ozone, Chem. Mater. 2008, 20, 6840–6846
137. Goswami J., Wang C.-G., Cao W., Dey S.K., MOCVD of Platinum Films from $(CH_3)_3CH_3CpPt$ and $Pt(acac)_2$: Nanostructure, Conformality, and Electrical Resistivity, Chem. Vap. Deposition No. 4, 2003, 9

138.Lewis F.D., Salvi G.D., Kanis D.R., Rainer M.A., Electronic Structure and Spectroscopy of Nickel(II), Palladium(II), and Platinum(II) Acetylacetonate Complexes, Inorg. Chem. 1993, 32, 1251-1258

139.Onuma S., Horioka K., Inoue H., Shibata S., The crystal structure of bis(acetylacetonato)platinum(II), Bull. Chem. Soc. Jpn., 53, 1980, 2679-2680

140.Battiston G.A., Gerbasi R., Rodriguez A., A Novel Study of the Growth and Resistivity of Nanocrystalline Pt Films Obtained from $Pt(acac)_2$ in the Presence of Oxygen or Water vapour, Chem. Vap. Deposition 2005, 11, No. 3

141.Di Bella S., Fragalá I., Granozz G., Electronic Structure of Transition-Metal Tetracoordinated Complexes. 1. Theoretical ab Initio and UV-Photoelectron Spectroscopy Study of Palladium(II) and Platinum(II) Square-Planar Acetylacetonate Complexes, Inorganic Chemistry, Vol. 25, 1986, No. 22

142.Yoshizawa M., Ono K., Kumazawa K., Kato T., Fujita M., Metal−Metal d−d Interaction through the Discrete Stacking of Mononuclear M(II) Complexes (M = Pt, Pd, and Cu) within an Organic-Pillared Coordination Cage, J. Am. Chem. Soc. 2005, 127, 31, 10800–10801

143.Merche D., Dufour T., Baneton J., Caldarella G., Debaille V., Job N., Reniers F., Fuel cell electrodes from organometallic platinum precursors: an easy atmospheric plasma approach, Plasma processes and polymers, 2016, Vol. 13, Issue 1, 91-104

144.Pearson R.G., Johnson D.A., The Rates and Mechanism of Substitution Reactions of Palladium(II)-Acetylacetonate Complexes, J. Am. Chem. Soc. 1964, 86, 19, 3983–3989

145.Queirós M. A. M., Robinson S.D., Complexes of the Platinum Metals. 13.1 ß-Diketonato Derivatives of Ruthenium, Osmium, and Iridium, Inorganic Chemistry, Vol. 17, 1978, No. 2

146.Süß D., Hubera S.E., Mauracher A., Comparative study of electronic-structure methods for platinum-containing molecules: bond lengths and bond dissociation energies, Eur. Phys. J. D, 2019, 73:135

147.Chen X., Chen J., Pan Z., Ye Q., Liu W., Yu Y., Chang Q., Novel Synthesis and Characterization of $[Pt(NH_3)_4](NO_3)_2$, Asian Journal of Chemistry Vol. 22, No. 8, 2010, 6493-6496

148.Lippert B., Lock C.J.L., Rosenberg B., Zvagulis M., cis-Di(nitrato(diamine))platinum(II), cis-$Pt(NH_3)_2(N0_3)_2$. Crystalline Structure and Vibrational Spectra, Inorganic Chemistry, Vol. 16, 1977, No. 6

149.Smolentsev A.I., Gubanov A.I., Zadesenets A.V., Plyusnin P.E., Baidina I.A., Korenev S.V., Structures of tetraammine salts $[Pt(NH_3)_4(NO_3)_2]$, $[Pd(NH_3)_4(NO_3)_2]$ and $[Pd(NH_3)_4]F_2H_2O]$, Journal of Structural Chemistry. Vol. 51, No. 4, 2010, pp. 709-713

150.von Kahlenberg V., Gelbrich T., Tessadria R., Klauser F., Crystal structure of cis-diamminebis (nitrito-jN)- platinum(II), Acta Cryst., 2015, E71, 366–370

151.Kinoshita K., Routsis K., Bett J.A.S., The thermal decomposition of platinum(II) and (IV) complexes, thermochimica Acta, vol. 10, Issue 1, 1974, 109-117

152.Oudenhuijzen M.K., Kooyman P.J., Tappel B., van Bokhoven J.A., Koningsberger D.C., Understanding the Influence of the Pretreatment Procedure on Platinum Particle Size and Particle-Size Distribution for SiO_2 Impregnated with $[Pt^{2+}(NH_3)_4](NO^{-}_3)_2$: A Combination of HRTEM, Mass Spectrometry, and Quick EXAFS, Journal of Catalysis 205, 2002, 135–146

153.Wang S., Sun Y. M., Wang Q., White J. M. J., Electron-beam induced initial growth of platinum films using $Pt(PF_3)_4$, Journal of vacuum science & technology B 22(4):1803 – 1806, 2004

154.Joshipura K. N., Mason N. J., Atomic-Molecular Ionization by Electron Scattering, Cambridge University Press, 2019

155.Laporta V., Celiberto R., Wadehra J. M., Theoretical vibrational-excitation cross sections and rate coefficients for electron-impact resonant collisions involving rovibrationally excited N_2 and NO molecules, Plasma Sources Sci. Technol. 21 (2012) 055018

156.Munro J., Harrison S., Fujimoto M., Tennyson J., A dissociative electron attachment cross-section estimator, 2012, J Phys: Conf Ser 388 012013

157.Lee J. W., Davidson K. L., Bush M. F., Kim H. I, Collision cross sections and ion structures: development of a general calculation method via high-quality ion mobility measurements and theoretical modeling, Analyst, 2017, 142, 4289–4298

158.Randolph S. J., Fowlkes J. D., Rack P. D., Focused, Nanoscale Electron-Beam-Induced Deposition and Etching, Critical Reviews in Solid State and Materials Sciences, 2006, 31:3, 55-89

159.Ma J., Mercer R. R., Barger M., Schwegler-Berry D., Cohen J. M., Demokritou P., Castranova V., Effects of amorphous silica coating on cerium oxide nanoparticles induced pulmonary responses, Toxicol Appl Pharmacol. 2015; 288(1): 63-73

160.Yang S., Yue W., Huang D., Chen C., Lin H., Yang X., A facile green strategy for rapid reduction of graphene oxide by metallic zinc, RSC Advances, 2012, 2, 8827–8832

161.de Vera P., Azzolini M., Sushko G., Abril I., Garcia-Molina R., Dapor M., Solov'yov I. A., Solov'yov A. V., Multiscale simulation of the focused electron beam induced deposition process, Sci Rep 10, 2020, 20827

162.Yakubovich A. V., Solov'yov A., Molecular dynamics simulations of bio-nano systems with MBN Explorer, Physics Procedia 40, 2013, 93 – 99

163.Komiya S., Kochi J.K., Reversible Linkage Isomerisms of ß-Diketonato Ligands. Oxygen-Bonded and Carbon-Bonded Structures in Gold(III) Acetylacetonate Complexes Induced by Phosphines, Journal of the American Chemical Society, j 99:11 / May 25, 1977

164.Wnuk J.D., Gorham J.M., Rosenberg S.G., van Dorp W.F., Madey T.-E., Hagen C. W., Fairbrother D. H., Electron beam irradiation of dimethyl acetylacetonate gold(III) adsorbed onto solid substrates, Journal of Applied Physics 107, 054301, 2010

165.Guzman J., Gates B.C., Reactions of $Au(CH_3)_2(acac)$ on γ-Al_2O_3: Characterization of the Surface Organic, Organometallic, Metal Oxide, and Metallic Species, Langmuir 2003, 19, 3897-3903

166.Zhongye Xie, Yan Tang, Yi Zhou, Qinyuan Deng, Surface and thickness measurement of transparent thin-film layers utilizing modulation-based structured-illumination microscopy, Vol. 26, No. 3, 5 Feb 2018, Optics Express, 2944

167.Engelhart D. P., Wagner R. J. V., Meling A., Wodtke A. M., Schäfer T., Temperature programmed desorption of weakly bound adsorbates on Au(111), Surface Science, Volume 650, 2016, Pages 11-16

168.Liberman A., Mendez N., Trogler W.C., Kummel A.C., Synthesis and surface functionalization of silica nanoparticles for nanomedicine, Surf Sci Rep. 2014 September-October; 69(2-3): 132–158

169.Cristoni S., Armelao L., Tondello E., Traldi P., Electrospray Ionization in the Study of Polycondensation of $Si(OEt)_4$, J. Mass Spectrom. 34, 1999, 1380–1382

170.Sayen S., Walcarius A., Electro-assisted generation of functionalized silica films on gold, Electrochemistry Communications 5 (2003) 341 – 348

171.Chun Y., Chen X., Yan A.-Z., Xu Q.-H., Chemical vapour deposition of $Si(OEt)_4$ on zeolite Hβ, Zeolites and Related Microporous Materials: State of the Art 1994, J. Weitkamp, H.G. Karge, H. Pfeifer and W. H. Blderich (Eds.), Studies in Surface Science and Catalysis, Vol. 84, 1035 – 1042

172.Rubio F., Rubio J., Oteo J.L., A FT-IR Study of the Hydrolysis of Tetraethylorthosilicate (TEOS), Spectroscopy Letters, 31(1), 1998, 199 – 219

173.Eo Y., Kim D., Bae B., Song K.-C., Lee T.-Y., Song S.-W., Coating of Tetraethylorthosilicate (TEOS)/Vinyltriethoxysilane (VTES) Hybrid Solution on Polymer Films, 1998, Journal of Sol - Gel Science and Technology 13, 409 – 413

174.Yio M.H.N., Wong H.S., Buenfeld N.R., 3D Monte Carlo simulation of backscattered electron signal variation across 2 pore-solid boundaries in cement-based materials, Cement and Concrete Research, 2016

175.Joy D. C., A Database of Electron-Solid Interactions, Scanning, 1995a, 17(4):270 – 275
176.Holm C., Simulation Methods in Physics 1, Institute for Computational Physics, Univ. of Stuttgart, 2012/2013
177.Fowkes F. M., Contact Angle, Wettability, and Adhesion, Chap. 6, Advances in Chemistry Series, Vol. 43, 1964, American Chemical Societies
178.Fowkes F. M., Chemistry and Physics of Interfaces, pp. 1-12, 1965, American Chemical Society, Washington, D.C.
179.Frieser R.G., Characterization of Thermally Grown SiO_2 Surfaces by Contact Angle Measurements, J. Electrochem. Soc.121, 1974, 669
180.Wolf D.E., Villain J., Growth with surface diffusion, Euro Phys. Lett., 13 (5), 1990, pp. 389-394
181.Seebauer E.G., Allen C.E., Estimating surface diffusion coefficients, Progress in Surface Science, Vol. 49, No. 3, 1995, pp. 265-330
182.Szekeres A., Alexandrova S., Lytvyn P., Kompitsas M., Oxidation of hydrogenated crystalline silicon as an alternative approach for ultrathin SiO_2 growth, Journal of Physics: Conference Series 10, 2005, 246–250
183.Wohllebe A., Hollander B., Mesters S., Dieker C., Crecelius G., Michelsen W., Mantl S., Surface diffusion of Fe and island growth of $FeSi_2$ on Si(111) surfaces, Thin Solid Films 287, 1996, 93-100
184.Sutton A. P., Chen J., Long-range Finnis–Sinclair potentials, Philosophical Magazine Letters, 1990, 61(3):139–146
185.Cagnetta F., Evans M. R., Marenduzzo D., Kinetic roughening in active interfaces, EPJ Web of Conferences 230, 2020, 00001
186.Korobtsov V. V., Balashev V. V., Pisarenko T.A., Chusovitin E. A., Markidonov E. V., Fe interaction with native SiO_2 on Si(001) studied by RHEED, e-J. Surf. Sci. Nanotech. Vol. 5, 2007, 45-50
187.Lengyel J., Pysanenko A., Swiderek P., Heiz U., Fárník M., Fedor J., Water-Assisted Electron-Induced Chemistry of the Nanofabrication Precursor Iron Pentacarbonyl, J. Phys. Chem. A 2021, 125, 9, 1919–1926
188.Gavagnin M., Wanzenboeck H.D., Belic D., Shawrav M.M., Persson A., Gunnarsson K., Svedlindh P., Bertagnolli E., Magnetic force microscopy study of shape engineered FEBID iron nanostructures, Phys. Status Solidi A 211, 2014, No. 2, 368-374
189.Lavrijsen R., Cordoba R. C., Schoenaker F. J., Ellis T. H., Barcones B., Kohlhepp J. T., Swagten H. J. M., Koopmans B., De Teresa J. M., Magen C., Ibarra M. R.,

Trompenaars P., Mulders J. J. L., Fe:O:C grown by focused-electron-beam-induced deposition: magnetic and electric properties, Nanotechnology 22, 2011, 025302

190.Gavagnin M., Wanzenboeck H. D., Shawrav M. M., Belic D., Wachter S., Waid S., Stoeger–Pollach S., Bertagnolli E., Focused Electron Beam-Induced CVD of Iron: A Practical Guide for Direct Writing, Chem. Vap. Deposition 2014, 20, 243–250

191.Philips J. M., Substrate selection for thin-film growth, MRS Bulletin/April 1995

192.Liu C. L., Cohen J. M, Adams J. B., Voter A. F., EAM study of surface self-diffusion of single adatoms of fcc metals Ni, Cu, Al, Ag, Au, Pd, and Pt, Surf. Sci. 253, 1991, 334-344

193.Liu S., Bönig L., Metiu H., Effect of small-cluster mobility and dissociation on the island density in epitaxial growth, Phys. Rev. B52, 1995, 2907-2913

194.Stoltze P., Simulation of surface defects, J. Phys.: Condens. Matter 6, 1994, 9495-9517

195.Boisvert G., Lewi L. J., Yelon A., Many-body nature of Meyer-Neidel compensation law for diffusion, Phys. Rev. Lett. 75, 1995, 469-472

196.Antczak G., Ehrlich G., Surface Diffusion. Metals, Metal Atoms, and Clusters, 2010, Cambridge University Press Peulon S., Legrand L., Antony H., Chaussé A., Electrochemical deposition of thin films of green rusts 1 and 2 on inert gold substrate, Electrochemistry Communications, 2003, Vol. 5, Issue 3, 208-213

197.Lilian L., François M., Refait Ph., Renaudin G., Lelaurain M., Génin J. M. R., Mechanisms of formation and transformation of Ni-Fe layered double hydroxides in SO_3^{2-} and SO_4^{2-} containing aqueous solutions, Solid State Sci., 2002

198.Baker T.A., Xu B., Liu X., Kaxiras E., Friend C.M., Nature of Oxidation of the Au(111) Surface: Experimental and Theoretical Investigation, J. Phys. Chem. C, Vol. 113, No. 38, 2009, 16561-16564

199.Portius P., Bühl M., George M. W., Grevels F.-W., Turner J. J., Structure and Dynamics of Iron Pentacarbonyl, Organometallics 2019, 38, 4288-4297

200.Hauchard C., Pépin C., Rowntree P., $Fe(CO)_5$ thin films adsorbed on Au(111) and on self-assembled monolayers: I. Structure, Langmuir 2005, 21, 9154-9165

201.Cahoon J. F., Sawye K. R., Schlegel J. P., Harris C. B., Determining transition-state geometries in liquids using 2D-Ir, Science 2008, 319, 1820-1823

202.Berry R. S., Correlation rates of intramolecular tunnelling processes with application to some group V compounds, J. Chem. Phys. 1960, 32, 933-938

203. Jang J. H., Lee J. G., Lee H., Xie Y., Schaefer H. F., III. Molecular structures and vibrational frequencies of iron carbonyls: $Fe(CO)_5$, $Fe_2(CO)_9$ and $Fe_3(CO)_{12}$, J. Phys. Chem. A 1998, 102, 5298-5304
204. Allmers T., Donath M., Growth and morphology of thin Fe films on flat and vicinal Au(111): a comparative study, New Journal of Physics 11, 2009, 103049
205. Cimatti I., Ninova S., Lanzilotto V., Malavolti L., Rigamonti L., Cortigiani B., Mannini M., Magnano E., Bondino F., Totti F., Cornia A., Sessoli R., UHV deposition and characterization of a mononuclear iron(III) β-diketonate complex on Au(111), Beilstein J Nanotechnol. 2014; 5: 2139–2148
206. Carraro G., Maccato C., Gasparotto A., Barreca D., Walter M., Mayrhofer L., Moseler M., Venzo A., Seraglia R., Marega C., An old workhorse for new applications: $Fe(dpm)_3$ as a precursor for low-temperature PECVD of iron(III) oxide, Phys Chem Chem Phys 2015, 17(17):11174-81
207. Zhang P., Mohimi E., Talukdar T. K., Abelson J. R., Girolami G. S., Iron CVD from iron pentacarbonyl: Growth inhibition by CO dissociation and use of ammonia to restore constant growth, Journal of Vacuum Science & Technology A 34, 2016, 051518
208. Lengyel J., Kočišek J., Fárník M., Fedor J., Self-Scavenging of Electrons in $Fe(CO)_5$ Aggregates Deposited on Argon Nanoparticles, J. Phys. Chem. C2016, 120, 7397-7402
209. Wanzenboeck H. D., Hochleitner G., Bertagnolli E., Perpendicular Iron Nanopillars by Electron Beam Induced Deposition, The Society for Micro- and Nanoelectronics – Biennial Report 2005/2006, 153-157
210. Sun X., Felicissimo M. P., Rudolf P., Silly F., NaCl multi-layer islands grown on Au(111)-(22 × √3) probed by scanning tunnelling microscopy, Nanotechnology 19, 2008, 495307
211. Rai A., Nayak J., Barman S. R., Chromium Nano-Islands on Au(111), e-J. Surf. Sci. Nanotech. Vol. 12, 2014, 49-52
212. Lu J., Bao D.-L., Qian K., Zhang S., Chen H., Lin X., Du S.-X., Gao H.-J., Identifying and Visualizing the Edge Terminations of Single-Layer $MoSe_2$ Island Epitaxially Grown on Au(111), ACS Nano 2017, 11, 1689−1695
213. Kara M., Sasabe H., Knoll W., Ordered nucleation of a self-assembled monolayer on Au(111) studied by scanning tunnelling microscopy, Thin Solid films 273, 1996, 66-69
214. Hanke F., Björk J., Structure and local reactivity of the Au(111) surface reconstruction, Phys. Rev. B 87, 2013, 235422

215.Mannie G. J. A., Lammich L., Li Y.-W., Niemantsverdriet J. W. H., Lauritsen J. V., Monolayer Iron Carbide Films on Au(111) as a Fischer–Tropsch Model Catalyst, ACS Catal. 2014, 4, 9, 3255–3260

216.Porrati F., Sachser R., Gazzardi G. C., Frabboni S., Huth M., Fabrication of FeSi and Fe3Si compounds by electron beam induced mixing of $[Fe/Si]_2$ and $[Fe_3/Si]_2$ multilayers grown by focused electron beam induced deposition, Journal of Applied Physics, 2016, 119, 234306

217.Demers H., Poirier-Demers N., Philips M. R., de Jonge N., Drouin D., Three-Dimensional Electron Energy Deposition Modeling of Cathodoluminescence Emission near Threading Dislocations in GaN and Electron-Beam Lithography Exposure Parameters for a PMMA Resist, Microsc. Microanal. 18, 2012, 1220-1228

218.Häupler B., Wild A., Schubert U. S., Carbonyls: Powerful Organic Materials for Secondary Batteries, Adv. Energy Materials, 2015, Vol. 5, 11, 1402034

219.Kumar T P R., Bjornsson R., Barth S., Ingólfsson O., Formation and decay of negative ion states up to 11 eV above the ionization energy of the nanofabrication precursor $HFeCo_3(CO)_{12}$, Chem. Sci., 2017, 8, 5949-5952

220.Jungwirth F., Knez D., Porrati F., Schuck A.G., Huth M., Plank H., Barth S., Vanadium and Manganese Carbonyls as Precursors in Electron-Induced and Thermal Deposition Processes. Nanomaterials 2022, 12, 1110

221.Porrati F., Barth S., Sachser R., Jungwirth F., Eltsov M., Frangakis A. S., Huth M., Binary Mn–Si nanostructures prepared by focused electron beam induced deposition from the precursor $SiH_3Mn(CO)_5$, J. Phys. D: Appl. Phys., 2018, 51, 455301

222.Kumar T P R. , Weirich P., Hrachowina L., Hanefeld M., Bjornsson R., Hrodmarsson H. R., Barth S., Fairbrother D. H., Huth M., Ingólfsson O., Electron interactions with the heteronuclear carbonyl precursor $H_2FeRu_3(CO)_{13}$ and comparison with $HFeCo_3(CO)_{12}$: from fundamental gas phase and surface science studies to focused electron beam induced deposition, Beilstein J. Nanotechnol. 2018, 9, 555–579

223.Thorman R. M., Jensen P. A., Yu J.-C., Matsuda S. J., McElwee-White L., Ingólfsson O., Fairbrother D. H., Electron-Induced Reactions of $Ru(CO)_4I_2$: Gas Phase, Surface, and Electron Beam-Induced Deposition, J. Phys. Chem. C 2020, 124, 19, 10593–10604

224.Chen X., Su Z., Zhang L., Tang M., Yu Y., Zhang L., Chen L., Iron Nanoparticle-Containing Silicon Carbide Fibers Prepared by Pyrolysis of $Fe(CO)_5$-Doped Polycarbosilane Fibers, Journal of American Ceramic Society, 2010, Vol. 93, 1, 89-95

225. Bilgilisoy E., Thorman R. M., Barclay M. S., Marbach H., Fairbrother D. H., Low Energy Electron- and Ion-Induced Surface Reactions of $Fe(CO)_5$ Thin Films, J. Phys. Chem. C 2021, 125, 32, 17749–17760

226. Massey S., Bass A. D., Sanche L., Role of Low-Energy Electrons (<35 eV) in the degradation of $Fe(CO)_5$ for Focused Electron Beam Induced Deposition Applications: Study by Electron Stimulated Desorption of Negative and Positive Ions, J. Phys. Chem. C 2015, 119, 22, 12708–12719

227. Henderson M. A., Ramsier R. D., Yates J. T., Low-energy electron induced decomposition of $Fe(CO)_5$ adsorbed on Ag(111), Surface Science, Vol 259, 1–2, 1991, 173-182

228. Indrajith S., Rousseau P., Huber B. A., Nicolafrancesco C., Domaracka A., Grygoryeva K., Nag P., Sedmidubská B., Fedor J., Kočišek J., Decomposition of Iron Pentacarbonyl Induced by Singly and Multiply Charged Ions and Implications for Focused Ion Beam-Induced Deposition, J. Phys. Chem. C 2019, 123, 16, 10639–10645

229. Zhao X., Di Q., Li M., Yang Q., Zhang Z., Guo X., Fan X., Deng K., Chen W., Zhang J., Fang J., Quan Z., Generalized Synthesis of Uniform Metal Nanoparticles Assisted with Tungsten Hexacarbonyl, Chem. Mater. 2019, 31, 12, 4325–4329

230. Nooraeipour M., Moghadam M., Tangestaninejad S., Mirkhani V., ohammadpoor-Baltork I., Iravani N., Multi-wall carbon nanotube supported tungsten hexacarbonyl: an efficient and reusable catalyst for epoxidation of alkenes with hydrogen peroxide, Journal of Coordination Chemistry, 2012, 65:2, 226-238

231. Guenzburger D., Baggio-Saitovitch E., De Paoli M. A., Manela H., On the photofragmentation of $Fe(CO)_5$. II. Molecular orbital studies of $Fe(CO)_n$, $1>n>5$, The Journal of Chemical Physics 80, 1984, 735

232. Mendes M., Regeta K., Ferreira da Silva F., Jones N. C., Hoffmann S. V., García G., Daniel C., Limão-Vieira P., Comprehensive investigation of the electronic excitation of $W(CO)_6$ by photoabsorption and theoretical analysis in the energy region from 3.9 to 10.8 eV, Beilstein J. Nanotechnol. 2017, 8, 2208–2218

233. Carden W. G., Pedziwiatr J., Abboud K. A., McElwee-White L., Halide Effects on the Sublimation Temperature of X–Au–L Complexes: Implications for Their Use as Precursors in Vapor Phase Deposition Methods, ACS Appl. Mater. Interfaces 2017, 9, 46, 40998–41005

234. Moonir Shawrav M., Wanzenboeck H. D., Belic D., Gavagnin M., Bethge O., Schinnerl M., Bertagnolli E., Mask-free prototyping of metal-oxide-semiconductor devices utilizing focused electron beam induced deposition, Phys. Status Solidi A211, 2014, No. 2, 375–381

235.Fleischer M., Weber-Bargioni A.,Virginia M., Altoe P., Schwartzberg A. M., James Schuck P., Cabrini S., Kern D. P., Gold Nanocone Near-Field Scanning Optical Microscopy Probes, ACS Nano 2011, 5, 4, 2570–2579

236.Huck C., Toma A., Neubrech F., Chirumamilla M., Vogt J., De Angelis F., Pucci A., Gold Nanoantennas on a Pedestal for Plasmonic Enhancement in the Infrared, ACS Photonics 2015, 2, 497−505

237.Pogrebnjak A., Pogorielov M., Viter R., Adhesive and Barrier Sublayers for Metal Nanofilms Active Elements of Hall Sensors, Nanomaterials in Biomedical Application and Biosensors (NAP-2019), Springer Proceedings in Physics, vol 244, 2020

238. Koops H. W. P., Weiel R., Kern D. P., Baum T. H., High-resolution electron-beam induced deposition, J. Vac. Sci. Technol. B 6(1), 1988

239.Curado N., GimØnez N., Miachin K., Aliaga-Lavrijsen M., Cornejo M. A., Jarzecki A. A., Contel M., Preparationof Titanocene–Gold Compounds Based on Highly Active Gold(I)-N-Heterocyclic Carbene Anticancer Agents: Preliminary in vitro Studies in Renal and Prostate Cancer Cell Lines, Chem. Med. Chem. 2019, 14, 1086 –1095

240. Bertranda B., Casini A., A golden future in medicinal inorganic chemistry: the promise of anticancer gold organometallic compounds, Dalton Trans., 2014, 43, 4209

241.Vallejosab S., Gràciaa I., Bravoa J., Figuerasa E., Hubálekb J., Cané C., Detection of volatile organic compounds using flexible gas sensing devices based on tungsten oxide nanostructures functionalized with Au and Pt nanoparticles, Talanta, Vol 139, 2015, Pages 27-34

242.Liu J., Liu J., Attarilar S., Wang C., Tamaddon M., Yang C., Xie K., Yao J., Wang4 J., Liu C., Tang Y., Nano-Modified Titanium Implant Materials: A Way Toward Improved Antibacterial Properties, Front. Bioeng. Biotechnol., Vol. 8, 2020, 576969

243.Galassi R., Simon Oumarou C., Burini A., Dolmella A., Micozzi D., Vincenzettic S., Pucciarellic S., A study on the inhibition of dihydrofolate reductase (DHFR) from Escherichia coli by gold(I) phosphane compounds. X-ray crystal structures of (4,5 – dichloro - 1H - imidazolate - 1 - yl) – triphenylphosphine - gold(I) and (4,5 – dicyano - 1Himidazolate – 1 - yl) – triphenylphosphine - gold(I), Dalton Trans., 2015, 44(7):3043-56

244.Scherer G. W., Structural Evolution of Sol-Gel Glasses, Yogyo-Kyokai-Shi, 95, [1], 1987

245.Soloviev A., Tufeu R., Sanchez C., Kanaev A. V., Nucleation Stage in the $Ti(OPri)_4$ Sol−Gel Process, J. Phys. Chem. B 2001, 105, 19, 4175–4180

246.Mathur S., Kuhn P., CVD of titanium oxide coatings: Comparative evaluation of thermal and plasma assisted processes, Surface and Coatings Technology, Vol. 201, Issues 3–4, 2006, 807-814

247.Pillai S. C., Periyat P., George R., McCormack D. E., Seery M. K., Hayden H., Colreavy J., Corr D., Hinder S. J., Synthesis of High-Temperature Stable Anatase TiO2 Photocatalyst J. Phys. Chem. C 2007, 111, 4, 1605–1611

248.Petrella A., Tamborra M., Curri M. L., Cosma P., Striccoli M., Cozzoli P. D., Agostiano A., Colloidal TiO_2 Nanocrystals/MEH-PPV Nanocomposites: Photo(electro)chemical Study J. Phys. Chem. B 2005, 109, 4, 1554–1562

249.Campostrini R., Carturan G., Pelli B., Traldi P., Hydrolysis and polycondensation of $Si(OEt)_4$: A mass spectrometry approach to the definition of reaction intermediates in the presence of acid or basic catalysts. Part 1, Journal of Non-Crystalline Solids, Vol 108, Issue 2, 1989, 143-149

250. Watanabe R., Yokoi T., Kobayashi E., Otsuka Y., Shimojima A., Okubob T., Tatsumia T., Extension of size of monodisperse silica nanospheres and their well-ordered assembly, Journal of Colloid and Interface Science, Vol 360, Issue 1, 2011, 1-7

251.Reddy K. R., Hassan M., Gomes V. G., Hybrid nanostructures based on titanium dioxide for enhanced photocatalysis, Applied Catalysis A: General, Vol 489, 2015, 1-16

252.Manzano M., Vallet-Regí M., Mesoporous Silica Nanoparticles for Drug Delivery, Adv. Funct. Mater.2020, 30, 1902634

253.Liab T., Shib S., Goel S., Shen X., Xie X., Chen Z., Zhang H., Li S., Qin X., Yang H., Wu C., Liu Y., Recent advancements in mesoporous silica nanoparticles towards therapeutic applications for cancer, Acta Biomaterialia, Vol 89, 2019, 1-13

254.Rosenholm J. M., Mamaeva V., Sahlgren C., Lindén M., Nanoparticles in targeted cancer therapy: mesoporous silica nanoparticles entering preclinical development stage, Nanomedicine Review, Vol. 7, 2011, No 1

255.Ju S., Nguyen V. L., Watekar P. R.; Kim B. H., Jeong C., Boo S., Kim C. J., Han W.-T., Fabrication and Optical Characteristics of a Novel Optical Fiber Doped with the Au Nanoparticles, Journal of Nanoscience and Nanotechnology, Vol 6, Number 11, 2006, pp. 3555-3558(4)

256.Belhadj Miled O., Hafedh B. O., Livage J., pH sensor based on a detection sol–gel layer onto optical fiber, Materials Science and Engineering: C, Vol 21, Issues 1–2, 2002, Pg 183-188

257.Ab Rahman I., Padavettan V., Synthesis of Silica Nanoparticles by Sol-Gel: Size-Dependent Properties, Surface Modification, and Applications in Silica-Polymer Nanocomposites—A Review, Journal of Nanomaterials, Vol 2012, 132424

258.Bret T., Jonckheere R., Van den Heuvel D., Baur C., Waiblinger M., Baralia G., Closing the gap for EUV mask repair, Proceedings Vol 8322, Extreme Ultraviolet (EUV) Lithography III; 2012, 83220C

259.Caminade A.-M., Majoral J.-P., Nanomaterials Based on Phosphorus Dendrimers, Acc. Chem. Res. 2004, 37, 6, 341–348

260.Zhao G., Giolando D. M., Kirchhoff J. R., Chemical Vapor Deposition Fabrication and Characterization of Silica-Coated Carbon Fiber Ultramicroelectrodes, Anal. Chem. 1995, 67, 2592-2598

261.Kopyra J., Rabilloud F., Wierzbicka P., Abdoul-Carime H., Energy-Selective Decomposition of Organometallic Compounds by Slow Electrons: The Case of Chloro(dimethyl sulfide)gold(I), J. Phys. Chem. A 2021, 125, 4, 966–972

262.Chang S.-Y., Uehara A., Booth S. G., Ignatyev C., Frederick J., Mosselmans W., Dryfea R. A. W., Schroeder S. L. M., Structure and bonding in Au(I) chloride species: a critical examination of X-ray absorption spectroscopy (XAS) data, RSC Adv., 2015, 5, 6912

263.Richardson J.H., Stephenson L.M., Brauman J.I., Photodetachment of electrons from trifluoromethyl and trifluorosilyl ions the electron affinities of CF_3 and SiF_3, Chem. Phys. Lett., 1975, 30, 17

264.Sirakov I., Becker B., Capote R., Kopecky S., Massimi S., Pronyaev V., Schillebeeckx P., Trkov A., Žerovnik G., Evaluation of Neutron Induced Reaction Cross Sections on Gold, JRC Scientific and Policy Reports, 2013, ISBN 978-92-79-28319-2

265.Fischer W., Baltz A. J., Blaskiewicz M., Gassner D., Drees K. A., Luo Y., Minty M., Thieberger P., Pshenichnov I. A., Measurement of the total cross section of gold - gold collisions at square root [sNN] = 200 GeV, Conference, 7th International Particle Accelerator Conference (IPAC'16),BEXCO, Busan, Korea, May 8 – 13, 2016

266.Hannaske R., Elekes Z., Beyer R., Junghans A., Bemmerer D., Birgersson E., Ferrari A., Grosse E., Kempe M., Kögler T., Marta M., Massarczyk R., Matic A., Schramm G., Schwengner R., Wagner A., Neutron total cross section measurements of gold and tantalum at the nELBE photoneutron source, Eur. Phys. J. A 49, 137 (2013)

267.Carden W. G., Thorman R. M., Unlu I., Abboud K. A., Fairbrother D. H., McElwee-White L., Design, Synthesis, and Evaluation of CF_3AuCNR Precursors for Focused Electron Beam-Induced Deposition of Gold, ACS Appl. Mater. Interfaces 2019, 11, 11976−11987

268.Ómarsson B., Engmann S., Ingólfsson O., Dissociative electron attachment to the complexation ligands hexafluoroacetylacetone, trifluoroacetylacetone and acetylacetone; a comparative experimental and theoretical study, RSC Adv., 2014, 4, 33222-33235

269.Weitzer A., Huth M., Kothleitner G., Plank H., Expanding FEBID-Based 3D-Nanoprinting toward Closed High-Fidelity Nanoarchitectures, ACS Appl. Electron. Mater. 2022, 4, 2, 744–754

270. Kolb F., Schmoltner K., Huth M., Hohenau A., Krenn J., Klug A., List E. J. W., Plank H., Variable tunneling barriers in FEBID based PtC metal-matrix nanocomposites as a transducing element for humidity sensing, Nanotechnology 24, 305501
271. Wartelle A., Pablo-Navarro J., Staňo M., Bochmann S., Pairis S., Rioult M., Thirion C., Belkhou R., de Teresa J. M., Magén C., Transmission XMCD-PEEM imaging of an engineered vertical FEBID cobalt nanowire with a domain wall, Nanotechnology 29, 4, 045704
272. Hinum-Wagner J., Kuhness D., Kothleitner G., Winkler R., Plank H., FEBID 3D-Nanoprinting at Low Substrate Temperatures: Pushing the Speed While Keeping the Quality, Nanomaterials 2021, 11, 1527
273. Fernández-Pacheco A., Skoric L., De Teresa J. M., Pablo-Navarro J., Huth M., Dobrovolskiy O. V., Writing 3D Nanomagnets Using Focused Electron Beams, Materials 2020, 13, 3774
274. Winhold M., Schwalb C. H., Porrati F., Sachser R., Frangakis A. S., Kämpken B., Terfort A., Auner N., Huth M., Binary Pt–Si Nanostructures Prepared by Focused Electron-Beam-Induced Deposition, ACS Nano 2011, 5, 12, 9675–9681
275. Thorman R. M., Kumar T. P. R., Fairbrother D. H., Ingólfsson O., The role of low-energy electrons in focused electron beam induced deposition: four case studies of representative precursors, Beilstein J. Nanotechnol. 2015, 6, 1904–1926
276. Lau Y. M., Chee P. C., Thong J. T. L., Ng V., Properties and applications of cobalt based material produced by electron-beam induced deposition, J. Vac. Sci. Technol. A. 20, 2002, 1295
277. Utke I., Michler J., Gasser P., Santschi C., Laub D., Cantoni M., Buffat P. A., Jiaoand C., Hoffmann P., Cross Section Investigations of Compositionsand Sub-Structures of Tips Obtained byFocused Electron Beam Induced Deposition, Adv. Eng. Materials, 2005,7, No. 5
278. Fernández-Pacheco A., De Teresa J. M., Córdoba R., Ibarra M. R., Magnetotransport properties of highquality cobalt nanowires grown by focused-electron-beam induced deposition, J. Phys. D: Appl. Phys., 2009, 42, 055005
279. Lukasczyk T., Schirmer M., Steinruck H. P., Marbach H., Electron-beam-induced deposition in ultrahigh vacuum: lithographic fabrication of clean iron nanostructures, Small 4, 2009, 841–6
280. Cordoba Castillo R. M., Barcones B., Roelfsema E., Verheijen M. A., Mulders J. J. L., Trompenaars P. H. F., Koopmans B., Functional nickel-based deposits synthesized by focused beam induced processing, Nanotechnology, 27(6), 2016, 1-11
281. Almeida T., McGrouther D., Kovacs A., Dunin-Borkowski R., McVitie S., Effect of annealing on the magnetic states of FEBID-grown cobalt nanopatterns examined by off-axis electron holography, Journal of Microscopy, Vol. 279, Issue 3 2020, pp. 217–221

282.Idigoras O., Nikulina E., Porro J. M., Vavassori P., Chuvilin A., Berger A., FEBID fabrication and magnetic characterization of individual nano-scale and micro-scale Co structures, Nanofabrication 2014; Volume 1: 23–34

283.Gazzadi G. C., Mulders J. J. L., Trompenaars P., Ghirri A., Rota A., Affronte M., Frabboni S., Characterization of a new cobalt precursor for focused beam deposition of magnetic nanostructures, Microelectronic Engineering, Vol 88, Issue 8, 2011, Pg 1955-1958

284.Belić D., Shawrav M. M., Gavagnin M., Stöger-Pollach M., Wanzenboeck H. D., Bertagnolli E., Direct-Write Deposition and Focused-Electron-Beam-Induced Purification of Gold Nanostructures, ACS Appl. Mater. Interfaces 2015, 7, 4, 2467–2479

285.Perentes A., Hoffmann P., Focused Electron Beam Induced Deposition of Si-Based Materials From SiOxCy to Stoichiometric SiO_2: ChemicalCompositions, Chemical-Etch Rates, and Deep UltravioletOptical Transmissions, Chem. Vap. Deposition 2007,13, 176–184

286.Perentes A., Hoffmann P., Oxygen assisted focused electron beam induced deposition of Si-containing materials: Growth dynamics, J. of Vac. Science & Technology B: Microelectronics and Nanometer Structures Processing, Measurement, and Phenomena 25, 2007, 2233

287.Dyck O., Zhang C., Rack P. D., Fowlkes J. D., Sumpter B., Lupini A. R., Kalinin S. V., Jesse S., Electron-beam introduction of heteroatomic Pt–Si structures in graphene, Carbon, Vol 161, 2020, Pages 750-757

288.Porrati F., Sachser R., Walz M. - M., Vollnhals F., Steinrück H. -P., Marbach H., Huth M., Magnetotransport properties of iron microwires fabricated by focused electron beam induced autocatalytic growth, J. Phys. D: Appl. Phys. 44, 2011, 425001

289.Hochleitner G., Steinmair M., Lugstein A., Roediger P., Wanzenboeck H. D., Bertagnolli E., Focused electron beam induced deposition of gold catalyst templates for Si-nanowire synthesis, Nanotechnology 22, 1, 2010, 015302

290.Porrati F., Kämpken B., Terfort A., Huth M., Fabrication and electrical transport properties of binary Co-Si nanostructures prepared by focused electron beam-induced deposition, Journal of Applied Physics 113, 2013, 053707

291.Chapman G., Masteghin M. G., Cox D. C., Clowes S. K., Focused electron beam deposited silicon dioxide derivatives for nano-electronic applications, Materials Science in Semiconductor Processing, Vol 147, 2022, 106736

292.Baum T. H., Jones C. R., Laser chemical vapor deposition of gold, Appl. Phys. Lett. 47 (5), 1985

293.Baum T. H., Jones C. R., Laser chemical vapor deposition of gold: Part II, J. Vac. Sci. Technol. B 4 (5), 1986

294.Prati L., Villa A., The Art of Manufacturing Gold Catalysts, Catalysts 2012, 2(1), 24-37

295.Feurer E., Suhr H., Preparation of Gold Films by Plasma-CVD, Appl. Phys. A 44, 1987, 171-175

296.Guzman J., Gates B.C., Reactions of Au(CH3)2(acac) on γ-Al_2O_3: Characterization of the surface organic, organometallic, metal oxide, and metallic species, Langmuir 2003, 19, 3897–3903

297.Okumura M., Tsubota S., Haruta M., Preparation of supported gold catalysts by gas-phase grafting of gold acethylacetonate for low-temperature oxidation of CO and of H_2, J. Mol. Catal. A 2003, 199, 73–84

298.Chen Y.J., Yeh C.T., Deposition of highly dispersed gold on alumina support. J. Catal. 2001, 200, 59–68

299.Basova T. V., Hassan A., Morozovaa N. B., Chemistry of gold(I, III) complexes with organic ligands as potential MOCVD precursors for fabrication of thin metallic films and nanoparticles, Coordination Chemistry Reviews, Vol 380, 2019, Pg 58-82

300.Winkler R., Schmidt F.-P., Haselmann U., Fowlkes J. D., Lewis B. B., Kothleitner G., Rack P. D., Plank H., Direct-Write 3D Nanoprinting of Plasmonic Structures, ACS Appl. Mater. Interfaces 2017, 9, 9, 8233–8240

301.Parkhomenko R. G., Trubin S. V., Turgambaeva A. E., Igumenov I. K., Deposition of pure gold thin films from organometallic precursors, Journal of Crystal Growth, Vol 414, 2015, Pg 143-150

302.Mäkelä M., Hatanpää T., Mizohata K., Räisänen J., Ritala M., Leskelä M., Thermal Atomic Layer Deposition of Continuous and Highly Conducting Gold Thin Films, Chem. Mater. 2017, 29, 14, 6130–6136

303.Carden W. G., Pedziwiatr J., Abboud K. A., McElwee-White L., Halide Effects on the Sublimation Temperature of X–Au–L Complexes: Implications for Their Use as Precursors in Vapor Phase Deposition Methods, ACS Appl. Mater. Interfaces 2017, 9, 46, 40998–41005

304.De Los Santos V. L., Lee D., Seo J., Lizbet Leon F., Bustamante D. A., Suzuki S., Majima Y., Mitrelias T., Ionescu A., Barnes C. H. W.,Crystallization and surface morphology of Au/SiO2 thin films following furnace and flame annealing, Surface Science 603, 2009, 2978–2985

305.Bessonov A. A., Morozova N. B., Gelfond N. V., Semyannikov P. P., Trubin S. V., Shevtsov Y. V., Shubin Y. V., Igumenov I. K., Dimethylgold(III) carboxylates as new precursors for gold CVD, Surface and Coatings Technology, Vol 201, 22–23, 2007, Pg 9099-9103

306.Lengyel J., Pysanenko A., Swiderek P., Heiz U., Fárník M., Fedor J., Water-Assisted Electron-Induced Chemistry of the Nanofabrication Precursor Iron Pentacarbonyl, J. Phys. Chem. A 2021, 125, 9, 1919–1926

307.Ryu Y. J., Yoo C. S., Physical and chemical transformations of iron pentacarbonyl under pressure, Journal of Physics: Conference Series 500, 2014, 022011

308.Wanzenboeck H. D., Hochleitner G., Bertagnolli E., Perpendicular Iron Nanopillars by Electron Beam Induced Deposition, The Society for Micro- and Nanoelectronics – Biennial Report 2005 – 2006

309.Thorman R. M., Matsuda S. J., McElwee-White L., Fairbrother D. H., Identifying and Rationalizing the Differing Surface Reactions of Low-Energy Electrons and Ions with an Organometallic Precursor, J. Phys. Chem. Lett. 2020, 11, 6, 2006–2013

310.Rodríguez L. A., Deen L., Córdoba R., Magén C., Snoeck E., Koopmans B., De Teresa J. M., Influence of the shape and surface oxidation in the magnetization reversal of thin iron nanowires grown by focused electron beam induced deposition, Beilstein J. Nanotechnol. 2015, 6, 1319–1331

311.Puydinger dos Santos M. V., Barth S., Béron F., Pirota K. R., Pinto A. L., Sinnecker J. P., Moshkalev S., Diniz J. A., Utke I., Magnetoelectrical Transport Improvements of Postgrowth Annealed Iron–Cobalt Nanocomposites: A Possible Route for Future Room-Temperature Spintronics, ACS Appl. Nano Mater. 2018, 1, 7, 3364–3374

312.Córdoba R., Han D. -S., Koopmans B., Manipulating the switching in modulated iron nanowires grown by focused electron beam induced deposition, Microelectronic Engineering, Vol 153, 2016, Pg 60-65

313.Fortouna Y., de Vera P., Verkhovtsev A., Solov'yov A. V., Molecular dynamics simulations of sodium nanoparticle deposition on magnesium oxide, Theoretical Chemistry Accounts, Vol 140, 2021, 84

314.Aviziotis I. G., Duguet T., Vahlas C., Boudouvis A. G., Combined Macro/Nanoscale Investigation of the Chemical Vapor Deposition of Fe from $Fe(CO)_5$, Adv. Mater. Interfaces 2017, 4, 1601185

315.Prosvetov A., Verkhovtsev A. V., Sushko G., Solov'yov A. V., Irradiation-driven molecular dynamics simulation of the FEBID process for $Pt(PF_3)_4$, Beilstein J. Nanotechnol. 2021, 12, 1151–1172

316.Chen X.-B., Fang W.-H., Phillips D. L., Theoretical Studies of the Photochemical Dynamics of Acetylacetone: Isomerization, Dissociation, and Dehydration Reactions, J. Phys. Chem. A 2006, 110, 4434-4441

317. Glessi C., Mahgoub A. , Hagen C. W., Tilset M., Gold(I) N-heterocyclic carbene precursors for focused electron beam-induced deposition, Beilstein J. Nanotechnol. 2021, 12, 257–269
318. Illenberger E., Momigny J., Gaseous Molecular Ions: An Introduction to Elementary Processes Induced by Ionization (Topics in Physical Chemistry), Steinkopff, 1992
319. Krishnan C. V., Garnett M., Hsiao H. S., Chu B., Solute-Solvent Interactions from Impedance Measurements: 'π –way' Conduction and Water Structure-Enforced Ion Pair Formation in Aqueous Lidocaine Hydrochloride, Int. J. Electrochem. Sci., 4, 2006, 1085 – 1099
320. Prabhudesai V.S., Nandi D., Krishnakumar E., On the presence of the $^4\Sigma_u$ resonance in dissociative electron attachment to O_2, J. Phys. B: At. Mol. Opt. Phys. 39, 2006, L277 – L283
321. Colliex C., Seeing and measuring with electrons: Transmission electron microscopy today and tomorrow – An introduction,' C. R. Physique 15, 2014, 101-105
322. Ray F. Egerton, Physical Principles of Electron Microscopy. An Introduction to TEM, SEM and AEM, Springer, 2005

ANNEX 1. $Fe(CO)_5$ COMPUTATIONAL PARAMETERS

The computational parameters used for the $Fe(CO)_5$ cross-section calculations are presented below. We declared a separate user defined basis set that can be viewed separately for O, C and Fe.

Atomic coordinates of $Fe(CO)_5$

Atom Label	X (angstroms)	Y (angstroms)	Z (angstroms)
Fe1	0	0	0
C2	0	-2.04	0
C3	0	0	1.846
C4	1.599	-0	-0.923
C5	-1.599	-0	-0.923
C6	0	2.04	0
O7	0	-3.144	0
O8	0	0	2.962
O9	2.565	-0	-1.481
O10	-2.565	-0	-1.481
O11	0	3.144	0

Table A1. Atomic coordinates for $Fe(CO)_5$ used in Quantemol-N cross-sections determination

Basis Set in SUPERMOLECULE format Fe:

20 7 0

4316265.0000000 8.048803E-06 -4.155954E-06 9.532178E-07 -2.063008E-07 -4.009367E-07 -6.966042E-07 0.0000000

646342.4000000 6.258306E-05 -3.231401E-05 7.414605E-06 -1.604169E-06 -3.189255E-06 -5.568036E-06 0.0000000

147089.7000000 0.0003290239 -0.0001699525 3.898393E-05 -8.438437E-06 -1.623079E-05 -2.813684E-05 0.0000000

41661.5200000 0.001387355 -0.0007171369 0.0001647152 -3.563151E-05 -7.15792E-05 -0.0001252418 0.0000000

13590.7700000 0.005023256 -0.002603625 0.000598598 -0.0001295998 -0.0002463958 -0.0004260787 0.0000000

4905.7500000 0.0161014 -0.008399109 0.00194239 -0.0004201534 -0.0008544907 -0.00149906 0.0000000

1912.7460000 0.04590034 -0.02434109 0.005687237 -0.001231954 -0.002307593 -0.003979103 0.0000000

792.6043000 0.1136154 -0.06251948 0.01501329 -0.003248922 -0.006728292 -0.01185686 0.0000000

344.8065000 0.2283869 -0.1365929 0.03452455 -0.007493717 -0.01366165 -0.02346734 0.0000000

155.8999000 0.3221159 -0.2312707 0.0649582 -0.01410102 -0.0306224 -0.05467736 0.0000000

72.2309100 0.2383661 -0.2383734 0.07716194 -0.0169160 -0.02631137 -0.0439382 0.0000000

32.7250600 0.07404667 0.03123837 -0.01873411 0.004218996 -0.009760183 -0.02376103 0.0000000

15.6676200 0.09214197 0.5086818 -0.3009185 0.0683381 0.1801906 0.3435928 0.0000000

7.5034830 0.0933979 0.4987695 -0.4554661 0.1098201 0.1529634 0.3192960 0.0000000

3.3122230 0.01573965 0.09033552 0.1286463 -0.04009005 0.05505413 -0.1343207 0.0000000

1.5584710 -0.0004186682 -0.006005337 0.7183316 -0.2174739 -0.9551364 -2.2210200 0.0000000

0.6839140 5.376318E-05 0.0002312454 0.4051743 -0.2465135 0.2586813 2.5711420 0.0000000

0.1467570 -3.816654E-05 -0.000564368 0.02168227 0.2731435 1.8340490 -0.2292404 0.0000000

0.0705830 4.319603E-05 0.000499226 -0.008343566 0.5748321 -0.9333240 -1.8324520 0.0000000

0.0314490 0.0000000 0.0000000 0.0000000 0.0000000 0.0000000 0.0000000 1.0000000

16 6 0

17745.6900000 0.0000410 -0.0000150 0.0000030 0.0000050 0.0000110 0.0000000

4200.7210000 0.0003690 -0.0001300 0.0000290 0.0000420 0.0000870 0.0000000

1364.4290000 0.0021290 -0.0007510 0.0001650 0.0002410 0.0005410 0.0000000

522.0806000 0.0093690 -0.0033290 0.0007340 0.0010850 0.0022260 0.0000000

221.4595000 0.0330970 -0.0119120 0.0026260 0.0038310 0.0085930 0.0000000

100.9096000 0.0944310 -0.0349330 0.0077250 0.0114230 0.0233390 0.0000000

48.4011500 0.2080770 -0.0799890 0.0177330 0.0257920 0.0588440 0.0000000

23.9853600 0.3323330 -0.1346360 0.0300550 0.0448180 0.0882890 0.0000000

12.1825000 0.3329870 -0.1385980 0.0310940 0.0445980 0.1231920 0.0000000

6.2422980 0.1568430 0.0302780 -0.0100480 -0.0111770 -0.0631860 0.0000000

3.1109440 0.0215490 0.3332160 -0.0883060 -0.1381340 -0.3549020 0.0000000

1.5099580 -0.0020950 0.4561530 -0.1298240 -0.1882850 -0.6197080 0.0000000

0.7108450 -0.0017390 0.2850510 -0.0769370 -0.1073990 0.8129860 0.0000000

0.2731900 -0.0003000 0.0461440 0.2126610 0.4448630 0.8191180 0.0000000

0.1042330 0.0000290 -0.0032490 0.5730610 0.6402390 -0.9017050 0.0000000

0.0382910 0.0000000 0.0000000 0.0000000 0.0000000 0.0000000 1.0000000

8 4 0

113.3440000 0.0035300 -0.0038900 0.0056950 0.0000000

33.6414000 0.0257840 -0.0284420 0.0420010 0.0000000

12.3310000 0.0991190 -0.1124290 0.1735400 0.0000000

4.9947800 0.2390730 -0.2742570 0.4101570 0.0000000

2.0728000 0.3571990 -0.3155460 0.1132520 0.0000000

0.8307530 0.3621880 0.0571090 -0.7696800 0.0000000

0.3091780 0.2364610 0.5636040 -0.0316430 0.0000000

0.1001300 0.0000000 0.0000000 0.0000000 1.0000000

2 2 0

3.2758000 1.0000000 0.0000000

0.7920000 0.0000000 1.0000000

1 1 0

2.0897000 1.0000000

Basis Set in SUPERMOLECULE format C:

13.0450960 0.53532814 0.0000000

3.5305122 0.44463454 0.0000000

2.9412494 0.0000000 -0.09996723

0.6834831 0.0000000 0.39951283

0.2222899 0.0000000 0.70011547

3 1 0

2.9412494 0.15591627

0.6834831 0.60768372

0.2222899 0.39195739

Basis Set in SUPERMOLECULE format O:

6 2 0

130.7093200 0.15432897 0.0000000

23.8088610 0.53532814 0.0000000

6.4436083 0.44463454 0.0000000

5.0331513 0.0000000 -0.09996723

1.1695961 0.0000000 0.39951283

0.3803890 0.0000000 0.70011547

3 1 0

5.0331513 0.15591627

1.1695961 0.60768372

0.3803890 0.39195739

This particular user defined basis set was used for all the calculations involving the $Fe(CO)_5$ molecule, from total cross sections to excitation cross-sections and DEA cross-sections as well as determination of the excited states involved in the DEA fragmentation of the molecule.

Smaller basis sets have been used for the O and C compared to the Fe. The Fe is expected to have a higher number of electrons around the nucleus and the complexity of the calculations increases. While for O and H with a reduced number of electrons a smaller basis set as 6-31G**, or 3-21 is more suitable reducing the memory utilized and the number of iterations in the calculations.

ANNEX 2. ACETYLACETONE FROM $ME_2AU(ACAC)$

A2.1 ACETYLACETONE KETO AND ENOL STRUCTURES

Atom	x	y	z
C(1)	-2.635	0.5851	-0.3823
C(2)	-1.2888	0	-0.837
O(1)	-1.2909	-0.4925	-1.9568
H(11)	-3.3807	0.4464	-1.1817
H(12)	-2.5123	1.6599	-0.1723
H(13)	-2.9684	0.0648	0.5301
C(3)	0	0	0
C(4)	2.635	-0.5851	-0.3823
C(5)	1.2888	0	-0.837
O(2)	1.2909	0.4925	-1.9568
H(51)	3.3807	-0.4464	-1.1817
H(52)	2.5123	-1.6599	-0.1723
H(53)	2.9684	-0.0648	0.5301
H(31)	0	0.8764	0.6681
H(32)	0	-0.8764	0.6681

Table A2.1.1 Keto structure of acetylacetone from Ref. [111]

Atom	x	y	z
C(1)	-2.5219	0	-0.0036
C(2)	-1.2132	0	-0.729
O(1)	-1.1903	0	-2.0431
H(11)	-2.3358	0	1.0826
H(12)	-3.0923	-0.9008	-0.2821
H(13)	-3.0923	0.9008	-0.2821
C(3)	0	0	0
C(4)	2.5219	0	-0.0036
C(5)	1.2132	0	-0.729
O(2)	1.1903	0	-2.0431
H(51)	2.3358	0	1.0826
H(52)	3.0923	0.9008	-0.2821
H(53)	3.0923	-0.9008	-0.2821
H(31)	0	0	1.102
H	0	0	-1.9812

Table A2.1.2 Keto structure of acetylacetone from Ref. [111]

A2.2. ACETYLACETONE FROM $ME_2AU(ACAC)$ GAS PHASE ANALYSIS

A2.2.1 INTRODUCTION OF ACETYLACETONE FROM $ME_2AU(ACAC)$

Acetylacetone is widely used as a solvent and part of Pt, Au, Cu(II), Co(II), Ni(II) and Zn(II) complexes has applications in cancer research, medicine, nanolithography, magnetic structures deposition. In this thesis analysis of $Me_2Au(acac)$ thin films using TPD is reported, with characterization of the broad range

of anion fragments obtained during ESD (see Surface Science Section, Chapter 8). Fragmentation and decomposition of the acac fragment is a major source of O and C contaminants in the FEBID nanostructures.

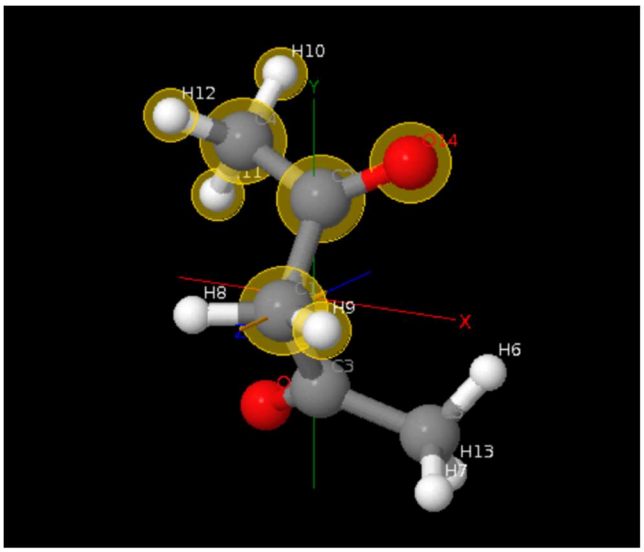

Fig A2.2.1.1. Acetylacetone Quantemol-N symmetry

A2.2.2 Previous Work

Ómarsson et al 2006 in [268] presents three anions arising from DEA of the acetylacetone recorded using a quadrupole mass spectrometer. The first anion CH_2 - $COCH_3^-$, has its resonance at an incident electron energy of 2 eV, 4.3 eV and 8.5 eV, result of the allowed transition from HOMO in π state to LUMO in π* state. Through the removal of an extra ligand to the methyl radical, the anion $COCH_3^-$ is obtained. The anion $COCH_3^-$, has its resonance peak at a value of 4.5 eV and 8.9 eV, and it was formed in the interaction of the $CH_3COCH_2COCH_3$ with an electron following the dissociation path: $CH_3COCH_2COCH_3 + e^- \rightarrow CH_2COCH_3 + COCH_3^-$. By the removal of a C – O ligand, CH_3COCH_2C is formed with the resonance peak falling at an incident electron energy of 8.6 eV. The CH_3^- (m/z 15) has only one peak of the resonance at an incident electron energy of 9 eV. The cited source reports the resonances for all anions as being high lying core-excited resonances.

Reference	DEA anion spectra	Electron Energy (eV)
Ref. [268] Ómarsson et al 2006	CH_2 - CH_3CO^- CH_3CO^- CH_3^-	2 /4.3 / 8.5 4.5 / 8.9 9

	CH_2 - CH_3COO^-	8.6
Present work (DFT, Gaussian 16) B3LYP/6-31G**	$COOH(C_2H_3)_2$	3.29
	$CH_2(C_2H_3)_2O$	9.80
	$COCH_2CH_3$	5.11

Table A2.2.2.1. DEA anion spectrum data from different sources

No H^- and O^- anions have been found present, result of the fragmentation of acetylacetone, in the work reported by Ómarsson et al 2006 [268], due to a high excess energy needed to fragment the precursor at low electron energy in DEA. The presence of the ionized excited parent (TNI) of the acetylacetone could not be determined experimentally, being very short lived (~fs). The threshold reported in [268] for the apparition of the anions are 3.42 eV (CH_3^-), 1.38 eV (CH_2 – CH_3CO^-), 2.76 eV (CH_3CO^-) and 3.58 eV (CH_2 – CH_3COO^-).

In enol form, the acetylacetone is in $S_2(\pi\pi^*)$ excited state in the Franck-Condon region (FC) [316] in singlet state at 266 nm excitation, undergoing a decay to the $S_1(n\pi^*)$ state by vibronic interaction, as a result the molecule relaxes to $T_1(\pi\pi^*)$ triplet state by spin-orbit coupling (SOC). The O – H – O bond goes through rotational isomerization and ligand breakage. The C = C bond converts to a single bond and the molecule reorganizes in keto state. The OH elimination happens from the lowest triplet state $T_1(\pi\pi^*)$ at a time constant of 247 ± 43 ps to singlet $S_2(\pi\pi^*)$.

Chen et al 2006 in [316] determined experimentally a number of five excited states involved in the dissociation of the acetylacetone compound, fragmentation taking place between E_0 π state to 1nπ* and E_0, E_1 π to 3nπ* allowed transition, ranging from 3 eV – 5 eV. The first three allowed transitions are from E0 π to 1nπ* at 4.70 eV, 4.04 eV and 3.57 eV, while the last two transitions are from E_1 π to 1nπ* at 3.68 eV and 3nπ* at 3.34 eV. Using the FERMI 100 fs pulse laser at 19.23 eV, the $S_2(\pi\pi^*)$ goes into $S_1(n\pi^*)$ state and further to $T_1(\pi\pi^*)$ through intermediary ultrafast crossing $S_1(n\pi^*)/T_2(n\pi^*)$. The enol form of acetylacetone is the AcAc form, with possible geometries C_s and C_{2v} in Ref. [111] symmetry point groups. The AcAc form is widely used for metal acetylacetonates.

Reference	Electronic states and cross-sections
Ref. [316] Chen et al 2006	1nπ* 4.70 eV 1nπ* 4.04 eV 1nπ* 3.57 eV 1nπ* 3.68 eV 3nπ* 3.34 eV
Present work (Quantemol-N)	1A 0 eV 3B 5.3 eV 3A 5.54 eV 1B 5.8 eV 1A 6.03 eV 3B 7.19 eV 3A 7.22 eV 1A 8.98 eV 3B 9.57 eV 3A 9.65 eV 1B 10.47 eV 1A 10.97 eV 1B 10.99 eV 3B 11.45 eV 1A 11.53 eV 3A 11.78 eV 3B 11.81 eV
Present work DFT calculations from Gaussian 16 in neutral state at B3LYP/6-31G**	1B 4.1586 eV 1A 4.3431 eV 1B 6.2289 eV 1B 7.8489 eV 1A 7.9950 eV 1B 8.1545 eV 1A 8.3696 eV 1B 8.4140 eV
Present work DFT calculations from Gaussian 16 in charged state at B3LYP/6-31G**	2B 2.7279 eV 2A 3.7552 eV 2B 3.8586 eV

	2A 4.0071 eV 2B 4.4309 eV 2B 4.8321 eV 2A 4.8696 eV 2A 4.8962 eV 3B 5.1239 eV

Table A2.2.2.2. DFT electronic states, cross-sections and resonances from different sources

Structure analysis of acetylacetone. Acetylacetone is a compound derived from acetone containing two ethyl groups (Fig A2.2.2.1). Acetylacetone is used as a radical in the synthetization of metal acetylacetonates, stabilizer agents for thin films in Ref. [107] and compounds containing metal atoms in Ref. [108], and in mixtures, as in the case of the TiO_2 thin films used for deposition of wash free surfaces for tunnel lamps and skyscraper windows in Ref. [109].

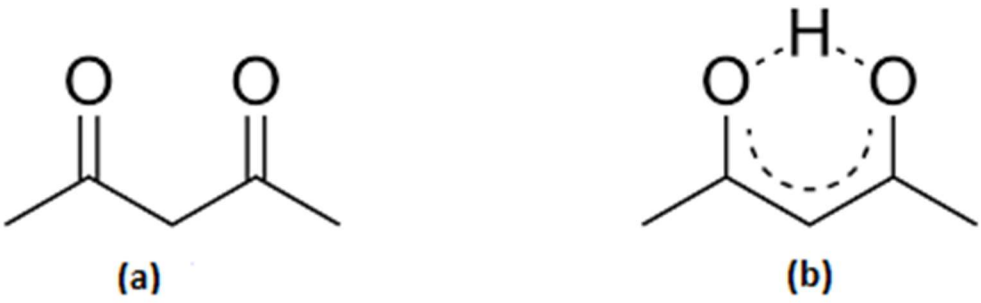

Fig A2.2.2.1. Acetylacetone in (a) keto form and (b) enol form

Acetylacetone can be in two structural forms and dynamic equilibrium: keto (ANNEX 2 Table A2.1.1) and enol (ANNEX 2 Table A2.1.2), both presented in Fig 4.2.4.1. For a concentration of 66 ± 5 % in vapour phase at 105 deg in enol form in Ref. [110], the hydrogen bond distances are O – O = 2.381 ± 0.020 Å for the short internal hydrogen with a linear symmetric structure, C – O = 1.315 ± 0.007 Å and C – C = 1.416 ± 0.010 Å for the hydrogen bond of the planar ring. The other distances are C – C = 1.497 ± 0.010 Å and the ring angles are OCC = 120.0 ± 1 .3 deg, CCC = 118.0 ± 2.5°. Non-ring angles are CCC = 120.0 ± 1.4 deg. In the keto form in Ref. [110], the two planar groups of the tautomer and the acetyl group are rotated with respect to each other at 48.6 ± 4 deg. The bond distances are C – O = 1.225 ± 0.010 Å, C – C = 1.540 ± 0.015 Å, the angles are OCC_0 = 120.0 ± 1.8 deg, CC_0C=114.0 ± 3.6 deg, CCC_0 = 125.0 ± 3.5 deg and the O – O = 2.767 ± 0.030 Å.

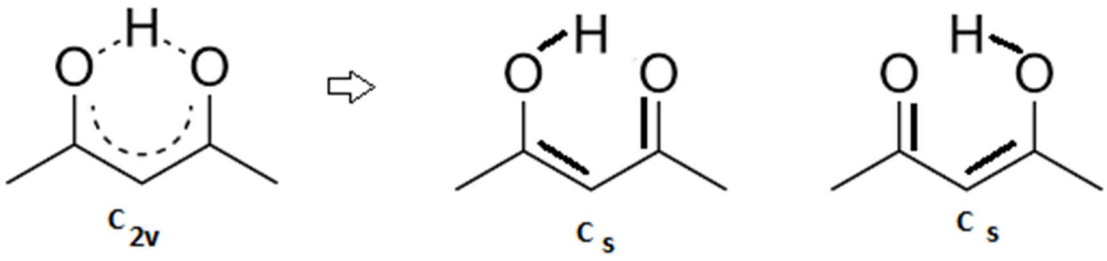

Fig A2.2.2.2. The enol tautomer geometry of AcAc in Ref. [111]

The vibrational spectrum of acetylacetone presents features showing C - O, C - C, C = C bonding. A comparative study in Ref. [112] with Ogoshi and Nakamoto 1966 [113] and Chiavassa et al 1993 [114], presents ab initio calculations at post Hartree-Fock level and the infrared spectrum of acetylacetone and d_6-acetylacetone from 300 cm^{-1} – 3200 cm^{-1}. The vibrational peaks corresponding to CH stretching modes (Fig A2.2.2.3) are at: 3090 cm^{-1} (0.38 eV), 2963 cm^{-1} (0.37 eV), 2960 cm^{-1} (0.37 eV).

For CH_3 in asymmetric plan [112] the vibrational peaks are at 3002 cm^{-1} (0.37 eV), 3004 cm^{-1} (0.37 eV), 2222 cm^{-1} (0.28 eV) and 2223 cm^{-1} (0.28 eV). In the out of plane asymmetric CH_3, the stretching modes are at 2963 cm^{-1} (0.37 eV), 2962 cm^{-1} (0.37 eV), 2255 cm^{-1} (0.28 eV) and 2256 cm^{-1} (0.28 eV). The low temperature infrared spectrum corresponding to C = C – C = O stretch to OH in plane bending mode and C = O + C - CH_3 stretch and in plane bending shows the vibrational frequencies at 1635 cm^{-1} (0.20 eV), 1600 cm^{-1} (0.20 eV) and 1575 cm^{-1} (0.20 eV).

Chiavassa et al 1993 [114] present frequency at 1300 cm^{-1} (0.16 eV) corresponding to C - O, C = O stretch and δ_{OH}, while in Ref. [112] assigns them to O – C = C - C and C = O stretch strongly coupled to δ_{OH}. At 1250 cm^{-1} (0.15 eV) Ogoshi and Nakamoto 1966 [113] assign the frequency to C - C + C = C, while Chiavassa et al 1993 [114] assign it to C - C, C = C and δ_{OH}.

The CH_3 modes (Table A2.2.2.3) are found at 930 cm^{-1} (0.12 eV), 397 cm^{-1} (0.05 eV), 640 cm^{-1} (0.08 eV), 1460 cm^{-1} (0.18 eV) in plane asymmetric deformation and 1455 cm^{-1} (0.18 eV), 1444 cm^{-1} (0.18 eV) and 1429 cm^{-1} (0.18 eV) shoulders to 1404 cm^{-1} (0.17 eV) resonance of CH_3 stretching mode. In the calculation of the fragmentation cross-sections a specificity or IR frequency of 2300 cm^{-1} (0.29 eV)/1800 cm^{-1} (0.22 eV) were used with an electron affinity of 1.46 eV and 1.85 eV. The simplest cases of loosing one H^- or one O^- through ligand breakage/fragmentation was considered and computed for a dissociation energy of 0.2 eV (<1 eV) to obtain the lowest lying resonance close to 0 eV, that would give the highest negative ion in number of atoms.

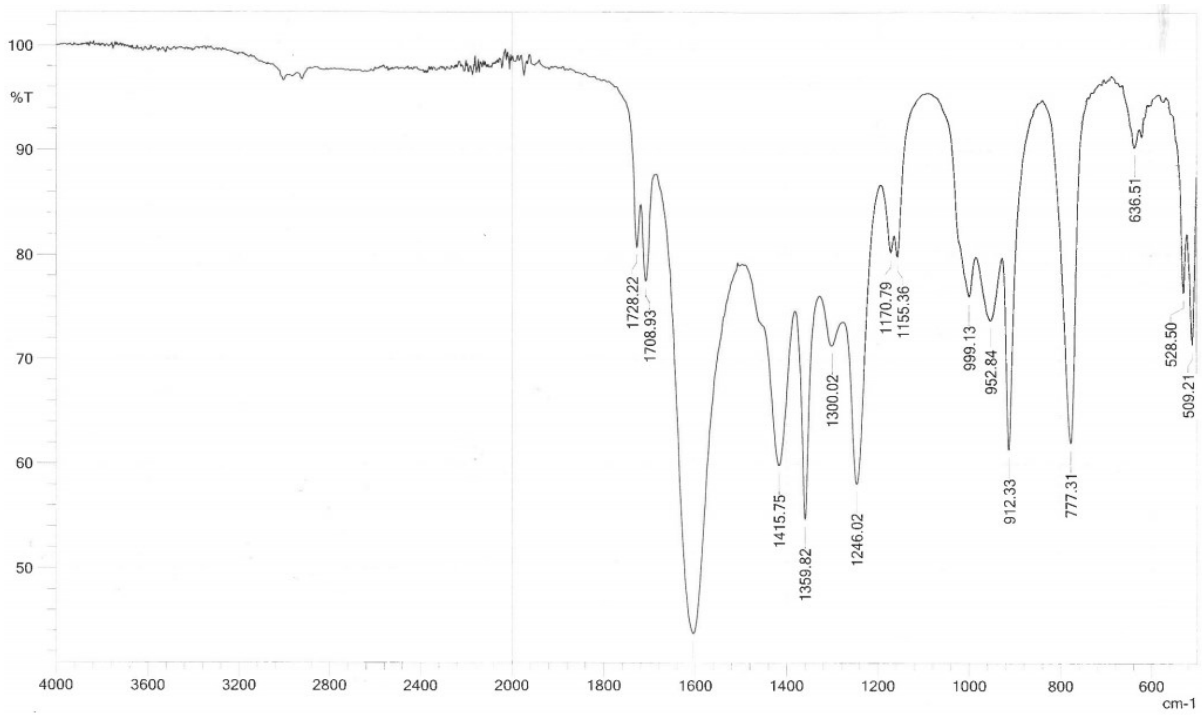

Fig A2.2.2.3. IR spectrum of acetylacetone

A2.2.3 Computational Details

The simulations were run using Gaussian 16 at DFT B3LYP/B3LYP/6-31G** and cross-section data derived using Quantemol-N.

A2.2.4 Results and Discussions

Quantemol-N Cross Sections Data. The structure of acetylacetone was imported from *NIST database* in enol form at 6-31G** level of theory. The symmetry of the molecule in ground state configuration at this level of theory is C_{2v}, but for simplification for our Quantemol-N calculations we used C_1 symmetry, reducing the computation time. The chosen symmetrical atoms are presented in Fig A2.2.1.1. The basis set used for our Quantemol-N calculations is cc-pVDZ with an R-matrix radius of 14. The molecular ground state of acetylacetone, result of the Quantemol-N simulation is $1b^2$, $1a^2$, $2b^2$, $2a^2$, $3a^2$, $4a^2$, $3b^2$, $5a^2$, $4b^2$, $6a^2$, $5b^2$ with the excited states used in the calculation of the cross-sections: 3B, 3A, 1B, 1A, 3B, 3A, 1A, 3B. The excitation cross-sections are presented in Fig A2.2.4.4 and the target excitation energies of singlet and triplet excited states are presented in Table A2.2.4.1 at the level of energy.

Using Quantemol-N software, the total electron scattering, and ionization cross-sections were evaluated for acetylacetone. The maximum value of the total cross-sections result of the simulation is 1.3 x 10^{-15} cm^{-1} (Fig A2.2.4.7). A number of two higher inflexion points are observed in the TCS of acetylacetone below 5 eV representing possible resonances. The fragmentation of acetylacetone has the result of two CH_3 radicals that would break through a vibrational – rotation resonance at higher than 2 eV energies with the result of an ionized parent and a negatively charged radical of COOC - CH_2^- or a negatively charged fragment CH_3^- at energies higher than 7 eV.

Singlet	A	0
Triplet	**B**	**5.3**
Triplet	**A**	**5.54**
Singlet	**B**	**5.8**
Singlet	**A**	**6.03**
Triplet	**B**	**7.19**
Triplet	**A**	**7.22**
Singlet	**A**	**8.98**
Triplet	**B**	**9.57**
Triplet	**A**	**9.65**
Singlet	B	10.47
Singlet	A	10.97
Singlet	B	10.99
Triplet	B	11.45
Singlet	A	11.53
Triplet	A	11.78
Triplet	B	11.81

Table A2.2.4.1. Excited States from Configuration Interactions of MO orbitals

The appearance of the excitation cross-sections or the appearance of their excited states lies between 5.4 eV (3B excited state) to 9.6 eV (3B excited state) (Fig A2.2.4.4). Singlet excited states 1B (5.9 eV excited state), 1A (6.10 eV excited state) and 1A (9 eV excited state) can be observed on the graph, yellow, green, and dark green curves. We can observe the similitude in shape of the resonances at (5.4 eV, 5.6 eV) representing (3A, 3B), as well as at (7.2 eV, 7.3 eV), while at (5.9 eV, 6.10 eV) representing (1A, 1B) and (9 eV, 9.6 eV) representing (1A, 3B) a difference in amplitude is observed between the two

similar shape resonances. The maximum falls between 2 and 3 x 10^{-16} cm^2, for the brown and light blue excited states corresponding to 3A and 3B.

The active space from CIS Configuration Interaction calculations with 11 frozen orbitals is 13a, 14a, 15a, 12b, 13b, 14b. The close coupling (CC) expansion method defining the type of collision interactions was used and the ionization energy with a value of 8.85 eV from experimental data NIST database. The number of CAS virtual orbitals used was 2: 2A and 2B, with 3 CAS open orbitals and 5 virtual orbitals. The excited target energies presented in Table A2.2.4.2 are close to the excited states appearance energies and can be seen highlighted in bold.

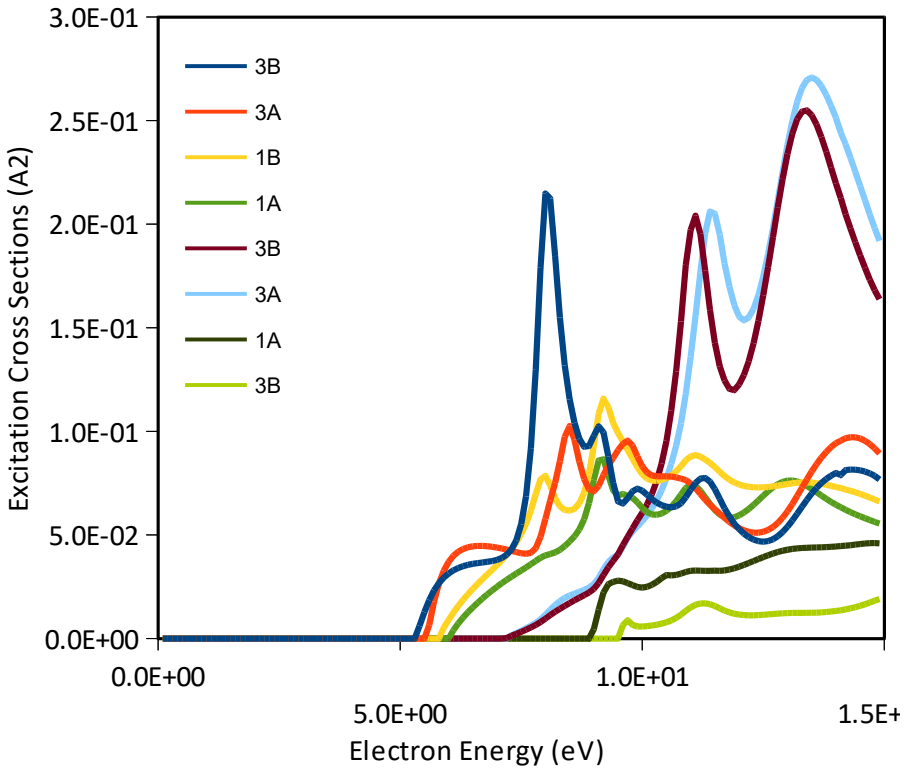

Fig A2.2.4.4. Excitation cross-sections of acetylacetone

A number of 17 vertical excitation energies (frequencies) have been computed with energies lying between -343.33 Hartree (3B excited state) to -343.77 Hartree (1A excited state). The number of 17 energies are calculated on only triplet and singlet excited states. The fragmentation of acetylacetone follows the steps presented in Fig A2.2.2.1 with the resulting fragments T_1, S_1, S_2 in π^* excited state. In agreement with Chen et al 2006 [115] from these 17 vertical excitation energies we prove the existence of three fragments, results of the dissociation of the acetylacetone: $CH_3COCH_2CH_2^-$, $HCOCH_2OCH^-$, $CH_2COCH_2^-$, $CH_2COCH_3^-$ and neutral fragments in neutral state OH, CH_3CO, CH_3COH and CH_2.

Ion	Neutral Fragment	Dissociation energy (kcal/mol)
$CH_2COCH_3^-$	CH_3CO	59.9
$CH_2COCH_2^-$	CH_3COH	46.6
$CH_3COCH_2CCH_3^-$	OH	90.3

Table A2.2.4.2. Fragmentation of acetylacetone with dissociation energies in Ref. [115]

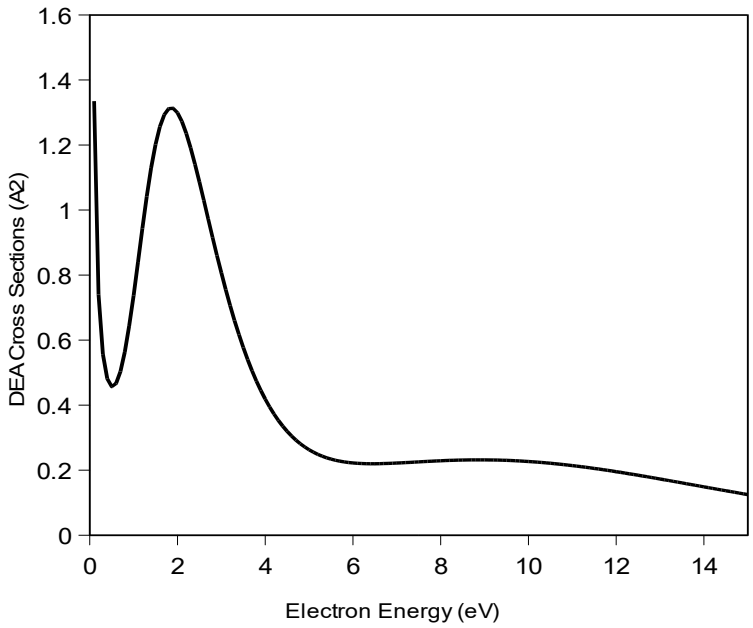

Fig A2.2.4.5. DEA Cross Sections of acetylacetone radical

In the derived DEA cross-section a resonance is observed below 1 eV (~0.1 eV), and another peak containing multiple resonances with a width of 3.2 eV can be seen at 1.9 eV, and a further broad peak from 6 eV to 15 eV, most probably corresponding again to multiple resonances. According to this, two of our ions with electron energies lower than 5 eV would have a resonance in the first peak and a second resonance in the third peak, while the third fragment corresponding to $CH_3COCH_2^-$ would have a resonance in the third peak. From our DFT calculations (Table A2.2.4.3) we obtained a fragmentation energy of the C – O bond of 9.80 eV with the anion $CH_2(C_2H_3)_2O^-$ in quartet state, and a maximum kinetic energy of 6.15 eV. The EA energies were calculated from the electronic energies corrected for zero-point energy corrections, while the bond dissociation energies are the energies calculated by Chen et al 2006 in [115] with a value of 3.92 eV for the particular anion. By breaking one C – H ligand we obtained a value of the incident electron energy of 22.03 eV, higher than the DEA 0 – 20 eV energy value, and a maximum kinetic energy of 21.91 eV making the apparition of the $CH_2COCH_2^-$ unlikely. The calculations were run using Gaussian 16 at B3LYP/6-31G**. The presence of H^- and O^- could not

be probed, the molecule needing a high amount of excess energy to form single H^- and O^- ionized fragments. A value of maximum kinetic energy of 1.02 eV was obtained for $CH_2COCH_3^-$ for an electron affinity of 0.42 eV [268] and an incident electron energy of 2 eV. The CH_2COCH_3 has multiple resonances peaking at 2 eV, 4.3 eV and 8.5 eV, with the highest intensity at 8.5 eV.

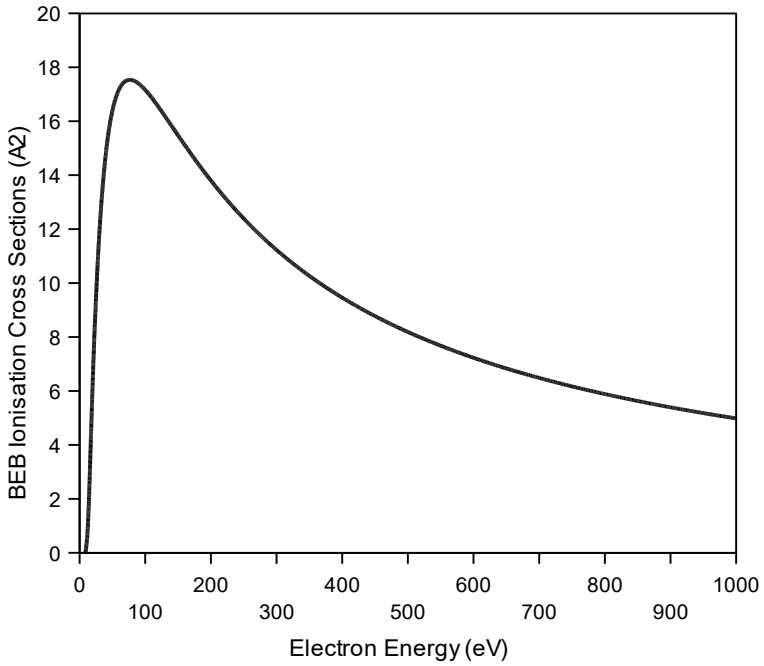

Fig A2.2.4.7. Total cross-sections of acetylacetone

Anion	Ei (eV)	EA (eV)	Ee (eV)	BDE (eV) [115]
$CH_2COCH_3^-$	2 / 4.3 / 8.5 [268]	0.42 [268]	1.02	2.60
$CH_2COCH_2^-$	22.03 (DFT)	1.90 (DFT)	21.91	2.02
$CH_3COCH_2CCH_3^-$	9.8 (DFT)	0.27 (DFT)	6.15	3.92

Table A2.2.4.3 Calculated excess energy of the anions

The value of the total cross-section of the acetylacetone decreases from 1350 $Å^2$ close to 0 eV to 100 $Å^2$ to 150 eV asymptotically. Almost one order of magnitude lower with values in the range of 160 $Å^2$ and with a visible peak, the cross-section distribution has a sharp decrease over a 0 - 2.5 eV range. At 3.5 eV a second peak is observed in the TCS graph with an intensity of 100 $Å^2$.

The Born-Bethe ionization cross-sections are shown to have a maximum value of 17.7 x 10^{-18} cm^2 (Fig a2.2.4.8) at 100 eV. At half maximum, an electron energy of 510 eV would correspond to a cross-section value of 8.5 x 10^{-18} cm^2.

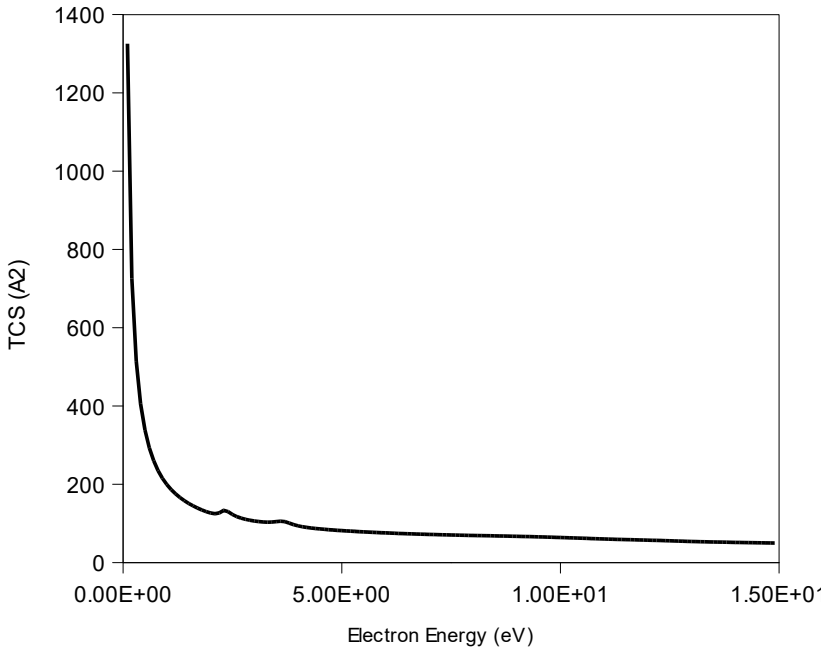

Fig A2.2.4.8. Ionization cross-sections of acetylacetone

A2.2.5 Summary and Conclusions

A cross-sections study of acetylacetone has been performed using Quantemol-N software, determining a wide range of cross-section types, from excitation cross-sections to DEA cross-sections and total cross-sections. The values of the dissociation energy has been taken from [268] and Chen et al 2006 [316] with specificities in the range of 1800 cm^{-1} to 2200 cm^{-1}. Values of the total cross-sections of 1350 $Å^2$ close to 0 eV to 100 $Å^2$ at 150 eV have been obtained from the simulations, while the DEA cross-sections present values of 1.15 $Å^2$ at 0 eV and 2 eV, and 0.3 $Å^2$ at 10 eV corresponding to the presence of the anions between 0 – 10 eV. The calculated excitation cross-sections for 17 states with values between 5.4 eV (3B excited state) to 9.6 eV (3B excited state) (Table 4.2.4.1). The apparition energies of the excitation cross-section are 5.2 eV (3B), 5.4 eV (3A), 5.6 eV (1B), 5.8 eV (1A), 7.5 eV (3B), 7.5 eV (3A), 9 eV (1A) and 9.5eV (3B), and have been presented in Fig 4.2.4.4. A set of DFT calculations of VEA, EA, BDE and maximum kinetic energies of the anions has been generated (Table A2.2.4.3) using DFT values of complexation energies and incident electron energies from [268]. The Born-Bethe ionization cross-section have been calculated over an energy range from 0 to 1000 eV, showing a maximum at 90 eV of 17.5 $Å^2$. The value of the maximum cross-section for the acetylacetone is lower with more than two orders of magnitude than for the metal compounds with cross-sections in the range of 10^{-16} cm^2, and the spectrum is shifted to the left with over 100 eV.

ANNEX 3. ACETYLACETONE RADICAL FROM $ME_2AU(ACAC)$

A3.1 STRUCTURE CHARACTERIZATION OF ACETYLACETONE RADICAL FROM $ME_2AU(ACAC)$ USING DFT CALCULATIONS

Geometry and molecule characterization

The acetylacetone radical from $Me_2Au(acac)$ was analyzed to surface – molecule interactions on Cu surface and SiO_2 substrate, Cu as the first deposition medium from the experimental work, and SiO_2 for comparison with the Cu simulations and experimental work.

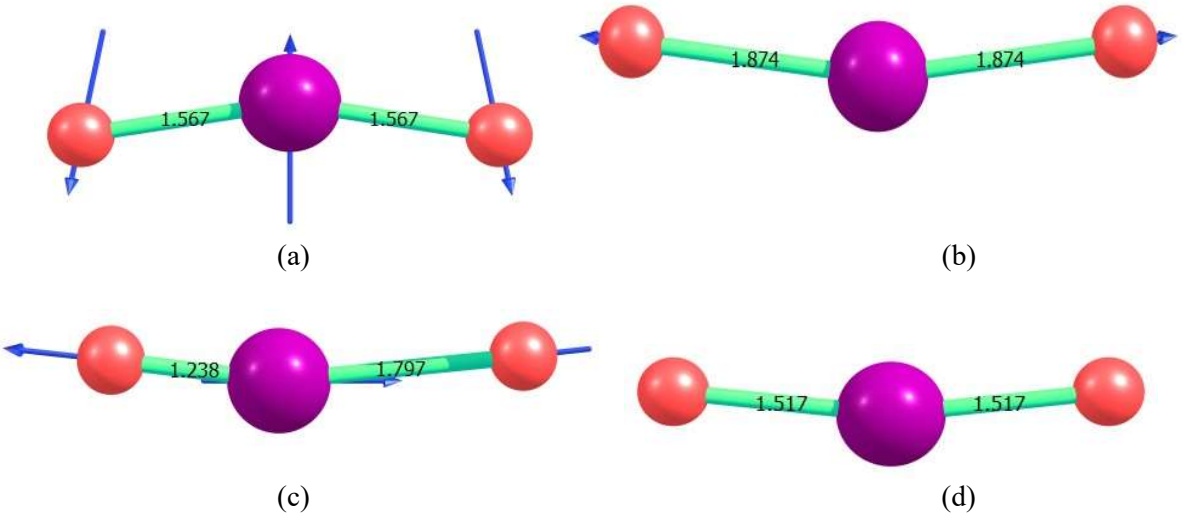

Fig A3.1.1. SiO_2 frequencies and oscillations (Si violet, O red) from the optimization step 258.4384 (A1 state) (b) 1002.5095 (A1 state) (c) 1452.9339 (B1 state) (d) B3LYP/6-31G** optimized geometry in ground state

For each of the three compounds of interest, the optimized geometry and frequencies were run using Gaussian 16 at B3LYP/6-31G** level of theory with the Si – O distance lower than the initial geometry characterized by a bond length of 1.5197 Å obtained from *NIST database* for the same level of theory B3LYP/6-31G** with the resulting value in the range of 0.24 Å higher, while the Cu – Cu bond distance through optimization remains at the same value of 2.4400 Å.

The acetylacetone molecule has a higher difference in the values of the bond lengths of the molecule in the ground state compared to the values imported from *NIST database* for B3LYP/6-31G** level of theory.

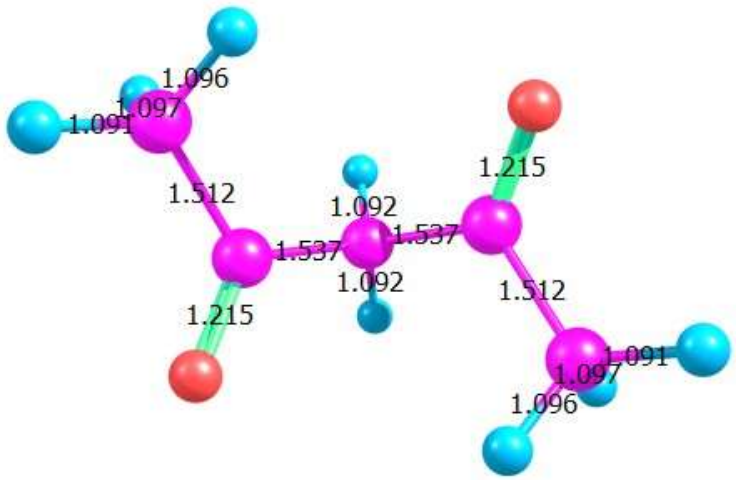

Fig A3.1.2 Acetylacetone optimized structure and bond lengths at B3LYP/6-31G**

(C violet, O red, H blue)

Complex	Initial geometry (Å)	Optimized bond lengths (Å)
SiO_2	1.5197	1.5173
Cu - Cu	2.4400	2.4400
$C_5O_2H_8$	C–C 1.5367, C–C 1.5106 C-O 1.2180 C-H 1.0910, C-H 1.0961, C-H 1.0971	C-C 1.537, C-C 1.512 C-O 1.215 C-H 1.096, C-H 1.097, C-H 1.091 C-H 1.092

Table A3.1.1. Bond lengths of SiO_2, acetylacetone and Cu – Cu

The C - C bond distance for the carbon bonded to the oxygen C(O) and carbon bonded to carbon C(C) with a value of the bond length C(O) - C(C) of 1.537 Å, while C(C) to carbon bonded to hydrogen C(H), C(C) – C(H) has a bond distance of 1.512 Å. The three C – H bonds of the methyl radicals have bond distances of 1.096 Å, 1.097 Å and 1.091 Å, close in value to each other are 0.003 Å – 0.0001 Å higher than the initial geometry taken from our reference database. The two O set on x axis to 180 deg orientation to the normal axis with a symmetry rotation angle of 180 deg to the central C atom have bond distances of 1.215 Å with 0.003 Å lower than the initial geometry bond length. The two axial ethyl groups, the C – H radicals have a bond distance of 1.092 Å placed at an angle of 120 deg between each other and 30 deg to the main y axis. The obtained structure from optimization is smaller overall than the

initial geometry, the only elongation observed is in the methyl radicals that have longer bond lengths to their three hydrogens.

Thermochemistry of the molecules

By default, the temperature for our calculations is 298.15 K. Based on the adjustment of this temperature a set of vibrational temperatures are computed to determine the zero-point vibrational energy, thermal corrections, and the thermal parameters such as entropy, thermal energy correction and heat capacity. The acetylacetone radical of $Me_2Au(Acac)$ formed in the surface irradiation and thermal desorption processes is characterized by an enthalpy of formation at 298.15 K of -384.40 kJ/mol reported by ***NIST database***, while our calculations done using the 6-31G** basis set at B3LYP level of theory report values of heat capacity of 28.038 cal/molK and an entropy of 90.236 cal/molK, their contribution coming from vibrational processes and almost 10% of vibrational processes the rotational and translational with equal values of 2.981 cal/molK (heat capacity) and translational and rotational process for the entropy of the molecular system. A second set of simulations was run using CCSD calculations of thermochemistry parameters presenting close values to the ones obtained for the B3LYP calculations. The highest contribution is the entropic contribution of translational processes of the atoms of the acetylacetone with a value of 39.720 cal/molK, while in the thermal energy the only contribution comes from the vibrational processes. A value of 83.861 kcal/mol (CCSD) of the thermal energy is reported 1.9 kcal/mol higher than the first value determined of 81.875 kcal/mol (B3LYP). A higher zero-point vibrational energy is reported for the acetylacetone radical from running CCSD calculations, with a value of 78.7107 kcal/mol, compared to the B3LYP calculations presenting a value of 76.6552 kcal/mol. The chemical accuracy of the thermochemistry calculations in Gaussian using the G1 (developed 1998) and G2 (developed 2007) is defined as being no more than 1kcal/mol or 4 kJ/mol in Ref [32] with the value decreasing to 0.33 kcal/mol for later methods as MP2, MP3, B3LYP methods. The accuracy of the calculation is highly dependent on the size of the basis set used as well, from this point of view the B3LYP to CCSD have discrepancies with up to 1.9 kcal/mol.

The SiO_2 molecule has a formation enthalpy reported by ***NIST database*** of -322.07 kJ/mol at 298.15 K and an entropy of 228.72 J/molK. The value of the entropy obtained from our calculations is in the range of 238.6475 J/molK at the B3LYP level of theory and 232.5264 J/molK at CCSD level of theory. The thermal energy for both levels of theory is due mostly to the changes due to vibrational processes with a value of 5.982 kcal.mol, in B3LYP calculations, and 6.409 kcal/mol from CCSD calculations. Comparatively, the values reported by ***NIST database*** for the heat capacity at the nominal temperature, 298.15 K, is 44.05 J/molK, while the one obtained from our calculations is 34.2187 J/molK at B3LYP level of

theory and 37.0489 J/molK at CCSD, both lower with up to 9.9 J/molK. The values obtained from CCSD/6-31G** calculations show higher similitude with lower discrepancies than the values obtained from B3LYP/6-31G**, although the non-optimized molecule was imported from *NIST database* at B3LYP/6-31G** level of theory and basis set. A zero-point energy of 4.3375 kcal/mol was obtained for CCSD/6-31G** calculations, and a value of 3.8797 kcal/mol from B3LYP/6-31G**. The thermal corrections and thermal energies have higher values at CCSD level of theory. When starting to calculate the Cu surface, a Cu – Cu interaction with a bond length value of 2.44Å is used at x axis plane. For our Cu – Cu interactions, all the thermal corrections and thermochemistry characteristics are lower at CCSD level than B3LYP/6-31G** level with a value of the sum of electronic and thermal energy of -3278.8547 Hartree/particle (CCSD) to -3280.3912 Hartree/particle (B3LYP). The value of entropy is mostly related to translational processes with a value of 61.077 cal/molK from B3LYP/6-31G** and a lower value of 57.978 cal/molK from CCSD/6-31G**. The heat capacity on the case of the Cu – Cu bond is not characterized by similar contributions from translational and rotational processes with the highest contribution coming from translational processes and a value of 6.944 cal/molK at B3LYP/6-31G** (6.755 cal/molK from CCSD/6-31G**). Similar contributions from the point of the highest type of contribution is in the case of the thermal energy with a value of 2.077 kcal/mol (B3LYP/6-31G**) from translational processes (2.136 kcal/mol at CCSD). The highest discrepancy between the two levels of theory we find in the calculation of the zero-point vibrational energy with a value of 0.0767 kcal/mol (B3LYP/6-31G**), 0.26 kcal/mol lower than the CCSD level of theory results.

Table A3.1.2. Thermochemistry characteristics of SiO_2, Cu-Cu and $C_5O_2H_8$ at B3LYP/6-31G** level of theory

	SiO_2		Cu - Cu		$C_5O_2H_8$	
	CCSD	B3LYP	CCSD	B3LYP	CCSD	B3LYP
$Corr._{ZPE}$	0.0069	0.0062	0.0005	0.0001	0.1254	0.1222
$Corr._{ThE}$	0.0102	0.0095	0.0034	0.0033	0.1336	0.1305
$Corr._{ThS}$	0.0112	0.0105	0.0043	0.0043	0.1346	0.1314
$Corr._{ThGFE}$	-0.0152	-0.017	-0.0232	-0.0248	0.0927	0.0885
Σ_{ZPE}	-439.0645	-439.92	-3278.8576	-3280.3944	-344.7068	-345.6839
Σ_{ThE}	-439.0612	-439.9167	-3278.8547	-3280.3912	-344.6986	-345.6755
Σ_{ThS}	-439.0602	-439.9158	-3278.8538	-3280.3903	-344.6976	-345.6746
Σ_{ThFE}	-439.0866	-439.9432	-3278.8813	-3280.4193	-344.7395	-345.7175

A3.2 Surface –Molecule Interactions of Acetylacetone Radical from $Me_2Au(acac)$ Using DFT Calculations

Acetylacetone/ (SiO_2 and Cu) molecule – surface interactions

A comparison is intended between the acetylacetone deposited on a SiO_2 surface and the acetylacetone as a radical obtained from the dissociation of $Me_2Au(acac)$ on Cu surface. The difference in values between the two surfaces is related mostly to the binding energy of the molecule to the specific material and the number of atoms bonded to the atoms of the substrate as well as their diversity. We used bonds with two atoms, in both cases, H and O, defining the O - Si - O and C atoms as separate unique bonds and calculations.

$$E_{ads} = (E_{n\ x\ molecules/surface} - E_{surface} - nE_{molecule}) / n \quad (A3.2.1)$$

The absorption of the molecules on the substrate is characterized by an absorption energy and a binding energy defined as E_{abs}, as the process where the molecules bind to the surface is not a process where the atoms accommodate themselves in holes, defects or become interstitial atoms. The characterization of the process is presented in more detail in Ref. [36] and the relation describing it is shown in (A3.2.1). TD-DFT in Ref. [29] calculations of the simple SiO_2 in Ref. [30] and $C_5O_2H_8$ molecules present the excited states and absorption characteristics of the compounds, as single molecules. Our focus though is on the deposition of the $C_5O_2H_8$ on SiO_2 surface and Cu surface with DOS (density of states) characterization, binding energies to O, C, H, and the absorption on the surface for $\sigma = 0.01, 0.03, 0.05, 0.07, \ldots, 2.5$.

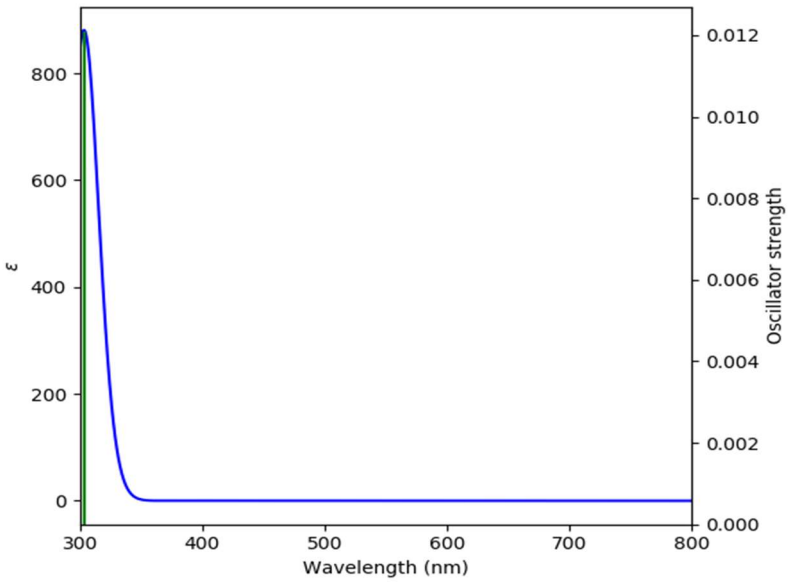

Fig A3.2.1. Absorption spectrum of acetylacetone with dependence on oscillator strength

Our calculations are done at a nominal temperature of 298.15 K for ground state single calculations, and a ramp of values reported from 160 K to 298 K for the molecule – substrate characterization. Separate density of states spectrums are calculated and visualized using Gaussian 16 at B3LYP/6-31G** level of theory and TD-DFT calculations for the excited states and GaussSum to determine the density of states (DOS) at certain excitations levels corresponding to the three molecules. The DOS for the two substrates is presented in Fig A3.2.2 (b) and (c).

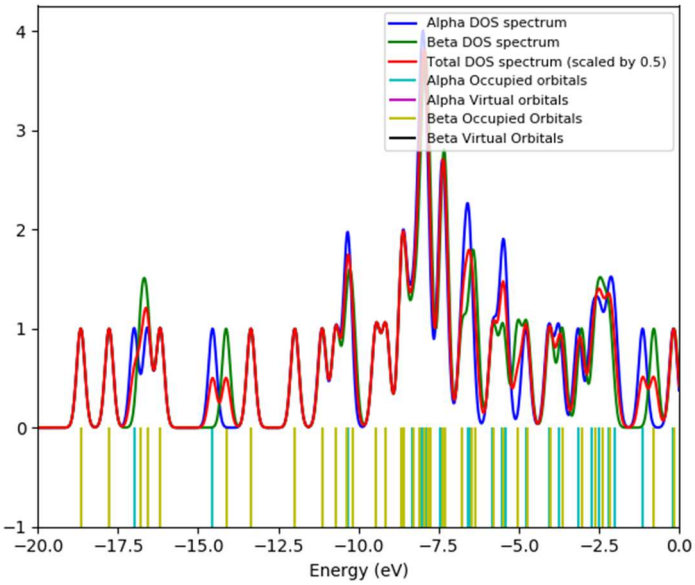

(a)

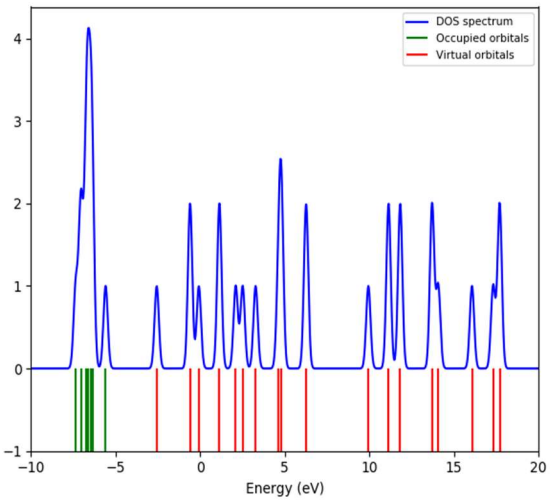

(b)

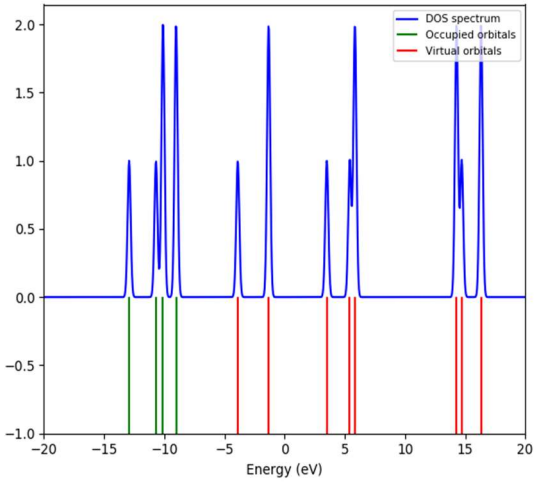

(c)

Fig A3.2.2. Density of states from GaussSum of acetylacetone on SiO_2 (a), Cu – Cu (b) and SiO_2 (c)

The single molecule density of states are obtained for acetylacetone at excited state 3 (root =3) with an electron energy of 4.0850 eV corresponding to a frequency of 303.51 nm and characterized by an oscillator strength of 0.0121 defining an allowed transition and representing a transition state that would lead to the release of one methyl radical through irradiation and fragmentation. Similar excitation states and transition states have been obtained for Cu – Cu interaction and SiO_2 molecule, with the excited states in singlet form at 2.5018 eV (495.58 nm and f=0.0032) for Cu – Cu interactions and singlet form at 4.9534 eV (250.30 nm and f = 0.0781) for SiO_2 molecule, respectively.

The binding energy of the molecule on the substrate is defined by the relation (A3.2.2.):

$$E_{binding} = E_{C5O2H8} + E_{SiO2} - E_{SiO2C5O2H8} \quad \text{(A3.2.2)}$$

The same relation would apply to calculation for the binding energy of the acetylacetone on the Cu substrate with Cu instead of SiO_2. The calculation of a molecule deposited on a section of a SiO_2 substrate calculated using B3LYP/cc-pVTZ basis set and level of theory has a value of -327.2117830 (*Hartree*), where the molecule binds to the O of SiO_2 by C. The binding energy of one C atom of the $C_5O_2H_8$ molecule with one or two of the O of SiO_2 has been calculated using the Gaussian 16 simulation. The energy value of a single SiO_2 molecule in Hartree is E(UB3LYP) = -439.9262308 (*Hartree*), while for a small section of a substrate where the molecule could accommodate to one of the O is in the range of -550.1580614 (*Hartree*).

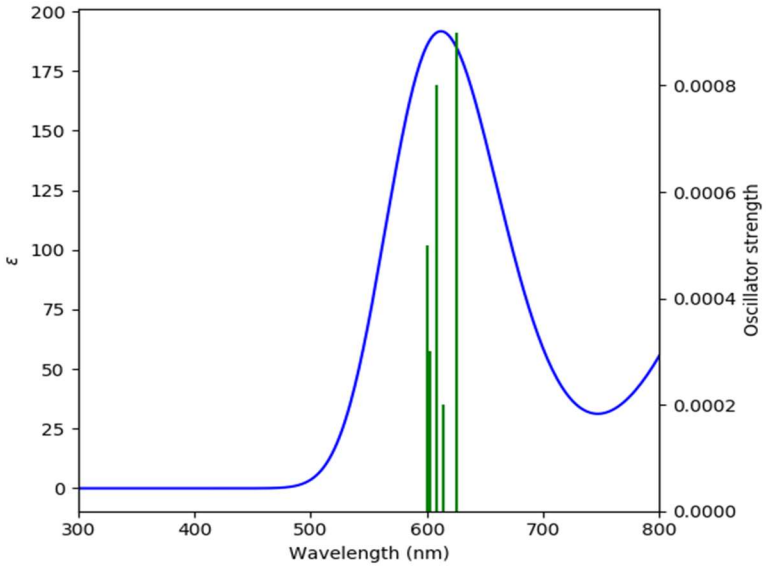

Fig A3.2.3. Acetylacetone on SiO_2 absorption spectrum bonded through one C atom

From using the relation (A4.2.2) we obtain a binding energy of the molecule to the thin monolayer of SiO_2 substrate through a C bond of -568.8721245 (*Hartree*). The biding energy of $C_5O_2H_8$ on SiO_2 using

the same type of calculations as for the C bond to the SiO_2 has a value of 1711.5528817 (*Hartree*) where the energy of the substrate and molecule accommodated on the substrate has a value of -2607.6367892 (*Hartree*) and the energy of the SiO_2 substrate itself is -550.1580614 (*Hartree*). The binding energy for an O and H atoms from $C_5O_2H_8$ bonded to the SiO_2 substrate has a value in this case of 1937.4145492 (*Hartree*), where the molecule on the SiO_2 substrate bonded by and O and an H has a value of -2833.4985467 (*Hartree*).

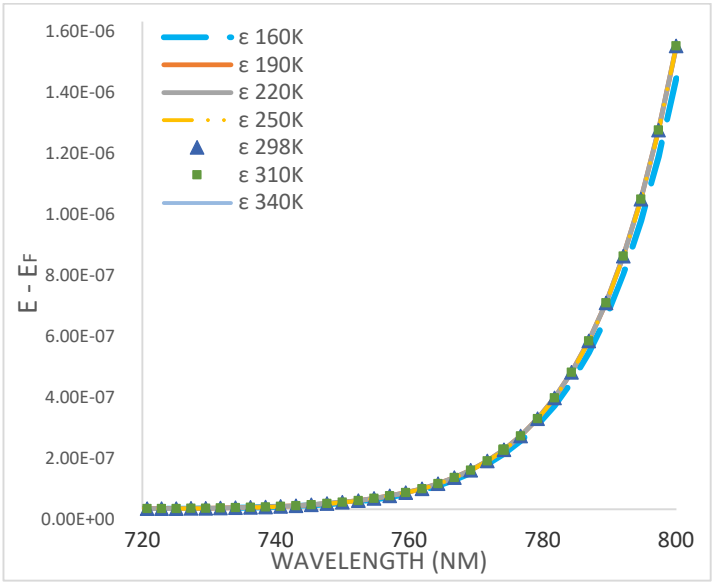

Fig A3.2.4. Absorption spectrum of nCu-$C_5O_2H_8$ with temperatures from 160 K – 310 K

In the case of Cu(110) substrate, a small area of five Cu atoms monolayer with an O bonding to $C_5O_2H_8$ was evaluated obtaining a total energy E(UB3LYP) = -8549.1029374 (*Hartree*), while just the monolayer has an energy of E(UB3LYP) = -8203.1672390 (*Hartree*). The binding energy of $C_5O_2H_8$ on the Cu(110) substrate has a final value of 0.0098523 (*Hartree*) result of only one O – Cu bond. A smaller binding energy is observed in the case of O from acetylacetone on Cu(110) compared to O from acetylacetone on SiO_2, where O from acetylacetone is bonded to one of the Si atoms of the substrate.

REFERENCES

[1] Komiya S., Kochi J.K., Reversible Linkage Isomerisms of ß-Diketonato Ligands. Oxygen-Bonded and Carbon-Bonded Structures in Gold(III) Acetylacetonate Complexes Induced by Phosphines, Journal of the American Chemical Society, j 99:11 / May 25, 1977

[2] Wnuk J.D., Gorham J.M., Rosenberg S.G., van Dorp W.F., Madey T.-E., Hagen C. W., Fairbrother D. H., Electron beam irradiation of dimethyl acetylacetonate gold(III) adsorbed onto solid substrates, Journal of Applied Physics 107, 054301, 2010

[3] Guzman J., Gates B.C., Reactions of Au(CH3)2(acac) on γ-Al2O3: Characterization of the Surface Organic, Organometallic, Metal Oxide, and Metallic Species, Langmuir 2003, 19, 3897-3903

[4] Zhongye Xie, Yan Tang, Yi Zhou, Qinyuan Deng, Surface and thickness measurement of transparent thin-film layers utilizing modulation-based structured-illumination microscopy, Vol. 26, No. 3, 5 Feb 2018, Optics Express, 2944

[5] Madey T.-E., Electron- and photon-stimulated desorption: probes of structure and bonding at surfaces, Science. 234 (Oct. 17, 1986)

[6] https://www.kimballphysics.com/downloadable/download/sample/sample_id/1327/

[7] http://instructor.physics.lsa.umich.edu/adv-labs/Mass_Spectrometer/MassSpecQMS.pdf

[8] https://www.hidenanalytical.com/wp-content/uploads/2016/06/RGA_Series_Widescreen.pdf

[9] Botman A, Mulders J.J.L., Hagen C.W., Creating pure nanostructures from electron-beam-induced deposition using purification techniques: a technology perspective, Nanotechnology 20 (2009) 372001 (17pp)

[10] Abdel-Samada S., Abdel-Baryb M., Kiliana K., Residual gas analysis in the TOF vacuum system, Vacuum 78 (2005) 83–89

[11] Squibb R.J., Sapunar M., Ponzi A., Richter R., Kivimäki A., Plekan O., Finetti P., Sisourat N., Zhaunerchyk V., Marchenko T., Journel L., Guillemin R., Cucini R., Coreno M., Grazioli C., Di Fraia M., Callegari C., Prince K.C., Decleva ., Simon M., Eland J.H.D., Došlić N., Feifel R., Piancastelli M.N., Acetylacetone photodynamics at a seeded free-electron laser, Nature Communications, 2018, 9:63

[12] Spiridonova J., Katerski A., Danilson M., Krichevskaya M., Krunks M., Acik I. O., Effect of the Titanium Isopropoxide: Acetylacetone Molar Ratio on the Photocatalytic Activity of TiO2 Thin Films, Molecules 2019, 24, 4326

[13] Steinbach J.F., Freiser H., Acetylacetone. In the Dual Role of Solvent and Reagent in Extraction of Metal Chelates, Analytical Chemistry, Volume 25, 1953, No. 6

[14] Tayyari S.F., Milani-nejad F., Vibrational assignment of acetylacetone, Spectrochimica Acta Part A56, 2000, 2679–2691

[15] Ogoshi H., Nakamoto K., Normal-Coordinate Analyses of Hydrogen-Bonded Compounds. V. The Enol Forms of Acetylacetone and Hexafluoroacetylacetone, J. Chem. Phys. 45, 1966, 3113

[16] Trivella A., Coussan S., Chiavassa T., Theulé P., Roubin P., Comparative study of structure and photo-induced reactivity of malonaldehyde and acetylacetone isolated in nitrogen matrices, Low Temperature Physics 32, 2006, 1042

[17] Chiavassa T., Verlaque P., Pizalla L., Roubin P., Vibrational studies of methyl derivatives of malonaldehyde: Determination of a reliable force field for β-dicarbonyl compounds, Spectrochim. Acta 50A, 1993, 343

[18] Lowrey A.H., George C., D'Antonio P., Karle J., Structure of Acetylacetone by Electron Diffraction, Journal of the American Chemical Society, 1971, 93:24

[19] Caminati W., Grabow J.-U., The C2v Structure of Enolic Acetylacetone, J. Am. Chem. Soc. 9 Vol. 128, 2006, No. 3, 857

[20] Prabhudesai V.S., Tadsare V., Ghosh S., Gope K., Davis D., Krishnakumar E., Dissociative electron attachment studies on acetone, The Journal of Chemical Physics 141, 2014, 164320

[21] Gil-Rubio J., Vicente J., Gold trifluoromethyl complexes, Dalton Trans., 2015, 44, 19432-19442

[22] Hasan M., Kozhevnikov I.V., Siddiqui M.R.H., Steiner A., Winterton N., Gold Compounds as Ionic Liquids. Synthesis, Structures, and Thermal Properties of N, N'-Dialkylimidazolium Tetrachloroaurate Salts, Inorg. Chem. 1999, 38, 25, 5637–5641

[23] Chang S.-Y., Uehara A., Booth S.G., Ignatyev K., Frederick J., Mosselmans W., Dryfe R.A.W., Schroeder S.L.M., Structure and bonding in Au(I) chloride species: a critical examination of X-ray absorption spectroscopy (XAS) data, RSC Adv. 2015, 5, 6912-6918

[24] Ye H., Trippel S., Di Fraia M., Fallahi A., Mücke O.D., Kärtner F.X., Küpper J., Velocity-map imaging for emittance characterization of multiphoton-emitted electrons from a gold surface, Phys. Rev. Applied 9, 2018, 044018

[25] Blaya M., Bautista D., Gil-Rubio J., Vicente J., Synthesis of Au(I) Trifluoromethyl Complexes. Oxidation to Au(III) and Reductive Elimination of Halotrifluoromethanes, Organometallics 2014, 33, 22, 6358–6368

[26] Galassi R., Oumarou C.S., Burini A., Dolmella A., Micozzi D., Vincenzettic S., Pucciarellic S., A study on the inhibition of dihydrofolate reductase (DHFR) from Escherichia coli by gold(I) phosphane compounds. X-ray crystal structures of (4,5 – dichloro – 1H – imidazolate – 1 – yl) triphenylphosphane - gold(I) and (4,5 – dicyano – 1Himidazolate – 1 – yl) – triphenylphosphane - gold(I), Dalton Trans., 2015, 44, 3043-3056

[27] Wozniak D.I, Hicks A.J., Sabbers W.A., Dobereiner G.E., Imidazolyl-Phenyl (IMP) Anions: A Modular Structure for Tuning Solubility and Coordinating Ability, Dalton Trans., 2019, 48, 14138-14155

[28] Visser B.R., Addicoat M.A., Gascooke J.R., Lawrance W.D., Metha G.F., First spectroscopic observation of gold(i) butadiynylide: Photodetachment velocity map imaging of the AuC4H anion, The Journal of Chemical Physics 145, 2016, 044320

[29] Jornet-Somoza J., Lebedeva I., Real-Time Propagation TDDFT and Density Analysis for Exciton Coupling Calculations in Large Systems, J. Chem. Theory Comput. 2019, 15, 6, 3743–3754

[30] El-Sayed A.-M. B., PhD Thesis, 2015, University College London

[31] Nagy B., Szakacs P., Csontos J., Rolik Z., Tasi G., Kallay M., High-Accuracy Theoretical Thermochemistry of Atmospherically Important Sulfur-Containing Molecules, J. Phys. Chem. A 2011, 115, 7823–7833

[32] Peterson K. A., Feller D., Dixon D. A., Chemical accuracy in ab initio thermochemistry and spectroscopy: current strategies and future challenges, Theor. Chem. Acc. 131, 2012, 1079

[33] Janet J. P., Zhao Q., Ioannidis E. I., Kulik H. J., Density functional theory for modelling large molecular adsorbate–surface interactions: a mini-review and worked example, Molecular Simulation, 2017 Vol. 43, Nos. 5–6, 327–345

[34] Merkx M. J. M., Sandoval T. E., Hausmann D. M., Kessels W. M. M., Mackus A. J. M., Mechanism of Precursor Blocking by Acetylacetone Inhibitor Molecules during Area-Selective Atomic Layer Deposition of SiO2, Chem. Mater. 2020, 32, 3335−3345

[35] Whitcher T. J., Wong W. S., Talik A. N., Woon K. L., Chanlek N., Nakajima H., Saisopa T., Songsiriritthigul P., Investigation into the Gaussian density of states widths of organic semiconductors, J. Phys. D: Appl. Phys. 49, 2016, 325106

[36] Boda A., Ali S. M., Shenoy K. T., Mohan S., Adsorption, Absorption, Diffusion, and Permeation of Hydrogen and Its Isotopes in bcc Bulk Fe and Fe(100) Surface: Plane Wave-Based Density Functional Theoretical Investigations, J. Phys. Chem. C 2019, 123, 23951−23966

[37] Engelhart D. P., Wagner R. J. V., Meling A., Wodtke A. M., Schäfer T., Temperature programmed desorption of weakly bound adsorbates on Au(111), Surface Science, Volume 650, 2016, Pages 11-16

ANNEX 4. PT BASED COMPOUNDS

"Everything is theoretically impossible, until it is done." Robert A. Heinlein

Platinum is a widely used precursor for FEBID and for the development of 3D structures at the nanoscale, whether it is photomask repair, photomask fabrication or sensitive sensor development. The challenges in working with platinum precursors comes from the lack of data available on the chemical reactions induced by electron beams and the lack of Pt atom implementation in current simulation packages (e.g. Quantemol-N) forces us to use density functional theory calculations for low-energy electron gas-phase analysis and surface studies. Multiple Pt containing precursors are used for deposition purposes, whether it is FEBID, MOCVD or CVD, with the aim of creating nanostructures, nanoparticles, thin films. The multitude of Pt complexes used can be divided by the organic part they contain: acac, hfac, tfac, broms, fluorides or carbonyl groups, a few of which are of interest in the present study: $Pt(acac)_2$, $Pt(NH_3)_4(NO_3)_2$ and $Pt(PF_3)_4$. Other Pt-containing precursors, cis-$PtCl(NH_3)_2$ and $Pt(CO)_2Cl_2$, have been analysed in FEBID studies using RAIRS and XPS. These two chlorines containing precursors, create deposits containing high content of Cl. In the case of $Pt(CO)_2Cl_2$, highly chloride contaminated deposits are obtained with Pt/Cl ratios of 1 : 1 in Ref. [127], needing extensive exposure to electron beams with density of 1.5 x 10^{19} e^-/cm^2 or over. At exposure rates of 6.6 x 10^{15} e^-/cm^2 and 199.3 eV half of the total chlorine goes into Cl $2p_{3/2}$ excited state forming $PtCl_2$. The FEBID of cis-$PtCl(NH_3)_2$ has been in Ref. [127] characterized by species detected by ESD using electron beams in the range of ~ 500 eV: NH_3^-, $NH_3 - H^-$, NH^-, N_2^-, $N_2 - N^-$, HCl^-; XPS studies show Pt(4f) and N(1s) signals, and DEA studies show the most abundant products are Cl^-, $Pt(NH_3)_2^-$ and NH_2^- (at 5.5 eV) representing the transitions from ground state HOMO to the lowest unoccupied orbital LUMO. The use of Br, I and F containing precursors is important for applications where C content in the final structure should be ~ 0 % (nanowires, nanotubes, and superconductors). The Pt – P bond is characterized by antibonding where the Pt 5d orbitals overlap with PF_3 σ orbitals, and bonding of Pt 5d overlapping P – F σ* empty orbitals.

A4.1 PT$(PF_3)_4$

Compared to $Pt(NH_3)_4(NO_3)_2$ and $Pt(acac)_2$, fluorine containing precursors such as $Pt(PF_3)_4$ are more widely used for deposition purposes as the fluorides are pumped away more easily and electron impact dissociation processes may leave only the Pt, releasing all the PF_3 radicals. $Pt(PF_3)_4$ and $(CH_3)_3PtCp(CH_3)$ experimental data in Ref. [128] of FEBID studies have shown a carbon content of 1.15 ± 0.1 %, double than that derived from carbon free Pt precursors, with a value of 0.57 ± 0.1 %. A decrease

of two orders of magnitude is observed for Pt interconnects compared to bulk Pt, one of the potential causes being the surface oxidation. Interconnects with low resistivity in the range of 0.24 x 10^{-3} Ωcm, while the standard $(CH_3)_3PtCp(CH_3)$ has a value of 0.2 Ωcm. Similar VRH behaviour is observed for $W(CO)_6$ and $(CH_3)_3PtCp(CH_3)$ at temperatures between 7 – 300 K, while in Ref. [129] the authors report conductivity values from low-electron irradiation of 1.28 x 10^5 $\Omega^{-1}cm^{-1}$, demonstrating that samples with sp^2 bonds have higher conductivity than samples with sp^3 bonds. Ritz and Bartell 1976 [130] experimentally determined the bond lengths and angles for the molecular structure as having values of Pt – P 2.229 Å, P – F 1.55 Å and <PtPF 118.9 deg. Table A4.1.1 presents data from Zlatar et al 2016 [131] with the $Pt(PF_3)_4$ symmetry point group as T_d. The molecular structure was calculated for the molecule using TDDFT calculations.

$Pt(PF_3)_4$	BDE (eV) in Ref. [131]	Resonances (eV) in Ref. [132]	Cross Sections (pm^2) in Ref. [132]	Type	Bond length(Å)
$Pt(PF_3)_3$	0.91	0.5	19800	Pt - PF_3	2.229 [130], 2.23 [133]
$Pt(PF_3)_2$	1.15	0.5 1.8	89 48	P - F	1.55 [130 - 133] 1.561 NIST
$Pt(PF_3)F$	-	2.1 5.9	25 121	Type	Angle(deg)
$PtPF_3$	1.49	5.9	96	<PtPF	97.7 NIST, 98.9 [133]
Pt	2.81	6	1.8	<XPF	119.6 NIST, 118.7 [133]

Table A4.1.1. $Pt(PF_3)_4$ structure: bond lengths (Å) and bond dissociation energy (BDE)

DEA of $Pt(PF_3)_4$ follows the schematics in relation (A3.1.1):

$$\begin{aligned} Pt(PF_3)_4 + e^- \rightarrow\ & Pt(PF_3)_4^* \rightarrow Pt(PF_3)^-_3 + PF_3 + e^- \\ & \rightarrow Pt(PF_3)^-_2 + (PF_3)_2 + e \\ & \rightarrow Pt(PF_3)F^- + (PF_3)_2 + PF_2 + e^- \\ & \rightarrow PtPF^-_3 + (PF_3)_3 + e^- \\ & \rightarrow Pt^- + (PF_3)_4 + e^- \end{aligned} \qquad (A4.1.1)$$

The ground electronic state of $Pt(PF_3)_4$ is $^1A_1$ and the symmetry configuration is D_{3h}. The excited states of $Pt(PF_3)_4$ in Ref. [131] are A_1, A_2, E, T_1, T_2 characterized by singlet and triplet allowed transitions, $^1T_2$ spin – and dipole allowed states, and $^3A_1 \rightarrow T_1$, $^3A_2 \rightarrow T_2$, $^3E \rightarrow T_1 + T_2$, $^3T_1 \rightarrow A_1 + E + T_1 + T_2$, $^3T_2 \rightarrow A_2 + E + T_1 + T_2$. In the DEA process, the induced dissociation will have resonances at electron energies between 0 and 12 eV in Ref. [132]. As the excited parent of the $Pt(PF_3)_4^-$ is short lived, its presence was not experimentally determined by mass spectrometry, compared to other compounds such as $Ti(OPr)_4^-$. Besides the five Pt containing negative fragments, close to 12.0 eV, May et al 2012 [132] reported the presence of F^- with cross-sections values in the range of ~87 pm^2. The P - Pt – P vibrational deformation energy is in the range of only 6meV compared to $Pt(acac)_2$ and $Pt(NH_3)_4(NO_3)_2$. Allan et al 2012 [134] by using DFT and experimental data found 5 shape resonances corresponding to vibrational excitations at 0.84 eV, 1.75 eV, 3.3 eV, 6.6 eV and 8.5 eV. The same Pt – P 5d and P – F σ* orbitals overlapping are reported similar to the data from Zlatar et al 2016 [131], while the parent excited states were assigned to Rydberg states at 5.8 eV, 6.8 eV, 7.4 eV, 8.4 eV and 11 eV.

Structure calculations of $Pt(PF_3)_4$. $Pt(PF_3)_4$ has the ground state configuration $^1A_1$ $(7e)^4$ $(6t_1)^6$ $(20t_2)^6$ $(8e)^4$ $(7t_1)^6$ $(14a_1)^2$ $(8t_1)^6$ $(1a_2)^2$ $(21t_2)^6$ $(9e)^4$ $(22t_2)^6$ $(23t_2)^0$ $(10e)^0$ $(9t_1)^0$ $(15a_1)^0$ $(16a_1)^0$ $(24t_2)^0$ $(25t_2)^0$ $(11e)^0$ $(17a_1)^0$ $(26t_2)^0$ $(10t_1)^0$ $(27t_2)^0$ in Ref. [131], in good agreement with our ground state DFT calculations from Gaussian 16 presenting the ground state of the neutral molecule as $^1A_1$: $(6s_0\ 5d_8\ 6p_1\ 7p_0)^1$ $(3s_1\ 3p_1\ 4p_0)^4$ $(2s_1\ 2p_5)^{12}$. The minimum energy for the converged structure from the DFT calculation of the structure of $Pt(PF_3)_4$ using LANL2DZ/B3LYP studies is E(RB3LYP) = -1343.49559431 Hartree. The orbital energies and kinetic energies (alpha) are presented in Table A4.1.2.

		1	2
69	O	-0.358223	2.227926
70	O	-0.346446	2.168793
71	O	-0.315889	1.983086
72	O	-0.312647	2.214204
73	O	-0.310166	2.172560
74	V	-0.137718	1.423954
75	V	-0.132390	1.741561
76	V	-0.121275	2.190377
77	V	-0.096142	1.797204
78	V	-0.093347	1.765180

Table A4.1.2. $Pt(PF_3)_4$ orbital energies for HOMO and LUMO

The total kinetic energy from orbitals has a value of 1.240465022141E+03 with a number of orbitals 1 – 162 orbitals. From Table A4.1.1 we observe that the LUMO orbital is orbital 74 with a kinetic energy of 2.019897 eV and the HOMO orbital is 73 with a kinetic energy of 2.339627 eV. For the calculation of the $Pt(PF_3)_4$ molecules we used a LANL2DZ basis set with different methods B3LYP/LANL2DZ, HF/LANL2DZ, MP2/LANL2DZ, MP4/LANL2DZ, MP4(SDTQ)/LANL2DZ with full population density.

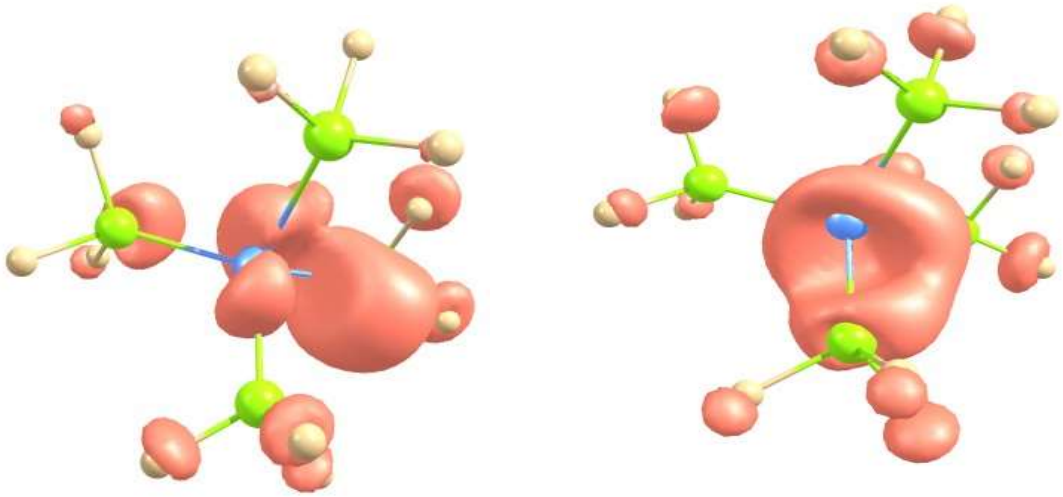

(a) (b)

Fig A4.1.1. $Pt(PF_3)_4$ orbitals LUMO (74) (a) and HOMO (73) (b)

The $Pt(PF_3)_4$ bond distances are expected to be shorter than the simple PF_3 radical, if taken separately. The bond distances for PF_3 are presented in Table A4.1.2 in comparison with the optimized structure for $Pt(PF_3)_4$. Comparatively, the bond length of P – F increase from the PF_3 to $Pt(PF_3)_4$, a smaller R(P – F) is observed in the PF_3 structure on *NIST database*, as well as $Pt(PF_3)_4$ structure from Gaussian 16 calculations (see Table A4.1.2).

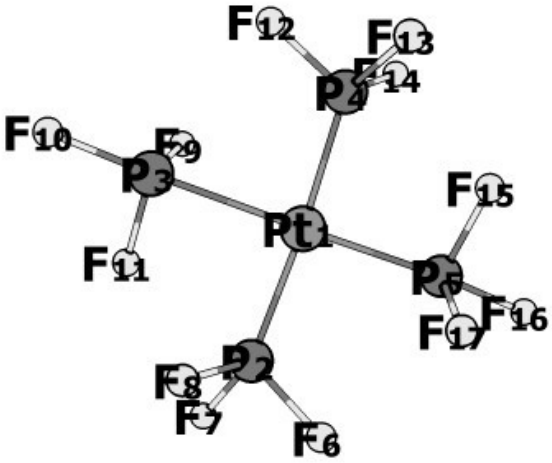

R[1, 2]	2.35701817
R[3, 9]; R[5, 15]	1.69799106
R[2, 8]	1.67562973
R[4, 13]	1.65878032

Fig A4.1.2. $Pt(PF_3)_4$ structure and bond distances

The Gaussian 16 code was run for both precursors, the $Pt(PF_3)_4$ and the PF_3 radical in neutral state, using the B3LYP/LANL2DZ basis set and method, following 16 cycles of structural optimization with a resulting energy $E(B3LYP)_{Pt(PF3)4}$ = 1343.53 Hartree, 52 % higher than the energy of a single PF_3 radical.

Compound	R(P – F) (Å)	H_{fg} (kcal/mol)	Energy (Hartree)
$Pt(PF_3)_4$	2.3_{eq}; 3.6_{ax}; 1.68-1.72	321.1	1343.5344
PF_3	1.561[NIST]; 1.599	228.8[NIST]; 640.938	640.952

Table A4.1.3. Bond distance, enthalpy, and energy of the system

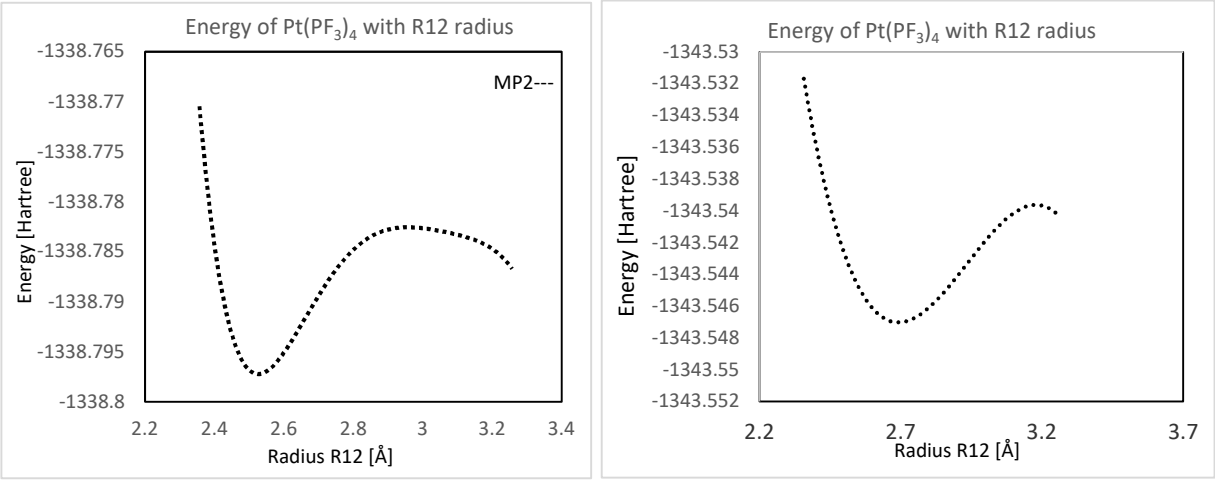

(a) (b)

Fig A4.1.3. Change in energy of $Pt(PF_3)_4$ with varying the radius between Pt(1) and P(2) at (a) MP2/LANL2DZ and (b) B3LYP/LANL2DZ level

The radius of Pt – P (1) bond was varied by 0.1 for 10 steps and at each point the structure was optimized and the energy of the system determined. The MP2/LANL2DZ and B3LYP/LANL2DZ were used to run the energy calculations for each of the steps. The data was not plotted on the same graph for comparison due to the high difference in the final energy value of the system, the values for MP2/LANL2DZ presenting a lower amplitude and less reliable value. It is easier to converge to a stable structure when varying one of the outer P – F bonds compared to varying the inner bond to the metal atom Pt – P. The zero-point energy and thermal corrections are calculated to correct (as their name says “corrections”) vibrations of the molecular system that persist for very high temperature values where an apparent immobility of the system is observed or for very low temperature values, where one would expect the system and substrate to be frozen. For higher temperatures, the values of the thermal energy and energy of the system need to have the correction factor added, see the values presented in the sums of the electronic and thermal energies and enthalpies (the values have the correction added to the final value).

Zero-point correction	0.032413 (Hartree/Particle)
Thermal correction to energy	0.057110
Thermal correction to enthalpy	0.058055
Thermal correction to Gibbs free energy	-0.033873
Sum of electronic and zero-point energies	-1343.502028
Sum of electronic and thermal energies	-1343.477331
Sum of electronic and thermal enthalpies	-1343.476386
Sum of electronic and thermal free energies	-1343.568314

Table A4.1.4. Thermal corrections of $Pt(PF_3)_4$ molecule from natural orbital population calculations

The entropy, enthalpy, and energy for a liquid, solid or gas are defined by the relation (A4.1.2):

$$\Delta G_i = \Delta H_i - T\Delta S_i \quad \text{(A4.1.2)}$$

The nominal temperature used for the system calculations is set as default to 298 K, room temperature. For the $Pt(PF_3)_4$ precursor, the calculated thermal corrections are taken at room temperature and nominal pressure of 1 atm. The values are presented in Table A4.1.5. The thermal energy correction is denominated as E(Thermal) in kcal/mol with a value of 35.526 kcal/mol. Besides the thermal energy correction, the constant volume molar capacity, CV, with a total value of 6.255 cal/mol·K, and entropy (S) with a value of 52.101 cal/mol·K are used. The precursors are not always used at room temperature, most of the time for deposition purposes they are used at values less that 100 K in Ref. [134], or for gas phase studies, where the temperature increases over 300 K.

	E(Thermal) kcal/mol	CV cal/mol-kelvin	S cal/mol-kelvin
Total	35.837	73.668	193.479
Electronic	0.000	0.000	0.000
Translational	0.000	2.981	44.782
Rotational	0.000	2.981	35.112
Vibrational	34.060	67.706	113.585

Table A4.1.5. Contributions from the three types of processes in the population analysis of orbitals

Each type of contribution from each type of process are presented in Table A4.1.5. The vibrations corresponding to the top (V = 0) have the highest contribution to the process (Table A4.1.5), followed by the translational process and the rotational process.

	Q	$Log_{10}(Q)$	ln(Q)
Total Bot	0.380761E+16	15.580652	35.875778
Total V = 0	0.308642E+31	0.308642E+31	70.204565
Electronic	0.100000E+01	0.000000	0.000000
Translational	0.502626E+09	8.701245	20.035357
Rotational	20.035357	20.035357	20.035357

Table A4.1.6. Vibrational parameter optimization

The vertical electron attachment energy (VEAE) of the system is calculated from the N+1 electron energy of the system minus the N-electron energy of the system. From these VEAE of the system the VEA or vertical electron energies can be calculated for the system. These VEA values are reported as the negative VEAE and are determined from the calculated values of the VEAE with the pole P3 calculations (see Table A4.1.7). The values of the VEAE are presented in Table A4.1.7.

	Orbital 74		Orbital 75	
	Alpha	Spin-orbital	Alpha	Spin-orbital
Koopmans Theorem	0.148E+00	4.015 eV	0.169E+00	4.599 eV
Conv. 2nd order pole	0.116E+00	3.158 eV	0.123E+00	3.346 eV
Conv. 3rd order pole	0.121E+00	3.290 eV	0.129E+00	3.530 eV
Renormalized P3 pole	0.120E+00	3.271 eV	0.129E+00	3.502 eV

Table A4.1.7. Summary of results for alpha spin orbital P3 coupling
for $Pt(PF_3)_4$ vertical electron affinities (LUMO and LUMO+1)

The first vertical excitation energy (VEE) is obtained from VEAE for LUMO+1 minus the VEAE for LUMO, in our calculation we obtain a value of VEE of -21.17 eV, the negative values of VEAE showing that the states are bound, but in our case only one state is bound corresponding to orbital 75. The values in Table A4.1.8 represent the vertical electron detachment energy (VEDE). The vertical ionization potential (VIP) of the $Pt(PF_3)_4$ molecule is the negative value of the VEDE. The values of VEDE are calculated for HOMO (75), HOMO-1 (74) and HOMO-2 (73). As all the values of VEDE are positive in the system and VIP is the negative of VEDE, the process in the $Pt(PF_3)_4$ is an exoenergetic process.

	Orbital 73		Orbital 74		Orbital 75	
	Alpha	Spin-orbital	Alpha	Spin-orbital	Alpha	Spin-orbital
Koopmans Theorem	0.113	3.082 eV	0.128E+00	3.492 eV	0.136	3.695 eV
Conv. 2nd order pole	0.0819	2.229 eV	0.873E-01	2.376 eV	0.114	3.100 eV
Conv. 3rd order pole	0.0866	2.355 eV	0.927E-01	2.522 eV	0.116	3.147 eV
Renormalized P3 pole	0.0859	2.336 eV	0.918E-01	2.499 eV	0.115	3.140 eV

Table A4.1.8. Summary of results for alpha spin-orbital P3 coupling for $Pt(PF_3)_4$ vertical ionization potentials (HOMO, HOMO-1 and HOMO-2)

Electron detachment will always be from the lowest occupied orbital to the highest unoccupied orbital, with implications for the fragmentation of the molecular compound. Through the excitation in the presence of an electron, the molecule would undergo a transition into a higher excited state and further stabilization at an energy higher than the initial system energy.

Study of the fragmentation using DFT calculations and Gaussian 16 software. In the study of the fragmentation processes of $Pt(PF_3)_4$, only the dissociation of the main four ligands Pt – PF_3 have been analysed as these are the most important processes leading to the decomposition of the precursor, though secondary electrons and related phenomena do take place at energies 0 – 20 eV that could cause the incomplete decomposition and formation of only intermediary products as F^-, PF^- and PF_2^-. The appearance energies for the available PF_3 radicals are in the range of 13 – 21 eV for dissociative ionization processes without the apparition of single fluorine ions.

	B3LYP/ LANL2DZ	HF/ LANL2DZ	MP2/ LANL2DZ	MP4/ LANL2DZ	MP4(SDTQ) / LANL2DZ
$E_{counterpoise}$ (Hartree)	-1343.52	-1336.92	-1338.71	-1338.8	-1338.8
E_{BSSE} (eV)	0.009	0.006	0.03	0.03	0.03
$\sum_{Fragments}$ (Hartree)	-1343.52	-1336.92	-1338.69	-1338.77	-1338.77
$E_{Complexation\ Raw}$ (kcal/mol)	-6.06	-3.53	-36.55	-39.2	-39.2
$E_{Complexation}$ Corr. (kcal/mol)	-0.64	0.55	-17.36	-17.64	-17.64

Table A4.1.9. Fragmentation of $Pt(PF_3)_4$ for the loss of one PF_3 ligand at 0.76 eV

The negative ions at their fragmentation energy have the electron energy as presented in Table A4.1.9. The value is close to 0 eV for the B3LYP level of theory with a value of 0.22 eV, while the value reported in the literature as the dissociation of the first Pt – PF_3 ligand is 0.5 eV.

Level of theory	B3LYP/ LANL2DZ	HF/ LANL2DZ	MP2/ LANL2DZ
$E_{ComplexationCorr.}$ (kcal/mol)	-5.08	-3.03	-45.54

Table A4.1.10. Complexation energy for negative ions for the loss of one PF_3

Dissociation values have been calculated for the molecule in neutral state with the formation of neutral fragments in the process of neutral dissociation. The values presented for the neutral dissociation of the $Pt(PF_3)_4$ into $Pt(PF_3)_3$ and PF_3 are presented in Table A4.1.10, the first appearance threshold has a value of 0.76 eV for a bond strength of -17.64 kcal/mol calculated at MP4 level of theory or close to ~0 eV at B3LYP level of theory.

For PF_3 bonds the complexation energy is in the order of 0 – 1 eV since the experimental value for the first excited state is similar to the excitation value of one PF_3 ligand at 0.76 eV (-17.54 kcal/mol).

	B3LYP/ LANL2DZ	HF/ LANL2DZ	MP2/ LANL2DZ	MP4/ LANL2DZ	MP4(SDTQ) / LANL2DZ
$E_{Counterpoise}$ (Hartree)	-1343.51	-1336.91	-1338.74	-1338.81	-1338.81
E_{BSSE} (eV)	0.02	0.02	0.03	0.04	0.04
$\sum_{Fragments}$ (Hartree)	-1343.47	-1336.90	-1338.70	-1337.78	-1337.78
$E_{Complexation}$ Raw (kcal/mol)	-37.46	-19.02	-41.21	-43.17	-43.17
$E_{Complexation}$ Corr. (kcal/mol)	-24.04	-9.12	-19.83	-19.20	-19.20

Table A4.1.11. Fragmentation of $Pt(PF_3)_4$ for the loss of two PF_3 ligands at 0.83 eV

The second and third ligands from our Gaussian calculations have values close to the values presented for a single ligand, 0.83 eV and respectively 0.63 eV. These values, considering the accuracy of the calculations, are very close to one another, suggesting a very small quantity of energy needed to break two or three Pt – PF_3 ligands. A source of error could be the stability of the ion in the case of dissociation of three ligands resulting a shorter life of the anion or a much faster and shorter-lived dissociation

process, a small cross-section value would be observed in this case characteristic to a very low yield value to electron energy.

	B3LYP/ LANL2DZ	HF/ LANL2DZ	MP2/ LANL2DZ	MP4/ LANL2DZ	MP4(SDTQ)/ LANL2DZ
$E_{Counterpoise}$ (Hartree)	-1343.50	-1336.91	-1338.73	-1338.80	-1338.80
E_{BSSE} (eV)	0.03	0.02	0.04	0.05	0.05
$\sum_{Fragments}$ (Hartree)	-1343.47	-1336.90	-1338.70	-1338.77	-1338.78
$E_{Complexation\ Raw}$ (kcal/mol)	-38.97	-18.62	-42.59	-45.05	-45.05
$E_{Complexation\ Corr.}$ (kcal/mol)	-22.54	-6.44	-16.66	-15.76	-15.76

Table A4.1.12. Fragmentation of $Pt(PF_3)_4$ with the loss of three PF_3 ligands at 0.68 eV

The fragmentation method we used in these Gaussian calculations might not be the most reliable method for determining the fragmentation thresholds, the multistep energy method could give better results in the present case. At the B3LYP level though, the $Pt(PF_3)_3$ resonance has a value of 0.98 eV, 0.48 eV higher than the experimental value of 0.5 eV. For the negative ions at the B3LYP level of theory the dissociation value is in the order of 0.94 eV (-21.59 kcal/mol). Both the $Pt(PF_3)^-_3$ and $Pt(PF_3)^-_2$ resonances are found to be at the same value of 0.5 eV, the second one presenting another peak at 1.8 eV. From our calculations, the resonance for the formation of the neutral $Pt(PF_3)_2$ is at 0.83 eV, 0.33 eV higher than experimental value in Ref. [132]. The experimental values for the negative ions are presented in Table A4.1.13.

Negative Ion	Pt^-	$PtPF^-_3$	$Pt(PF_3)^-_2$	$Pt(PF_3)^-_3$	F^-
Dissociation energy (eV)	6.0	5.9	0.5; 1.8	0.5	12.0

Table A4.1.13. Negative ion formation of $Pt(PF_3)_4$ exposed to electron beams from Ref. [135]

In Ref. [135], the resonances corresponding to the formation of a $Pt(PF_3)F^-$ anion, through double fragmentation of $Pt(PF_3)_4$ in $PtPF_3 + 3(PF_3)$ and of PF_3 in P and F, and recombination of $PtPF_3$ with F, are all shape resonances, while the resonance responsible for the formation of a F^- anion is a core shape resonance.

	B3LYP/ LANL2DZ	HF/ LANL2DZ	MP2/ LANL2DZ	MP4/ LANL2DZ	MP4(SDTQ) /LANL2DZ
$E_{Counterpoise}$ (Hartree)	-1343.50	-1336.96	-1338.78	-1338.78	-1338.78
E_{BSSE} (eV)	0.03	0.03	-0.01	0.07	0.07
$\sum_{Fragments}$ (Hartree)	-1343.39	-1336.86	-1338.63	-1338.64	-1338.64
$E_{Complexation\ Raw}$ (kcal/mol)	-87.51	-44.82	-88.23	-132.61	-132.61
$E_{Complexation\ Corr.}$ (kcal/mol)	-66.13	-65.80	-95.21	-91.51	-91.51

Table A4.1.14. Fragmentation of $Pt(PF_3)_{4\ for}$ the loss of four PF_3 ligands at 3.97 eV

In the formation of the neutral Pt, the dissociation electron energy from our calculations has a value of 3.97 eV at the MP4 level of theory and a value of 4.13eV at the B3LYP level of theory, 2 eV lower than the experimental value for the formation of the negative ion Pt^- declared to be at 6.0 eV in Ref. [135]. Allan et al 2012 [134] determines the HOMO and LUMO as $22t_2^{-1}$ and $23t_2$, and the band assigned to it corresponds to the 5.9 eV resonance responsible for the formation of $PtPF^-_3$. Similar excitation and orbital data are presented in Ref. [136] with the HOMO and LUMO orbitals as $22t_2$ 73 and $23t_2$ 74 orbitals.

Excited states of $Pt(PF_3)_4$ using Gaussian 16 calculations. For the calculation of the excited states, in the CIS functional has been employed a number of 44 states to be analysed. The first state, a transition from the σ-state to π*-state, HOMO 73 to LUMO 74 is close to the first fragmentation energy of 0.76 eV with the first excited state at a value of 0.7411 eV. The transition for the cleavage of the fourth PF_3 ligand is the transition from higher excited state orbital 73 to lower lying excited state orbital 76 in $^1A_1$ state, the energy falling around 3.81 eV. For the 44 excited states, the resonances lie between 0.74 eV to 8.05 eV, more excited states can be run up to 100 states and 10 eV. From CIS calculations we obtained 34 excited states up to 8.1868 eV, the energies for these excited states are presented in Table A4.1.15. The first excited state $2A_1$ at an energy of 1.2974 eV is a forbidden state seen from the value of the oscillator strength (f = 0); all other states are allowed transitions from the $^1A_1$ initial configuration. The excited states at 6.3334 eV and 6.3564 eV, corresponding to states 10 and states 11, are overlapping transitions from the ground state configuration to $^2A_1$, with oscillator strengths higher than 0, similar to states 18 $^2A_1$ and 19 $^2A_1$ very close in values to 7.1389 eV and 7.1567 eV, states 26 $^2A_1$ and 27 $^2A_1$, with values of 7.6597 eV and 7.6821 eV, states 28 $^3A_1$ and 29 $^2A_1$, at 7.8108 eV and 7.8266 eV, states 32 $^2A_1$ and 33 $^2A_1$, with values of 8.1226 eV and 8.1451 eV.

$2A_1$	**$2A_1$**	**$2A_1$**	**$2A_1$**	**$2A_1$**	**$2A_1$**	**$3A_1$**	**$2A_1$**

1.2874eV	1.8197eV	2.3384eV	2.8356eV	4.8615ev	4.9818eV	5.5123eV	6.0446eV
$3A_1$	**$2A_1$**	**$2A_1$**	**$2A_1$**	**$3A_1$**	**$3A_1$**	**$3A_1$**	**$2A_1$**
6.3334eV	6.3564eV	6.5093eV	6.5662eV	6.7449eV	6.8352eV	6.8971eV	6.9696eV
$2A_1$	**$2A_1$**	**$2A_1$**	**$2A_1$**	**$2A_1$**	**$2A_1$**	**$3A_1$**	**$2A_1$**
6.1739eV	7.1389eV	7.1567eV	7.2131eV	7.2534eV	7.3095eV	7.3941eV	7.4797eV
$2A_1$	**$2A_1$**	**$2A_1$**	**$2A_1$**	**$2A_1$**	**$3A_1$**	**$2A_1$**	**$2A_1$**
7.6597eV	7.6821eV	7.8266eV	8.0064eV	8.0603eV	7.8108eV	8.1226eV	8.1451eV
$3A_1$							
8.1868eV							

Table A4.1.15. Excited states up to 8.18 eV from $Pt(PF_3)_4$

We determine the excited states from TDDFT at the LANL2DZ/B3LYP level obtaining three excited states up to 1.3 eV with oscillator strengths of 0.2877 eV (*f = 0.0000*), 0.5355 eV *(f = 0.0000*) and 1.2610 eV (*f = 0.0000*), all representing forbidden transitions from a lower LUMO to a higher HOMO.

Excited State 1: 2.000-A 0.2877 eV 4309.36 nm f=0.0000 <S**2>=0.750

Excited State 2: 2.003-A 0.5355 eV 2315.44 nm f=0.0000 <S**2>=0.753

Excited State 3: 2.002-A 1.2610 eV 983.20 nm f=0.0000 <S**2>=0.752

On the other hand, the CIS calculations, although known to be less accurate, produced excited states that lie in the allowed transition region, at values of 0.7411 eV (*f = 0.0091*) and 1.3409 eV (*f = 0.0469*).

Excited State 1: Singlet-A 0.7411 eV 1673.02 nm f=0.0091 <S**2>=0.000

Excited State 2: Singlet-A 1.3409 eV 924.60 nm f=0.0469 <S**2>=0.000

For $Pt(PF_3)_4$, the TDDFT does not give us any allowed transitions and its absorption cross-sections interdependence with the oscillator strength cannot be plotted, the values presented in Fig 6.1.5 correspond only to CASSCF and CIS calculations.

Ee	f	∫ε(ν)d(ν)
0.7411	0.0091	3.89E+06
1.3409	0.0469	2.00E+07

Table A4.1.16. $Pt(PF_3)_4$ absorption coefficient and oscillator strength interdependence for n = 1.846988

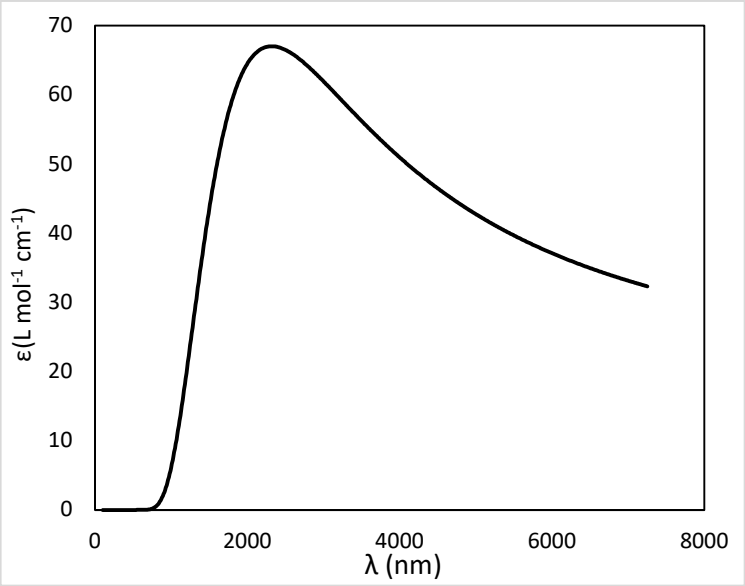

Fig A4.1.4. $Pt(PF_3)_4$ absorption cross-sections interdependence with oscillator strength

$Pt(PF_3)_4$					
				∫ε(v)d(v)	
f	Ee	n	A	*f* = 0.0091	*f* = 0.0469
0.0091	0.7411	0.4	1.08E-08	8.43E+05	4.34E+06
0.0469	1.3409	0.5	8.64E-09	1.05E+06	5.43E+06
		0.6	7.20E-09	1.26E+06	6.51E+06
		0.7	6.17E-09	1.47E+06	7.60E+06
		0.8	5.40E-09	1.69E+06	8.69E+06
		0.9	4.80E-09	1.90E+06	9.77E+06
		1	4.32E-09	2.11E+06	1.09E+07
		1.1	3.93E-09	2.32E+06	1.19E+07
		1.2	3.60E-09	2.53E+06	1.30E+07
		1.3	3.32E-09	2.74E+06	1.41E+07
		1.4	3.09E-09	2.95E+06	1.52E+07
		1.5	2.88E-09	3.16E+06	1.63E+07
		1.6	2.70E-09	3.37E+06	1.74E+07
		1.7	2.54E-09	3.58E+06	1.85E+07
		1.8	2.40E-09	3.79E+06	1.95E+07
		1.9	2.27E-09	4.00E+06	2.06E+07

Table A4.1.17. Absorption coefficient (integral) and oscillator strength of $Pt(PF_3)_4$ excited states (CIS level of calculation)

As at TDDFT level the oscillator strength has values of 0.00001, representing only forbidden transitions, the absorption dependence of the excited states has been sampled on excited states obtained at CIS level of calculations with electron energy values < 1 eV. A separate CASSCF study makes use of an active space of (9, 18), 9 orbitals with 18 electrons in the 9 orbitals, computing the excited states. The occupation of the orbitals is presented in Fig A4.1.5, with only alpha orbitals present. An alteration of excited state 7 with the excited state 12 is done, with a $^3A_1$ symmetric state in 7 and a $^2A_1$ symmetric state in 12.

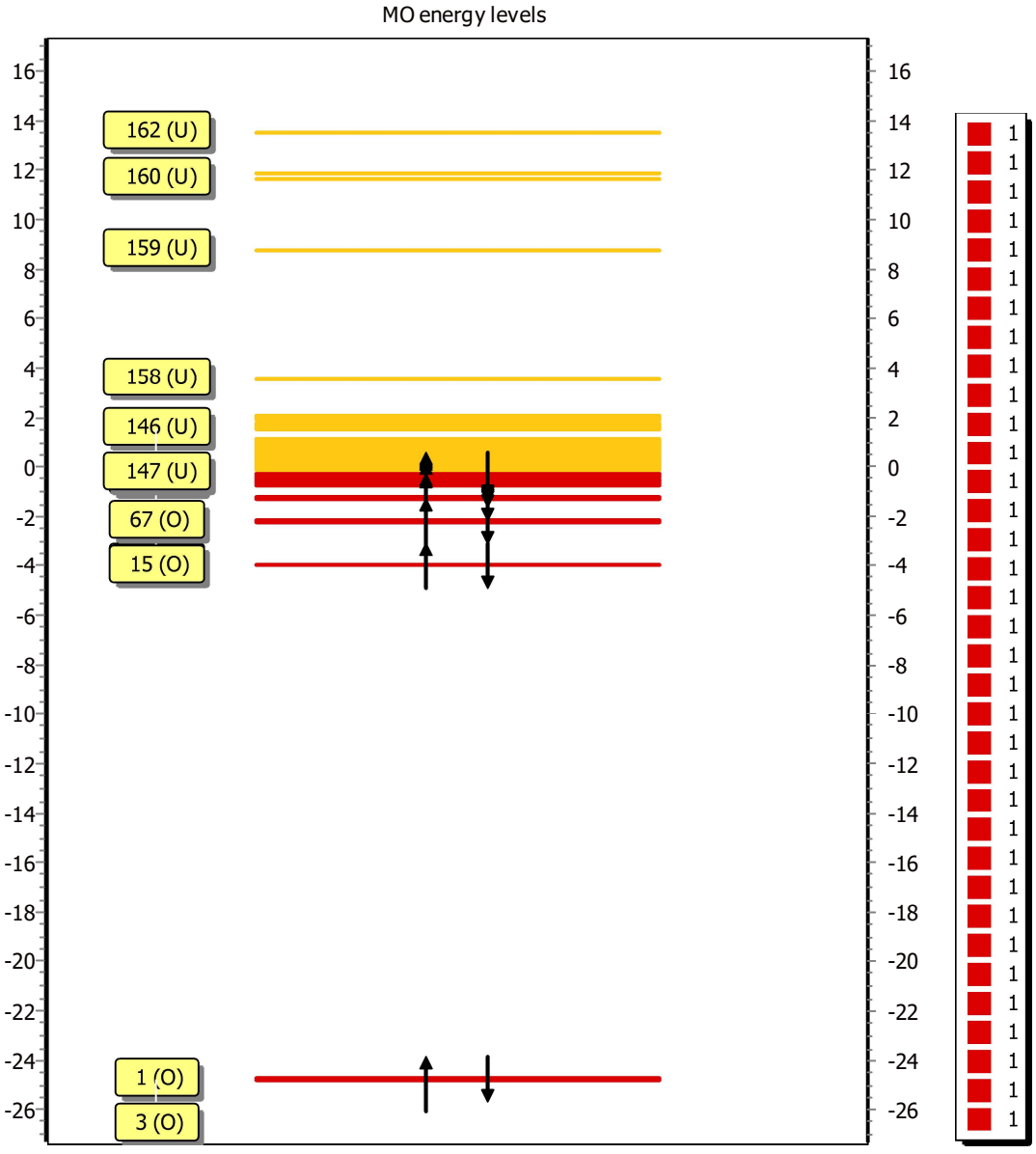

Fig A4.1.5. $Pt(PF_3)_4$ MO CASSCF diagram of optimized structure at B3LYP/LANL2DZ level of theory

The fragmentation pathway for the exothermic energy exchange between two fragments, part of the molecule characterizing a dissociation reaction is presented below. At B3LYP/LANL2DZ level of theory and CIS/TDDFT, the calculation was carried using one photon excitation energy and two fragments.

$$Pt(PF_3)_4^* \rightarrow Pt(PF_3)_3^- + PF_3 \qquad (A4.1.6)$$

The excited parent $Pt(PF_3)_4^*$ was taken in a negative doublet state while the higher mass fragment was defined as being a negative ion as a doublet with a negative charge -1; the second fragment is in neutral state. From the EET analysis of the excitation energy transfer of $Pt(PF_3)_4$, the excitation rate obtained for the energy transfer between the molecule and the two fragments (relation (A4.1.6)), we obtained an excitation rate of 1.4333 eV for the neutral fragment and an excitation rate of 0.7383 eV for the negative fragment $Pt(PF_3)_3$, with the molecule characterized by an excitation energy of 0.6950 eV.

A4.2 Pt(acac)$_2$

$Pt(acac)_2$ has a D_{3h} molecular symmetry and a mass of 393.3 amu. In FEBID studies in Ref. [137], the carbon content of the Pt nanostructures deposited using $Pt(acac)_2$ could be less than 1 %. The platinum from $Pt(acac)_2$ is extensively used for thin film deposition on substrates such as TiO_2 and Al_2O_3 in Ref. [136] in the form of oxides on the two substrates or only Pt on Al_2O_3, the difference coming in the temperature of deposition, 120-130 °C in the first case and over 140 °C in the second case.

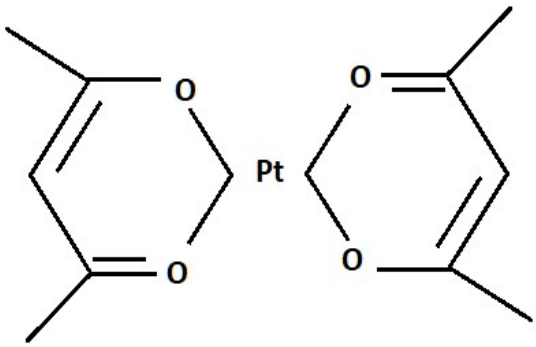

Fig A4.2.1. $Pt(acac)_2$ precursor

Gas phase studies of this compound are scarce, and mostly reports are of deposition studies in Ref. [136, 138 - 140] determining the deposition rate coefficient at different temperature rates and in different experimental conditions: MOCVD, CVD and atomic layer deposition. The $Pt(acac)_2$ precursor bond distances and angles in Ref. [139] are presented in Table A4.2.1.

$Pt(acac)_2$	Bond distance (Å) and angles (deg)
Pt - O	1.99
C - O	1.3
C - C	1.39
C - CH_3	1.51
<CCC	127
<OCC	127
<$OCCH_3$	114
<OPtO	96

Table A4.2.1. $Pt(acac)_2$ structure in Ref. [139]: bond lengths (Å) and angles (deg)

The electronic structure of $Pt(acac)_2$ determined using experimental data and pseudopotential valence-only ab-initio method in Ref. [141] presents molecular orbitals with the corresponding electronic energy bands (A, B, C, D, E, G, J) determined from the calculations as: $3b_{2g}$ corresponding to A at 7.6 eV, $2b_{1u}$ corresponding to C at 8.54 eV, $8a_g$ corresponding to B at 8.28 eV, $2b_{3g}$ corresponding to D at 8.90 eV, $7a_g$ corresponding to E and F bands at 9.27 eV and 9.70eV, the $2b_{2g}$, $5b_{2u}$, $6b_{3u}$, $5b_{1g}$, $1a_u$ orbitals correspond to G and J bands with ionization energies of 9.85 eV, 10.43 eV, 10.90 eV and 11.71 eV, and further orbitals $6a_g$, $5b_{3u}$, $1b_{3g}$, $1b_{1u}$, $1b_{2g}$, $5a_g$. All ligand – to - metal charge transfer σ symmetry for metal coordinates in planar square symmetry are characterized by empty s and d_{xy} metal orbitals. The $3b_{2g}(\pi_3)$ HOMO orbital in 5d state corresponding to band A has a small contribution to MOs. The metal – to - ligand orbitals with bonding and nonbonding character show higher energy levels compared to antibonding metal – to - ligand orbitals. The orbitals populations are s, p_σ, p_π, $5d_\sigma$ (x^2-y^2, z^2, xy), $5d_\pi$ (xz, yz) in Ref. [141] with overlapping d_{z^2} and p_z orbitals in the Pt – Pt cage linkage in Ref. [142]. The populations corresponding to the Pt – O linkage have stronger metal ligands with σ and π type interactions and a d_{xz} higher contribution to the HOMO orbitals of $Pt(acac)_2$ than other similar compounds, increasing twice in amplitude compared to the case of $Pd(acac)_2$ precursor in Ref. [143], π and π* interactions. The bonding and nonbonding MOs stabilize, and the antibonding MOs destabilize. The same comparison comes in the case of tfac and hfac Pd precursors that have lower fragmentation energy compared to the acac Pt precursors. Previous ab-initio calculations performed for Pd(II) acetylacetonate complexes present a similar behaviour in Ref. [141, 144 - 145], not only in the electronic structure charge transfer process, but as well in substitution reactions. A more in-depth analysis of the (acac) radical has been presented in ANNEX 4 Acetylacetone section.

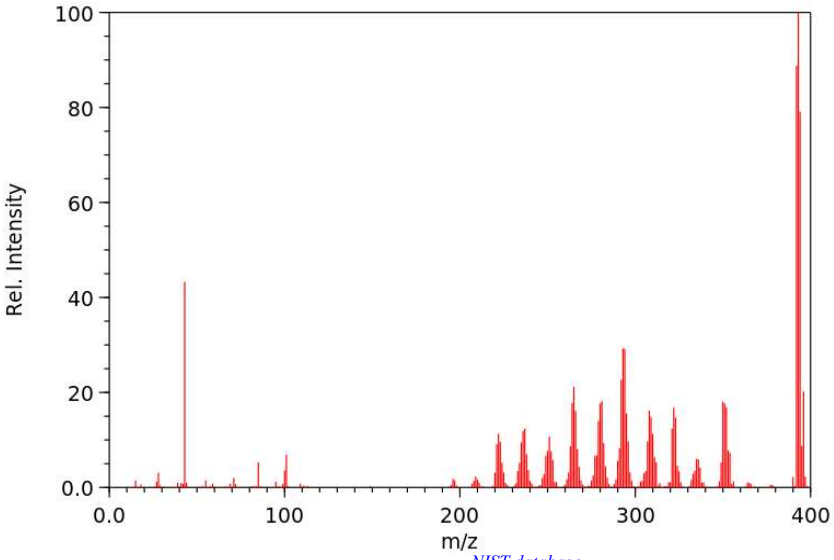

Fig A4.2.2. $Pt(acac)_2$ mass spectrum NIST database (in ground state)

The masses visible in the $Pt(acac)_2$ mass spectrum are m/z 43, 222, 237, 251, 265, 281, 294, 308, 322, 350, 393, and other possible masses are present but with very low ratios m/z 101, 197 and 209. The possible negative fragments, result of low electron energy interactions, are formed by loosing H, methyl radicals and O branches, with the organic elements results of the dissociation: H^-, CH^-_3, CH^-_2, CH^-, $COOH^-$: $PtO_4C_7H_7$ (m/z 350), $PtO_3C_6H_7$ (m/z 322), $PtO_3C_5H_7$ (m/z 294), $PtO_2C_4H_6$ (m/z 281), $PtOC_4H_6$ (m/z 265), $PtO_3C_3H_4$ (m/z 251), PtC_3H_6 (m/z 237) and PtC_2H_3 (m/z 222).

DFT calculations of $Pt(acac)_2$

The ground state configuration of the $Pt(acac)_2$ from literature data in Ref. [139] is $^1A_1$ in good agreement to the optimized ground state $^1A_1$ configuration we obtained from our DFT Gaussian 16 calculations: $(6s_0\ 5d_5\ 6p_0\ 6d_0)^1\ (2s_1\ 2p_5\ 3p_0)^4\ (2s_0\ 2p_3\ 3p_0)^4\ (2s_1\ 2p_3\ 3p_0)^6\ (1s_0)^{14}$. The minimum energy for the converged structure of $Pt(acac)_2$ from the energy optimization using LANL2DZ/B3LYP is E(RB3LYP) = -809.541302307 Hartree. The orbital energies and kinetic energies (alpha) for HOMO and LUMO orbitals calculated using Gaussian 16 are presented in Table A4.2.2.

		1	2
58	O	-0.255381	2.573772
59	O	-0.249412	1.588761
60	O	-0.244639	2.289257
61	O	-0.232736	2.059844

62	O	-0.212055	2.303541
63	V	-0.062537	1.882728
64	V	-0.053079	2.047634
65	V	-0.034726	3.296612
66	V	0.028277	0.439548
67	V	0.041656	0.406695

Table A4.2.2. $Pt(acac)_2$ orbital energies for HOMO and LUMO

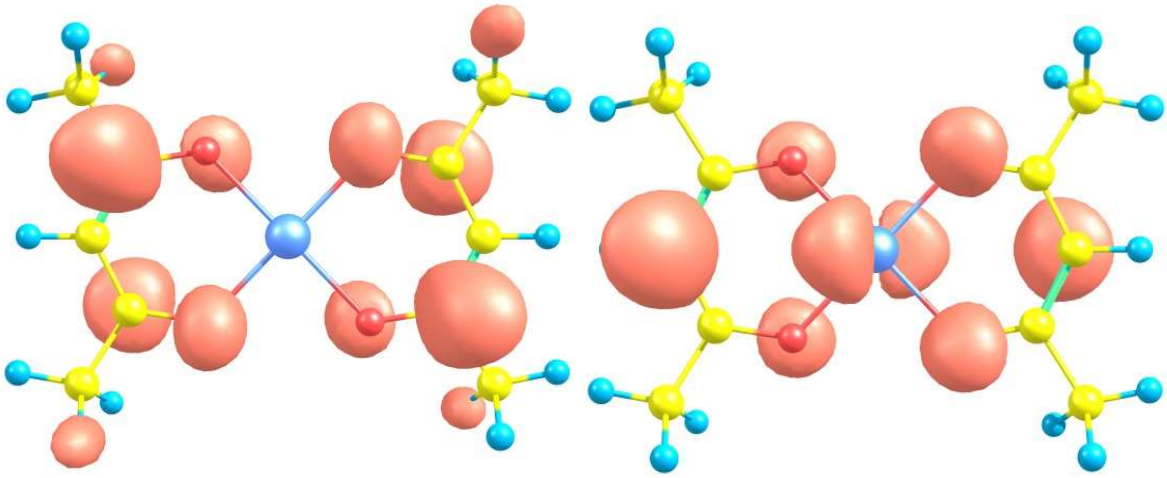

Fig A4.2.3. $Pt(acac)_2$ orbitals LUMO (63) (left) and HOMO (62) (right)

The value of the total kinetic energy from the orbital has a value of 7.240017E+02 for a number of 176 assigned orbitals to $Pt(acac)_2$ molecule. The LUMO orbital is orbital number 63 with an orbital energy of 2.303540 eV and HOMO orbital is the orbital number 62 with an orbital energy of 2.30 eV.

The thermal corrections for energies and zero-point corrections are run at room temperature (298 K) and 1 atm. For temperatures higher than room temperature or lower than room temperature, to the final value calculated in the simulation we add the values of correction to energy 0.255660 and enthalpy 0.246604. The updated values are presented in Table A4.2.3. The zero-point correction is included in the calculation and does not have to be added to the final value.

Zero-point correction	0.228108 (Hartree/Particle)
Thermal correction to energy	0.245660
Thermal correction to enthalpy	0.246604

Thermal correction to Gibbs free energy	0.180946
Sum of electronic and zero-point energies	-809.313265
Sum of electronic and thermal energies	-809.295713
Sum of electronic and thermal enthalpies	-809.294769
Sum of electronic and thermal free energies	-809.360427

Table A4.2.3. Thermal corrections of $Pt(acac)_2$ molecule from natural orbital population calculations

The enthalpy of formation obtained from the Gaussian 16 simulation with the optimized geometry presented in Fig A4.2.4 has a value of 809.29 kJ/mol, similarly the entropy and thermal free energy for the $Pt(acac)_2$ have been computed and are in good agreement with the values presented in Ref. [139], 809.295713 kJ/kmol and respectively 809.360427 kJ/kmol. The values of the bond distances, enthalpy of the system and energy are presented for each particular radical, CH, CH_3 and acac, and the main precursor molecule, in comparison with values from *NIST* database and literature are presented in Table A4.2.4.

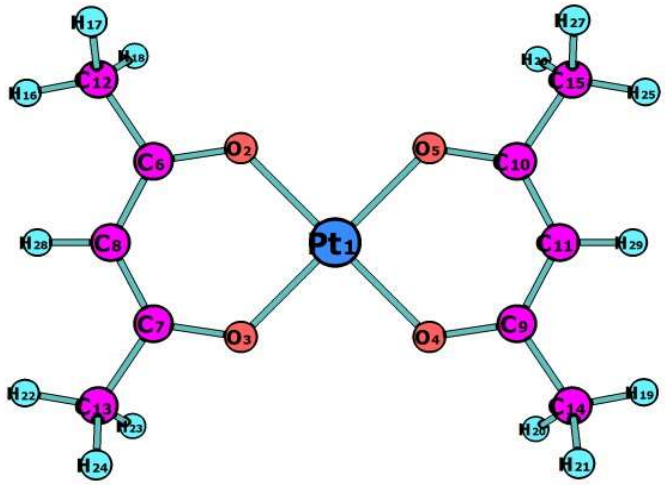

R[1, 2]	2.0252Å
R[2, 6]	1.3116Å
R[6, 8]	1.4136Å
R[8, 28]	1.083Å
R[6, 12]	1.514Å
R[12, 16]	1.0934Å
R[12, 17]	1.0972Å
R[12, 18]	1.0967Å

Fig A4.2.4. $Pt(acac)_2$ optimized structure and bond distances

The bond lengths for the optimized structure of $Pt(acac)_2$ are obtained with the natural population analysis with LANL2DZ/B3LYP basis set (see ANNEX 2 for detailed values and calculations). With the ground state in C_{4v} configurations a set of bond lengths for each of the fragments is obtained: Pt – O, C - CH_3, C – CH and O – C. The bonds lengths in the $Pt(acac)_2$ are similar to the ones in simple acetylacetone, with values in the range of ~1.0927 Å, smaller by 0.03 than in the ethyl where a value of the bond length of 1.120 Å is presented by *NIST database*; a value of 1.1718 Å lower by 0.4 is obtained from DFT calculations. The asymmetric structure calculated from DFT has C8 – H28 with values between 1.5 – 1.5586 Å (CH) and C12 – H17 with values between 1.09 – 1.0993 Å (CH_3). The energy change with

the variation of radius R12, Pt1 – O2, has been investigated at B3LYP and HF levels of simulation. The complexity of the method determines the accuracy of the simulation result, higher methods (e.g. B3LYP) giving better results to the variation of the radius. The plots of the two methods (see Fig A4.2.5) applied to the variation of the radius are presented in Fig A4.2.5. For this particular precursor, an elongation of the Pt – O bond compared to the PtO_2 or Pt_2O_3, a shortening of the C – H bond in ethyl radicals and an elongation of the C – H bonds of the methyl radicals are expected. A comparison of the bonds for each of the radicals ethyl, methyl, acac and the $Pt(acac)_2$, with energy and enthalpy of formation is presented in Table A4.2.4.

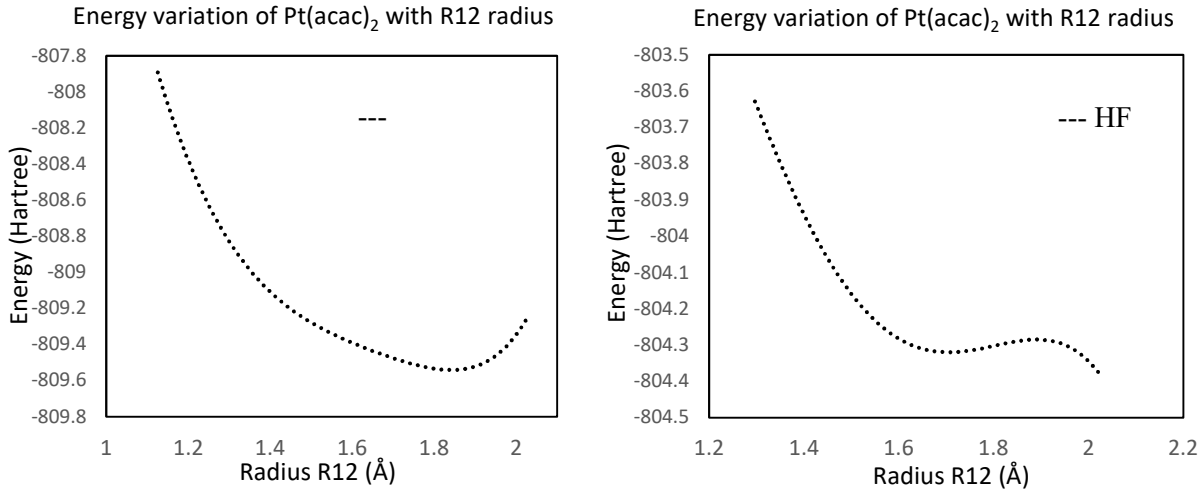

Fig A4.2.5. Change in energy of $Pt(acac)_2$ with varying the radius between Pt(1) and O(2) at (left) B3LYP/LANL2DZ and (right) HF/LANL2DZ level

Compound	R(C-H) (Å)	Energy (Hartree)	Hgf (kcal/mol)
$Pt(acac)_2$	1.083[(a)]; 1.0972[(b)]	724.0017	193.426
PtO_2	-	269.604	124.187
acac	1.0927[(b)]; 1.0971[(a)]*NIST; 1.5 -1.56; 1.09	345.476	91.874 NIST
CH_3	1.079[(b)]NIST; 1.1286; 1.9546	39.674	35.062 NIST
CH	1.120[(a)]NIST; 1.1718	38.420	142.399 NIST

* B3LYP/6-31+G**; (a) CH; (b) CH_3

Table A4.2.4. Bond distance, energy and enthalpy of formation of the system

The individual contributions to the enthalpy of formation and thermal corrections for energy, enthalpy and entropy were calculated and are presented in Table A4.2.5 corresponding to the total vibrational correction coming from electronic translations, rotational translations and translational movements of the precursor's molecules.

	Q	log10 (Q)	ln(Q)
Total Bot	0.589735E-83	-83.229343	-191.642645
Total V = 0	0.493052E+22	21.692893	49.949732
Electronic	0.100000E+01	0.000000	0.000000
Translational	0.306290E+09	8.486132	19.540042
Rotational	0.350636E+07	6.544857	15.070090

Table A4.2.5. Vibrational parameter optimization of $Pt(acac)_2$ molecule

The total thermal energy of the system is 154.154 kcal/mol, with a heat capacity of the system in the range of ~61.594 cal/mol·K and an entropy of 52.101 cal/mol·K. The rotational and translational parameters have similar values, representing 0.5 % of the total thermal energy of the system and 4.8 % of the heat capacity of the final system and 2.4 % - 3.2 % of the entropy of the system.

	E(Thermal) Kcal/Mol	CV Cal/Mol-Kelvin	S Cal/Mol-Kelvin
Total	154.154	61.594	138.189
Electronic	0.000	0.000	0.000
Translational	0.889	2.981	43.798
Rotational	0.889	2.981	32.928
Vibrational	152.376	55.632	61.463

Table A4.2.6. Contributions from the three types of processes in the population analysis of orbitals

The energy values of LUMO and LUMO+1 orbitals determined from renormalized partial third-order methods (p3+ pole), representing the vertical electron attachment energy VEAE, are used to determine the vertical excitation energy of the system. The vertical excitation energy is the VEAE of LUMO+1 minus the VEAE of LUMO, corresponding to a value of -0.337 eV. The positive values of the VEAE show that both states of the system are unbound. The VEA of the system would be the negative value of VEAE, in our case the system being an endoenergetic system.

	Orbital 63	Orbital 64

	Alpha	Spin-orbital	Alpha	Spin-orbital
Koopmans Theorem	2.93E-01	7.969 eV	2.95E-01	8.029 eV
Conv. 2nd order pole	2.61E-01	7.095 eV	2.47E-01	6.730 eV
Conv. 3rd order pole	2.62E-01	7.123 eV	2.50E-01	6.790 eV
Renormalized P3 pole	2.62E-01	7.119 eV	2.49E-01	6.782 eV

Table A4.2.7. Summary of results for alpha spin orbital P3 coupling for $Pt(acac)_2$ vertical electron affinity for LUMO and LUMO+1 orbitals

From the vertical electron detachment energy (VEDE) for the HOMO (63), HOMO-1 (62) and HOMO-2 (61) for the $Pt(acac)_2$, the vertical ionization potential is determined using the negative value of the VEDE. Since all our VEDE values for all orbitals are positive, the process being an exoenergetic process of an electron detaching from the system. Table A4.2.8 presents the value for vertical ionization potentials of the orbitals 61, 62 and 63: 6.407 eV, 6.726 eV and 7.119 eV.

	Orbital 61		Orbital 62		Orbital 63	
	Alpha	Spin-orbital	Alpha	Spin-orbital	Alpha	Spin-orbital
Koopmans Theorem	2.67E-01	7.267 eV	2.84E-01	7.731 eV	2.93E-01	7.969 eV
Conv. 2nd order pole	2.36E-01	6.421 eV	2.45E-01	6.673 eV	2.61E-01	7.095 eV
Conv. 3rd order pole	2.35E-01	6.405 eV	2.48E-01	6.735 eV	2.62E-01	7.123 eV
Renormalized P3 pole	2.35E-01	6.407 eV	2.47E-01	6.726 eV	2.62E-01	7.119 eV

Table A4.2.8. Summary of results for alpha spin-orbital P3 coupling for $Pt(acac)_2$ vertical ionization potentials for HOMO, HOMO-1 and HOMO-2 orbitals

The HOMO-1 and HOMO-2 are expected to have higher energy and higher occupation of the electronic states than the HOMO orbitals, and the LUMO. The transition from the HOMO to LUMO in the case of $Pt(acac)_2$ is a π to π^* transition, where an electron undergoes detachment through ionization and filling another open space into a lower occupied orbital with a structural transition of the molecule to π^*. The transition is always taking place from higher energy to lower energy and the system's energy from lower energy to final higher energy.

Study of the fragmentation using DFT functionals for calculations

The same hierarchy in the accuracy of the result (HF as the least accurate method, B3LYP as more reliable) is observed in the study of the fragmentation of one to multiple molecular bonds compared to experimental data of $Pt(acac)_2$, higher differences being observed for HF/LANL2DZ and MP2/LANL2DZ compared to the B3LYP/LANL2DZ and MP4(SDTQ)/LANL2DZ. The loss of one H of one of the acac branches should be a spontaneous process with little release of energy and high cross-sections. The Gaussian 16 study of the fragmentation process indicates the electron energy necessary to release one H atom to be ~3.36 eV that could be assigned to the higher stability of the complex and the strong bonding in the CH and CH_3 radicals. In the B3LYP study, the precursor has a dissociation threshold of 4.3 eV compared to the MP4 and MP4(SDTQ) with values of 3.6 eV or HF with a value of 3.25 eV.

	B3LYP/ LANL2DZ	HF/ LANL2DZ	MP2/ LANL2DZ	MP4/ LANL2DZ	MP4(SDTQ)/ LANL2DZ
$E_{Counterpoise}$ (Hartree)	-809.543	-804.368	-805.829	-805.981	-805.981
E_{BSSE} (eV)	0.004	0.003	0.01	0.006	0.006
$\sum_{Fragments}$ (Hartree)	-809.385	-804.249	-805.707	-805.857	-805.857
$E_{Complexation\ Raw}$ (kcal/mol)	-102.110	-76.810	-80.010	-80.970	-80.970
$E_{Complexation\ Corr.}$ (kcal/mol)	-99.500	-74.870	-76.490	-77.380	-77.380

Table A4.2.9. Fragmentation of $Pt(acac)_2$ by the loss of one H at 3.36 eV

The loss of one H in the simple acac radical from our Gaussian calculations has a value of 3.44 eV, compared with the value provided by the literature in Ref. [146] of ~ 0 eV, lower than our calculations showing a higher stability of the acac/$Pt(acac)_2$ compared to $Pt(acac)_2$/acac. The basis set used for the acac radical is 6-31G(d, p). The level of simulation used for our comparative calculations is B3LYP. The threshold for the dissociation of one H from the acac radical in $Pt(acac)_2$ has higher bond strength value than in acac (see for comparison Table A4.2.10).

$E_{Counterpoise}$ (Hartree)	E_{BSSE} (eV)	$\sum_{Fragments}$ (Hartree)	$E_{Complexation\ Raw}$ (kcal/mol)	$E_{Complexation\ Corr.}$ (kcal/mol)
-345.705	0.039	-345.578	-103.50	-79.33

Table A4.2.10. Fragmentation of acac radical by losing one H at B3LYP/6-31G(D, P) level of theory

The loss of one H from the CH group has a value of 4.55 eV (-104.88 kcal/mol), compared to the threshold for CH_3 with a value of 9.70 eV (-223.64 kcal/mol). Both calculations have been done at B3LYP level of theory using a 6-31G(d, p) basis set. A higher-than-expected value for the dissociation of $Pt(acac)_2$ into $Pt(acac)(COOCH{=}C_3H_3)^-$ and CH_3 takes place at a value of -543.950 kcal/mol corresponding to an electron energy of 21.4 eV (see values Table A4.2.11), the value of the energy making it a very improbable fragmentation pathway.

	B3LYP/ LANL2DZ	HF/ LANL2DZ	MP2/ LANL2DZ	MP4/ LANL2DZ	MP4(SDTQ)/ LANL2DZ
$E_{Counterpoise}$ (Hartree)	-809.531	-804.349	-805.796	-805.954	-806.000
E_{BSSE} (eV)	0.016	0.022	0.04	0.032	0.032
$\sum_{Fragments}$ (Hartree)	-808.665	-803.402	-804.975	-805.213	-805.213
$E_{Complexation\ Raw}$ (kcal/mol)	-554.140	-608.280	-539.440	-485.220	-513.680
$E_{Complexation\ Corr.}$ (kcal/mol)	-543.950	-594.400	-515.040	-465.090	-493.550

Table A4.2.11. Fragmentation of $Pt(acac)_2$ by the loss of one CH_3 at 21.4 eV

Another possible fragmentation pathway, more plausible for our Pt precursor is the dissociation to $Pt(COOH)CH_3$ and $(CH)_4(acac)$ with values of 12.36 eV, for low-energy dissociative electron attachment complexation. The values for the fragmentation threshold of the $Pt(acac)_2$ into $Pt(COOH)CH_3$ and $(CH)_4(acac)$ from our Gaussian 16 calculations are presented in Table A4.2.12.

$E_{Counterpoise}$ (Hartree)	E_{BSSE} (eV)	$\sum_{Fragments}$ (Hartree)	$E_{Complexation\ Raw}$ (kcal/mol)	$E_{Complexation\ Corr.}$ (kcal/mol)
-805.927	0.059	-805.473	-322.15	-285.04

Table A4.2.12. Fragmentation of $Pt(acac)_2$ by the loss of one $(CH)_4(acac)$ (fragment left $Pt(COOH)CH_3$) at 12.36 eV and MP4(SDTQ)/LANL2DZ level of theory

The ionization potentials follow the relation (A4.2.1) for our calculations, both $^+$ state and negative ion formation:

$$E_{ionization} = E[Pt(acac)_2^+] - E[Pt(acac)_2] \text{ or } E[Pt(acac)_2^-] - E[Pt(acac)_2] \quad (A4.2.1)$$

$E_{Counterpoise}$	E_{BSSE} (eV)	$\sum_{Fragments}$ (Hartree)	$E_{Complexation\ Raw}$ (kcal/mol)	$E_{Complexation\ Corr.}$ (kcal/mol)

(Hartree)				
-805.954	0.032	-805.737	-156.29	-136.25

Table A4.2.13. Fragmentation of $Pt(acac)_2$ by the loss of one acac radical at 5.91 eV and MP4(SDTQ)/LANL2DZ level of theory

Excited states of $Pt(acac)_2$ using Gaussian 16 calculations. For the $Pt(acac)_2$ simulations we calculated 107 states up to 6.7035 eV. The excited states 27 – 32 would reach an energy of 4.4 – 4.8 eV, where the main excited states responsible for fragmentation lie in the 4 – 6 eV energy range. The state 29 lies between 6 eV and 6.7 eV, while the numbered 26 excited state is around ~ 5 eV. The first 32 excited states are presented in Table A4.2.14.

$2A_1$	**$2A_1$**	**$2A_1$**	**$3A_1$**	**$2A_1$**	**$3A_1$**	**$3A_1$**	**$2A_1$**
0.9080ev	1.0790eV	2.0366eV	2.6778eV	2.6828eV	2.6923eV	3.0971eV	3.2068eV
$2A_1$	**$2A_1$**	**$3A_1$**	**$2A_1$**	**$3A_1$**	**$2A_1$**	**$2A_1$**	**$3A_1$**
3.2386eV	3.2960eV	3.3084eV	3.4187eV	3.4281eV	3.4338eV	3.6220eV	3.6403eV
$2A_1$	**$2A_1$**	**$2A_1$**	**$2A_1$**	**$2A_1$**	**$2A_1$**	**$2A_1$**	**$2A_1$**
3.7229eV	3.7925eV	3.9703eV	4.0840eV	4.0852eV	4.1146eV	4.1398eV	4.2835eV
$2A_1$	**$2A_1$**	**$2A_1$**	**$2A_1$**	**$2A_1$**	**$2A_1$**	**$2A_1$**	
4.4068eV	4.4181eV	4.4837eV	4.4951eV	4.5920eV	4.6452eV	4.7054eV	

Table A4.2.14. The first 32 excited states of $Pt(acac)_2$ up to 4.7 eV

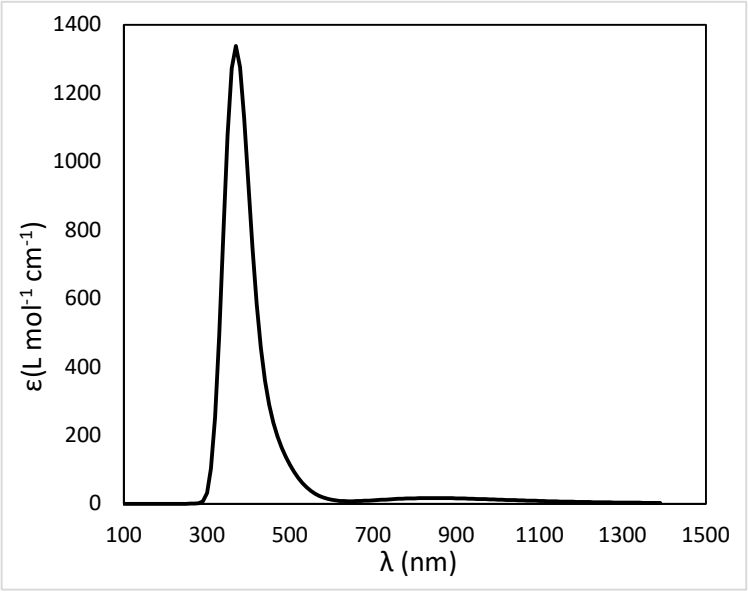

Fig A4.2.6. Pt(acac)2 absorption coefficient and oscillator strength for a refractive index of 1.741913

The excited states 1, 3 – 9, 11 – 18, 20, 22 – 25 and 29 – 32 have oscillator strength 0 and are forbidden transitions, the rest of the transitions are from $^2A_1$ to $^2A_1$, while the $^2A_1$ to $^3A_1$ are all forbidden transition states. From SCF density analysis, all alpha and opposed sign beta virtual and occupied orbitals are in singlet – A_1 state, and the determined geometry through configuration interaction CIS(50-50) for NStates = 32/20/107 is $^2A_1$, similar to the one obtained in the Natural Population analysis.

$Pt(acac)_2$

				∫ε(ν)d(ν)		
f	Ee	n	A	*f* = 0.0013	*f* = 0.0003	*f* = 0.0002
0.0013	0.4743	0.4	1.08E-08	1.20E+05	2.78E+04	1.85E+04
0.0003	0.6385	0.5	8.64E-09	1.50E+05	3.47E+04	2.31E+04
0.0002	0.8255	0.6	7.20E-09	1.81E+05	4.17E+04	2.78E+04
		0.7	6.17E-09	2.11E+05	4.86E+04	3.24E+04
		0.8	5.40E-09	2.41E+05	5.56E+04	3.70E+04
		0.9	4.80E-09	2.71E+05	6.25E+04	4.17E+04
		1	4.32E-09	3.01E+05	6.94E+04	4.63E+04
		1.1	3.93E-09	3.31E+05	7.64E+04	5.09E+04
		1.2	3.60E-09	3.61E+05	8.33E+04	5.56E+04
		1.3	3.32E-09	3.91E+05	9.03E+04	6.02E+04
		1.4	3.09E-09	4.21E+05	9.72E+04	6.48E+04
		1.5	2.88E-09	4.51E+05	1.04E+05	6.94E+04
		1.6	2.70E-09	4.81E+05	1.11E+05	7.41E+04
		1.7	2.54E-09	5.12E+05	1.18E+05	7.87E+04
		1.8	2.40E-09	5.42E+05	1.25E+05	8.33E+04
		1.9	2.27E-09	5.72E+05	1.32E+05	8.80E+04

Table A4.2.16. Absorption coefficient (integral) and oscillator strength of the excited states of $Pt(acac)_2$ (TDDFT level of calculation)

TDDFT calculations of $Pt(acac)_2$ show the presence of the three transitions under 1 eV, with oscillator strengths different than zero representing all allowed transitions from lower lying orbitals to higher excited state orbitals. The result of the calculations is 0.6385 eV (*f = 0.0013*), 0.6385 eV (*f = 0.0003*) and 0.8255 eV (*f = 0.0002*).

Excited State 1: 2.045-A 0.4743 eV 2613.92 nm f=0.0013 <S**2>=0.795

Excited State 2: 2.802-A 0.6385 eV 1941.87 nm f=0.0003 <S**2>=1.712

Excited State 3: 2.874-A 0.8255 eV 1502.00 nm f=0.0002 <S**2>=1.815

We know that Pt has a refractive index of 2.32694, while acac has a refractive index of 1.4494, where n_i can be estimated, though not with remarkably high accuracy, using:

$$n_i = (1 * RI_{Pt} + 2 * RI_{acac})/ 3 \quad \text{(A4.2.2)}$$

The resulting n_i value is 1.741913.

The vibrational frequencies are 2613 nm (= 3827.02 cm^{-1}), 1941 nm (= 5151.98 cm^{-1}) and 1502 nm (= 6657.79 cm^{-1}).

The dependence of oscillator strength on absorption cross-sections is defined by the relation (A4.2.3):

$$f_{ij} = 4\pi\varepsilon_0 (m_e c/\pi e^2) \int \sigma_{ij}(\nu)\, d\nu \qquad \text{(A4.2.3)}$$

where m is the mass of an electron, e is the charge of an electron and c is the speed of light in vacuum and $4\pi\varepsilon_0$ has a value of 0.667 $cm^2 s^{-1}$.

The obtained excited state from CIS corresponding to the same energy range as the excited state obtained in TDDFT is presented below.

Excited State 1: 2.026-A 0.9080 eV 1365.49 nm f=0.0000 <S**2>=0.776

Comparing the excited states from CIS(50 - 50, N = 17) with 50 – 50 singlet and triplet states and 17 excited states calculated at CIS and LANL2DZ/B3LYP level and LANL2DZ/B3LYP TDDFT, we find that the first one gives us only one excited state under 1 eV at an electron energy of 0.9080 eV, and it is a forbidden transition, while the second one as presented in the last paragraph has three excited states representing allowed transitions. The absorption UV/Vis visible plot (Fig A4.2.6) has been calculated using three oscillators with values different than zero obtained from TDDFT calculations of the molecule at 2613.92 nm (0.4743 eV, f=0.0013), 1941.87 nm (0.6385 eV, f=0.0003) and 1502 nm (0.8255 eV, f=0.0002).

Ee	f	∫ε(ν)d(ν)
0.4743	0.0013	5.24E+05
0.6385	0.0003	1.21E+05
0.8255	0.0002	8.06E+04

Table A4.2.15. $Pt(acac)_2$ absorption coefficient and oscillator strength interdependence for a refractive index of 1.741913

The absorption cross-sections dependence on oscillator strength is plotted to different excited states evaluation methods (CASSCF, CIS, TDDFT) and *f* varied from 0.5 to 2.5. See Table A4.2.17. An EET (electronic energy transfer) or resonance energy transfer (RET), usually based on earlier CIS/TDA/TDDFT (TD) calculations presents the excitation transfer in an excited molecule by a photon/electron giving the excitation rate of the fragmentation process (overlap of absorption spectrum between the molecule and the fragments, donor to acceptor).

$$Pt(acac)_2^* \rightarrow PtO_2C_2H_3^- + O_2C_2H_{11} \quad (A4.2.4)$$

The chemical reaction is following the pathway presented in relation (A4.2.4). The electron energy transfer excitation rate of the neutral fragment is 0.4931 eV while the excitation rate of the ionized fragment is 0.0854 eV, where the main photoionization energy for the $Pt(acac)_2$ has a value of 0.4078 eV. The ionization state of the ionized parent molecule is a negative doublet, with the resulting fragment or part of the molecule in negative singlet and the second fragment in neutral state.

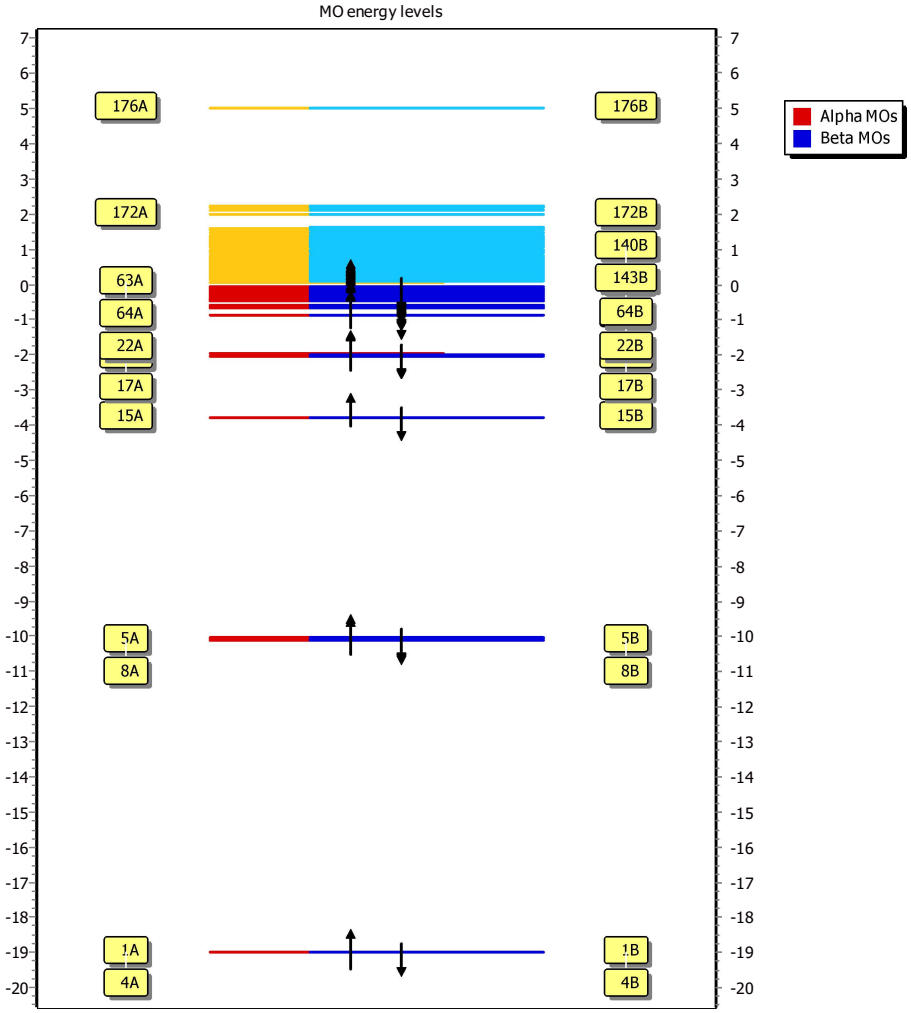

Fig A4.2.7. $Pt(acac)_2$ MO diagram with level of occupancy and energy for each orbital calculated at CASSCF(11, 17) /LANL2DZ level of theory

A thorough analysis of MO population is necessary for choosing the active space, for our $Pt(acac)_2$ calculations being CASSCF(11, 17), 11 orbitals with 17 electrons. The excited states in orbitals (4, 12), (5, 13), (6, 15), (11, 17) have been interchanged for the creation of the active space of orbitals

characterizing the molecule. All orbitals that were interchanged with the CASSCF calculations are in $^3A_1$ excited state and have been reconfigured to $^2A_1$.

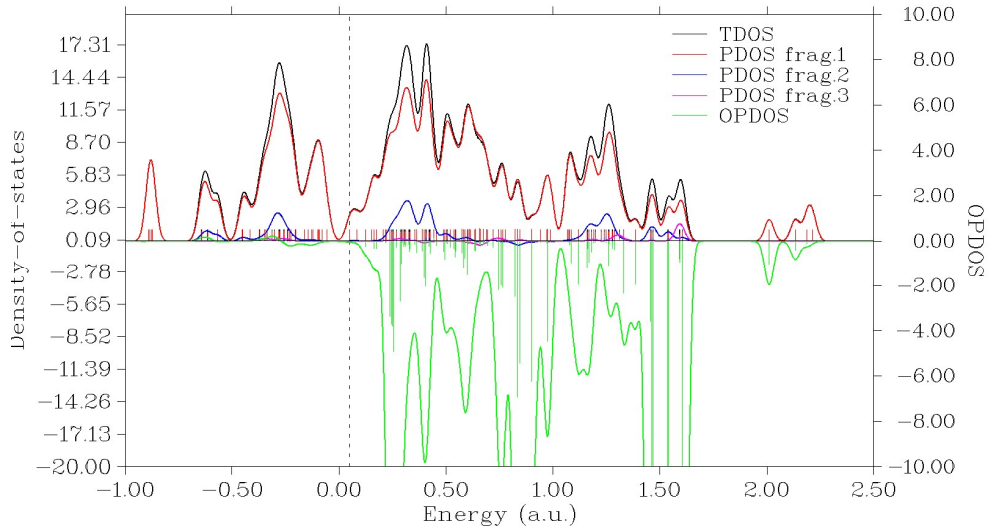

Fig A4.2.8 TDOS, PDOS and OPDOS of CH_3 (fragment 1), H (fragment 2), Pt(acac)CH($COOH_2$) (fragment 3) Pt(acac)$_2$ fragments

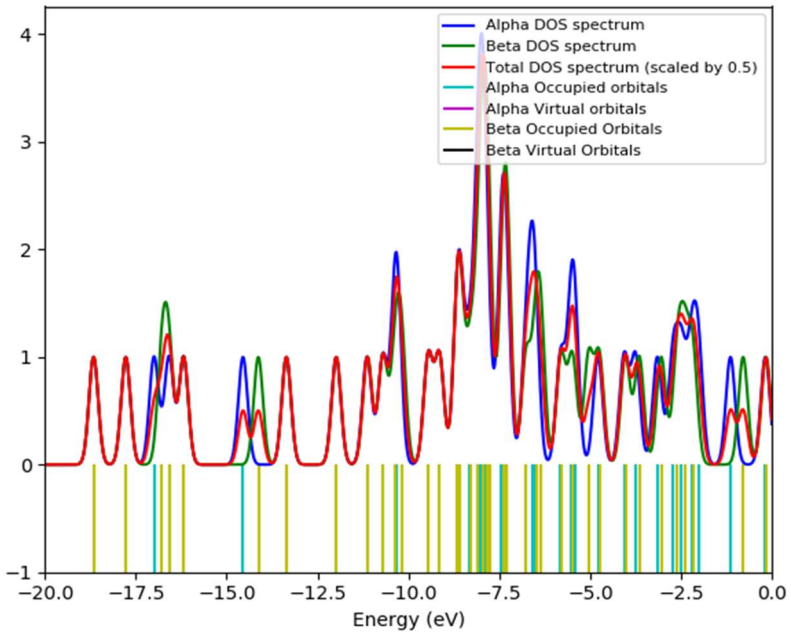

Fig A4.2.9 TDOS of Pt(acac)2 obtained from GaussSum

The density of states spectrum obtained from running CIS/TDDFT simulations using Gaussian 16 and Multiwfn for graph data processing is presented in Fig A4.2.8 considering three fragments of the

molecule with all characteristic functions s, p, d, xy, xz, x^2-y^2. The density of states of $Pt(acac)_2$ depending on the molecular orbitals occupancy (Fig A4.2.7) alpha and beta is presented in Fig A4.2.9.

A4.3 Pt$(NH_3)_4(NO_3)_2$

$Pt(NH_3)_4(NO_3)_2$ has been synthesized by Chen et al 2010 [147] in 2010 in a four-step process, its analysis revealing that it could make a good candidate for Pt nanostructures/nanoparticles precursor deposition by FEBID through its lack of C or Cl, though its analysis is limited to the positive ions. The four-step process involves the use of K_2PtCl_4 and replaces the water in the last step with ammonia, see relation (A4.3.1) for detailed schematics.

$$cis\text{-}[Pt(NH_3)_2(H_2O)_2](NO_3)_2 + 2NH_3 \rightarrow [Pt(NH_3)_4](NO_3)_2 \quad (A4.3.1)$$

The structure of the molecule in its ground state is C_{4v}. The structure, bond length (Å) and angles (deg) of the $Pt(NH_3)_2(NO_3)_2$ in Ref. [148] are presented in Table A4.3.1.

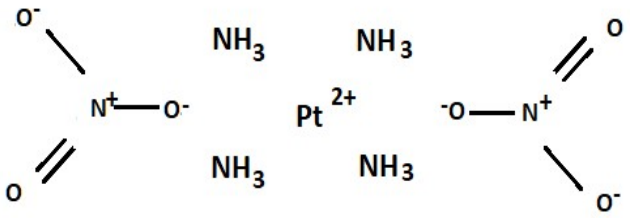

Fig A4.3.1. $Pt(NH_3)_4(NO_3)_2$ precursor

$Pt(NH_3)_4(NO_3)_2$	Bond lengths(Å) and angles(deg)
Pt – N	1.99; 2.00
Pt – O	1.99; 2.03
O – N	1.19; 1.30
N – O	2.91; 3.37
<NPtN	93
<NPtO	88.0 – 89.9
<PtON	119 - 120
<ONO	116 - 123

Table A4.3.1. $Pt(NH_3)_4(NO_3)_2$ structure [148]: bond lengths (Å) and angles (deg)

Different configuration and structural data for the molecule is available in Ref. [150] with 0.2Å and 10-50deg difference to the ones presented in Table A4.3.1 from Ref. [148]. The distances metal-to-N have values in the range of 2.021 – 2.047 Å: M – N(1) 2.042Å, M – N(2) 2.035 Å, M – N(3) 2.021 Å, M – N(4) 2.047 Å, and angles in the range of 89.7 – 90.1 deg: N(1) – M – N(2) 89.7 deg, N(1) – M – N(2) 90.3 deg, N(3) – M – N(4) 89.9 deg, N(3) – M – N(4) 90.1 deg. Our IR spectrum from the density functional theory calculations at B3LYP level (Fig A4.3.8) shows peaks at 537.606 cm^{-1} that we assign to Pt – N and 685.269 cm^{-1} that we assign to Pt – O, compared to 508 cm^{-1} attributed to the same Pt – N bond in Ref. [150]. The $\nu_3(NO^-_3)$ assigned in Ref. [150] at 833 cm^{-1} is found at 859.78 cm^{-1} in our spectrum and the N – H stretchings at higher values up to 100 cm^{-1} over the 3272 cm^{-1}, but still in good agreement, with our values of 3313 cm^{-1} and 3447.239 cm^{-1}. Lower values are obtained for δ_a(HNH) and $\nu_3(NO_3)$ at 1178.598 cm^{-1} and 1470.568 cm^{-1}.

The $Pt(NH_3)_2(NO_3)_2$ fragment or platinum p-salt was used as early as 1931 by Keitel and Zschiegner for electroplating. The structure of the molecule changes with the loss of two NH_3 bonds in $Pt(NH_3)_4(NO_3)_2$ to D_{3h} geometry in ground state. The Pt – N bonds in Ref. [150] to amine ligands have a length of 2.039 Å and 2.052 Å, being longer than Pt – N bonds to the monodentate nitrite groups 1.995 Å and 2.001 Å. The N1 – Pt - N2 has a 93.06 deg angle and the NO_2 planes are at an angle of 38.6 deg and 61.6 deg and twisted to an angle of 62.4 deg. Each $Pt(NH_3)_2(NO_3)_2$ has 18 hydrogen-bonding interactions linking to the eight surrounding molecules, forming a Bravais lattice (used to describe organization of atoms in a crystal using 3-dimensional 14 possible configurations), two four point, four two point and two one point.

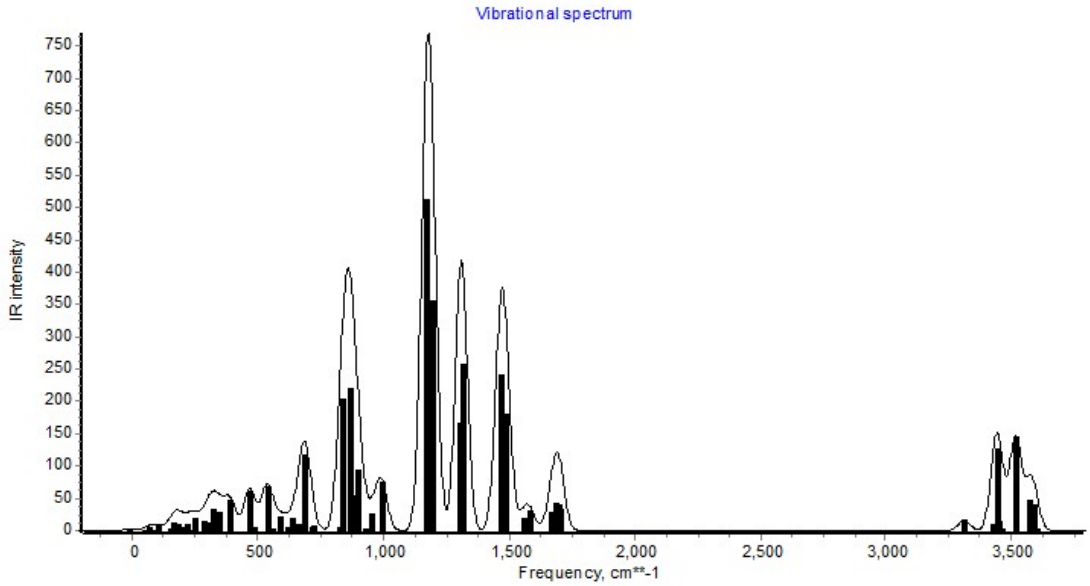

Fig A4.3.2. IR intensity spectrum of $Pt(NH_3)_4(NO_3)_2$ from GaussSum

The $Pt(NH_3)_4(NO_3)_2$ ligands may be broken by heat treatment of the sample. Similar behaviour as most precursors presenting a higher stability in air than in hydrogen, is reported in Ref. [151], while in H_2 forms neutral $Pt(NH_3)_2H_2$ (at temperatures in the range of 80 - 100 °C) in Ref. [152]. According to Ref. [148], a modification in the bond angles is observed in the $Pt(NH_3)_2(NO_3)_2$ structure with the bond angles O(4) – N(4) – O(5) of 117 deg and O(1) – N(3) – O(3) of 116 deg, as well as the angles between the NO_3 planes and ligand planes in the range of ~73.3 deg and 87.2 deg, where the dihedral angles between two nitrate planes are 80.6 deg. Other negative ions, results of dissociation processes are: N_6O_3 (m/z 132), HN_3O_6 (m/z 133), NH_6O_3 (m/z 139), PtH_5N_2 (m/z 228), PtH_6N_2 (m/z 229), PtH_6NO (m/z 231), PtH_7N_3 (m/z 244), PtH_7N_2O (m/z 246) and PtO_3H_5 (m/z 248). With stripping of a $(NH_3)_2$ radical, the $Pt(NH_3)_2(NO_3)_2$ is in a D_{3h} configuration and the reduction of this symmetry state to C_{2v} or C_{2h} removes the E' extra energy corresponding to the excited state and the main ground excited state A_2" induces six vibrational modes. Exciting the molecule through electron-molecule collision or ionization, due to lower bond strength with NH_3 and NO_3, would remove one or multiple H, NH, NH_3 and NO, NO_3 fragments. The presence of O fragment is expected to be at higher energies than H and fragments containing H to be in the range of ~ 6 - 7 eV.

$Pt(NH_3)_4(NO_3)_2$ Density of States (DOS) analysis

The structure of the molecule is created based on the structures of NH_3 and NO_3 from NIST database and the bond lengths of Pt – N and Pt – O reported in Ref. [149] and optimized according to Table A4.3.2 bond lengths. A schematic of the initial configuration used for our optimization steps is presented in Fig A4.3.4 and the values are indicated in Table A4.3.2.

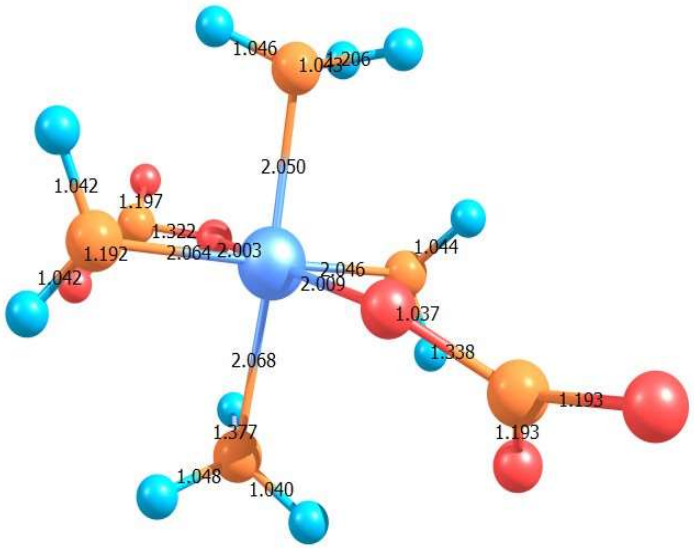

Fig A4.3.4. Tetraammineplatinum nitrate ($Pt(NH_3)_4(NO_3)_2$) molecular structure from ChemCraft

The bond distances obtained from the optimization of the structure are 0.2 Å higher than the value presented in Ref. [149] of 1.99 Å with an initial configuration of 2.050 Å and after optimization configuration of 2.097 Å for the Pt – N bond length, while the equatorial bonds of Pt – N and Pt – O have lower bond distances than the axial one with values of 2.046 Å initial configuration (from *NIST database*) and 2.051 Å final configuration (optimized configuration).

	Initial Configuration	Optimized Configuration
Pt - N	2.046_{eq}; 2.050	2.051eq, 2.097
N - O	1.197	1.258
Pt - O	2.009	2.058
N - H	1.042	1.024
<PtNO>	111; $109_{dihedral}$	$111.9;109.58_{dihedral}$
<PtNH>	90; $107_{dihedral}$	$87.89; 108.6_{dihedral}$

Table A4.3.2. Bond lengths and angle of $Pt(NH_3)_4(NO_3)_2$

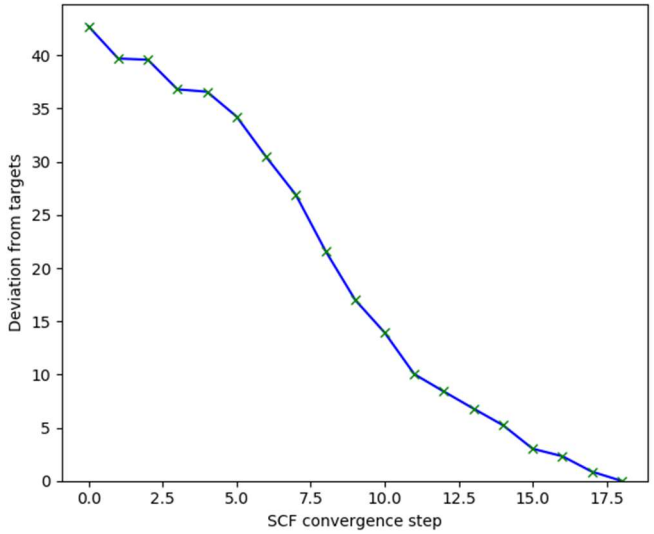

Fig A4.3.5 Convergence steps to optimization of $Pt(NH_3)_4(NO_3)_2$

The O – N bond distances are higher, close to the values of N - O bond distances of 1.322 Å, while the reported value of the N – O (1.193 Å) has a very high discrepancy with the calculated value of 2.91 Å. The configuration optimized angles are though in close agreement with the initial configuration built with a C_{4v} symmetry, with a difference of no more than 0.2 deg, and as well in close agreement with the ones reported in Ref. [149]. The $Pt(NH_3)_4(NO_3)_2$ seems to be a less stable structure than the lower mass $Pt(NH_3)_2(NO_3)_2$, that has been more extensively used and has higher symmetry in optimization. The

instability of the molecule would have, as a result, lower energy bonds to H, one of the outer four bonds of O or in highly inhomogeneous cases the release of a NH_3 radical, all three representing transition structures of the molecule.

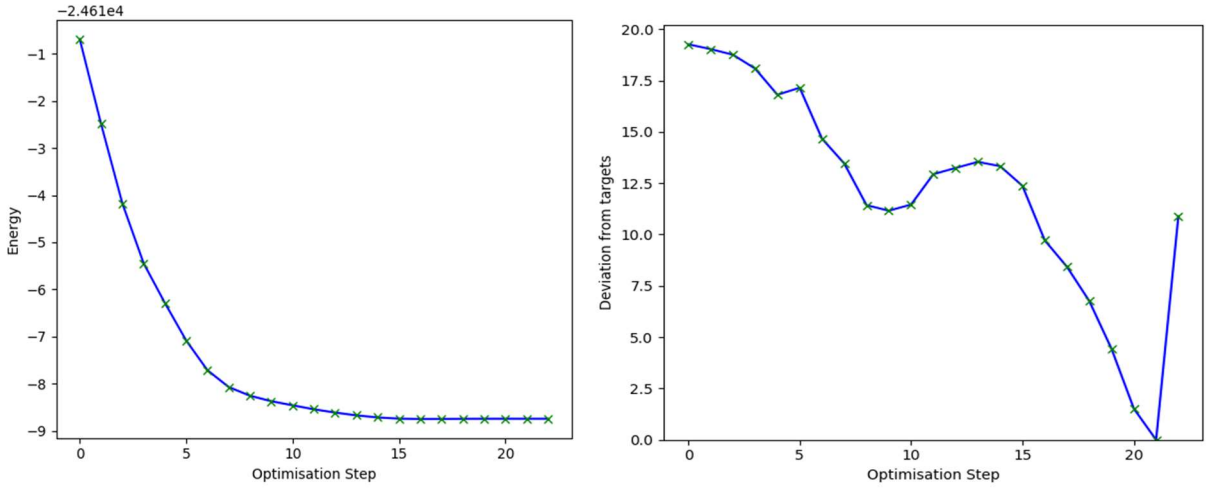

Fig A4.3.6 Optimization target and steps for $Pt(NH_3)_4(NO_3)_2$

From the SCF convergence calculations we can monitor, using the optimization steps and the number of cycles, the deviation from the target (minimum optimized geometry) using GaussSum, that calculates for each energy the difference between the current state and the final state. Using the B3LYP/LANL2DZ level of theory and basis set we obtained a mean value of convergence steps/optimization steps of 18 (convergence steps, Fig A4.3.5) and 20 (optimization steps, Fig A4.3.6), where the deviation from the target has a value of 0. The minimum energy for the optimized structure at the B3LYP/LANL2DZ level of theory is E(UB3LYP) = -904.7223697 Hartree. The $Pt(NH_3)_4(NO_3)_2$ is excited to a higher energetic state as negatively charged doublet, with two occurring fragments of $Pt(NH_3)_3(NO_3)_2$ and a ground state neutral singlet NH_3. At HF/LANL2DZ level of theory, the fragmentation energy has a value of -9.29 kcal/mol corresponding to 0.40 eV.

Ion/Fragment	E_{BSSE} (Hartree)	$E_{Counterpoise}$ (Hartree)	$E_{Fragmentation}$ (kcal/mol)
$Pt(NH_3)_3(NO_3)_2^-$	0.00606597	-899.457270921	-9.29
$Pt(NH_3)_4(NO_3)NO_2^-$	0.00655068	-904.784164116	-128.66
$Pt(NH_3)_4(NO_3)$	0.01670993	-899.446626963	-276.35

Table A4.3.3 $Pt(NH_3)_4(NO_3)_2$ ions fragmentation energies

The fragmentation of $Pt(NH_3)_4(NO_3)_2$ into negative charged fragments, anions, as a result of dissociative electron attachment processes, takes place at rather low energies, close to zero with a spontaneous release

of H, that would keep the structure's symmetry in an ionizing environment, to fragmentation of higher mass radicals as NH_3 at electron energies of 0.40 eV by charging the molecule found in doublet state with negative charge resulting the $Pt(NH_3)_3(NO_3)_2^-$ ionized fragment and the neutral NH_3 fragment.

Excited states of $Pt(NH_3)_4(NO_3)_2$ using Gaussian 16 calculations. The dissociation of the compound into the negative higher mass charged fragment and one O is predicted to take place as in relation (A4.3.2) at an electron energy of 5.57 eV:

$$Pt(NH_3)_4(NO_3)_2^- \rightarrow Pt(NH_3)_4(NO_2)_2NO^- + O \qquad \text{(A4.3.2)}$$

The breakage of one ligand to a NH_3 radical in this way would need less electron energy than breaking a ligand to an O or NO_3 radical. The fragmentation with the result of a higher mass fragment $Pt(NH_3)_4(NO_3)^-$ has an electron energy value of the dissociative electron attachment resonance from the doublet π* to negatively charged ionic doublet result of fragmentation π* of 11.98 eV.

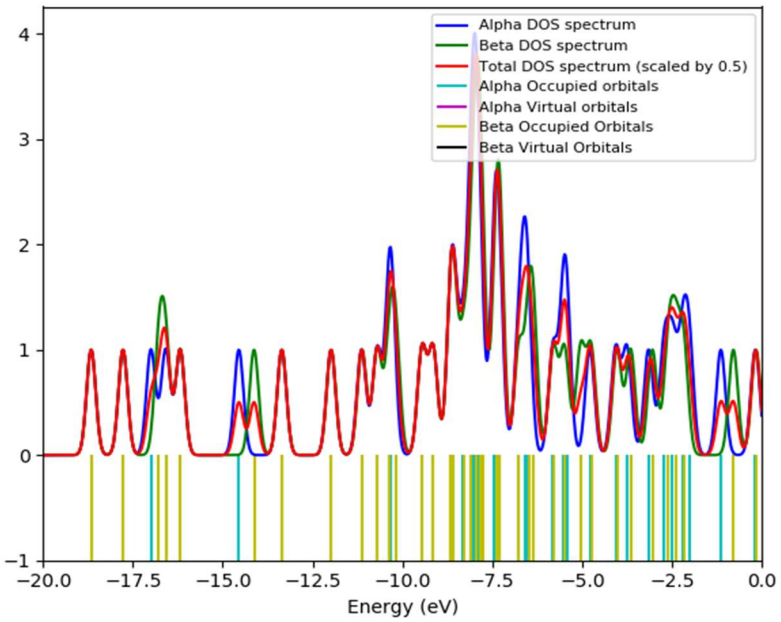

Fig A4.3.7 MO-DOS and HOMO/LUMO of $Pt(NH_3)_4(NO_3)_2$

The MO-DOS spectrum of HOMO and LUMO orbitals are presented in Fig A4.3.8. A total of 150 orbitals have been calculated from B3LYP/LANL2DZ calculations with the HOMO orbital as 59 and the LUMO orbital as 60. The density of states from TDDFT calculations using Gaussian 16 is presented in Fig A4.3.8 and Fig A4.3.9 using GaussSum. The peak of the HOMO falls at an energy of -0.24 eV (see Fig A4.3.9) with an allowed occupation for the electronic states of ~2 states/eV. The same value is observed for the LUMO of the molecule with similar amplitude of the peak. Our TDDFT/CIS calculations give us a number of 30 excited states (see Table A4.3.4 and A4.3.5) with energies 0eV to 4.5 eV.

$2A_1$	$2A_1$	$2A_1$	$2A_1$	$2A_1$	$2A_1$
0.2650eV	0.6431eV	0.7306eV	1.2412eV	1.6447eV	1.7521eV
$2A_1$	$3A_1$	$3A_1$	$3A_1$	$3A_1$	$3A_1$
3.0773eV	3.1564eV	3.1601eV	3.6338eV	3.6646eV	3.6659eV
$2A_1$	$2A_1$	$3A_1$	$2A_1$	$3A_1$	$3A_1$
3.7203eV	3.7205eV	3.7947eV	3.8197eV	3.8319eV	3.8319eV
$3A_1$	$2A_1$	$2A_1$	$3A_1$	$3A_1$	$3A_1$
4.0541eV	4.1569eV	4.1826eV	4.2734eV	4.3052eV	4.3220eV
$2A_1$	$2A_1$	$2A_1$	$2A_1$	$2A_1$	$2A_1$
4.3411eV	4.3611eV	4.3673eV	4.3713eV	4.3801eV	4.4768eV
$2A_1$					
4.5043eV					

Table A4.3.4 Excited States from TDDFT calculations at B3LYP/LANL2DZ level of theory from GaussSum

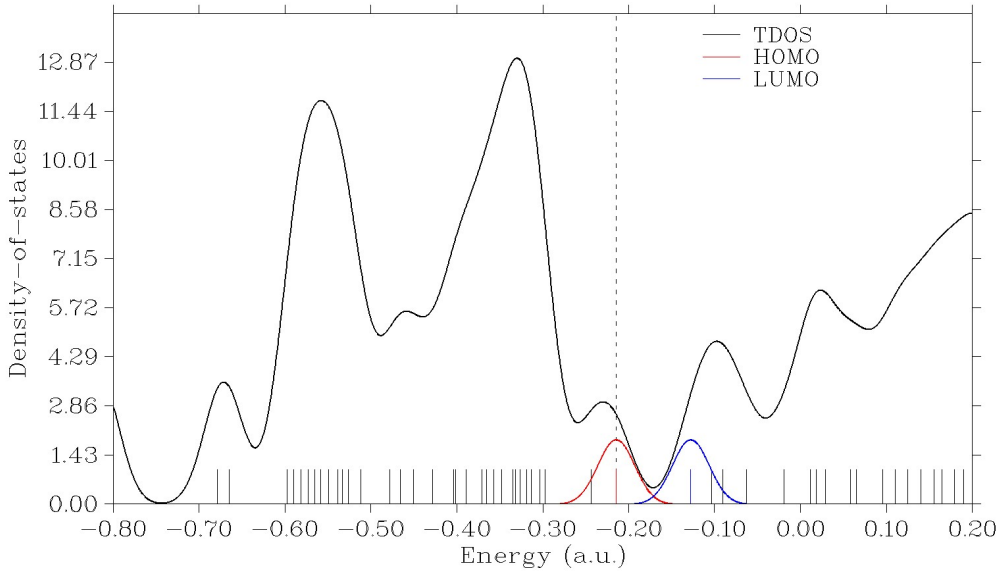

Fig A4.3.8 TDOS and orbital electronic level of occupancy from GaussSum

Excited State	Energy (eV)	Wavelength (nm)	Oscillator Strength	S**2
2.025-A	0.4848eV	2557.61nm	0.0004	0.775
2.029-A	0.6244eV	1985.67nm	0.0108	0.780
2.005-A	1.4480eV	856.23 nm	0.0000	0.755

2.016-A	2.3613eV	525.08 nm	0.0002	0.767
3.312-A	2.7271eV	454.64nm	0.0000	2.492

Table A4.3.4 Excited states from TDDFT/CIS calculations at B3LYP/LANL2DZ level of theory

The results of the electron energy transfer process from fragment 1 $Pt(NH_3)_3(NO_3)_2$ in neutral state π, to fragment 2 NH_3 radical in neutral state σ of the $Pt(NH_3)_4(NO_3)_2$, has an energy difference between the two states of 0.0455 eV. The distance between the higher mass fragment and the lower mass fragment of 0.815 Å is reported from the electron energy transfer simulations. The energy transfer for the second fragment corresponding to the lower mass NH_3 in state 1 has a value of 0.0699 eV, while the higher mass fragment has an energy transfer of 0.0244 eV. Based on our TDDFT of the excited states of $Pt(NH_3)_4(NO_3)_2$ and oscillator strength the absorption cross-sections spectrum (Fig A4.3.10 (b)) is presented from 300nm and 800nm.

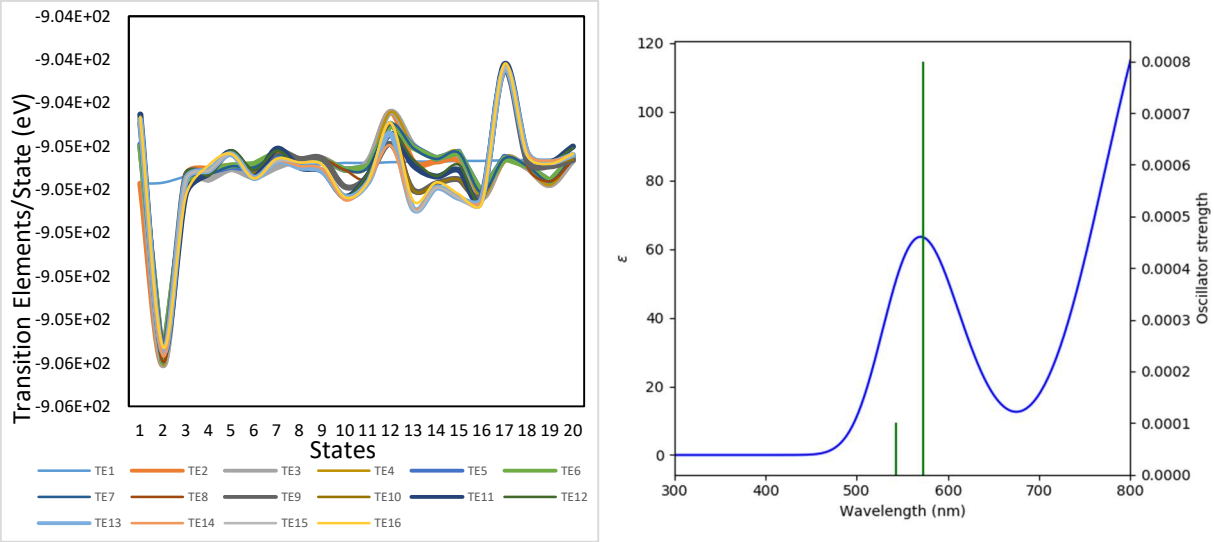

Fig A4.3.9 $Pt(NH_3)_4(NO_3)_2$: (left) density of states of states 1 – 20 (right) absorption spectrum from GaussSum

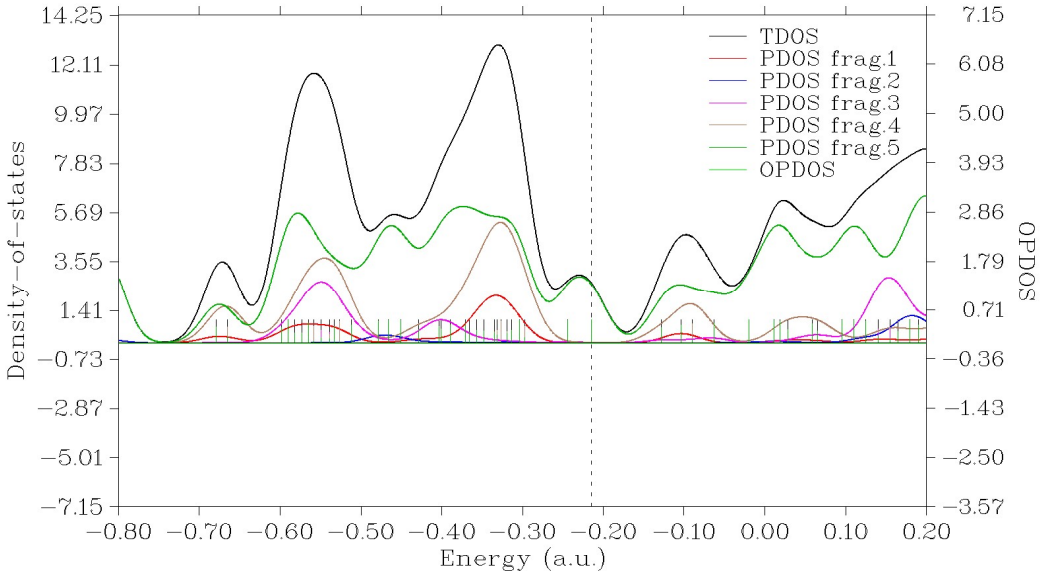

Fig A4.3.10 TDOS/PDOS for $Pt(NH_3)_4(NO_3)_2$: fragment 1 = O, fragment 2 = H, fragment 3 = NH_3, fragment 4 = NO_3, fragment 5 = $Pt(NH_3)_2(NO_3)NH$

The spectrum of partial density of states and total density of states reveals the highest contribution coming from Pt – N binding. The partial density of states follows closely the total density of states, with a density value of 3 at HOMO energy of -0.24 eV.

At an energy of -0.40 eV to -0.50 eV the number of electrons increases for fragment 2 representing the H in agreement with the change in TDOS/PDOS curves while the rest of the fragments go to 0. A decrease of the amplitude of TDOS and increase of NH_3 contribution is observed at -0.40 eV. The HOMO orbital is mostly dominated by the Pt population at -0.24 eV. Further, comparing the PDOS with the smaller fragment 1, 2 and 3 PDOS we observe a contribution from the binding of NH_3 and NO_3 between 0.0 eV and 0.1 eV, while between 0.1 eV and 0.2 eV the contribution comes mostly from the binding of NO_3 and Pt electronic states.

A4.4 Conclusions To Annex 4

The three Pt containing compounds, $Pt(PF_3)_4$ $Pt(acac)_2$ and $Pt(NH_3)_4(NO_3)_2$ studied in this chapter have attracted a lot of attention from the FEBID community since they have been shown to produce high purity Pt nanostructures, achieving levels of 60 % in Ref. [154]. This chapter focused on the fragmentation of different type of ligands Pt – N, Pt – C and Pt – P through a cleavage mechanism

characteristic to low electron energy dissociative electron attachment processes between 0 – 25 eV. Compared to the $Pt(PF_3)_4$ precursor molecule that removes all four PF_3 radicals leaving pure Pt, the $Pt(acac)_2$ molecule does not allow a full fragmentation of all ligands in the DEA process. The third precursor, the $Pt(NH_3)_4(NO_3)_2$ is characterized by a high volatility making it a good FEBID precursor, DEA removes all ligands to NH_3 and NO_3 leaving pure Pt. A DFT analysis of the three compounds compared to available experimental data shows good agreement of the obtained values from calculations and the experimentally determined values from the literature.

A4.4 Supplementary Data

Structures used for DFT calculations.

Structure of $Pt(PF_3)_4$ from Gaussian 16 Optimization (a) standard structure (b) optimized structure

Atom	X (Å)	Y (Å)	Z (Å)
Pt1	-0.4200	0.7087	0.0709
P2	-0.5067	3.1446	-0.1626
P3	-0.3259	-1.6982	0.3077
P4	1.9990	0.7359	-0.1225
P5	-2.8230	0.5975	0.3641
F6	-2.0166	3.0931	-0.8808
F7	-0.5561	4.8165	-0.2277
F8	0.8105	3.1649	-1.1937
F9	2.5445	1.2340	1.3793
F10	3.6638	0.7410	-0.2938
F11	1.4893	0.2402	-1.6386
F12	0.2376	-1.9584	1.8620
F13	-0.2774	-3.3667	0.4320
F14	-0.8869	-1.4769	-1.2545
F15	-2.2505	0.9866	1.8881
F16	-4.4774	0.5325	0.6116
F17	-3.4325	0.2079	-1.1460

(a)

Atom	X (Å)	Y (Å)	Z (Å)
Pt1	-0.1041	-0.0142	0.2951
P2	0.4276	2.1624	0.8766
P3	0.9155	1.8208	-0.2345
P4	-2.4584	0.5637	-0.5754
P5	1.9330	-0.3906	-1.7520
F6	0.8512	-3.4447	0.2322
F7	0.5006	-2.2790	2.4684
F8	-1.5115	-2.9816	1.0871
F9	-3.6744	-0.0254	0.4439
F10	-2.9485	2.1844	-0.6115
F11	-3.1361	0.0793	-2.0470
F12	2.2602	1.4643	2.1118
F13	-0.1065	2.3551	2.3964
F14	1.4044	3.3466	0.6007
F15	3.4939	-1.1715	-1.8917
F16	2.7075	0.9222	-0.9344
F17	0.5272	0.9354	-2.1382

(b)

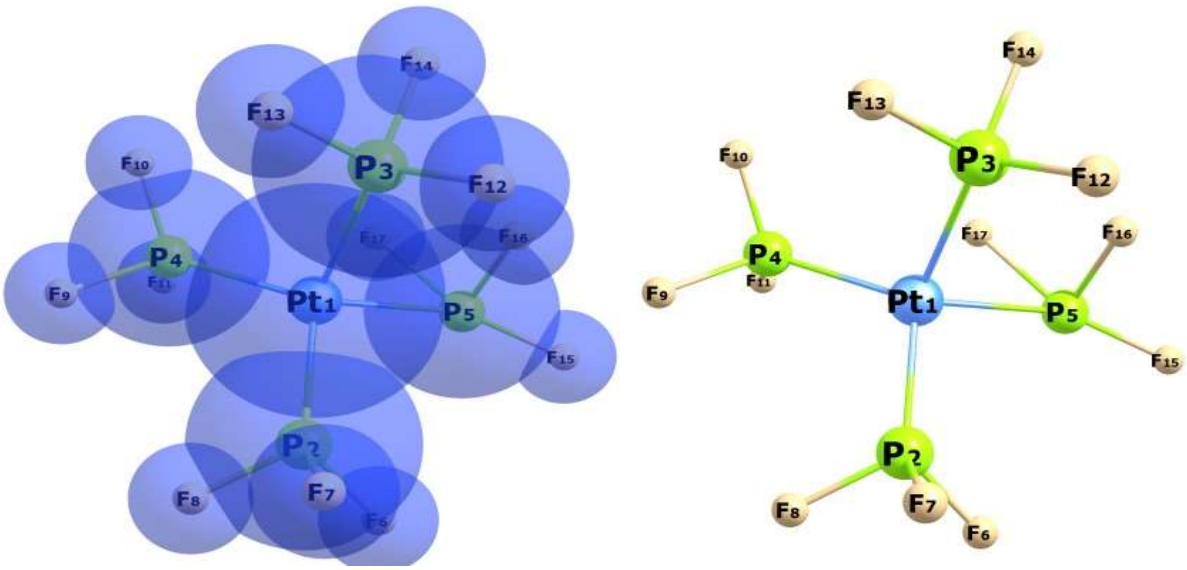

(a) (b)

Fig A4.4.1. $Pt(PF_3)_4$ molecule: (a) with van der Waals forces/electronic cloud (b) basic type 1 structure

Atomic types:

From B3LYP/LANL2DZ:

Summary of Natural Population Analysis:

		Natural Population				
Atom	No	Charge	Core	Valence	Rydberg	Total
Pt	1	-0.65442	67.97838	10.65671	0.01933	78.65442
P	2	2.55669	10.00000	2.41856	0.02475	12.44331
P	3	2.48229	10.00000	2.49423	0.02348	12.51771
P	4	2.56717	10.00000	2.41091	0.02193	12.43283
P	5	1.79212	10.00000	3.19070	0.01718	13.20788
F	6	-0.71083	1.99998	7.70871	0.00213	9.71083
F	7	-0.70865	1.99998	7.70666	0.00201	9.70865
F	8	-0.71225	1.99998	7.71027	0.00200	9.71225
F	9	-0.72202	1.99998	7.72063	0.00141	9.72202
F	10	-0.72203	1.99998	7.72041	0.00164	9.72203

F	11	-0.71876	1.99998	7.71729	0.00148	9.71876
F	12	-0.72430	1.99998	7.72288	0.00144	9.72430
F	13	-0.72986	1.99998	7.72846	0.00142	9.72986
F	14	-0.72662	1.99998	7.72482	0.00182	9.72662
F	15	-0.77707	1.99999	7.77438	0.00271	9.77707
F	16	-0.73896	1.99999	7.73692	0.00205	9.73896
F	17	-0.75251	1.99999	7.74963	0.00288	9.75251

==========

* Total *	0.00000	131.97818	113.89217	0.12965	246.00000

Natural Population

Effective Core	100.00000
Core	31.97818 (99.9318% of 32)
Valence	113.89217 (99.9054% of 114)
Natural Minimal Basis	245.87035 (99.9473% of 246)
Natural Rydberg Basis	0.12965 (0.0527% of 246)

Atom	No	Natural Electron Configuration
Pt	1	[core]6S(0.71)5d(8.84)6p(1.11)6d(0.01)7p(0.01)
P	2	[core]3S(1.15)3p(1.27)4p(0.02)
P	3	[core]3S(1.41)3p(1.08)4p(0.02)
P	4	[core]3S(1.33)3p(1.08)4p(0.02)
P	5	[core]3S(1.73)3p(1.46)4p(0.02)
F	6	[core]2S(1.92)2p(5.79)
F	7	[core]2S(1.92)2p(5.79)
F	8	[core]2S(1.92)2p(5.79)
F	9	[core]2S(1.93)2p(5.80)
F	10	[core]2S(1.93)2p(5.79)
F	11	[core]2S(1.92)2p(5.79)
F	12	[core]2S(1.92)2p(5.80)
F	13	[core]2S(1.93)2p(5.80)
F	14	[core]2S(1.93)2p(5.80)

F 15 [core]2S(1.94)2p(5.84)
F 16 [core]2S(1.93)2p(5.81)
F 17 [core]2S(1.93)2p(5.82)

From MP4(SDQT)/LANL2DZ:

Summary of Natural Population Analysis:

Natural Population

Atom	No	Charge	Core	Valence	Rydberg	Total
Pt	1	-0.94308	67.98584	10.94290	0.01434	78.94308
P	2	2.14321	10.00000	2.82775	0.02905	12.85679
P	3	2.10877	10.00000	2.86585	0.02537	12.89123
P	4	2.13321	10.00000	2.84295	0.02384	12.86679
P	5	1.90639	10.00000	3.06937	0.02424	13.09361
F	6	-0.59420	1.99999	7.59106	0.00315	9.59420
F	7	-0.58780	1.99999	7.58473	0.00309	9.58780
F	8	-0.59068	1.99999	7.58764	0.00305	9.59068
F	9	-0.60146	1.99999	7.59875	0.00271	9.60146
F	10	-0.59701	1.99999	7.59433	0.00270	9.59701
F	11	-0.59515	1.99999	7.59249	0.00267	9.59515
F	12	-0.60212	1.99999	7.59951	0.00262	9.60212
F	13	-0.61560	1.99999	7.61282	0.00280	9.61560
F	14	-0.59470	1.99999	7.59198	0.00273	9.59470
F	15	-0.66827	1.99999	7.66393	0.00435	9.66827
F	16	-0.63003	1.99998	7.62677	0.00327	9.63003
F	17	-0.67147	1.99999	7.66623	0.00525	9.67147
* Total *		-0.00000	131.98570	113.85907	0.15523	246.00000

Natural Population

Effective Core	100.00000
Core	31.98570 (99.9553% of 32)

Valence	113.85907 (99.8764% of 114)
Natural Minimal Basis	245.84477 (99.9369% of 246)
Natural Rydberg Basis	0.15523 (0.0631% of 246)

Atom	No	Natural Electron Configuration
Pt	1	[core]6S(0.49)5d(9.48)6p(0.97)6d(0.01)
P	2	[core]3S(1.26)3p(1.56)4p(0.02)
P	3	[core]3S(1.40)3p(1.46)4S(0.01)4p(0.02)
P	4	[core]3S(1.37)3p(1.48)4p(0.02)
P	5	[core]3S(1.73)3p(1.34)4S(0.01)4p(0.02)
F	6	[core]2S(1.93)2p(5.66)
F	7	[core]2S(1.93)2p(5.66)
F	8	[core]2S(1.93)2p(5.66)
F	9	[core]2S(1.93)2p(5.66)
F	10	[core]2S(1.93)2p(5.66)
F	11	[core]2S(1.93)2p(5.66)
F	12	[core]2S(1.93)2p(5.67)
F	13	[core]2S(1.93)2p(5.68)
F	14	[core]2S(1.93)2p(5.66)
F	15	[core]2S(1.94)2p(5.72)
F	16	[core]2S(1.94)2p(5.69)
F	17	[core]2S(1.94)2p(5.73)

Structure of $Pt(acac)_2$ from Gaussian 16 Optimization (a) optimized structure (b) standard structure

Pt	0.00000	0.00000	0.00000
O	-1.39630	1.46687	-0.00022
O	-1.39630	-1.46686	0.00019
O	1.39630	-1.46686	0.00022
O	1.39630	1.46686	-0.00021
C	-2.69181	1.26192	0.00036
C	-2.69181	-1.26192	-0.00041
C	-3.32887	0.00000	-0.00005
C	2.69182	-1.26191	0.00073

Pt	0.00200	-0.00300	0.00006
O	1.38208	1.46049	-0.00019
O	1.38209	-1.46051	-0.00006
O	-1.38209	-1.46049	0.00024
O	-1.38208	1.46049	0.00015
C	2.64181	1.25527	-0.00013
C	2.64184	-1.25527	-0.00003
C	3.27895	0.00001	0.00006
C	-2.64182	-1.25526	-0.00006

C	2.69182	1.26192	-0.00071
C	3.32887	0.00000	0.00003
C	-3.50974	2.53595	0.00497
C	-3.50974	-2.53595	-0.00477
C	3.50973	-2.53595	0.00526
C	3.50974	2.53595	-0.00538
H	-4.58375	2.33370	-0.02891
H	-3.27948	3.11511	0.90794
H	-3.22872	3.15469	-0.85585
H	4.58384	-2.33365	-0.02500
H	3.23140	-3.15288	-0.85777
H	3.27664	-3.11702	0.90625
H	-4.58380	-2.33367	0.02691
H	-3.27778	-3.11639	-0.90648
H	-3.23032	-3.15347	0.85746
H	4.58381	2.33367	0.02624
H	3.27770	3.11623	-0.90717
H	3.23040	3.15363	0.85677
H	-4.41232	0.00000	-0.00008
H	4.41232	0.00000	0.00005

(a)

C	-2.64182	1.25527	-0.00017
C	-3.27895	0.00000	-0.00028
C	3.46882	2.51849	-0.00020
C	3.46883	-2.51849	0.00007
C	-3.46885	-2.51847	-0.00023
C	-3.46882	2.51849	0.00018
H	4.54769	2.31672	0.00047
H	3.21031	3.12150	-0.88531
H	3.20923	3.12226	0.88407
H	-4.54771	-2.31668	0.00066
H	-3.20915	-3.12246	0.88386
H	-3.21044	-3.12127	-0.88552
H	4.54768	-2.31673	0.00044
H	3.20945	-3.12200	0.88459
H	3.21003	-3.12175	-0.88479
H	-4.54768	2.31671	-0.00046
H	-3.21026	3.12136	0.88538
H	-3.20927	3.12240	-0.88401
H	4.36861	0.00003	0.00014
H	-4.36860	0.00002	-0.00052

(b)

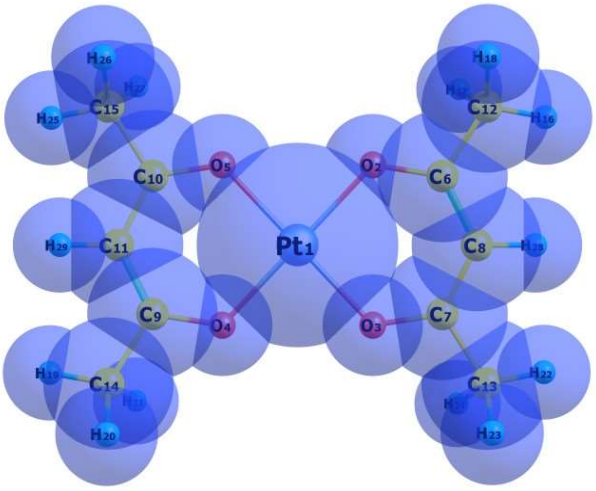

(a)

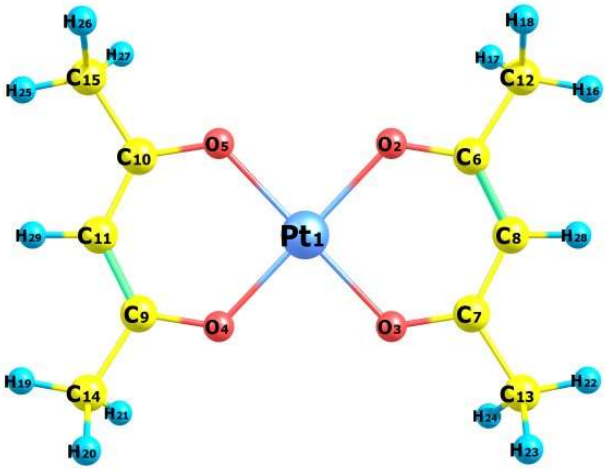

(b)

Fig A4.4.2 $Pt(acac)_2$ molecule: (a) with van der Waals forces/electronic cloud (b) basic type 1 structure

Atomic types:

From B3LYP/LANL2DZ:

Summary of Natural Population Analysis:

Natural Population

Atom	No	Charge	Core	Valence	Rydberg	Total
Pt	1	4.05583	67.99215	5.93505	0.01696	73.94417
O	2	-0.86488	1.99984	6.85030	0.01474	8.86488
O	3	-0.86488	1.99984	6.85030	0.01474	8.86488
O	4	-0.86488	1.99984	6.85030	0.01474	8.86488
O	5	-0.86488	1.99984	6.85030	0.01474	8.86488
C	6	0.15640	1.99923	3.81866	0.02571	5.84360
C	7	0.15640	1.99923	3.81865	0.02571	5.84360
C	8	-0.73233	1.99915	4.72011	0.01307	6.73233
C	9	0.15640	1.99923	3.81866	0.02571	5.84360
C	10	0.15639	1.99923	3.81866	0.02571	5.84361
C	11	-0.73233	1.99915	4.72011	0.01307	6.73233
C	12	-1.05033	1.99926	5.04364	0.00744	7.05033
C	13	-1.05033	1.99926	5.04363	0.00744	7.05033
C	14	-1.05033	1.99926	5.04363	0.00744	7.05033
C	15	-1.05033	1.99926	5.04363	0.00744	7.05033
H	16	0.32771	0.00000	0.67158	0.00071	0.67229
H	17	0.31212	0.00000	0.68515	0.00273	0.68788
H	18	0.31340	0.00000	0.68397	0.00264	0.68660
H	19	0.32771	0.00000	0.67157	0.00071	0.67229
H	20	0.31332	0.00000	0.68403	0.00264	0.68668
H	21	0.31219	0.00000	0.68509	0.00272	0.68781
H	22	0.32771	0.00000	0.67158	0.00071	0.67229
H	23	0.31216	0.00000	0.68512	0.00272	0.68784
H	24	0.31336	0.00000	0.68400	0.00264	0.68664
H	25	0.32771	0.00000	0.67158	0.00071	0.67229
H	26	0.31216	0.00000	0.68511	0.00272	0.68784

H	27	0.31335	0.00000	0.68401	0.00264	0.68665
H	28	0.31558	0.00000	0.68312	0.00129	0.68442
H	29	0.31558	0.00000	0.68312	0.00129	0.68442

==========

* Total *	0.00000	95.98380	87.75468	0.26153	184.00000

Natural Population

Effective Core	60.00000
Core	35.98380 (99.9550% of 36)
Valence	87.75468 (99.7212% of 88)
Natural Minimal Basis	183.73847 (99.8579% of 184)
Natural Rydberg Basis	0.26153 (0.1421% of 184)

Atom	No	Natural Electron Configuration
Pt	1	[core]6S(0.68)5d(5.09)6p(0.16)6d(0.01)
O	2	[core]2S(1.68)2p(5.17)3p(0.01)
O	3	[core]2S(1.68)2p(5.17)3p(0.01)
O	4	[core]2S(1.68)2p(5.17)3p(0.01)
O	5	[core]2S(1.68)2p(5.17)3p(0.01)
C	6	[core]2S(0.82)2p(3.00)3p(0.02)
C	7	[core]2S(0.82)2p(3.00)3p(0.02)
C	8	[core]2S(1.05)2p(3.67)3p(0.01)
C	9	[core]2S(0.82)2p(3.00)3p(0.02)
C	10	[core]2S(0.82)2p(3.00)3p(0.02)
C	11	[core]2S(1.05)2p(3.67)3p(0.01)
C	12	[core]2S(1.20)2p(3.85)3p(0.01)
C	13	[core]2S(1.20)2p(3.85)3p(0.01)
C	14	[core]2S(1.20)2p(3.85)3p(0.01)
C	15	[core]2S(1.20)2p(3.85)3p(0.01)
H	16	1S(0.67)
H	17	1S(0.69)
H	18	1S(0.68)
H	19	1S(0.67)

H 20 1S(0.68)
H 21 1S(0.69)
H 22 1S(0.67)
H 23 1S(0.69)
H 24 1S(0.68)
H 25 1S(0.67)
H 26 1S(0.69)
H 27 1S(0.68)
H 28 1S(0.68)
H 29 1S(0.68)

ANNEX 5. MACHINE LEARNING AND IMAGE PROCESSING FOR MOLECULAR PHYSICS

A5.1 VELOCITY MAP IMAGING IMAGE ANALYSIS

For the data analysis, a program in Python is used, and more relevant to the present work OpenCV and Scikit-learn modules of Python. Similar work has been developed using MATLAB in Institutes in India for the Velocity Map image processing. Though easy to use, MATLAB needs a work license and occupies much more disk space. On the other hand, Python is an open-source software, the files are relatively small and the length of the program code much smaller. The Python analysis code developed here goes through multiple image processing steps, from which some are going to be presented further. A CCD camera is used to acquire the images. The files are saved in black & white *bmp format. Depending on the acquisition time set and the counts wanted, between 10 and 200 files are created for each negative fragment.

Fragments relative to environment / CCD camera:

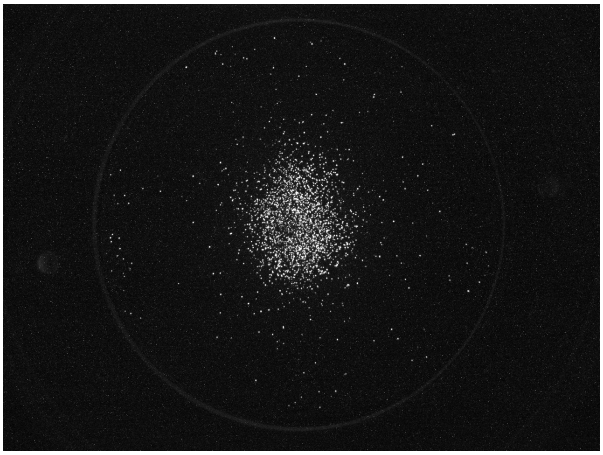

(1a)

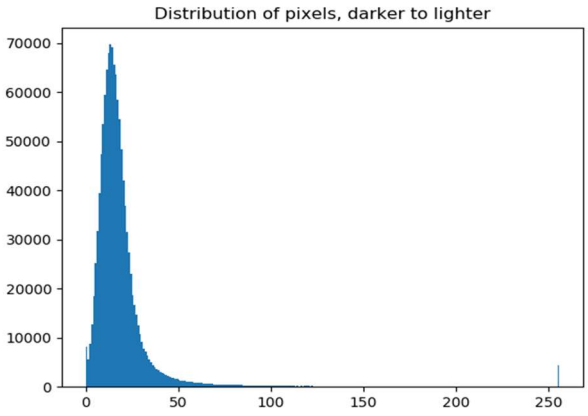

(1b)

Fig A5.1.1. (1a) $Fe(CO)_3^-$ fragment at 10 V lens, 300 V, 100 V negative extraction pulse, 1.55 A magnetic field, delay 8.69 μs and (1b) pixel distribution for $Fe(CO)_3^-$

**Code from Open-CV tutorial*

```
import cv2

import numpy as np
```

```
from matplotlib import pyplot as plt

img = cv2.imread('home.jpg', 0)

plt.hist(img.ravel(), 256, [0,256]); plt.show()
```

The pictures collected in the file are added to form the velocity map image.

```
arr=np.zeros((h, w), np.float)

for im in imlist:

        imarr=numpy.array(Image.open(im), dtype=numpy.float)

        arr=arr+imarr/N
```

The final output is presented in Fig A5.1.2 for $Fe(CO)_4^-$.

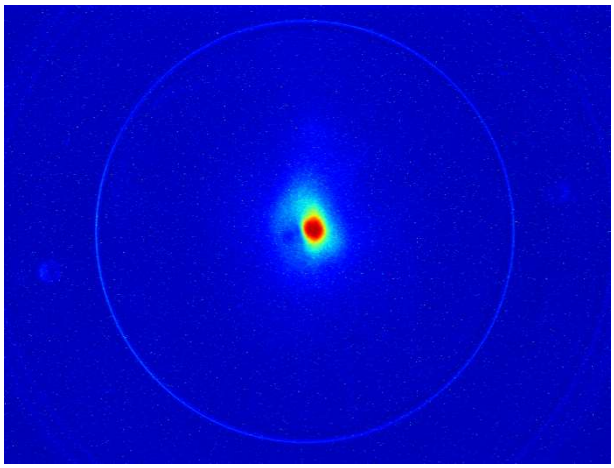

Fig A5.1.2. Negative fragment $Fe(CO)_4^-$

Manipulated pictures analysis showing pixel distribution on colors:

**Code from Open-CV tutorial*

```
import cv2

import numpy as np
```

```
from matplotlib import pyplot as plt



img = cv2.imread('home.jpg')

color = ('b','g','r')

for i, col in enumerate(color):

histr = cv2.calcHist([img], [i], None, [256], [0,256])

plt.plot(histr, color = col)

plt.xlim([0, 256])

plt.show()
```

The output of the code is presented in Fig A5.1.3.

CCD Camera Noise Theory

There are multiple types of noise that can appear in the pictures as a result of the parameters of the CCD camera or the quality of it. The most common CCD camera pictures types of noise are:

1. Gaussian Noise
2. Heavy Tailed Noise
3. Salt and Pepper Noise
4. Quantization and Uniform Noise
5. Photon Counting Noise
6. Photographic Grain Noise
7. Dark Noise
8. Red Noise
9. Speckle

(a) **Gaussian Noise.** The density function of Gaussian noise is expressed by the relation:

$$P_q(x) = (2\pi\sigma^2)^{-1/2}\, e^{-(x-\mu)^2/2\sigma^2} \qquad \text{(A5.1.1)}$$

where the values of Gaussian noise are limited to ±3σ. The Gaussian distribution function is based on the Central Limit Theorem.

If the Central Limit Theorem cannot cover all the noise appearing in the picture, the so called Heavy Tailed Noise effect is the one creating the extra noise. According to that, everything that is not approximately Gaussian, is Tail effect. The tails are the approximation of the noise for values of large x, $|x| \rightarrow \infty$. If the Tail effect grows even stronger, the Heavy Tailed effect takes place, that means that the gaussian function $p_q(x)$ drops with a more attenuated slope to 0. The Heavy Tailed models used are: Laplacian or double exponential, negative exponential, Alpha stable, Gaussian mixture models, generalized gaussian.

(b) **Salt and Pepper Noise.** The effect of salt and pepper noise is the appearance of white and black pixels (dots) on the pictures. The phenomenon can be expressed by the relation:

$$\Pr[|X - Y| = 2^i] = \varepsilon\,(1 - \varepsilon)^{B-1} \tag{A5.1.2}$$

where, $X = \Sigma_{i=0}^{B-1} b_i 2^i$, B is the number of bits, ε is the crossover probability, i = 1, 2, …, B-1. The most significant bit is $\varepsilon 4^{B-1}$, and $\varepsilon(4^{B-1} - 1)/3$ all the other bits.

(c) **Quantization and Uniform Noise.** The Quantization and Uniform noise are the noise created by converting a random variable into a discrete one or a discrete one to a smaller variable.

$$E[q] = 1/D \int_{-D/2}^{D/2} sds \tag{A5.1.3}$$

where $-D/2 \leq q \geq D/2$, q is uniformly modeled and independent of a, and b = Q(a) = a + q.

(d) **Photon Counting Noise.** The distribution characterizing photon counting noise is called Poisson noise distribution function. The distribution takes the form:

$$P(a = k) = e^{-\lambda}\lambda^k / k! \tag{A5.1.4}$$

where k =0, 1, 2, … and λ is the Poisson parameter.

(e) **Photographic Grain Noise.** The photographic grain noise is pretty similar to photon counting noise and depends on if they are faster or slower. The photographic grain noise in a given area A is characterized by the relation:

$$\Pr[N = k] = \left(\int_k^L p^k \ (1 - p)^{L-k} \right) \tag{A5.1.5}$$

where L is the number of grains, p is proportional to the number of photons.

(f) **Speckle**. The speckle noise is the effect of either a coherent light source (photon, radar, and electron) or the effect of atmospheric conditions. It is one of the most complex type of noise. As our compounds are in a chamber with little light from the outside the environmental noise is limited to the effect of electrons and heat lamps in Ref. [6].

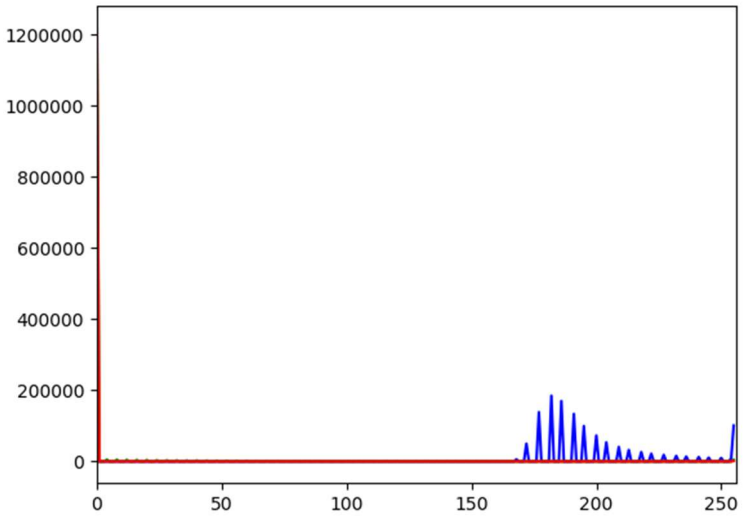

Fig A5.1.3. Color pixels distribution for $Fe(CO)_4^-$

The output of the CCD camera is affected by noise. A part of the pixels that look like negative fragments at a more thorough look are CCD noise.

The final pictures have been processed to remove the noise coming from the CCD camera.

```
img = cv2.imread(img)

b,g,r = cv2.split(img)

rgb_img = cv2.merge([r, g, b])

dst = cv2.fastNlMeansDenoisingColored(img, None, 10, 10, 7, 21)

b,g,r = cv2.split(dst)

rgb_dst = cv2.merge([r, g, b])

plt.imsave('pic' + str(i) +'.jpg', rgb_dst, cmap='jet')
```

The difference between the velocity map image and the processed picture can be clearly seen.

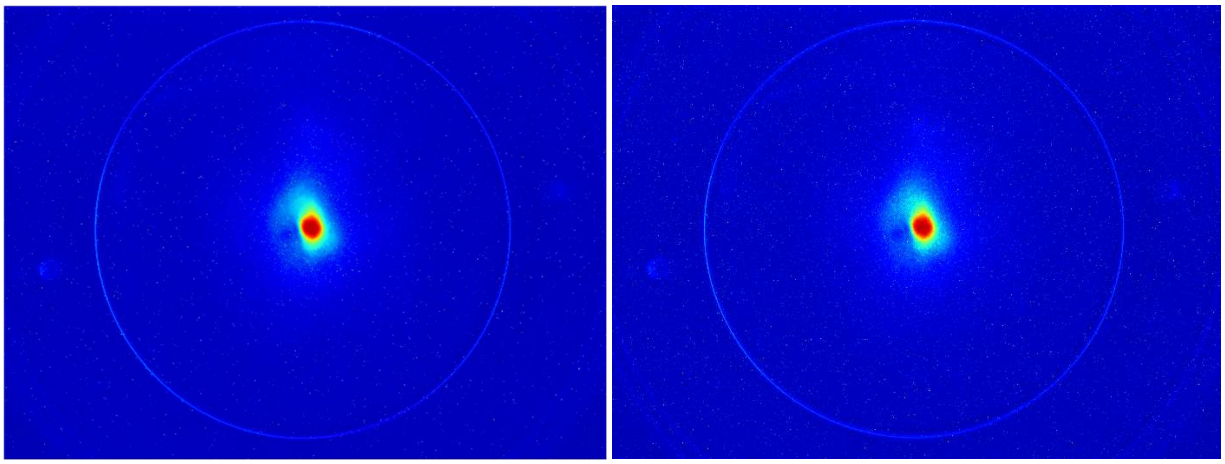

(4a) (4b)

Fig A5.1.4. (4a) $Fe(CO)_4^-$ with noise processing; (4b) $Fe(CO)_4^-$ without processing

Finding the area of interest and making a contour:

```
import argparse

import imutils

import cv2

ap=argparse.ArgumentParser()

ap.add_argument("-i", "--A:\\Maria\\Expenses\\MARIA\\Fe(CO)5\\0.2 eV - Fe(CO)4\\test1.png",
help="path to the input image")

args=vars(ap.parse_args())

image=cv2.imread("A:\\Maria\\Expenses\\MARIA\\Fe(CO)5\\0.2 eV - Fe(CO)4\\test1.png")

gray=cv2.cvtColor(image, cv2.COLOR_BGR2GRAY)

print image.shape

blurred=cv2.GaussianBlur(gray, (5,5), 0)
thresh=cv2.threshold(blurred, 60, 255, cv2.THRESH_BINARY)[1]
```

```
cnts=cv2.findContours(thresh.copy(), cv2.RETR_EXTERNAL, cv2.CHAIN_APPROX_SIMPLE)
```

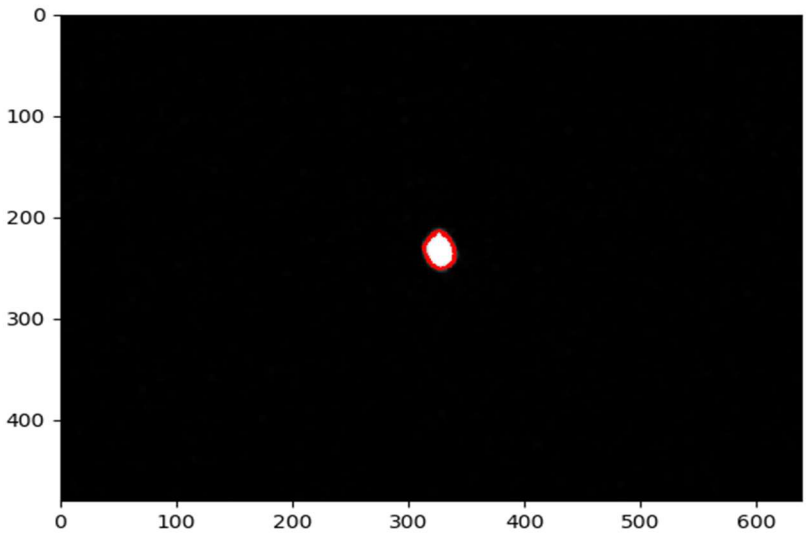

Fig A5.1.5. Contour of $Fe(CO)_4^-$ Velocity Map Imaging

Finding the center point of the area in the contour:

```
cnts=cnts[0] if imutils.is_cv2() else cnts[1]

for c in cnts:

        M=cv2.moments(c)

        cX=int(M["m10"] / M["m00"])

        cY=int(M["m01"] / M["m00"])

        cv2.drawContours(image, [c], -1, (0,255,0),2)

        cv2.circle(image, (cX, cY), 7, (0,0,0), -1)

        cv2.putText(image, "center", (cX-20, cY-20), cv2.FONT_HERSHEY_SIMPLEX, 0.5,
(255,255,255), 2)

        cv2.imshow("Image", image)
```

```
        cv2.imwrite("Image", image)

        cv2.waitKey(0)
```

The values of the center point are:

```
>>> (cX, cY)
(653, 466)
```

Processing the number of counts in the images:

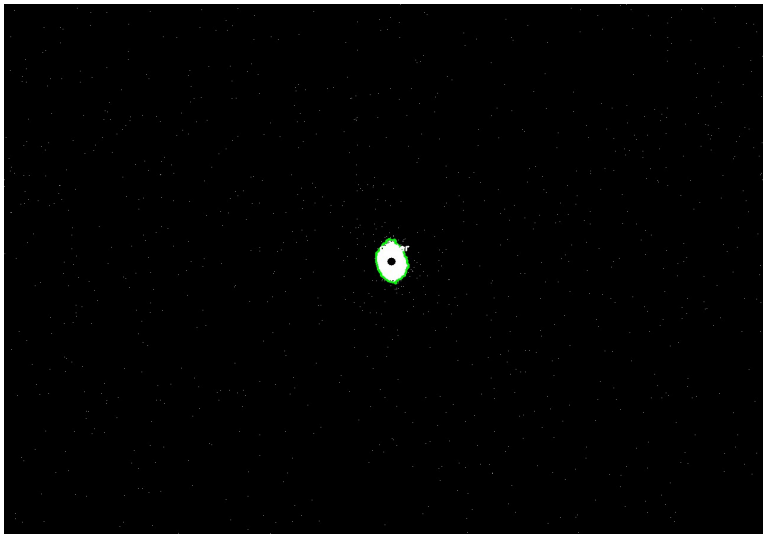

Fig A5.1.6. $Fe(CO)_4^-$ contour area with center point marked

```
from skimage import io, filters
from scipy import ndimage
import matplotlib.pyplot as plt
from skimage import measure

im=io.imread("image", as_gray=True)
val=filters.threshold_otsu(im)
counts=ndimage.binary_fill_holes(im>val)
plt.imshow(counts, cmap='gray')
plt.show()
labels=measure.label(counts)
print(labels.max())
print('coverage is %f' %(counts.mean()))
```

A5.2 Bond Determination, Structure Solvation and PES Using AI and ML

Newer approaches to molecular physics simulations are the use of neural networks to optimize molecular structures, create new molecular designs, and calculate characteristics and bond interactions between different molecules and surfaces. In other words, everything that is possible today running quantum molecular calculations for molecular dynamics (MD) or bond energies using molecular simulation software can be done more efficient by using machine learning algorithms (ML) and artificial intelligence (AI). The built neural network (NN) in Ref. [7] is subsided by a Random Forest algorithm designed with 4 neurons and 3 hidden layers, while the first layer has 8 neurons, the second and the third layers both have 12 neurons. To map all obtained data a Least Square Fit Regression model is used representing the dependence of bond energy on the bond length:

$$E = lR^{-2} + m \quad \text{(A5.2.1)}$$

where l, m are constants of a given atomic pair.

Charges have been obtained using the Mulliken charged method and the error for the newly built neural network are 5.34 % for the test with a mean absolute error of 1.837 kcal/mol in Ref. [7], while the best Mulliken charged NN had a relative error of 5.04 % with a maximum absolute error of 4.988 kcal/mol. Sampling techniques specific to the data collected in Ref. [9] require different methods integrated to the main framework Spectral Gap Optimization of Order Parameters (SGOOP) and AI – MD Reweighted Autoencoded Variational Bayes for Enhanced Sampling (RAVE): temperature based (TB), collective variable (CV) and reaction coordinate (RC), metadynamics, umbrella – sampling (US) and adaptive biasing force (ABF).

Feng et al in Ref. [7] employed a Random Forest algorithm to hop its neural network composed of 100 decision trees and 3 depths each, the results of which have been compared to the MD simulation of bond breaking energies from DFT calculations, representing a resource saving tool for optimization of chemical reactions and molecular design using Merz – Kollman atomic charge distribution. The chemical activity, stability and flexibility have been calculated in Ref. [7] by using 8000 sets of quantum computational data, out of which 7200 sets have been used for training and 800 sets were used for testing. Neural networks have been used in Ref. [8, 16] to estimate potential energy surfaces using Behler – Parinello (one of the first networks applied to molecular science), DTTN (Deep Tensor Neural Network), SchNet, Continous Convolutions and VAMPnets in Ref. [8, 11, 16] (for kinetics calculations). Wu et al in Ref. [11] makes use of a different neural network and database, MoleculeNet, comprising of a collection of public datasets, based on building SMILES strings to model molecules, and 3D coordinates of molecular structures.

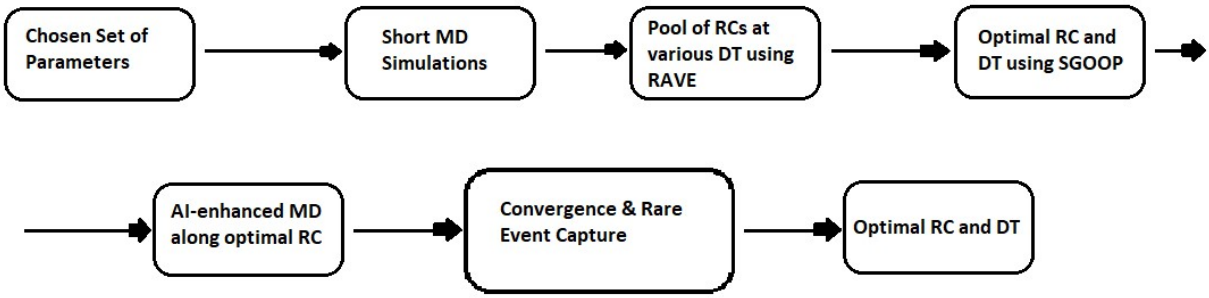

Fig A5.2.1. Sampling techniques using NN with SGOOP and RAVE in Ref. [9]

A better approach to creating viable molecular structures and defining molecular dynamic problems, as well as characterizing potential energy surfaces, bond breaking energies and transition structures, the ML and AI algorithms come with a multitude of approaches in the methods they adopt, everything that was built for MD simulations can be transposed and transformed in neural network approaches with great success in reducing the time needed for computation as well as scalability of the process.

The flow of the process in Ref. [9] to achieve the best reaction coordinate result is presented in Fig A5.2.1. Starting from running a short MD simulation on a set of parameters, then in the second step create a pool of RCs at different characteristic times using RAVE, select the RC in the third step on the SGOOP and then with the selected RC perform a MD simulation and check the convergence to allow the selection of optimal RC. A bigger database used for the extraction of molecular properties is Inorganic Crystal Structure Database (ICSD) in Ref. [10] containing more than 190000 entries of organic and inorganic molecules. The training is done either supervised or unsupervised using radial distribution functions, Voronoi tessellations, property-labelled material fragments, and Naive Bayers classifiers to train the selected data, with newer approaches and challenges in the use of neural Turing machines and imitation learning.

Different approaches to NNs has been intended in Ref. [12] with a variety of methods based on the use of kernels, based on Coulomb matrix, SOAP (smooth overlap of the atomic positions), HDAD (histogram of distances, angles and dihedrals), BOB (bag of bonds), BAML (bonds, angles and machine learning), MBTR (many-body tensor representations), MPNN (message passing neural networks), DTNN (deep tensor neural network), HIP - NN (hierarchically interacting particle neural network) and SchNet. Reinforcement learning for quantum calculations of molecular materials and designs is presented in detail in Ref. [13]. The inverse design through high – throughput virtual screening (HTVS) makes use of generative models for converging the desired properties and chemical space characteristics of the molecular environment by the use of variational encoders (VAEs), generative adversarial networks (GANs) and reinforcement learning (RL). The recurrent neural network (RNN) used in combination with the reinforcement learning algorithm runs one step at the time in an incremental sequence. The

reinforcement learning comes as a learner that needs to act in a certain environment, in SMILES for example, using a Monte Carlo Tree search algorithm (MCTS).

The active learning is modelled by the relation (A5.2.2) for molecules larger than a threshold defined as γ:

$$\delta F/\delta \Theta_m(\Theta, x^*) = \Sigma_i \, \delta V(n_i)/\delta \Theta_m (\Theta, x^*) \quad (A5.2.2)$$

where x* is defining atomic environments.

The machine learning model (ML) defines the total loss function (A5.2.3) based on N number of molecules, F the function predicting a certain property of molecules, y called labels and Θ is a free parameter:

$$L(\Theta) = \Sigma^n_{j=1}(y_j - F(\Theta, x^{(j)})^2 \quad (A5.2.3)$$

$$F(x) = \Sigma_i \, V(n_i) \quad (A5.2.4)$$

where $n_i = \{(r_{ij}, z_j)\}$ is the locality in Ref. [12] in the model.

The moment tensor potentials are:

$$V(n_i) = \Sigma_\alpha \, \zeta_\alpha \, B_\alpha(n_i) \quad (A5.2.5)$$

where ζ_α are linear parameters and the functions describe the evolution of the tensor are presented in (A5.2.6) and (A5.2.7) in Ref. [12]:

$$f_\mu(r, z_i, z_j) = \Sigma_k \, c^{(k)}_{\mu, zi, zj} \, Q^{(k)}(r) \quad (A5.2.6)$$

$$Q^{(k)}(r) = T_k(r) \, (R_{cut} - r)^2 \quad (A5.2.7)$$

The two types of parameters are the intensive quantity characterizing the HOMO/LUMO level and extensive quantity defining the atomization energy.

Computational expenses. The solvation free energy of a compound, example of H_2O in Ref. [15], comes with high computational expenses for regular MD simulations and force – field errors resulting from the reduced space available to compute. Comparatively ML simulations have been carried and presented with the MD based simulations. The ML predictions have been calculated using methods such as LASSO, random forest regression (RFR), gradient tree boosting (GTB) and support vector regression (SVR). Based on Kirkwood-Buff method, the MD simulations work with force – fields designed for vapour equilibrium of 1 % and solvation free energy in the range of 0.6 – 1.8 RMSE compared to the ML values of 0.5 (GTB), 0.3 (SVR), 0.6 (RFR) and 0.7 (LASSO).

The simulation of amorphous silicon (a-Si) using DFT-MD simulation at 10^{11} K/s rate required 16 million core hours on Archer facility, while running it with GAP improved the efficiency of the process reducing the number of core hours to 40000 presented by Deringer et al [14], that obtained for a number of 4096 atoms on GAP-MD a δ value of -51 ppm (inverse height H^{-1} of 0.57) while experiments show a value of

-38.3 ppm (inverse height 0.58). Newer approaches in reduction of computational time for large scale molecular simulations come from the limitations of traditional deep learning methods that are overcome by the application of newer neural network methods in the field of deep learning in Ref. [16]. Examples of neural networks adapted to the calculation type are CNNs (convolutional neural networks) in computer vision and RNNs (recurrent neural networks) in context dependent language semantics. The deep learning neural networks though still have deficiencies that need to be fixed: importance sampling and dimensionality reduction, reduced by the use of deep unsupervised learning (generative learning). The GNNs (or graph based neural networks) use nodes denoted n_i to define the characteristics of each particle i, where each node receives information from its neighbours m_i. Their main characteristics is smoothness as all the weights matrices during training need to be normalized, through a process called spectral normalization, a method mostly applied to generative adversarial networks (GANs) and energy-based models (EBMs).

A5.3 Conclusions To Annex 5

The developments in artificial intelligence and machine learning greatly reduce the time needed for the molecular simulations and as well the memory that one needs to allocate for the same job. As presented in Section A5.2 Computational Resources a reduction in the time needed to run MD simulations from 16 million core hours to 40000 core hours is the future of molecular simulations and MD generally, and is the application of neural networks and AI algorithms to solve the same problems that could not be run, due to the large computational resources necessary, or the time needed that would be too long. MLAtom, SGOOP, and other newly developed molecular databases and frameworks contain data of specific molecules to multiple experimental resources that can be run 16 mil / 40000 faster.

References

[1] Irie K., McKinnon A. E., Unsworth K., Woodhead I. M., A Technique for Evaluation of CCD Video-Camera Noise, IEEE Transactions on Circuits and Systems for Video Technology, 2008, Vol. 18, No.2

[2] Mayne A.J., Dujardin G., Atomic and Molecular Manipulation, Elsevier, 2011, Volume 2

[3] Solem J.E., Programming Computer Vision with Python, O'Reilly, 2012, First Edition

[4] Aiazzi B., Alparone L., Baronti S., Selva M., Stefani L., Unsupervised estimation of signal-dependent CCD camera noise, EURASIP Journal on Advances in Signal Processing 2012, 2012:231

[5] Douglas K.M., Modeling Noise for Image Simulations, http://kmdouglass.github.io/posts/modeling-noise-for-image-simulations/

[6] Boncelet C., Image Noise Models, The Essential Guide to Image Processing (Second Edition), 2009, Pages 143-167

[7] Feng C., Sharman E., Ye S., Luo Y., Jaing J., A neural network protocol for predicting molecular bond energy, SCIENCE CHINA Chemistry, 2019, Volume 62, Issue 12:1698-1703

[8] Nóe F., Tkatchenko A., Müller K.-R., Clementi C., Machine learning for molecular simulation, Annu. Rev. Phys. Chem. 2020. 71:361–90

[9] Pant S., Smith Z., Wang Y., Tajkhorshid E., Tiwary P., Confronting pitfalls of AI-augmented molecular dynamics using statistical physics, J. Chem. Phys. 153, 2020, 234118

[10] Butler K.T., Davies D.W., Cartwright H., Isayev O., Walsh A., Machine learning for molecular and materials science, Nature, Vol. 559, 2018, 547-555

[11] Wu Z., Ramsundar B., Feinberg E. N., Gomes J., Geniesse C., Pappu A.S., Leswing K., Pande V., MoleculeNet: a benchmark for molecular machine learning, Chem. Sci., 9, 2018, 513-530

[12] Gubaev K., Podryabinkin E. V., Shapeev A. V., Machine learning of molecular properties: Locality and active learning, J. Chem. Phys. 148, 2018, 241727

[13] Sanchez-Lengeling B., Aspuru-Guzik A., Inverse molecular design using machine learning: Generative models for matter engineering, Science 361, 2018, 360–365

[14] Deringer V. L., Bernstein N., Bartók A. P., Cliffe M. J., Kerber R. N., Marabella L. E., Grey C. P., Elliot S. R., Csányi G., Realistic Atomistic Structure of Amorphous Silicon from Machine - Learning – Driven Molecular Dynamics, J. Phys. Chem. Lett. 2018, 9, 2879−2885

[15] Gebhardt J., Kiesel M., Riniker S., Hansen N., Combining Molecular Dynamics and Machine Learning to Predict Self - Solvation Free Energies and Limiting Activity Coefficients, J. Chem. Inf. Model. 2020, 60, 11, 5319–5330

[16] Zhang J., Lei Y.-K., Zhang Z., Chang J., Li M., Han X., Yang L., Yang I., Gao Y. Q., A Perspective on Deep Learning for Molecular Modelling and Simulations, J. Phys. Chem. A 2020, 124, 34, 6745–6763

ANNEX 6. STUDIES OF GOLD CONTAINING COMPOUNDS USED AS PRECURSORS IN FEBID; A GAS-PHASE STUDY

Gold compounds have been investigated for their suitability as FEBID precursors mainly in the past five to six years. High ratios of Au : C (~7 : 1) have been obtained in the nanostructures created using the FEBID process with purities similar to those achievable in iron nanostructures. Using dimethyl gold (III) trifluoroacetylacetonate Ref. [100], purities of 91 at% Au in the structures have been obtained with the addition of H_2O jets to the precursor gas compared with 15 at% to 31 at% Au contents without the addition of H_2O. Higher purities in Au nanostructures have been obtained using MeAuCO and ClAuCO in Ref. [101-102], with a content of Au in the nanostructures of 95 at% at a deposition temperature of 40 – 45 °C. FEBID technology has been widely applied to a range of applications in the electronics industry and CMOS/MOSFET capacitors development [233], to atomic force microscopy manufacturing tips for the scanners [234], nanoantennae by the use of PMMA and Au in the deposition of plasmonic gold nanostructures [235], and Hall sensors through deposition of Au nanofilms on sapphire [236]. Gold FEBID nanostructures [233] have improved conductivity with resistivity values as low as 8.8 μΩcm. Commercially obtained precursors as $Me_2Au(acac)$ have wide applications to nanostructures embedded in nanocrystalline graphite [17] reaching grain sizes close to 12 – 14 nm at temperatures close to 300 °C, while $Me_2Au(tfac)$ with the addition of H_2O gives structures with Au content as high as 90 at% [9]. Earlier FEBID studies of the $Me_2Au(tfac)$ [237] as early as 1988 report deposition purities of the nanostructures of 40 at% Au, 55 at% C and 1.5 at% O, by the use of a modified-vector scan electron-beam lithography system. By using dimethyl - gold(III) – trifluoro - acetylacetonate ($Me_2AuCF_3(acac)$) Au – Fe nanoalloys for nanoelectronic applications have been obtained in the EBI - CVD process with 34 at% Au, 9 at% O, and 57 at% C and height of 0.54 μm, and a deposition rate 3 times higher than the Fe deposition rate. In the biomedical field of FEBID tiocene – Au compounds [238] with Au deposition to form active Au(I) – N - heterocyclic carbene as anticancer agents have been developed targeting renal and prostate cancer cells. Other sources report oxidation studies of Au compounds [239], cyclometallated Au(III) complexes (C, N – donor ligands), Au - N – heterocyclic (NHC) carbene complexes and Au alkynyl complexes, that in biological compounds at nanometre level can inoculate O atoms and degrade the metal atom reducing the Au(III) to Au(I). In combination with metal atoms, nanomodified titanium and Au nanoparticles [241] have been studied to antibacterial properties with good results, titanium on its own not having antibacterial properties. Two Au containing compounds have been studied to their effect on bacteria as E. Coli [104], ((triphenylphosphine) - gold(i) - (4,5 –

dicyanoimidazolyl - 1H - 1yl) and on (triphenylphosphine) - gold(i) - (4,5 – dichloroimidazolyl - 1H - 1yl), looking at their inhibitory properties by testing the E. coli dihydrofolate reductase (DHFR). The developments in the use of Au nanoparticles in gas sensing devices [240] have allowed the detection of volatile organic compounds. Combinations of W_xO_y + Au and Pt allow the filtration, checks and sensing of different organic elements in rooms, chambers and environment. For the purpose of our study of the suitability of precursors for FEBID processes, deposition of thin films of $Me_2Au(acac)$ and mass spectroscopy of 4,5-dichloro – 1,3-diethyl – imidazolyl (trifluoromethyl) gold(I) have been carried at low electron energy irradiation in the range of 0 – 25 eV complemented with stability studies of the precursors, and, VEA and VEDE DFT calculations at B3LYP/Def2TZVPP level of theory.

A6.1. 4,5-DICHLORO – 1,3-DIETHYL – IMIDAZOLYL (TRIFLUOROMETHYL) GOLD(I)

4,5-dichloro – 1,3-diethyl – imidazolyl (trifluoromethyl) gold(I) is used in advanced materials fabrication (insulators and alloys), in the pharmaceutical industry having a high ability to inhibit enzymes and the presence of the metal centre activating biological changes of the organic ligand in catalysed reactions Ref. [103] and reductive elimination/migratory insertion reactions by the addition in between two ligands of a new metal atom in Ref. [104]. 4,5-dichloro – 1,3-diethyl – imidazolyl (trifluoromethyl) gold(I) compound is one of the compounds synthesized by the Department of Chemistry from the University of Oslo, Norway, as part of the ELENA project, designed for FEBID and DEA applications.

Synthesis of compound. 4,5-dichloro – 1,3-diethyl – imidazolyl (trifluoromethyl) gold(I) has the linear formula of $C_8H_{10}Cl_2N_2AuF_3$ and the mass of 459.05 amu. The schematics of the compound is presented in Fig A6.1.1.

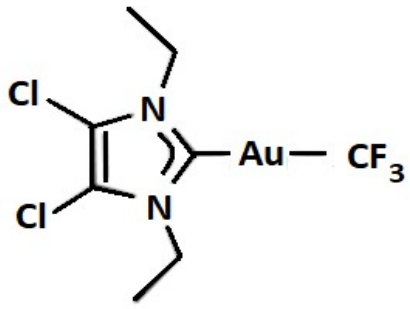

Fig A6.1.1 Schematics of 4,5-dichloro – 1,3-diethyl – imidazolyl (trifluoromethyl) gold(I)

The synthesis of the compound follows the steps in Fig A6.1.2, and from its structure we can easily determine that it is a methyl gold-based compound. The closest commercially available compound is IPr-Au-CF_3.

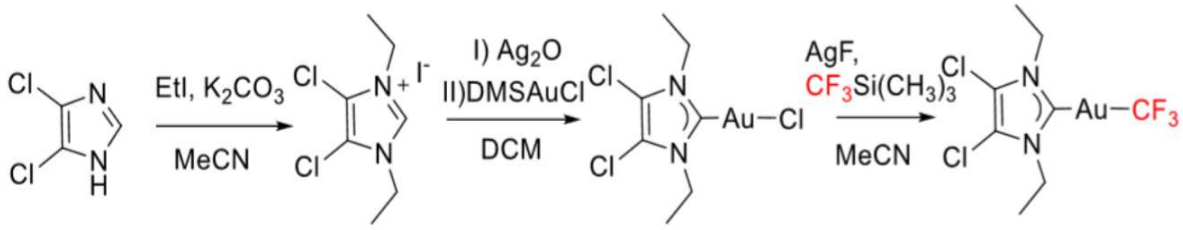

Fig A6.1.2. Synthetization of 4,5-dichloro – 1,3-diethyl – imidazolyl (trifluoromethyl) gold(I)

A6.1.1 Previous Work

The scarce research work on Au-compounds makes the comparison of the work with previous literature data difficult, as the 4,5-dichloro – 1,3-diethyl – imidazolyl (trifluoromethyl) gold(I) compound has been newly designed for this particular project. A set of precursors containing Me radicals and CF_3 are analysed for their anion data and fragmentation (Table A6.1.1.1). Blaya et al 2014 [25] through experimental NMR studies detected two of the anions of $Au(CF_3)_2L$ (L=NHC or $P(OMe)_3$) and $Au_2(CF_3)_2(\mu\text{-dppe})$ as $Au(CF_3)_2^-$ and $Au(C_6F_5)_2^-$, while the behaviour of compounds containing Br and Cl through the higher electronegativity of the Cl and Br radicals tend to form AuX_4^- (X = Cl, Br). Kopyra et al 2021 [261] in the study of $ClAuS(CH_3)_2$ using a quadrupole mass spectrometer analyser detected a number of anions ranging from 0.2 eV (Cl^-) to 8.6 eV (CSH_2^-) for a vertical electron detachment of 0.0745 eV and vertical electron affinity of 0.10648 eV. The dissociation of the $ClAuS(CH_3)_2$ compound is characterized by a transition from σ to π* symmetry, from HOMO with an orbital energy of -6.755 eV to LUMO with an orbital energy of 2.415 eV.

Reference	DEA anion	Electron Energy (eV)
Ref. [25] Blaya et al 2014 $Au(CF_3)_2L$ (L=NHC or $P(OMe)_3$) $Au_2(CF_3)_2(\mu\text{-dppe})$	$Au(CF_3)_2^-$ $Au(C_6F_5)_2^-$ AuX_4^- (X = Cl, Br)	*Anions obtained from reaction, NMR study
Ref. [261] Kopyra et al 2021 $ClAuS(CH_3)_2$	Cl^- S^- CH_2S^- $ClAuH\cdots SH^-$	0.2 / 0.7 4.6 / 7.2 / 8.1 - 8.4 0.6 / 8.6 2.3 / 2.9

Ref. [14] Carden et al 2019 $CF_3AuCNMe$	$M - H^-$ CF_3AuCN^-	*mass spectrum presented only; yields / (m/z)
Present work (VMI)	Cl^-	0.85 / 5.2
	CF_3^-	0.88 / 7.1
	$CH_4N_2Cl^-$	0.84
	$C_4H_9N_2Cl_2^-$	0.82 / 3.2
	$H_4N_2F_2Au^-$	0.82 / 4.7
	$C_5H_8AuCl^-$	0.90 / 4.7 / 9.2
	$C_5H_9NFAuCl^-$	0.85 / 5.6
	$C_7H_{10}N_2AuCl_2^-$	0.86
	$C_8H_{10}Cl_2N_2AuF_3^-$	0.86

Table A6.1.1.1. DEA anion spectrum data from different sources and comparison with current work

The electron affinity and bond strengths defines the M – L bond between the metal and the L = F, Cl, Br, I with antibonding character. According to Blaya et al [25], the bond strength, dissociation energy and anions would follow the rule $F^- > Cl^- > Br^- > I^-$. Higher bonding energy is assigned to CF_3 compared to Cl, and higher to Cl compared to CH_3. Br – M and I – M are weaker bonds in Au compounds, one of the main purposes they are highly sought in designing of the precursors for focused electron beam induced deposition purposes. On the other hand, S will have a higher bond strength to a metal like Au, compared to C, though at high and very high temperatures the C – Au is more stable forming carbene lattices with metal atoms embedded [239], one of the most important applications in the carbon/carbene nanotubes development. N in combination with H in Au compounds would form hydrogenated nitrogen bonds between the molecules, where the Au would be in the centre of the framework surrounded by F and Cl atoms characterized by a higher electronegativity. A higher content of H_2O would change the lattice to Cl – N – H_2O bonds and oxidation of the metal with time and increase in temperature.

Reference	Electronic states and excitation cross-sections
Ref. [264] Sirakov et al 2013 Au atom	1.0698×10^{-22} cm^2 total cross-sections at 0.0253 eV between 200 keV to 5 MeV (neutron cross-section)

Ref. [265] Fischer et al 2016 Au atom	2.185 x 10^{-22} cm^2 total cross-sections (neutron cross-sections)
Ref. [266] Hannaske et al 2013 Au atom	7.5 x 10^{-22} cm^2 total cross-section at 3.5 MeV (neutron cross-section)
Present work (Quantemol-N)	*Excitation cross-section data missing as the Au atom is not implemented in the Quantemol-N software
Present work DFT calculations from Gaussian 16 in neutral state at B3LYP/Def2TZVPP	1A 4.5726 eV 1A 5.3364 eV 1A 5.4276 eV 1A 5.4392 eV 1A 5.5289 eV 1A 5.6655 eV 1A 5.6850 eV 1A 5.8209 eV 1A 5.8959 eV 1A 6.1231 eV 1A 6.1454 eV 1A 6.2935 eV 1A 6.3836 eV 1A 6.3839 eV 1A 6.4548 eV 1A 6.4675 eV 1A 6.4936 eV 1A 6.6320 eV 1A 6.6978 eV 1A 6.7178 eV 1A 6.8246 eV 1A 6.8414 eV
Present work	2A 2.8584 eV 2A 3.1330 eV

DFT calculations from Gaussian 16 in charged state at B3LYP/Def2TZVPP	2A 3.2165 eV 2A 3.8830 eV 3A 3.9369 eV 2A 4.3089 eV 2A 4.4307 eV 2A 4.5041 eV 2A 4.6242 eV 2A 4.7247 eV 2A 4.7879 eV 2A 4.8295 eV 2A 4.8439 eV 2A 4.8533 eV 2A 4.9216 eV 2A 4.9832 eV 2A 5.0134 eV 2A 5.0617 eV 2A 5.1034 eV 2A 5.1367 eV 2A 5.1675 eV 2A 5.1822 eV 3A 5.2287 eV 2A 5.3024 eV 2A 5.3694 eV 3A 5.4309 eV

Table A6.1.1.2. DFT electronic states, cross-sections and resonances from different sources and comparison with current work

The cross-section data is available only for the Au atom, the 4,5-dichloro – 1,3-diethyl – imidazolyl (trifluoromethyl) gold(I) due to its novelty does not have any available cross-section data in the scientific literature. The three cited sources (Table A6.1.1.2), present very different values of the cross-sections; a total cross-section is presented in [265] with a value of 2.185 x 10^{-22} cm^2, total cross-sections from neutron measurements. A lower cross-section is presented by the Berkely Scientific Report from 2013 [264] with a value of 1.0698 x 10^{-22} cm^2 total cross-sections at 0.0253 eV between 200 keV to 5 MeV (neutron cross-section). The highest value, in high discrepancy compared to the work in [264] and [266]

is the value presented by Hannaske et al 2013 [266] with a value of 7.5 x 10^{-22} cm^2 total cross-section at 3.5 MeV from neutron measurements. XANES experimental studies of dichloroaurate (I) (gold (I) chloride species) in Ref. [105], of the white line of $[AuCl_2]^-$ ions show weak Au $2p_{3/2}$ → 5d transition. The density of states (DOS) analysis resembles that the weak transition is the result of an Au 6s/5d hybrid partially occupied to the highest energy level occupied HOMO orbital. From the laser ablation of $[Au(CF_3)Cl]^-$ anion in Ref. [104], the dipole allowed transitions $p_{3/2}$ → d and $p_{3/2}$ → s and the presence of 6s/5d transition from the relativistic 6 states and 3d → 5d hybridization of the unoccupied HOMO states appear as characteristics of the Au – Cl bond. The bond distance Au – Cl for a resultant $[AuCl]^-$ anion is 2.27 Å in Ref. [105], similar in scattering processes to the Au(III) anion $[AuCl_4]^-$. For our DEA studies of the 4,5-dichloro – 1,3-diethyl – imidazolyl (trifluoromethyl) gold(I) complex, that could only be the result of recombination once fragmentation has occurred, a double CH_2 bond as intermediary and a C - N – Au bond would need to be broken for the transition to take place. The compound with the presence of ethyl and methyl radicals would increase the cross-section value at least two orders of magnitude compared to the values of the simple Au compound, placing the maximum of the peak between 150 eV and 200 eV.

5.1.2. Experimental Set-up

The experimental set-up of the VMI is presented in Section 1 Chapter 2 of the thesis. In a typical VMI set-up the vapours of the compound enter the chamber at 90 degrees (perpendicular) to the electron beam, and they are guided towards the MCP by a set of plates, called pusher, puller and extractor with different polarities and two Helmholz coils keeping the magnetic field for levitation inside the chamber at a certain level prior established by the user.

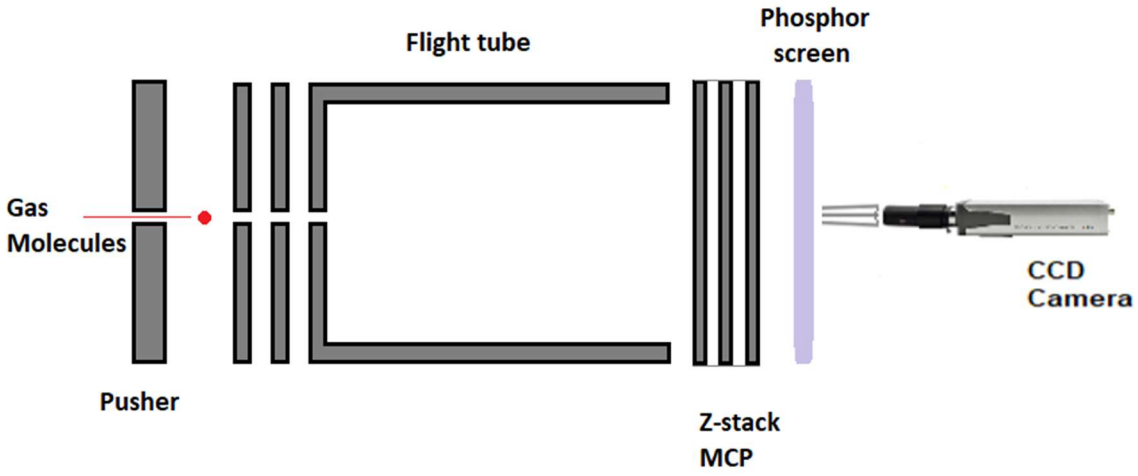

Fig A6.1.2.1 VMI and MCP assembly set-up

The MCP detector has three channel plates with Chevron patterns according to the ion velocities; once the ions have passed the detector they are projected on a phosphor screen and imaged by using an industrial CCD camera. The ions will show up on the CCD camera as a 2D projection of a ion Newton sphere. The VMI is used in time-of-flight mode only for this compound as its vaporization pressure is too low to be imaged.

5.1.3. Results and Discussions

Bond lengths and angles. Using Gaussian 16 software we ran ab-initio and DFT calculations of the structure and main characteristics of the 4,5-dichloro – 1,3-diethyl – imidazolyl (trifluoromethyl) gold(I) precursor. Bond distances of Au to different organic radicals are presented in Ref. [25].

Compound	Au – C bond distance value [Å]
PMe_3 – Au - C	2.056 – 2.075
$PPN[Au(CF_3)_2]$	2.059 – 2.073
$[Au(CF_3)(PPh_3)]$	2.05
$[Au(CF_3)(CO)]$	2.05

Table A6.1.3.2. Bond distances for Au(I) compounds in Ref. [25]

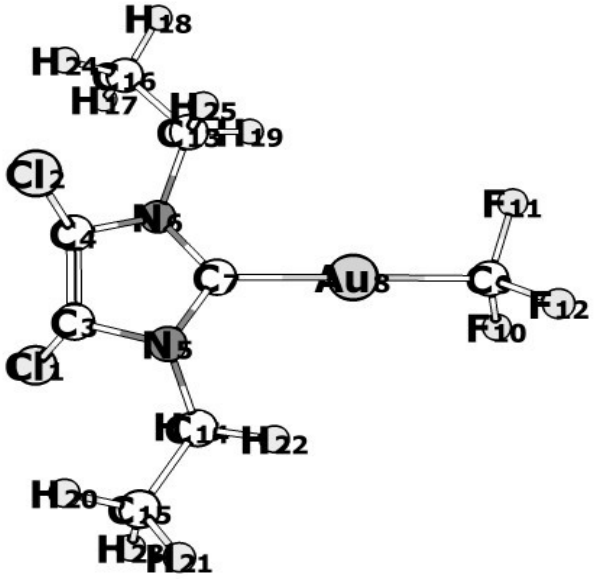

Type of bond	Bond lengths (Å)
Au8 – C7	2.065
Au8 – C9	2.076
C7 – N5	1.356
N5 – C3	1.384
C3 – Cl1	1.702
C3 – C4	1.357
N5 – C14	1.469
C13 – C16	1.523
C13 – H19	1.087
C13 – H25, C16 –	1.089
C16 – H17/24	1.090
C9 – F10	1.372

Fig A6.1.3.3 The 4,5-dichloro – 1,3-diethyl – imidazolyl (trifluoromethyl) gold(I) precursor structure from Gaussian 16 at B3LYP/Def2TZVPP level of theory

The calculated bond distances between different atoms of the precursor are presented in Fig A6.1.3.3. The Au8 – C9 distances is 2.065 Å, 0.008 Å higher in value than the values obtained from the literature for other precursors used for deposition (Table A6.1.3.1 and Table A6.1.3.2). The bond distance of Au8 – C7 is 2.075 Å, higher than to the carbon – nitrile ring. Each bond to the nitrile has a value of 1.356 Å of the C7 – N5. No direct bond between Au and Cl is made. Both methyl groups have C16 – H17 bond distances of 1.090 Å. The fluorine bond lengths are C9 – F10 with values of 1.372 Å. The two C3 – Cl1 bond distances obtained from our calculations are 1.702 Å, while the C13 – H19 bond distances are 1.087 Å. The C13 – H19 bond distances are 1.087 Å, both symmetric to the symmetry axis containing the C7, Au8 and the CF_3 fluorine group. The space group of the molecule is D_{3h}, with the symmetry on the Au8 atom and C7 atom axis. The two methyl groups are rotated 90 deg to the symmetry axis, similar behaviour is seen in the case of the two bonds, to Cl and H from C4 and C3.

DEA Anion Formation To $C_8H_{10}F_3Cl_2N_2Au$. Dissociative electron attachment of $C_8H_{10}F_3Cl_2N_2Au$ (4,5-dichloro – 1,3-diethyl – imidazolyl (trifluoromethyl) gold(I)) was studied using a velocity sliced map imaging equipment with the precursor's molecules being introduced into the vacuum chamber in gas-phase at a pressure of ~10^{-7} mbar. The resulting mass spectrum reveals a large number of negative ions (see Table A6.1.3.4) with masses m/z 35, 69, 79, 155, 267, 300, 334, 389 and 408. The lightest masses acquired from the dissociation of the compound are Cl^- at m/z 35 and CF_3^- at m/z 69.

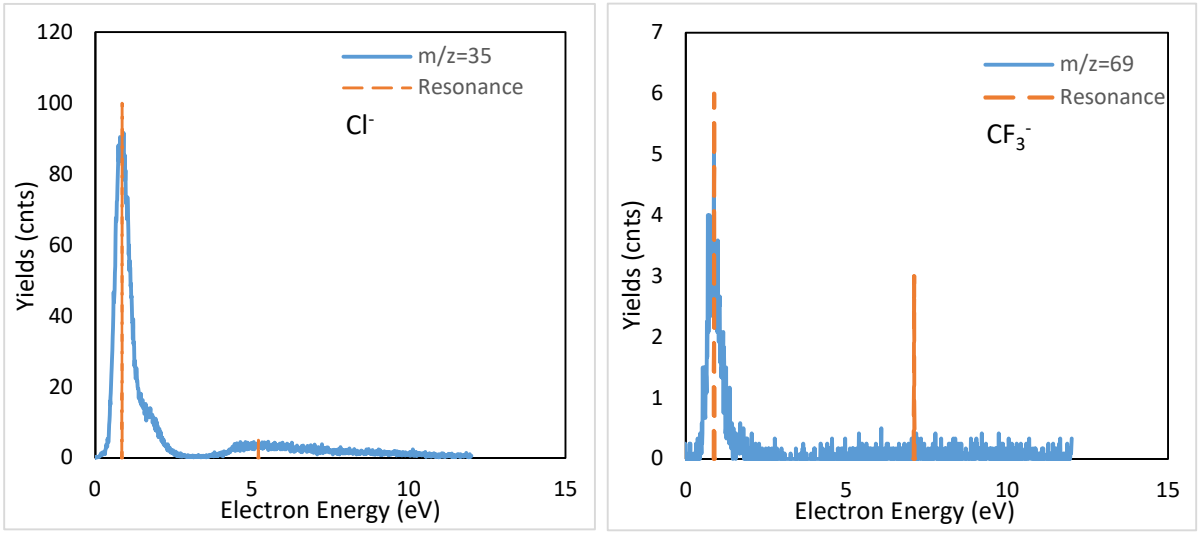

Fig A6.1.3.4 Yields to electron energy spectrum of Cl^- (left) CF_3^- (right) between 0 and 12 eV

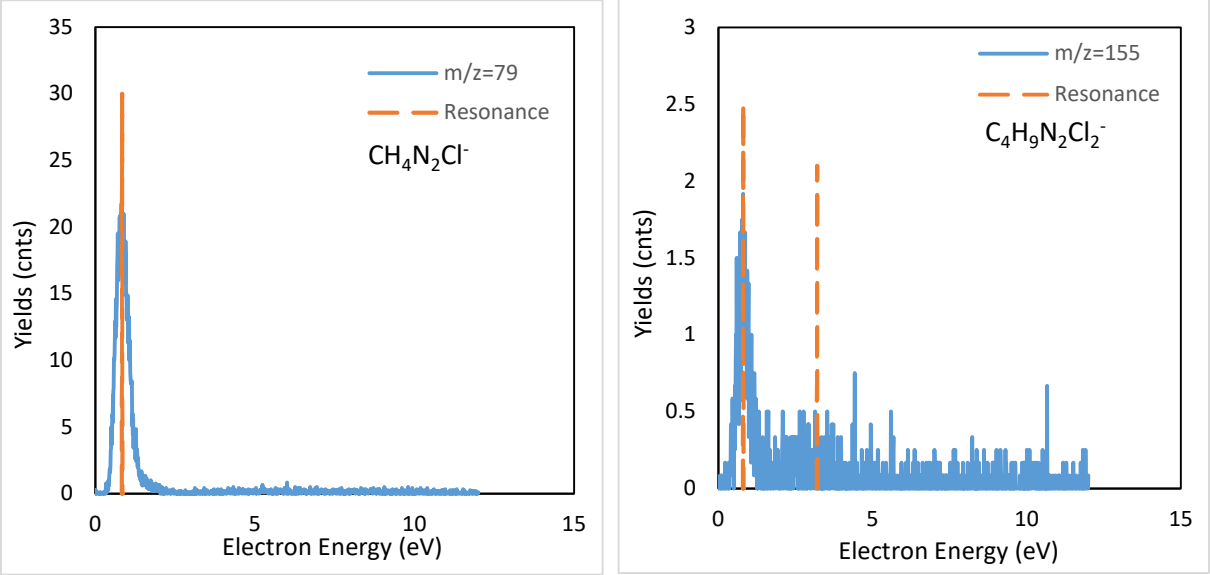

Fig A6.1.3.5 Yields to electron energy spectrum of $CH_4N_2Cl^-$ (left) $C_4H_9N_2Cl_2^-$ (right) between 0 and 12 eV

The Cl^- anion yield presents two resonance peaks: a high cross-section, low area peak at 0.81 eV with the FWHM width of the resonance of 2.41 eV and a second wider resonance of the same anion with the maximum of the resonance at 5.3 eV and a FWHM width of 5.98 eV. A smaller amplitude anion is the CF_3^- anion with the maximum peak of the resonance found at an incident electron energy of 0.81 eV with a FWHM width of 1.61 eV; the second resonance peak of the CF_3^- anion is found at 7.1 eV, with extremely low amplitude and a broad resonance peak. Higher masses anions, still containing only organic material, are m/z 79 corresponding to $CH_4N_2Cl^-$ and m/z 155 $C_4H_9N_2Cl_2^-$. The m/z 79 has only a single resonance peak at 0.84 eV. The mass m/z 155 corresponding to $C_4H_9N_2Cl_2^-$ has its first resonance peak at 0.82 eV and a second resonance peak at 3.2 eV. In the FEBID process these four anions with m/z up to 155 represent sources of C, F and N contamination in the structure. The intent is to create and use higher mass anions, through dissociation at higher than 0.5 keV incident electron beam characteristic (characteristic process at 1 keV, 2 keV and 5 keV). The anions at lower energies containing Au can deposit secondary metallic structures that can create electronic interferences in magnetic structures, while the organic parts are more easily pumped away. The first gold containing anion fragment $H_4N_2F_2Au^-$ at mass m/z 267 has a first resonance peak at an incident electron energy of 0.82 eV; and a much lower amplitude of the second peak of the resonance with a maximum at 4.7 eV. Anions observed with masses m/z 300 and m/z 334 are found to correspond to higher ethane containing anions of $C_5H_8AuCl^-$ and $C_5H_9NFAuCl^-$. The mass m/z 300 presents three resonances at 0.90 eV, 4.7 eV and 9.2

eV. The higher mass anion at m/z 334 corresponding to $C_5H_9NFAuCl^-$ has a low energy resonance peak at 0.85 eV with a width of 1.4 eV, while there is tentative evidence for a higher mass resonance.

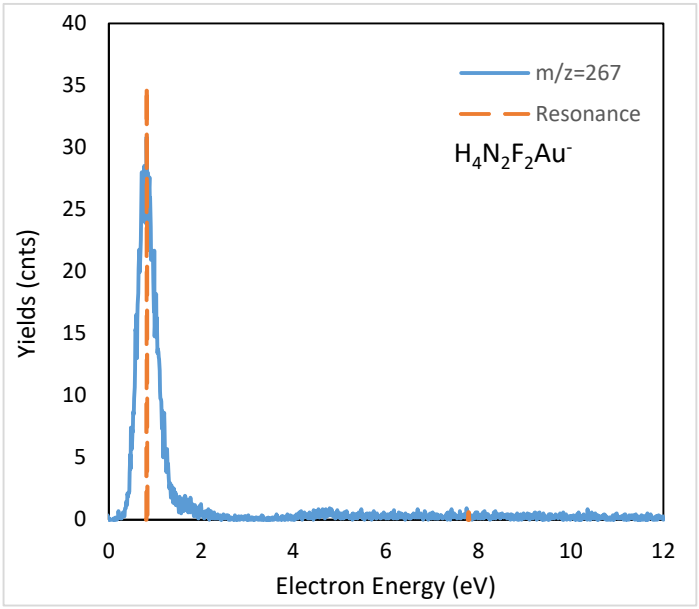

Fig A6.1.3.6 Yields to electron energy spectrum of $H_4N_2F_2Au^-$ between 0 and 12 eV

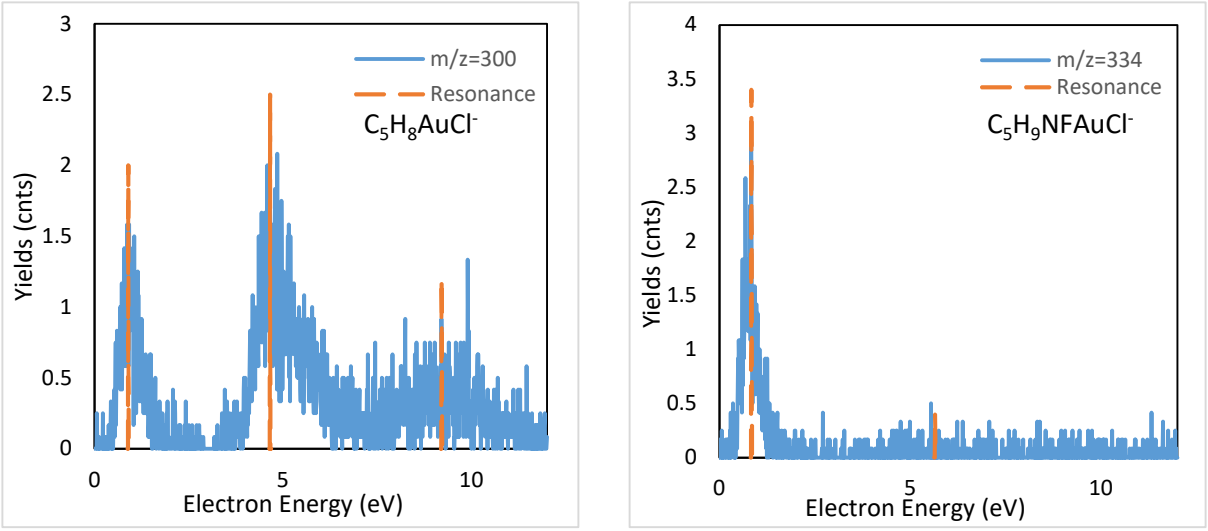

Fig A6.1.3.7 Yields to electron energy spectrum of $C_5H_8AuCl^-$ (left) $C_5H_9NFAuCl^-$ (right) between 0 and 12 eV

The anion with m/z 389 corresponding to $C_7H_{10}N_2AuCl_2^-$ has a low energy resonance peak at 0.86 eV. The highest anion found at mass m/z 408 corresponding to $C_7H_{10}N_2FAuCl_2^-$ has its first peak resonance at 0.86 eV. The second peak of the resonance is hard to distinguish from the noise and its presence is arguable, higher resolution velocity sliced map imaging could prove its existence with more reliable

output. All the anions with their characteristics of the 4,5 - dichloro – 1,3-diethyl – imidazolyl (trifluoromethyl) gold(I) precursor are presented in Table A6.1.3.3.

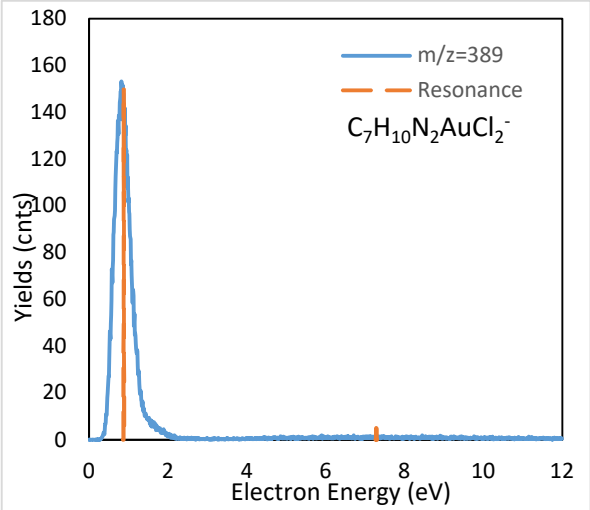

Fig A6.1.3.8 Yields to electron energy spectrum of $C_7H_{10}N_2AuCl_2^-$ between 0 and 12 eV

Mass (m/z)	Resonance [eV]	Negative Ion
35	0.81 /5.3	Cl^-
69	0.81 / 7.1	CF_3^-
79	0.84	$CH_4N_2Cl^-$
122	0.85	$C_2H_6NCl^-$
155	0.82 /3.2	$C_4H_9N_2Cl_2^-$
267	0.82 / 4.7	$H_4N_2F_2Au^-$
300	0.90 / 4.7 / 9.2	$C_5H_8AuCl^-$
334	0.85 / 5.6	$C_5H_9NFAuCl^-$
389	0.86	$C_7H_{10}N_2AuCl_2^-$
408	0.86	$C_8H_{10}Cl_2N_2AuF_3^-$

Table A6.1.3.3 Negative ions of 4,5-dichloro – 1,3-diethyl – imidazolyl (trifluoromethyl) gold(I)

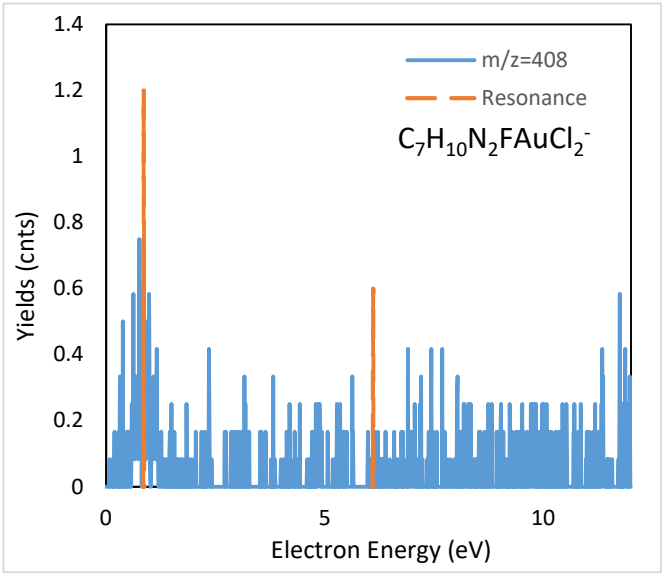

Fig A6.1.3.9 Yields to electron energy spectrum of $C_7H_{10}N_2FAuCl_2^-$ between 0 and 12 eV

EA (Electron Affinities) and BDE (Bond Dissociation Energies). The BDEs and EAs of the anions Cl^-, CF_3^-, $H_4N_2F_2Au^-$ and $C_7H_{10}N_2AuCl_2^-$ have been calculated at B3LYP/ Def2TZVPP level of theory using Gaussian 16 software. Values between 0.53 eV (Cl^-) and 0.97 eV of the bond dissociation energies have been calculated, with electron affinities of the anions between 0.0001 eV (Cl^-) to 0.16 eV (CF_3^-).

The excess energy for each particular anion is calculated using the BDE and EA of the anion using the relation Ee = EA – BDE + Ei, where Ee is the excess energy, Ei is the electron incident energy and BDE is the bond dissociation energy. The excess energies (see Table 5.1.3.4) have values between 0.03 eV for an incident electron energy of 0.86 eV in the case of the anion $C_7H_{10}N_2AuCl_2^-$. The excess energy of the anions is the calculated maximum of the kinetic energy.

Anion	EA (eV)	BDE (eV)	Ei (eV)	Ee (eV)
$C_7H_{10}N_2AuCl_2^-$	0.06	0.89	0.86	0.03
$H_4N_2F_2Au^-$	0.021	0.97	4.7	3.75
Cl^-	0.0001	0.59	0.85	0.26
CF_3^-	0.16	0.53	0.88	0.47

Table A6.1.3.4 Calculated excess energy of anions $AuCl_2N_2C_8H_{10}F_3$ at DFT B3LYP/cc-pVTZ level of theory

VEA (Vertical electron affinity) and EA (Electron affinity). The vertical electron attachment energies and electron affinities have been calculated at B3LYP/Def2TZVPP using Gaussian 16. The highest

counts anions (Table A6.1.3.5) have been calculated. The dissociation of the parent in anions and neutral fragments follows the path:

$$C_8H_{10}N_2Cl_2AuF_3 + e^- \rightarrow C_7H_{10}N_2Cl_2Au^- + CF_3 \quad (1)$$

$$C_8H_{10}N_2Cl_2AuF_3 + e^- \rightarrow C_7H_{10}N_2Cl_2Au + CF_3^- \quad (2)$$

$$C_8H_{10}N_2Cl_2AuF_3 + e^- \rightarrow H_4N_2F_2Au^- + C_8H_6Cl_2F \quad (3)$$

$$C_8H_{10}N_2Cl_2AuF_3 + e^- \rightarrow C_2H_6NCl^- + C_6H_4NClF_3 \quad (4)$$

To obtain the electron affinity EA, the relation EA = [Ee(optimized neutral) + ZPE(optimized neutral)] – [Ee(optimized anion)+ZPE(optimized anion)] [267] was used.

The values of the VEA range from 0.506 eV for the highest mass anion $C_7H_{10}N_2AuCl_2^-$ to 1.090 eV for $H_4N_2F_2Au^-$. The values of the VEA have been calculated using the HOMO and LUMO orbital energies for a transition from the ground state π to higher excited state π*. The highest vertical electron affinity is obtained for the $H_4N_2F_2Au^-$ anion with a value of 3.9009 eV.

Ions	$C_7H_{10}N_2AuCl_2^-$	$H_4N_2F_2Au^-$	$C_2H_6NCl^-$	CF_3^-
VEA(eV)	0.506	1.090	0.561	2.820 [263] *VDE
EA(eV)	3.0327	3.9009	2.9781	3.3157

Table A6.1.3.5. Electron affinities of ions $C_7H_{10}N_2AuCl_2^-$(m/z 389), $H_4N_2F_2Au^-$(m/z 267), $C_2H_6NCl^-$ (m/z 79) and CF_3^- (m/z 69)

Cross Section Data. DEA cross-sections using Quantemol-N were not possible as the Au atom has too many target electrons and at the present moment it is not implemented in the software. A software limitation of 17 atoms for a molecular structure is imposed.

A6.1.4 Summary and Conclusions

Gold compounds are rather new to the nano – deposition industry, but have received a lot more interest in nano – biomedical sciences. 4,5-dichloro – 1,3-diethyl – imidazolyl (trifluoromethyl) gold(I) with its linear formula $C_8H_{10}F_3Cl_2N_2Au$ was synthesized at the University of Oslo for this project. DEA of $C_8H_{10}F_3Cl_2N_2Au$ results in formation of nine anions resulting from a series of resonances. In the fragmentation of the precursor a number of five Au – containing anions and four organic anions have been obtained results of the collision with an electron. The Au – containing anions are masses over 200 amu with low count rates, rather noisy in the range of 200 – 300 amu presenting sharp peaks with low

FWHM width. The five anions have resonances falling at 0.82 eV and 4.7 eV for m/z 267 ($H_4N_2F_2Au^-$), 0.9 eV, 4.7 eV and 9.2 eV for m/z 300 ($C_5H_8AuCl^-$), 0.85 eV and 5.6 eV for m/z 334 ($C_5H_9NFAuCl^-$), 0.86 eV for m/z 389 ($C_7H_{10}N_2AuCl_2^-$) and 0.86 eV for m/z 408 ($C_8H_{10}Cl_2N_2AuF_3^-$). The lower mass anions containing only organic radicals have low counts under 100 counts, the only anion containing higher number of counts is Cl^- with the resonance peaks at 0.85 eV and 5.2 eV, a FWHM width of 2.1 eV (0.85 eV resonance) and 8.2 eV (5.2 eV resonance), and a maximum number of counts of 92 cnts. The other organic anions are m/z 69 (CF_3^-) with resonance peaks at 0.88 eV and 7.1 eV, m/z 79 ($CH_4N_2Cl^-$) with resonance peaks at 0.84 eV and m/z 155 ($C_4H_9N_2Cl_2^-$) with resonance peaks at 0.82 eV and 3.2 eV. The electron affinities (EA) and bond dissociation energies (BDE) have been calculated for $C_7H_{10}N_2AuCl_2^-$ (m/z 389) with an EA of 0.06 eV and a BDE of 0.89 eV, $H_4N_2F_2Au^-$ (m/z 267) with an EA of 0.021 eV and a BDE of 0.97 eV, Cl^- (m/z 35) with an electron affinity close to 0 of approximately 0.0001 eV and a BDE of 0.59 eV, while the CF_3^- (m/z 69) has an EA of 0.16 eV and a BDE of 0.53 eV. The excess energy representing the maximum obtained kinetic energy is in the range of 0.03 eV for $C_7H_{10}N_2AuCl_2^-$ to 3.75 eV for $H_4N_2F_2Au^-$. A higher number of calculations of particular anions is presented in Table 5.1.3.4 (excess energy) and Table 5.1.3.5 (vertical electron affinity), with higher discrepancies in Table 5.1.3.5 coming from the reorganization of the molecular orbitals calculated for HOMO, LUMO and LUMO-1 compared to the value of 2.820 eV obtained in [263].

A6.2. Acetylacetone from $Me_2Au(acac)$ Gas Phase Analysis

Acetylacetone data is found in ANNEX 2 for cross-section and gas-phase studies and ANNEX 3 deposition of the acetylacetone radical on Cu(110) surface.

A6.3 Conclusions To ANNEX 6

Electron impact induced dissociation of $C_8H_{10}Cl_2N_2AuF_3$ designed for this particular study at the University of Oslo in their Chemistry Department, was analysed using mass spectrometry, with anions ranging from mass m/z 35, corresponding to Cl^-, to the highest fragment at mass m/z 408 $C_7H_{10}N_2FCl_2Au^-$, produced by incident electron energies between 0 eV and 12 eV. The second compound studied in this chapter in Section 5.2, is the acetylacetone radical which is formed in the dissociation of $Me_2Au(acac)$ for which a set of DEA cross-sections in Interaction Orbitals (IH) mode was produced using Quantemol-N. The fragmentation energies, excited states, and values of the cross-sections of the acac radical, part of a high number of acetylacetonate – metal compounds are of interest to the FEBID

process in gas-phase and at the surface. The nine anions of the $C_8H_{10}Cl_2N_2AuF_3$ obtained by dissociative electron attachment spread over an electron energy range of 0 eV to 12 eV. Five anions have resonances falling at 0.82 eV and 4.7 eV for m/z 267 ($H_4N_2F_2Au^-$), 0.9 eV, 4.7 eV and 9.2 eV for m/z 300 ($C_5H_8AuCl^-$), 0.85 eV and 5.6 eV for m/z 334 ($C_5H_9NFAuCl^-$), 0.86 eV for m/z 389 ($C_7H_{10}N_2AuCl_2^-$) and 0.86 eV for m/z 408 ($C_8H_{10}Cl_2N_2AuF_3^-$), while the organic radicals anions have resonances for m/z 35 Cl^- at 0.85 eV and 5.2 eV, m/z 69 CF_3^- with resonance peaks at 0.88 eV and 7.1 eV, m/z 79 $CH_4N_2Cl^-$ with a resonance peak at 0.84 eV, and m/z 155 $C_4H_9N_2Cl_2^-$ with resonance peaks at 0.82 eV and 3.2 eV.

The bond dissociation energies and electron affinities of the anions have been calculated using DFT simulations at B3LYP/cc-pVTZ level of theory with values in the range of 0.06 eV $C_7H_{10}N_2AuCl_2^-$ (m/z 389) EA and 0.021 eV $H_4N_2F_2Au^-$ (m/z 267) EA and BDE of 0.89 eV $C_7H_{10}N_2AuCl_2^-$ and 0.97 eV $H_4N_2F_2Au^-$. The Cl^- (m/z 35) anion has an electron affinity close to 0 of approximately 0.0001 eV and a BDE of 0.59 eV, while the CF_3^- (m/z 69) has an EA of 0.16 eV and a BDE of 0.53 eV. Excess energies in the range of 0.03 eV for $C_7H_{10}N_2AuCl_2^-$ to 3.75 eV for $H_4N_2F_2Au^-$ have been obtained representing the maximum kinetic energies. A number of 21 excited states from CIS calculations of the molecule in ground state have been obtained representing allowed transitions from 1A to $1A_1$' at 4.5726 eV, 5.3364 eV, 5.4276 eV, 5.4392 eV, 5.5289 eV, 5.6655 eV, 5.6850 eV, 5.8209 eV, 5.8959 eV, 6.1231 eV, 6.1454 eV, 6.2935 eV, 6.3836 eV, 6.3839 eV, 6.4548 eV, 6.4675 eV, 6.4936 eV, 6.6320 eV, 6.6978 eV, 6.7178 eV, 6.8246 eV and 6.8414 eV.

The Quantemol-N cross-section could not be run due to the lack of implementation of the Au atom in the software and the high number of atoms in the molecule. A study of cross-sections has been run for the acetylacetone radical from the $Me_2Au(acac)$ with good results. A number of 17 excited states have been obtained from CI Orbital Configuration mode in Quantemol-N software representing allowed transitions from 2A ground state to 1A 0.000001 eV, 3B 5.3 eV, 3A 5.54 eV, 1B 5.8 eV, 1A 6.03 eV, 3B 7.19 eV, 3A 7.22 eV, 1A 8.98 eV, 3B9.57 eV, 3A 9.65 eV, 1B 10.47 eV, 1A 10.97 eV, 1B 10.99 eV, 3B 11.45 eV, 1A 11.53 eV, 3A 11.78 eV and 3B 11.81 eV. A value of the DEA cross-sections of 1.15 $Å^2$ between 0 eV and 2 eV, and 0.3 $Å^2$ at 10 eV corresponding to the presence of the anions between 0 – 10 eV was obtained. A value of the maximum total cross section of 13 x 10^{-16} cm^2 characterizes the radical, while the ionization cross sections over 0 to 1000 eV range have a maximum value of 17.5 $Å^2$ at 90 eV. The excited states from the excitation cross-section show appearance energies at 5.4 eV, 5.6 eV - 3A, 3B as well as at 7.2 eV, 7.3 eV – 3A, 3B, with similar shapes, while at 5.9 eV, 6.10 eV representing 1A, 1B and 9 eV, 9.6 eV representing 1A, 3B curves, a difference in amplitude is observed between the two similar shape resonances.

ANNEX 7

Type of deposit	Dwell Time (us)	Loops (number)	Beam current [pA]
6 points	1.325/ 2.456/ 3.564/ 4.634/ 5.741/ 6.880	345/ 1102/ 2203/ 3301/ 4112/ 5734	24
6 points	10.325/ 12.456/ 13.564/ 14.634/ 15.741/ 16.886	1345/ 2102/ 3203/ 4301/ 5112/ 6734	24
6 points	20.325/ 22.456/ 23.564/ 24.634/ 25.741/ 26.886	10345/ 12102/ 13203/ 14301/ 15112/ 16734 & 1000	24
6 points	30.325/ 32.456/ 33.564/ 34.634/ 35.741/ 36.886	1000	24
6 points	40.325/ 42.456/ 43.564/ 44.634/ 45.741/ 46.886	1000	24
6 points	50.325/ 52.456/ 53.564/ 54.634/ 55.741/ 56.886	1000	24
6 points	80.325/ 82.450/ 83.564/ 84.634/ 85.741/ 86.886	1000	24
6 points	2.350/ 12.350/ 22.350/ 32.350/ 42.350/ 52.350	1000, 1300, 2000, 2500, 3000, 1800, 1500, 4000	24
6 points	1/ 5/ 10/ 15/ 20/ 25	4000	24
6 points	30/ 35/ 40/ 45/ 50/ 55	4000	24
6 points	20.325/ 22.325/ 24.325/ 26.325/ 28.325/ 30.325	1300	24
6 points	10.325/ 12.325/ 14.325/ 16.325/ 18.325/ 20.325	1300	24
6 points	30.325/ 32.325/ 34.325/ 36.325/ 38.325/ 40.325	1300	24
6 points	16	1300	24
6 points	30	1300	24
6 points	10	1300	24
6 points	20	1300	24
6 lines	5	1300	24

6 lines	0.7	500	24
6 lines	0.45	500	24
6 lines	0.7	700	24
6 lines	0.35	1300	24
5 lines	0.7	1300	24
Text	0.35	500	24

Table A7.1. Deposition of $Si(OEt)_4$ on Au(111)/silica, 8 months old deposits

Type of deposit	Dwell Time (us)	Loops (no)	Beam current [pA]	Beam voltage [eV]
7 lines	0.7	650	28	1000
7 lines	0.35	1300	28	1000
6 points	4.03/ 4.23/ 4.43/ 4.63/ 4.83/ 5.03	1000	28	1000
7 points	0.25/ 1.25/ 2.25/ 3.25/ 4.25/ 5.25/ 6.25	2600	28	1000

Table A7.2. Deposition of $Si(OEt)_4$ on Au(111)/silica, one day old deposits

Structure	Height (nm)	Width (nm)	Dwell time	Loops	Structure	Height (nm)	Width (nm)	Dwell time	Loops
Profile 1	123.1	350	350	1000	Point 1	1338	783	4300	1000
Profile 7	128	350	350	1000	Point 2	831	248	4230	1000
Profile 2	129.3	350	350	1000	Point 3	419.5	351	4430	1000
Profile 6	126.5	350	350	1000	Point 4	1032	480	4630	1000
Profile 3	168.8	350	350	1000	Point 5	1229	574	4830	1000
Profile 4	160.8	350	350	1000	Point 6	1628	619	5030	1000
Profile 5	165.1	350	350	1000	Point 7	590	405	4250	1000
Profile 8	88.9	341	700	1300	Point 8	487	365	250	1000
Profile 14	89.9	341	700	1300	Point 9	515	381	1250	1000
Profile 9	87	320	700	1300	Point 10	534	381	2250	1000
Profile 13	82	320	700	1300	Point 11	547	376	5250	1000
Profile 10	62.4	310	700	1300	Point 12	563.6	384	3250	1000

Profile 11	62.9	340	700	1300					
Profile 12	62.4	330	700	1300					

Table A7.3. Characteristics of the 12 hours old deposits

	Dwell time	Loops	Si	O	C	Au	N	C'	O'	Si'	N'	Au'
Bkg	0	0	0.9	2.3	34	63	0	48	1.6	1.4	0	42.7
Profile 1	350	1000	10.1	27	45	18	0	55	32	11.1	2	0
Profile 2	350	1000	10.8	27	44	18	0	58	21	8	13.4	0
Profile 3	350	1000	9.5	27	45	18	0	65	26	9.4	0	0
Profile 4	350	1000	11.4	28	41	20	0	53	25.3	9.9	11.4	0
Profile 5	350	1000	9.4	30	44	17	0	56	27.5	9	0	5.8
Profile 8	700	1300	12.3	33	47	8.1	0	53	28.2	8.9	9.7	0
Profile 9	700	1300	10.6	32	48	8.7	0	46	31.9	10.6	11.4	0
Profile 10	700	1300	12.1	33	47	7.9	0	51	23.9	9.3	15.4	0
Profile 11	700	1300	12.3	33	47	7.8	0	55	28.8	9.6	4	0
Profile 12	700	1300	12.4	33	47	7.4	0.8	49	30.2	10.4	10.8	0

Table A7.4. Composition calculations for the 8 months old deposits (‘)
and 12 hours old deposits ()

	Dwell time	Loops	C/C'	O/ O'	Si/ Si'
Bkg	0	0	0.709	1.438	0.643
Profile 1	350	1000	0.816	0.856	0.91
Profile 2	350	1000	0.754	1.3	1.35
Profile 3	350	1000	0.703	1.042	1.011
Profile 4	350	1000	0.764	1.115	1.152
Profile 5	350	1000	0.782	1.076	1.044
Profile 8	700	1300	0.88	1.16	1.382
Profile 9	700	1300	1.05	1.013	1
Profile 10	700	1300	0.914	1.389	1.301
Profile 11	700	1300	0.858	1.128	1.281
Profile 12	700	1300	0.967	1.076	1.192

Table A7.5 Ratios calculations for the 8 months old deposits (‘) and
12 hours old deposits ()

	Pillar 1	Pillar 2	Pillar 3	Pillar 4	Pillar 5	Pillar 6
D8 Width	0.37	0.503	0.255	0.709	0.158	0.915
D8 Height	1.278	1.894	0.906	2.283	0.655	2.454
D9 Width	0.545	0.794	0.345	0.958	1.745	*
D9 Height	1.895	2.759	1.329	3.404	3.87	
D10 Width	1.026	1.244	0.848	1.228	2.303	*
D10 Height	3.534	3.828	3.31	4.18	4.332	
D11 Width	0.373	0.513	0.259	0.695	0	0.994
D11 Height	1.13	1.669	0.843	2.233	0	2.709

Table A7.6. Profiles height and width for 8 months old deposits in μm; * last two structures merged over time

	Line1 (nm)	Line 2 (nm)	Line 3 (nm)	Line 4 (nm)	Line 5 (nm)	Dwell Time (us)	Loops (no)
D1 Height	163.8	168.8	140.8	177	152.8	700	700
D1 Weight	370	300	280	300	330	700	700
D2 Height	311.6	296.2	283.9	287.1	291.7	450	500
D2 Weight	330	330	330	410	330	450	500
D3 Height	103.2	107.1	117.1	120.4	116.6	700	500
D3 Weight	320	280	280	370	300	700	500
D4 Height	146.2	196	161.6	173.4	175.7	350	900
D4 Weight	240	320	350	280	280	350	900
D5 Height	289.6	288	290.7	0	0	350	1300
D5 Weight	272	247	239	0	0	350	1300
D6 Height	278.6	283.6	291.9	0	0	1000	1300
D6 Weight	285	291	309	0	0	1000	1300
D7 Height	158.5	168.5	176.3	188.6	173.3	350	1300
D7 Weight	322	289	289	289	330	350	1300
D8 Height	329.8	346.1	363.8	401	379.2	700	1300
D8 Weight	445	520	396	396	384	700	1300
D9 Height	237.9	224.4	203.6	259.5	199.4	350	900
D9 Weight	361	299	289	330	309	350	900

Table A7.7. Line width and height for 8 months old deposits

ARTICLES LIST

1. Pintea M., Mason N. J., Tudorovskaya M., Velocity Map Imaging and Cross Sections of $Fe(CO)_5$ for FEBIP Applications, Eur. Phys. J. D (2022) 76:160

2. Pintea M., Mason N. J., Tudorovskaya M., Dissociative Electron Attachment Cross Sections for $Ni(CO)_4$, $Co(CO)_3NO$, $Cr(CO)_6$, *Chemistry* **2022**, *4*, 1060-1075

3. Pintea M., Mason N., Peiró-Franch A., Clark E., Samanta K., Glessi C., Schmidtke I. L., Luxford T., Dissociative Electron Attachment to Gold(I) Based Compounds: 4,5-dichloro – 1,3 diethyl – imidazolyl trifluoromethyl gold(i), Front. Chem., 19 June 2023, Sec. Physical Chemistry and Chemical Physics, Volume 11-2023, DOI: 10.3389/fchem.2023.1028008

4. Mason N. J., Pintea M., Csarnovics I., Fodor T., Szikszai Z., Kertész Z., Structural Analysis of $Si(OEt)_4$ Deposits on $Au(111)/SiO_2$ Substrates at the Nanometer Scale Using Focused Electron Beam-Induced Deposition, *ACS Omega* Article ASAP, DOI: 10.1021/acsomega.3c00793